Methodological Developments for Sodium, Phosphorus and Lithium MRI at high magnetic field : Applications to clinical research at 3 and 7 Tesla.

Arthur Coste

To cite this version:

Arthur Coste. Methodological Developments for Sodium, Phosphorus and Lithium MRI at high magnetic field : Applications to clinical research at 3 and 7 Tesla.. Imaging. Université Paris Saclay (COmUE), 2017. English. NNT : 2017SACLS229 . tel-01696539

HAL Id: tel-01696539
https://theses.hal.science/tel-01696539
Submitted on 30 Jan 2018

NNT : 2017SACLS229

THÈSE DE DOCTORAT
DE
L'UNIVERSITÉ PARIS-SACLAY
PRÉPARÉE À
L'UNIVERSITÉ PARIS-SUD

Unité d'Imagerie par Résonance Magnétique et de Spectroscopie
NeuroSpin - ISVFJ - DRF - CEA

École Doctorale n°575
Electrons, Photons et Science du Vivant

Spécialité : Physique et Imagerie Médicale

par

ARTHUR COSTE

Développements méthodologiques pour l'IRM à haut champ magnétique du sodium, du phosphore et du lithium : applications en recherche clinique à 3 et 7 Tesla.

Thèse soutenue à Gif-sur-Yvette, le 20 Octobre 2017 :
Composition du jury :

Monsieur	YANNICK CRÉMILLIEUX	Directeur de Recherche CNRS ISM, Université de Bordeaux	Président
Monsieur	JEAN-PHILIPPE RANJEVA	Directeur de Recherche CNRS CRMBM, Université Aix Marseille	Rapporteur
Monsieur	XAVIER MAÎTRE	Chargé de Recherche CNRS IR4M, Université Paris Sud	Examinateur
Monsieur	SANDRO ROMANZETTI	Chargé de Recherche Hôpital Universitaire d'Aachen	Examinateur
Monsieur	DENIS LE BIHAN	Directeur de Recherche CEA NeuroSpin	Directeur
Madame	CÉCILE LERMAN	Ingénieur de Recherche CEA NeuroSpin	Encadrante

PhD Thesis

Methodological Developments for Sodium, Phosphorus and Lithium MRI at high magnetic field : Applications to clinical research at 3 and 7 Tesla

Arthur Coste
Engineer, M.Sc.

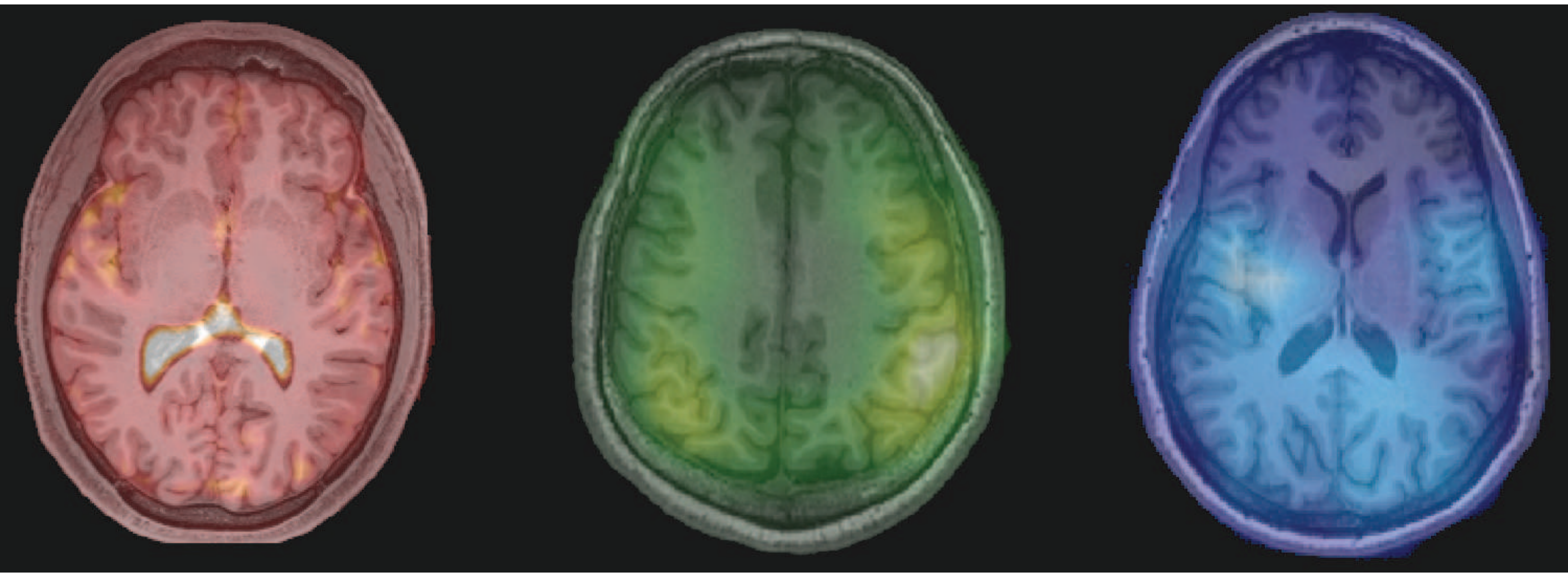

PhD Supervisor
Pr. Denis Le Bihan
Director of NeuroSpin

PhD Advisor
Dr. Cécile Lerman
Research Engineer

PhD Advisor
Dr. Fawzi Boumezbeur
Research Engineer

PhD defended on October 20^{th} 2017

NMR Imaging and Spectroscopy Unit
NeuroSpin, Fundamental Research Division
CEA, Université Paris-Saclay

Contents

Acknowledgments

This thesis is the result of three years of work at NeuroSpin and what is presented in this document is only a limited view of everything that occurred during this time. Many people contributed, more or less directly, to make these three years highly interesting and I would like to express them my gratitude and appreciation.

I would like to first thank Denis LE BIHAN, for supervising this work and giving me the opportunity to work in such an interesting and amazing place as NeuroSpin, the Institute he founded. And also for supporting my idea in founding and organizing an annual scientific event at NeuroSpin. I also thank Cyril POUPON for welcoming me in his NMR Spectroscopy and Imaging Unit and for supporting some of the non-proton hardware developments.

I thank Cécile LERMAN for her kind and regular support and for helping me design this research work. Thanks for your precious advice and for also letting me look into other aspects of MRI and Image Processing sometimes quite far from my research topic (bone and rodent MRI, sulci extraction, 3D volume rendering...).

I'm also really grateful to Fawzi BOUMEZBEUR for his major contributions and always interesting and fascinating discussions about cellular biology, pre-clinical experiments and medical applications. Thanks for allowing me to work on pre-clinical machines with rodents, on your Bipolar Disorder Lithium project and for helping me perform NMR Spectroscopy experiments. Thanks for your careful and rigorous remarks and corrections about my verbose prose and my overflowing obsessional vocabulary.

Alexandre VIGNAUD also contributed, with precious and valuable scientific advice, to improve my knowledge about MRI and Physics and to help me designing experimental protocols and apprehend the whole complexity of MRI. Thanks for your time, for sharing your knowledge and for reminding me to focus while I dispersed myself on far too many investigations and research projects.

I would like to especially thank Sandro ROMANZETTI for a stimulating and productive collaboration on Sodium MRI, and also for inviting me several times at Aachen University Hospital. It was always a pleasure to come, stay in your clinical research team, learn new things, make nice human multi-nuclei acquisitions, have interesting discussions and the overview of a medical research environment. I also thank Kathrin REETZ and her neurology team at Aachen University Hospital for welcoming me several time and supporting our human explorations.

I also thank Guillaume MADELIN from New York University Medical Center for careful and rigorous paper review.

I deeply thank Lisa LEROI for a nice collaboration on simultaneous multiparametric mapping applied to Sodium MRI as well as her collaborators: Ludovic DE ROCHEFORT from CRMBM, Mathieu SANTIN and Romain VALABREGUE from Paris Brain and Spine Institute.

I acknowledge Nicolas CHAUFFERT for his time to introduce me to his work on Compressed Sensing and Non Linear Inverse Problem solving and for allowing me to adapt his methods for my research.

I wish to thank NeuroSpin permanent researchers: Alexis AMADON, Nicolas BOULANT, Philippe CIUCIU and Vincent GRAS for nice and stimulating discussions and contributions to broaden my scientific knowledge about their research domains. I also thank Franck MAUCONDUIT, Clinical Scientist at Siemens Healthcare, for his support and help in developing pulse sequences on various software versions for different MR scanners.

I thank Franz HOZER and Josselin HOUENOU, psychiatrists at Paris Public Hospital (AP-HP), for their support and interest in the application of my developments to their Lithium MRI research project.

I would also like to thank the reviewers: Jean-Philippe RANJEVA and Yannick CREMILLIEUX who kindly accepted to read and evaluate my work and Xavier MAITRE for accepting to attend my defense.

I would like to thank France Life Imaging (FLI) and the CEA funding program for their financial support during these 3 years, allowing me to attend interesting and stimulating conferences and support hardware developments and experiments. I would like to thank the Société Francaise de Résonance Magnétique en Médecine et Biologie (SFRMBM) and the International Society for Magnetic Resonance in Medicine (ISMRM) for awarding me fellowships.

Carrying on during those 3 years was possible with the support of my PhD colleagues and friends: Gaël SAIB for sharing good and bad times together and about 15 000 km in train, my deskmate Lisa LEROI who endured my spreading desk mess, Raphael TOMI-TRICOT for challenging Particle Physics experiments with unconventional accelerators and because "*jouer avec Tomi c'est jamais fini*", Emilie POIRION for challenging imaging and computer science questions and interesting discussions about clinical applications, Jacques STOUT my X-men colleague, Loubna EL GUEDDARI who laughed even to the worst of my jokes, Achille TEILLAC an old colleague from engineering school, Hamza CHERKAOUI, Carole LAZARUS, Justine BEAUJOIN, Amicie DE PIERREFEU and Yann LEGUEN. Also with older doctoral students Marianne BOUCHER, Gabrielle FOURNET and Allegra CONTI for always nice discussions, Remi MAGNIN, Alfredo LOPEZ KOLKOVSKY, Mathieu DUBOIS, Zo RAOLISON for your cooking recipes and musical references and Guillaume RADECKI for photography tips. And also Laura DUPAS, David GAY, Robin BONICEL, Vera FELDMAN, Morgane LEGARREC, Cedric DE BRAS DE FER and Hannaé CARRIE. Some colleagues from CEA-Mircen, Clémence LIGNEUL and Jéremy PEPIN. I had fun, great times and discussions with all of you. Thanks particularly to Marianne for your friendship and amazing and idealistic discussions about photography, life, science and research.

A special thank goes to my friends of the NeuroBreakfast and SpinDating Teams, Marianne, Gabrielle, Valentina, Carole and Benoit, for organizing nice events and giving me the opportunity to take responsibilities to create and organize scientific and social events. To Regine TREBOSSEN, Frederic DOLLÉ and the PhD Student Day organizing committee for allowing me to participate.

I'm grateful to many other persons who helped me for experiments, phantom design and conception, hardware management, administrative handling and more personal discussions: Benoit LARRAT, Sebastien MERIAUX, Michel LUONG from the Research Institute on the Universe Fundamental laws (IRFU), Vincent LEBON and Lucie HERTZ PANNIER for valuable personal advice and support, Pierre BRUGIERE, Marie France HANG, Marilyne HEVIN DELAMARE, Nathalie BLANCHO, Christine DOUBLÉ, Boucif DJEMAI, Françoise GEFFROY, Edouard CHAZEL, Eric GIACOMINI, Joël COTTON, Denis FOURNIER, Jérémy BERNARD and Jean-Christophe GINEFRI. I acknowledge Benjamin MARTY and Theresa GERHALTER from Paris Myology Institute for interesting discussions about their applications of Sodium MR Spectroscopy. I thank the MR staff of NeuroSpin: Séverine BECUWE-DESMIDT, Chantal GINISTY, Séverine ROGER and Lionel ALIROL for their support and for allowing me to do unscheduled evening, night, early morning or weekend acquisitions.

I also would like to deeply thank people who trusted and offered me opportunities to teach and lecture in various domains despite constrains I had.
At ESCPE Lyon, Catherine BURNIER and Jean-Pierre BRUANDET, for trusting me to design and create a complete lecture and practical work on Nuclear Magnetic Resonance and Magnetic Resonance Imaging, participate in teachings in Numerical Optimization and Image Processing, Nicole GACHE, for trusting me to handle Signal Processing practical work and Random Signals teachings, Jean Marie BECKER for Applied Mathematics and Damien ROHMER for programming.
At ESME Paris, Sebastien MAIZY, Maxime OSSONCE, Antonin BOURGEOIS and Hamid OULD, for trusting me in handling Signal Processing, Programming, Electrical Engineering and Physical measurements practical work.
This teaching experience was sometimes challenging but always pleasurable and allowed me to learn new things and new ways to communicate around scientific problems.

I want to thank people who trusted me and allowed me to learn and discover many things prior to this thesis and whose influence was significant on undertaking this work.
Jean Marie BECKER for inspiring me with amazing maths applications when I was student.
Guido GERIG, for allowing me to work on cutting edge DTI research projects in his former neuroimaging lab (UCNIA) at the Scientific Computing and Imaging Institute in the United States of America, and also for offering me the incredible opportunity to complete my engineering degree at the School of Computing of the University of Utah, where I could widely broaden my scientific background and attend highly interesting courses.
Sylvain GOUTTARD for his kind support and help while working both in the US and also at BioClinica and Clément VACHET for his kind supervision.
Joël SCHAERER for supervising my industrial research internship at BioClinica and for sharing his knowledge about programming and allowing me to work on highly interesting and stimulating projects.

I also would like to thank few old friends, who shared a part of the path which led me to undertake this thesis. Alexandre B, Grégoire S, Xavier D, Lisa B and the BG's team of CPE.

Finally, the most important thank of all will go to my family. My parents Isabelle and Philippe for their unswerving support over the years and especially in the hardest periods. I also would like to thank them for supporting my next project which is going to be even longer and far way more complicated. My sister Pauline and my brother Victor for sharing my infinite doubts and questions and my older cousins, particularly Sophie, for showing me the way. I dedicate this work to them and to all my family members who suffered and are suffering from neurodegenerative diseases and particularly my grand mother. I know it's not much but I hope I've brought some tools that could be used for further explorations.


CYPRIEN
LUCIE
NICOLE
LILY
JEAN
MARGUERITTE
ALFREDO
BENJAMIN
DAMIEN
JEAN LOUIS
CLÉMENT
BRIGITTE
SOPHIE
MICHEL
JEAN-MARIE
MARIANNE
PHILIPPE
GREGOIRE
RAPHAËL
GUIDO
ALFREDO
LISA
DENIS
XAVIER
VINCENT
LAURA
FRANCK
VICTOR
AMICIE
CYRIL
MARYLINE
NICOLE
ACHILLE
ERIC
EMILIE
ALEXANDRE
CÉDRIC
SÉVERINE
ALLEGRA
LISA
JUSTINE
VALENTINA
CHANTAL
HAMID
ISABELLE
GUILLAUME
CÉCILE
GAËL
FRANCK
CYRIL
HANNAE
ELODIE
DENIS
DAVID
SÉBASTIEN
EDOUARD
KEVIN
SANDRO
ISABELLE
ACHILLE
BRIGITTE
HAMZA
JOËL
PIERRE
SYLVAIN
DENIS
FAWZI
HAMID
VICTOR
CAMILLE
MARIE FRANCE
NICOLAS
ROBIN
LUCIE
JÉRÉMY
LOUBNA
CAROLE
KATHRIN
LISA
BENJAMIN
CÉDRIC
VINCENT
ALEXANDRE
MARIE FRANCE
ERIC
NANCY
MATHIEU
GABRIELLE
FRÉDÉRIC
LIONEL
MÉDÉRIC
SANDRO
CATHERINE
ALEXIS
REMI
JEANNINE
BOUCIF
FRANÇOISE
DELPHINE
DAVID
LUCIE
JACQUES
BENOIT
GAËL
ALEXIS
MAXIME
VERA
GUILLAUME
FAWZI
JACQUES
NICOLAS
MICHEL
LILY
ROBIN
MORGANE
PAULINE
PHILIPPE
JUSTINE
NICOLAS
BENJAMIN
CHANTAL
ALEXANDRE
CAROLE
EDOUARD
PAULINE
ROMAIN
PAUL
AMICIE
LOUBNA
FRANZ
DAMIEN

Introduction

After thirty years of unending developments in hardware and software, Magnetic Resonance Imaging (MRI) has become the most powerful tool to explore the anatomy, function and metabolism of the human body non-invasively. Among its biggest achievements MR researchers have helped in deciphering the brain cytoarchitecture non-invasively using high resolution anatomical images as well as functional information acquired using functional MRI (fMRI [OGAWA 1990]) and structural organization explored through water diffusion properties (DWI/DTI [LE BIHAN 1985]). In particular, the wider availability of high and ultra-high magnetic fields (UHF) for clinical explorations opens the way for more extensive explorations of the human brain as it increases significantly the amount of signal available for MRI and therefore the quality of acquired images [STUCHT 2015]. Exotic (X) nuclei such as Carbon-13 (^{13}C) [VALETTE 2017], Oxygen-17 (^{17}O) [HOFFMANN 2011], Sodium-23 (^{23}Na) [HILAL 1985, MADELIN 2013] or Phosphorus (^{31}P) [BENDEL 1969] are usually studied using MR spectroscopy (MRS) as they exhibit lower NMR sensitivity than ^{1}H and relatively low *in vivo* concentrations compared to water. Undoubtedly, MR Imaging of those X-nuclei could be an even more exciting perspective of *in vivo* UHF NMR. Indeed, the cartography of the related metabolites or electrolytes would allow scientists to study brain physiology, energy metabolism, neurotransmission or pharmacology from complementary points-of-view.

NeuroSpin is a research center dedicated to the development of UHF MRI and its applications to Neurosciences and translational biomedical research. NeuroSpin is part of the Fundamental Research Division of the French Atomic Energy Commission (CEA) and its Life Sciences Frédéric Joliot Institute located at the CEA center of Saclay. NeuroSpin possesses a unique platform for both clinical and preclinical investigations with a 3 T and a 7 T clinical scanners as well as three preclinical spectrometers at 7 T, 11.7 T and 17 T. Recently, NeuroSpin welcomed the world first clinical 11.7 T magnet [VEDRINE 2008, QUETTIER 2017] designed and developed by CEA physicians from its Institute of Research into the Fundamental Laws of the Universe (Irfu) who designed the magnets for the European Organization for Nuclear Research (CERN) circular particles accelerator: Large Hadron Colider (LHC). Additionally, a Magnetoencephalography apparatus (MEG) and Electroencephalography sensors (EEG) are available to explore the time-courses of brain activity at higher temporal resolution. About 200 scientists, medical doctors, engineers, technicians and students in physics, applied mathematics, data sciences and neurosciences work together at NeuroSpin to push the boundaries of brain imaging and our understanding of its full complexity in normal and pathological conditions. Our work benefited from NeuroSpin's rare environment and set of expertise as MR scientists from the NMR Imaging and Spectroscopy Unit (UNIRS) are pursuing their ambition to develop Sodium-23, Phosphorus-31 and Lithium-7 MRI at 7 T and higher.

The first Sodium (^{23}Na) images were obtained in 1985 by HILAL *et al.* [HILAL 1985]. Our interest in Sodium MRI stems from its involvement in cellular homeostasis and viability. Despite being the second most abundant NMR visible nucleus in the human body, those first ^{23}Na MR images suffered from a very low spatial resolution and were not particularly attractive for clinical research. In the past decade, major developments were made leading to spatial resolution as high as 1 mm isotropic at 7 T or 9.4 T [QIAN 2012a, MIRKES 2015]. Using Ultra-Short Echo-Time (UTE) acquisitions combined with dedicated non-Cartesian sampling trajectories such as the Twisted Projection Imaging [BOADA 1997c] or the Fermat Looped, ORthogonally Encoded Trajectories (FLORET) [PIPE 2011], those developments were enabled by improved hardware components, in particular advanced dual-resonance ^{23}Na-^{1}H coil designs [SHAJAN 2016]. Pioneering studies were conducted using Sodium MRI on various brain diseases ranging from tumors to neurodegenerative diseases. Among them, multiple sclerosis has probably been studied the most with Sodium MRI demonstrating an increased Sodium concentration in lesions compared to healthy subjects even in normal appearing white matter [INGLESE 2010, ZAARAOUI 2012, PALING 2013, MAAROUF 2014, EISELE 2015, BILLER 2016, MAAROUF 2017]. Yet, the robustness of concentration quantification remains an open issue. Moreover, the specificity and relevance of the reported Sodium changes deserve a more thorough investigation and modeling.

Phosphorus MR Imaging shares common challenges with Sodium Imaging with even lower *in vivo* concentrations and NMR sensitivity. The detection and quantification of phosphorylated metabolites levels is usually conducted using MR Spectroscopy approaches.
The study of Adenosine TriPhosphate (ATP) and PhoshoCreatine (PCr) is highly relevant to probe energy metabolism [CHAUMEIL 2009]. Recently, it was shown that spectrally selective ^{31}P MRI sequences could be an exciting alternative to MRS Imaging [LU 2013, PARASOGLOU 2016].

Lithium is the first line treatment for patients suffering from Bipolar Disorder (BP). Despite its very low *in vivo* concentration (inferior to 1 mmol.L^{-1}) and quite a long T_1 relaxation time (superior to 3 seconds in tissues [MOORE 2003, SMITH 2011] and up to 20 seconds in liquids [KOMOROSKI 2004]), probing the brain distribution of Lithium can be achieved using ^{7}Li MRSI/MRI as demonstrated by [LEE 2012, BOADA 2010] in recent years.

This PhD thesis aimed at developing an efficient and adaptable platform for non-proton MRI at high and ultra-high magnetic fields. The first objective was to develop state-of-the-art Sodium MRI sequences and dedicated reconstruction and post-processing pipelines. Benefiting from our collaboration with Dr. Sandro ROMANZETTI, we implemented the TPI [BOADA 1997c] sequence for Sodium MRI at 7 T. In parallel, various non-Cartesian reconstruction methods were implemented with the help of Dr. Nicolas CHAUFFERT for non-linear methods [CHAUFFERT 2015].
The second objective was to develop a more accurate and robust method for quantifying non-proton MR signals using a Variable Flip Angle (VFA) approach.
The third objective was to develop a multigradient echoes approach as an alternative for Multiple Quantum Filtering (MQF) methods to disentangle intra- and extra-cellular contributions to ^{23}Na NMR signal.
From the premise of our previous experiences in ^{31}P MRSI at 7 T [LOPEZ KOLKOVSKY 2015], the fourth objective was to adapt the TPI sequence for spectrally selective Phosphorus MRI and evaluate its benefits.
Finally, those developments were validated *in vitro* and applied in clinical research settings at 3 T or 7 T. The application of the VFA approach to Sodium MRI was first validated on healthy volunteers with Drs Sandro ROMANZETTI and Kathrin REETZ at Aachen University Hospital. Patients suffering from Alzheimer's or Huntington's diseases are currently examined with the same protocol. A proof-of-concept study was conducted at NeuroSpin to evaluate the sensitivity of our spectrally selective ^{31}P 3D-TPI sequence and compare obtained PCr and ATP maps to ^{31}P 2D-MRSI data. In the context of our first ^{7}Li MRI study conducted at 7 T (BipLi7 project) in collaboration with Pr. Frank BELLIVIER (Inserm UMR-S1144, AP-HP) and Drs. Josselin HOUENOU and Franz HOZER (NeuroSpin, AP-HP, Fondation FondaMental), we applied our non-proton imaging platform to map brain Lithium concentration and its longitudinal relaxation time in bipolar patients.

Outline of the manuscript

This dissertation is composed of four sections. The first section elaborates on the context, challenges and objectives of this doctorate (Chapter 1). The second section presents our experimental setup (Chapter 2) and our developments of a complete acquisition and reconstruction framework for X-nuclei MRI using non-Cartesian sampling schemes (Chapter 3). The third section details the post-processing and quantification methods developed and validated on dedicated home-made phantoms : the variable flip angle (VFA) approach (Chapter 4) as well as explorations around multiparametric quantitative mapping (Chapter 5) and compartmentalization (Chapter 6). *In vivo* Sodium (Chapter 7), Phosphorus (Chapter 8) and Lithium MRI (Chapter 9) proof-of-concept studies are presented in our final section.

CHAPTER 1

Non Proton Nuclear Magnetic Resonance Imaging

Contents

In this first chapter, a short introduction to NMR and a current state-of-art are proposed for the non-expert. Additionally, we discuss briefly some of the challenges and opportunities for the use of *in vivo* NMR Spectroscopy and Imaging of non-proton nuclei to study brain metabolism, physiology or pharmacology in normal or pathological conditions. Supplementary details about NMR physics and applications to both Spectroscopy and Imaging can be found in [HAACKE 1999, BERNSTEIN 2004, DE GRAAF 2007].

1.1 NMR Principles

1.1.1 NMR Phenomenon

The Nuclear Magnetic Resonance (NMR) phenomenon was first described by I. RABI [RABI 1938]. For this discovery, he received the Physics Nobel Prize in 1944. Soon, F. BLOCH and E. M. PURCELL developed NMR Spectroscopy to study molecular structures for analytical chemistry [BLOCH 1946, PURCELL 1946]. For their groundbreaking achievements, they shared the Physics Nobel Prize in 1952. Later in the 70s, NMR was extended to imaging following the ideas of P.C. LAUTERBUR [LAUTERBUR 1973] and Sir P. MANSFIELD [MANSFIELD 1977] to encode spatially the NMR signal. In 2003, the Medicine and Physiology Nobel prize was awarded to both of them. As indicated by its name, the NMR phenomenon involves the nucleus of atoms possessing a non-nul spin. For an atom with an odd number of protons and/or neutrons, the nucleus has a quantized intrinsic angular magnetic momentum $\vec{\mu}$ proportional to its half-integer spin $\vec{S}$:

$$\vec{\mu} = \gamma_X \vec{S} \tag{1.1}$$

The nuclear spin $\vec{S}$ depends on the nucleus composition (arrangement of elementary quarks and gluons). Hydrogen is the most commonly studied element in NMR and its nucleus is usually refered to as ^{1}H or proton. Since it possesses a single nucleon, its spin is equal to 1/2. In addition to ^{1}H, many other atoms can be investigated using NMR such as Lithium ^{7}Li [RENSHAW 1985, BOADA 2010, LEE 2012], Boron ^{11}B [GLOVER 1992, BENDEL 1998], Fluorine ^{19}F [MCFARLAND 1985, RUIZ-CABELLO 2011], Sodium ^{23}Na [HILAL 1985, MADELIN 2013], Phosphorus ^{31}P [BENDEL 1969, LU 2013], Chlorine ^{35}Cl [NAGEL 2014], Potassium ^{39}K [ADAM 1987, PARRISH 1997, UMATHUM 2013]. For three of the most important atoms in biology and chemistry: Carbon, Nitrogen and Oxygen, their most abundant isotopes are not detectable using NMR. However, labeling strategies can be adopted to detect stable isotopes ^{13}C [DAY 2007, VALETTE 2017], ^{15}N [MOONEY 1969] and ^{17}O [HOFFMANN 2011] and study brain biochemistry. Also, some mostly inert atoms can be studied as gases such as Helium ^{3}He [KOBER 1999] or Xenon ^{129}Xe [ALBERTS 1994]. Table 1.1 summarizes their basic NMR properties. The nuclear sensitivity of a given nuclei is function of its nuclei quantum spin number I and gyromagnetic ratio γ according to:

$$S \propto |\gamma^3| \times (I(I+1)) \tag{1.2}$$

NMR exploits the interaction of the nuclear magnetic moment $\vec{\mu}$ with an external static magnetic field B$_0$. This magnetic field modifies the orientation of a nuclear magnetic moment (here the spin would be $\frac{1}{2}$) by orienting it either parallelly or anti-parallelly to its own direction (Zeeman splitting effect - Figure 1.1). A different energy level is associated to each quantic state leading to an energy gap ΔE:

$$\Delta E = \gamma \hbar B_0 = \hbar \omega_0 \tag{1.3}$$

Isotope	Spin	Natural Abundance (%)	Relative Sensitivity†	Gyromagnetic Ratio $\gamma/2\pi$ (MHz.T^{-1})	NMR frequency at 7T (MHz)
^{1}H	1/2	99.985	1.00	42.58	298.03
^{2}H	1	0.015	1.45×10^{-6}	6.54	45.75
^{3}He	1/2	1.4×10^{-4}	5.75×10^{-7}	32.43	227.04
^{7}Li	3/2	92.4	0.272	16.55	115.82
^{11}B	3/2	80.42	0.133	13.66	95.61
^{13}C	1/2	1.108	1.76×10^{-4}	10.70	74.93
^{14}N	1	99.63	1.0×10^{-3}	3.08	21.54
^{15}N	1/2	0.370	3.86×10^{-6}	-4.32	-30.21
^{17}O	5/2	0.037	1.08×10^{-5}	5.77	40.40
^{19}F	1/2	100	0.834	40.05	280.36
^{23}Na	3/2	100	9.27×10^{-2}	11.26	78.83
^{27}Al	5/2	100	0.21	11.09	77.66
^{31}P	1/2	100	6.65×10^{-2}	17.24	120.65
^{35}Cl	3/2	75.53	3.55×10^{-3}	4.17	29.2
^{39}K	3/2	93.10	4.75×10^{-4}	1.99	13.92
^{129}Xe	1/2	26.44	5.71×10^{-3}	11.78	82.44

Table 1.1: NMR Properties of various nuclei of interest for biomedical research. † Relative sensitivity is given as the product of NMR sensitivity and natural abundance compared to ^{1}H.

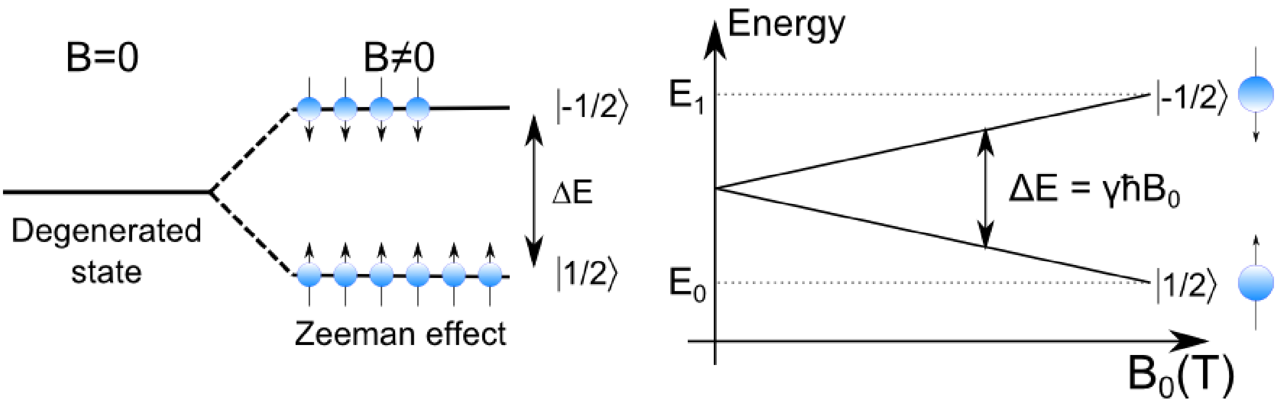

Figure 1.1: Zeeman splitting of a $\frac{1}{2}$ spin system and its evolution according to the static magnetic field strength.

Let us consider a biological sample, one can define a macroscopic nuclear magnetization $\vec{M}$ as the sum of all individual nuclear magnetic moments:

$$\vec{M_0} = N_{E_0}\vec{\mu_Z} + N_{E_1}\vec{\mu_Z} = \gamma\left(\frac{h}{4\pi}\right)(N_{E_0} - N_{E_1}) \tag{1.4}$$

The difference in populations on the two energy levels can be derived from the Maxwell-Boltzmann statistics:

$$\frac{< N_{E_i} >}{N} = \frac{1}{e^{(\varepsilon_i - \mu)/K_B T}} = \frac{1}{Z}e^{(-\varepsilon_i)/K_B T} \tag{1.5}$$

which describes the average distribution of non-interacting particles over various energy states at thermal equilibrium with N being the total number of particles, N$_{E_i}$ the number of particles on energy levels i, ε_i the energy of level i, μ the chemical potential, T the temperature and Z the partition function defined by:

$$Z = \sum_i e^{(-\varepsilon_i)/K_B T}. \tag{1.6}$$

As the lower energy level E$_0$ is slightly lower than E$_1$, the corresponding state is more populated:

$$(N_{E_0} - N_{E_1}) \approx \frac{Nh\nu}{2K_B T}. \tag{1.7}$$

The later term of this relation is referred to as polarization and is rather small at room temperature: only few parts per million (*ppm*). Increasing the strength of B$_0$ results in increasing the polarization and the subsequent macroscopic magnetization at thermal equilibrium:

$$\vec{M_0} = \left(\frac{\gamma_X h}{2\pi}\right)^2 \left(\frac{NB_0}{4K_B T}\right) \qquad \text{[De Graaf 2007]} \tag{1.8}$$

At this stage, one should notice that the magnetization depends on the strength of the static magnetic field, the number of nuclei and their gyromagnetic ratio. One can also notice that reducing the temperature T of the sample can also increase the polarization. This "brute-force" approach is one of many adopted to achieve hyperpolarization of isotopes such as ^{13}C, ^{15}N, ^{3}He or ^{129}Xe [Abragam 1978, Golman 2003].

1.1.2 Radiofrequency excitation

To observe the longitudinal magnetization M$_0$ created by the static magnetic field B$_0$, the precessional motion of the spins must be detected. This can be achieved by using a second orthogonal magnetic field B$_1$ to flip M$_0$ towards the transverse plane. For an efficient energy transfer and rotation of the magnetization, this B$_1$ field must be oscillating at the Larmor frequency ω_0 to satisfy the resonance condition :

$$\omega_0 = 2\pi f_0 = \gamma B_0 \tag{1.9}$$

As shown in Table 1, these Larmor frequencies lie in the radiofrequency (RF) band, ie in the MHz range depending on the field strength and the gyromagnetic ratio of the nucleus of interest. In order to apprehend the time evolution of the magnetization vector M(t) during the radiofrequency excitation, one can write the following equation:

$$\frac{dM_x(t)}{dt} = \gamma M(t) \times B(t) = \gamma M(t) \times (B_0 + B_1(t)) \tag{1.10}$$

In the laboratory frame of reference, the radio-frequency field B$_1$(t) can be written as :

$$B_1(t) = 2B_{1_{max}} \cos(2\pi\nu t) = B_1^+(t) + B_1^-(t) \tag{1.11}$$

with:

$$\begin{aligned} B_1^+ &= \frac{1}{2}(B_{1,x} + iB_{1,y}) \\ B_1^- &= \frac{1}{2}(B_{1,x} - iB_{1,y}) \end{aligned} \tag{1.12}$$

For convenience, NMR is best described in a rotating frame of reference, rotating about B$_0$'s direction at the frequency ω. The z' axis of the rotating frame is consequently collinear with the z axis

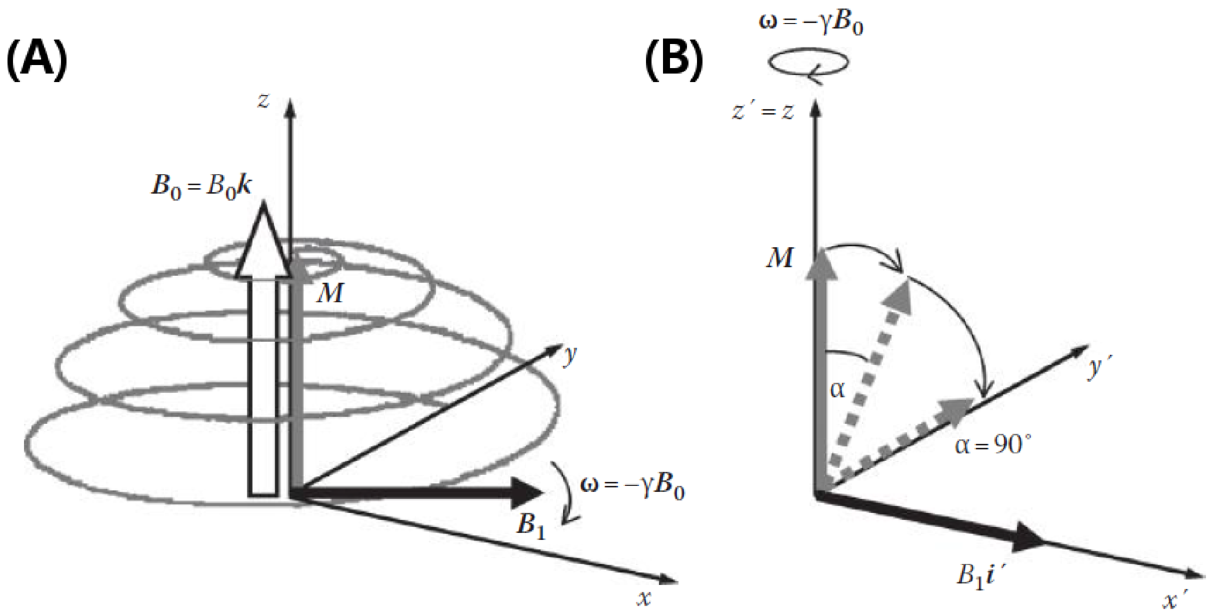

Figure 1.2: Effect of a radiofrequency field B_1 on the longitudinal magnetization M, represented in the laboratory frame (A) or in the rotating frame (B) [FLOWER 2012].

of the laboratory frame as illustrated on Figure 1.2. In the laboratory frame, the evolution of the magnetization vector M(t) = (M_x(t),M_y(t),M_z(t)) is described by a set of phenomenological ordinary differential equations (ODE) called BLOCH equations [BLOCH 1946] (here a spin $\frac{1}{2}$ is considered):

$$\begin{aligned}
\frac{dM_x(t)}{dt} &= \gamma\left(M(t) \times B(t)\right)_x - \frac{M_x(t)}{T_2} = \gamma\left(M_y(t)B_z(t) - M_z(t)B_y(t)\right) - \frac{M_x(t)}{T_2} \\
\frac{dM_y(t)}{dt} &= \gamma\left(M(t) \times B(t)\right)_y - \frac{M_y(t)}{T_2} = \gamma\left(M_z(t)B_x(t) - M_x(t)B_z(t)\right)_y - \frac{M_y(t)}{T_2} \\
\frac{dM_z(t)}{dt} &= \gamma\left(M(t) \times B(t)\right)_z - \frac{M_z(t) - M_0}{T_1} = \gamma\left(M_x(t)B_y(t) - M_y(t)B_x(t)\right)_z - \frac{M_z(t) - M_0}{T_1}
\end{aligned} \tag{1.13}$$

In the rotating frame, the magnetization vector M′(t) = (M'_x(t),M'_y(t),M'_z(t)) have the following components:

$$\begin{aligned}
M'_x &= M_x \cos(\omega t) + M_y \sin(\omega t) \\
M'_y &= M_y \cos(\omega t) - M_x \sin(\omega t) \\
M'_z &= M_z
\end{aligned} \tag{1.14}$$

The BLOCH equations can then be reformulated as follow considering B=B$_0\vec{z}$:

$$\begin{aligned}
\frac{dM'_x(t)}{dt} &= \omega_0 M'_y(t) - \frac{M'_x(t)}{T_2} \\
\frac{dM'_y(t)}{dt} &= -\omega_0 M'_x(t) - \frac{M'_y(t)}{T_2} \\
\frac{dM'_z(t)}{dt} &= -\frac{(M'_z(t) - M_0)}{T_1}
\end{aligned} \tag{1.15}$$

This radiofrequency field can be generated using an electromagnetic coil loop whose plane is orthogonal to B$_0$. Its application results in the rotation of the magnetization toward the transverse plane. The effective rotation or flip angle (FA)α depends on the intensity and duration (τ) of the excitation or transmission field B$_1^+$:

$$\alpha = \gamma \int_0^{\tau} B_1^+(t)dt = \gamma B_1^+ \tau \tag{1.16}$$

As operating NMR frequencies increases with the static magnetic field strength, the wavelength of the transmission field decreases and can lead to B$_1^+$ field inhomogeneities and severe artifacts depending on the design of the radiofrequency coil, the size of the studied organ and its dielectric properties [Collins 2011].

1.1.3 The NMR Experiment

In pulsed NMR, the most basic experiment is referred to as the pulse-acquire experiment. A RF pulse is applied at the Larmor frequency leading to the rotation of the longitudinal magnetization M$_0$ onto the transverse plane. Ideally, a 90° nutation angle is achieved to obtain a maximum transverse magnetization. In the laboratory frame of reference, the precession of the spins lead to the emission of a radiofrequency signal named Free Induction Decay (FID) (Figure 1.3):

$$\begin{aligned} M_x(t) &= M_0 e^{-t/T_2^*} \sin(\omega_0 t) \\ M_y(t) &= M_0 e^{-t/T_2^*} \cos(\omega_0 t) \\ M_z(t) &= M_0(1 - e^{-t/T_1}) \end{aligned} \tag{1.17}$$

This FID can be picked up by our RF coil as an electromotive force ε according to Faraday's law of induction :

$$\varepsilon = -\frac{\Delta\Phi}{dt} \qquad \text{with} \qquad \Delta\Phi = \int_S B \cdot dS \tag{1.18}$$

With $\Delta\Phi$ being the variation of the magnetic flux created by the rotating electromagnetic field and S the surface of the coil loop. The NMR signal intensity is proportional to M$_x$(t)+M$_y$(t). NMR signals are acquired according to the spatially variant reception profile B$_1^-$(r) of our coil:

$$\Delta\Phi(t) \propto \int_V B_1^-(r) \frac{\partial M_{xy}(r,0)}{\partial r} e^{+2i\pi\nu t} dr \tag{1.19}$$

whith $\frac{\partial M_{xy}(r,0)}{\partial r}$ being the density of magnetization in the sample at position r.

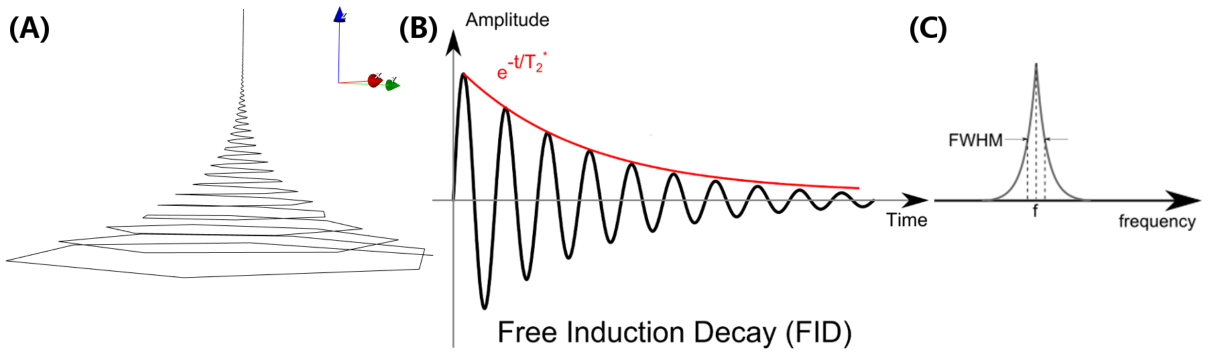

Figure 1.3: Precession of the magnetization vector in the laboratory frame (A) and corresponding Free Induction Decay signal (B) and NMR spectrum (C).

The FID is converted into a NMR spectrum by the use of a Fourier transformation [Bracewell 1965]. Such transformation allows to bijectively convert a time-domain signal f(t) into a frequency-domain spectrum F(ν):

$$F(\nu) = \int_{-\infty}^{+\infty} f(t)e^{-2i\pi\nu t}dt \qquad f(t) = \frac{1}{2\pi}\int_{-\infty}^{+\infty} F(\nu)e^{+2i\pi\nu t}d\nu \tag{1.20}$$

This NMR spectrum is a complex signal with an absorption (real) and a dispersion (imaginary) component. After phase correction, the absorption spectrum (or in some occasion the modulus to avoid phase correction) can be exploited to identify the many resonance peaks from the sample. Notably, the full width at half maximum (FWHM) of the Lorentzian lineshape of the absorption resonances can be used to estimate directly the effective transverse relaxation rate T_2* as:

$$FWHM = \frac{1}{\pi T_2^*} \tag{1.21}$$

1.1.4 Relaxation Times

The time constants T_1 and T_2 in the Bloch equations represent the phenomenological relaxation times of the spin system: T_1 is referred to as the longitudinal or spin-lattice relaxation time and T_2 as the transverse or spin-spin relaxation time. As illustrated by Figure 1.4, T_1 corresponds to the reconstitution of the longitudinal magnetization at thermodynamic equilibrium, while T_2 corresponds to the disappearance of the transverse magnetization. Both relaxation times vary according to the physical environment of the spins. These variations depend on the Larmor frequency, shielding effects (σ), the correlation time (τ_C) and the main magnetic field strength (B_0) and are given by:

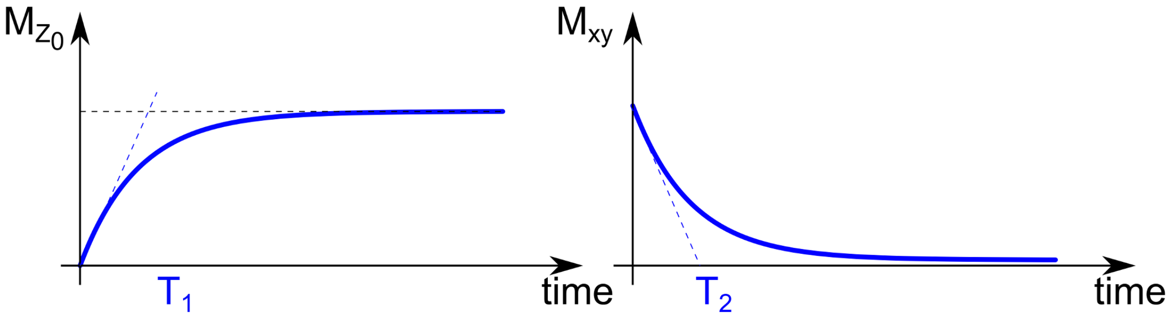

Figure 1.4: Mono exponential models of: longitudinal magnetization regrowth of constant time T_1 and transverse magnetization decay of constant T_2.

$$\frac{1}{T_1} = \frac{2}{15}\gamma^2 B_0^2(\sigma_{||} - \sigma_{\perp})^2\tau_C \qquad \frac{1}{T_2} = \frac{7}{45}\gamma^2 B_0^2(\sigma_{||} - \sigma_{\perp})^2\tau_C \qquad \text{[De Graaf 2007]} \tag{1.22}$$

where $\sigma_{||}$ and $\sigma_{\perp}$ are the longitudinal and transverse projections of the shielding effects. The correlation time corresponds to the average time for a molecule to rotate over 1 rad. For highly mobile molecules in solutions τ_C can be as short as few femtoseconds while it increases with medium density and can be as long as few microseconds in solid media. Each individual spin is subject to a slightly varying magnetic field due to its chemical environment, leading to a loss of coherence between neighboring spins reflected in the transverse relaxation rate. Moreover, non-random para-magnetic inhomogeneities such as blood flow or iron deposits further accelerate the transverse relaxation rate leading to the definition of an apparent relaxation rate T_2^* defined as:

$$\frac{1}{T_2^*} = \frac{1}{T_2} + \gamma \Delta B_{inhomogeneities} \tag{1.23}$$

1.1.5 Spatial encoding

Spatial encoding is the basis for any MRI methods. This is usually achieved by combining three different methods relying on the use of space (and time) varying magnetic fields called gradients. These gradients are produced by three resistive electromagnetic coils generating ideally linear spatial magnetic field variation along X, Y and Z directions.

The first method is the slice selective excitation for which a gradient is concomitantly applied with the excitation RF pulse operating at a given frequency as illustrated by Figure 1.5. As the local magnetic field experienced by spins differs according to their spatial coordinates, it is possible to excite selectivity a subset of the sample. The second encoding method is based on frequency variations induced by the gradient coils during the acquisition of the NMR signal. Indeed, the application of a gradient field changes the precession frequency of nuclei along a given direction:

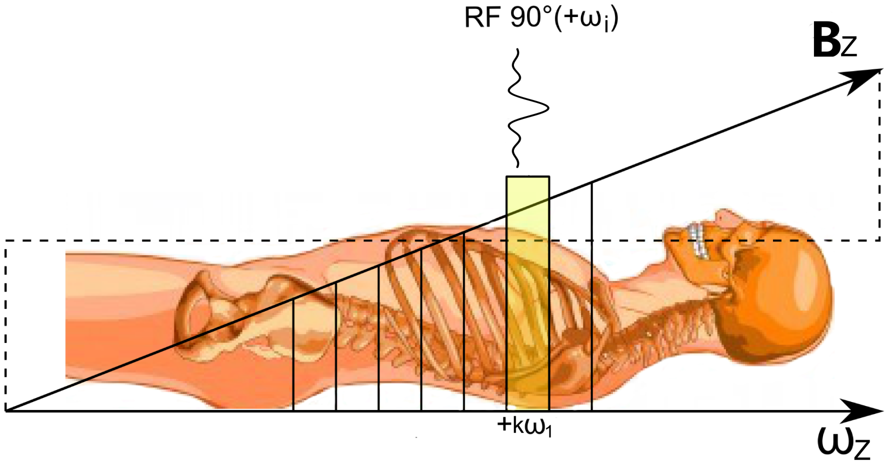

Figure 1.5: Slice selective excitation of a human torso using a sinc RF pulse applied concomitantly with a gradient along the Z direction. Slice selection can be iterated along this direction by using the same RF pulse at different operating frequencies: $\omega_i = k\omega_1$ with $k \in [\![-\frac{N}{2}, \frac{N}{2}]\!]$.

$$\omega_0 = \gamma B_0 \rightarrow \omega_i(r) = \gamma(B_0 + G(r)) \tag{1.24}$$

In the case of a simple 1D frequency encoding and for a monochromatic NMR signal, the application of an inverse Fourier transformation allows to recover a profile of the spin density along the considered direction. The third method is referred to as phase encoding and is useful for polychromatic NMR signal and constitutes the basis for Chemical Shift Imaging. Integration of the frequency variations brought by the gradients after excitation lead to a space-varying phase of the transverse magnetization. As this phase holds during the acquisition of the NMR signal, the adequate iteration of those phase encoding steps (= gradient intensities) along one or more directions allows to sample the Fourier or K (spatial frequencies)-space. By applying a inverse Fourier transformation, the matrix of NMR signals is reverted into an MR image in the space domain. Figure 1.6 illustrates the canonical 2D Gradient Recalled Echo (GRE) sequence with the sequential application of the RF pulse for slice selection and the use of frequency and phase-encoding gradients to sample the K-space and obtain a 2D MRI Figure 1.7. In this example of Cartesian Sampling of the k-space, regularly spaced lines (frequency encoding or readout) are acquired each repetition time (TR), the orthogonal coordinates corresponding to the incremental phase encoding steps.

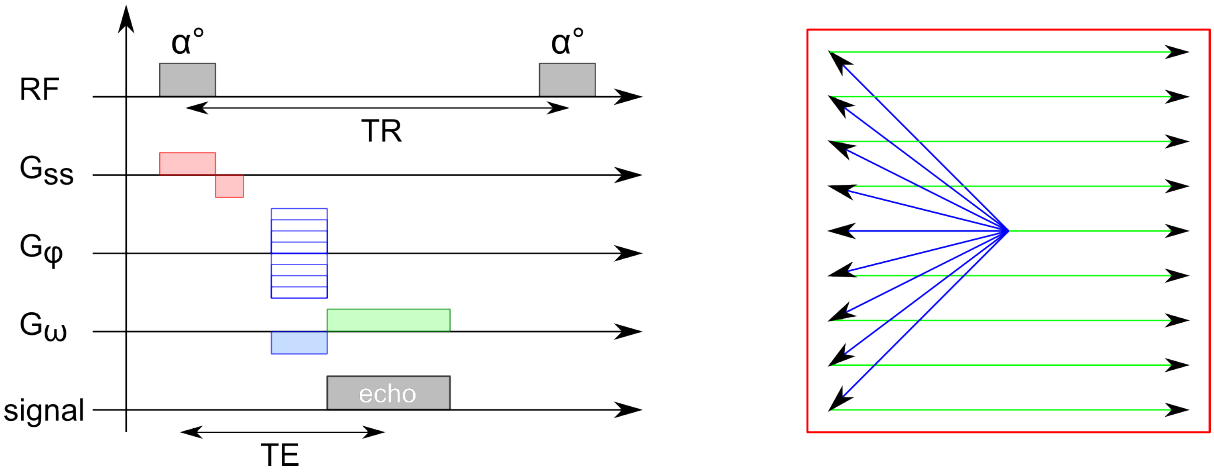

Figure 1.6: Chronogram of a 2D Gradient Recalled Echo (GRE) sequence (left) and associated sampling pattern in K space (right). RF: transmission channel; $G_S S$: slice selection (and slice refocusing in negative) gradients; G_φ: phase encoding gradients; G_ω: dephasing (negative) and rephasing gradients for frequency encoding and creation of an gradient-echo.

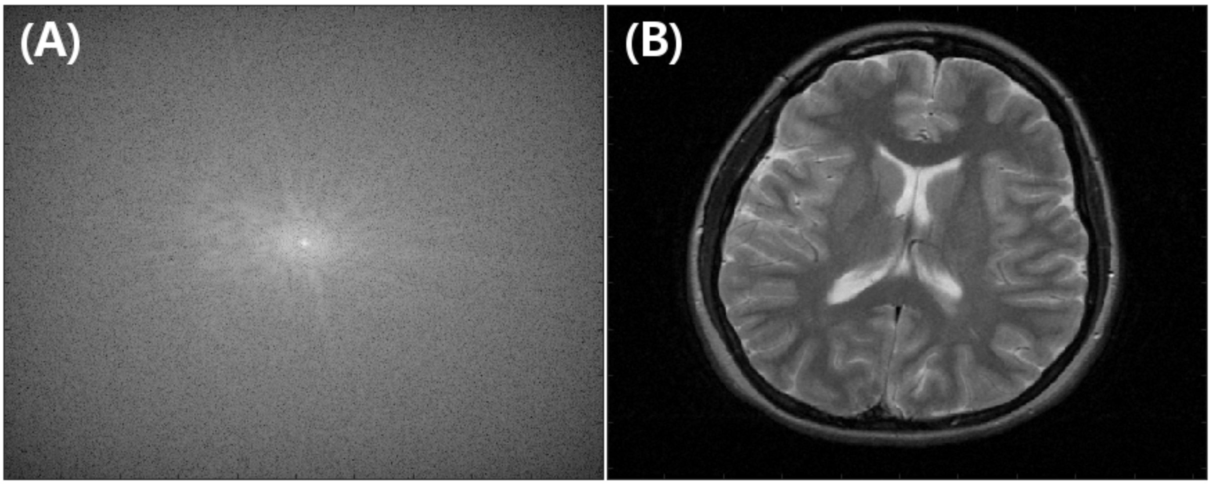

Figure 1.7: Logarithm of the modulus of complex frequency-domain NMR data (A) and the modulus of the associated reconstructed image through 2D discrete inverse Fourier transform (B).

1.1.6 NMR Spectroscopy

A priori, the NMR signal is the sum of contributions from spins experiencing diverse chemical or electronic environments leading to a complex NMR spectrum as illustrated by Figure 1.8 for *in vivo* ^{1}H MRS of the rat brain at 17T. By default, ^{1}H MRS signal is dominated by the water signal (corresponding to some 80 moles per liter of protons in brain tissue). Water suppression schemes reduce the water signal drastically (by few thousand folds) facilitating the acquisition of a neurometabolic profile from which up to 20 metabolites can be detected and quantified [Lopez-Kolkovsky 2016]. Although ^{31}P sensitivity is much lower than ^{1}H, ^{31}P MRS is an interesting technique to explore energy and membrane metabolism *in vivo*. Usually, MRS data are obtained from a region-of-interest using single-voxel spectroscopy (SVS) sequences such as STEAM [Frahm 1969, Granot 1986], PRESS [Bottomley 1987] or LASER [Slotboom 1991, Garwood 2001]. However, MR Spectroscopic Imaging (MRSI) or Chemical Shift Imaging (CSI) can also be performed by adding phase encoding steps to SVS or non-localized sequences leading to metabolite concentrations maps [Brown 1982, Maudsley 1983] as illustrated by Figure 1.9.

In addition to the static metabolite concentrations, dynamic information can be obtained using MRS when using chemical exchange saturation or magnetization transfer approaches. Indeed energy storing metabolites: PhosphoCreatine and Adenosine TriPhosphate (ATP) can be probed and their consumption and synthesis rates can be estimated using magnetization transfer [Du 2007]. These past ten years, these Chemical Exchange Saturation Transfer (CEST) approaches have been quite popular in particular when applied to ^{1}H MRI to indirectly map pH, the concentrations of metabolites (PCr, Glc, Glu...) or semi-mobile proteins with labile hydrogens, the temperature or some enzyme activity [van Zijl 2011]. Such explorations being performed in both pre-clinical and clinical environments with healthy subject and also on patients suffering from various diseases such as brain tumors, neurodegenerative diseases or to study pharmacology non-invasively [Castillo 1996, Ross 2001].

Finally, structural information can also be inferred from diffusion-weighted MRS data with the possible inference of neuronal and astrocytic morphological features [Palombo 2016].

1.1.7 NMR Imaging

Since its advent during the 80s, NMR imaging or MRI has become the best imaging modality to investigate non-invasively soft tissues and articulations in humans and animals *in vivo*. Conventional MRI relies on mapping water content using diverse T_1 and T_2/T_2* relaxation weightings to emphasize contrast between normal and abnormal tissue types. As explained previously, MRI manipulates and detects only a fraction (around $1/10^5$) of the available protons. As a consequence, the intrinsic sensitivity of MRI is much lower than high energy imaging modalities such as Positron Emission Tomography (PET) or Computed tomography (X-ray CT). However, MRI benefits from the sensitivity of the NMR signal to various other physical properties. MRI can be divided into several main applications.

First, the biggest application is anatomical MR Imaging. Studies are mostly performed using T_1, T_2/T_2^* weighted images as illustrated in Figure 1.10. Those anatomical images can be exploited using advanced post-processing methods to study brain morphology and extract volumetric and surfacic measurements such as cortical thickness or sulci depths for instance.

The second application of MRI is Diffusion Weighted Imaging [Stejskal 1965, Le Bihan 1985] (DWI). DWI and its tensor description (DTI) use the Brownian motion of water molecules to infer brain structure in particular white matter tracts as illustrated in Figure 1.11. Recent diffusion protocols requires more directions so as to obtain more precise modeling of crossing fiber bundles or short fibers: High Angular Resolution Diffusion Imaging (HARDI) [Tuch 2002], QBall [Tuch 2004], Diffusion Spectrum Imaging [Wedeen 2005], Neurite Orientation Dispersion and Density Imaging (NODDI) [Zhang 2012] and others.

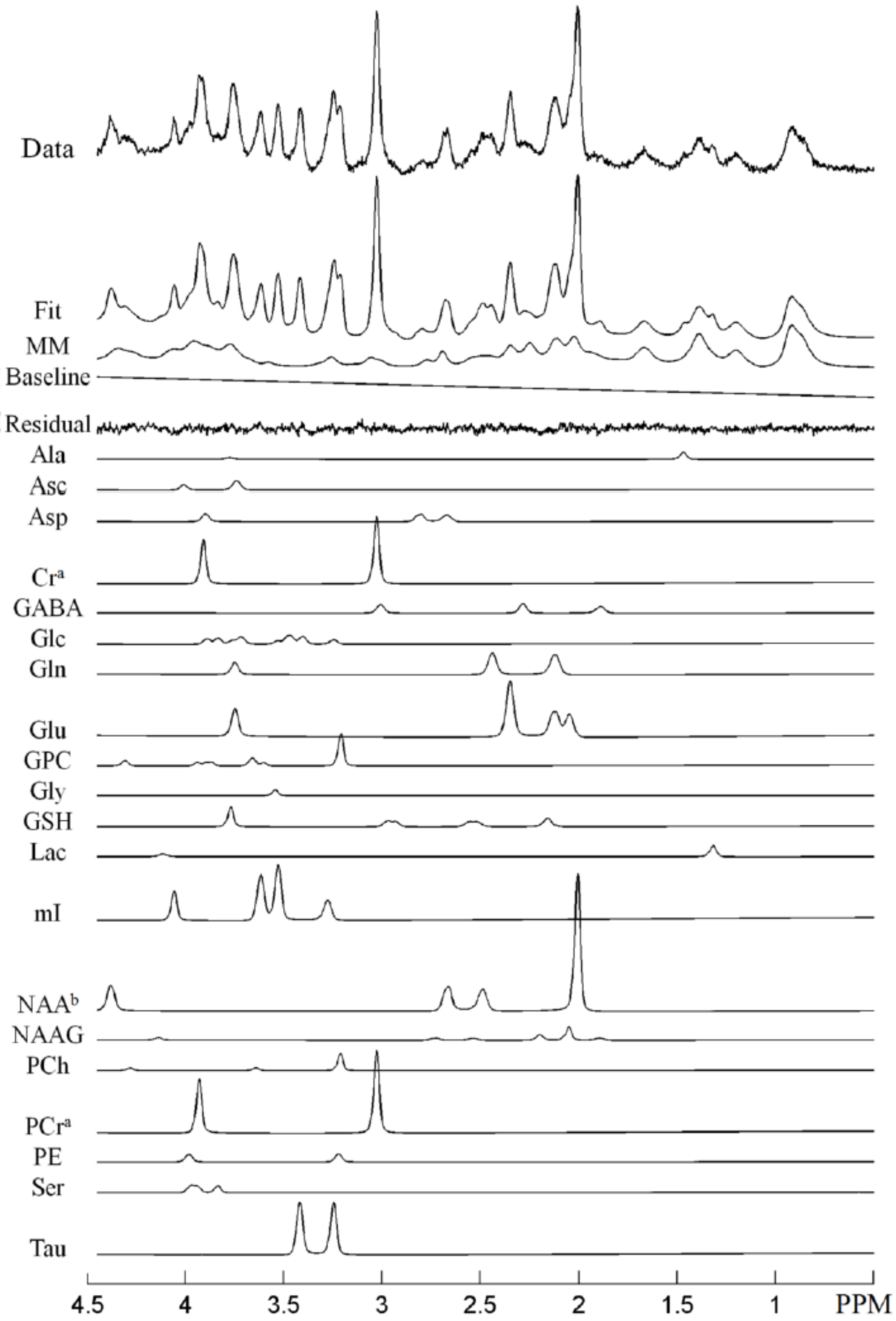

Figure 1.8: ^{1}H Spectrum acquired *in vivo* from a rat brain at 17 T and its spectral decomposition obtained with LCModel (Courtesy of Alfredo LOPEZ KOLKOVSKY). Abreviations: MacroMolecules (MM), Alanine (Ala), Ascorbic Acid (Asc), Aspartate (Asp), Creatine (Cr), Gamma-Aminobutyric acid (GABA), Glucose (Glc), Glutamine (Gln), Glutamate (Glu), GlyceroPhosphorylCholine (GPC), Glycine (Gly), Glutathione (GSH), Lactate (Lac), Myo-Inositol (mI), N-Acetyl-Aspartate (NAA), N-Acetyl-Aspartate-Glutamate (NAAG), PhosphoCholine (PCh), PhosphoCreatine (PCr), Phosphorylethanolamine (PE), Serine (Ser) and Taurine (Tau).

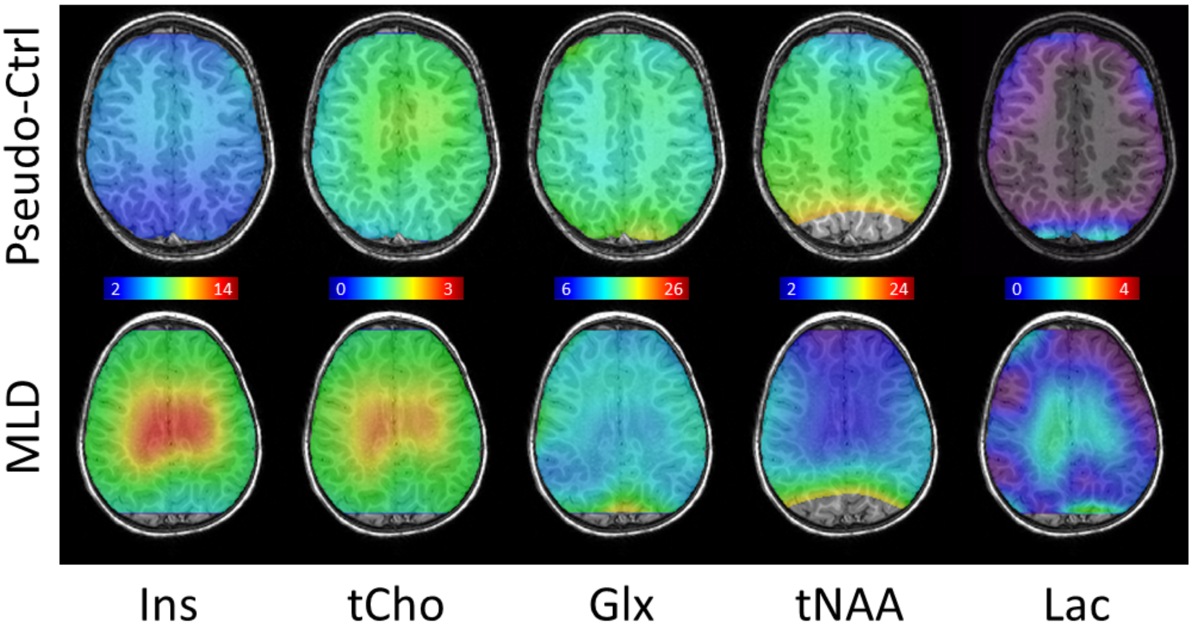

Figure 1.9: Metabolic maps obtained after spectral decomposition with LCModel (Courtesy of Fawzi Boumezbeur). 1H MRSI data were acquired from pseudo-control children (suffering from unilateral focal epilepsy) and children affected by the juvenile form of metachromatic leucodystrophy (MLD). Majors signs of neurodegeneration and neuroinflammation [Blanc 2016] can be observed. Abbreviations: Inositol (Ins), Choline (Cho), Glx= Glutamate (Glu) + Glutamine (Gln), N-Acetyl-Aspartate (NAA), Lactate (Lac).

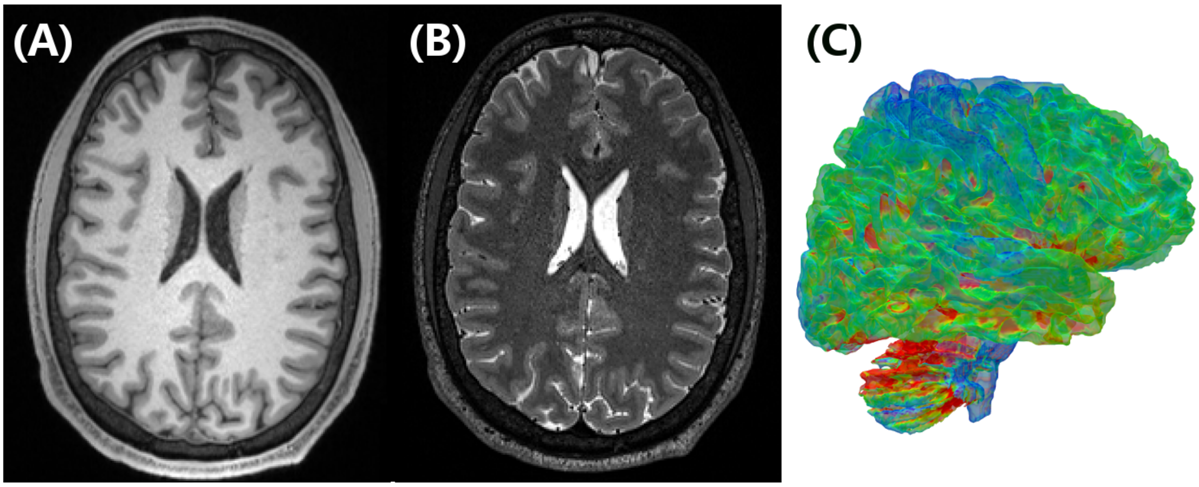

Figure 1.10: Examples of T_1 (A) (Turbo Flash TR/TE/FA/TA=2400 ms/2.36 ms/8°/7′02") and T_2 (B) (SPACE TR/TE/TA=3200 ms/567 ms/3′17") weighted images acquired at 3 T at a millimetric resolution (A. Coste and S. Romanzetti) and a cortical thickness 3D map (C) ([Coste 2014]).

The third application is MR Angiography (MRA). MRA uses dedicated MR pulse sequences with or without contrast agents to image arteries and vessels conveying blood in the brain Figure 1.12. Many sequences exist to acquire angiograms, here are some examples: time of flight (TOF) [Nishimura 1990] or phase contrast [Dumoulin 1989] and contrast-enhanced 3D spoiled gradient-echo sequences following the injection of a Gadolinium-based contrast agent (to shorten blood's T_1).

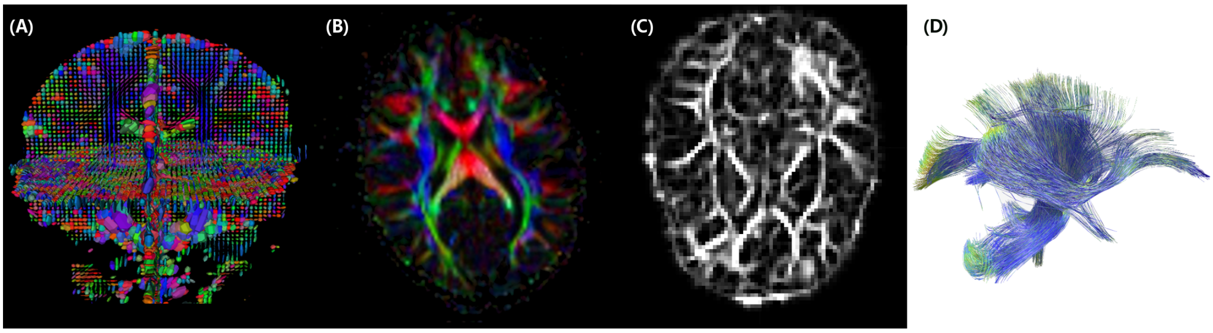

Figure 1.11: (A) Diffusion Tensor Visualization, (B) RGB colored Fractional Anisotropy map, (C) curvature Fractional Anisotropy map and (D) example of tracts of white matter ([COSTE 2013]).

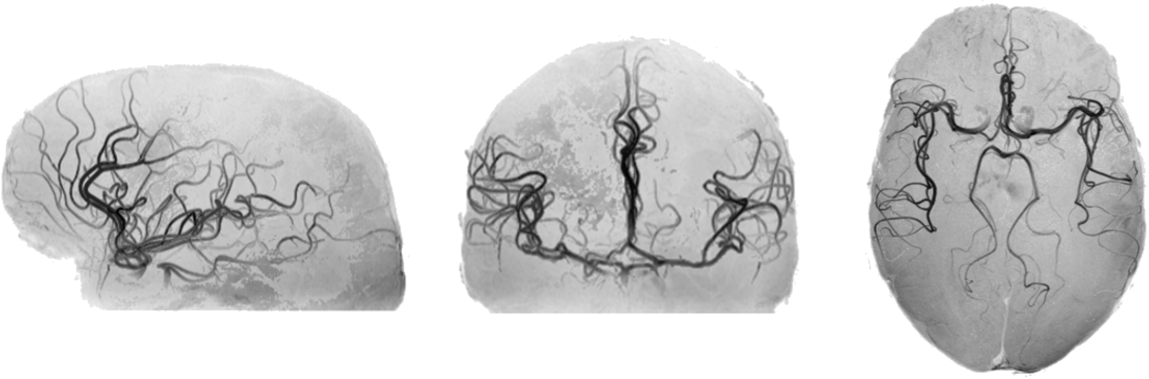

Figure 1.12: Sagittal, Coronal and Axial views of an intensity inverted Maximum Intensity Projection (MIP) MR Angiography of arteries of the brain using a TONE Pulse with FA $\in [10°, 30°]$ Time of Flight sequence with TR/TE=20 ms/5.8 ms , resolution = $0.5\times0.5\times0.1$ mm^3 [SAIB 2017].

The fourth application is functional MRI (fMRI). fMRI relies on the Blood Oxygen Level Dependent effect (BOLD) [OGAWA 1990]. BOLD corresponds to a lengthening of T_2/T_2^* relaxation times following the paraxodycal decrease in the concentration of paramagnetic deoxyhemoglobin due to neuronal activity and the concomitant local increase of blood flow. In task-related fMRI, activation maps can be computed from the application of the General Linear Model [FRISTON 1994, FRISTON 1999] which looks for correlations between stimulus presentation and BOLD contrast changes. In resting-state fMRI, functional networks are inferred from co-variance maps between pixels. Figure 1.13 illustrates the activation map for a language task (Broca area, Brodmann 44,45).

Finally, MRI can be used to assess other physico-chemical properties such as relaxation constants [WEISKOPF 2013], temperature [YOUNG 1994], elastometric properties [MARIAPPAN 2010], myelin [GLASSER 2011] or iron content [HAACKE 2004, DE ROCHEFORT 2009]. Some of them can be used as quantitative biomarkers to monitor tissue changes and better characterize disease progression (Figure 1.14). Quantitative MRI approaches open the way to a more personalized medicine as parametric maps are less dependent on hardware. Many techniques are currently used or under development such as: Look Locker in FISP [SCHMITT 2004], QRAP-test[WARNTJES 2007] and its

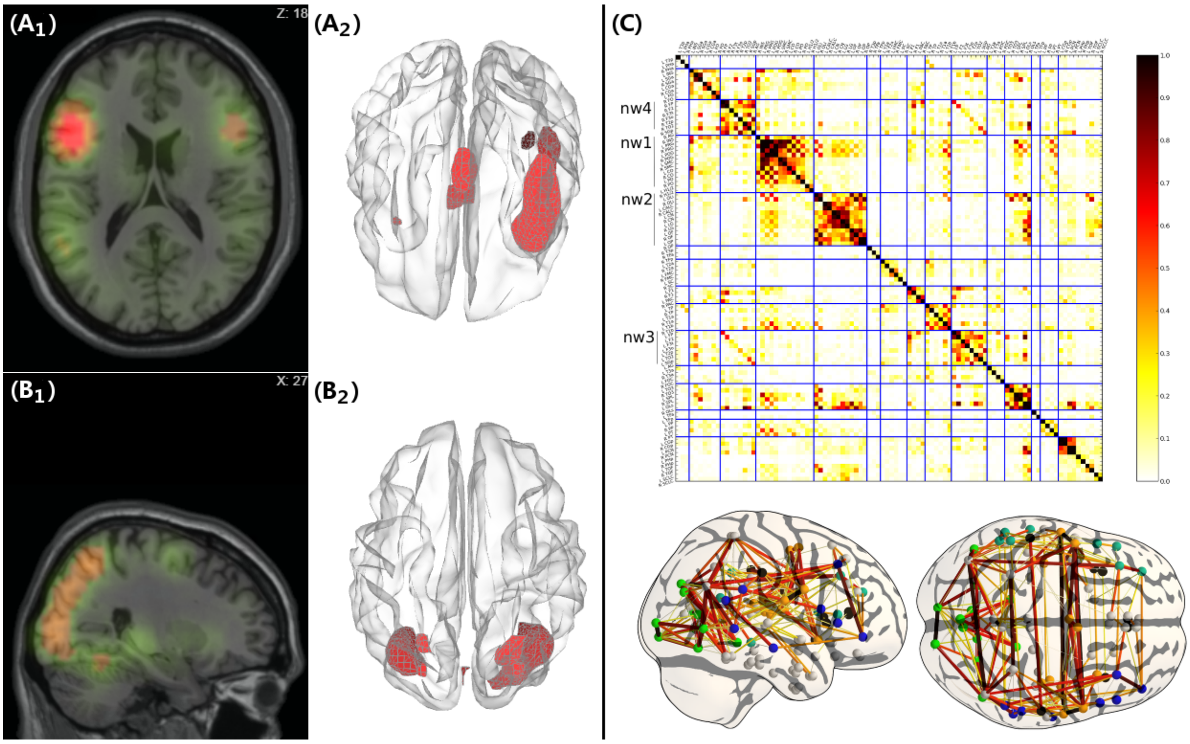

Figure 1.13: Activation maps for a language task (A_1) and a vision task (B_1) and their associated 3D localization (A_2 and B_2) [Toro 2016]. (C) Example of a functional connectivity network and corresponding co-variance matrix [Phlypo 2014].

improvement QRAP-master [Warntjes 2008], MR Fingerprinting [Ma 2013], TESS [Heule 2014], SMART [Sukstanskii 2016] or QUICS [de Rochefort 2015, de Rochefort 2016c].

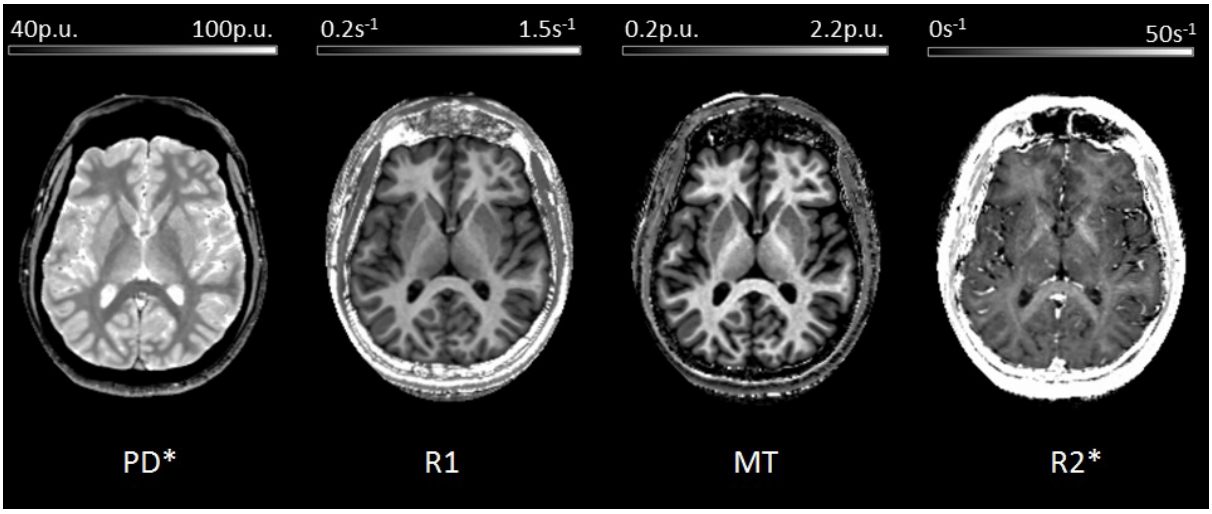

Figure 1.14: Maps of apparent proton density (PD*), longitudinal relaxation rate (R_1=1/T_1), magnetization transfer (MT) ratio and effective transverse relaxation rate (R_2*=1/T_2*) [Weiskopf 2013].

1.2 Non-Cartesian Acquisitions and Data Reconstruction

Frequency and phase encoding concepts have been introduced previously when considering a Cartesian sampling of k-space. However, non-Cartesian sampling schemes have been proposed to sample more efficiently the Fourier space. As a consequence of their nature, dedicated reconstruction algorithms are needed.

1.2.1 Non Cartesian sampling schemes

Gradients are responsible of the trajectory described in Fourier space according to:

$$\vec{k}(t) = \vec{k}(0) + \gamma \int_0^t \vec{G}(\tau) d\tau \tag{1.25}$$

Non-Cartesian sampling trajectories can be used to minimize the echo-time (TE) for spins with a short T_2*. Indeed, to perform Cartesian sampling, frequency encoding gradients have to be "ramped up" to a constant value so as to induce a regular spatial frequency shift and an uniform sample distribution. In ultra-short TE (UTE) sequences, the idea is to exploit this "ramp time" to encode spatial information more rapidly. As a consequence, the sampling density will no longer be uniform.

1.2.1.1 Radial Sampling

The design of the radial readout was first proposed by LAUTERBUR [LAUTERBUR 1973]. As illustrated by Figure 1.15, one can see that both gradients are used at the same time to create a radius in Fourier space which, in the case of non-Cartesian sampling, is called a "spoke". Gradients are defined by:

$$G(t) : \begin{cases} G_x(i) = G_0 \cos\left(\frac{2\pi i}{N}\right) \\ G_y(i) = G_0 \sin\left(\frac{2\pi i}{N}\right) \end{cases} \qquad i \in \mathbb{N} \qquad \text{[HAACKE 1999]} \tag{1.26}$$

and the following parametric equation:

$$s(t) : \begin{cases} x(t) = at \\ y(t) = bt \end{cases} \qquad \text{with } (a, b) \in \mathbb{R}^{*2} \text{ and t } \in \mathbb{R}^{+} \tag{1.27}$$

with G_0 being the gradient amplitude necessary to sample the central row which corresponds to a Cartesian row. When the two gradients are played together this leads to a radial sampling trajectory, starting from the center and reaching the outer part of K-space. In accordance with the objective of reducing TE, one does not wait for the gradients to reach their plateau and directly starts sampling the signal after excitation. This last point leads to a non-uniform spatial sampling in Fourier space (signal is always sampled at the same frequency). As illustrated by Figure 1.15, lesser spatial frequencies are more densely sampled than the higher spatial frequencies. This Variable Density Scheme (VDS) is particularly interesting for X-MRI and its low SNR and spatial resolution. However, one must consider this non-uniform sampling density in the reconstruction process and for the estimation of the resulting point-spread function (PSF).
The radial scheme can be optimized by adjusting the number of spokes and the angular increment between spokes. The so-called golden angle of value of 111.25° [WINKELMANN 2007] is particularly interesting when adopting a sparse or Compressed Sensing (CS) [LUSTIG 2007] oriented approach allowing for an eventual reduction in acquisition time. The 2D sampling scheme was later generalized in 3D by JERECIC [JERECIC 2002].

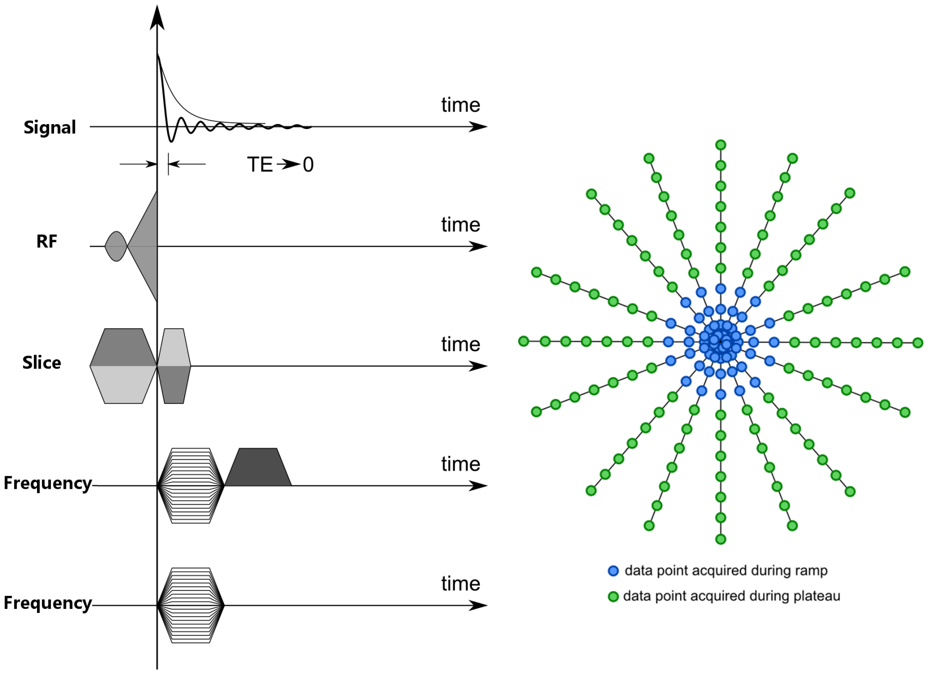

Figure 1.15: Chronogram of a 2D GRE UTE radial sequence and its associated sampling pattern.

1.2.1.2 Spiral Sampling

The spiral sampling sequence was introduced in 1986 by AHN [AHN 1986]. It is defined by the following gradients:

$$G(t) : \begin{cases} G_x(t) = G_0 \cos(\theta(t)) \\ G_y(t) = G_0 \sin(\theta(t)) \end{cases} \qquad \text{[HAACKE 1999]} \tag{1.28}$$

and the following parametric equation:

$$s(t) : \begin{cases} x(t) = at\cos(t) \\ y(t) = at\sin(t) \end{cases} \qquad \text{with } a \in \mathbb{R}^* \text{ and t } \in \mathbb{R}^+ \tag{1.29}$$

Variations of the trajectory, for instance starting in the outer parts of the Fourier space and going

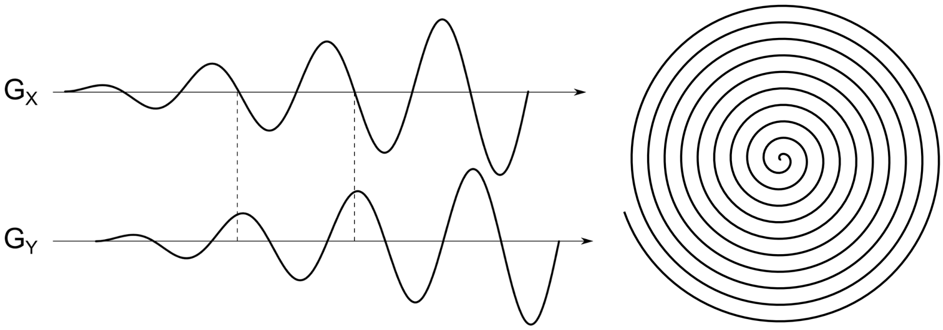

Figure 1.16: Sequence diagram of a 2D Spiral sequence and its associated sampling pattern.

toward the center were also proposed later. A 3D extension of the spiral sampling scheme were also developed, for instance the Fermat Loop ORthogonaly Encoded Trajectory (FLORET) [Pipe 2011] which is shown below in Figure 1.17.

1.2.1.3 Radial and Spiral Combination

Radial and spiral schemes were elegantly combined to yield the TWisting Radial Lines [Jackson 1992] (TWIRL), and later generalized for 3D MRI with the Twisted Projection Imaging (TPI) [Boada 1997c] also illustrated in Figure 1.17. These trajectories are characterized by two distinct sections: first a radial one and then a spiral one to encode the higher spatial frequencies. The length of the radial section is an important "tuning" parameter.

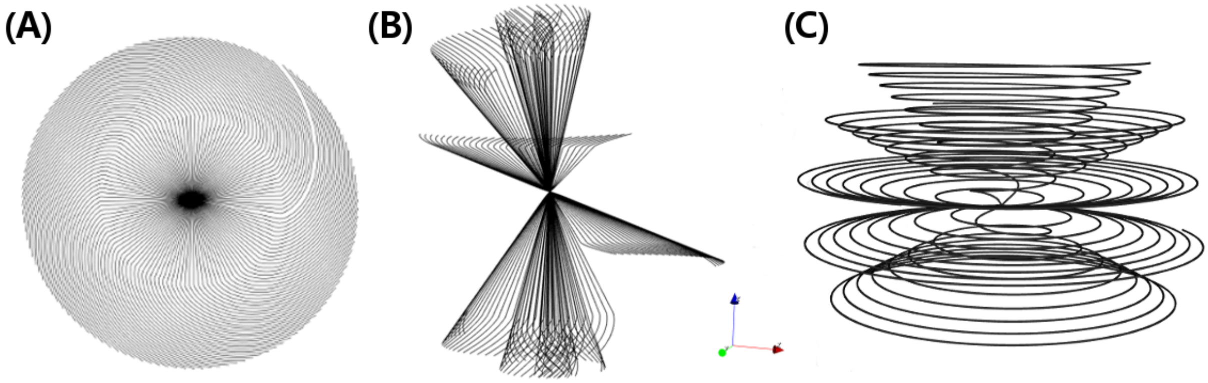

Figure 1.17: VTK-based [Schroeder 2006] rendering of the TWIRL (A) TPI (B) and FLORET (C) sampling schemes.

1.2.1.4 Other Non Cartesian Schemes

Over the years, other non-Cartesian sampling schemes have been proposed such as the Rosette trajectory [Noll 1997], RARE spiral [Block 1997] or the Circular trajectory [Zhou 1998]. One can design its own trajectory in Fourier space and by derivation of equation 1.25 obtain the associated gradient currents to play on the MR scanner. However, one should consider hardware constrains such as the maximum intensity and slew rate of the gradient coils so that:

$$||G(t)|| \leq G_{max} \qquad ||\dot{G}(t)|| = \left\| \frac{dG(t)}{dt} \right\| \leq Slew_{max} \qquad \forall t \in [0, T] \tag{1.30}$$

Consequently, a MR trajectory belongs to the following set:

$$\mathcal{S}_T = \left\{ s : [0, T] \to \mathbb{R}^3, ||\dot{s}(t)|| \leq \gamma_X G_{max}, ||\ddot{s}(t)|| \leq \gamma_X S_{max}, \forall t \in [0, T] \right\} \tag{1.31}$$

The consideration of these constraints led to a physically plausible trajectory design which was the subject of N. Chauffert's PhD thesis [Chauffert 2015].

1.2.2 Reconstruction of non-Cartesian Data

With non-Cartesian sampling trajectories, MRI data can not be reconstructed using the standard Inverse Fourier Transform (IFT). As the acquired points no longer lie over an homogeneous equispaced rectangular grid, dedicated reconstruction algorithms were developed thanks to the ever increasing capacities of computer that enables more sophisticated data processing.

1.2.2.1 Gridding

Gridding methods were the first to be proposed as they are the easiest to implement and were not computationally expensive. The principle is to back-project the acquired points onto a Cartesian grid and then apply the IFT.

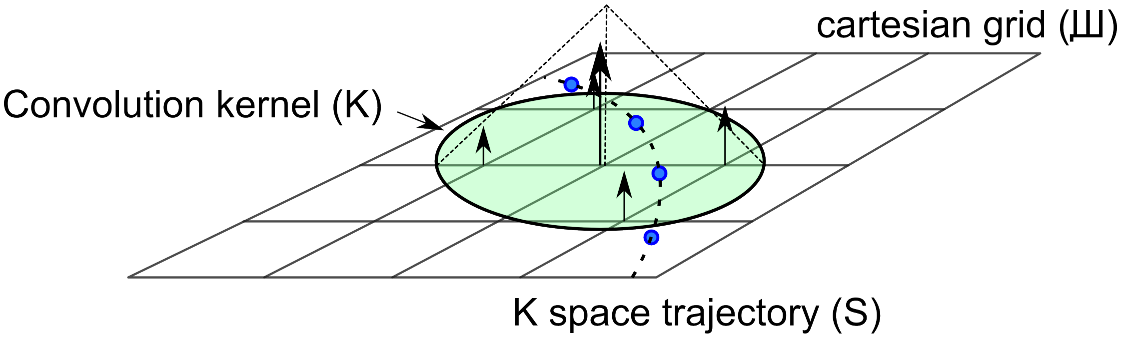

Figure 1.18: Principle of the gridding technique.

The gridding method uses a weighting convolution kernel that goes through the acquired trajectory and weights grid points according to their distance with the sampled point. The most widely used kernel is the Kaiser-Bessel kernel for its convenient mathematical properties [Jackson 1991]. Here is a presentation of the algorithm:

Let $M(u,v)$ be a signal sampled along some non-Cartesian trajectory:

$$S(u,v) = \sum_{i}^{N} {}^2\delta(u-u_i, v-v_i) \tag{1.32}$$

composed of N points and where ${}^2\delta(x,y)$ is the 2D Dirac distribution. The sampled data is then:

$$M_s(u,v) = M(u,v).S(u,v) \tag{1.33}$$

Depending on the sampling scheme, samples distribution $S(u,v)$ may not be uniform so it is necessary to take it into account by introducing a density correction function $\rho(u,v)$. The density adapted data is then:

$$M_{sw} = \frac{M_s(u,v)}{\rho(u,v)} = \frac{M(u,v).S(u,v)}{\rho(u,v)} \tag{1.34}$$

To adequately distribute the sampled value onto the associated grid points, adapted data is convoluted by a weighting kernel $K(u,v)$ such as:

$$M_{swc} = M_{sw} * K(u,v) = \frac{M(u,v).S(u,v)}{\rho(u,v)} * K(u,v). \tag{1.35}$$

The kernel K(u) is a separable Kaiser-Bessel kernel defined by:

$$K(u) = \frac{1}{W} I_0 \left(\beta(1-2\frac{u}{W})\right)^2 \tag{1.36}$$

with I_0 being the zero-order Bessel function of the first kind and W the width of the kernel and β is defined according to:

$$\beta = \pi\sqrt{\frac{W^2}{a^2}((a-0.5)^2) - 0.8}. \qquad \text{[Beatty 2005]} \tag{1.37}$$

with a being an over-sampling factor.
We can then sample the previously adapted and convoluted data onto a Cartesian grid:

$$\text{ш}(u,v) = \sum_{i=0}^{N}\sum_{j=0}^{N}{}^{2}\delta(u-i, v-j) \tag{1.38}$$

leading to the following equation of the gridded data:

$$M_{swcg} = M_{swc}.\text{ш}(u,v) \tag{1.39}$$

$$M_{swcg} = \left(\frac{M(u,v).S(u,v)}{\rho(u,v)} * K(u,v)\right).\text{ш}(u,v) \tag{1.40}$$

Finally, we apply the inverse Fourier transform to get the reconstructed image :

$$m(x,y) = \mathcal{F}^{-1}(M_{swcg}(u,v)) \tag{1.41}$$

$$\mathcal{F}^{-1} : F(u,v) \rightarrow f(x,y) = \frac{1}{MN}\sum_{u=0}^{M-1}\sum_{v=0}^{N-1} F(u,v)e^{2i\pi\left(\frac{ux}{M}+\frac{vy}{N}\right)} \tag{1.42}$$

Moreover, applying the convolution kernel from the non-Cartesian grid to the regularly spaced grid also introduces the Fourier Transform of the kernel which can degrade image quality if uncorrected. Two correction methods are possible: the first option consists of deapodization of the image by dividing by the Fourier Transform of the Kernel as follow :

$$m_d(x,y) = \frac{m(x,y)}{\mathcal{F}^{-1}(K(u,v))} \tag{1.43}$$

In the case of the Kaiser-Bessel Kernel, its Fourier Transform is given by:

$$k(x) = \frac{\sin(\sqrt{\pi^2 W^2 x^2 - \beta^2})}{\sqrt{\pi^2 W^2 x^2 - \beta^2}} \tag{1.44}$$

The second strategy consists in the use a larger Cartesian grid to reduce the effect of apodization by the kernel. This last aspect was also evaluated for our implementation and is presented in Chapter 3.

1.2.2.2 Non-Uniform and NonEquispaced Fourier Transform

The lack of a dedicated and adapted transformation to directly reconstruct non-conventionally sampled Fourier space has been problematic for long years. To tackle this issue, several research groups have proposed methods to define a Fourier transform that will take into account the sparsity, the inhomogeneous and irregular distribution of MR data in K-space. In 1993, Dutt proposed the Non-Uniform Fast Fourier Transform (NUFFT)[Dutt 1993]. It was improved by Fessler [Fessler 2003] in 2003 and in 2008 Keiner and colleagues proposed the NonEquispaced Fast Fourier Transform (NFFT) [Keiner 2008].

NUFFT principle

The expression of the regular Discrete Fourier Transform (DFT) is:

$$X_k = \sum_{n=0}^{N-1} x_n e^{-2i\pi kn/N} \tag{1.45}$$

This equation makes the assumption of a uniform and evenly spaced data as for instance being sampled on a grid with a constant spacing Δ_s such as $s_n = s_0 + n\Delta_s$ leading to $x_n = x(s_n)$. In the general case of non Cartesian sampling, this assumption no longer holds and we need to compute:

$$X_k = \sum_{t=1}^{N} x(s_t) e^{-2i\pi k s_t} \tag{1.46}$$

where $x(s_t)$ is now evaluated at samples locations s_t.

A comparison between the NUFFT algorithm and Kaiser-Bessel gridding was made and found that both were very similar, as one can easily notice because the NUFFT algorithm is equivalent to a Gaussian kernel based gridding method [SARTY 2001].

NFFT principle

The NFFT algorithm [KEINER 2008] is based on a collection of different samples at possible frequencies $k \in Z^d$, where d is the dimension of the K-space, in the multi-index set:

$$I_{\mathbf{N}} := \left\{ \mathbf{k} = (k_t)_{t=0,\dots,d-1} \in Z^d : -\frac{N_t}{2} \leq k_t < \frac{N_t}{2},\ t = 0,\dots,d-1 \right\}, \tag{1.47}$$

where $\mathbf{N} = (N_t)_{t=0,\dots,d-1}$ is the multibandlimit, i.e., $N_t \in 2N$. For a finite number of given Fourier coefficients $\hat{f}_{\mathbf{k}} \in C$, $\mathbf{k} \in I_{\mathbf{N}}$, a fast evaluation of the trigonometric polynomial:

$$f(\mathbf{x}) := \sum_{\mathbf{k} \in I_N} \hat{f}_{\mathbf{k}} \mathrm{e}^{-2\pi \mathrm{i} \mathbf{k}\mathbf{x}} \tag{1.48}$$

is done at given nonequispaced nodes $\mathbf{x}_j \in T^d$, $j = 0, \dots, M-1$, from the d-dimensional torus as well as the adjoint problem, the fast evaluation of sums of the form:

$$\hat{h}_{\mathbf{k}} := \sum_{j=0}^{M-1} f_j \mathrm{e}^{2\pi \mathrm{i} \mathbf{k}\mathbf{x}_j} \qquad \textbf{with} \qquad f_j = f(x_j). \tag{1.49}$$

1.2.3 Non-Linear Iterative Inverse Problem Reconstruction

An other way to reconstruct MR images is to formulate it as an inverse problem where one aims at simulating the MR image via the minimization of an objective function that measures the distance between the model and experimental signals [GUERQUIN-KERN 2011]. The acquired image is modeled with a finite Field of View (FOV) defined by M coefficients $\mathbf{c}[p]$ defined as vector $\mathbf{c}$. The MR data-formation can be modeled using the following equation:

$$\mathbf{m} = \mathbf{E}\mathbf{c} + \mathbf{b} \tag{1.50}$$

where $\mathbf{E}$ is the MRI system matrix and $\mathbf{b}$ a residual vector representing the effect of noise and MR machine imprecisions on measurements. We are then exploiting the idea that an object can be well described by a sparse representation. This sparse representation is composed of few non-null coefficients in a orthonormal basis of M functions. In our case, we rely on the discrete wavelet transform (DWT) that bijectively maps coefficients $\mathbf{c}$ to the wavelet coefficients ω. The DWT being represented by matrix $\mathbf{W}$, we have:

$$\mathbf{c} = \mathbf{W}\omega \Rightarrow \omega = \mathbf{W}^{-1}\mathbf{c}. \tag{1.51}$$

If we define $\mathbf{M} = \mathbf{EW}$, we end up with the following problem to solve:

$$\mathbf{m} = \mathbf{M}\omega + \mathbf{b}. \tag{1.52}$$

We are looking for an optimal solution $\omega^\star$ which is a minimizer of a cost function involving two terms. The first term is a data fidelity term $\mathcal{F}(b)$ and the second a regularization term $\mathcal{R}(\omega)$ that penalizes undesirable solutions and promotes sparsity. The problem is described by the following equation:

$$\omega^\star = \arg\min\left(\mathcal{F}(\mathbf{m} - \mathbf{M}\omega) + \lambda\mathcal{R}(\omega)\right) \tag{1.53}$$

where $\lambda \in \mathbb{R}^+$ is balancing the two constraints. In MRI, we usually assume $\mathbf{b}$ to be a realization of white Gaussian processes which enforces the choice of a quadratic norm such as:

$$\mathcal{F}(\mathbf{b}) = ||\mathbf{b}||_2^2. \tag{1.54}$$

Such problem is ill-conditioned, due to sub-sampling. This is why the use of a suitable regularization function $\mathcal{R}(\omega)$ is required. Regarding the wavelet regularization term, the l_1-norm is properly reflecting sparsity and own nice mathematical properties such as convexity. Indeed, the l_1-norm promotes sparsity because when one minimizes it, the optimal solution is the null vector. Therefore, we will favor solution with wavelet coefficients of small l_1-norm. The final problem to be solved is formulated as follows:

$$\omega^\star = \arg\min\left(\frac{1}{2}||\mathbf{m} - \mathbf{M}\omega||_2^2 + \lambda||\Phi x||_1\right) \tag{1.55}$$

Where $\Phi x = \omega$ are the wavelet coefficients associated with the image. The minimization function combines the Least Square reconstruction of the image based on the data with a sparsity promoting term in the wavelet domain. Some modifications of the reconstruction formula exists with, for instance, the addition of a total variation (TV) constraint on the image such as:

$$\omega^\star = \arg\min\left(\frac{1}{2}||\mathbf{m} - \mathbf{M}\omega||_2^2 + \lambda||\Phi x||_1 + \beta||x||_{TV}\right) \qquad \text{[Behl 2016]} \tag{1.56}$$

Where the TV constraint is defined based on the modulus of the derivative in x and y directions: D$_x$ and D$_y$ and usually computed using second order finite differences or a combination of first and second order [Geman 1995] in a anisotropic form:

$$R_{TV}(x) = \sum_i |D_x(x_i)| + |D_y(x_i)| \qquad \text{[Block 2007]} \tag{1.57}$$

or an isotropic form defined by:

$$R_{TV}(x) = \sqrt{(D_xI)^2 + (D_yI)^2} \tag{1.58}$$

Non-linear reconstruction algorithms possess the property of automatically handling non-uniform sampling densities and consequently do not require a density compensation before reconstruction and a deapodization after. We used the FISTA [Beck 2009] algorithm to solve Equation 1.55. It is a special instance of Proximal gradient method, a generalized form of projection used to solve non-differentiable convex optimization problems.

This method has already been applied to ^{1}H MRI [Huang 2012] and has demonstrated its efficacy. In the aforementioned paper, validation of the method was based on SNR measures which shadow a possible structural modification of the image particularly in low SNR acquisitions. Instead, we explored this aspect using a structural similarity index (SSIM) accounting for localized changes (for details see [Wang 2004]):

$$SSIM(x,y) = l(x,y).c(x,y).s(x,y) = \frac{(2\mu_x\mu_y + c_1)(2\sigma_x\sigma_y + c_2)(2cov_{xy} + c_3)}{(\mu_x^2 + \mu_y^2 + c_1)(\sigma_x^2 + \sigma_y^2 + c_2)(\sigma_x\sigma_y + c_3)} \qquad \text{[Wang 2004]} \tag{1.59}$$

1.3 State-of-the-art in X-MRI

The study of non-proton nuclei with NMR is as old as MRS itself [Bendel 1969, Mooney 1969] while MRI applications appeared some 15 years later [Hilal 1985]. During this PhD thesis, we were interested in three different nuclei: Lithium-7 (^{7}Li), Sodium-23 (^{23}Na) and Phosphorus-31 (^{31}P). While Phosphorus has a $\frac{1}{2}$ spin like Hydrogen, Sodium and Lithium have a $\frac{3}{2}$ spin as summarized in Table 1.1. Due to their low gyromagnetic ratio and natural abundance, their relative sensitivities (compared to ^{1}H) are 6.65×10^{-2} for ^{31}P, 0.272 for ^{7}Li and 9.27×10^{-2} for ^{23}Na. Additionally, their *in vivo* concentrations are several order of magnitude lower than the water content of brain tissue. As a consequence, MRI of these X-nuclei must account for the low available NMR signal by adapting the spatial and temporal resolutions. Fortunately, the signal-to-noise ratio (SNR) is a function of their relaxation times and the strength of the static magnetic field:

$$SNR \propto B_0^{\frac{7}{4}} \left(\frac{T_2^*}{T_1}\right)^{\frac{1}{2}} \qquad \text{[Hoult 1976, Hoult 1979]} \tag{1.60}$$

A recent paper [Pohmann 2016] provides a more precise analysis of the relationship between field strength and SNR as: SNR $\propto$ $B_0^{1.65}$. Therefore, the achievable temporal and spatial resolutions of X-MRI has significantly been improved by the use of more intense magnetic fields opening the way for more ambitious clinical research studies with X-MRI.

1.3.1 NMR of 3/2 spin nuclei

For nuclei such as Sodium or Lithium with a $\frac{3}{2}$ spin, Zeeman splitting leads to four possible energy levels. This higher, non-integer, quantum spin number reflects the non-spherical distribution of nucleon creating an electrical quadrupolar moment with the surrounding electronic cloud. Consequently, electric field gradients (EFG) are generated by the electronic distribution around the nucleus. In comparison, nuclei with a $\frac{1}{2}$ spin present a spherical charge distribution and the interaction of the nuclei with its electronic cloud exists but is direction independent leading to a null quadrupolar moment (eQ). As illustrated by Figure 1.19, nuclei with a spin greater or equal to 1 display an asymmetry of charges that can be of two types either prolate (case C) with a positive quadupolar moment ($eQ > 0$) or oblate (case D) with a negative quadrupolar moment ($eQ < 0$). The four differ-

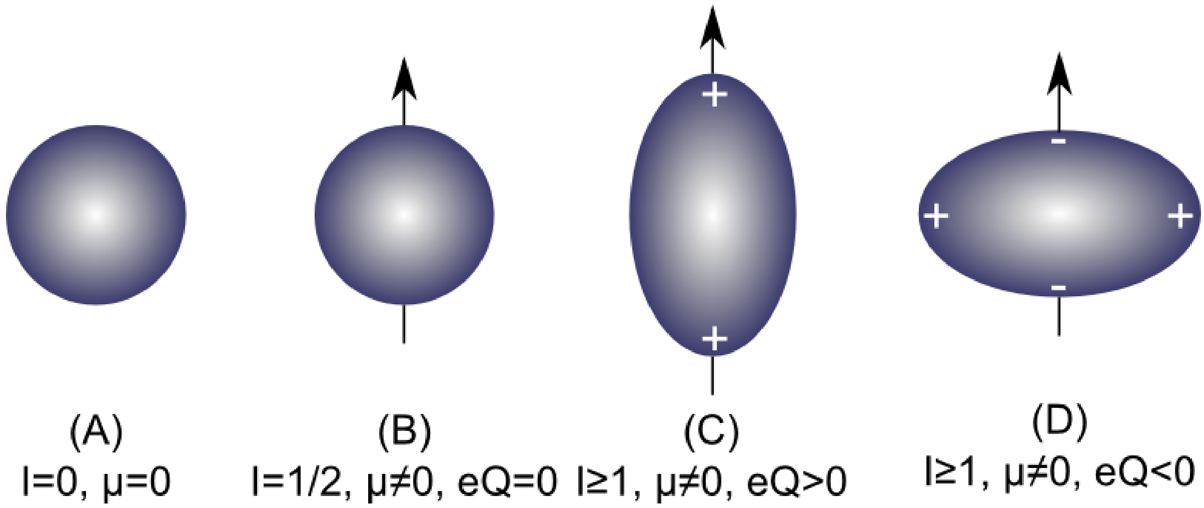

Figure 1.19: Nucleus shape depending on its spin quantum number and electronic quadrupolar moment [Drago 1992].

ent energy levels created by Zeeman splitting: $\{\frac{3}{2}, \frac{1}{2}, -\frac{1}{2}, -\frac{3}{2}\}$ lead to three possible transitions:

$$\begin{cases} (1): \frac{3}{2} \rightarrow \frac{1}{2} \\ (2): \frac{1}{2} \rightarrow -\frac{1}{2} \\ (3): -\frac{1}{2} \rightarrow -\frac{3}{2} \end{cases} \tag{1.61}$$

Transitions (1) and (3) are satellite transitions and (2) is the central transition. The energy levels structure and energy difference between transitions is highly dependent on the chemical environment and the physical state of the nuclei. When Sodium Chloride (NaCl) is dissolved into pure water, its NMR spectrum only presents a single resonance corresponding to the equal energy gaps between those 4 states. In this particular case, the quadrupolar interaction is averaged to zero as the system experiences rapid motion (with short correlation time τ_C) and all orientations of the EFG are equally probable. However, in solid state environments, Sodium experiences very strong residual quadrupolar interactions (RQI) which shifts energy levels as illustrated by Figure 1.20.

Biological tissues present various physico-chemical properties leading to a mixed NMR behavior of strongly quadrupolar nuclei such as Sodium. Due to the slow modulation of the quadrupolar coupling ω_Q with macromolecules, both satellite and central transitions coexist (more or less) at the same Larmor frequency but with different relaxation constants T_1 and T_2. Multiple Quantum Coherences (MQC) exists with the appearance of Double and Triple Quanta Coherences (DQC/TQC) as illustrated by Figure 1.21. These coherences are associated with bi-exponential longitudinal and transverse relaxation processes. Magnetization can be described with the following equations:

$$\begin{cases} M_{x,y}(t) = M_0 \sin(\omega_0 t)(0.6e^{-t/T_{2f}} + 0.4e^{-t/T_{2s}}) \\ M_z(t) = M_0(1 - 0.2e^{-t/T_{1f}} - 0.8e^{-t/T_{1s}}) \end{cases} \tag{1.62}$$

where $T_{1s/f}$ and $T_{2s/f}$ are respectively the slow and fast longitudinal and transverse relaxation times. The ratios between the two relaxation components are derived from the quantum mechanical description of the temporal evolution of the spin system through its Hamiltonian operator. For Sodium, the Hamiltonian operator is the sum of: a Zeeman Hamiltonian, a Radio Frequency Hamiltonian (describing the influence of a RF pulse), and a Quadrupolar Hamiltonian such as:

$$H = H_Z + H_{RF} + H_Q \tag{1.63}$$

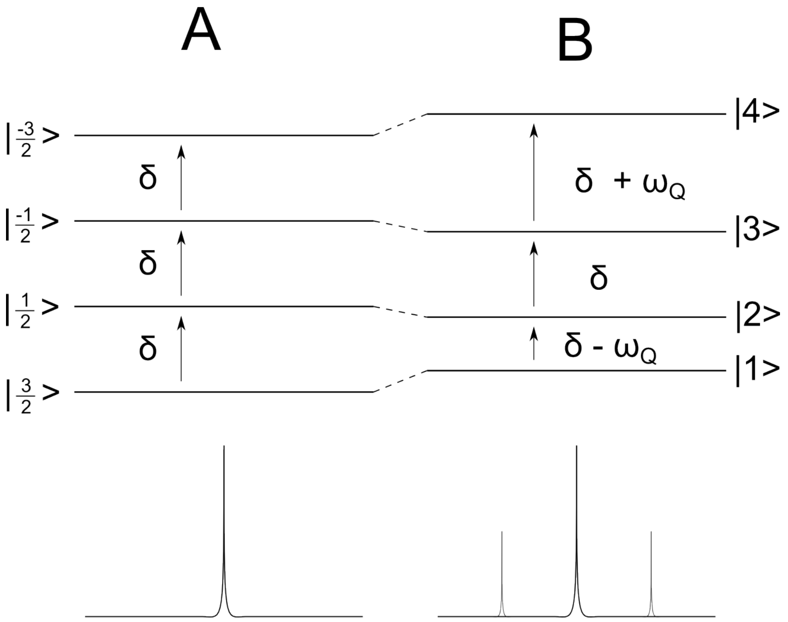

Figure 1.20: Energy levels and corresponding MR spectra for a spin 3/2 in liquid (A) or solid-state (B) environments [Rooney 1991].

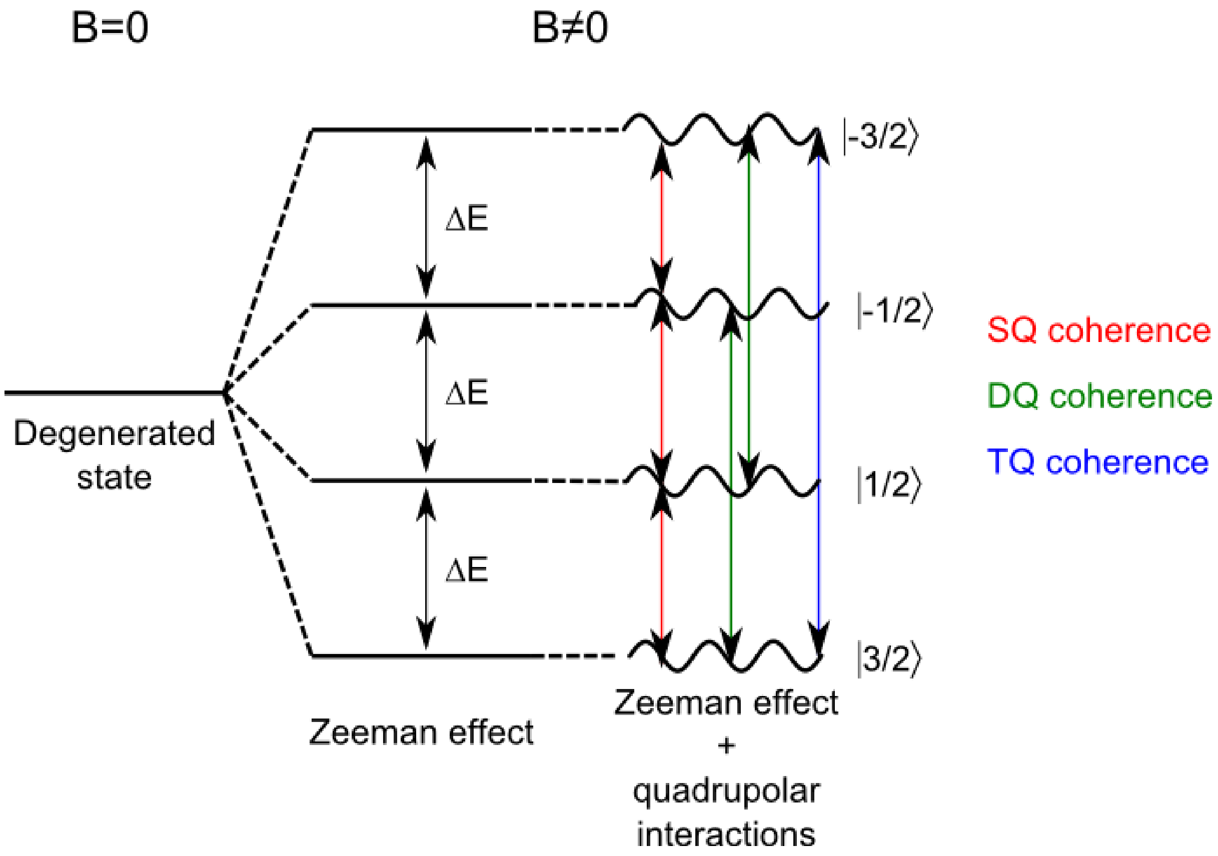

Figure 1.21: Zeeman splitting and the influence of the quadrupolar interactions for $\frac{3}{2}$ spin nuclei in a nonzero average EFG such as brain tissues (adapted from [Van Der Maarel 1989]).

Analysis of this Hamiltonian involves the Irreducible Spherical Tensor Operator model and will not be presented here but details can be found elsewhere

[Van Der Maarel 1989, Van Der Maarel 2001, Van Der Maarel 2003].

1.3.2 Sodium-23 MRI

We detail here the main methods used to acquire Sodium MR Images. Two families of sequences currently exist based on the number of RF pulses used and the coherence selection. The role of a MR pulse sequence is to create a coherence pathway which corresponds to the coherence orders taken by the magnetization during the sequence. All experiments start with a zero order coherence (magnetization along the z axis) and should end with a coherence order of -1 ($T_{1\pm1}$) corresponding to the transverse magnetization. Different pathways with multiple quanta coherences and phase cycling can also lead to this final coherence order.

1.3.2.1 Single Quantum Imaging

The Single Quantum (SQ) Imaging of Sodium corresponds to the measurement of the MR signal from all sodium nuclei contained in a sample. A single RF excitation pulse is used without phase cycling which creates a single coherence of the Sodium nucleus. The Total Sodium Concentration (TSC) remains the most common measurement reported in ^{23}Na MRI to examine variations of sodium concentration in relation to pathological processes.

To perform a TSC measurement, state-of-the-art acquisition is a Spin Density (SD) weighted acquisition with an ultra-short echo time and a relatively long TR. Initial developments made with standard sampling sequences were not very efficient [Parrish 1997]. As stated before, non-Cartesian sampling schemes allowed to further reduce TE and increase SNR. Main sequences are: 2D Radial Sampling, 2D Twisting Radial Lines (TWIRL)[Jackson 1992], 3D Radial [Nielles-Vallespin 2007, Nagel 2009b, Eisele 2015], Twisted Projection Imaging [Boada 1997c, Boada 1997a, Lu 2010a, Atkinson 2011], FLORET (Fermat Looped, ORthogonally Encoded Trajectories) [Pipe 2011], Cones [Gurney 2006, Riemer 2014], PETRA (Pointwise Encoding Time reduction with Radial Acquisition) [Grodzki 2012] combining Cartesian and Non Cartesian sampling, SPRITE (Single-Point Ramped Imaging with T_1-Enhancement) [Mastikhin 1999, Szomolanyi 2001, Halse 2003] [Romanzetti 2006]. Most Sodium MRI explorations have until now been conducted on 3T MR scanner with spatial resolutions of 3 to 4 mm isotropic. Higher resolution of 1x1x5 mm^3 can, for instance, be achieved at ultra high field (7 T and 9.4 T) [Mirkes 2016] using an Acquisition Weighted Stack Of Spirals (AWSOS)[Qian 2008, Qian 2012a] sampling trajectory. Parallel imaging techniques have been evaluated to reduce the length of some acquisitions, for instance TPI [Qian 2009].

1.3.2.2 Multiple Quantum Filtering

In organized media, the satellite and central transitions or fast and slow components of Sodium [Chen 1993] can be exploited to investigate its physico-chemical environment. While single quantum UTE sequences detect both components, the different multiple quantum coherences (MQC) can be detected using Multiple Quanta Filtering (MQF) sequences [Jaccard 1986]. There are two types of MQF : the Double Quanta Filtering (DQF) [Tsang 2015] and the Triple Quanta Filtering (TQF) [Fiege 2013, Mirkes 2015] where the NMR signal is manipulated to select the second or third coherence orders supposedly coming from the intracellular compartment. Each acquisition is based on a specific phase cycle scheme [Wimperis 1992].
MQF sequences are sensitive to B_0 inhomogeneities [Tanase 2005, Matthies 2010, Fleysher 2010, Tsang 2013]. Characterization of the TQF signal dependency to B_0 allowed a possible correction

by acquiring a B_0 map and adapting the phase cycle [TANASE 2005]. Another solution lies in the introduction of a refocusing pulse at half of the preparation time τ as proposed by [JACCARD 1986].

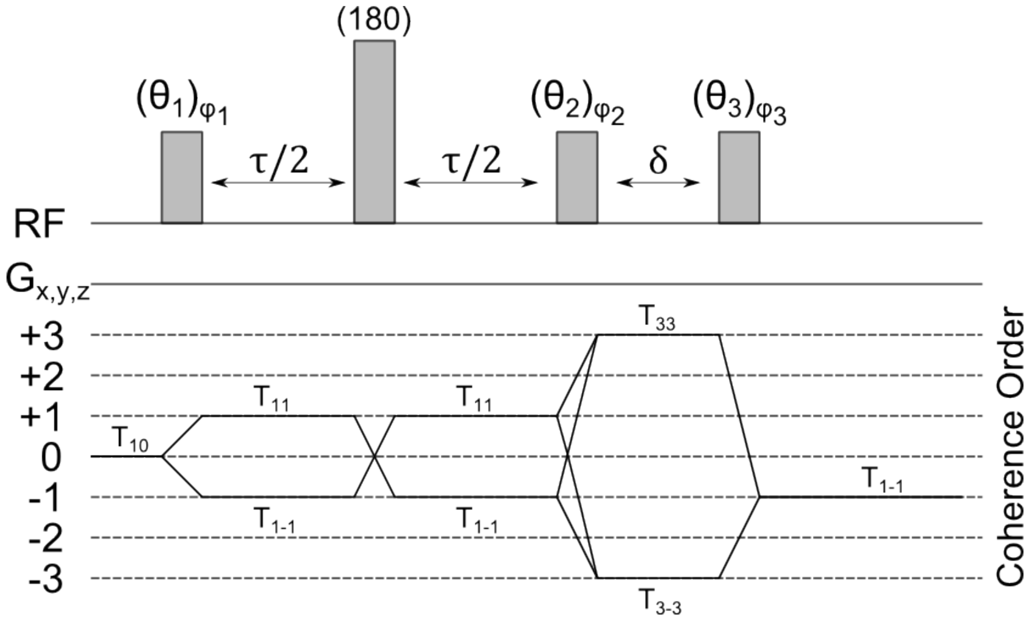

Figure 1.22: B_0 insensitive Multiple Quanta Filtered sequence with coherence order transfers from [JACCARD 1986].

Applications of MQF to clinical research have been performed at various static field intensities from 3 T to 9.4 T [HANCU 1999, BOADA 2005, FLEYSHER 2012, FIEGE 2013, PETRACCA 2016]. TQF has been more used than DQF due to its 50% higher signal [CHUNG 1990]. Nonetheless, TQF suffers from a very low sensitivity of about 1/10 of SQ. This leads to longer acquisition times and lower spatial resolution. Moreover, the use of at least three 90 degrees pulses which are heavily repeated through phase cycles leads to a very important SAR. The addition of a 180 degrees refocusing pulse for B_0 homogeneity increases even more this aspect. Finally, it seems that TQF signal is dependent on both the fast and slow T_2 relaxations of signal which makes rigorous quantification difficult. Alternative methods have been proposed to achieve comparable signal weighting or computations with fewer pulses or more SNR: Quadrupolar Jump and Return [LEE 2009], Biexponential-weighted and Difference Image Method (DIM): Gradient Selected DIM (gsDIM) [BENKHEDAH 2013], Phase Cycling DIM (pcDIM)[BENKHEDAH 2013] and 2 pulses DIM (2P-DIM) [BENKHEDAH 2014].

1.3.2.3 Clinical Applications

In addition to some preclinical applications mostly in rodents [SCHEPKIN 2006, NEUBERGER 2007, HARRINGTON 2011], ^{23}Na MRI has been used for clinical research by a few research groups during the past decades.

Brain

The ^{23}Na MRI studies of brain diseases were recently reviewed [SHAH 2015]:

- Multiple Sclerosis: In a pioneering study, performed on a clinical 3T MR scanner, it was shown that it was possible to correlate local the Total Sodium Concentration (TSC) increase

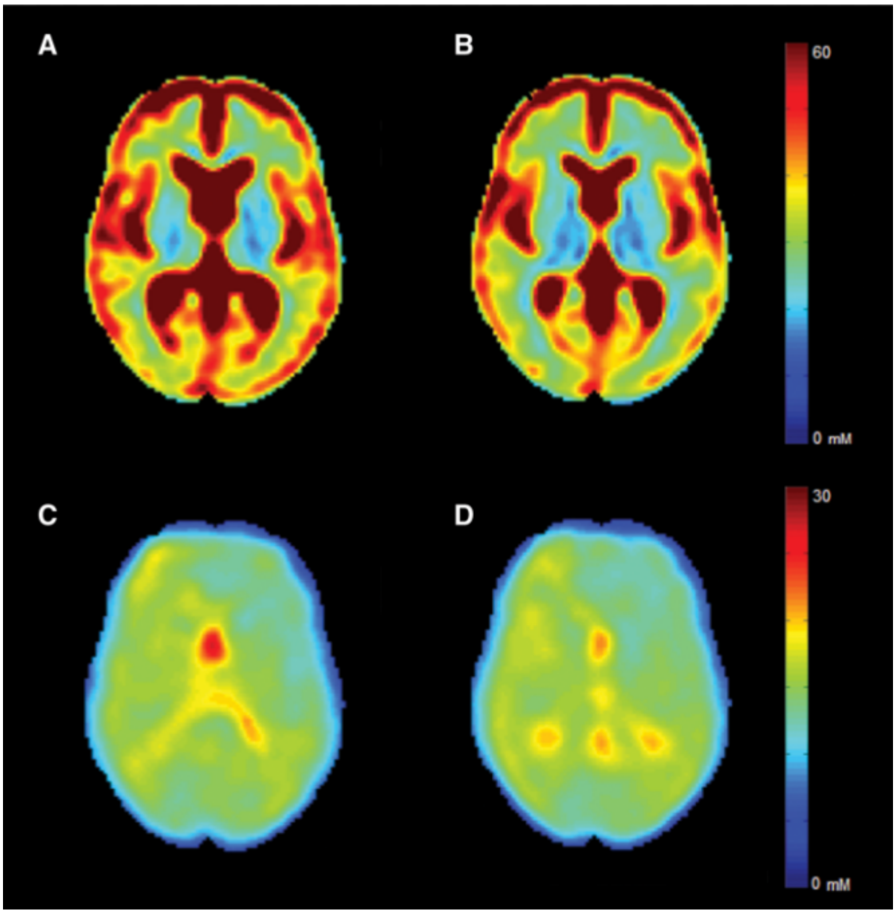

Figure 1.23: Sodium MRI of the brain of a Multiple Sclerosis patient (left) and healthy control (right). The top row presents Total Sodium Content (TSC) and the bottom row the Intracellular Sodium Content [PETRACCA 2016] acquired with a TQF sequence [FLEYSHER 2012].

with lesions. Comparison with ^{1}H T_2 weighted MR Images confirmed that these sodium increased concentration areas were located at exactly the same locations as lesions classically detected with a hyper signal [INGLESE 2010]. Another study, conducted on a larger cohort, showed two important results. First, it confirmed that it was possible to correlate the TSC increase with the development of the disease. Second, that it was possible to quantify the state of the disease between early RRMS (Relapsing Remitting Multiple Sclerosis) and advanced RRMS based on Sodium distribution which presents a significant increase between both stages [ZAARAOUI 2012]. Ongoing studies are now performed at 7 T by CRMBM researchers (CNRS U7339, Aix-Marseille University) with more patients [MAAROUF 2014, MAAROUF 2017]. In another study, cortical sodium concentrations were shown to be significantly higher in all subgroups of multiple sclerosis patients compared to healthy controls [PALING 2013]. Further TSC measurements for MS patients were performed in 2015 and concluded that TSC was a sensitive biomarker of the severity of chronic tissue abnormalities in MS and could reflect the opening of the blood-brain-barrier and vasogenic tissue edema in contrast-enhancing lesions [EISELE 2015]. All application of Sodium MRI to study MS were recently reviewed [PETRACCA 2015]. Moreover, a description of the biological and biochemical origins of the Sodium accumulation in MS can be found in [STYS 2005] and [WAXMAN 2008]. Notably, the role of astrocytes in the framework of MS has also been investigated in 2010 [BLACK 2010].

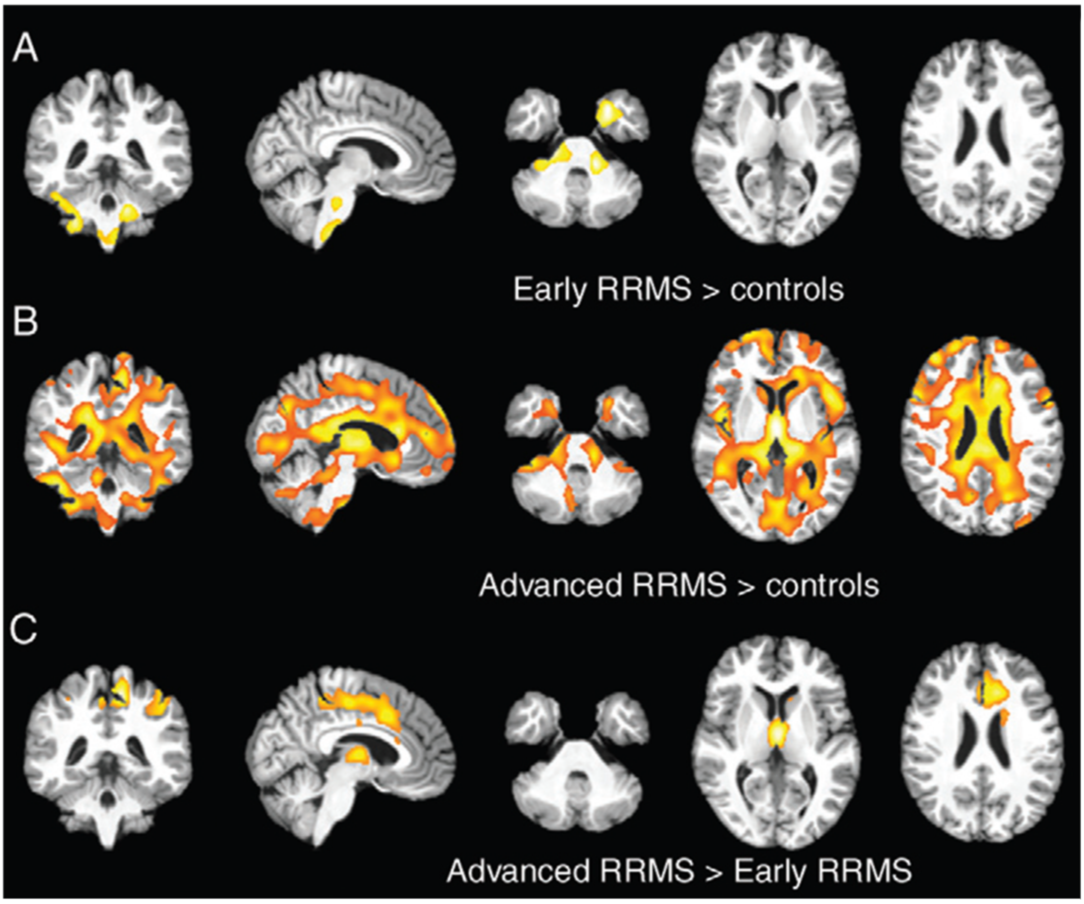

Figure 1.24: Statistical comparison (Z-score) of the TSC maps from early RRMS (A) and advance RRMS (B) stages of Multiple Sclerosis (MS) patients versus controls subjects (C)[Zaaraoui 2012].

- Alzheimer's Disease: A 2009 study investigated the putative link between TSC variations and neuronal death occurring in patients suffering from Alzheimer's Disease (AD). This hypothesis relates diminishing cellular vitality/viability caused by the disease with increased total sodium concentrations in the hippocampus [Mellon 2009]. Considering the variability of AD, this preliminary study would deserve a follow-up. As of mid-2017, no other studies of AD involving Sodium MRI has been published.

- Huntington's Disease: In 2012, an early study showing a TSC increase in patients suffering from Huntington's disease compared to controls was published [Reetz 2012]. As for MS or AD, increased TSC values were found in the striatum, a structure known to be strongly affected by the disease, but also in other structures across the brain.

- Cerebral hemorrhage and Stroke: These acute conditions have been investigated using sodium MRI as large sodium concentration variations can be observed [Shimizu 1992, Thulborn 2005, Tsang 2011]. More recently, sodium MRI has been suggested as a predictive marker for penumbra viability in combination with perfusion MRI [Wetterling 2015].

- Tumors: Patients suffering from brain tumors were explored quite early with sodium MRI in 2005 [Babsky 2005] and later in 2011 [Nagel 2009a]. It has been suggested that sodium MRI could help in classifying neoplasias at an early stage so as to improve and individualize patient management in neuro-oncology [Biller 2015].

Other organs or tissues

Other organs have also been studied using Sodium MRI. Whole Body Sodium MRI was performed [Wetterling 2012] few years ago using 5 time slots of 10 minutes. The resulting ^{23}Na MRI shows that sodium is ubiquitous but is mostly concentrated in the eyes, brain, heart and bladder as illustrated by Figure 1.25.

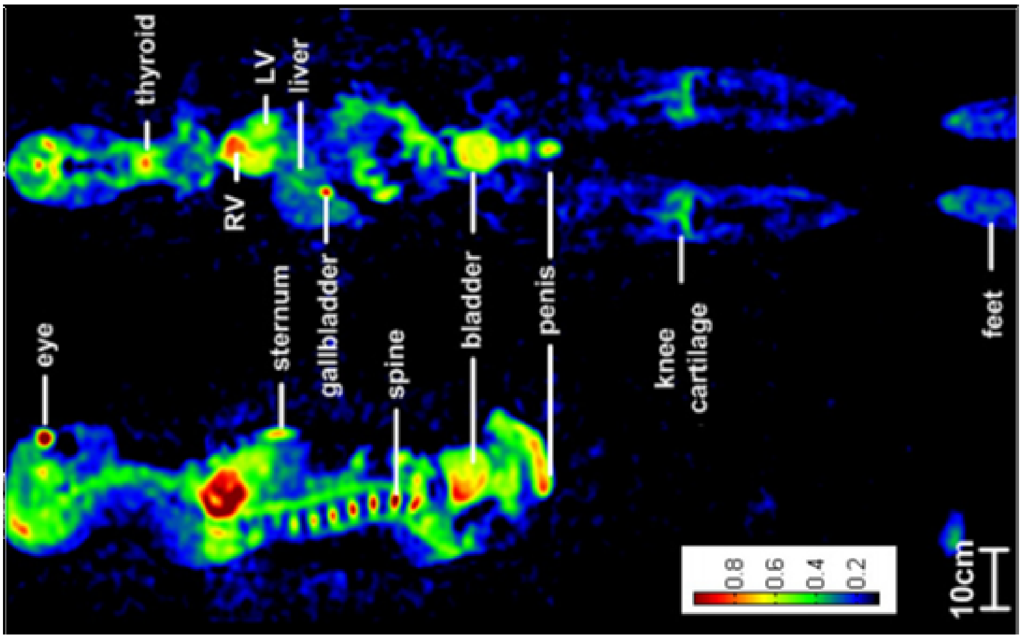

Figure 1.25: Sagittal and coronal views of a whole body sodium MR Image[Wetterling 2012].

Those organs were studied with ^{23}Na MRI:

- Increased intracellular concentrations of Sodium following myocardial infarction [Ouwerkerk 2005, Ouwerkerk 2008, Gai 2015, Graessl 2015, Bottomley 2015];
- Kidneys [Maril 2006, Haneder 2013, Zöllner 2015];
- Exploration of skin Sodium storage capacities [Linz 2014];
- Cartilage [Watts 2011, Madelin 2012, Zbýn 2015, Lee 2016];
- Muscles and tendons[Weber 2011, Nagel 2011, Bangerter 2016];
- Breast cancer [Ouwerkerk 2007];
- Spine [Haneder 2014, Malzacher 2015].

1.3.3 Phosphorus-31 MRSI and MRI

With *In vivo* ^{31}P NMR, non-invasive studies of energy metabolism, pH and membrane turnover can be performed. As illustrated in Figure 1.26, ^{31}P MRS or MRSI approaches allow to estimate phosphorylated metabolites (adenosine triphosphate (ATP), phosphocreatine (PCr), phosphomonoesters (PME), phosphodiesters (PDE), inorganic phosphate (Pi) and few others) alterations in regions-of-interest or map their distribution in the brain[Chaumeil 2009, Martin 2007, Kauv 2017, Du 2017] or other diseased organs such as muscles [Chance 2006, Bendahan 2006, Kemp 2007] [Hooijmans 2017], the heart [Ingwall 1982, Bottomley 2009, Stoll 2016], the liver [Norén 2004],

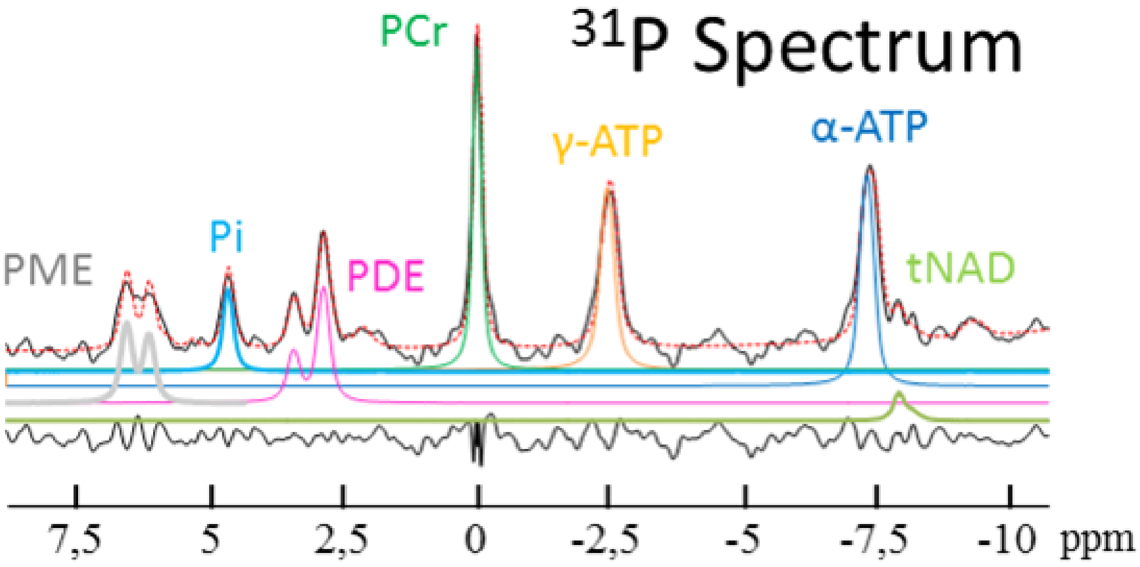

Figure 1.26: ^{31}P Spectrum acquired from a healthy human brain at 7 T and its spectral decomposition obtained with LCModel (Courtesy of Alfredo LOPEZ KOLKOVSKY). Abreviations: adenosine triphosphate (ATP), phosphocreatine (PCr), phosphomonoesters (PME), phosphodiesters (PDE), inorganic phosphate (Pi) and nicotinamide adenine dinucleotide (NAD).

the prostate [KOMOROSKI 2011] or the breast [KLOMP 2011, VAN DER KEMP 2014]. As ATP stocks are quite limited, its synthesis is a permanent process orchestrated by the mitochondrion. Consequently, several pathological or physiological processes modulating cellular activity can be probed using static or (better) dynamic ^{31}P MRS [LAYEC 2011]. As cellular stress and mitochondrial dysfunction are suspected to play key roles in various neurodegenerative diseases at asymptomatic stages, quantifying the metabolic state of the brain and its energy synthesis capacity could be of high interest as early biomarkers.

Unfortunately, ^{31}P MRSI suffers from a poor spatial resolution (and specificity) due to the low concentrations of those phosphorylated metabolites (up to 3-4 mmol/L for PCr). As CSI sequences require a 2D or 3D phase encoding scheme, their acquisition times are also quite long. At 7 T, typical *in vivo* ^{31}P CSI exhibits 10 mL voxels for an approximate acquisition time of 20 minutes [LEI 2003, VAN DER KEMP 2013, RODGERS 2014]. To further improve these acquisitions, more efficient sequences were proposed such as the echo-planar spectroscopic imaging (EPSI) [MANSFIELD 1984, MATSUI 1985, POSSE 1994] allowing a 3D coverage in some 10 minutes at a spatial resolution of $15 \times 15 \times 30$ mm^3 [KORZOWSKI 2017].

An alternative approach is to focus on one or two phosphoryraled metabolites such as ATP or PCr and use spectrally selective sequences to acquire images of their spatial distribution using ^{31}P MRI [LU 2013]. Promising applications of ^{31}P MRI were performed using adapted and optimized non-Cartesian sampling sequences [LU 2013, PARASOGLOU 2016] as illustrated by Figure 1.27. Interesting methods exploiting the Nuclear Overhauser Effect (NOE) or the Multi-point Dixon sequence were proposed for ^{31}P MRI [RINK 2016].

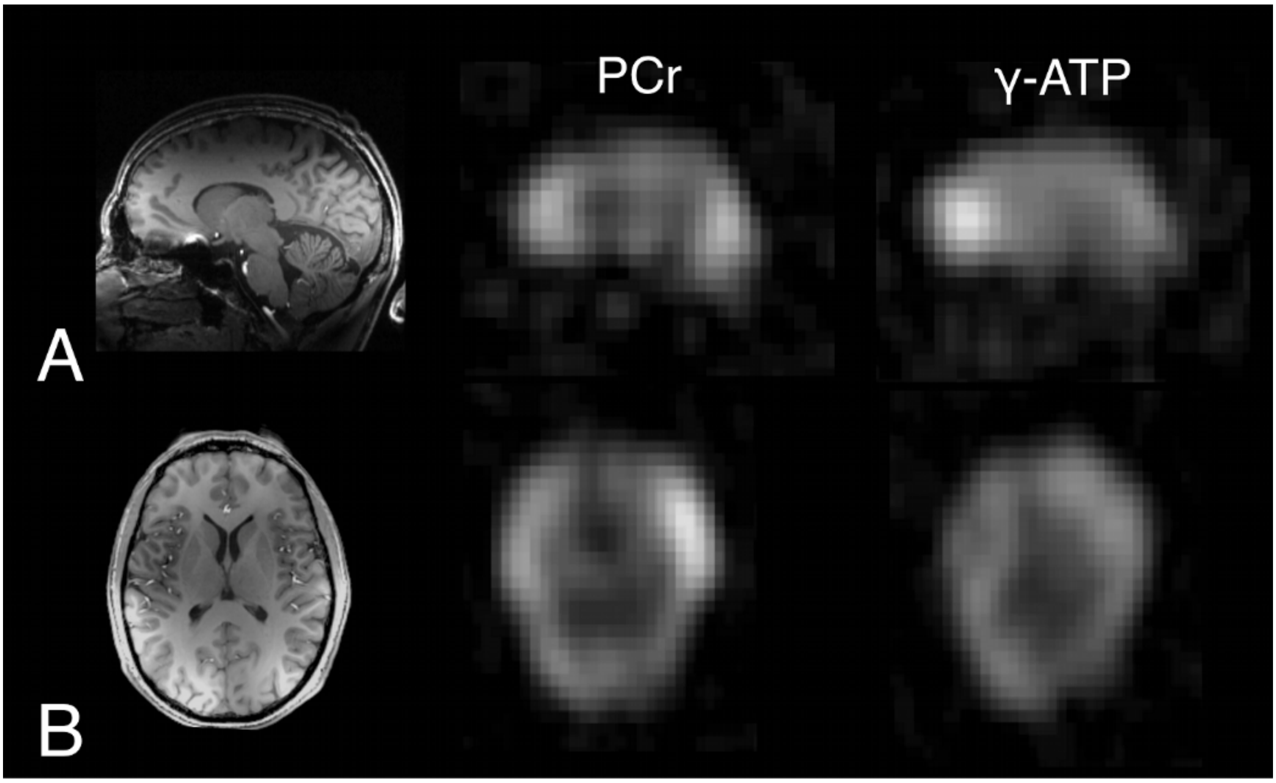

Figure 1.27: PCr and ATP maps obtained at 7 T with a 14mm isotropic resolution in 15 minutes for each metabolite [Parasoglou 2016].

1.3.4 Lithium-7 MRSI and MRI

Bipolar disorder (BP) is a high prevalence psychiatric disease where patients alternate between periods of deep depression and high happiness. In depression periods, symptoms can be as serious as self mutilation and suicide. The mechanics of this disorder are poorly understood and lithium salts are currently the reference treatment as they modify neuron functioning. A complete review about the history of Lithium therapy can be found in [Shorter 2009]. Already several clinical research studies of bipolar patients treated with lithium salts have been conducted using ^{7}Li MRS or MRSI despite the challengingly low signal available mostly at 3 T [Renshaw 1985, Renshaw 1988, Gonzalez 1993, Soares 2001, Smith 2011, Lee 2012, Cousins 2013]. Similarly to Sodium, Lithium is an electrolyte Li^{+} presenting a single NMR peak. Therefore, there is very little interest in using MRS or MRSI sequences and its distribution can be readily obtained with optimized imaging sequences leading hopefully to faster, larger brain coverage and overall more efficient acquisitions. To our knowledge, a single ^{7}Li MRI study was conducted at 7 T using an Acquisition Weighted Stack of Spirals (AWSOS) [Boada 2010] with very promising results as illustrated by Figure 1.29. Ongoing ^{7}Li MRI studies are underway at New York University Medical Center (Center for Advanced Imaging Innovation and Research) and at Newcastle University (Institute of Neuroscience).

1.4 Objectives and Challenges

X-MRI offers an opportunity to get access to metabolic, physiological or pharmacological data through the concentrations (or relaxation times) of various metabolites or electrolytes and their

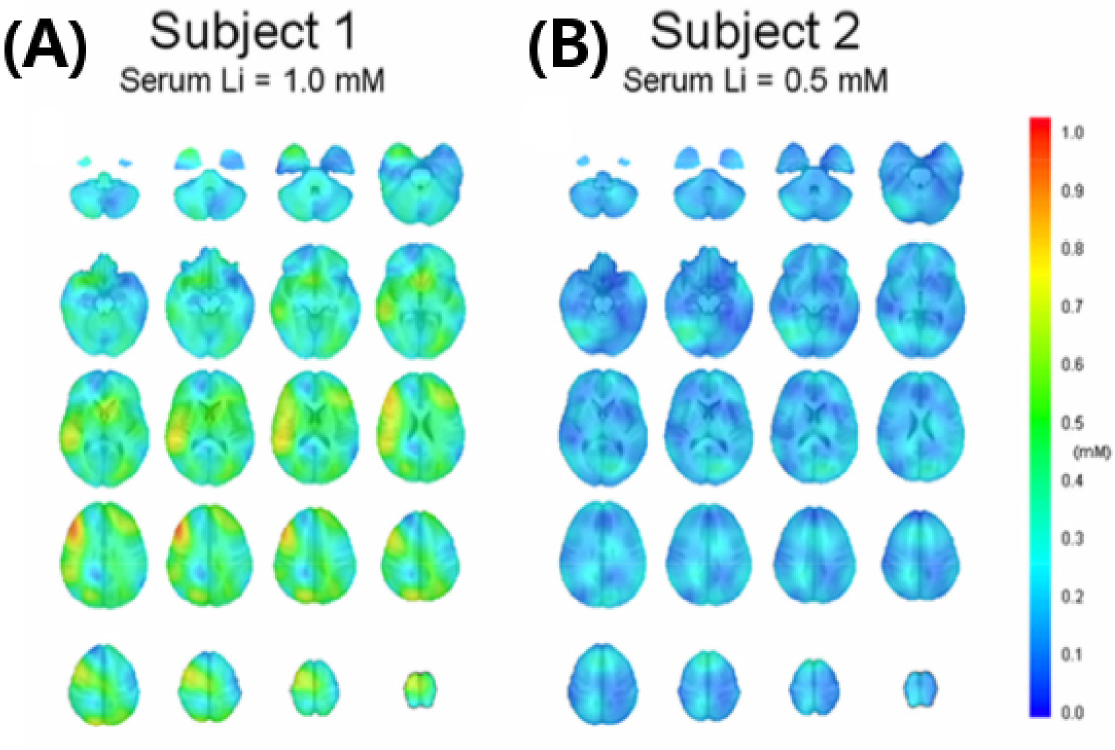

Figure 1.28: Lithium distributions in two bipolar patients obtained at 4T using ^{7}Li MRSI [Lee 2012].

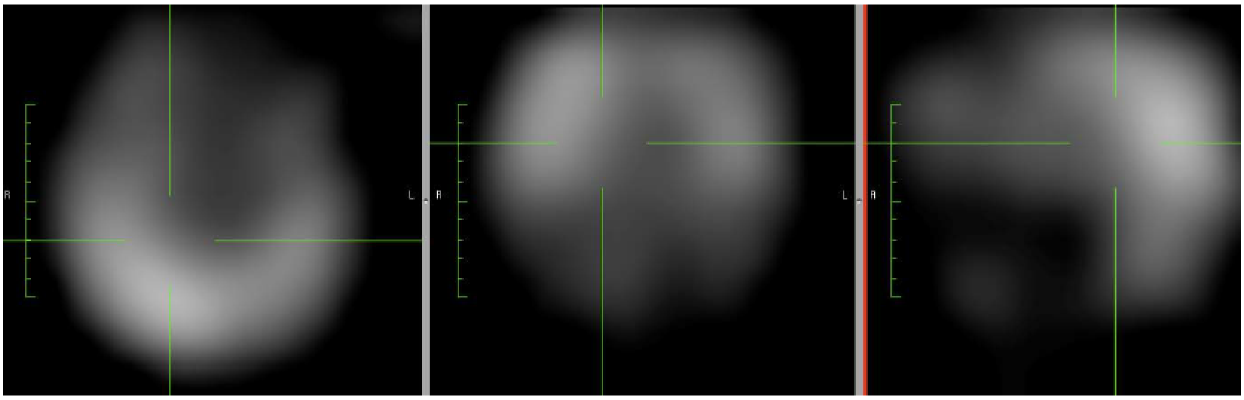

Figure 1.29: Axial, Coronal and Transverse brain Lithium images obtained from a patient suffering from Bipolar Disorder at 7 T (TR/TE/TA=1 s/0.6 ms/32 min) [Boada 2010].

spatial distribution in the brain.

How to perform robust concentration measurements is currently an important and challenging question in the non-proton MRI community as a condition for a wider clinical applicability and interest. Moreover, low spatial specifity, SNR and long acquisition times are also considerable limitations to clinical applications. Fortunately, the wider availability of high magnetic fields (3 T) in hospitals and ultra-high magnetic fields ($\geq$ 7 T) in research centers should help in overcoming those challenges [Ugurbil 2014].

This thesis aims at tackling three general challenges of non-proton MRI:

- Acquisition time reduction
- Spatial resolution improvement
- Robust quantification estimation

The additional challenge of cellular compartmentalization of ^{23}Na NMR signal was also explored. NeuroSpin laboratory is dedicated to the non-invasive exploration of the brain from rodents to Human using NMR Spectroscopy and Imaging. The recent arrival of the world first Human 11.7 T magnet strongly motivates non-proton developments. Indeed, this unique field should allow pushing the limits of X-MRI and reach unprecedented sensitivity and resolution without the drawbacks of dielectric artifacts thanks to their lower gyromagnetic ratios.

Our Sodium and Phosphorus MRI explorations benefited from the clinical interest of neurologists: Dr. Kathrin REETZ from Aachen University Hospital and Dr. Julien LAGARDE from Saint Anne Hospital (Paris Public Hospital). A scientific collaboration was established and strengthened with this thesis with Dr. Sandro ROMANZETTI from Aachen University Hospital for methodological developments. A secondary collaboration with Dr. Guillaume MADELIN from the Center for Biomedical Imaging of the department of Radiology of New York University medical center was also established regarding the FLORET sequence used in Aachen. These collaborations allowed us to validate our developments in a clinical environment. An internal collaboration with Dr Nicolas CHAUFFERT and Dr. Philippe CIUCIU about Compressed Sensing and image reconstruction allowed me to adapt Nicolas' work to non-proton MRI. It allowed to first explore both retrospective and prospective acquisition under-sampling to reduce acquisition time. And second to improve image reconstruction with the use of advanced and more sophisticated reconstruction algorithms. A collaboration with Lisa LEROI, PhD student of Dr. Alexandre VIGNAUD on quantitative MRI in collaboration with Dr. Ludovic DE ROCHEFORT from CRMBM at Aix-Marseille University, Dr. Romain VALABREGUE and Dr. Mathieu SANTIN from Paris Brain and Spine Institute enabled the application of simultaneous multiparametric quantitative method to Sodium MRI. The collaboration with Dr. Josselin HOUENOU, Dr. Franz HOZER, Pr. Franck BELLIVIER (APHP) and Jacques STOUT, a fellow PhD student of our group working on ^{7}Li MRI allowed me to apply my developments to the study of lithium treated BP patients. Finally, the internal collaboration with Dr. Michel LUONG from the *Institut sur les lois fondamentales de l'Univers* and the electrical engineering and mechanical teams of NeuroSpin allowed me to get involved in both RF coil and phantom developments.

As no prior non-proton MR Imaging explorations (except for ^{19}F MRI) were ever carried out at NeuroSpin, an important goal of this thesis was the development of a complete acquisition, reconstruction and post-processing environment for X-MRI as well as hardware developments and quality control processes.

CHAPTER 2

Hardware Characterization

Contents

This chapter is dedicated to the description of our experimental set-up for ^{23}Na, ^{31}P and ^{7}Li MRI at 3 or 7 Tesla. Our radiofrequency coils, test-objects and imaging protocols have been characterized and evaluated in regards to our methodological, safety and quality-control objectives.

2.1 NMR Systems

2.1.1 General System overview

To perform *in vivo* NMR Spectroscopy or Imaging of an animal or a Human volunteer, horizontal dedicated spectrometers are needed. A MR scanner is composed of 3 main components: a superconductive electromagnet to create the static magnetic field B_0, a transmission and reception radiofrequency coil to manipulate the sample magnetization and acquire NMR signals and a set of gradient coils to encode the spatial position of the spins. Several other components are also involved such as high power amplifiers, frequency synthesizers and pulse modulators to generate the radio-frequency (RF) waves, signal pre-amplification and demodulation circuits, Analog-to-Digital Converters (ADC), Digital-to-Analog Converters (DAC) and computer hardware to control all those electronic elements, manage the flow of NMR data and reconstruct the images. A simplified overview of this architecture is presented on Figure 2.1.

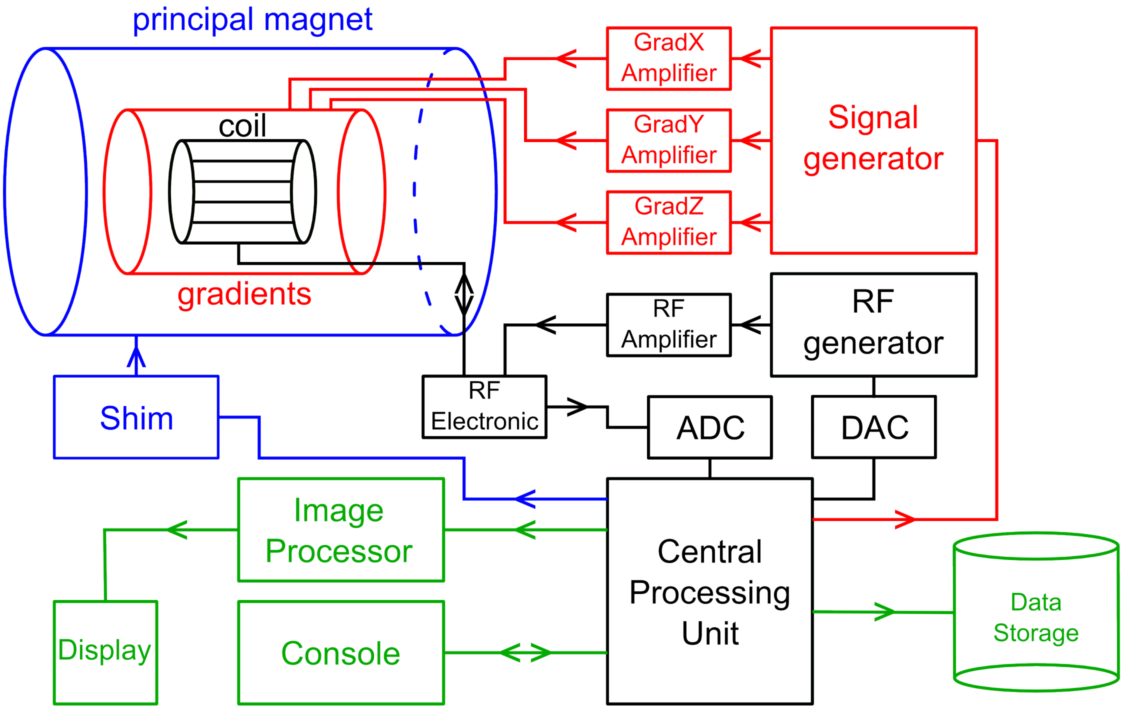

Figure 2.1: Schematic of a MR system and its hardware (reproduced from [Clare 1997]).

2.1.2 Characteristics of our MR scanners

2.1.2.1 3 T PRISMA Mr Scanner

NeuroSpin's 3 T wide-bore scanner (⌀ 600 mm) is a Siemens (Erlangen, Germany) Prisma-fit system (upgraded in 2016). It offers enhanced features compared to previous generations:

- improved gradient performances with 80 $mT.m^{-1}$ strength and a 200 $T.m^{-1}s^{-1}$ slew rate simultaneously on all three axes in addition to other features such as a force-compensated design for reduced vibrations and ultra-high-performance cooling;

- for conventional ^{1}H NMR, a body coil with 2 independent transmit channels to alleviate transmission artifacts in large organs.

- Tim 4G integrated receiving architecture with 64 independent channels for faster acquisitions or higher SNR as well as a fully digital transmit and receive channels;

- a broad-band transmit channel for X-NMR.

The scanner is interfaced with the latest Syngo operating system version E11. A PRISMA 3 T MR scanner with similar characteristics was used for our ^{23}Na experiments at Aachen University Hospital but the Syngo version was D13.

2.1.2.2 7 T MAGNETOM MR Scanner

Since its opening in 2007, NeuroSpin is equipped with a 7 T Siemens Magnetom MR scanner (first in France) dedicated to methodological developments and clinical research with advanced methods. As of mid-2017, some 50 7 T MR scanners have been installed all over the world (mostly in Western Europe and the USA). Our 7 T NMR Spectrometer has the following characteristics:

- AC84 Head-only gradient coil with max intensity of 80 $\mathrm{mT.m^{-1}}$ and a 333 $\mathrm{T.m^{-1}s^{-1}}$ slew rate on all axis. This gradient coil should be replaced by a SC72 whole-body gradient coil in 2018;
- 8 Transmit (Tx) and 32 Receive (Rx) channels for ^{1}H;
- a broad-band RF amplifier and transmit channel for non-proton nuclei.

This 7 T scanner still runs on the old VB17 Syngo operating system.

2.1.2.3 11.7 T Iseult MR Scanner

Despite the fact that the 11.7T Iseult clinical research MR scanner has been welcomed at NeuroSpin only few weeks ago, we wanted to share some information about its design and expected characteristics. This unique magnet was designed by scientists from the *Institut de Recherche sur les lois Fondamentales de l'Univers* (CEA-DRF-IRFU) who are experts on magnets and superconductivity. The design of the magnet is different from the state-of-the-art and is made from 170 double pancakes niobium/titanium wires through which some 1500 A are planned to run. The helium bath will be cooled at 1.8 K, below the 4 K of other MRI magnets so as to reach a superfluid state. It shall operate with Siemens hardware and operating system (Syngo) version B17. It is 5 m long and has a diameter of 5.4 m with wide-bore diameter of 900 mm prior to gradient insertion and a final bore of 650 mm (gradient coil SC72 and shim coils up to the third order).

Figure 2.2: NeuroSpin's 3 T PRISMA-fit (left) and 7 T MAGNETOM (center) MR Scanners (Siemens Healthcare, Erlangen, Germany) plus a peak at the "naked" 11.7 T Iseult magnet (CEA-IRFU) (right).

2.1.2.4 Static Magnetic Field B_0

Mapping the static field is of importance as its heterogeneities can lead to some significant artifacts and errors. In spite of the available "shimming" approaches to homogenize the static magnetic field over the whole brain or a region-of-interest using dedicated or generic shim coils (for details read [JUCHEM 2017, STOCKMANN 2017]), B_0 mapping techniques are useful to monitor, control and eventually correct for those heterogeneities in post-processing. The most common method to map

B_0 relies on the acquisition of two GRE images at echo-times adequately spaced. From the phase differences between those two images, B_0 field variations can be estimated as:

$$\Delta B_0 = \frac{\Delta\phi}{2\pi\Delta TE} \quad (2.1)$$

Figure 2.3 presents an example of this technique applied *in vivo* at 3 T. One can notice the more intense variations at the level of frontal cortex due to the presence of air in frontal sinuses (and the subsequent magnetic susceptibility interface). Even though B_0 mapping and shimming should be performed using the more abundant ^{1}H signal, they can be perform using X-NMR, in particular ^{23}Na signal. With the help of Franck MAUCONDUIT who modified the shimming step for X nuclei applications, it is now possible to acquire two phase images using two echoes in a standard non proton SPGR sequence and compute a B_0 map which is used by the scanner shimming system making X-nuclei shimming possible.

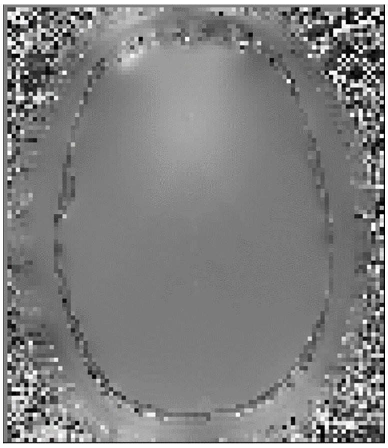

Figure 2.3: *in vivo* B_0 map of a Human head obtained at 3 T (from A. COSTE and S. ROMANZETTI).

2.1.2.5 Gradient system

The gradient system is typically composed of three pairs of coils which are of two different types to operate in the three spatial directions. The first type is the saddle Golay coils used to create field variations perpendicular to the direction of the static magnetic field. The second type is the Helmholtz coil placed along the direction of the field.

Ideal gradient profiles are usually assumed so as to guarantee the linearity and regularity of Cartesian trajectories in the Fourier space. For fast imaging sequences such as echo-planar, echo-volumic imaging or non-Cartesian trajectories, such approximation is not satisfactory and gradient imperfections (non-linearity, delays and eddy currents) must be controlled and corrected [BRODSKY 2009]. It is possible using a dedicated sequence to measure the precision of the gradient system by estimating the performed trajectory and compare it with theory. The fidelity of our gradients was validated using the LPM sequence [PAPADAKIS 1997, SCHNEIDER 2011].

2.2 Coils

As I worked at developing and validating MRI of three different nuclei ^{23}Na, ^{31}P and ^{7}Li at 3 or 7 T, different coils were used during my PhD thesis. This section presents each coil and their characteristics. For our home-made RF transceiver coil for non-human primate ^{23}Na MRI, its design and characterization was realized in collaboration with our colleagues of the Coil Design and Prototyping cell: Michel LUONG (CEA/IRFU), Eric GIACOMINI, Edouard CHAZEL and Marie-France HANG.

2.2.1 Calibration Steps

2.2.1.1 Tuning and Matching

Before any NMR experiment, it is important to check the 50 Ohm impedance adaptation (matching) of our transmission and reception RF coil elements at the operating frequency (tuning). For most coils, the tuning and matching are performed *a priori* by the manufacturer assuming a standard electronic load corresponding to an average head.

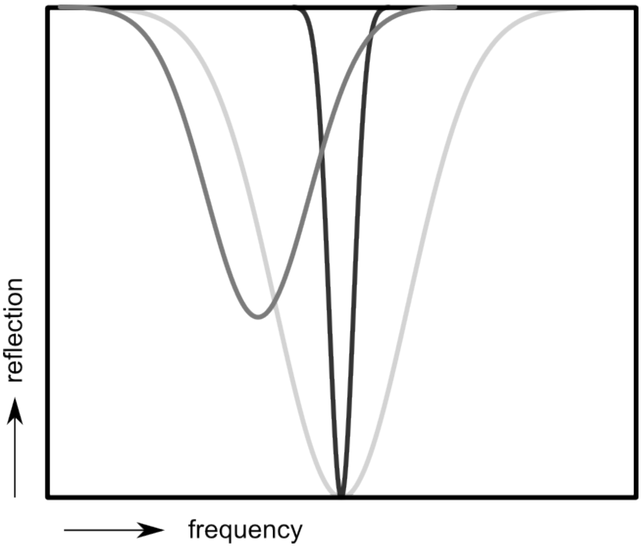

Figure 2.4: Power reflection coefficient of a RF coil element around its operating frequency (radiofrequency sweep or wobble) without (black), or with a load before (dark gray) and after proper tuning or matching (ligh gray) (adapted from [DE GRAAF 2007]).

However, some RF coils can be tuned and matched according to their specific load. Most of the time, variable capacitors are positioned in the resonating circuits to adjust their complex impedance and resonance frequency. As illustrated by Figure 2.4, the fulfilment of both conditions maximize the transmission efficiency and minimize reception losses due to power reflection along the transmission or reception chains.

2.2.1.2 Reference Voltage

Calibration of the reference voltage (or power) of the transmission channel is usually realized at the beginning of each NMR experiment by evaluating the voltage that need to be applied to realize a a 90° flip angle with a 500 microsecond square pulse (or a 180° FA with a 1 millisecond pulse). For Siemens scanners, this calibration step is automatically implemented for ^{1}H channels . But it has to be performed manually for X-nuclei explorations. A simple and generic approach is to acquire a serie of non-localized Free Induction Decay (FID) spectra while sweeping the range of possible voltages. If TR is sufficiently long (TR > 5 T_1) and the B_1^+ profiles not too inhomogenous, the 90° flip angle is reached when the NMR signal is maximized as illustrated by Figure 2.5.

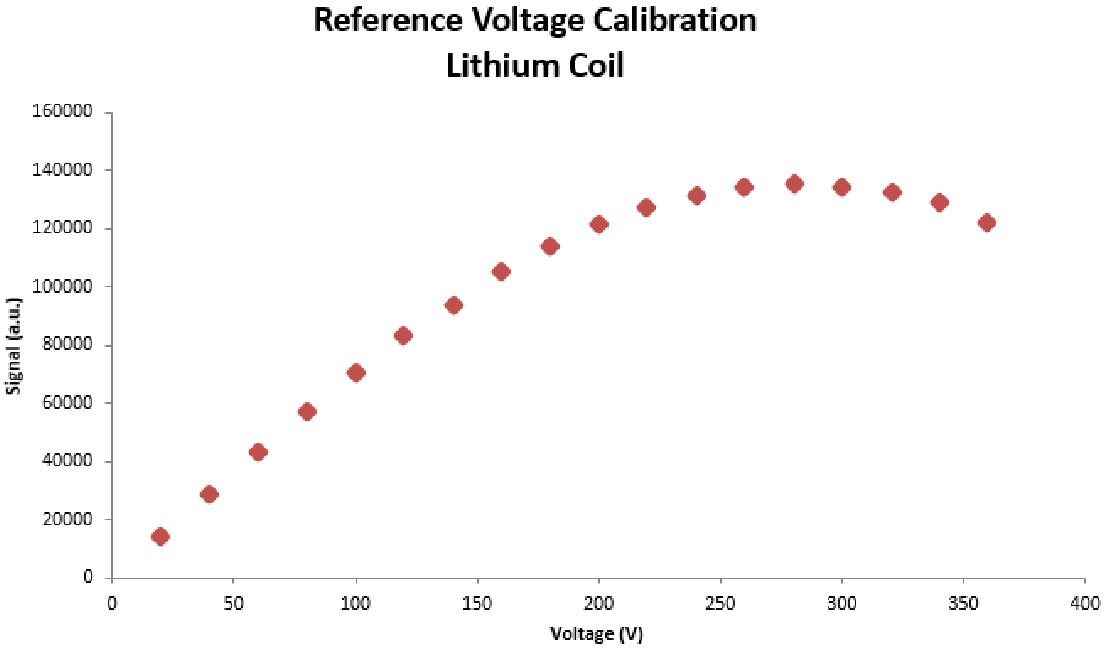

Figure 2.5: Reference voltage calibration for our dual resonance ^{1}H/^{7}Li birdcage coil. A value of 280V was set for our ^{7}Li channel.

As the reference voltage varies with the load this calibration should be repeated for each new subject. For time purpose, the voltage sweeping resolution can be lowered significantly and the response curve can be interpolated from few acquired samples. This method, based on 4 or 5 spectroscopic acquisitions was implemented by Franck MAUCONDUIT (Siemens) and was used during most of our X-MRI experiments at 7 T and as part of our quality control process presented later.

2.2.1.3 B_1 Mapping

Beyond the reference voltage, a better approach is to assess B_1^+ profiles of the coil via the map of the effective flip angle or the map of the required voltage to achieve a targeted flip angle. Three methods are presented.

The XFL sequence corresponds to a Magnetization prepared FLASH sequence and was developed by Alexis AMADON [AMADON 2010]. With the XFL sequence, the coil transmission field is computed from two acquisitions where the first one is acquired following a low intensity saturation pulse. Figure 2.15 shows our sodium coil transmission profile obtained with the XFL sequence.

The Double Angle Method (DAM) [STOLLBERGER 1988, CUNNINGHAM 2006] consists in two separate acquisitions with the same parameters except for a double flip angle realized for one acquisition. Based on the magnitude of reconstructed images, the transmission field map can be computed using:

$$\alpha(r) = \arccos\left(\frac{|I_{2\alpha}(r)|}{2|I_{\alpha}(r)|}\right) \qquad \text{[Stollberger 1988]} \tag{2.2}$$

This method is pretty convenient to use on clinical MR scanners as it can readily be performed with a standard GRE acquisition sequence and do not require to install any new sequence. We used it for our *in vivo* explorations at 3 T and results are presented in Chapter 4.

The Actual Flip Angle Imaging (AFI) sequence [Yarnykh 2007] is another transmission profile mapping sequence. As both previous methods, it is also based on two GRE signal acquisitions but with distinct TR that could be merged into the same imaging acquisition. It uses the ratio of the resulting longitudinal magnetization for both TR where the second TR has to be significantly longer than the first (four or five times):

$$r = \frac{S_2}{S_1} = \frac{1 - E_1 + (1 - E_2)E_1\cos(\alpha)}{1 - E_2 + (1 - E_1)E_2\cos(\alpha)} \qquad \text{[Yarnykh 2007]} \tag{2.3}$$

When TR are short enough that the first order approximation of the exponential terms can be used leading to:

$$\alpha \approx \arccos\left(\frac{r\frac{TR_2}{TR_1} - 1}{\frac{TR_2}{TR_1} - r}\right) \qquad \text{[Yarnykh 2007]} \tag{2.4}$$

The AFI is well suited for exploration of flip angles comprised between 50° and 60° as demonstrated by an error minimization computation. The sequence can be upgraded to a "BAFI" sequence allowing to estimate the static field map by means of two echoes. The AFI method was improved [Nehrke 2009, Choi 2014] and combined with a Variable Flip Angle (VFA) approach for longitudinal relaxation time mapping known as VAFI [Hurley 2012].

Other methods are available such as the Bloch-Siegert Shift [Sacolick 2007] (BSS), Dual Refocusing Echo Acquisition Mode (DREAM) [Nehrke 2012] or Phase Sensitive (PS) [Morrell 2008] but were not explored during this thesis.

2.2.1.4 Reception Gain

Each MR scanner also possesses internal analogical signal amplifiers of various possible gains. For non-proton MR explorations with low signal intensity, reception gain has to be set to higher values than for hydrogen. Depending on MR scanner vendor and operating systems, gains can be modified individually or globally. Moreover, when working with DICOM format, for image encoding, an additional conversion factor can be added to convert the ADC numerical range to the 12 bits storage capacity of DICOM images. A conversion gain (called FFT factor on Siemens systems) has to be manually set for this purpose. Incorrect setting of this gain can jeopardize resulting image dynamic by either saturating some areas or compressing the integer resulting range. For our explorations, choice was made to work with raw data stored on a 32 bits floating value type. Post-processing was carried out conserving the same numerical type and dynamic to maintain numerical precision.

2.2.2 Proton Birdcage Coil

A single channel Tx/Rx ^{1}H birdcage coil (Invivo Corp., Gainesville, FL, USA) (Figure 2.6) was used on the 7T scanner to test several sequences and explore our reconstruction algorithm at higher spatial resolutions thanks to the high SNR in ^{1}H MRI.

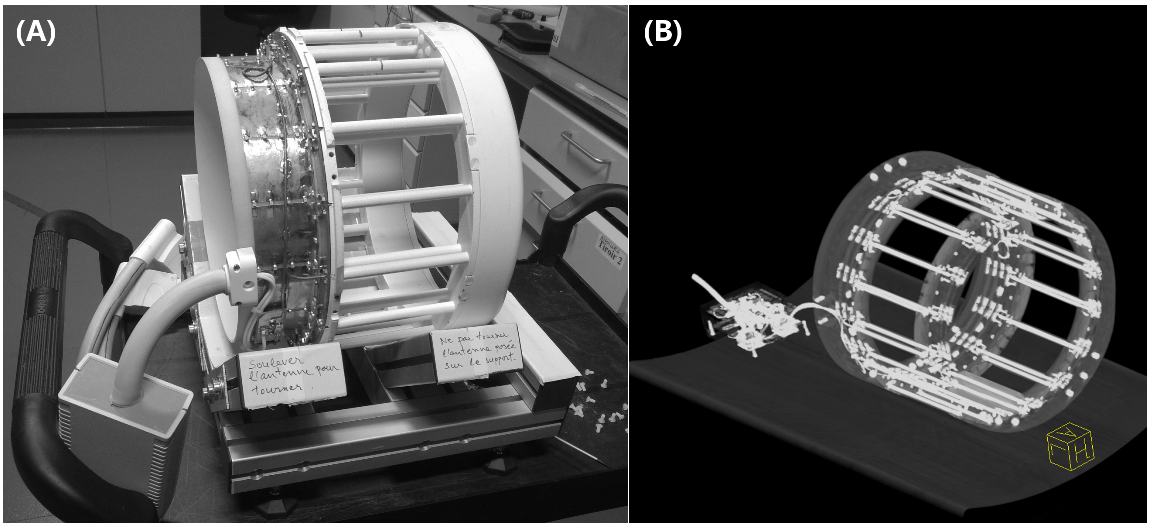

Figure 2.6: ^{1}H 1Tx/1Rx birdcage coil (A) with its X ray image (B) (courtesy of Lisa LEROI and Alexandre VIGNAUD).

2.2.3 Phosphorus Phased Array Coil

Phosphorus experiments were performed at 7 T using an eight transmit and eight receive channels (8Tx/8Rx), dual resonance ^{1}H/^{31}P phased array coil manufactured by Resonant Research Incorporated (RRI, Billerica, MA, USA) presented in Figure 2.7. The coil is made of two parts, the bottom one embed 5 loops and the top part the remaining 3. This design was proposed by N. AVDIEVICH [AVDIEVICH 2011] to maximize the sensitivity in selected area using B_1 shimming approaches at the expense of the overall B_1^+ field homogeneity for the circular polarization (CP) mode.

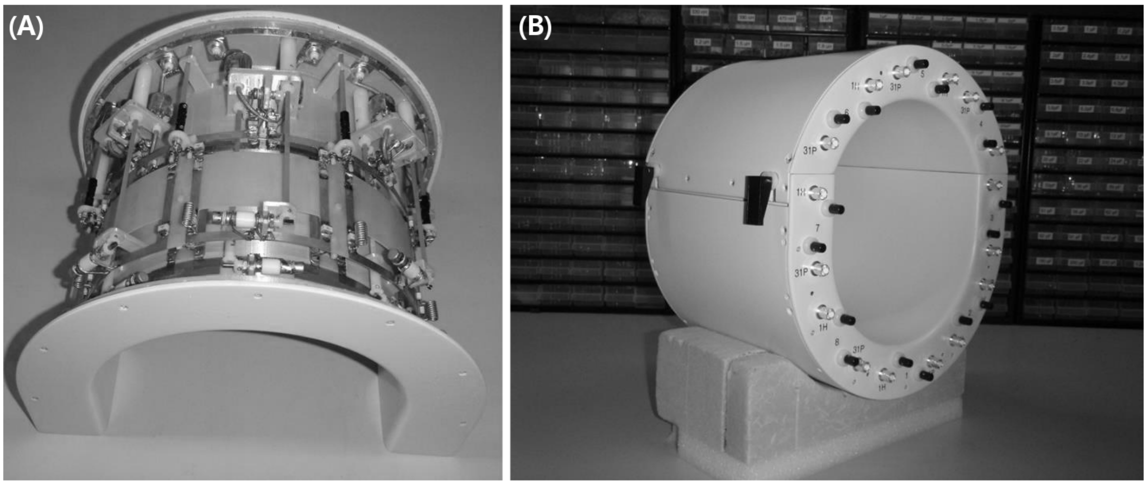

Figure 2.7: Pictures of the pTx 8Tx/8Rx dual tune ^{1}H/^{31}P coil (Courtesy of Alfredo LOPEZ KOLKOVSKY).

Manual tune and match is possible with this coil using variable capacitors visible on Figure 2.7. Manual voltage calibration was performed for the Phosphorus channel as illustrated by Figure 2.8 and using an homogeneous ellipsoidal phantom described later.

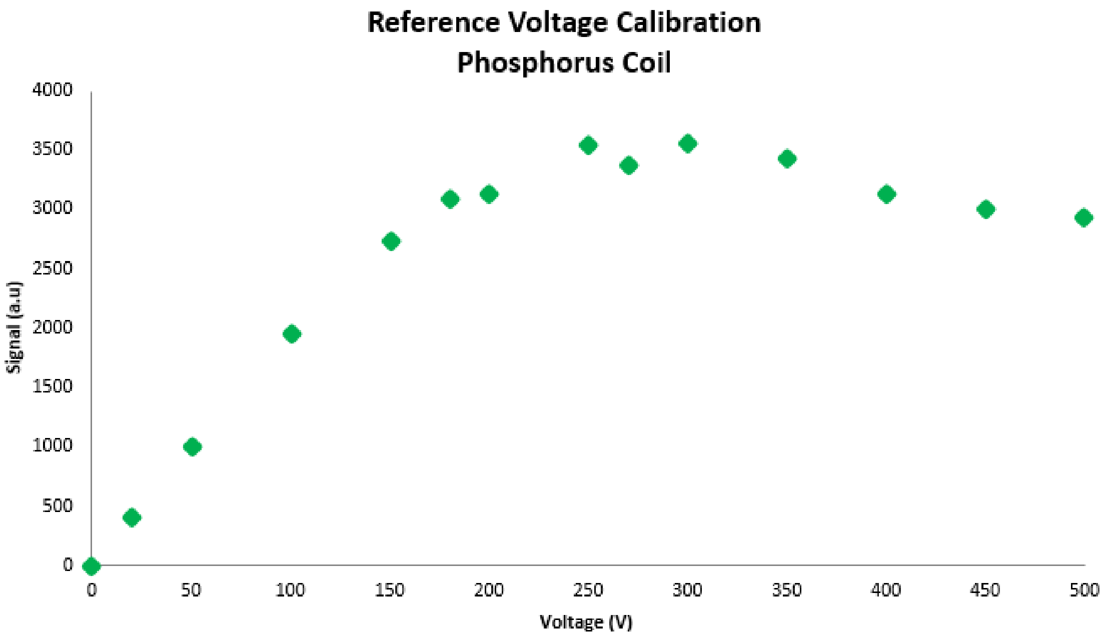

Figure 2.8: Plot of the amplitude of each acquired non localized spectra for a reference voltage calibration process of the ($^{1}H/^{31}P$) coil.

2.2.4 Lithium Birdcage Coil

Lithium experiments were performed at 7 T using a dual resonance $^{1}H/^{7}Li$ 1Tx/1Rx birdcage coil manufactured by Rapid Biomedical (Rimpar, Germany). This generic design was chosen to maximize the interior diameter of the coil and improve the comfort of the bipolar patients (Figure 2.9). No manual tune and match was possible for this coil. Manual voltage calibration using an homogeneous ellipsoidal phantom (described in a following section) was performed for the ^{7}Li channel as illustrated by Figure 2.5.

2.2.5 Sodium Birdcage Coil

A dual resonance $^{1}H/^{23}Na$ 1Tx/1Rx birdcage coil (Rapid Biomedical, Rimpar, Germany) was used for 3 T Sodium MRI at Aachen University Hospital. Excepted some minor differences, this design is similar to the Lithium birdcage coil as illustrated on the right panel of Figure 2.9.

2.2.6 Design and Realization of a non-human primate Sodium coil

As Sodium MRI explorations started at NeuroSpin with this PhD thesis, development of a dedicated RF coil was mandatory. With the prospect of *in vivo* ^{23}Na MRI at 11.7 T of non-human primates in the coming years, we designed and realized a hemi-volumic single channel ^{23}Na coil. As illustrated by figure 2.10, the home-made coil is composed of two distinct resonating circuits: a first coil positioned on top of the monkey head (in the sphinx position) and a second coil (divided into two parts) covering both sides of the monkey head. Loops were printed on a flexible conductive material to be then fixed onto the semi-cylindrical shape of the coil (Figure 2.12). A dedicated electronic hardware circuit was added at the back of the coil to handle the power transmission for excitation and signal amplification for reception. The electrical diagram of the coil's hardware can be summarized according to Figure 2.11. The two resonant circuits are merged as a single transmit and

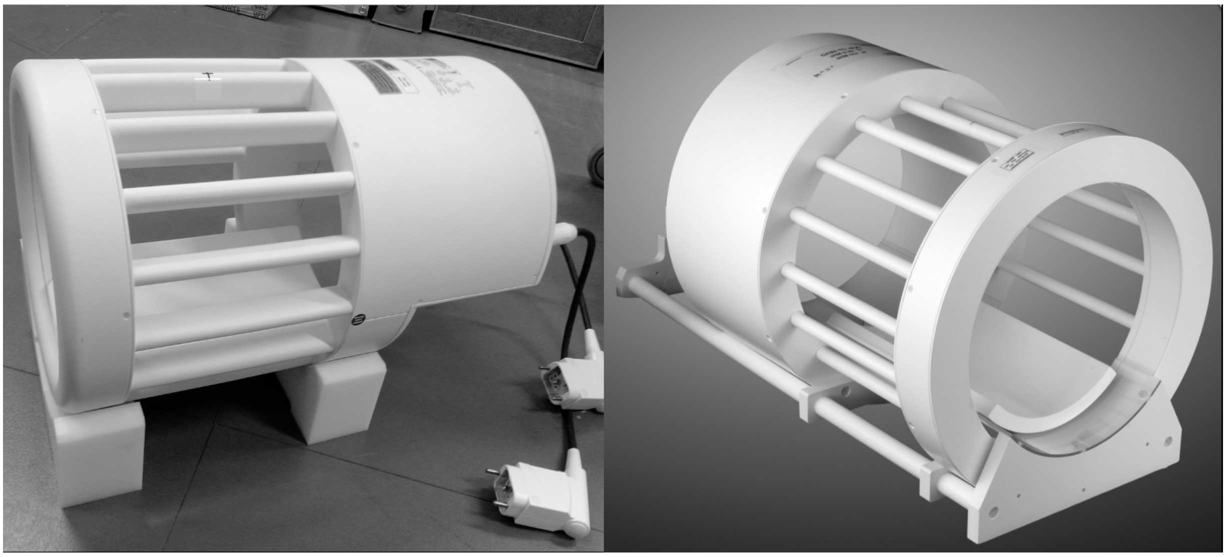

Figure 2.9: Picture of the Rapid Biomedical ^{1}H/^{7}Li 1Tx/1Rx birdcage coil (left) (courtesy of F. BOUMEZBEUR) and picture of the Rapid Biomedical ^{1}H/^{23}Na 1Tx/1Rx birdcage coil (right).

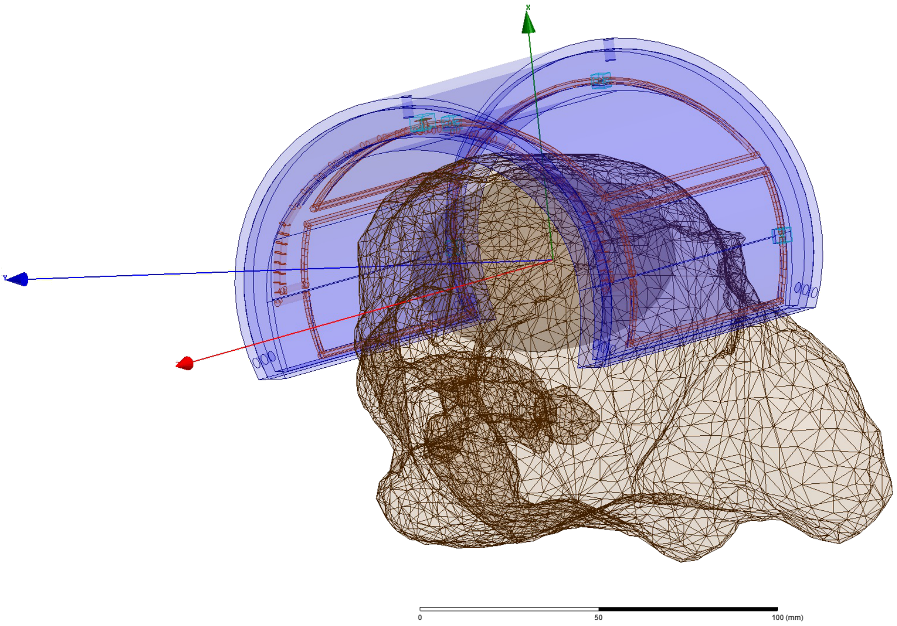

Figure 2.10: 3D model of the Sodium coil design on a non human primate head model(courtesy of Marie-France HANG).

receive channel. Commutation between transmission and reception is ensured using a "TR switch" driven by a TTL (Transistor Transistor Logic) signal provided by the MR scanner. A TTL signal is a digital signal used for hardware synchronization. "Balun" elements were used to convert coaxial loop connections to electronic printed circuit board (PCB) striped circuits. On the receive channel, an analogical signal preamplifier was added. Specific software setup is needed for each and every RF coil. For this home-made coil, a mock proton channel was declared so the system could operate. Due to this mock ^{1}H channel, automated calibrations were disabled. Using the voltage calibration method presented before, a reference voltage of 100 V was evaluated *in vitro* as illustrated by

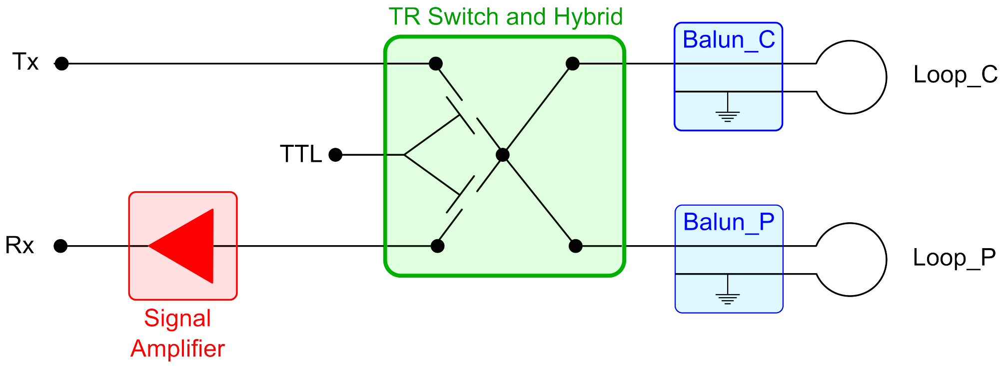

Figure 2.11: Simplified diagram of the electrical part of the coil.

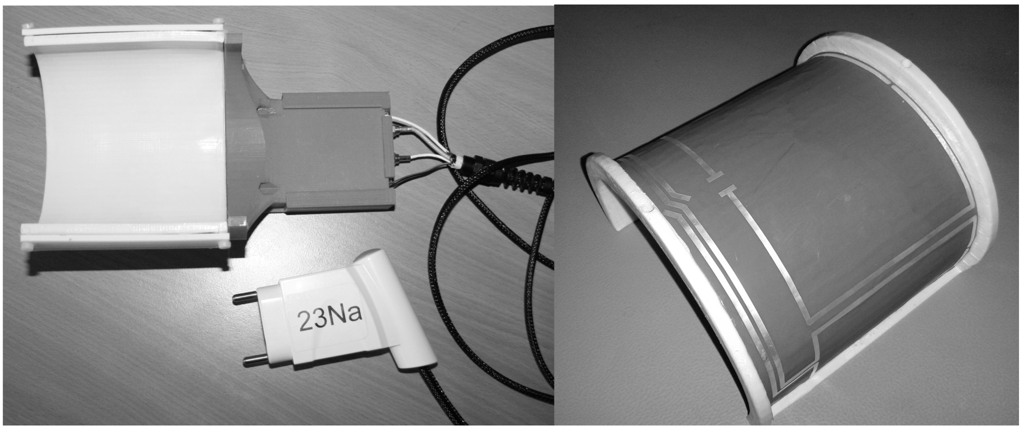

Figure 2.12: Picture of our homemade single transmit single receive non-human primate Sodium coil (left) and a model of the contained loops (right).

Figure 2.13.
Simulations of the B_1^+ field were computed using HFSS (Figure 2.14) and compared to *in situ* maps obtained using the XFL sequence (Figure 2.15) using a low flip angle (5°) and then interpolated. Indeed, spatial variations of both reception and transmission fields in homogeneous media can be smoothed with large width kernels or fitted using low order spatial polynomials. Both B_1 field profiles are in agreement with slightly better transmission and reception efficiency on the right side of the coil.

2.3 Test Objects

Test-objects or "phantoms" are important components for methodological development, *in vitro* validation, but also for quality control purposes in clinical environment. For instance, they are used for calibration and to evaluate longitudinal hardware evolution and stability. Phantoms are designed to display specific physico-chemical properties (concentrations, density, diffusion coefficent or relaxation properties). Many phantoms were made and used during this PhD thesis.

2.3.1 Concentration

The following phantoms were used to test and validate concentration quantification pipelines or to be used as external references of concentration:

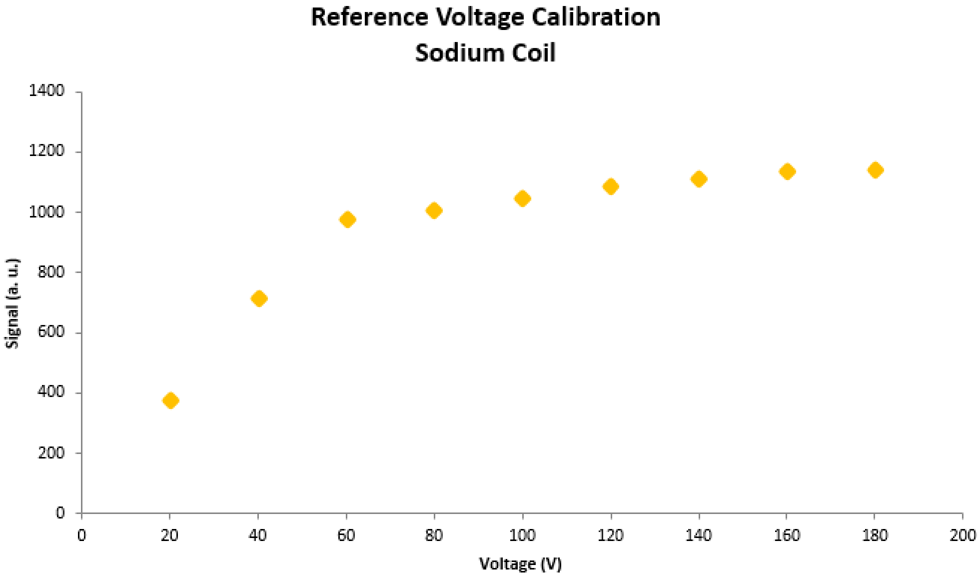

Figure 2.13: Voltage calibration curve of our homemade sodium coil. Calibration was performed on an homogeneous cylinder filled with saline solution at 150 mmol.L^{-1}.

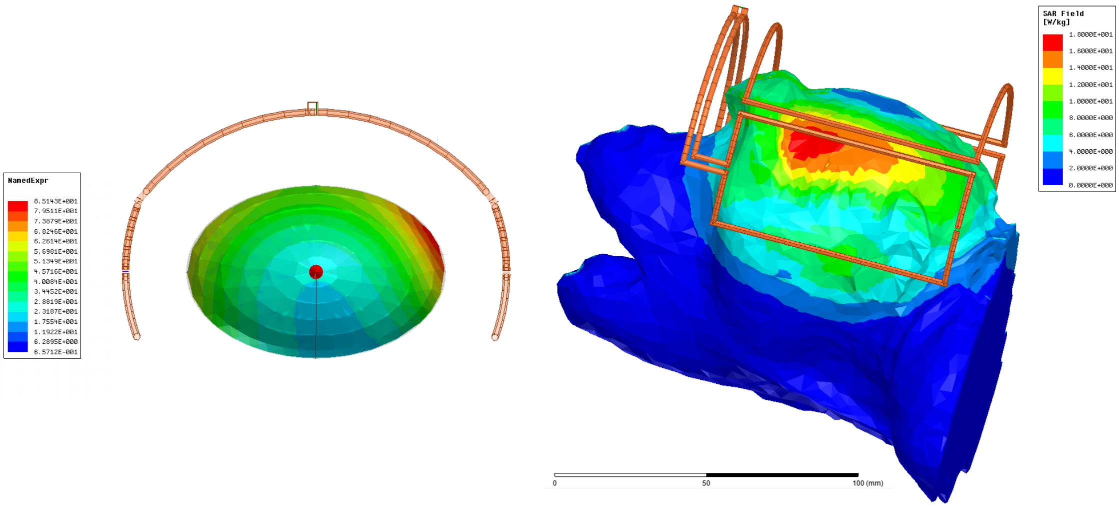

Figure 2.14: Simulations of the B_1^+ field of the coil using HFSS (courtesy of Marie-France HANG).

- Phantoms 31P-7T-1 and 7Li-7T-1 (Figure 2.16);
- Phantom 31P-7T-2 (Figure 2.17);
- Phantom 23Na-3T-1 and 7Li-7T-2 (panels A and B)(Figure 2.25);
- Phantom 23Na-7T-1 (Figure 2.18).

2.3.2 Spectral Selectivity

Two phantoms (ref=31P-7T-3 and ref=31P-7T-4) were realized to validate the spectral validity of our non-Cartesian SSFP sequence for ^{31}P MRI. As illustrated by Figure 2.19, both consisted in different

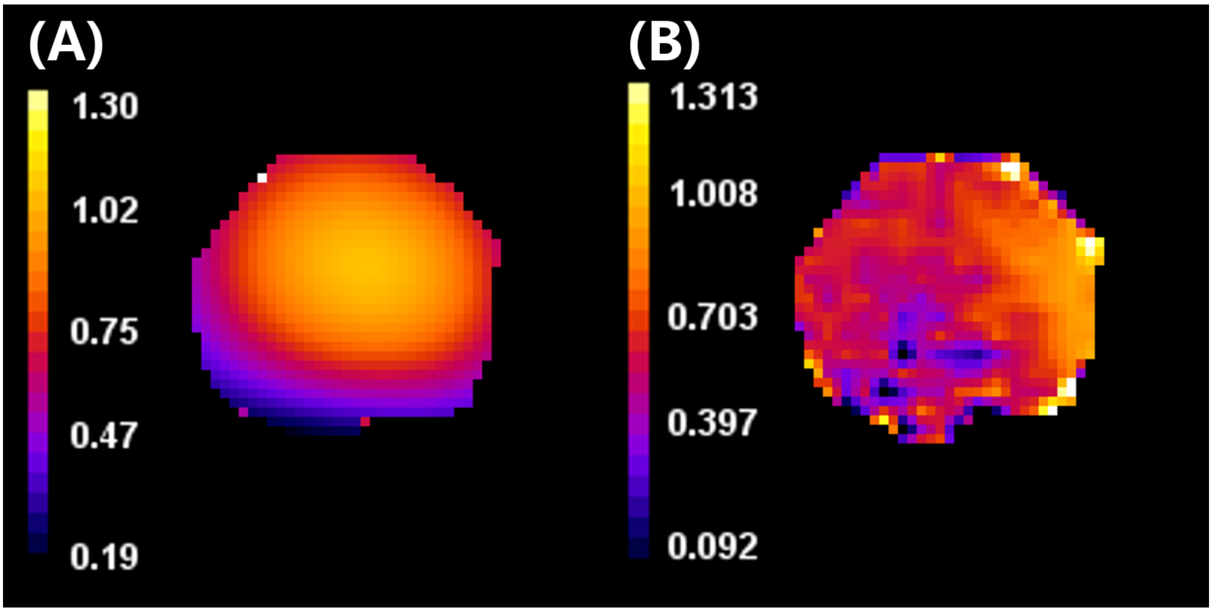

Figure 2.15: Maps of reception (A) and transmission (B) profiles of our homemade Sodium coil.

compartments filled with either PBS (*i.e.* Pi), PCr or ATP at various concentrations.

2.3.3 Resolution

Resolution phantoms are useful to check on the actual spatial resolution achieved using a given K-space trajectory or the consequences of a certain parametrization of our reconstruction algorithms. In addition of phantom 31P-7T-2 (Figure 2.17), two other phantoms were used:

- Phantom 1H-7T-1 (Figure 2.20);
- Phantom 23Na-7T-2 (Figure 2.21).

While phantom 1H-7T-1 was a Bruker resolution phantom that we recovered from our old 3 T whole-body MR scanner, phantom 23Na-7T-2 was made to test our non human primate ^{23}Na coil and the pulse sequences developed for ^{23}Na MRI at 7 T. The design of the disk and its holes of different sizes was modeled using blender [The Blender Foundation] and J. BERNARD built it.

2.3.4 Relaxation

In order to validate the quantification of relaxation rates using either the VFA (Chapter 4) or the QUICS (Chapter 5) approaches, phantoms 23Na-3T-1 and 23Na-7T-1 were prepared with 50mL tubes containing agarose gels of various density (Figure 2.18). The cylinder was made by J. BERNARD, from NeuroSpin's mechanic team, to fit the dimensions of our homemade Sodium coil. It allows to insert various objects inside as tube holders or disks with holes for resolution studies as illustrated on Figure 2.21.

Besides for external referencing purposes, *in vitro* longitudinal and transverse relaxation rates were also measured from phantoms 31P-7T-1 and 7Li-7T-1 using non-localized or SVS T_1 and T_2-weighted ^{31}P (Figure 2.22) or ^{7}Li MR spectra (Figure 2.23).

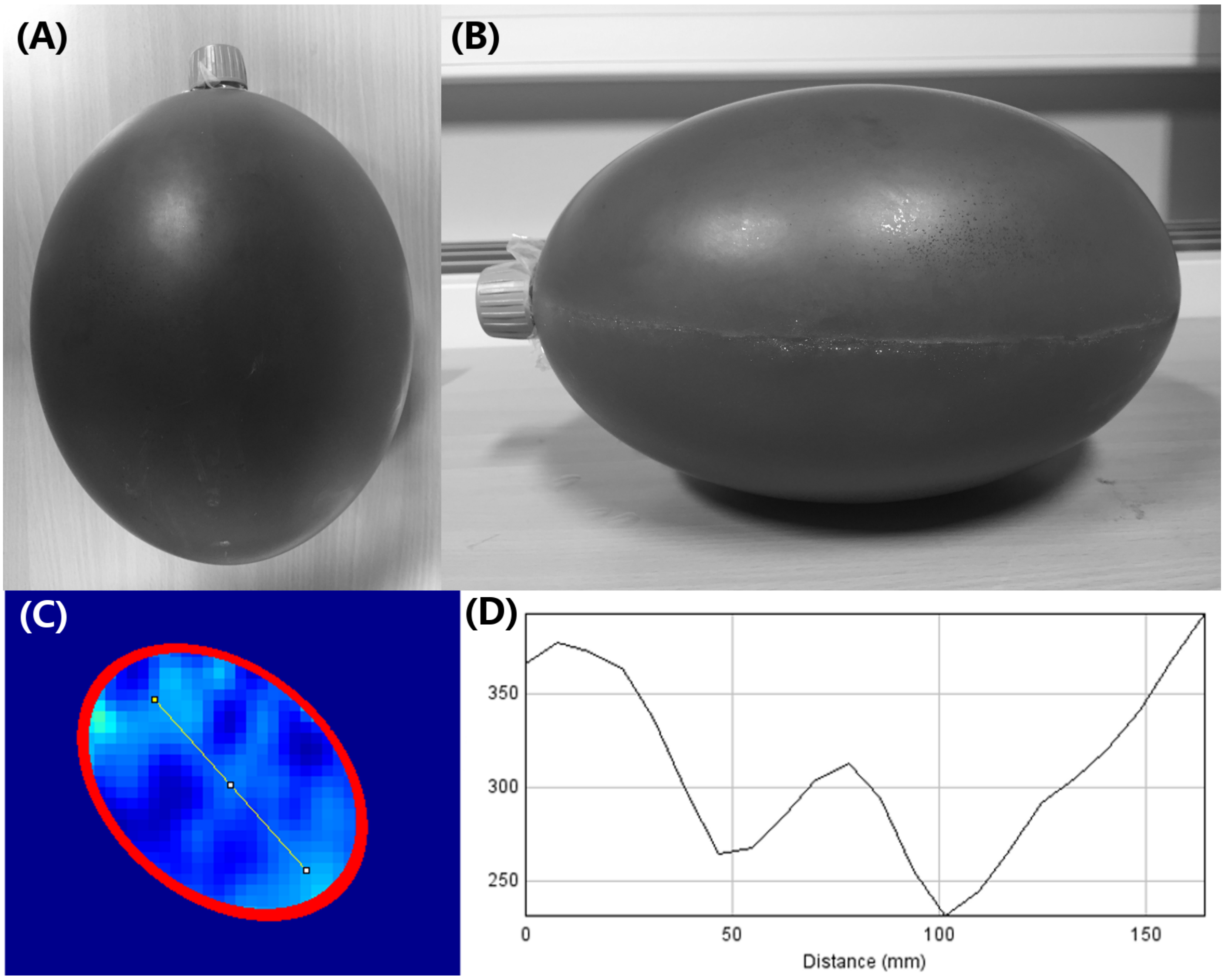

Figure 2.16: Ellipsoidal 4.2 L phantom (ref=7Li-7T-1 and ref=31P-7T-1) (A,B) used to measure the B_1 coil profiles (C) of our dual resonance ${}^{1}\mathrm{H}/{}^{31}\mathrm{P}$ or ${}^{1}\mathrm{H}/{}^{7}\mathrm{Li}$ RF coils with the XFL sequence. The same phantoms were also used as external reference of concentrations as this phantom presents a load similar to a Human head. One can notice the heterogeneous transmission profile of our ${}^{31}\mathrm{P}$ phased array coil (D) plotted along the yellow line of panel (C).

2.3.5 Diffusion

To test the quantification of the apparent diffusion coefficient using the QUICS sequence (Chapter 5), phantom 23Na-7T-X was prepared with 150 mL glass bottles containing NaCl solutions with different sucrose (Sigma-Aldricht) content to modify their viscosity.

2.3.6 Combined phantom

For our explorations in Sodium at 3 T, we used an identical phantom design as used for phosphorus spectral explorations (31P-7T-4) and illustrated in Figure 2.25. The four large tubes ($\oslash$ 28 mm) contain agarose gel at either 2% or 6% with Sodium concentrations of 50 or 150 mmol.L^{-1}. The set of small tubes ($\oslash$ 10 mm) are filled with saline solution at different concentrations matching the bioscale [25,150] mmol.L^{-1}.

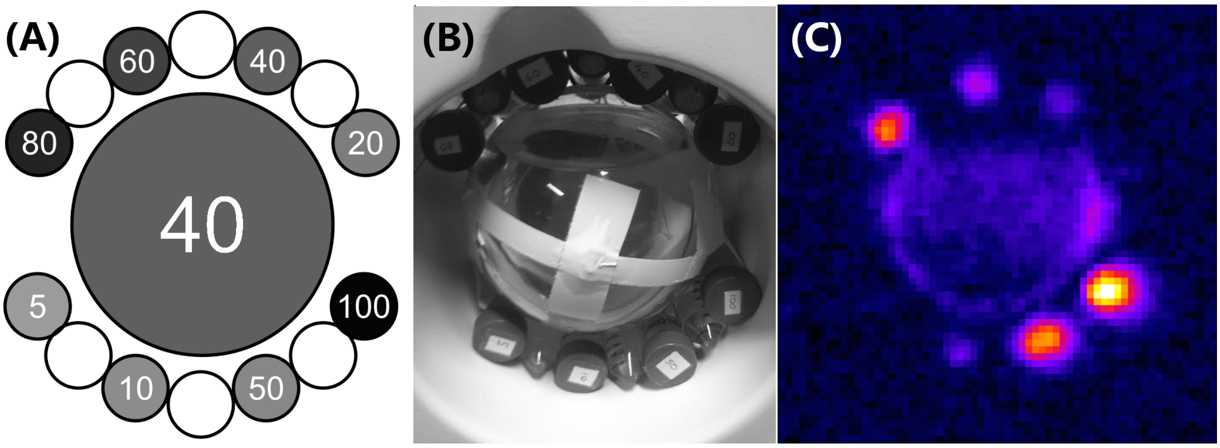

Figure 2.17: Schematic of our second 7 T Phosphorus phantom (ref=31P-7T-2)(A), its setup in the $^{1}H/^{31}P$ coil (B) and an example of ^{31}P TPI image obtained using a 3D non-Cartesian SSFP sequence (C). The 2 L sphere (⌀ 160 mm) and its two galleries of 50 mL tubes (⌀ 28 mm) filled with phosphate buffer solution (PBS) at known concentrations has been used to evaluate the sensitivity of our ^{31}P MRI sequence.

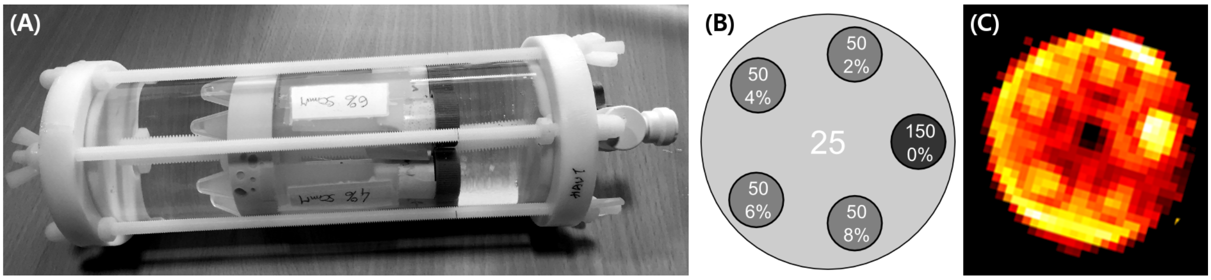

Figure 2.18: Picture of our 7 T Sodium Relaxation phantom (ref=23Na-7T-1) (A), its associated diagram (B) and sodium MR Image non-Cartesian SPGR acquisition (C). The concentration in Sodium is indicated in mmol.L^{-1} as well as the agarose density in tubes. Removing the tube holder allows to obtain an homogeneous cylinder (ref=23Na-7T-E).

2.4 Compliance with Regulations

MR scanners and RF coils are medical devices for which compliance to regulations is a prerequisite to Human explorations. The clinical application of our developments made us explore those regulatory aspects to ensure clinical viability of our research protocols.

Specific Absorption Rate (SAR) corresponds to the power dissipated by the RF coil into the subject. SAR limitations are set to avoid any injury due to excessive local (over 10 g) or global (less than 10 W/Kg or 3.2 W/Kg averaged over 10 minutes) transfer of energy (mostly as heat in tissues) [IEC 2015]. For this PhD thesis, standard SAR evaluation was computed by the MR scanners and all our sequences were able to pass this first step.

Another regulation about patient comfort and safety consists in limiting noise produced by gradients during the experiment to a maximum mean value of 99 dB
[IEC 2010]. The use of earplugs and noise absorbing ear protections enables a possible increased value of the mean measured noise of the sequence to 119 dB. Our clinical protocols were subjected

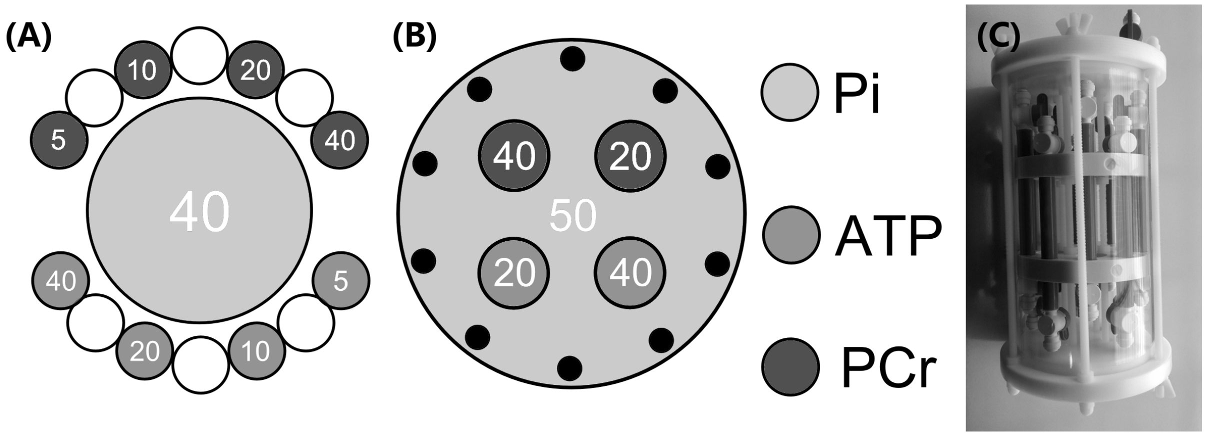

Figure 2.19: Schematic of phantoms 31P-7T-3 and 31P-7T-4 used to validate the spectral selectivity of our ^{31}P MRI sequence. The first one consists in a 2L sphere with two galleries of 50 mL tubes (A). The second one consists in a cylinder we designed (B) and its picture (C). All indicated concentrations are in mmol.L^{-1}.

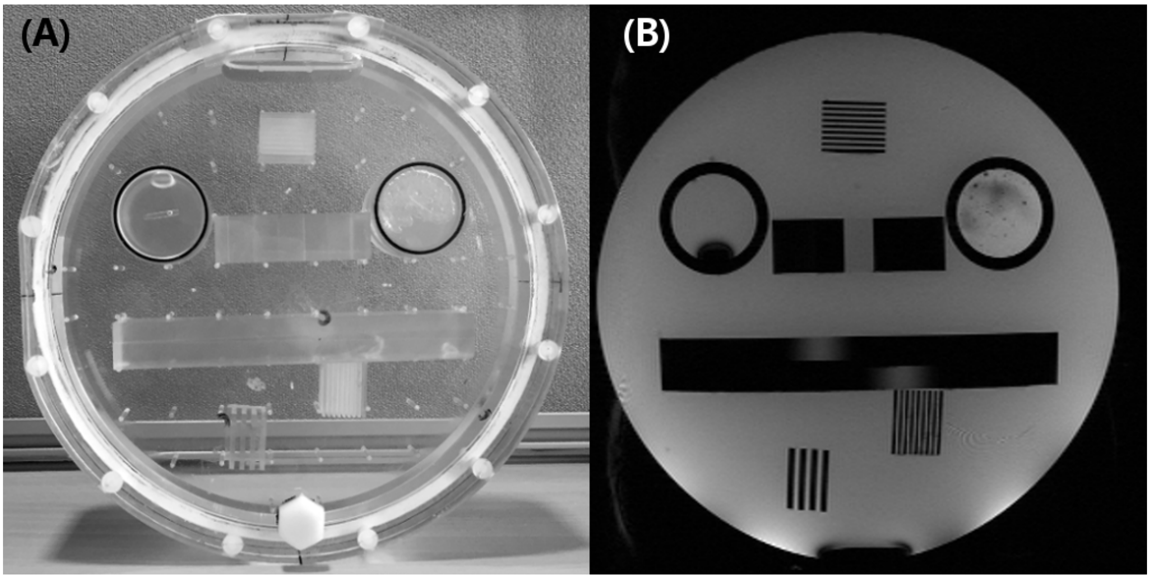

Figure 2.20: Picture (A) and reference ^{1}H MRI (B) of the Bruker resolution phantom (ref=1H-7T-1).

to noise measurements prior to human explorations using a RION NA-28 microphone placed in the coil on the side of a phantom mimicking the head. Compared to the very noisy T_{1w} MPRAGE sequence (average = 114 dB and peak=127.7 dB), our relatively low-resolution X-MRI acquisitions generated moderate noises (average < 90 dB / peak $\approx$ 100 dB).

2.5 Coil Quality Control

A very important aspect to ensure good image quality and consistency for *in vivo* studies is to be able to maintain identical acquisition characteristics over time. Therefore, it is mandatory to regularly evaluate hardware performances and asses their stability. With the help of Alexandre VIGNAUD and Franck MAUCONDUIT a quality control pipeline for our non proton studies was developed. Placing of the coil and the phantom on the MR scanner was achieved using a dedicated holder

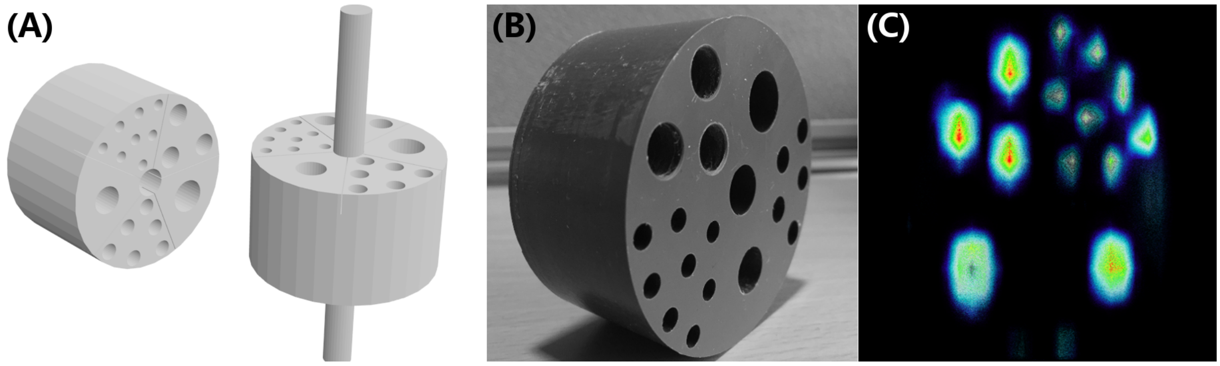

Figure 2.21: 3D views (A) and picture (B) of our resolution phantom (ref=23Na-7T-2) and its ^{23}Na MRI at 7 T (C). Holes diameters are 12,10,8,6 and 4 mm.

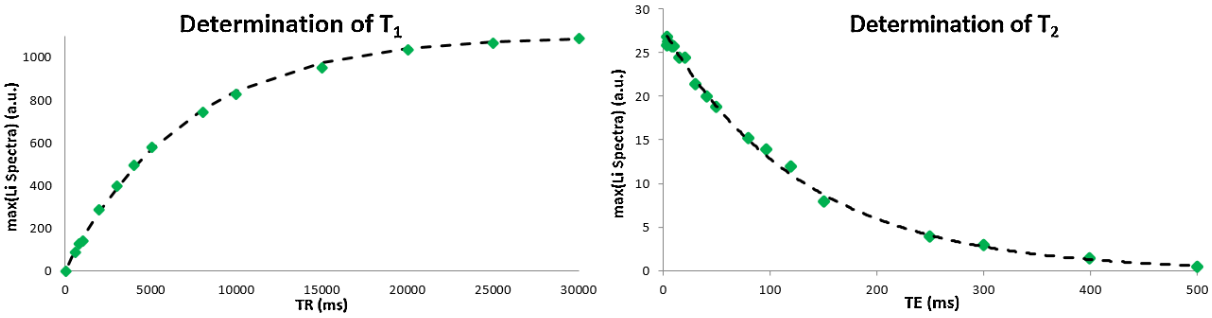

Figure 2.22: Determination of ^{31}P longitudinal (left) and transverse (right) relaxation rates *in vitro* using a mono-exponential model. Using PRESS acquisitions, the progressive saturation method (TR $\in$ [200,30000] ms) yielded a T_1 of about 7 s. By increasing the echo-time (TE $\in$ [5,500] ms), a T_2 of about 170 ms was estimated. Measurements were made on a spherical phantom filled with PBS solution at 50mmol.L^{-1}.

to get reproducible measurements. The pipeline is composed of either standard or home-made acquisitions sequences and used a dedicated spherical Siemens spectroscopy phantom containing Sodium and Lithium Chloride. The following procedure is now run on a regular basis prior to any new acquisition of lithium-treated bipolar patient:

- Standard ^{1}H 2D GRE (Localizer) to ensure proper functioning of the ^{1}H channel;
- Noise estimation using two ^{1}H GRE EPI acquisitions with FAs of 8° and 80°
- Reference Voltage estimation using ten ^{1}H GRE EPI acquisitions with angles linearly distributed in [8°, 80°] for the ^{1}H channel;
- ^{7}Li Reference Voltage estimation using five non localized FID spectra;
- Assessment of ^{7}Li B_1^+ map and mean flip angle in phantom using the XFL sequence;
- SNR estimation on a standard Cartesian ^{7}Li GRE sequence.

All parameters are saved and plotted over time, any significant variation are interpreted as a sign of possible hardware malfunction. Figure 2.26 and Figure 2.27 illustrate some results obtained for the

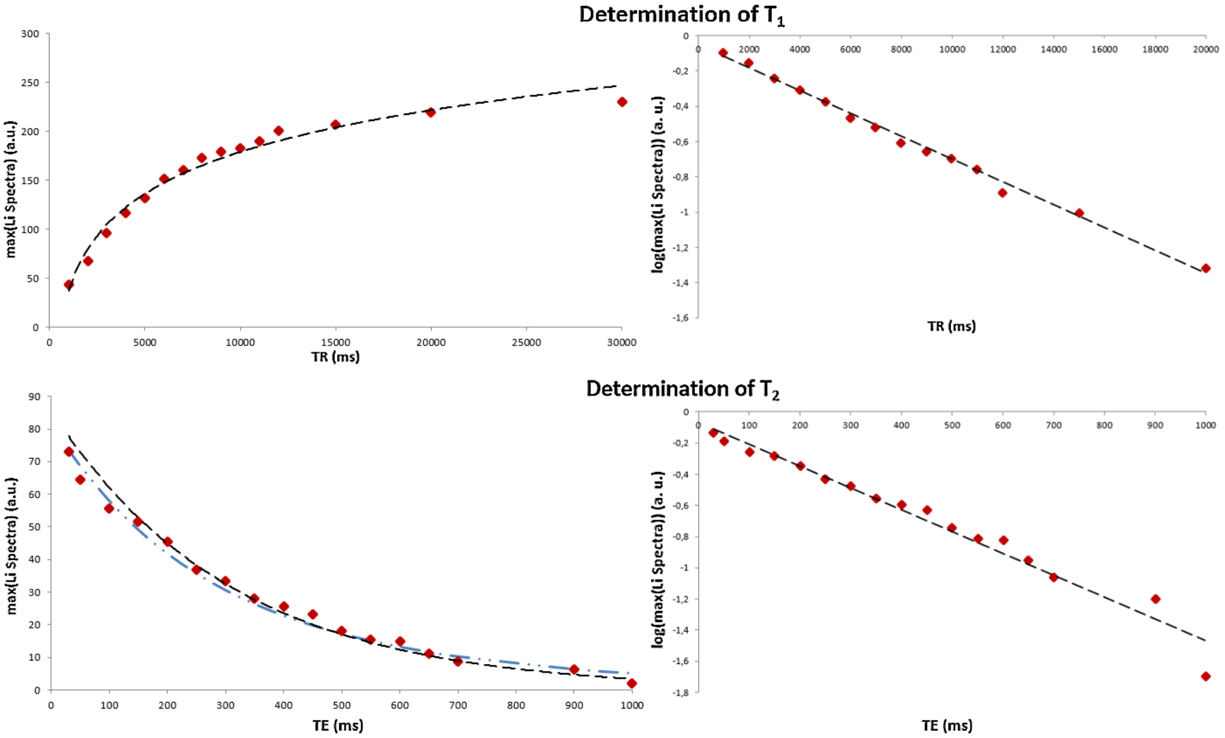

Figure 2.23: Determination of ^{7}Li longitudinal (top) and transverse (bottom) relaxation rates *in vitro* using a mono-exponential (left) and their corresponding semi-logarithmic linear fits (right). Using PRESS acquisitions, the progressive saturation method (TR $\in$ [400,20000] ms) yielded a T_1 of about 14 s. By increasing the echo-time (TE $\in$ [30,1000] ms), a T_{2mono} of about 310 ms was estimated. Notably, a bi-exponential fit of the transversal decay yielded a slightly better fit with a T_{2s} of 220 ms and T_{2f} of 510 ms (blue dash-dotted curve).

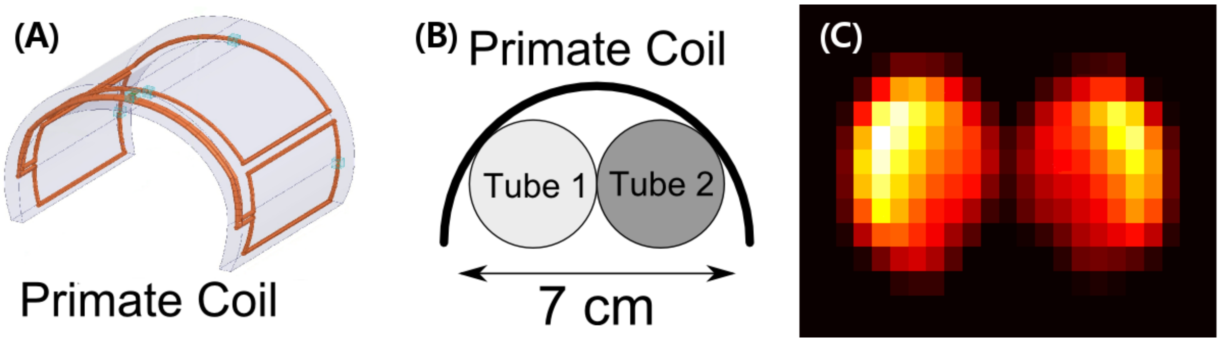

Figure 2.24: Design of the sodium primate coil (A) and schematic of the diffusion composed of two 150 mL glass bottles (B). Associated magnetization map (C) computed using the QuICS protocol presented in Chapter 5.

Hydrogen and Lithium channels. This Quality Control protocol enables the longitudinal follow-up of coil properties and guarantee constant image quality and the validity of some of our post-processing pipeline. Thanks to Franck MAUCONDUIT, such follow-up is now an inline tool of our 7 T MR scanner.

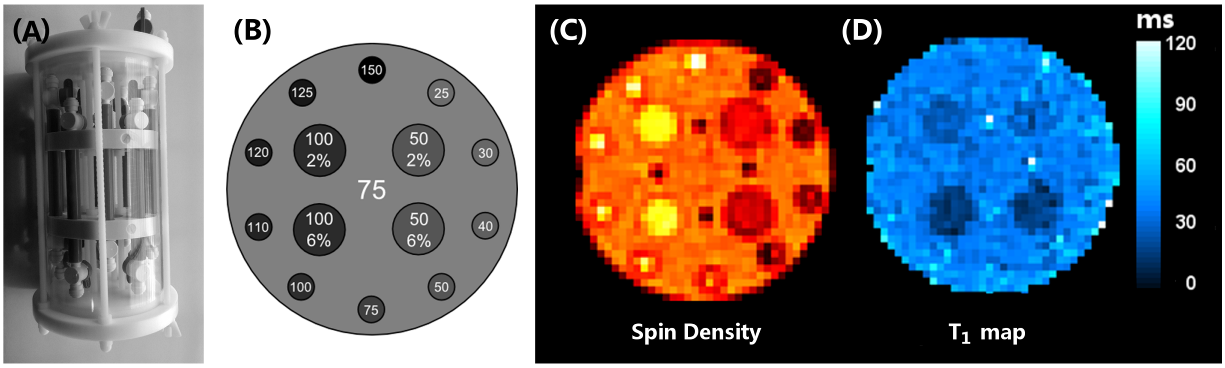

Figure 2.25: Picture (A) and schematic of the phantom with the theoretical sodium and agarose gel (in %) content (B). A spin density acquisition (TR/TE/FA/TA = 300 ms/0.1 ms/90°/18′) allows to observe the different sodium content in the different compartments (C) and a 2 angles VFA acquisition (TR/TE/FA1/FA2/TA = 20 ms/0.1 ms/25°/55°/18′)(detailed in Chapter 4) allows to obtain a T_1 map (D).

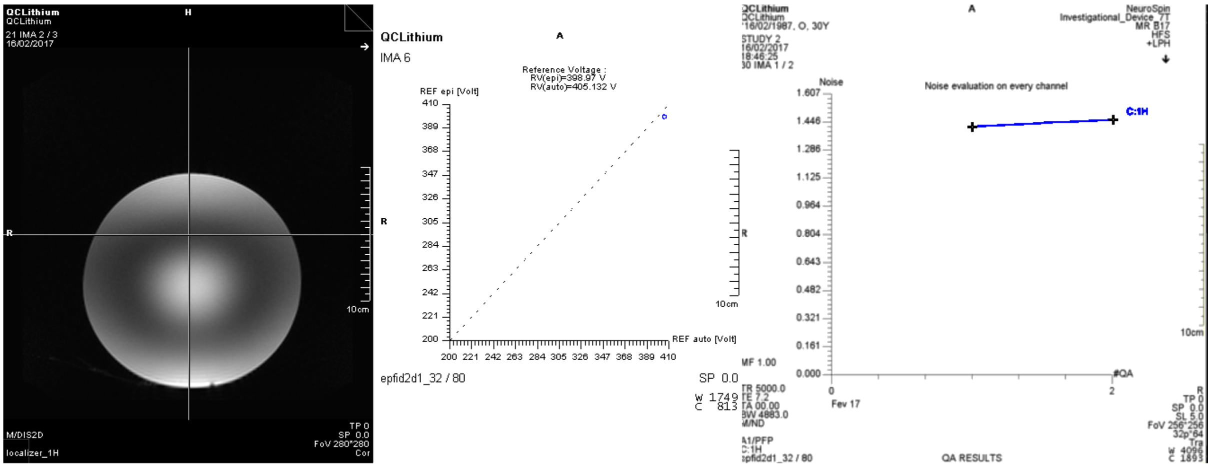

Figure 2.26: Results of the Quality Control protocol for the ^{1}H channel. The left panel shows one slice of the Localizer. The center panel shows a reference voltage correlation plot between the scanner automated process and a homemade sequence. The right panel shows the noise evaluation of the proton channel.

2.6 Conclusion and Perspectives

In this chapter, several important components of this PhD thesis were presented. Indeed, a rigorous assessment of hardware properties is a prerequisite for an efficient development, validation and parametrization of our imaging protocols. Moreover, the ability to map static B_0, transmit B_1^+ and receive B_1^- fields is often necessary for advanced data post-processing corrections.

During this PhD, a complete non-human primate surface sodium coil was designed, built, characterized and validated. I implemented all aforementioned calibration and characterization steps and circumvented many limitations of the Siemens operating system (coil files, automated voltage calibration and non-proton shimming). Other non-proton RF coils were also characterized as a preliminary step for our clinical explorations and as part of our Quality-Control procedure. All those methods should be useful beyond the scope of this PhD. Our Quality Control pipeline was imple-

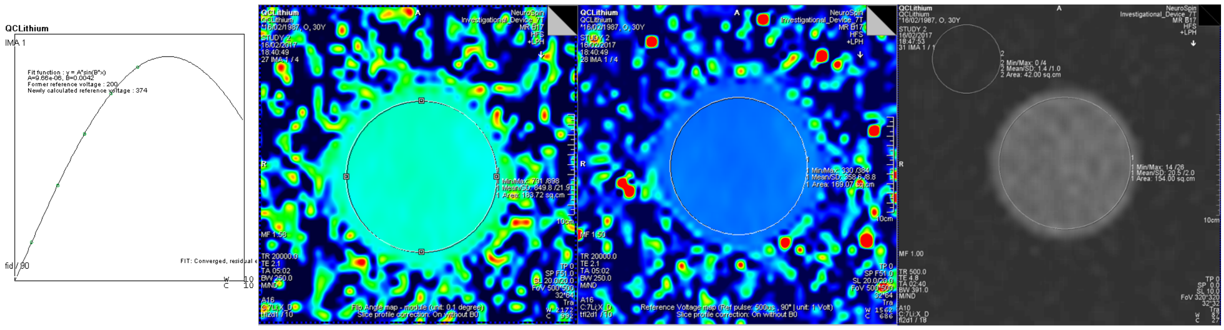

Figure 2.27: Results of the Quality Control protocol for the ^{7}Li channel. The left panel shows the automated Reference Voltage estimation based on non-localized spectra. The two center panels illustrates the flip angle map and the associated voltage map acquired with the XFL sequence. The right panel shows a standard Cartesian SSFP image (TR/TE/TA=500 ms/4.8 ms/2'40") acquired for SNR estimation and followup. Acquisitions are made on a standard Siemens spectroscopy phantom.

mented for all non-proton coils to help in assuring a robust image quality for future longitudinal, follow-up or multi-centric X-MRI studies.

A dedicated set of phantoms with different design and physico-chemical properties such as relaxation rates, concentrations, diffusion coefficients, resolution or composition were used to test and validate our MR pulse sequences and post-processing developments.

Working on multiple MR scanners was a challenge as every environment was different. Depending on the intensity of the static magnetic field or the design of the RF coil, some hardware calibration or characterization steps are bound to be more critical than others. In the scope of the future implementation of non-proton MRI at 11.7 T, it is our belief that most of these developments should be relevant.

CHAPTER 3

MR Pulse Sequences and Image Reconstruction

Contents

NMR study of non-proton nuclei remains a minor field for clinical research due to its many challenges introduced in Chapter 1. Yet, the advent of ultra-high magnetic field MR scanners such as the 7 T Magnetom or the newly minted 11,7 T Iseult magnet hold the promise of improving significantly the achievable sensitivity, as well as the anatomical specificity and coverage for X-MRI. During this PhD thesis, I aimed at establishing an efficient and adaptable platform for the acquisition and reconstruction of concentration maps for various nuclei: ^{23}Na, ^{31}P and ^{7}Li.

Thanks to our collaboration with Drs. Sandro ROMANZETTI (Uniklinik Aachen, Department of Neurology, Aachen University) and Guillaume MADELIN (Center for Advanced Imaging Innovation and Research, New York University Medical Center), we based our methodological developments regarding dedicated pulse sequences on the 3D UTE sequences: Twisted Projection Imaging (TPI) and Fermat Looped Orthogonally Encoded Trajectory (FLORET). For our tinkering with the reconstruction algorithm FISTA, presented in Chapter 1, we benefited from the help of Dr. Philippe CIUCIU and the work of his former PhD student Nicolas CHAUFFERT [CHAUFFERT 2015]. In this chapter, those developments and other explorations are reported in details.

Parts of this Chapter were submitted and presented at the annual meetings of the International Society for Magnetic Resonance in Medicine conference in 2016 or the European Society for Magnetic Resonance in Medicine and Biology in 2015.

3.1 Ultra-short Echo-Time Sequences

3.1.1 Gradient Recalled Echo Sequences

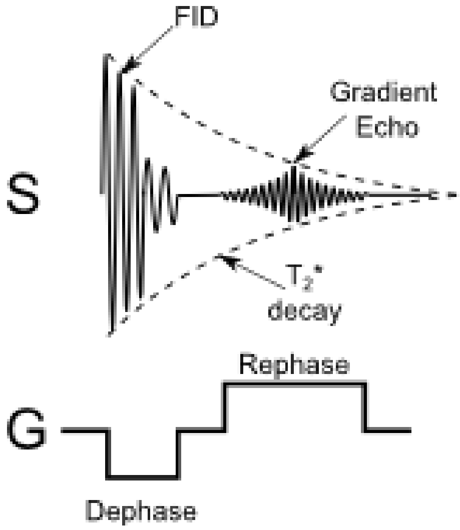

Figure 3.1: NMR signal in a GRE acquisition [ELSTER 2016].

The Gradient Recalled Echo (GRE) sequence exploits a single RF pulse to either excite the whole brain or a large slab for 3D MRI or a single slice for its 2D multislice variant. Immediately after the excitation, the Free Induction Decay (FID) loses some of its coherence due to the application of a gradient pulse along the readout direction (dephasing) followed by a reverse gradient pulse for frequency encoding. A "gradient echo" is generated during the readout as the transverse dephasing acquired during the first gradient pulse is compensated by the second gradient pulse. GRE sequences presents several advantages: (i) they do not require the use of high energy RF pulses such as the refocalisation pulse of the Spin-Echo (SE) sequences; (ii) low flip angles and adequately short TR can be used to reduce the acquisition time. Another consequence of using low flip angle is that GRE images are usually less affected by B_1^+ heterogeneities. Moreover, the excitation pulse duration can be easily shorten in order to reduce the echo-time. Compared to SE sequences, the GRE sequences are sensitive to non-random static field heterogeneities such as iron deposit or susceptibility discontinuities at air-tissue interfaces. As a consequence, T_2^* weighted images are obtained using GRE sequences. GRE sequences can also be spoiled to ensure that before each new TR and the application of the next RF-pulse, the steady-state magnetization has no remaining transverse component. Spoiling can be performed by three different methods: by setting TR in the order of five times T_2 to reach natural spoiling of the transverse component, by applying spoiling gradients with variable amplitudes at the end of each TR or by radiofrequency spoiling performed by changing the phase of the RF-carrier according to a predefined formula. The recommended method is RF spoiling thanks to its efficiency, spatial uniformity and the absence of associated eddy currents.
The application of spoiling in a gradient recalled echo sequence has consequences. Indeed when no spoiling is applied it is possible to accumulate residual magnetization from one TR to the next which can lead to an increased amount of signal but at the expense of a mixed T_1 and T_2 contrast and some B_0 artifacts. Indeed as dephasing also accumulates it can create areas where signal cancels out creating black stripes in the resulting image. Moreover, in order to obtain the desired T_1-weighting in GRE acquisitions, a sufficient number of dummy scans are performed to allow the longitudinal magnetization to reach a steady state. Typically, the number of dummy scans is set so that the total duration of this preliminary stage is equal to 5 or 10 times the T_1.

3.1.1.1 Spoiled Gradient Recalled Acquisition in Steady State

Spoiled Gradient Recalled Acquisition in Steady State (SPGR/FLASH) sequence is a special kind of GRE sequence where the remaining transverse magnetization is spoiled after having been sampled during readout. Spoiling is realized using both gradient and RF spoiling. In such sequence, signal behavior is complex and defined, in the case of a Spoiled GRE by:

$$S_{spoil} \propto \rho B_1^- \frac{1-E_1}{1-\cos(\alpha)E_1} \sin(\alpha) E_2^* \qquad \text{[BERNSTEIN 2004]} \tag{3.1}$$

where

$$
\begin{aligned}
E_1 &= e^{-TR/T_1} \\
E_2 &= e^{-TR/T_2} \\
E_2^* &= e^{-TE/T_2^*}
\end{aligned}
\tag{3.2}
$$

Where α is defined in Chapter 1 by equation 1.16 and the magnetization M_0 is given by $M_0=\rho B_1^-$. For a given nucleus, three tuning parameters: TE, TR and FA (through B_1^+) are adjusted to achieve the desired contrast. For any considered TE and TR values, a FA maximizes the resulting NMR signal. This value is known as Ernst Angle and defined by:

$$\alpha_E = arccos(e^{-TR/T_1}) \qquad \text{[Bernstein 2004]} \tag{3.3}$$

Such angle is of high interest in non-proton MRI when the first challenge is to maximize signal and avoid unnecessary losses due to an improper flip angle.

3.1.1.2 Steady State Free Precession Acquisition

For the Balanced Steady-state free precession MRI (bSSFP/FISP) sequence, the residual transverse magnetization after readout is preserved to achieve a better Signal to Noise Ratio (SNR) which can be used to enhance sensitivity. For this reason, the SSFP sequence is widely used for challenging applications such as cardiac and fetal imaging. The general definition of the signal in SSFP is given by:

$$S \propto \rho B_1^- \tan\left(\frac{\alpha}{2}\right)\left(1 - \frac{(1 - E_1\cos(\alpha))(1 - E_2^2)}{\sqrt{p^2 - q^2}}\right) \qquad \text{[Bernstein 2004]} \tag{3.4}$$

with

$$
\begin{aligned}
p &= 1 - E_1\cos(\alpha) - E_2^2(E_1 - \cos(\alpha)) \\
q &= E_2(1 - E_1)(1 + \cos(\alpha))
\end{aligned}
\qquad \text{[Bernstein 2004]} \tag{3.5}
$$

The application of rewinding gradients with reverse polarity before the end of the TR allows insuring stability of the phase of the MR signal in each repetition time and to aid in the development of coherent transverse magnetization:

$$S_{balanced} \propto \rho B_1^- \frac{1 - E_1}{1 - (E_1 + E_2)\cos(\alpha) + E_1E_2}\sin(\alpha)e^{-TE/T_2} \qquad \text{[Bernstein 2004]} \tag{3.6}$$

In the case where TR $\ll$ T_1 and TR $\ll$ T_2 previous equation can be simplified to:

$$S_{balanced} \propto \rho B_1^- \frac{1}{1 + \cos(\alpha) + (1 - \cos(\alpha))(T_1/T_2)}\sin(\alpha) \qquad \text{[Bernstein 2004]} \tag{3.7}$$

3.1.2 Ultra-short Echo-time Imaging

Both SPGR and SSFP sequences can be optimized to minimize their echo-time so as to sample the FID as soon as possible and limit the rapid loss of signal from strongly quadrupolar nuclei or nuclei with a limited mobility. This is particularly the case for Hydrogen in solid environments such as bones, strongly bounded to molecules with a mean T_2 at about a dozen microseconds [Du 2010, Horch 2010, Bae 2012] or in the case of Sodium [Madelin 2014]. Ultra-short Echo-time (UTE) Imaging enables the use of echo-times as low as 50 μs [Robson 2003]. The main limitations are the excitation pulse duration and the need for a phase encoding gradient or a dephasing gradient before starting the acquisition. Therefore, the use of a non-Cartesian sampling scheme relying solely on frequency encoding pulses is required. To reach even lower TE, zero echo-time (ZTE) [WEIGER 2011] or SWIFT (Sweep Imaging with Fourier Transformation) sequences [IDIYATULLIN 2006] can be considered. However, their application for non-proton MRI is still a work-in-progress [MADELIN 2013].

3.2 Non-Cartesian sampling schemes

As introduced in Chapter 1, space encoding consists in probing the spatial frequency space also referred as Fourier space or k-space. For our UTE sequences, echoes are sampled during the readout gradient pulse at a sampling frequency s_F usually expressed in Hz or Hz per pixel. In our implementation, we prefer to use a number of samples and the dwell time to define our readouts. Once the k-space is satisfyingly sampled, the set of complex signals ($c_i(k) \in \mathbb{C}$) is converted into module and phase images using the inverse Fourier transform as presented in Chapter 1 in equation 1.42.

In this section, the different sampling schemes we used are presented. Sequences are of two types depending if they only excite a single slice (2D sequences) or the whole volume-of-interest (3D sequences). The use of a 3D sequence is offering a larger signal compared to 2D sequences as the whole volume is excited and contributes to the produced signal. In the particular case of non-proton MRI with reduced available signal, 3D sequences are recommended. Non-selective excitation is usually achieved using rectangular RF pulse with a duration ranging from 50 to 500 μ allowing to reach an effective echo-time defined by:

$$TE = \frac{\tau_{RF}}{2} + \Delta T \tag{3.8}$$

where ΔT should be set at the minimal delay needed to commute from transmission to reception. Depending on the studied nuclei and particularly its longitudinal relaxation time, the use of 2D multi-slice acquisition, interleaved or not, and acquired within a single TR can become competitive compared to 3D sequences.

An interesting advantage of non-Cartesian sampling schemes is their better robustness to undersampling which allows to significantly reduce the number of acquired spokes as shown later in this chapter. Furthermore, acquiring the center of k-space at each repetition enables an increased SNR in reconstructed images which is of interest in non-proton MRI as well as a better robustness to motion.

3.2.1 2D Radial UTE

The 2D radial sampling scheme is the oldest sampling scheme as it was proposed by LAUTERBUR in his seminal paper about MR Imaging [LAUTERBUR 1973]. It is composed of a slice selection module followed by a centered out radius encoding of Fourier space as illustrated in Chapter 1 by Figure 1.15. Our 2D radial sequence consists in a half-sinc Variable-Rate Selective Excitation (VERSE) pulse [CONOLLY 1988]. The use of such truncated pulse allows to significantly reduce TE while preserving the slice profile but requires the acquisition of two averages with opposed slice selection gradient polarity. Both averages are summed to reconstruct the images as if it was acquired with a complete sinc pulse. Radial sampling is then performed by sampling the gradient echo during the ramp as well as during the plateau of the readout gradient pulse. Consequently, spatial frequency spacing is not linear leading to an higher density of samples at the center of the k-space. Improvements can be obtained using a density adapted sampling obtained with optimized gradients [KONSTANDIN 2011]. To respect the Nyquist-Shannon sampling theorem, one has to acquire enough spokes (N_s) to regularly cover the Fourier space:

$$N_s > 2\pi N_{pix} \tag{3.9}$$

Where $Npix$ represents the number of acquired samples along a single spoke. Therefore, for an image size of 128×128 meaning 64 samples per radius, one should acquire at least 402 spokes. This number is significantly higher than the number of lines required for a standard Cartesian sampling (*i.e.* 128).

3.2.2 3D TPI Sampling

The Twisted Projection Imaging (TPI) UTE sequence has been designed for Sodium imaging by Boada et al [BOADA 1997a]. It is based on the Projection Imaging (PI) technique which enables the use of short and ultra-short echo-time but further improve its sampling efficiency. It is a 3D generalization of the 2D TWIsting Radial Lines (TWIRL) sampling scheme [JACKSON 1992] which can be seen as a mix between the radial and spiral sampling schemes. As illustrated by panel (A) of Figure 3.2, the projection imaging technique aims at sampling an even number of spherical segment (N_s) in the Fourier space. Segments are separated by a distance equal to the inverse of the FOV and are defined by their polar coordinate:

$$\theta_n = \frac{n}{N_s}\pi \tag{3.10}$$

Projections are then placed along these circles as illustrated by Figure 3.2. The design of TPI relies on three optimization in order to improve efficiency: first, the Fourier space trajectory can twist to preserve the sample density, second the noise variance is minimized when sample density is uniform throughout Fourier space and finally a 3D constant sampling with spherical symmetry is optimal for SNR efficiency. Moreover, in 3D, sample density for spherically symmetric distribution is constant if the number of samples inside a thin spherical shell is proportional to the volume of the shell. Consequently this leads to formulate TPI equations:

$$\begin{cases} \dot{k} = \frac{dk}{dt} = \frac{\alpha}{k^2} \\ \dot{k}^2 + k^2(\dot{\theta}^2 + \sin^2(\theta)\dot{\phi}^2) = \bar{\gamma}^2 G^2 \end{cases} \qquad \text{[BOADA 1997a]} \tag{3.11}$$

With G being the gradient strength, $\bar{\gamma} = \gamma/2\pi$, α is an unknown constant, k the spatial frequency, θ and ϕ are polar and azimuthal angles. One can notice that both equations in 3.11 are Ordinary Differential Equations (ODE). The first one is a First Order Non Linear ODE which owns a closed form solution given by:

$$k(t) = \left(3\bar{\gamma}Gk_0^2 t + k_0^3\right)^{1/3} \tag{3.12}$$

The second equation has an infinite number of solutions since it embeds two time dependent unknowns whose solution can be analytically determined by setting a time dependent variable to a constant value independently leading to :

$$\text{If} \qquad \theta = 0 \rightarrow \dot{k}^2 + k^2(\dot{\theta}^2 + \sin^2(\theta)\dot{\phi}^2) = \bar{\gamma}^2 G^2 \equiv \dot{k}^2 + k^2\dot{\theta}^2 = \bar{\gamma}^2 G^2 \tag{3.13}$$

with the associated solution:

$$\phi(t) = \frac{1}{2}\left(\chi(t) + \arctan\left(\frac{1}{\chi(t)}\right)\right) + \phi_0 \qquad \chi(t) = \sqrt{\frac{k^4}{k_0^4} - 1} \tag{3.14}$$

$$\text{If} \qquad \phi = 0 \rightarrow \dot{k}^2 + k^2(\dot{\theta}^2 + \sin^2(\theta)\dot{\phi}^2) = \bar{\gamma}^2 G^2 \equiv \dot{k}^2 + k^2(\sin^2(\theta_0)\dot{\phi}^2) = \bar{\gamma}^2 G^2 \tag{3.15}$$

with the associated solution:

$$\theta(t) = \frac{1}{2\sin(\theta_0)}\left(\chi(t) + \arctan\left(\frac{1}{\chi(t)}\right)\right) + \theta_0 \qquad \chi(t) = \sqrt{\frac{k^4}{k_0^4} - 1} \tag{3.16}$$

Consequently, equations of k(t) and $\theta(t)$ represent the "spiral like" trajectory on the surface of a disk parallel to the K$_X$-K$_Y$ plane and equations of k(t) and $\phi(t)$ represent the "helix like" trajectory on the surface of the cone $\theta(t)$=θ_0. The trajectory is composed of an inner radial core and an outer spiral shell whose respective length is controlled by a tuning parameter.

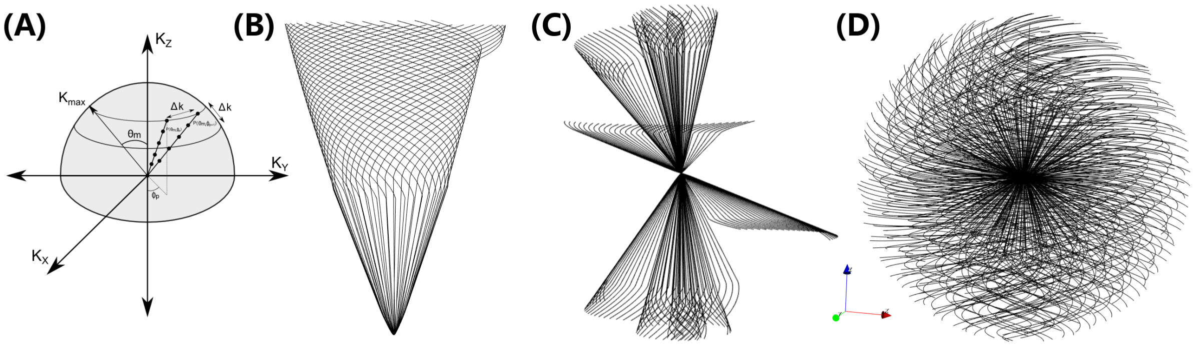

Figure 3.2: Principle of PI sampling theory (A) and view of a cone on which spokes are projected (B), a partial view of multiple cones (C) and a full view of TPI sampling trajectory (D). 3D views were made using VTK [Schroeder 2006].

The ratio of the linear part of each spoke is of importance to establish the optimal sampling rate as it is known that spiral sampling has a better spatial coverage efficiency than radial. When considering a completely 3D radial sampling scheme, the required number of spokes to respect Nyquist-Shannon sampling theorem is given by:

$$N_s = 4\pi\left(\frac{Matrix}{2}\right)^2 \qquad \text{[Konstandin 2014]} \tag{3.17}$$

where matrix is the number of voxel of the reconstructed image. As image resolution increases, the number of projections becomes practically unfeasible therefore massive under sampling factors are applied. For instance an undersampling factor of 10 can be found in literature for human sodium exploration [Nielles-Vallespin 2007]. As TPI spokes lie on concentric cones, the first step is to determine the number of cones (N$_c$) that densely cover the sampled spherical Fourier space:

$$N_c = \frac{\pi \times FOV}{2 \times Resolution} \qquad \text{[Boada 1997b]} \tag{3.18}$$

where FOV and Resolution are spatial dimensions in mm. Cones are then covered by spokes with an homogeneous angular spacing leading to a number of spokes defined by:

$$N_s = 2pN_c \sum_i \sin\left(\frac{i\pi}{N_c}\right) \qquad \text{[Engel 2015]} \tag{3.19}$$

where p is the linear ratio of the spoke. The lower p gets, the lower the number of spokes is as the spiral sampling is more important and covers more efficiently Fourier space than radial spokes.

3.2.3 3D FLORET Sampling

The 3D Fermat Looped Orthogonally Encoded Trajectory [PIPE 2011] is similar to TPI and based on a 2D variable density Fermat spiral Fourier space trajectory b$_x$(t), b$_y$(t) defined by:

$$k_r = c\theta^{1/2} \qquad \text{with } c = \sqrt{\frac{N}{2\pi\alpha_0 FOV^2}} \qquad \text{[PIPE 2011]} \tag{3.20}$$

where k$_r$ and θ are the trajectory polar coordinates radius and angle and c is determining the variable pitch rate to get a uniform inter-trajectory spacing. The 3D approach is realized by projecting these spirals onto 3D cones organized in different rotating hubs and defined by:

$$\begin{cases} k_x(t) = \cos(\alpha) b_x(t) \\ k_y(t) = \cos(\alpha) b_y(t) \\ k_z(t) = \sin(\alpha)\sqrt{b_x(t)^2 + b_y(t)^2} \end{cases} \tag{3.21}$$

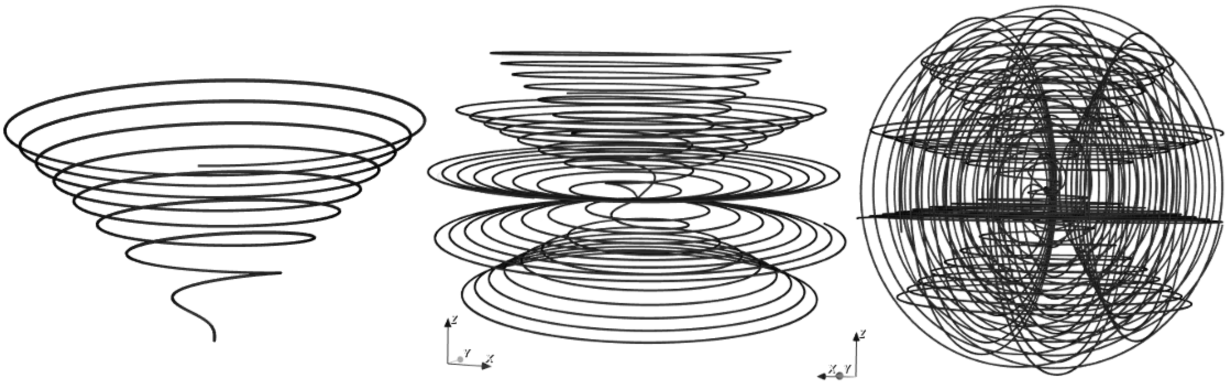

Figure 3.3: Single FLORET Spiral (A), a single hub with few spirals (B) and 3 interesting hubs of few spirals (C). Visualization of trajectory was made using VTK.

Figure 3.3 illustrates a single 3D spiral with its conical shape along the z axis (left), a hub is created by a dense staking of spirals, few of them are represented (center) and finally the spherical sampling pattern is obtained when acquiring multiple intersecting hubs with different orientations.

Other sampling schemes such as stars or cones can be used for non-proton MRI and have been compared at 9.4 T for brain Sodium Imaging [ROMANZETTI 2014]. The FLORET sequence authorizes under-sampling that can be performed on either single or multiple hubs. The use of multiple hubs enables sampling of some parts of Fourier space several times within a single acquisition.

3.2.4 Comparison

In order to define the most suitable sequence to use for our explorations, we relied both on the literature and on some comparisons and explorations we made. An advanced comparison study between the most commonly used sequence in Sodium MRI: Cartesian Gradient Echo, 3D Cones, Twitsted Projection Imaging (TPI), 3D Radial and 3D Density-Adapted Radial (DAR) was already reported in literature [ROMANZETTI 2014]. Authors compared both SNR and the Point-Spread-Function (PSF) of aforementioned sequences and showed that the TPI sampling scheme was the most suitable for both *in vitro* and *in vivo* Sodium MRI as it presents a highly homogenous and efficient k-space sampling along with the use of ultra-short echo-times. Indeed, as presented on Figure 3.4 the PSF of TPI is the closest to the Cartesian GRE sampling.

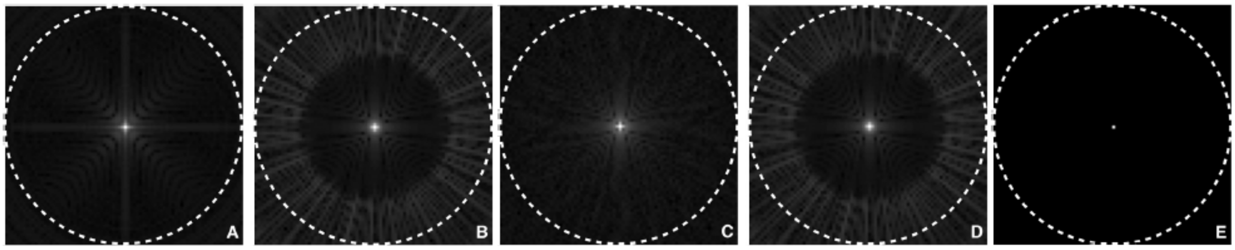

Figure 3.4: Point Spread Functions of TPI (A), Density-Adapted 3D Radial (B), Cones (C), 3D Radial (D) and GRE (E) from [Romanzetti 2014]. Acquisition were made with no under-sampling.

Consequently, those results led us to choose the 3D TPI sequence for our non-proton explorations to benefit from the gain in SNR brought by the 3D excitation as well as the optimal k-space coverage with a reduced spread to reach satisfying spatial image resolution.

3.2.4.1 3D Cartesian vs TPI for ^{31}P MRI

Early in this thesis, we started by exploring those aspects for a fast Phosphorus MR Imaging application [Coste 2016]. We compared a standard Cartesian SSFP sequence with the same acquisition made with the TPI sampling scheme. Acquisition parameters were: TR/TE = 100/4.5 ms, FA = 10°, isotropic FOV of 320mm at 5mm isotropic resolution, 1 average. The choice of TE was driven by limitations of the Cartesian sampling sequence. TPI linear ratio p was set to 0.75 and a number of spokes was taken equivalent to the Cartesian acquisition to 4096. Such spoke number is about twice lower than the required number to meet Nyquist-Shannon sampling requirements. Comparison between obtained images is presented on Figure 3.5 confirming the benefits of TPI compared to the Cartesian sampling sequence.
Prospective undersampled acquisitions were performed to reduce acquisition time. Panels (c) to (d) still allow to distinguish the phantom despite the reduced TA. However, for panels (e) and (f), image quality is too significantly degraded. SNR measurements were made to confirm the gain of combining the non-Cartesian sampling with the non-linear iterative reconstruction as illustrated on Figure 3.6 where each lines illustrate the SNR in TPI acquisition and the single symbols the SNR in equivalent ROIs of the Cartesian acquisition. Interestingly, similar SNR were obtained for the Cartesian sampling and the massively under-sampled (under-sampling factor of about 30 and fourteen times shorter acquisition time) TPI acquisition presented on panel (f).

3.2.4.2 Point Spread Function exploration

As TPI was chosen to be our reference sequence for non-proton explorations at NeuroSpin, I also explored the PSF associated with the TPI sampling scheme. Indeed, as the PSF corresponds to the impulse response of our sampling trajectory it brings valuable information about the spatial spread of data. It is dependent on two factors: the signal readout duration and the effective magnetization transverse decay (T_2^*). The PSF was computed using the gridding reconstruction of the TPI trajectory. We simulated different possible signal decays by either varying the readout duration or the T_2^* to evaluate their influence. As one can notice on Figure 3.7, a long readout time compared to T_2^* results in a enlargement of the PSF creating blurred reconstructed images.

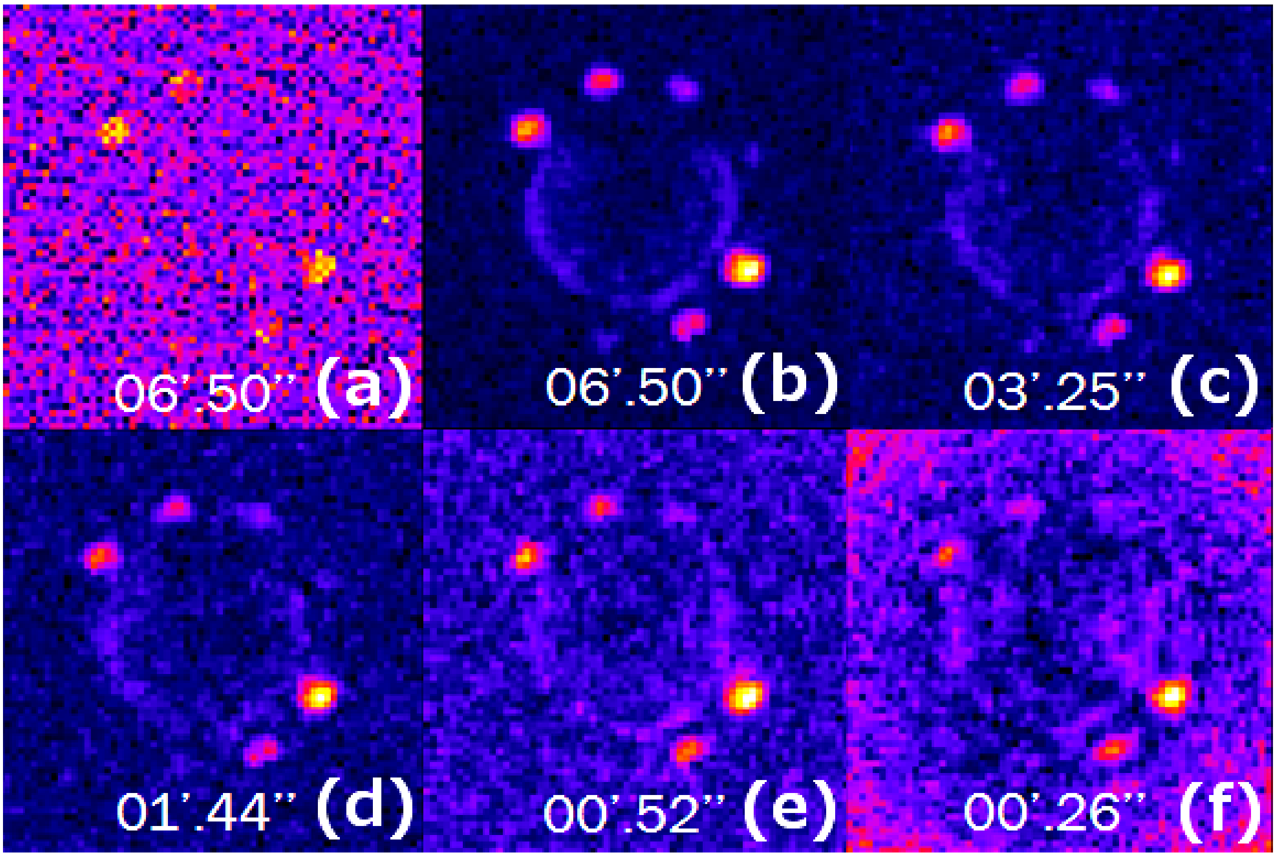

Figure 3.5: Comparison between the Cartesian FISP (a), TA-equivalent TPI (b) and under-sampled acquisitions (c-f) [Coste 2016].

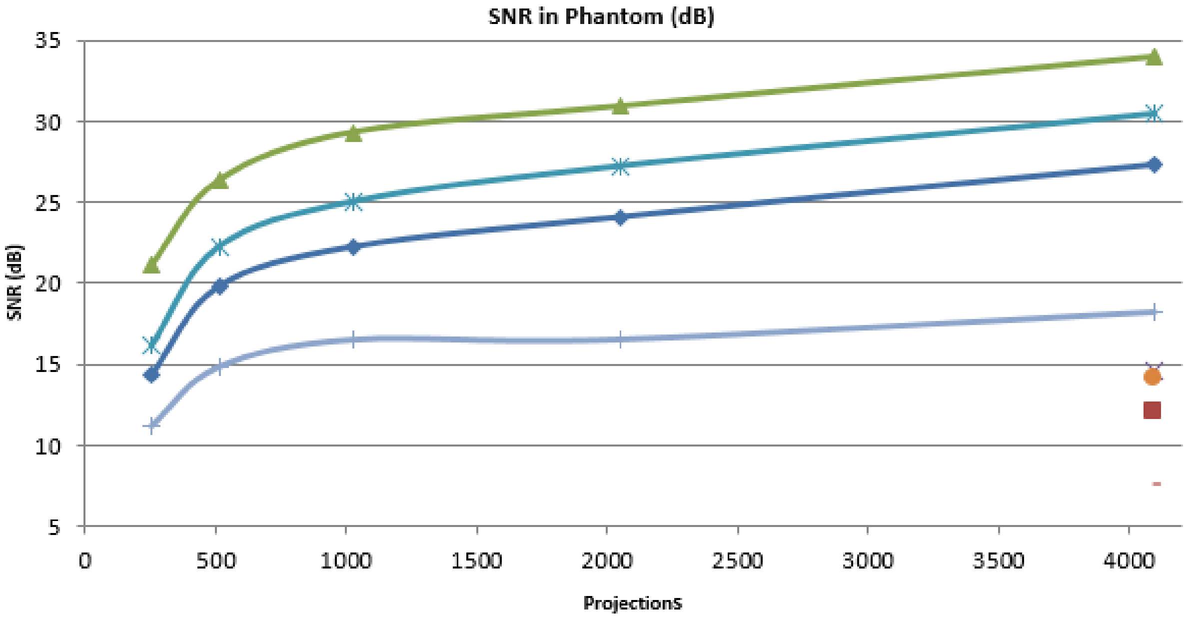

Figure 3.6: Plot of SNR in 4 different ROIs according to the number of spokes of the TPI acquisitions (solid lines) and compared to the Cartesian acquisition (symbols) [Coste 2016].

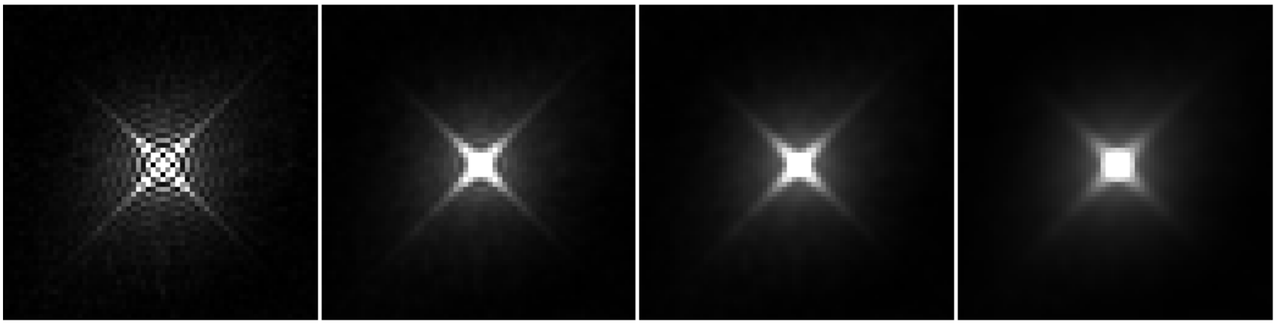

Figure 3.7: TPI PSF with increasing readout duration 0 ms, 10 ms, 20 ms and 30 ms for a constant T_2^* of 12 ms.

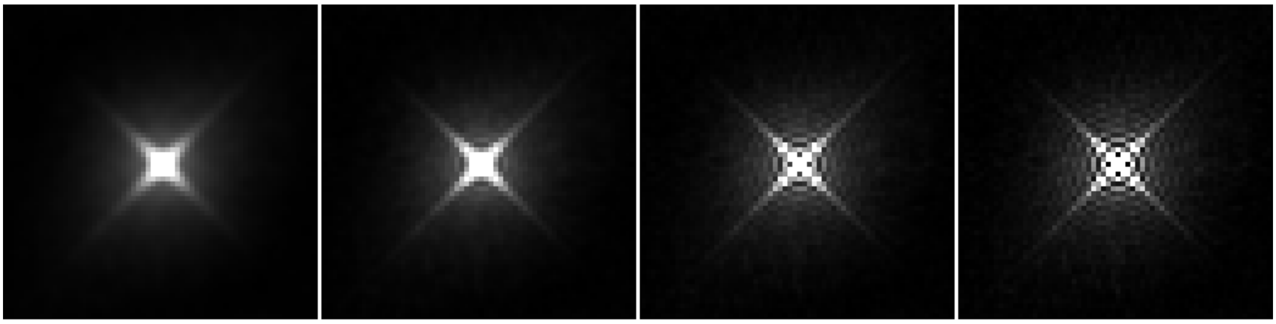

Figure 3.8: TPI PSF increasing T_2^* 6 ms, 12 ms, 60 ms, infinite for a constant readout time of 20 ms.

As noticeable on Figure 3.8, in the case of a nuclei with short T_2^* and quite long readout the blurring effect is present, but for nuclei with long T_2^* the PSF is sharper. These simulations confirm the link between PSF spreading and readout duration and shows us that readout duration should be comparable to T_2^* to limit blurring. Being able to estimate the acquisition PSF can be of interest for advanced deconvolution based image analysis. In the case of non-linear iterative regularized inverse problem based algorithms, there is no easy way to evaluate the PSF, due to the non-linear nature of the reconstruction process. But explorations can be made using Volterra series used to model non-linear processes [De Figueiredo 2006]. So depending on the reconstruction technique, a "reconstruction" PSF can be added when considering possible denoising or smoothing effects of the reconstruction algorithm.

3.3 Image Reconstruction

When MR data are sampled using the standard Cartesian scheme, images can be reconstructed using an inverse discrete Fourier transform which is given for 2D MRI by:

$$\mathrm{S}(x,y) = \sum_{m=0}^{\mathrm{M}-1}\sum_{n=0}^{\mathrm{N}-1} s(m,n)\cdot \mathrm{e}^{-2i\pi\left(\frac{xm}{\mathrm{M}}+\frac{yn}{\mathrm{N}}\right)} \tag{3.22}$$

where indexes m and n represent the index of the discrete k-space coordinates k_x and k_y and x and y the discrete image spatial coordinates.

When using non-Cartesian sampling schemes, direct use of the standard inverse discrete Fourier transform is no longer possible as Fourier space is neither homogeneously nor uniformly sampled meaning that sample do not cover the full k-space and are not identically spaced. As introduced in Chapter 1, three types of methods are currently available to reconstruct data acquired using a non-Cartesian sampling scheme: gridding, dedicated inverse Fourier transform or non linear iterative inverse problem based methods. All three approaches were used during this PhD thesis and compared in order to evaluate their respective advantages and drawbacks. This section presents some results that helped us in choosing reconstruction parameters as well as reconstruction methods.

3.3.1 Deapodization and Density Compensation in Gridding Algorithm

When using a gridding algorithm described by:

$$m(x,y) = \mathcal{F}^{-1}\left(\left(\frac{M(u,v).S(u,v)}{\rho(u,v)} * K(u,v)\right).\text{Ш}(u,v)\right) \tag{3.23}$$

two important points are to consider: the gridding kernel $K(u,v)$ and the density compensation function $\rho(u,v)$. Both aspects have been widely studied in the literature with various kernels and a good consensus has been reached with the recommended use of the Kaiser-Bessel kernel [JACKSON 1991]. The apodization effect brought by the use of such kernel requires proper correction. One possible correction lies in reconstructing acquired data on a larger grid. Therefore, we studied the influence of the grid size on the reconstructed image.

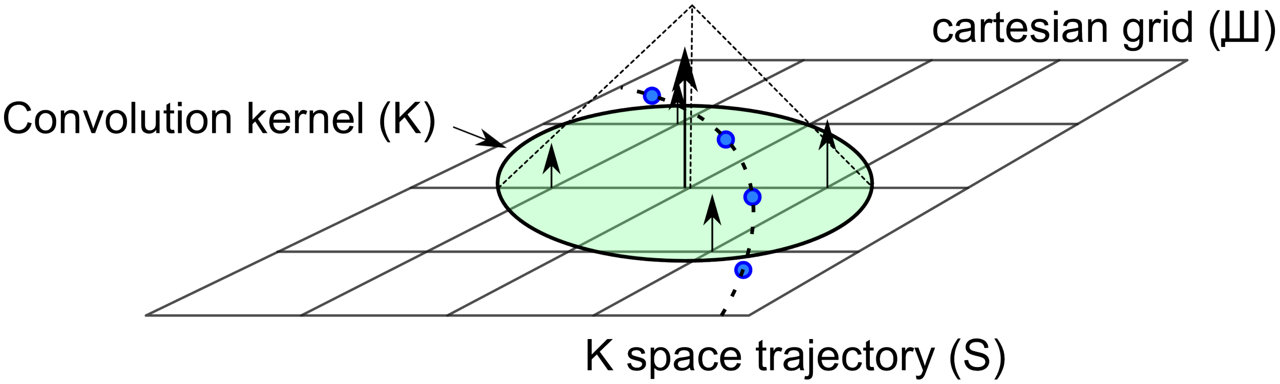

Figure 3.9: Principle of the gridding method.

As illustrated by Figure 3.10, the increase of reconstruction grid size lead to a reduction of the apodization effect that tends to lower the image intensity on its borders. When increasing the grid size, we observed that the homogeneity of the image intensity was restored. Indeed for a unity grid size reconstruction their is about 90% difference between the center and the sides of the image. This signal intensity difference is decreased to about 30% when doubling the grid size and remained stable when the grid size was tripled as illustrated by the resulting profiles along the X-axis.

Regarding the density compensation function, among all the methods available, we chose to use a Voronoi diagram [VORONOI 1908] based density compensation [RASCHE 1999]. This method aims at computing a partition of a spatial domain based on a distribution of points called "seeds". Regions obtained after partition are called "cells" and consist of all points closer to a given seed than to any other. In our application, the point distribution S is the spatial location of Fourier space samples. For two distinct samples p and q of S , the dominance of p over q is defined as the subset of the

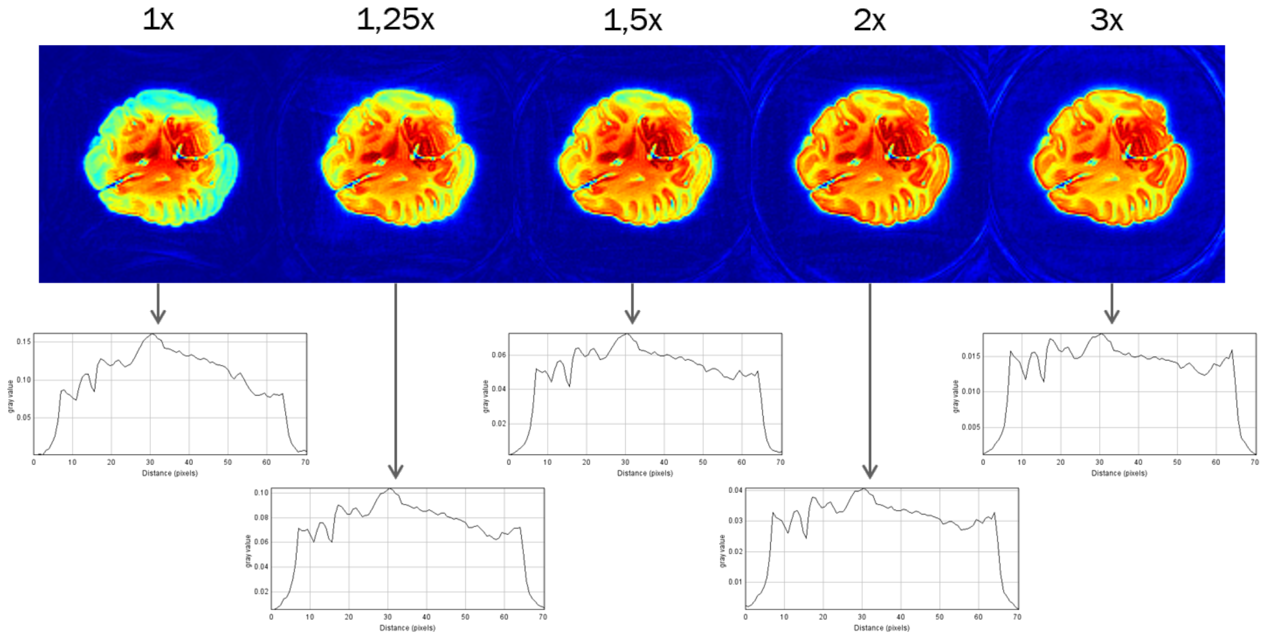

Figure 3.10: Influence of the reconstruction grid size for deapodization. These ^{1}H MRI data were acquired *post-mortem* on a baboon brain at 7 T using a 2D radial UTE sequence.

plane being at least as close to p as to q:

$$dom(p,q) = \left\{x \in \mathbb{R}^2 \middle| d(x,p) \leq d(x,q)\right\} \qquad \text{[Rasche 1999]} \tag{3.24}$$

where d is the standard Euclidean distance of $\mathbb{R}^n$:

$$d(p,q) = d(q,p) = \sqrt{\sum_{i=1}^{n}(p_i - q_i)^2} \tag{3.25}$$

$dom(p,q)$ is a closed half-plane bounded by the perpendicular bisector of p and q. The area of a site $p \in S$ is the portion of the plane lying in all of the dominances of p over the remaining areas in S:

$$cell(p) = \bigcap_{q \in S - \{p\}} dom(p,q) \qquad \text{[Rasche 1999]} \tag{3.26}$$

The sum of all partitions of the plane defined by equation 3.26 is the Voronoi diagram of S. The area of the cell associated to each point is computed, normalized and used as a weighting constant. The Voronoi diagram is the dual of Delaunay's triangulation of the points distribution [DELAUNAY 1934]. Figure 3.11 illustrates the computed Voronoi diagram for a 2D radial sample distribution.

Influence of the density compensation function was explored through a comparison of images reconstructed with a uniform density, a linear density and a Voronoi diagram based density in the case of the 2D radial sequence as illustrated in Figure 3.12.

The influence of the density compensation function is clearly visible. Indeed, when a uniform weighting is applied all samples have the same weight and since the density is more important in the center of Fourier space, the resulting image is blurred due to the dominance of low spatial frequencies. The use of a linear weighting function enables to reduce the weight of central samples and favor higher frequencies which reduce blurring. Finally, the use of a distribution adapted

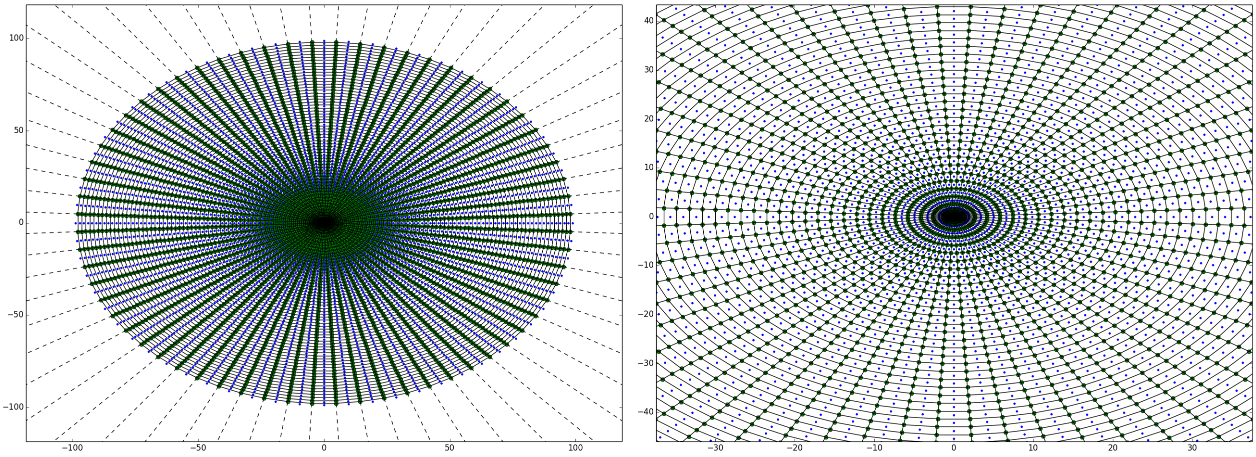

Figure 3.11: Example of the computed 2D Voronoi diagram of a Radial Fourier sample distribution (left) where each sample is represented as a blue dot and a zoom at the center (right) to better visualize the increasing cell area which provides an increasing weight with increasing distance from the center.

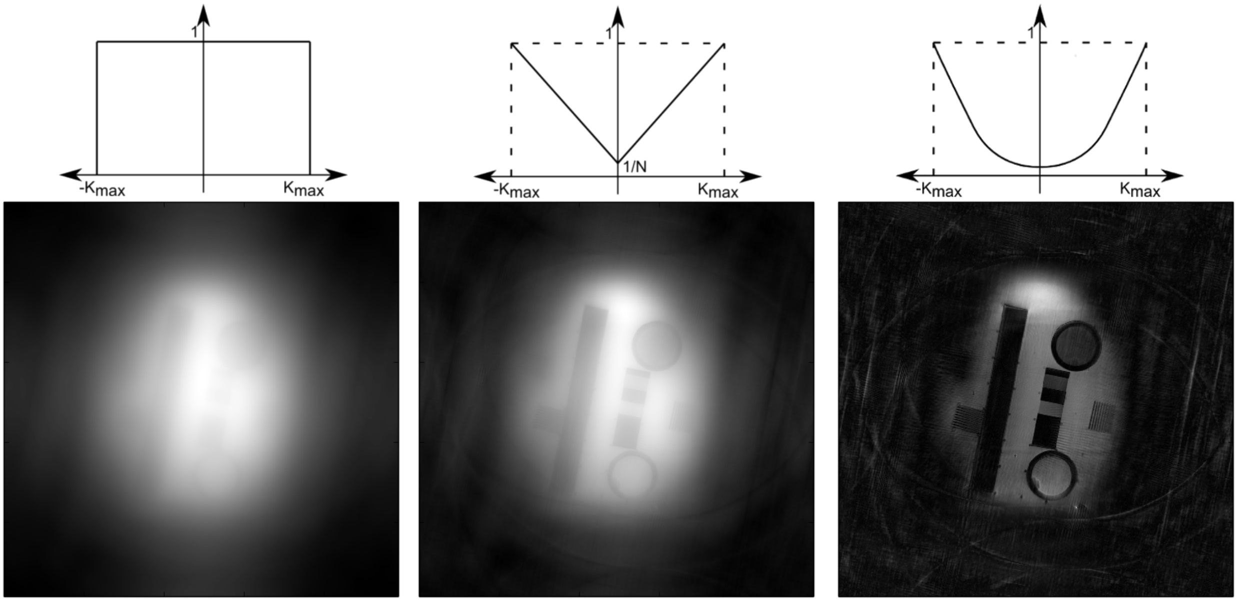

Figure 3.12: Comparison of different density compensation functions: uniform, linear and Voronoi diagram based and their impact on reconstructed images.

weighting function based on Voronoi's diagram enables to correctly reconstruct the image. Such method was also applied to optimize non-Cartesian trajectories developed by Nicolas CHAUFFERT. Figure 3.13 illustrates one example of such trajectories with a zoom showing its convolutions and the associated Voronoi parcellation. Such trajectories were developed with an optimized sampling density to reduce acquisition time by an efficient non-Cartesian Fourier space sampling. Non-linear iterative inverse problem based reconstruction were then used for an optimal image reconstruction. While such techniques are currently explored for high resolution imaging, they also have potential applications to X-MRI where reduction of the acquisition time could lead to the acquisition of more

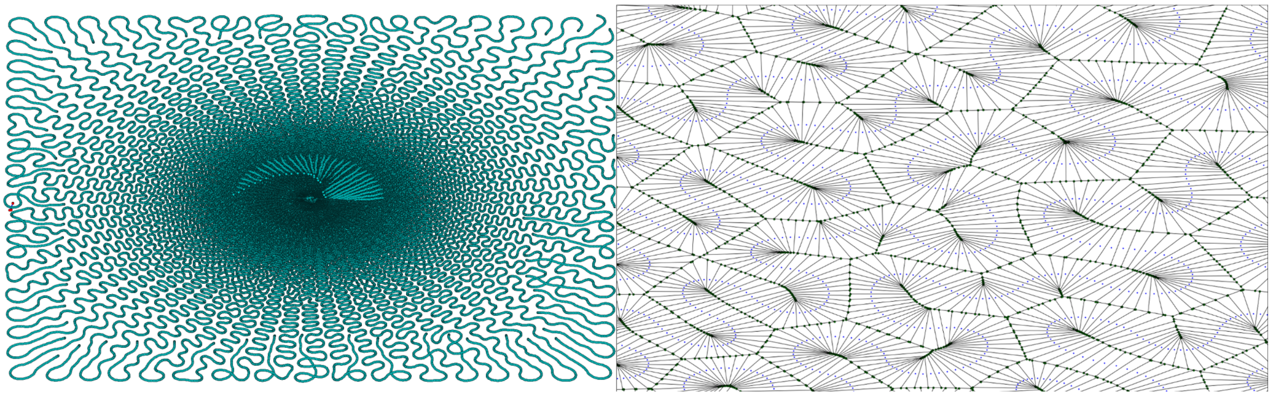

Figure 3.13: Optimized trajectory developed by Nicolas CHAUFFERT and a zoom on the associated 2D Voronoi Diagram.

averages to improve SNR.

3.3.2 Retrospective Under-Sampling

Once MR data are acquired with a given sampling pattern, it is always theoretically possible to reconstruct images as if they were acquired with a different sampling pattern, as illustrated by Figure 3.14. Different schemes were tried on a fully sampled data set: a radial "golden angle" approach consisting in acquiring a set of radii separated by a constant angle Φ defined by:

$$\left\{ n\Phi_G[2\pi] \middle| \Phi_G = \frac{180}{\phi}, n \in \mathbb{N}, n < N \right\} \qquad \text{with} \qquad \phi = \frac{1+\sqrt{5}}{2} \tag{3.27}$$

where N is given by 3.9. a spiral scheme defined by:

$$\begin{cases} x = t\cos(t) \\ y = t\sin(t) \end{cases} \tag{3.28}$$

a Fibonacci spiral viewed as an approximation of the golden spiral and defined by:

$$\begin{cases} \theta = \frac{2n\pi}{\Phi^2} \\ r = c\sqrt{n} \end{cases} \qquad \text{[VOGEL 1979]} \tag{3.29}$$

and finally a 2D random walk algorithm with the following rule:

$$\begin{cases} \theta = rand(361) \\ x = x + \cos(\theta) \end{cases} \tag{3.30}$$

As those retrospective sampling schemes do not account for all constraints or phenomena of MRI such as limited gradient slew rates or T_2^* decay, those explorations should be considered with caution. Therefore we chose to explore other under-sampling patterns where applied trajectories are not violating the MR acquisition physics as illustrated by Figure 3.15.

By only removing few acquired spokes randomly, NMR acquisition physics are not violated. Besides, the stochastic removal of spokes is consistent with the Compressed Sensing theory introduced in Chapter 1. Consequently a study was made to explore the robustness of the radial acquisition to such under-sampling process. We considered a fully sampled 2D Radial proton MRI data set

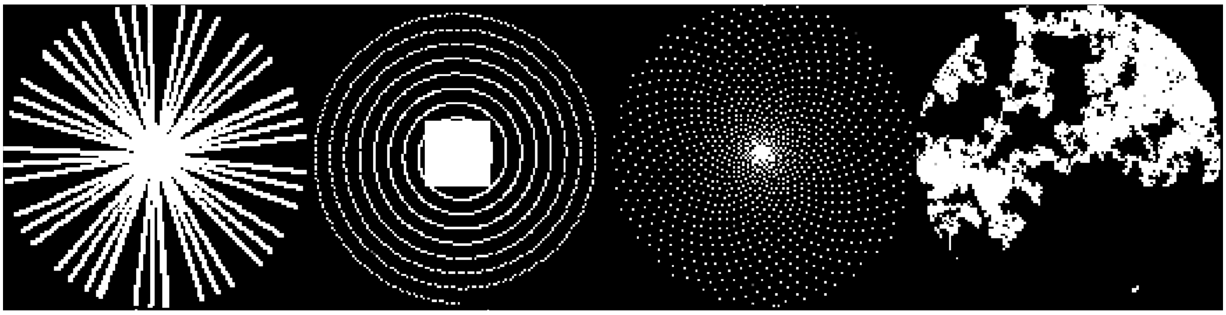

Figure 3.14: Retrospective sampling schemes applied to a low resolution fully sampled 2D Radial data set: (from left to right) Golden angle 2D Radial, Square Center and spiral out, Fibonacci spiral and 2D Random walk.

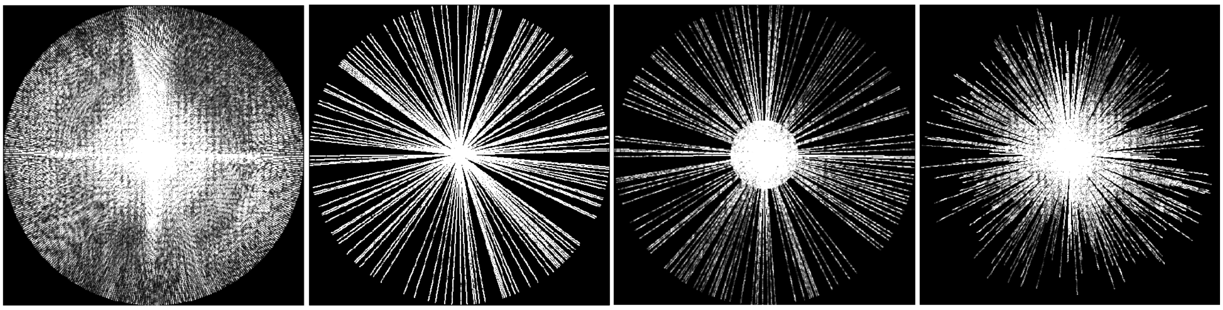

Figure 3.15: Physically plausible retrospective sampling schemes applied to a high resolution fully sampled 2D Radial data set: (from left to right) Full radial sampling, random radial sampling, Center and random radii and random radii of random length.

acquired on the resolution phantom 1H-7T-1. Then we retrospectively removed up to 97% of acquired projections to study the consequences as illustrated on Figure 3.16. Radial artifacts already appear after removing 10% of projections but their influence on overall image quality is quite low but it increases with projection removal. After 60% of removed spokes, the image quality is strongly affected by artifacts but the object is still recognizable. When only 10% of projections remains, the object become unrecognizable.

Such experiment illustrates the fact that retrospective random spoke removal is possible up to 70% and even more with high SNR data sets. It can therefore be considered to significantly reduce acquisition time while maintaining the theoretical spatial resolution. However, this strategy could have obvious consequences on the actual PSF and the SNR as observed when applying it to *in vivo* Sodium data sets acquired at 3 T and presented in Chapter 7. Indeed, with lower SNR removing spokes strongly affects image quality.

3.3.3 Reconstruction Method Comparison

Compressed sensing allows if performed adequately to achieve similar MR Image quality than fully sampled data while reducing the number of sampled spatial frequencies in k-space. As this approach could be useful to push the limits of non-proton MR applications, we conducted few tests to compare different sparse image reconstruction techniques. First we looked at the evolution of SNR when applying the gridding and the non-linear iterative methods on retrospectively undersampled Phosphorus MRI 2D radial data acquired at 7 T on a simple phantom model composed

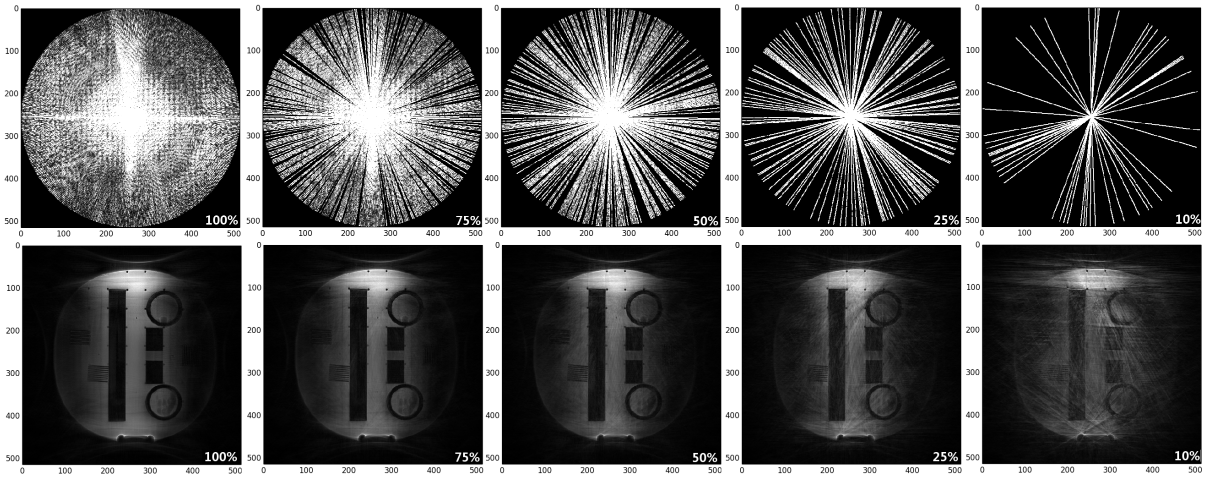

Figure 3.16: Retrospective under-sampling schemes applied to a high resolution full 2D Radial by stochastic removal of spokes and corresponding reconstructed images. From left to right, sampling factors are 1, 0.75, 0.5, 0.25 and 0.1.

of a single compartment with PBS and water tubes to create holes. Four separate acquisitions with sampling factors of 1, 0.75, 0.5 and 0.25 were performed and reconstructed with both algorithms [Coste 2015]. Results are presented on Figure 3.17 showing minor SNR degradation due to under-sampling. For all k-space, the intrinsic denoising and smoothing of FISTA produces notably higher SNR compared to gridding. As a consequence, the use of non-linear iterative algorithms (here based on FISTA) should be recommended to reconstruct MR data sampled using non-Cartesian trajectories.

This superiority of FISTA over gridding was confirmed by a second test using more Phosphorus MRI 2D radial images acquired at 7 T with an increasing number of excitation and reconstructed with both algorithms (Figure 3.18).

As comparison of SNR values can be misleading due to the denoising and smoothing properties of those algorithms, we chose to use another image quality metric : the Structural Similarity Index (SSIM). Between two images of size $N \times N$, SSIM is defined as:

$$SSIM(x,y) = l(x,y).c(x,y).s(x,y) = \frac{(2\mu_x\mu_y + c_1)(2\sigma_x\sigma_y + c_2)(2cov_{xy} + c_3)}{(\mu_x^2 + \mu_y^2 + c_1)(\sigma_x^2 + \sigma_y^2 + c_2)(\sigma_x\sigma_y + c_3)} \quad \text{[Wang 2004]} \tag{3.31}$$

with $\mu^2_{x/y}$, $\sigma^2_{x/y}$ and $cov_{x/y}$ are the mean, the variance and the covariance of x and y, and c_i are constants to stabilize the measure according to the image dynamic range.

As illustrated by the SNR and SSIM curves shown in Figure 3.19, FISTA is indeed superior to gridding for both metrics. However, the difference of behaviors between both methods in SSIM is more subtle and point at a inflexion point at which the gridding algorithm is not able to denoise images and maintain structural similarity and SNR.

In order to explore further this comparison for low SNR images (which is more realistic), we then looked at undersampled ^{31}P MRI data from a single excitation (Figure 3.20). Again, the denoising and smoothing behavior of FISTA is confirmed even for acquisitions presenting a low SNR.

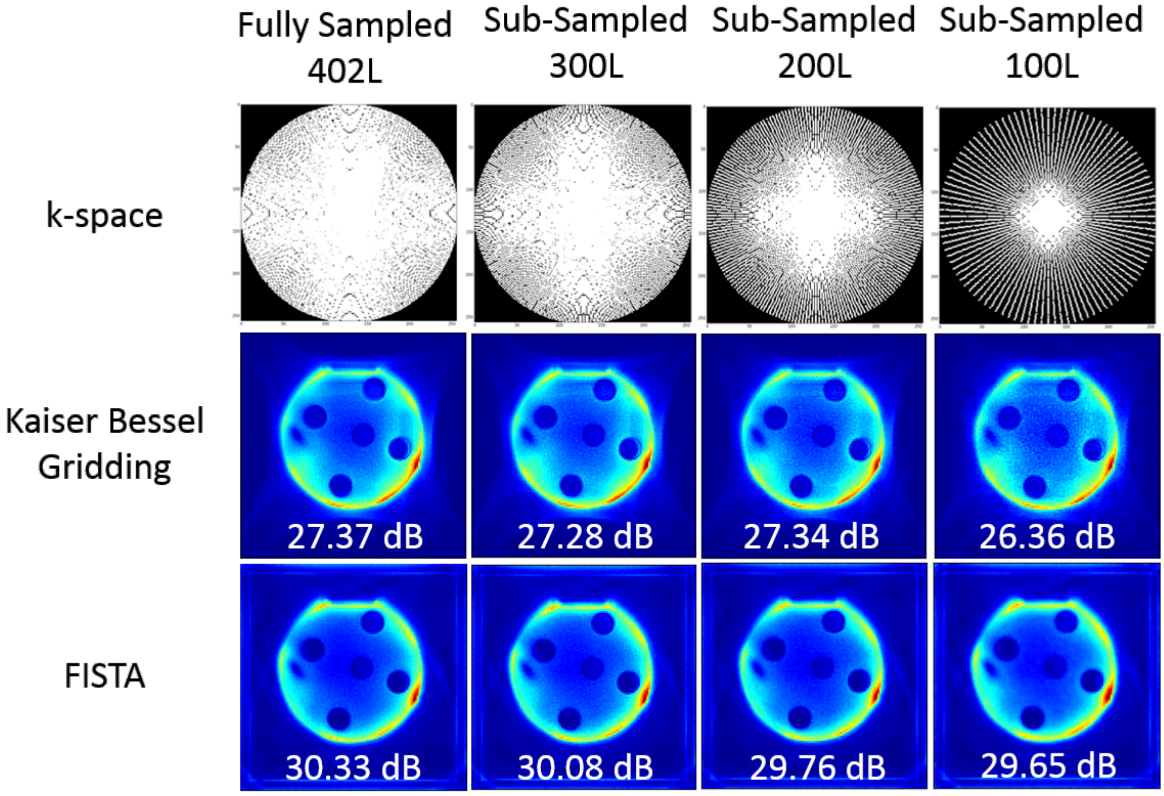

Figure 3.17: Comparison between gridding and FISTA on 2D radial retrospectively under-sampled Phosphorus MRI data [COSTE 2015]. First line: spoke removal from the fully sampled 2D radial acquired Fourier space; second and third lines: reconstructed images with regridding or FISTA methods and corresponding average SNR values in dB.

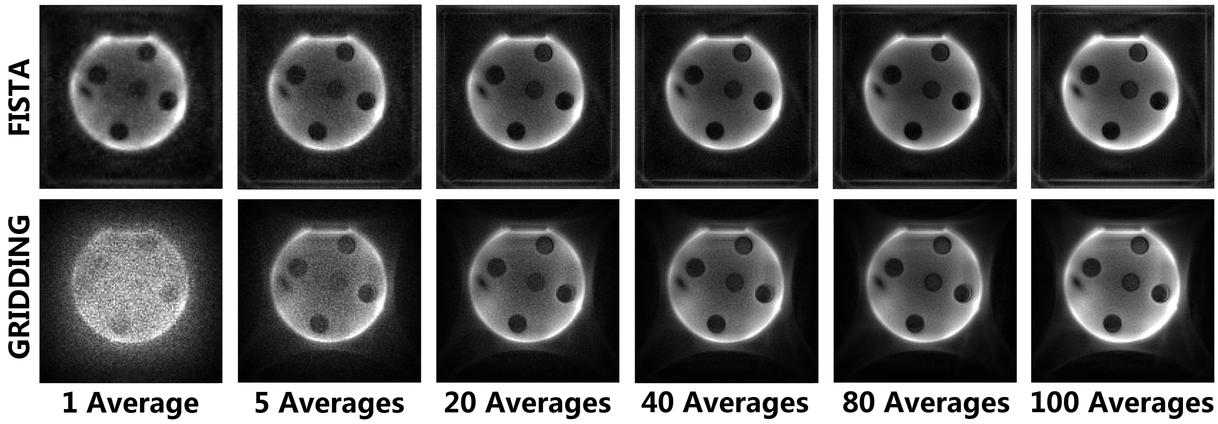

Figure 3.18: Reconstructed images with FISTA (top row) and Kaiser Bessel gridding (bottom row) with various number of excitation.

3.3.4 Study of the Non Linear Iterative algorithm

A deeper exploration of reconstruction algorithms is beyond the scope of this PhD thesis. Nevertheless, some tests were performed to get a better understanding of the influence of the regularization

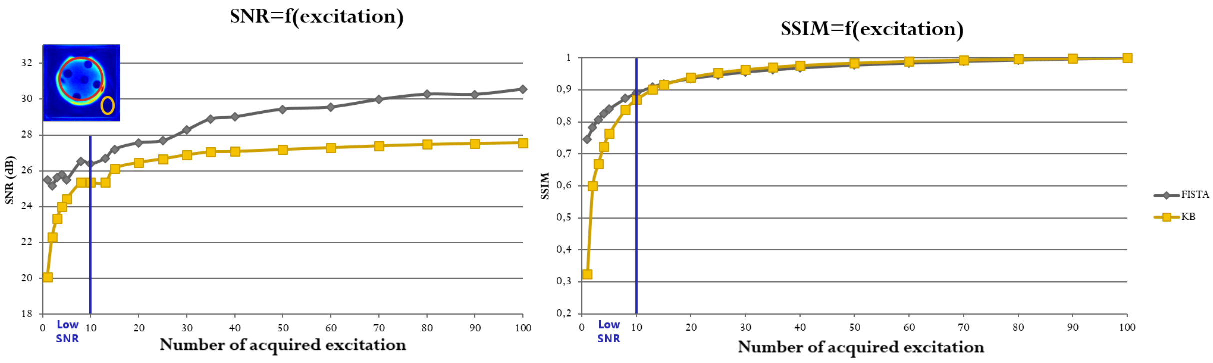

Figure 3.19: SNR and SSIM measurements according to the number of excitation.

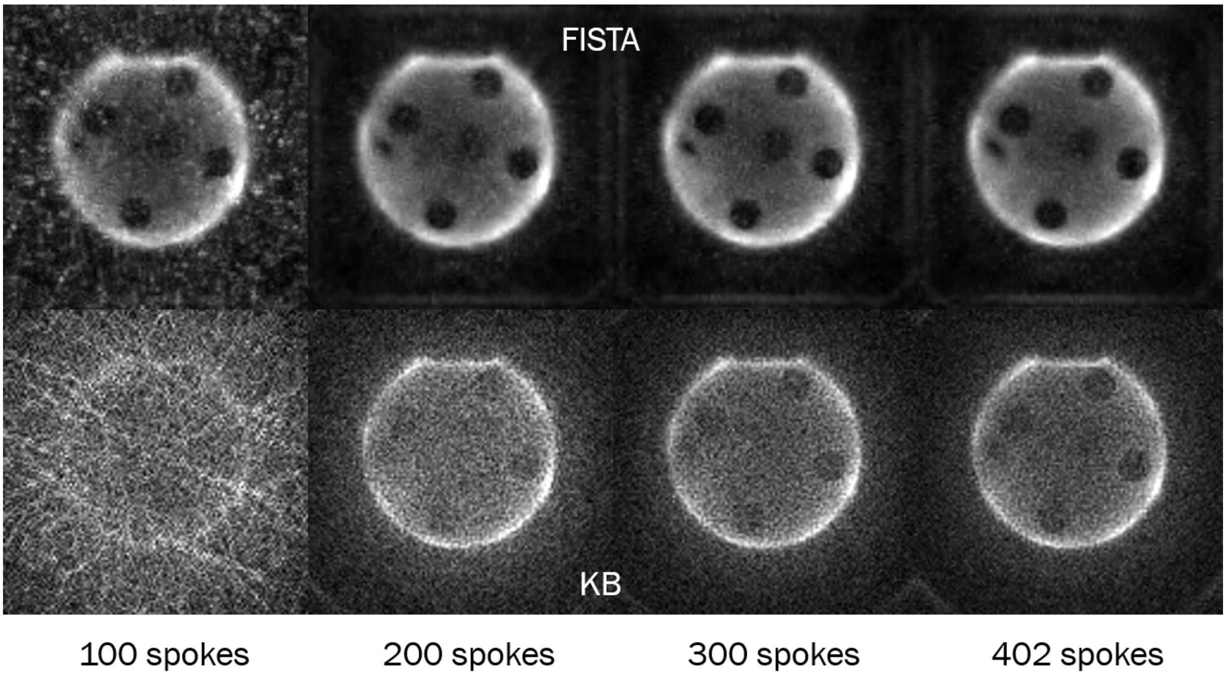

Figure 3.20: Comparison of FISTA (top row) and Kaiser Bessel Gridding (bottom row) reconstruction methods on low SNR ^{31}P MRI data (single average) with sampling ratios of 0.25, 0.5, 0.75 and 1.

term and the number of iterations of these algorithms as they are important tuning parameters. For convenience, this short study was performed using a single slice of a proton T_2 weighted acquisition acquired with a Cartesian sampling and with a native resolution of 512×512 pixels. Image was then interpolated to smaller size to match common matrix size of non-proton MRI as illustrated by Figure 3.21.

An image size of 64×64 was chosen as it matches the resolution of our *in vivo* sodium acquisitions. As samples were homogeneously distributed over k-space, the inverse fast Fourier transform (2D iFFT) could be applied to reconstruct a magnitude image used as reference for our computations.

In order to find a practical combination of regularization weights and number of iterations (for images with comparable SNR and spatial resolution), the image was reconstructed using our non-

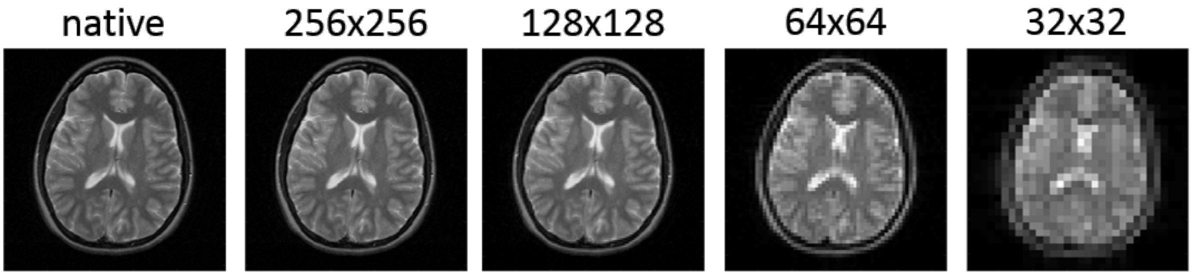

Figure 3.21: Test image re-sampled at different resolutions.

linear iterative wavelet regularized inverse problem based reconstruction code (programmed on Python) based on FISTA [BECK 2009] as described in Chapter 1 by:

$$\omega^\star = \arg\min \left(\frac{1}{2} ||\mathbf{m} - \mathbf{M}\omega||_{l_2}^2 + \lambda ||\Phi x||_{l1} \right). \tag{3.32}$$

In the absence of a deterministic method to find this optimum couple, we repeated the reconstruction for various set of parameters. To modulate SNR, a Gaussian noise of increasing intensity was added to the Fourier space complex data prior to image reconstruction. As confirmed in Figure 3.22, an increased Rician noise was observed on the modulus image [GUDBJARTSSON 1995].

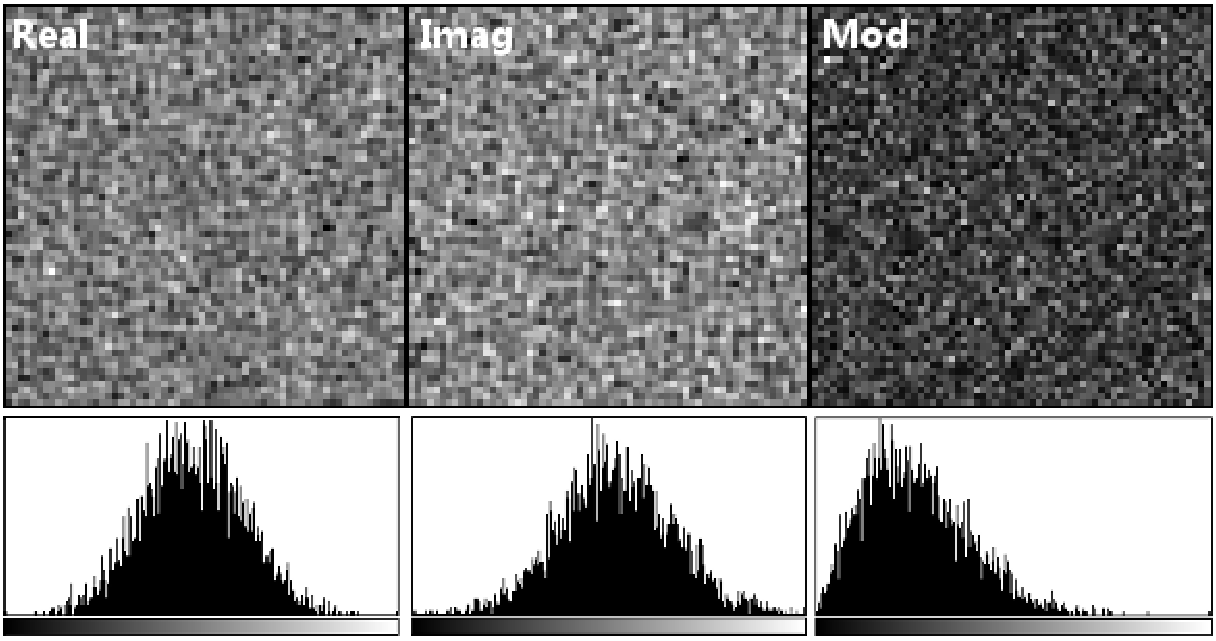

Figure 3.22: Gaussian noise distributions in image real (left), imaginary (center) parts and Rician distribution in magnitude image (right).

Figure 3.23 summarizes the SSIM values measured when exploring of all those parameters (noise level, number of iterations and regularization weight). In brief, we observed that 1000 or even 500 iterations were sufficient to ensure convergence of the energy minimization problem. We also noticed that the noise level had minor impact on the convergence. For the considered range of SNR, stronger regularization ($\lambda > 0.2$ for 1000 iterations) have a negative impact on the SSIM.

Beyond these tests, exploration of a possible influence of the type of wavelet: Daubechies, Symlet or Coiflet was done and no significant changes were observed when using one or another. Nevertheless, other basis functions, shearlet or curvelet (extensions of wavelets), are currently explored for other high resolution MRI applications [Tsai 2012, Zhang 2015].

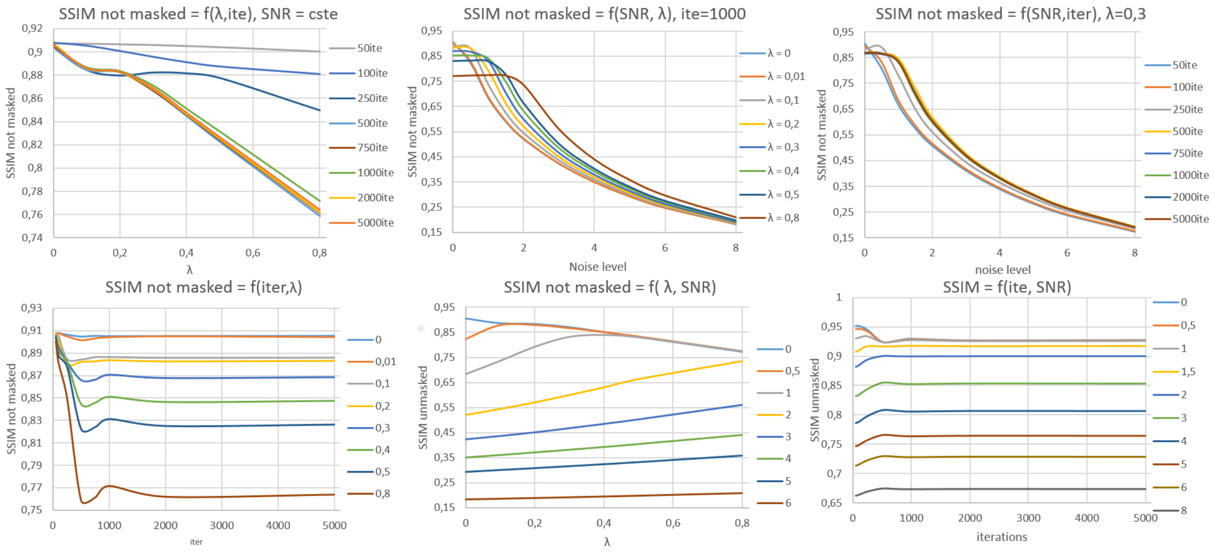

Figure 3.23: Impact on SSIM values compared with the iFFT reconstruction for variations of all parameters. Data were considered unmasked meaning that the large background noise variability leads to lowered SSIM values. Masking data does not change the behavior but improves SSIM numerical values. For the center and right plots curves illustrates the addition of noise with a factor ranging from 0.5 to 8 times the initial noise of the image.

3.4 Conclusion and perspectives

As explained in this Chapter, two families of UTE sequences are available for our X-MRI protocols: SPGR or SSFP sequences. Depending on our choice of one or the other, different signal dependencies to T_1, T_2* relaxation times and B_0 and B_1 fields should be considered for post-processing of our X-MRI data. As demonstrated by Romanzetti *et al.* [Romanzetti 2014], we chose to use the TPI non-Cartesian trajectory, and confirmed its superiority towards Cartesian sampling.

Our experiments to compare reconstruction algorithms allowed to better understand the behavior of the gridding algorithm that was implemented during this thesis and explore other methods based on the NUFFT or NFFT algorithms as well as non-linear iterative algorithms. We could observed the denoising and smoothing behavior brought by the non-linear iterative wavelet regularized algorithm based on FISTA.
While the benefits of such algorithms are of interest, the difficulty in setting the regularization weight and the number of iterations of the algorithm as they are dependent on data SNR would have required a deeper commitment to this problematic. As our implementation of the gridding reconstruction is fast and provides satisfying results for low resolution non-proton MRI, our subsequent X-MRI data were first reconstructed using gridding.

Our home-made gridding code was programmed on Python (The Python Foundation) allowing

a flexible use so as to reconstruct X-MRI from raw data acquired on different MR scanners (Siemens and Bruker). Furthermore, the use of 3D sampling sequence came along code improvements and developments to handle this new dimension and reconstruct data. Many Python functions were coded to make data compatible with all reconstruction algorithms. The use of raw data coming from acquisitions with multiple receiving channels and with multiple echoes also required the development of dedicated functions. Software limits were reached with our largest data set obtained for high resolution ^{1}H MRI acquisitions with 32 or more receiving channels. A final version of our code should be available for sharing as no license is needed.
On the contrary, the use of FISTA algorithm using Matlab requires a license and is dependent on several external libraries such as the NNFT which currently run solely on Linux station. For future *in vivo* Sodium applications, we used the NUFFT algorithm implemented in Matlab by Dr. Guillaume MADELIN.

Finally, this work demonstrates the potential of combining non-Cartesian sampling scheme with non-linear iterative reconstruction technique to attempt massively under-sampled acquisitions of high resolution X-MRI at ultra-high magnetic field.

CHAPTER 4

X-nuclei Concentration and Longitudinal Relaxation Time Quantification

Contents

The ultimate goal of non-proton MRI is to provide non-invasively specific, reliable and quantitative information about physiology, metabolism or pharmacology to biologists, pharmacologists, physicians or neuroscientists despite the relative scarcity of NMR signal and their limited temporal and spatial resolutions. In this chapter, we present a possible answer to this challenge in the form of a concentration and longitudinal relaxation time quantification pipeline for X-MRI *in vivo*. At the origin of this work, our collaboration with Dr. Sandro ROMANZETTI (Department of Neurology, Aachen University Hospital) and Dr. Guillaume MADELIN (Center for Biomedical Imaging, Department of Radiology, New York University) gave us the opportunity to implement and validate the Variable Flip Angle (VFA) method as a viable alternative to conventional steady-state spin density (SD) approach for ^{23}Na MRI at 3 T. This approach was later adapted for ^{31}P and ^{7}Li MRI at 7 T at NeuroSpin. Clinical research applications are presented later in Chapters 7, 8 and 9.

Parts of this Chapter were submitted as abstracts to the International Society for Magnetic Resonance in Medicine conference in 2017. Parts of this chapter are under review for publication in Magnetic Resonance in Medicine:
A.COSTE, F. BOUMEZBEUR, A. VIGNAUD, G. MADELIN, K. REETZ, D. LE BIHAN, C. RABRAIT-LERMAN and S. ROMANZETTI, Sodium Concentration and T_1 assessment in the human brain using a Variable Flip Angle approach at 3T.

4.1 The SD Approach

The SD approach consists in a single UTE acquisition with a 90° excitation flip angle and a long TR to minimize any relaxation effects and map the full magnetization. A non-Cartesian sampling scheme is preferred in most current implementations such as cones [RIEMER 2014], 3D Radial [INGLESE 2010, ZAARAOUI 2012, MAAROUF 2014, MAAROUF 2017], TPI [LU 2010a] or FLORET [MADELIN 2014, COSTE 2017]. Acquisition times (TA) are typically longer than 15 minutes and can be as long as 40 minutes [ZAARAOUI 2012] depending on the magnetic field strength and the spatial resolution achieved.

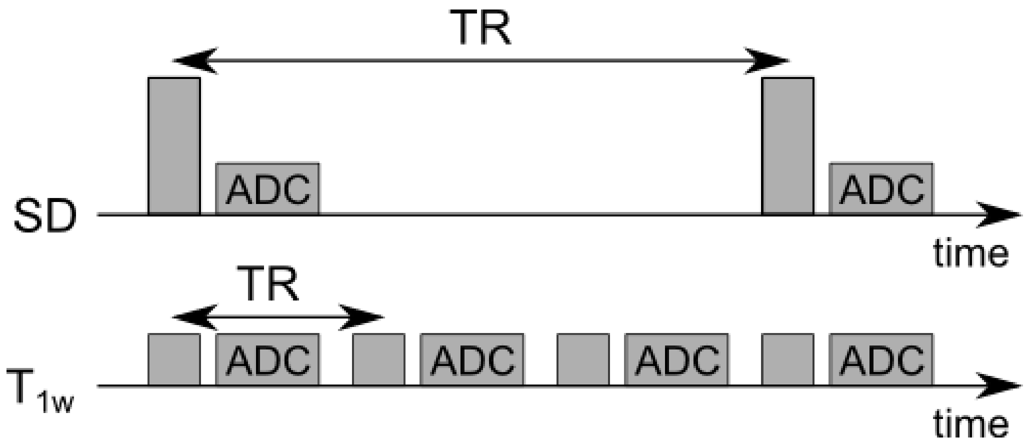

Figure 4.1: TR differences between Spin Density (SD) and T_1 weighted (T_{1w}) acquisitions allow to increase sampling efficiency.

To estimate quantitative concentrations, external phantoms with known sodium concentration are usually placed in the FOV and scanned together with the subject. Ideally, the phantoms should display similar dielectric or relaxometric properties than the brain or one of its compartment. Typically sodium chloride solutions are used to match the properties of CSF and agarose gels with increasing density can be used to mimic brain tissues (or cartilage) properties.

Depending on the exact parametrization of the SD UTE acquisitions, the signal equation can be simplified or corrected for T_1 relaxation effects and B_1^+/B_1^- inhomogeneities. Measuring signal intensity in each external reference allows to draw a calibration curve between signal intensities and estimated concentrations. The final step converts the corrected intensity ($\propto \rho$ (spin density)) map to a concentration map.

4.1.1 Implementation

To compare our VFA pipeline with the state-of-the-art method, we also implemented spin-density weighted Sodium acquisitions with parameters TE/TR=0.1/120 ms and FA=90°. As external references of concentrations, we used two 50 mL tubes located inside the phantom. Both phantoms were filled with sodium chloride at 50 and 100 mmol.L^{-1} and 2% or 6% of agarose (ref=23Na-3T-1). Intensity calibration was performed with both pair of tubes for comparison. In order to account for transmission and reception heterogeneities, The B$_1^+$ field was assessed using the Double Angle Method (DAM) [STOLLBERGER 1988], producing a B$_1^+$ field map based on two images with doubled nutation angle:

$$B_1^+ = \arccos\left(\frac{|I_{2\alpha}|}{2|I_\alpha|}\right) \qquad \text{[STOLLBERGER 1988]} \tag{4.1}$$

The computed B$_1^+$ map was then fitted using an 8th order polynomial function to preserve slow spatial variations while eliminating most of the noise from the transmission profile. Other filtering or smoothing techniques were evaluated such as a Gaussian Kernel, mean or median filter. However, no significant differences were observed on the TSC or T$_1$ maps between those techniques (data not shown). Since our ^{23}Na MRI data were obtained using a birdcage coil at 3T with moderate B$_1^+$ inhomogeneities, further explorations may be required for other X-nuclei or acquisitions at higher magnetic fields. In application of the reciprocity principle [HOULT 2000], the reception profile was considered identical to the acquired transmission profile.

To correct for residual T$_1$ and T$_2^*$-weighting, a correction factor can be considered as defined by:

$$f_{corr} = \left(\frac{1-e^{\frac{-TR}{T_1}}}{1-cos(\alpha)e^{\frac{-TR}{T_1}}}\left(0.6e^{\left(\frac{-TE}{T_{2f}^*}\right)} + 0.4e^{\left(\frac{-TE}{T_{2s}^*}\right)}\right)\right)^{-1} \qquad \text{[MADELIN 2010, MIRKES 2015]} \tag{4.2}$$

If images are acquired with an ultra-short echo-time, the exponential decay terms in equation 4.2 converge to 1 leading to a simplified correction factor:

$$f_{corr} = \frac{1-cos(\alpha)e^{\frac{-TR}{T_1}}}{1-e^{\frac{-TR}{T_1}}} \tag{4.3}$$

A plot of the required correction factor depending on TR and T$_1$ of studied tissue is presented later on Figure 4.16. T$_1$ values of our phantoms were estimated with MRS as explained in Chapter 2. Global T$_1$ values can also be estimated *in vivo* using MR spectroscopy leading to a spatially invariant correction factor. However, extracting brain masks for each brain compartments (grey, white matter and CSF) and use T$_1$ values from the literature should be a better alternative when no T$_1$ map is available. Unfortunately, we did not find the time necessary to program the necessary routines. The regression curves exploited multiple voxels within each calibration tube and analytic chemistry measurements were performed to control for the actual sodium concentration in those external references so as to get a more accurate concentration quantification.

4.2 The VFA approach

The Variable Flip Angle (VFA) method [CHENG 2006, PREIBISCH 2009, SABATI 2013] exploits two (or more) T$_1$-weighted images to evaluate both the total Sodium concentration (TSC) and the longitudinal relaxation time T$_1$. Contrary to the SD approach, no assumption has to be made regarding the global or local values of T_1. Hopefully, this should have a positive impact on the precision and robustness of the TSC measures. Moreover, considering the low ratio between signal acquisition duration and TR for the SD approach (typically in the range [0.05, 0.16] [ZAARAOUI 2012, RIEMER 2014, BILLER 2016]), one can expect an improved normalized SNR with the VFA mapping method.

4.2.1 Theory

The quantification of TSC using the VFA approach relies on the resolution of a linear system of equations of two unknowns (a, b) such as:

$$\frac{S}{\sin\left(B_1^+\alpha\right)} = a\frac{S}{\tan\left(B_1^+\alpha\right)} + b \tag{4.4}$$

Therefore at least two Steady State Spoiled Gradient Echo acquisitions are required. T_1 and M_0 are then determined by linear regression such as :

$$\begin{aligned} T_1 &= -\frac{TR}{\log(a)} \\ kM_0 &= -\frac{b}{1-a} \end{aligned} \tag{4.5}$$

To compute a spin density image, the relaxation and transmission corrected magnetization map M_0 is corrected for the coil reception profile:

$$\rho = k\frac{M_0}{B_1^-} \tag{4.6}$$

4.2.2 Choice of Repetition Time

The first step is to determine an optimal TR for acquisitions as it will constrain the used Flip Angles of the VFA method. To do so, quantum mechanical simulations where performed under Specific Absorption Rate (SAR) constrains to determine the shorter possible TR [STOBBE 2008]. SAR is the amount of RF energy deposited in the patient and is limited by official regulations to 3.2 W.kg^{-1} for the head [IEC 2015]. SAR depends on TR, the applied Flip Angle, the duration of the excitation pulse (τ_{RF}) and the static field intensity such as:

$$SAR \propto \frac{\alpha^2 B_0^2}{TR\tau_{RF}} \tag{4.7}$$

In collaboration with Sandro ROMANZETTI, quantum mechanical simulations considering residual quadrupolar interactions were performed to determine the optimal TR. Simulations of time normalized SNR were made to determine, under SAR constrains, the pulse duration and the TR value which maximizes the SNR per unit of time. Results are showed in Figure 4.2 and on which one can see that a maximum is reached on panel (B) for a 500 μs rectangular pulse with a TR of 20 ms and a flip angle of 55°.

The dissipated energy is measured based on the patient weight (m) and the power dissipated by the coil during an excitation cycle TR:

$$SAR_g = \frac{1}{m} \times \frac{V_{ref}}{L} \times \frac{\tau_{RF}}{TR} \tag{4.8}$$

where V_{ref} is the reference voltage, L is the Load of the coil and τ_{RF} is the duration of the RF pulse. Therefore, for a similar object, reducing TR leads to a global SAR increase. During the optimization of our protocol, we made sure that determined flip angles never exceeded SAR limits. Simulations were validated *in vitro* at 3 T with phantom experiments and confirmed later during *in vivo* explorations.

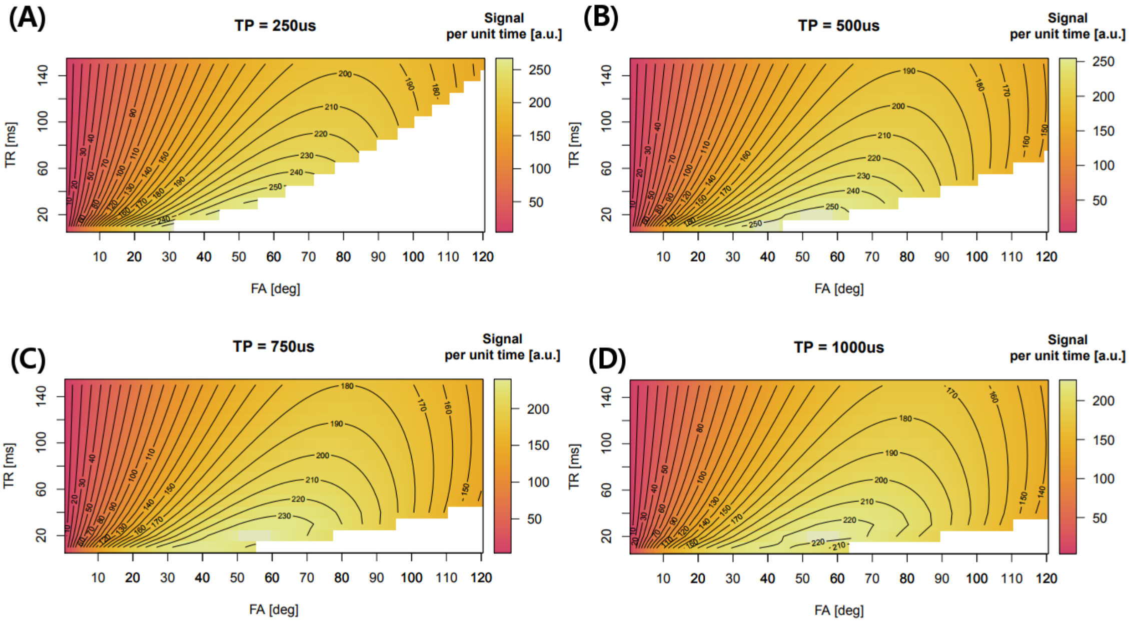

Figure 4.2: Simulations of SNR per unit of time, under SAR constrains for an increasing pulse duration from 250 μs to 1 ms.

4.2.3 Choice of Flip Angles

The choice of optimal flip angles for VFA method is important in order to maximize SNR and thus the quality of obtained images [Sabati 2013]. In SPGR acquisitions, the signal intensity is given by:

$$S = k\rho B_1^- \frac{1-e^{-TR/T_1}}{1-cos(\alpha)e^{-TR/T_1}} sin(\alpha) \left(0.6e^{-TE/T_{2f}^*} + 0.4e^{-TE/T_{2s}^*}\right) \tag{4.9}$$

The optimization method relies on solving a system of equations of two unknowns T_1 and M_0 (equal to ρB_1^- in eq 4.9). In the case of two images perfectly acquired at distinct flip angles α_1 and α_2, meaning that no transmit or receive heterogeneity is involved yet, equation 4.9 can be linearized as:

$$kM_0E = \frac{b}{1-a} = \frac{AS_1S_2}{BS_2 - CS_1} \tag{4.10}$$

Where

$$\begin{aligned}
A &= \sin(\alpha_2)\tan(\alpha_1) - \sin(\alpha_1)\tan(\alpha_2) \\
B &= \tan(\alpha_1)\sin(\alpha_1)(\sin(\alpha_2) - \tan(\alpha_2)) \\
C &= \tan(\alpha_2)\sin(\alpha_2)(\sin(\alpha_1) - \tan(\alpha_1)) \\
E &= 0.6e^{-TE/T_{2f}^*} + 0.4e^{-TE/T_{2s}^*} \\
a &= \text{slope of regression} \\
b &= \text{y intercept}
\end{aligned} \tag{4.11}$$

The use of ultra-short TE authorizes the approximation of E to one as $e^{-TE/T_{2f}^*} \rightarrow 1$. To optimize the choice of flip angles, we aimed at minimizing the noise deviation in the computed M_0 map as given by:

$$\sigma_{M_0} = \sqrt{\left(\frac{\partial M_0}{\partial S_1}\right)^2 + \left(\frac{\partial M_0}{\partial S_2}\right)^2}\,\sigma_S \tag{4.12}$$

Where σ_S is the noise in each image. Using equation 4.10, it is possible to compute each partial derivative of M_0 as:

$$\frac{\partial M_0}{\partial S_1} = \frac{ABS_2^2}{k(BS_2 - CS_1)^2} \qquad \frac{\partial M_0}{\partial S_2} = -\frac{ACS_1^2}{k(BS_2 - CS_1)^2} \tag{4.13}$$

leading to the formulation of the resulting noise on the M_0 image as:

$$\sigma_{M_0} = A\frac{\sqrt{B^2S_2^4 + C^2S_2^4}}{k(BS_2 - CS_1)^2}\sigma_S \tag{4.14}$$

To maximize SNR in the resulting M_0 map, it is therefore necessary to find the pair of angles (α_1,α_2) minimizing equation 4.14 while matching SAR constrains based on previously determined TR.

4.3 Post-processing

Computation of Sodium concentration map is achieved through the use of the acquired B_1^+ map and the two FLORET Sodium images with distinct flip angles. Solving Equation 4.5 allows to simultaneously compute a T_1 and a M_0 map. The use of phantom images with the volunteers are then used to compute the calibrating factor k of Equation 4.9. Figure 4.3 summarizes this post-processing pipeline.

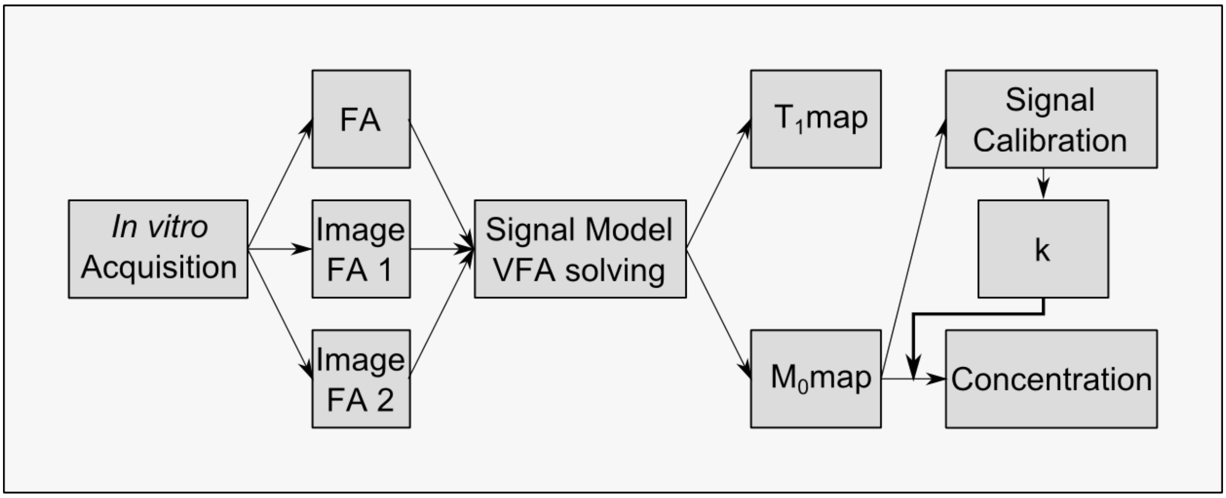

Figure 4.3: Schematic of the VFA post-processing pipeline to reach quantitative Sodium concentration and T_1 maps.

4.4 Sensitivity to patient motion

One major issue of long acquisition duration is possible patient or volunteer motion. Indeed, when undertaking an MRI exam people tend to loose track of passing time and after a while cannot concentrate to avoid motion. Therefore small motion can occur during acquisitions which leads to image blurring.

4.4.1 Fractionated acquisitions

To investigate this issue and attempt to alleviate its consequences, we used shorter acquisition blocks that could be realigned before being added to limit the eventual blurring due to motion.

The question of the duration of each block is not trivial as each block should have enough SNR to be independently reconstructed yet the acquisition should be short enough to capture (some of) the subject motion. After a few tests, we noticed that the minimum duration should be about 3 minutes. Depending on the spatial resolution of our image, the reconstruction method (or the field strength), it may be possible to go slightly below this limit.

4.4.2 Motion estimation and Image Reconstruction

To reconstruct the final motion corrected image all blocks are first individually reconstructed. Magnitude images are used to estimate a rigid transformation between the first and the other blocks. Four by four transformation matrix are considered:

$$T = \left(\begin{array}{ccc|c} a_{11} & a_{12} & a_{13} & T_x \\ a_{21} & a_{22} & a_{23} & T_y \\ a_{31} & a_{32} & a_{33} & T_z \\ \hline 0 & 0 & 0 & 1 \end{array}\right) \tag{4.15}$$

The motion correction matrices are then separately applied to both the imaginary and real part of reconstructed images to place them into the same space. Images are then corrected using the Homodyne phase reconstruction where a low pass filtering of each complex image is made and applied as:

$$I_H(x)e^{-i\Phi_L(x)} = I_H(x)\frac{I_L^*(x)}{|I_L(x)|} \qquad \text{[BERNSTEIN 2004]} \tag{4.16}$$

The final reconstructed and corrected image is then computed according to:

$$I = \sum_{block=1}^{N} I_{H,block}(x) \tag{4.17}$$

and illustrated by Figure 4.4.

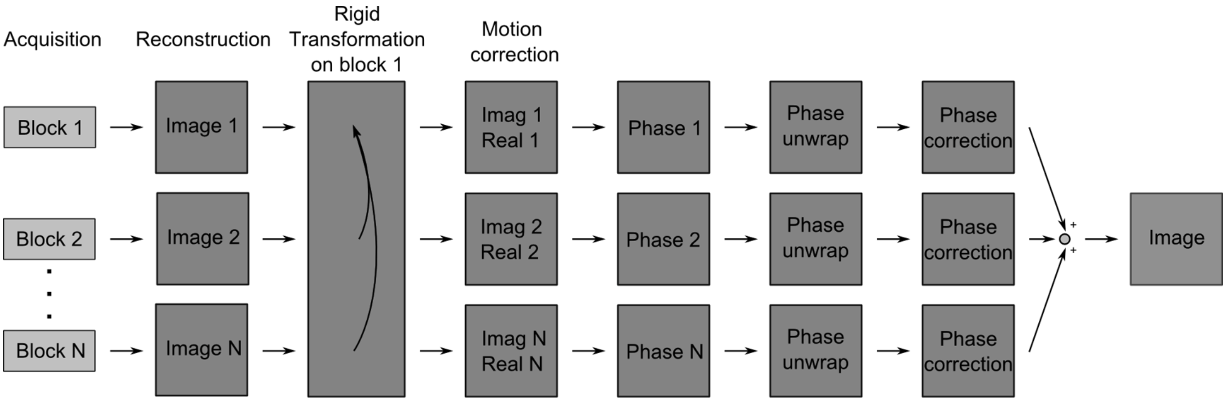

Figure 4.4: Motion correction and image reconstruction pipeline.

Finally, to improve image quality, a Non Local Mean Filter (NLM) [BUADES 2005] was applied on all reconstructed images. The algorithm aims at considering a weighting mean of a group of pixels to perform denoising of a target pixel according to:

$$u(p) = \frac{1}{\int_\Omega f(p,q)dq} \int_\Omega v(q) f(p,q) dq \tag{4.18}$$

Where p and q are two pixels, u(p) is the filtered value of p and v(q) the filtered value of q and f(p,q) a weighting function often defined as Gaussian function of the local mean value B of considered pixels.

$$f(p,q) = e^{-\frac{|B(q)-B(p)|^2}{h^2}} \tag{4.19}$$

4.5 TR and flip angles determination

TR determination was based under the SAR constraint to respect energy deposition regulations. The objective being to determine the shortest possible TR allowing VFA. In equation 4.7, one can notice that three parameters can be chosen (α,τ_{RF}, TR) and one (B_0) is defined by the hardware characteristics. To simplify simulations, we chose a relatively short pulse of 750 μs duration to minimize relaxation effects that can occur during RF pulses because of the imperfect transmission profile. The determination of possible flip angles is then possible depending on chosen TR. Numerical simulations were made by implementing equation 4.14 using Python (The Python Foundation). As variables S_1 and S_2 embed TR in their formulation, we could study the influence of TR on resulting noise. A range of $[1, 100]$ ms was used for TR and all possible values of both α_1 and α_2 were covered. For a given TR value, results can be presented as 2D symmetric convex maps whose minimum value is obtained for the two most suitable angles.

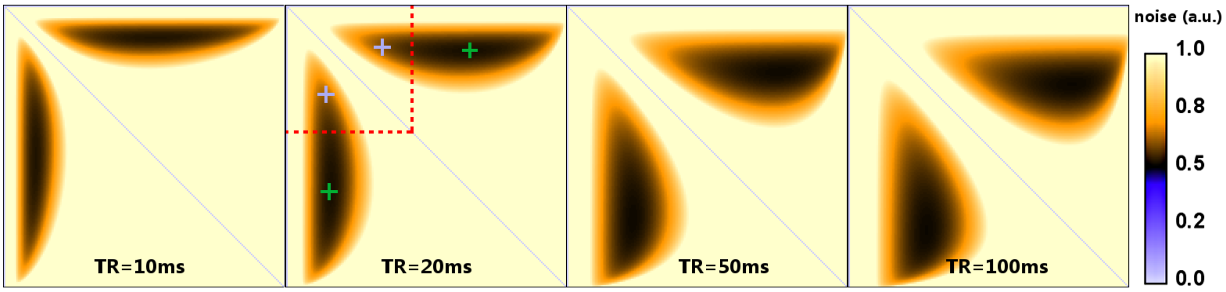

Figure 4.5: Simulation results of noise in M_0 image according for four different TR values 10, 20, 50 and 100 ms. Color map has been adapted for display to easily locate areas of minimal noise. Axis corresponds to α_1 and α_2 interchangeably. On the second panel corresponding of our chosen TR is plotted the SAR limit (red dashed line), the optimal flip angles (green crosses) and the chosen flip angle (light blue crosses).

Figure 4.5 confirms that the optimal FA values maximizing SNR in the magnetization image computed with the VFA method is as expected dependent on TR. As TR increases, the area of optimal SNR is moving toward larger flip angles. Based on our simulations, an optimal TR of 20 ms was selected. At such value, the lower noise in M_0 image is obtained using Flip Angles of respectively 28° and 117° (green crosses on Figure 4.5). Due to SAR limitations and considering a safety factor of 20%, a compromise on the value of α_2 was to be made leading to our choice to acquire one image at the Ernst angle of Sodium in tissues considering a T_1 of 35 ms [MADELIN 2014]:

$$\alpha_E = \arccos\left(e^{-TR/T_1}\right) = \arccos\left(e^{-0.02/0.035}\right) \approx 55^\circ \tag{4.20}$$

As a consequence, we set α_1 at the value of 25° will allow to limit the increase of noise in resulting image based on our numerical simulations.

4.6 *In vitro* Validation

The VFA and SD approaches were first tested and compared using a specially designed phantom (ref=$23Na - 3T - W$). This cylindrical phantom was designed with internal tube holders. In the periphery, 16 mL tubes were positioned containing sodium chloride solutions at concentrations ranging from 25 mmol.L^{-1} to 150 mmol.L^{-1}. At the center, four 50 mL tubes containing 2% or 6% agar gels with Sodium (NaCl) concentrations of 50 mmol.L^{-1} or 100 mmol.L^{-1}. The rest of the phantom was filled a sodium chloride solution at 75 mmol.L^{-1}. The phantom design is illustrated by panel (A) of Figure 4.8

4.6.1 Acquisition protocol

Our ^{23}Na MRI protocol consisted in VFA acquisitions with previously chosen angles of 25° and 55° performed with a 750 μs RF pulse and TR of 20ms, a ultrashort TE of 100μs at an isotropic spatial resolution of 4 mm. And a SD imaging protocol of similar TE and varying TR from 100 ms to 300 ms. TR values were incremented in order to evaluate the precision of the SD method according to the different T$_1$s of ^{23}Na in our different tubes. RF and gradient spoiling were applied to reach a steady-state similar to a SPGR sequence. FLORET sampling was realized with 3 hubs at angle $\alpha_0 = 45°$ and composed of 100 projections each. 3 signal averages were acquired for each 3 minutes acquisition block. Optimized acquisition parameters are presented in Table 4.1.

	SD	VFA	DAM	Unit
TE	0.1	0.1	0.1	ms
TR	[100,300]	20	80	ms
FA	90	25/55	60/120	degree (°)
TA	18	9/9	2/2	min
BandWidth	130	130	130	Hz/pixel
Resolution	4 iso	4 iso	6 iso	mm
Matrix	64 iso	64 iso	64 iso	voxel
FOV	256 iso	256 iso	384 iso	mm

Table 4.1: Acquisition parameters for our Sodium MRI protocol.

4.6.2 Denoising

Figure 4.6 illustrates the denoising effect of the Non Local Mean filtered used to improve image quality as background noise is significantly reduced and smoothing inside the phantom does not spread signal as illustrated in profile plots which is of particular interest.

4.6.3 Acquisition Efficiency

For fair comparison of both approach, TA was kept constant. As TA depends on TR, the number of averaged excitation (N$_E X$) had to be adjusted:

$$TA = TR \times Nb_{Projections} \times N_E X \tag{4.21}$$

Figure 4.7 illustrates the sampling efficiency of each acquisition based on the time-normalized SNR (tSNR) values calculated according to:

$$tSNR = \frac{SNR}{\sqrt{TA}} \tag{4.22}$$

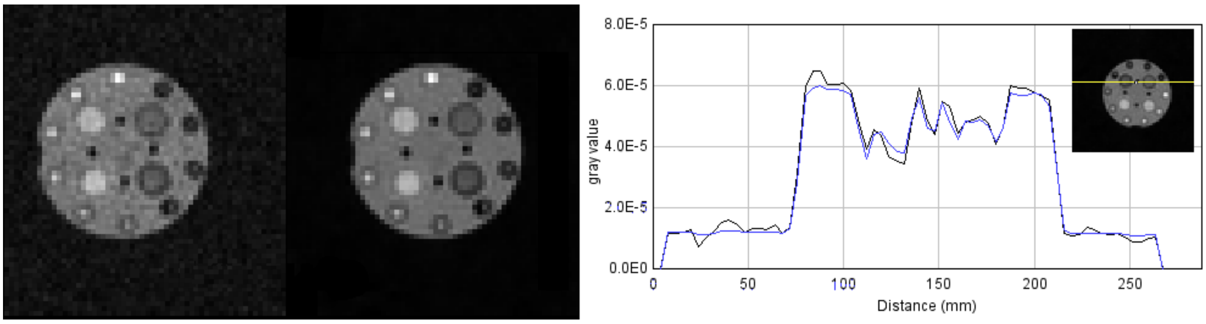

Figure 4.6: Effect of the Non Local Mean Filtered applied on Sodium data to reduce noise (blue line is the profile on the denoised image).

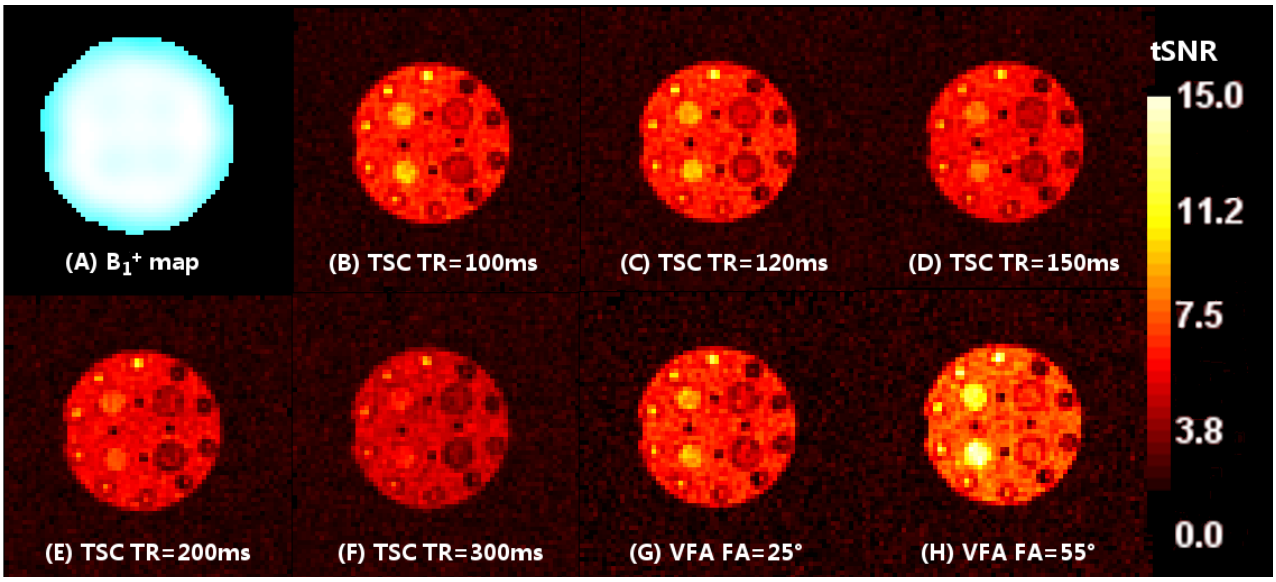

Figure 4.7: From B to H: tSNR maps for the different TSC acquisitions compared to VFA with flip angles 25° and 55°. A: B_1^+ profile. Due to the low resonance frequency of Sodium at 3T, about 34MHz, the transmission field is largely homogeneous.

As expected, tSNR decreases with increasing TR and the use of the Ernst Angle at shorter TR lead to an optimal accumulation of signal and sensitivity.

4.6.4 VFA vs SD TSC maps

Figure 4.8 presents the originally acquired and reconstructed TSC or T_1 maps for the VFA and the SD methods. The homogeneity of the corresponding transmission field can be appreciated from panel (A) of Figure 4.7. The whole correction pipeline was applied to SD acquisitions and compared to the concentration map obtained using VFA. The calibration between signal intensity and Sodium concentration was performed using the 2% agarose tubes (on top of the phantom).

At first glance, all TSC maps seem consistent to one another with a slightly better SNR and smoothness for the TSC map acquired with SD approach and the shortest TR of 100ms. As the TR increase, the values in the SD TSC maps converges towards the ones of the VFA TSC map. The quantitative analysis of these TSC maps confirms these observations and is summarized in Figure 4.9.

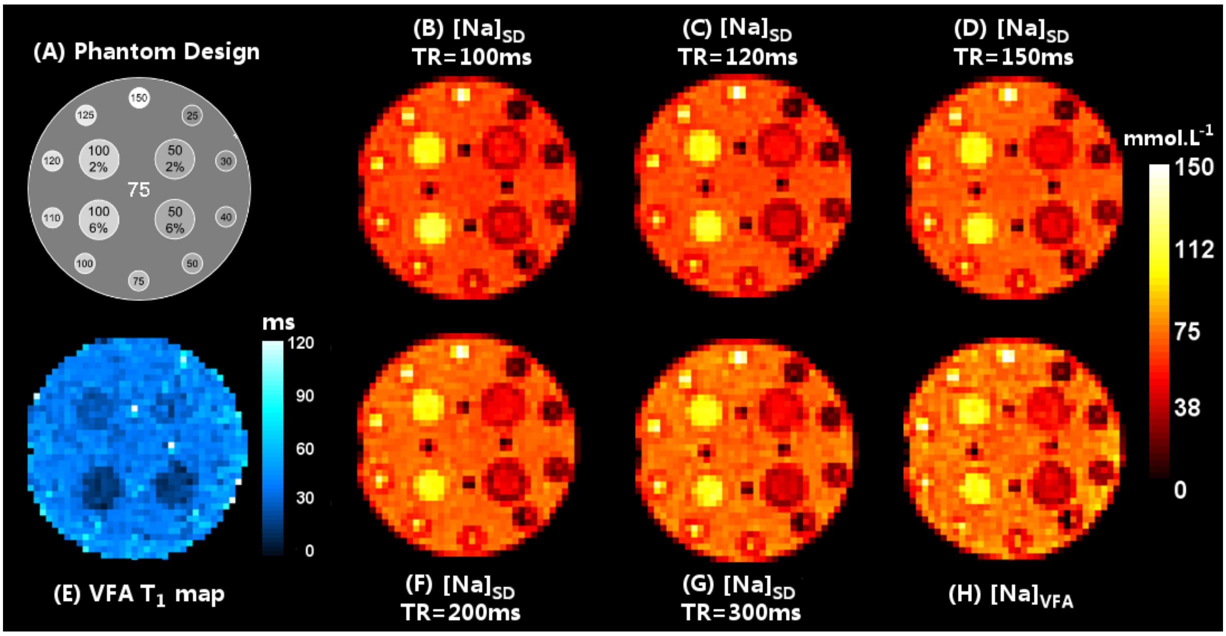

Figure 4.8: Computed concentration maps for the different acquisitions comparing SD with varying TR ([100,300] ms) and VFA.

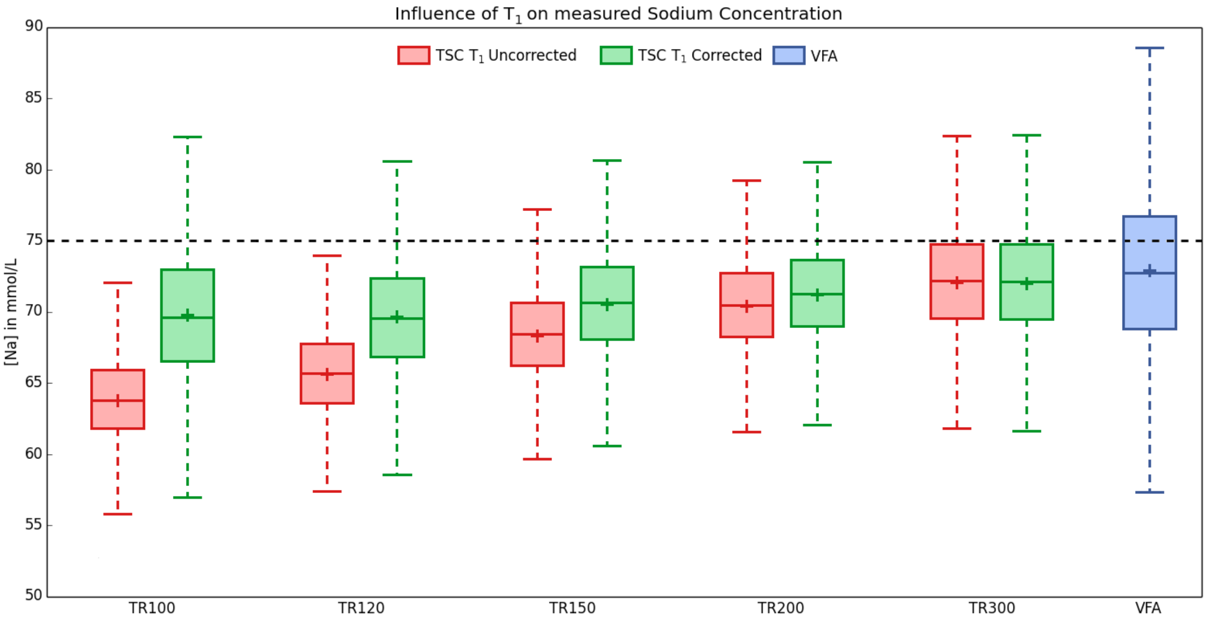

Figure 4.9: TSC values in the central liquid compartment of the phantom for the VFA approach and the SD acquisitions at TR of 100 ms, 120 ms, 150 ms, 200 ms, 300 ms with and without T$_1$ correction. (Details about box-plots can be found in Annex 9.4).

As expected the VFA method yields the more accurate estimation of TSC in the central compartment of the phantom as well as in the two 6% agarose tubes as presented in Figure 4.10.
When considering the 6% agarose tubes as our references of concentrations, noticeably higher con-

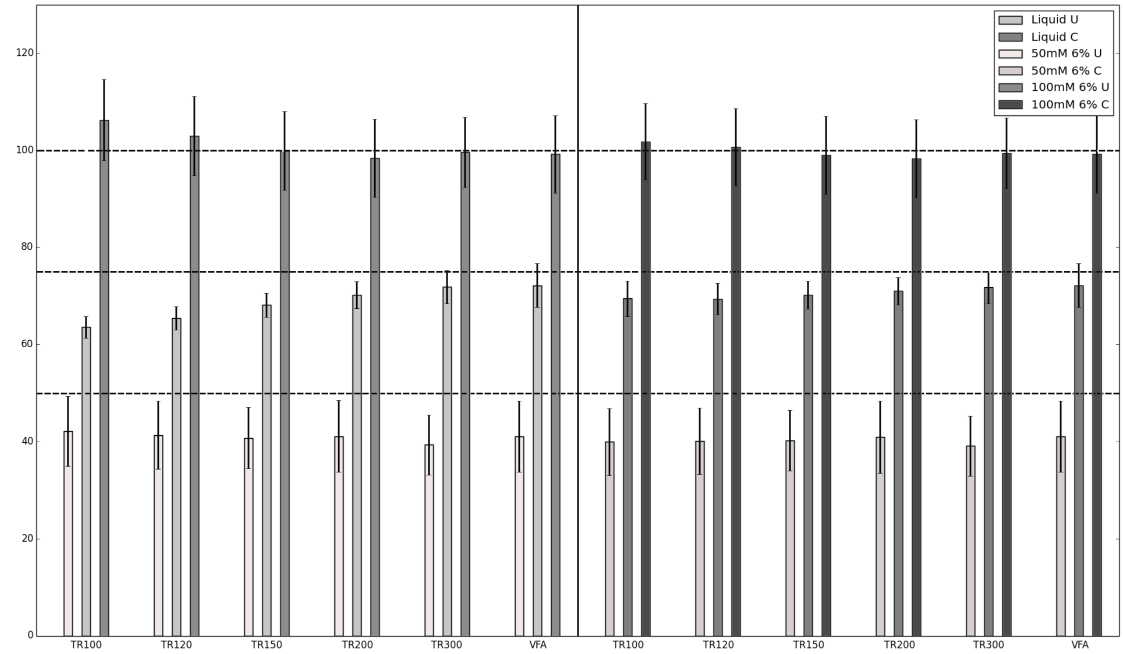

Figure 4.10: Concentration measurements in different compartments using 2% agarose tubes for calibration. On the left part of the plot is the T_1 uncorrected SD data (U) and on the right is SD data corrected with VFA T_1 map (C).

centrations were estimated (Figure 4.12) than when the 2% agarose tubes were used for calibration. Therefore, higher errors were computed as illustrated on Figure **??**.
This discrepancy should be attributed to the faster T_2* decay in the 6% vs the 2% agar gels which could lead to overestimation of sodium concentration. As for the previous measurements, the TSC estimations from the VFA approach are comparable to the values obtained with the SD approach and a TR of 300ms. For the SD approach with TR of 200ms and below, quantification errors can be as high as 12% if no T_1 correction is applied or about 4% when T_1 saturation effects are accounted for using the T_1 map from the VFA approach (Figure 4.13).

4.6.5 VFA T_1 map

Panel (E) in Figure 4.8 shows the T1 map extracted from the VFA pipeline. For the main compartments, the resulting distribution of T_1 values are detailed in Figure 4.14. A expected, a longer T_1 of 41.6 ± 5.9 ms was measured using VFA in the liquid compartment while average T_1s of 29.7 ± 4.7 ms and 19.6 ± 5.1 ms were measured respectively in the 2% and 6% agarose gels.

4.6.6 Limitations of the VFA approach

In spite of the satisfactory estimation of average T_1 and TSC values using the VFA approach, one must also consider the large spread of our T_1 values and the larger spread of TSC values from VFA compared to the SD acquisitions. This is the cost to pay for simultaneously estimating TSC and T_1 maps from two images with shorter TA (even if the intrinsic tSNR is higher for these acquisitions).
As summarized in Figure 4.15, when proper corrections for residual T_1-weighting are applied, the average TSC values are directly comparable whatever acquisition is performed. These data demonstrate : (i) the VFA approach allows to obtain T_1-independent concentration measurements; (ii) a

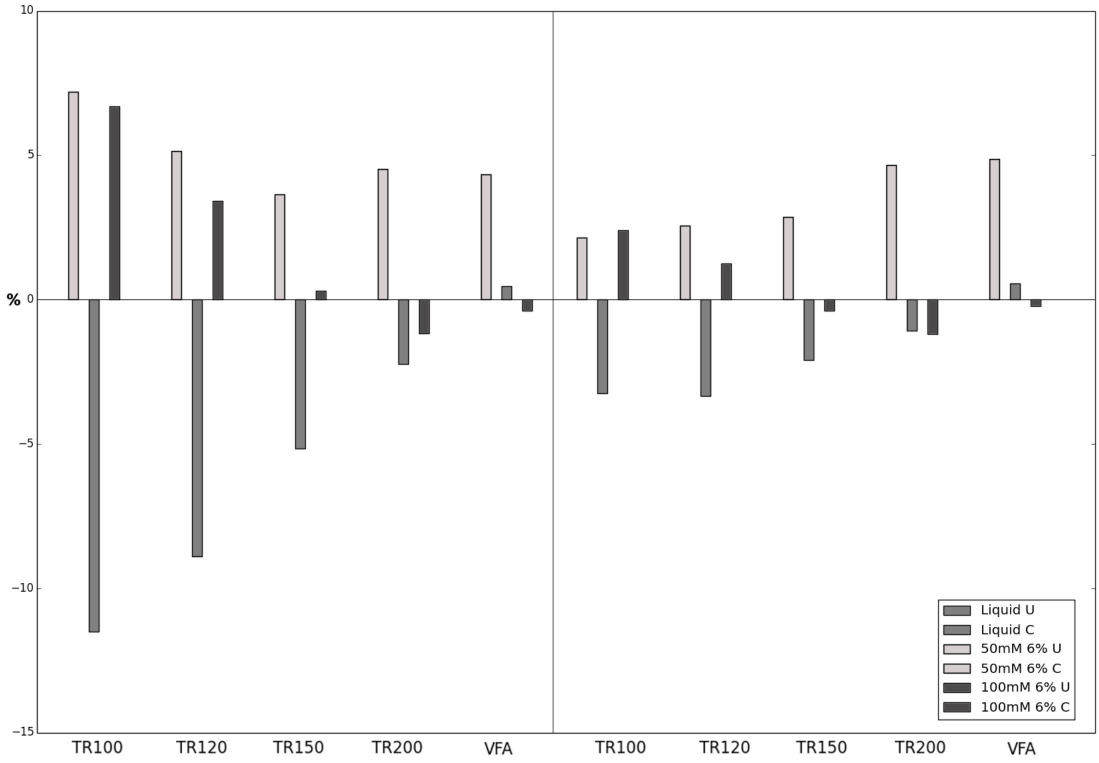

Figure 4.11: Relative concentration error normalized to TR 300 ms taken as reference. On the left part of the plot is the T_1 uncorrected SD data (U) and on the right is SD data corrected with VFA T_1 map (C).

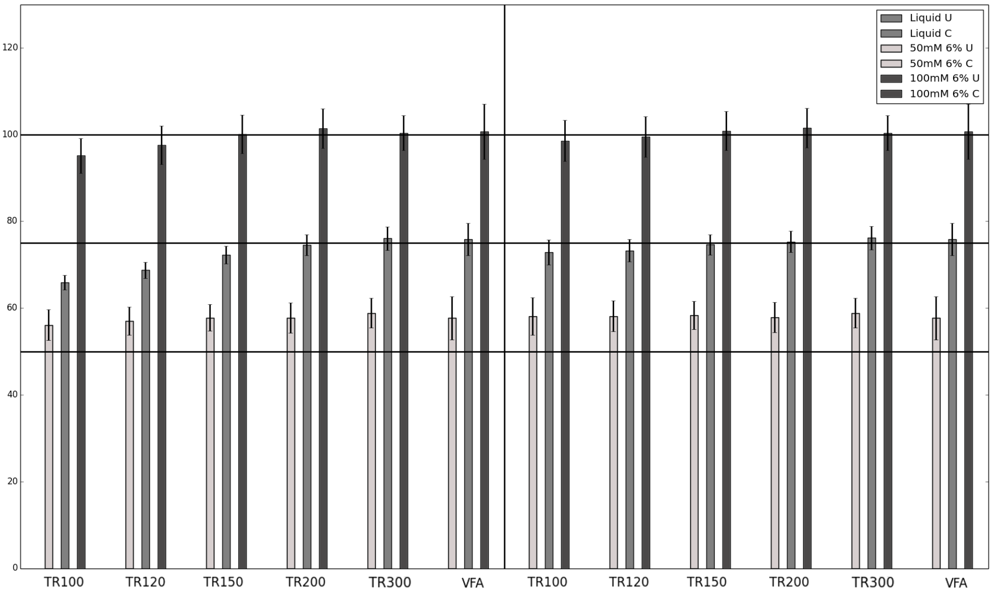

Figure 4.12: Concentration measurements in different compartments using 6% agarose tubes for calibration. On the left part of the plot is the T_1 uncorrected SD data (U) and on the right is SD data corrected with VFA T_1 map (C).

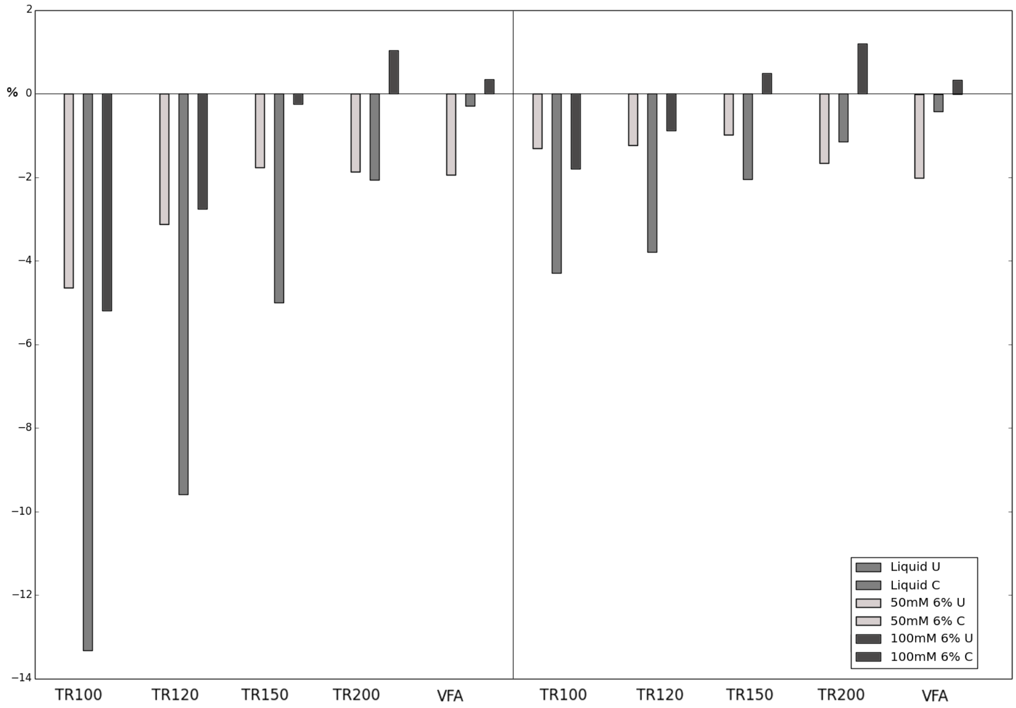

Figure 4.13: Relative concentration error normalized to TR 300 ms taken as reference. On the left part of the plot is the T_1 uncorrected SD data (U) and on the right is SD data corrected with VFA T_1 map (C).

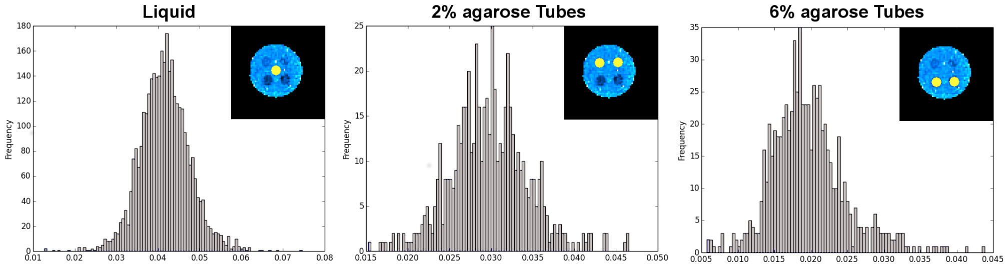

Figure 4.14: T_1 distributions (in s) at the heart of the internal compartment (left), in the 2% agarose tubes (center) and in the 6% agarose tubes (right).

SD acquisition with a long enough TR (Figure 4.16) is a competitive approach; (iii) relative short TR (to boost SNR) should be considered with caution unless T_1s are known and can be accounted for.

4.7 Conclusions and Perspectives

As non-proton MR images intrinsically suffer from the modest *in vivo* levels of electrolytes or metabolites, optimizing the SNR per unit of time and volume is a priority. In the case of ^{23}Na MRI, the use of UTE with non-Cartesian sampling scheme is the obvious choice to efficiently sample k-space and limit the loss of signal due to the fast T_2^* decay which is in the case of white matter in the range of [0.8,3] ms for the short component and in the range [15,30] ms for the long.

However, X-MRI and ^{23}Na MRI in particular focus on estimating and exploiting concentrations

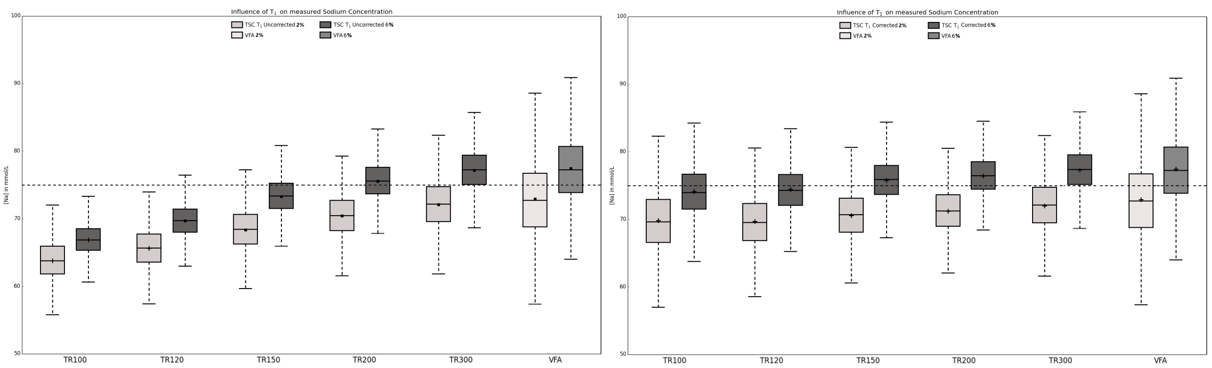

Figure 4.15: Concentration measurements in the central liquid compartment depending on used tubes for calibration on TSC T_1 uncorrected data (left) and T_1 corrected data (right).

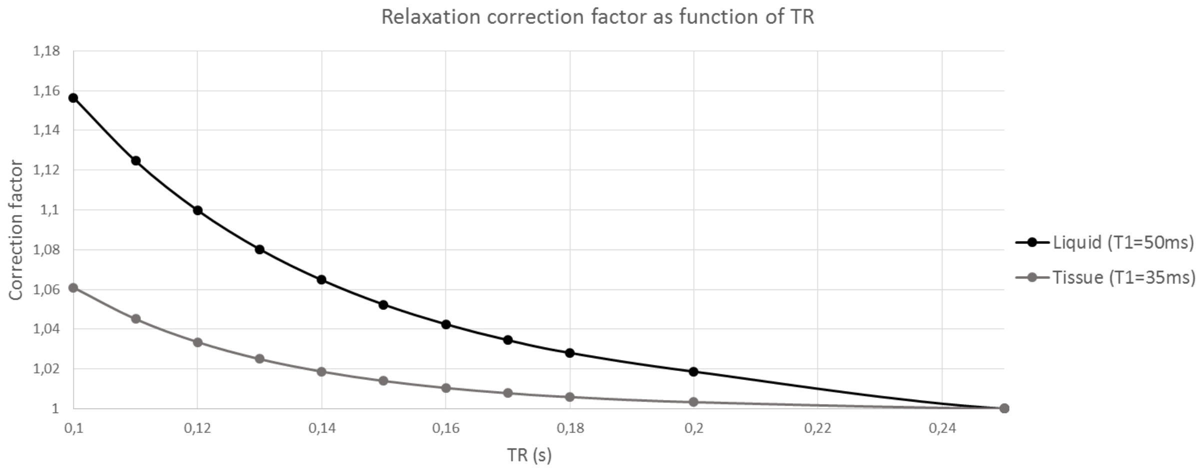

Figure 4.16: Correction factor for two distinct T_1 based on equation 4.2.

changes in pathological conditions. Therefore, the challenge is to obtain in the most efficient way, precise and robust concentration maps.

In this context, our VFA acquisition pipeline should be of high interest as it manages to boost signal accumulation without increasing the acquisition time, while extracting simultaneously accurate T_1 and TSC values.

Numerical simulations were performed to determine optimal acquisition parameters to maximize the robustness of the quantification pipeline and guarantee the clinical feasibility of our VFA approach.

Our *in vitro* tests have confirmed the precision of our quantification pipeline (with negligible errors for TSC - less than 2%)and its superiority compared to SD acquisitions when residual T_1-weighting are not accounted for properly (TR< 200 ms). With the broad use of TR as short as 120 ms in several clinical studies [INGLESE 2010, ZAARAOUI 2012, PALING 2013, RIEMER 2014, MAAROUF 2014], TSC errors as high as 10% in CSF (and in the eyes) and of about 4% in tissues should be expected.

Regarding the limitations of our VFA method, we can identify several axis of improvement. First, the estimation of the T_1 maps could be tackled differently so as to limit the spread of our T_1 distributions and accordingly improve the smoothness of our VFA TSC map. Regularization weigths could be added to our "Signal model solver". Masks could be extracted from reference ^1H images to constrain spatially the fit of homogenous T_1s for each compartments. Also, additional T_1-weighted acquisitions at other flip angles could be considered to increase the robustness of T_1 and M_0 estimation but at the cost of an increased acquisition time.

Finally, *in vivo* applications of our VFA approach are presented in Chapters 7 and 9, confirming the potential of this promising alternative to SD imaging for quantitative X-MRI.

CHAPTER 5

Simultaneous Quantitative Multiparametric exploration of X-nuclei Properties

---

Contents

Contrary to the transmission rate of an X-ray beam for CT, the NMR signal is sensitive to a multitude of physico-chemical properties (water content, diffusion coefficient, magnetic susceptibility, Young's modulus, pH, temperature,...) of the nucleus of interest or its environment. While this complexity is an opportunity to create multiple contrasts using MRI, it is also a challenge as the evolution of our MRIs during a pathological or physiological process can reflect the changes of more than one of these properties. Even more problematic is the possibility for the MRI signal intensity or contrasts to differ between MRI scanners or from one day to another on the same MRI.

In order to mitigate this limitation of MRI (especially for multicentric or longitudinal studies), quantitative MRI approaches have been proposed: Look-Locker [SCHMITT 2004], QRAPTEST and QRAPMASTER [WARNTJES 2007, WARNTJES 2008], Magnetic Resonance Fingerprinting (MRF) [MA 2013], Double Echo and Triple Echo Steady State (DESS/TESS) [WELSCH 2009, HEULE 2014], Magnetization Prepared DESS [STÖCKER 2014], Diffusion Weighted DESS [GRAS 2016]. Inversion Recovery (IR) and Multiple Gradient Echo (MGE) are among the simpler and most used methods to estimate T_1 and T_2 relaxation constants. Recently, Ludovic DE ROCHEFORT (CRMBM, UMR 7339, Aix-Marseille University) has devised a new method for quantitative, multiparametric MRI using a SSFP sequence with multiple contrasts (QuICS) [DE ROCHEFORT 2015, DE ROCHEFORT 2016c]. In collaboration with Lisa LEROI whose PhD thesis is dedicated to the development of high-resolution quantitative ^{1}H MRI in a clinically viable time, we have explored the possible application of QuICS to assess simultaneously Sodium relaxation times and diffusion coefficient at 7 Tesla.

Parts of this Chapter were submitted as an abstract at the International Society for Magnetic Resonance in Medicine conference in 2017. Parts of this chapter are under review for publication as a note in Magnetic Resonance in Medicine:
A.Coste, L. Leroi, L. De Rochefort, M. Santin, R. Valabregue, F. Mauconduit, D. Le Bihan, C. Poupon, F. Boumezbeur, C. Rabrait-Lerman and A. Vignaud, Multi-parametric mapping of ^{23}Na spin density, T_1, T_2 and ADC at 7 Tesla based on Multi-contrast unbalanced SSFP.

5.1 Quantitative Imaging using Configuration States: QuICS

Quantitative Imaging using Configuration States (QuICS) is one of the latest method proposed for multiparametric quantitative MR imaging [de Rochefort 2015, de Rochefort 2016c]. The aim of the method is to robustly and simultaneously assess a magnetization map M_0, the longitudinal relaxation rate R_1, the transverse relaxation rate R_2 and a mono-dimensional estimation of an Apparent Diffusion Coefficient (ADC) while correcting for heterogeneities of the static magnetic field B_0 and coil transmission profile B_1^+.

This method relies on a multiparametric SSFP acquisition with the associated pulse sequence diagram depicted by Figure 5.1.

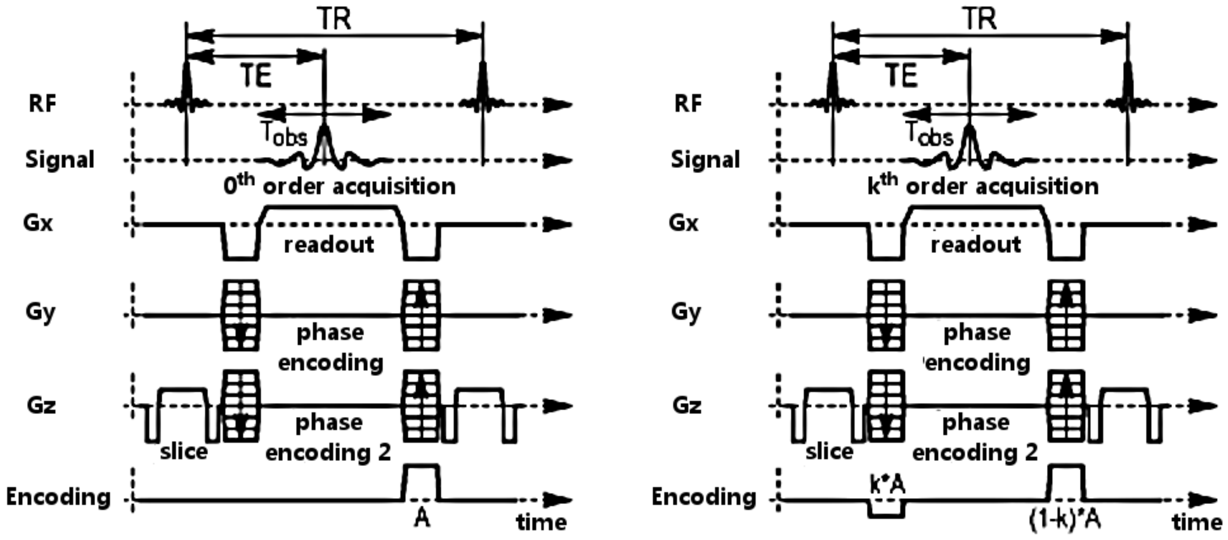

Figure 5.1: QuICS method: SSFP sequence diagram showing iterations of the spoiling gradient and the set of possible varying parameters: TE, TR, flip angle and spoiling momentum (referred to as A). The left panel illustrate the 0^{th} order volume acquisition and the right panel the k^{th} order volume acquisition where spoiling momentum is changed (other parameters: TR, TE and FA could also be changed) (translated from [de Rochefort 2016a]).

5.1.1 Signal modeling

As detailed previously in Chapter 3, Gradient Recalled Echo sequences can be either balanced, *i.e.* when all gradients are refocused between the RF pulses, or unbalanced, when a constant spoiling gradient area remains on a fixed axis. Balanced sequences are sensitive to B_0 inhomogeneity as phase accumulation between TRs is leading to the so-called banding-artifacts [EPSTEIN 1996]. Application of a gradient spoiling aims at creating a dephasing greater than 2π within one voxel such that the banding artifact is unapparent as all phases between 0 and 2π are present within the voxel and the measured signal corresponds to an average. Without loss of generality, the spoiling gradient axis is denoted z here but it can be applied on any physical axis (in practice, the direction varies among manufacturer and sequences). The gradient temporal waveform $G(t)$ is chosen such that a constant area remains between two TRs. This area is proportional to a spatial frequency shift:

$$\Delta k_z = \frac{1}{a} = \frac{\gamma}{2\pi} \int_0^{TR} G(t)dt \tag{5.1}$$

which is inversely proportional to a distance a called spoiling distance and corresponding to a 2π dephasing between two TRs. In such situation, magnetization can be described in space (as M(z)) or in terms of spatial frequencies. The latter description was proposed twenty-six years ago and is referred to as the "configuration states" description [PAULY 1991, LE ROUX 1993] or the "extended phase graph" description [HENNIG 1991a, HENNIG 1991b, SCHEFFLER 1999, WEIGEL 2015]. After several excitations at constant RF amplitude, a steady state is reached in which multiple orders are maintained within each voxel. Longitudinal and transverse relaxation magnetization after the n^{th} excitation can be decomposed into discrete complex Fourier series, as done in the extended phase graph theory, or similarly into polynomials P_n and Q_n as:

$$\begin{aligned} P_n &= \sum_{k=-\infty}^{k=+\infty} \sum_{j=-\infty}^{j=+\infty} p_{j,k,n} Y^{-j} Z^{-k} = \sum_{k=-\infty}^{k=+\infty} P_{k,n}(Y) Z^{-k} \\ Q_n &= \sum_{k=-\infty}^{k=+\infty} \sum_{j=-\infty}^{j=+\infty} q_{j,k,n} Y^{-j} Z^{-k} = \sum_{k=-\infty}^{k=+\infty} Q_{k,n}(Y) Z^{-k} \end{aligned} \tag{5.2}$$

where Y describes the phase such that the RF spoiling is considered using an apparent spatial frequency Δk_y as:

$$Y = e^{-2i\pi \Delta k_y a} \tag{5.3}$$

and where Z describes the spatial modulation between two excitations and is characterized by the total gradient area between two consecutive RF pulses along the Z direction as:

$$Z = e^{-2i\pi k_z z} \tag{5.4}$$

In this framework, magnetization components for each configuration state k are real numbers and the RF pulse action, which is modulated in amplitude and phase, is deduced from three numerical operations: linear filtering, linear combinations and index shifting. Indeed, the application of a spoiling gradient after the n^{th} excitation will lead to a coefficient shift of the transverse magnetization Q_n before the next excitation as described by:

$$Q_{n+1} = Z^{-1} \times Q_n \tag{5.5}$$

Similarly, the relaxation can be modeled as an attenuation of the signal according to:

$$\begin{aligned} P_{n+1} &= (1 - E_1) + E_1 \times P_n \\ Q_{n+1} &= E_2 \times Q_n \end{aligned} \tag{5.6}$$

with:

$$\begin{aligned} E_1 &= e^{-TR/T_1} \\ E_2 &= e^{-TR/T_2} \end{aligned} \tag{5.7}$$

Diffusion can be seen as a Gaussian filtering of acquired signal given by:

$$\begin{aligned} P_{n+1} &= D_P \star P_n \\ Q_{n+1} &= D_Q \star Q_n \end{aligned} \tag{5.8}$$

With

$$\begin{aligned} D_P &= \sum_{k=-\infty}^{k=+\infty} \left(e^{-DTR\left(\frac{2\pi}{a}\right)^2}\right)^{k^2} Z^{-k} \\ D_Q &= \sum_{k=-\infty}^{k=+\infty} \left(e^{-DTR\left(\frac{2\pi}{a}\right)^2}\right)^{k^2+k+\frac{1}{3}} Z^{-k} \end{aligned} \tag{5.9}$$

introducing D as the free diffusion coefficient. Finally, RF spoiling is modeled as a convolution of the longitudinal and transverse polynomials:

$$\begin{aligned} P_{n+1} &= S_v \star P_n \\ Q_{n+1} &= S_v \star Q_n \end{aligned} \tag{5.10}$$

with

$$S_v = \sum_{k=-\infty}^{k=+\infty} Y^{-kv} Z^{-k} \tag{5.11}$$

A second order recurrence relation on Q_n can be established as:

$$-a_n Q_{n-1} + b_n Q_n - c_n Q_{n+1} = r_{-1}\delta_{n+1,0} + r_0 \delta_{n,0} \tag{5.12}$$

where a_n,b_n,c_n,r_{-1},r_0 can be expressed as functions of Y, E_1, E_2, D_P, D, TR, FA and δ the Dirac function. Finally P_n will be deduced from:

$$d_n P_n = e_n Q_n - d_n Q_{n-1} \tag{5.13}$$

where e_n and d_n can be expressed as functions of Y, E_1, E_2, D, TR, FA leading to an efficient SSFP complex signal calculation for a given set of acquisition parameters.

To further emphasize the options in unbalanced sequences, an additional quadratic RF cycling is usually performed. It was originally proposed by ZUR with a spoil increment of 117° to reduce stimulated echo formation [ZUR 1991] and provides a steady-state closer to the one obtained for T_1-weigthed fully spoiled sequences. This spoiling increment varies as a function of the implementation, which is a source of limited reproducibility among manufacturer. Indeed, it has been shown that very different steady-states are obtained, in particular with small spoiling increments (few degrees) producing a T_2-weigthed contrast [GANTER 2006, BIERI 2011, DE SOUSA 2012].

As can be seen, multiple contrasts influenced by T_1, T_2 and ADC can be obtained using SSFP sequences and the configuration state description is adapted to analyze and describe them. This is the framework chosen here to deal with the Bloch-Torrey magnetization simulation and extraction of quantitative parameters from several contrasts obtained using SSFP. The Bloch Torrey equation is defined as:

$$\frac{dM}{dt} = \gamma_X M \times B - \frac{M_x\vec{i} + M_y\vec{j}}{T_2} - \frac{(M_z - M_0)\vec{k}}{T_1} + \nabla \cdot D \nabla M \qquad \text{[TORREY 1956]} \tag{5.14}$$

A more detailed description of the signal can be found in [DE ROCHEFORT 2016a].

5.1.2 Numerical simulations

For our experiments, GRE acquisitions with a fixed gradient spoil area and direction, as well as fixed RF pulse amplitude were considered, and only RF phase cycling was used to modulate the contrast from one acquisition to another. Additionally, we only acquired the m_{xy_0} state. Figure 5.2 provides examples of the SS transverse magnetization for k=0 state for all possible spoiling increments. This illustrates theoretical transverse magnetization complex signals for a voxel resulting from the k=0 state. Targeted acquisition parameters are presented in Table 5.1. The associated complex plane where each cross corresponds to a different RF spoiling increment, sampled for each degree from 0 to 360°. The maximum real value with null imaginary part corresponds to an RF spoiling increment of 0°/360°. It is represented in the complex plane to emphasize the signal variation with RF spoiling increment.

Parameter	targeted value	Unit
T_1	60	ms
T_2	50	ms
ADC	$1.3\text{x}10^{-9}$	$m^2 s^{-1}$
Spoiling range	[0,360]	degrees
Spoiling increment	1	degree
TR	10	ms
TE	3.2	ms
FA	45	degrees
resolution	6x6x6	mm^3
spoiling distance a	0.128	mm

Table 5.1: Targeted parameters used for simulations.

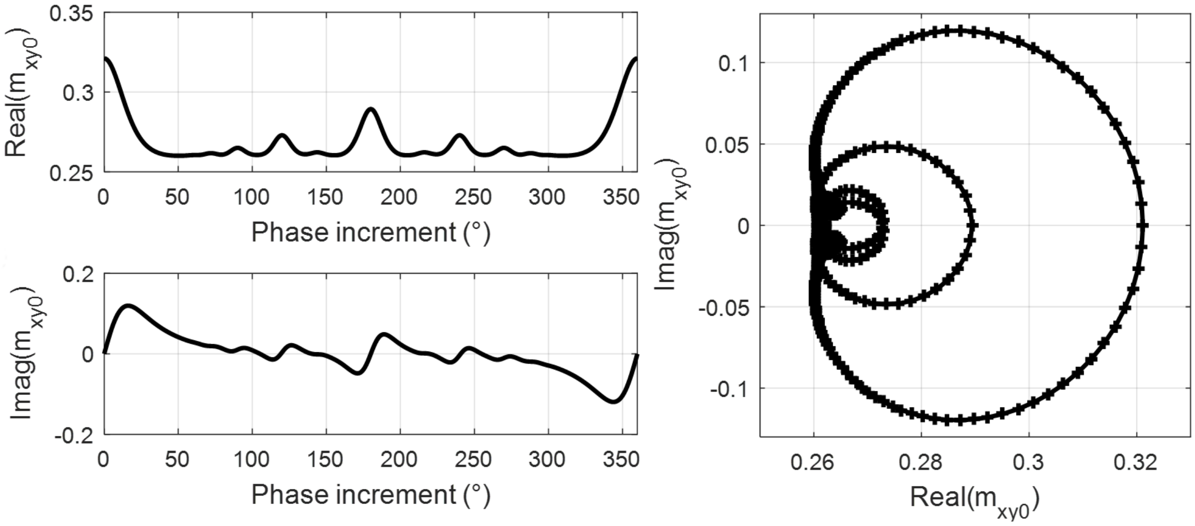

Figure 5.2: Real (top left) and imaginary (bottom left) parts of the theoretical transverse magnetization signal and the associated complex plane (right).

Figure 5.3 highlights the contrasts obtained with parameters presented in Table 5.1 and different T_1(left), T_2(center) and ADC (right) values. Obviously, the sensitivity of QuICS to changes in T_1, T_2

or ADC differs.

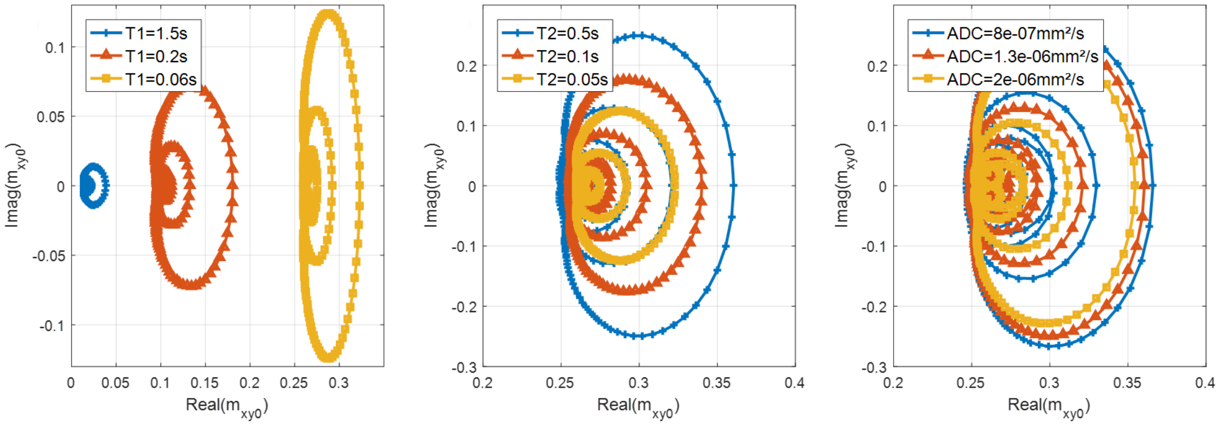

Figure 5.3: Complex representations of simulated signals for different T_1(left), T_2(center) and ADC(right).

5.1.3 Parameters extraction

To perform the quantitative extraction from the multiple SSFP signals, for each voxel in an image, the measurement are grouped into a single measurement vector:

$$S = [s(j)] = M_0 \times [m_{xy0}(j, T_1, T_2, ADC, \alpha)] + \eta = M_0 \times S_{model} + \eta \tag{5.15}$$

where η represents the acquisition noise and in which s(j) denotes the result of measurement j with a different set of acquisition parameters. M_0 is the voxel spin density multiplied by the coil sensitivity (B_1^-) at the voxel location, with additional T_2^* decay and phase accumulation at echo time. Finally, $m_{xy0}(j, T_1, T_2, ADC, \alpha)$ is the normalized SSFP signal for the voxel that depends on relaxation, diffusion and the effective flip angle at the voxel location as simulated in Figure 5.3. The principle of the quantification is then expressed by the least squares minimization of:

$$argmin_{\alpha, T_1, T_2, ADC} ||S - M_0 \times S_{model}(\alpha, T_1, T_2, ADC)||^2 \tag{5.16}$$

Where S_{model} is a vector containing discrete theoretical signal for each set of α, T_1, T_2, ADC obtained from the Bloch-Torrey equation. The flip angle is considered as a variable to be determined here. Indeed, the effective flip angle is usually different from the nominal flip angle due to B_1^+ being inhomogeneous. The degree of inhomogeneity is usually limited at low field or for non-proton nuclei with volume transmit coil, but becomes quite significant at ultra-high field or for surface coils.

Post-processing was performed with Matlab (The Mathworks, Natick, USA) based on the DICOM magnitude and phase images. Global phase drifts were first removed, assuming a linear temporal evolution between the first and last scans acquired in the same conditions. A gradient-echo phase map was estimated using the complex sum of volumes with 0° and 180° RF phase increments. It was then subtracted from all volumes providing the SSFP phase-induced maps independent of TE and corrected for B0 inhomogeneities.

A Gauss-Newton algorithm was implemented in Matlab including a numerical evaluation of the Jacobian matrix. The initialization parameters were selected by generating a limited dictionary of 32×32 values of T_1 and T_2 at fixed ADC (2.10^{-9}) and the nominal flip angle. The set minimizing the norm in Equation 5.16 was selected as a starting point for the subsequent Gauss-Newton iterations. The procedure was repeated until relative variations of the parameters were small enough (10^{-6} relative variations).

As robust concentration estimation is the main objective in non-proton MRI, we also wanted to assess this parameter. To compute a concentration map, magnetization images M$_0$ were corrected for reception profile:

$$\rho = \frac{M_0}{B_1^-} \tag{5.17}$$

Reception profile B$_1^-$ was determined using the reciprocity principle from the transmission profile B$_1^+$. Finally, to estimate concentration, the intensity of the obtained spin density image was calibrated using reference acquisitions with concentrations of 50 and 150 mmol.L^{-}1. Other acquisitions were performed changing the concentration of one tube to 30, 50 and 100 mmol.L^{-}1 concentrations and keeping the 150 mmol.L^{-}1. Reacquisition of an image with the 50 and 150 mmol.L^{-}1 tubes allowed to perform a test/retest experiments to evaluate the reproducibility of our measurements.

5.2 In vitro validation for ^{23}Na MRI at 7 T

5.2.1 Protocol optimization

To determine the most adequate acquisition parameters to assess accurately the sodium relaxations (R$_1$=1/0.06 s^{-1}, R$_2$=1/0.05 s^{-1}) and diffusion properties (ADC=1.3x10^{-6} mm^2/s), brute-force Monte-Carlo SSFP signal simulations were performed. M$_0$ was estimated from the expression of the signal:

$$M_0 = \frac{S}{\sigma} \times \frac{1}{\tan\left(\frac{\alpha}{2}\right)\left(1 - \frac{e^{-TR/T_1} - \cos(\alpha)(1-e^{-2TR/T_2})}{\sqrt{p^2-q^2}}\right)} \quad \text{[Bernstein 2004]} \tag{5.18}$$

Where S is the mean signal over a ROI, σ is the noise standard deviation, α is the Flip Angle, and

$$\begin{cases} p = 1 - e^{-TR/T_1} cos(\alpha) - e^{-2TR/T_2}\left(e^{-TR/T_1} - \cos(\alpha)\right) \\ q = e^{-TR/T_2}(1 - e^{-TR/T_1})(1+\cos(\alpha)) \end{cases} \tag{5.19}$$

based on the SNR measured on a non-selective 3D SSFP acquisition at the targeted resolution, FA and TR presented in Table 5.1 and with a RF spoiling increment of 0°.

To consider the variability of encountered flip angles due to the coil profile, values in the range [0°, 100°] were explored with a precision of 1°, using 10.000 draws per flip angle. To avoid SNR variations due to the coil reception profile, M$_0$ was adapted according to the studied flip angle. Spoiling gradient momentum was also studied, using the notation "N$_{RO}$" which represents the ratio between the pixel size along the readout direction (Δx) and the spoiling distance a such that:

$$N_{RO} \times a = \Delta x \tag{5.20}$$

Therefore, if N$_R O$= 0, the sequence is balanced and if N$_{RO}$ $\geq$1, the sequence is spoiled. Our considered N$_{RO}$ range varied from 1 to 47 which is the maximum achievable value with our MR scanner. The latter was the maximum reachable momentum according to our system limits for our chosen TR (20 ms) and pixel size, leading to a spoiling distance of 128 μm.

Simulated QuICS experiments and subsequent estimations of sodium NMR properties for various

FA and N_{RO} are shown in Figure 5.4. Monte-Carlo simulations were also performed to evaluate the resulting bias in quantitative maps. In simulations, M_0 was adjusted according to the targeted flip angle. Figure 5.4 illustrates that choosing a flip angle higher than 40° and the highest spoiling gradient momentum avoids any bias and leads to the most accurate estimations. Indeed, results obtained with FA below 40° cannot be considered because a large bias and uncertainty in the estimations are observed.

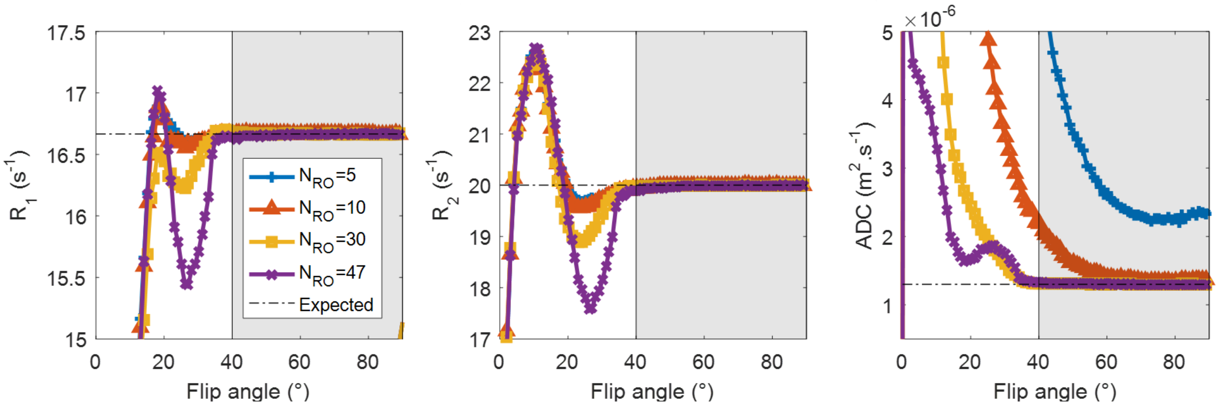

Figure 5.4: Results of Brute-force Monte-Carlo simulations of sodium R_1, R_2 and ADC as a function of flip angle and spoiling gradient momentum (N_{RO}) applied in the readout direction.

5.2.2 Data acquisitions

Acquisitions were performed at NeuroSpin on the 7T MR scanner (Magnetom, Siemens Healthcare, Erlangen, Germany) at room temperature (21°C) using our home made hemi-cylindrical non human primate single channel (1Tx/1Rx) Sodium transceiver coil. Acquisitions consisted in 3D non-selective Cartesian unbalanced SSFP sequences. From the optimization process described before, we extracted the N_{RO} and flip angle (α) needed to obtain reliable results, when sampling RF spoiling increments were varied from 0° to 10° and 350° to 360° by 2° steps, and from 20° to 140° by 10° steps. Thus, N_{RO} was set to 47 and flip angle α to 45°. Scanning parameters were TR/TE=20 ms/3.2 ms, bandwidth=220 Hz per pixel. The image resolution was 6 mm^3 isotropic in a 192×192×160 mm^3 field-of-view. Using 25 averages, the acquisition time of a volume was 7 minutes, leading to a total acquisition time of TA of 5h20 (320 minutes). As such explorations are conducted on phantom, this long acquisition time is not a limitation.

5.2.3 Data analysis

Total sodium concentration maps were computed from the ratio between M_0 and B_1^-, where the sensitivity profile B_1^- was estimated from the flip angle distributions, by application of the reciprocity principle [HOULT 2000]. The concentrations were estimated for each adjacent tube using the tube of 150mM as a reference of concentration. Due to the hemi-volumic coverage of our coil illustrated before in Figure 5.5, a substantial sensitivity bias was observed across our SSFP images. To limit the impact of this inhomogeneous SNR on the estimation of NMR properties of ^{23}Na, a region-of-interest (ROI) was defined in each phantom keeping the upper part of our phantom where the FA was systematically higher than 40°,(Figure 5.4). To avoid errors due to partial volume on the edge of tubes, maps were estimated over 6 slices, which leads to a more robust estimation.

5.2.4 First experiment

A first set of experiments was conducted to evaluate available signal and determine the achievable temporal and spatial resolution when considering a minimal SNR. Explorations were performed using an homogeneous cylindrical phantom with a 7 cm diameter and filled with an aqueous sodium chloride solution at 150 mmol.L^{-1} matching physiological concentration in human fluids (ref=23Na-7T-1-E). The setup is illustrated by panel A of Figure 5.5. Our images are shown in Figure 5.6.

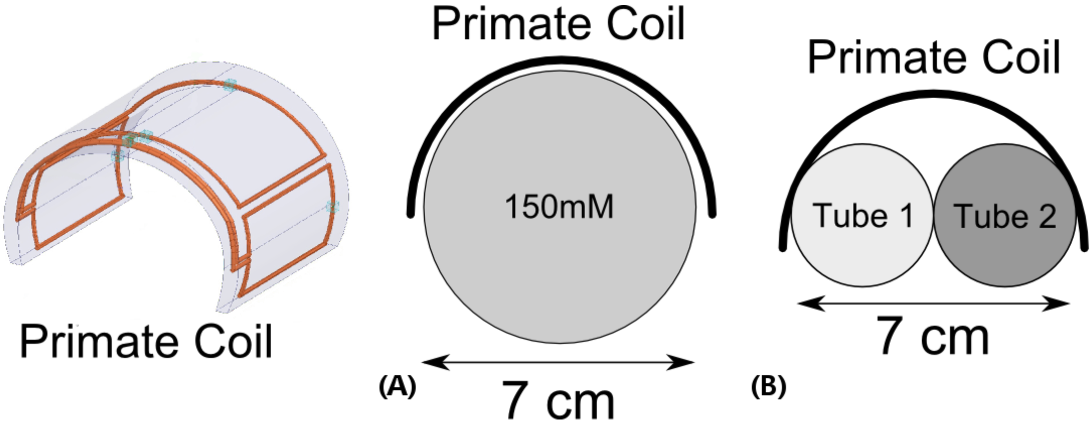

Figure 5.5: Experimental setup for 23Na QuICS experiments with the homogeneous cylindrical phantom 23Na-7T-Z (A) or with two phantoms (B).

As already shown in Chapter 2, our hemi-volumic ^{23}Na coil possess a heterogeneous transmission profile. Considering this flip angle map, the homogeneity of our quantitative T_1, T_2 and ADC maps are evaluated over the upper half of the phantom. Average measures are presented in Table 5.2 along values from the literature [GOODMAN 2005, BABSKY 2008, RIBEIRO 2010, MADELIN 2013, SHAH 2015]. Overall, these first results were quite encouraging as the differences with those previously reported values were small.

Parameter	QuICS measurement	Reference*	Unit
T_1 (R_1)	58 (17.3±1.43)	50-55	ms (s^{-1})
T_2 (R_2)	50 (19.9±2.13)	55-65	ms (s^{-1})
ADC	1.11±0.5x10^{-9}	1.15x10^{-9}	$m^2 s^{-1}$

Table 5.2: Quantitative measurements on aqueous Sodium at physiological concentration. (∗) Literature references given in [GOODMAN 2005, MADELIN 2013, SHAH 2015].

Applying state-of-the-art methods to obtain independent T_1 and T_2 values was not possible as the available MRI or MRS sequences did not allow sufficiently short inversion or echo-times. For similar reasons, it was not possible to obtain independent estimation of the ADC.

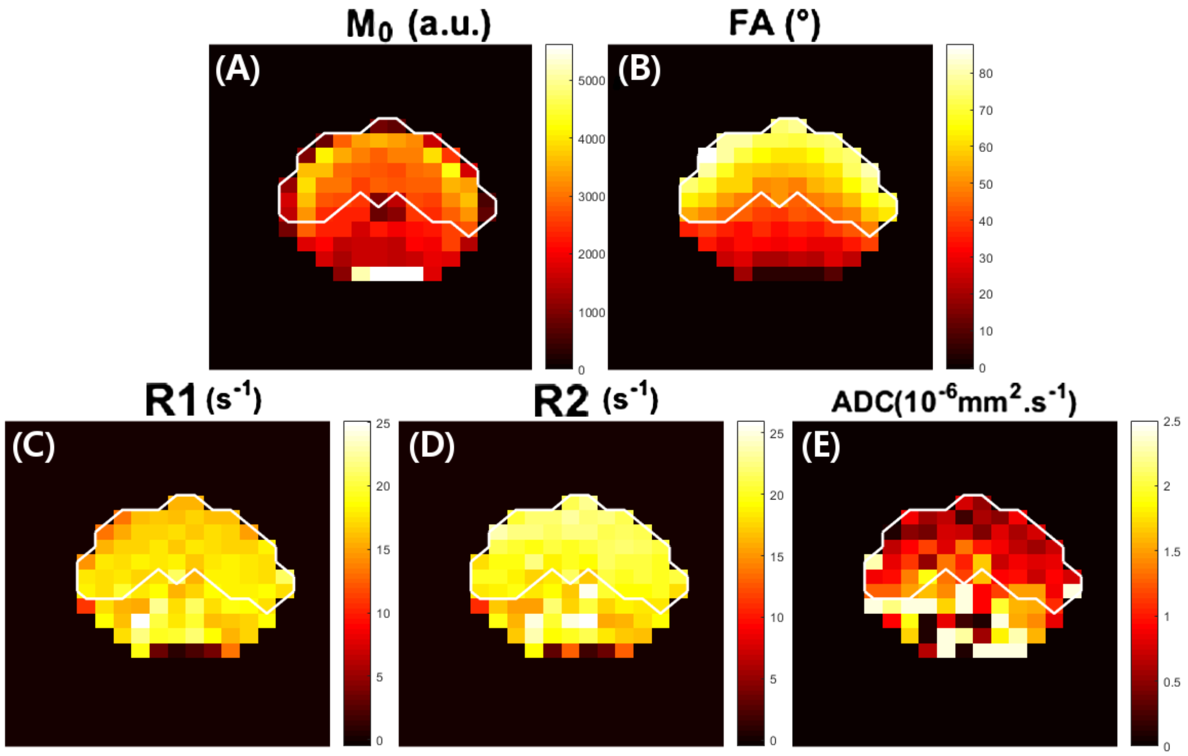

Figure 5.6: Resulting quantitative maps on the homogeneous cylindrical phantom. ROis were defined manually in areas for which the effective flip angle was above 40°.

5.2.5 Second experiments

A second set of experiments was performed to explore the sensitivity of the QuICS method to variations of the relaxation, concentration and diffusion parameters. Two smaller cylindrical phantoms were used: one was always kept as a reference while the second was changed to probe varying properties as illustrated by panel B of Figure 5.5.

5.2.5.1 Relaxation

To study the sensitivity of the method to relaxation parameter variations, we investigated agar gels to reduce both T_1 and T_2 relaxation times.

Parameter	Aqueous	2% agar	Unit
T_1	58.3±9.3	45±11.2	ms
T_2	53.6±7.0	28.5±4.9	ms

Table 5.3: T_1 and T_2 measurements for aqueous and 2% agar environments.

As expected, a denser environment created by higher agarose content led to a decrease of both relaxation times. One can notice that no significant changes in ADC was observed.

5.2.5.2 Concentrations

Sodium concentration measurements were reproducible and stable. As illustrated by Figure 5.8, our concentration measurements are within a 3% error margin demonstrating the precision of the

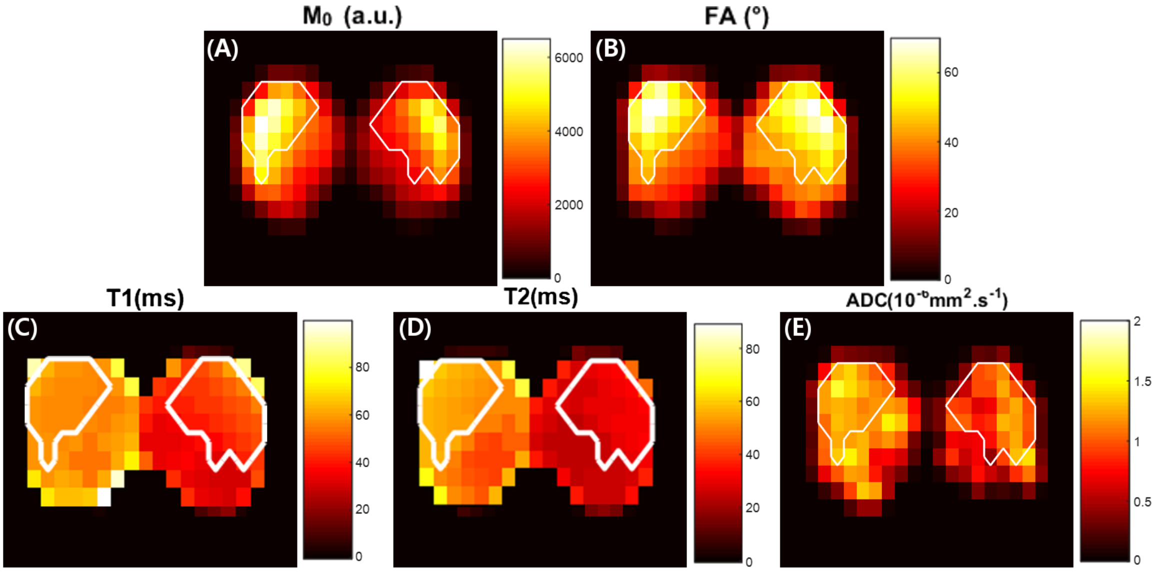

Figure 5.7: Quantitative maps comparing aqueous and 2% agar environments.

QuICS method for estimating spin density.

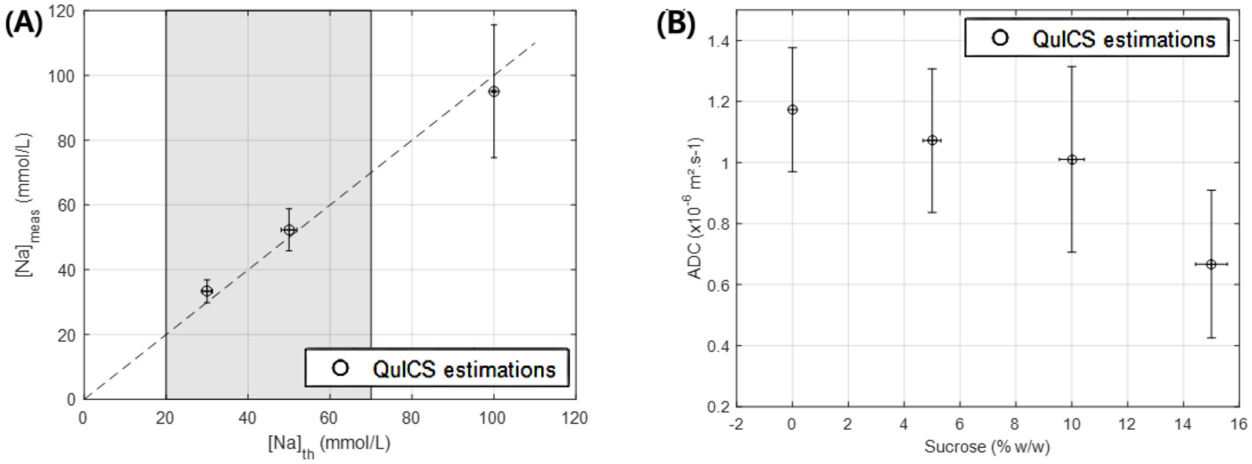

Figure 5.8: Sodium measurements vs theoretical concentrations (left) and diffusion coefficient estimations vs sucrose content (right). Measures are displayed with associated standard deviation and type B uncertainties for chemistry dilutions, as established in [ISO 1993].The concentration range corresponding to targeted brain applications is represented as the shaded area. The dashed line is the first bisector representing a perfect match between measures and theoretical values.

5.2.5.3 Diffusion

As illustrated on the right panel of Figure 5.8, the QuICS method managed to characterize the decrease of ADC values with increasing (from 5 to 15% w/w) sucrose content (Sigma-Aldrich, Saint Louis, USA) to increase the viscosity. These measures matches previous studies from [LAUBACH 1998, HARA 2014, WINFIELD 2016]. Unfortunately, the spread of these measurements is significant due to the low SNR of our ^{23}Na acquisitions (and the moderate sensitivity of QuICS to ADC changes).

Nevertheless, this demonstration of the QuICS method to estimate the mono-dimensional ADC of a short lived nucleus such as ^{23}Na remains a remarkable feat and should be considered to conduct unprecedented *in vivo* study of Sodium diffusion using MRI in preclinical research.

5.2.6 Further improvements

To evolve towards a clinically viable protocol, a significant time reduction needs to be achieved. With accurate optimization, it is possible to acquire only a limited set of contrasts and therefore reduce scanning time to about an hour and 20 minutes. Nevertheless, depending on the choice of the gradient spoiling momentum (N_{RO}) and chosen contrasts, the uncertainty on parameter extraction can increase. As illustrated by Figure 5.4, reducing the spoiling momentum will lead to a large uncertainty on ADC measurement. An acquisition was performed and allowed to obtain similar estimated values for T_2 and ADC as illustrated by Figure 5.9. Indeed a T_2 of 53.2 $\pm$ 5.5 ms and and ADC of 1.2 $\pm$ 0.687 $mm^2.ms^{-1}$ were obtained. Unfortunately, this shorter acquisition degraded the estimation of T_1 which is estimated to be 71.9 $\pm$ 9.65 ms.

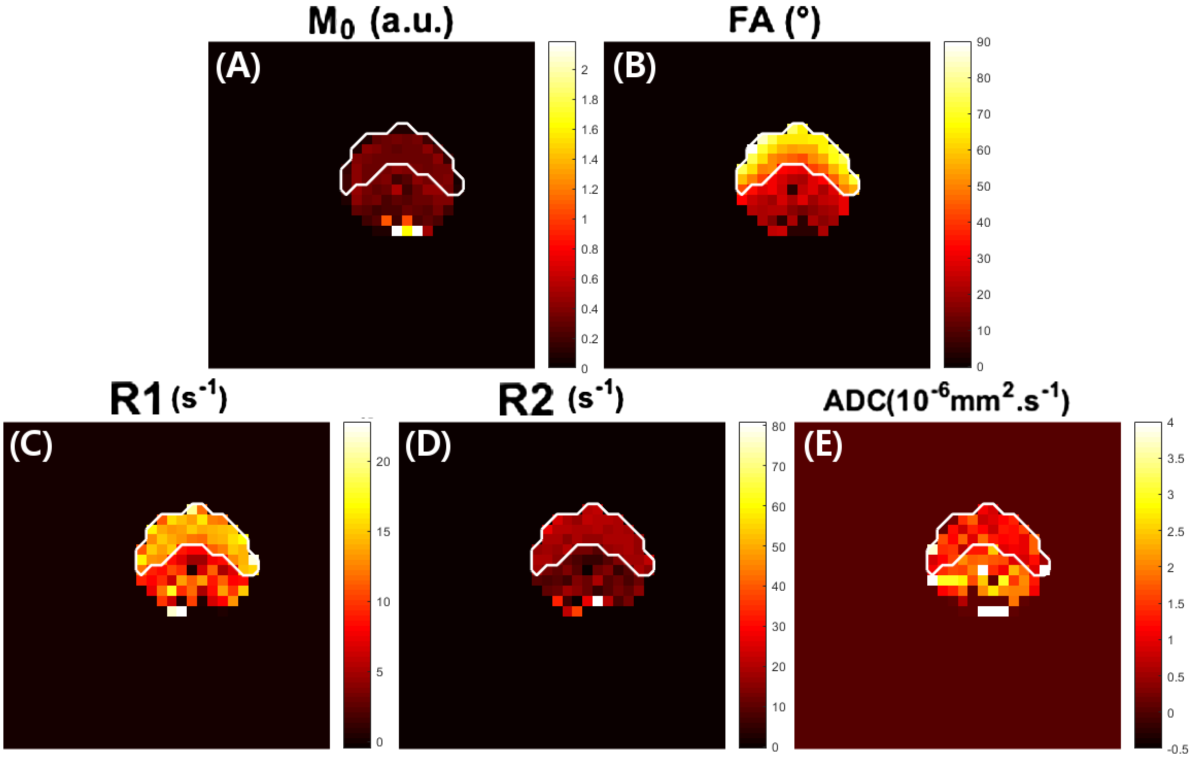

Figure 5.9: Results of an optimized QuICS acquisition of 78 minutes at a spatial resolution of 6 mm isotropic.

Regarding to the ability to quantify ADC, only one spoiling gradient was applied here leading to a single diffusion sensitivity of the sequence. Acquiring several volumes with different spoiling gradient amplitudes could also enhance the precision in the determination of the ADC coefficient [DE ROCHEFORT 2016c].

Moreover, acquisitions could be shortened to include only the most informative flip angles, RF and gradient spoiling steps. An optimization algorithm based on Fisher information matrix and Cramér-Rao lower bound [ANASTASIOU 2004, ALEXANDER 2008, ZHAO 2016, VALABRÈGUE 2016] could be used for this purpose leading to a significant acquisition time reduction.

Signal sampling efficiency and information collection can be improved by acquiring multiple echoes during each repetition time TR. Such optimization, illustrated by Figure 5.10, corresponds to the acquisition of multiple orders parameters presented in Table 5.1. Influence on the complex plane representing signals is presented in Figure 5.11. A new degree of freedom can also be gained by changing the TR from one volume to an other to assess different signal variations as illustrated by complex planes of Figure 5.11. Such optimization would allow to reduce the number of measurements to be made and therefore the total acquisition time.

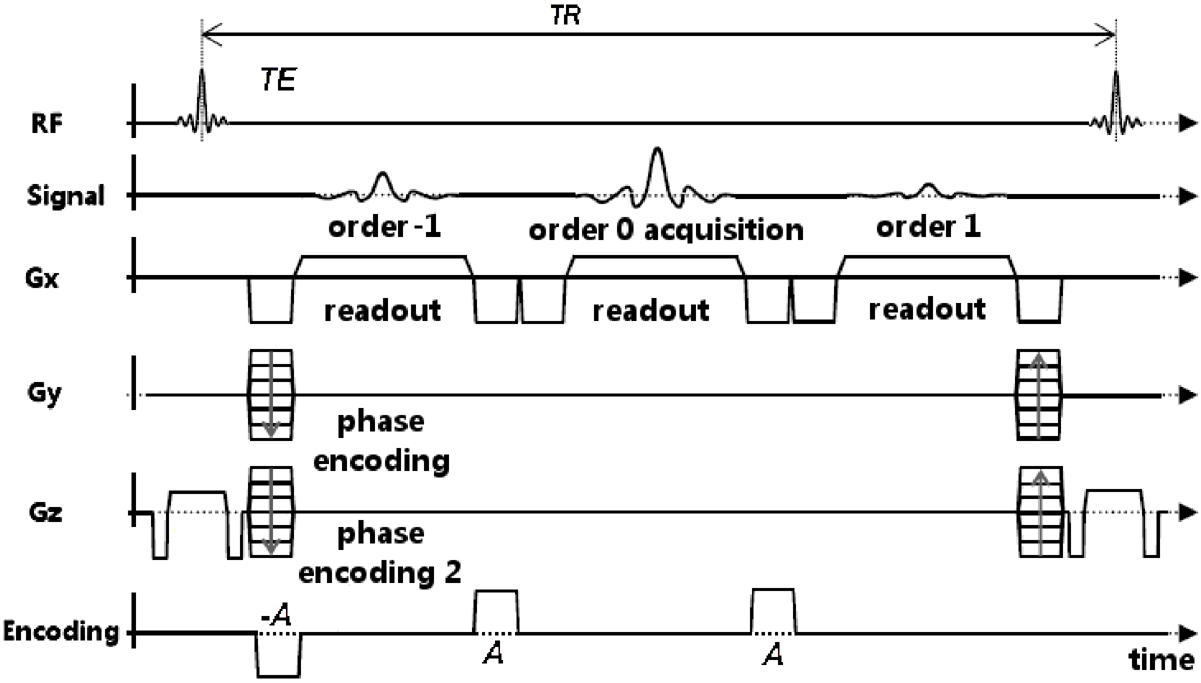

Figure 5.10: Multiple orders (echoes) acquisition in the QuICS sequence.

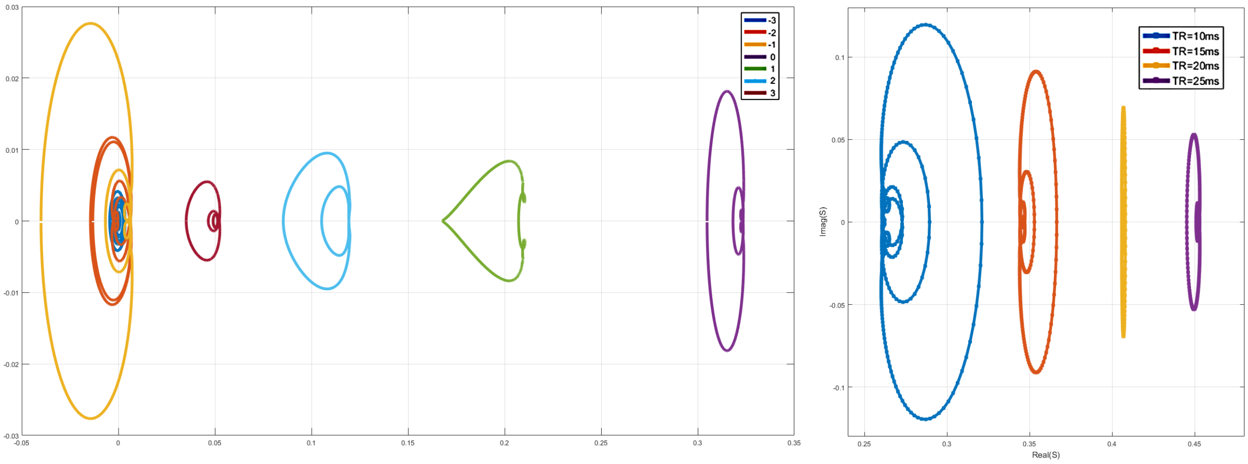

Figure 5.11: Influence of multiple echoes acquisition (left) and TR variations (right) on signal representation in complex planes.

Finally, to improve SNR and resolution of our images, the use of a non-Cartesian sampling scheme, as presented in Chapter 1, and an ultra-short echo-time would be of interest [Coste 2016].

In addition to the issue of the acquisition time, the post-processing can also be a concern if it gets too long. Dictionary-based multi-parametric methods, such as MR Fingerprinting, come with a long post-processing step [Cloos 2016] while in our framework, the analytic extraction of quantitative maps directly from DICOM images was achieved in approximately ten minutes and could be further improved using parallel computing which opens perspectives for clinical work flow optimization. Implementation of parallel algorithms on GPUs is also of interest when combined to non Cartesian sampling associated with previously described non-linear iterative methods.

Finally, the QuICS method would benefit from the use of an homogenous coil for transmission and multiple receiving elements [Shajan 2016]. In this case, the sensitivity profile of the coil would have to be corrected using a dedicated post-processing algorithm (and possibly a pre-calibration procedure) to extract total sodium concentration [Parker 2014].

5.3 Conclusion and Perspectives

The use of simultaneous multiple parameter extraction methods is of growing interest across the MRI community as quantitative measurements could well be the answer for the reproducibility and interpretability problems encountered in multicentric or longitudinal clinical research studies. As of 2017, no prior applications of a simultaneous multiparameter extraction of Sodium properties was reported as the short relaxation rates of ^{23}Na limits most of these methods.

In this small feasibility study, we managed to implement QuICS and adapt it to extract ^{23}Na ADC, TSC, T_1 and T_2 maps *in vitro*. Estimated relaxation times rates at 21°C were in agreement with values from the literature obtained using non-localized Inversion-Recovery and spin-echo sequences at 22°C and the same magnetic field (7T) [Nagel 2016]. Estimation of the mono-dimensional apparent diffusion coefficient of Sodium *in vivo* could be of interest in the scope of separating intra- and extra-cellular components or to validate some models. This perspective is even more exciting knowing that such diffusion measurements have not been reported so far.

Chapter 6

Towards Compartmentalization

Contents

Previously depicted pipelines (SD, VFA or QuICS) are aiming at estimating the total concentration of our nucleus-of-interest, but does not inform us about its compartmentalization, *e. g.* its relative distribution between intra- or extra-cellular compartments. In the case of Sodium, it is expected that in pathological conditions, sodium levels would vary more drastically in the cytosol of stressed/diseased neurons due to the dysfunction of the Na+/K+ ATPase pump which transfers three intracellular sodium ions out of the cell in exchange for two extracellular potassium ions into the cell [Murphy 2009]. As a consequence, alterations of the intracellular sodium concentration rather than the total sodium concentration would be a more specific and sensitive biomarker for clinical research studies. Unfortunately, the disentanglement of the intra- and extra-cellular components from the total ^{23}Na NMR signal is quite challenging with numerous interesting methods but very few satisfying applications to date. In this chapter, we are presenting some of the preliminary work done to tackle this problem (mostly for ^{23}Na MRI).

6.1 State-of-the-art

6.1.1 Biochemical Processes

As Sodium is not homogeneously distributed between intra- and extra-cellular compartments, a strong Sodium concentration gradient exists between these compartments and is tightly regulated by various biochemical processes at the boundary of the cell [Rose 1994, Murphy 2009]. Indeed, cell membranes contain different ion channels which transport various ions across the membrane such as Sodium, Potassium, Chloride or Calcium. As passive processes would lead to an equilibrium in ion concentrations between the intra- and extra-cellular compartments (Fick's law of diffusion), these ion channels consume energy to maintain ion gradients across the membrane which are crucial to drive numerous cellular functions. Among others (Sodium / Calcium Exchanger (Na^+/Ca^{2+} (NCX)), Sodium Hydrogen exchanger (Na^+/H^+ (NHE)), Na^+/HCO_3^- co-transporter proteins, Na^+/Mg^{2+} and $Na^+/K^+/Cl^-$ cotransporters), the Na^+/K^+ -Adenosine Triphosphatase pump (Na+/K+ ATPase) acts to maintain/regenerate the trans-membrane potential (difference of electric potential between the intra- and extra-cellular compartments) typically in the -40 to -80 mV range. In the case of Sodium, the typical intra- and extra-cellular concentrations are in the [10,20] and [140,150] $mmol.L^{-1}$ range respectively. Two possible compartmental models are currently used by the ^{23}Na MRI community when trying to separate intra- and extra-cellular contributions: a two- or a three-compartments model. The two-compartments model considers only an extra-cellular compartment mostly composed of extra-cellular fluids and blood vessels of high sodium concentration and an intra-cellular compartment (mostly cellular cytoplasm) with a slightly increased density, compared to the more liquid extra-cellular compartment, and a 10-fold lower concentration. The three-compartments model uses the same two compartments but adds a third one composed of ^{23}Na associated with cellular membranes and proteins and which is not NMR-visible in the context of liquid-state NMR.

6.1.2 Physical Properties

Sodium NMR response exhibits a strong dependence to the ionic environment because of the important quadrupolar moment and can lead to a bi-exponential transverse signal decay in tissues. Following a 90° excitation, the time-evolution of the magnetization is given by:

$$\begin{cases} M_x(t) = M_0(0.6e^{-t/T_{2f}} + 0.4e^{-t/T_{2s}}) \\ M_y(t) = M_0(0.6e^{-t/T_{2f}} + 0.4e^{-t/T_{2s}}) \\ M_z(t) = M_0(1 - 0.2e^{-t/T_{1f}} - 0.8e^{-t/T_{1s}}) \end{cases} \tag{6.1}$$

The bi-exponential behavior of the longitudinal recovery is hardly observed and is not considered in practice [JACCARD 1986] leading to a mono-exponential approximation:

$$M_z(t) = M_0(1 - e^{-t/T_1}) \tag{6.2}$$

Thanks to reasonably long and distinct T_2/T_2^* relaxation times for the fast and slow components typically in the [0.8,5] ms and [15,20] ms ranges, the bi-exponential nature of the transverse relaxation decay has been reported numerous time *in vitro* in agarose gels [ANDRASKO 1974] and *in vivo* [PAYNE 1990]. Quite early in the development of ^{23}Na MRI [PERMAN 1986], alterations to the transverse relaxation decay has been associated to changes in the mobility of the ^{23}Na nuclei [HEILER 2011]. Consequently, several teams have tried to explore either the bi-exponential T_2 decay of ^{23}Na or its different coherence pathway as a proxy of its cellular compartmentalization.

6.1.3 Compartmental Modeling

The Total Sodium Concentration measurement performed in clinical studies is interesting and can be correlated with various diseases (introduced in Chapter1). Unfortunately most interesting variations occur in the intra-cellular compartment where an increase of Sodium concentration traduces a failure of cellular regulation mechanisms. Two possible models are currently used when trying to separate intra- and extra-cellular Sodium contributions: a two- or a three-compartments model.

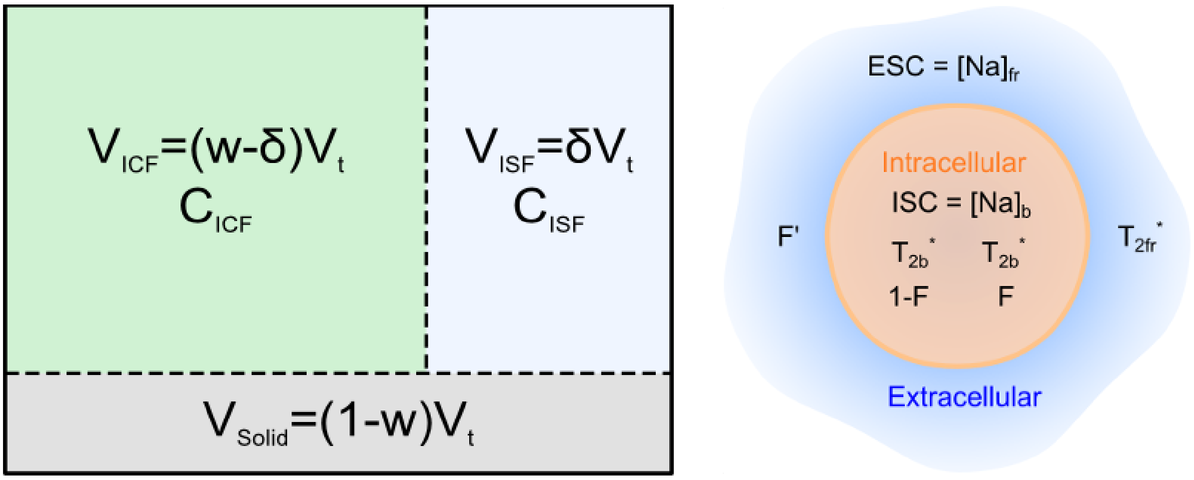

Figure 6.1: Schematics of the three and two compartments model

The three-compartments model involves 2 liquid compartments and a semi-solid one: the intracellular fluid (ICF) of concentration C$_{ICF}$ in the range [10,20] mmol.L^{-1}, the interstitial fluid (ISF) (to which the vascular fraction is added) with concentration C$_{ISF}$ in the range [140,150] mmol.L^{-1} and a compartment composed of sodium bound to cellular membranes and proteins at an unknown concentration. This semi-solid compartment is considered to represent 20% of the total volume in a pixel leading to a volume fraction of $w = 0.8$ for both ICF and ISF fluid. In normal brain tissues, the ISF fraction δ is also around 20%. As the sodium in the semi-solid compartment is not NMR-visible, the measured TSC correspond to:

$$TSC = \frac{[Na^+]_{ICF}V_{ICF} + [Na^+]_{ISF}V_{ISF}}{V_{ICF} + V_{ISF} + V_{SS}} \tag{6.3}$$

By introducing the notations of Figure 14, where w is the liquid volume fraction, we have:

$$TSC = \frac{[Na^+]_{ICF}(w-\delta) + [Na^+]_{ISF}\delta}{w} \tag{6.4}$$

The model complexity can be tuned by reducing the number of unknown parameters. Usually the extracellular concentration is known and considered fixed between 140 and 150 mmol.L^{-1}. In some models [Lu 2010b] the intracellular fluid concentration is also considered fixed, leaving the extracellular space volume fraction as the sole parameter of interest:

$$\delta = \frac{w\,(TSC - [Na^+]_{ICF})}{[Na^+]_{ISF} - [Na^+]_{ICF}} \tag{6.5}$$

Such parameter can be of interest in pathologies where the extracellular space expands along with cellular death such as in stroke or tumor. In less acute conditions, the intracellular concentration is often considered as unknown along with the intracellular volume as its variations are in interest to assess possible metabolic dysfunction that could lead to a modification of the ionic balance [Madelin 2014]. Tissue variations of the water volume fraction w which is for instance about 0.7 in WM and about 0.85 in GM can bring a more robust parameter estimation.

The two-compartments model considers an extracellular compartment composed of interstitial fluids and blood vessels with a high sodium concentration and an intracellular compartment with a slightly increased density and a 10-fold lower concentration. In each compartments, Sodium exhibits a bi-exponential decay characterized by a fast and a slow transverse relaxation rates supposedly distinct for the two compartments. Alternatively, this model can be used to describe sodium as being either free or bound. For bound sodium, T_2 relaxation decay is bi-exponential with a fast and a short component. However for free moving sodium, T_2 relaxation decay is mono-exponential with a long relaxation time. In this case, the total ^{23}Na signal in a voxel is described by a T_1 and T_2-weighted sum of the contributions from both compartments according to:

$$s(t) = V_b C_b \eta_b \left[a_{b,f} e^{-t/T_{2b,f}} + a_{b,s} e^{-t/T_{2b,s}} \right] + V_{fr} C_{fr} a_{fr} \eta_{fr} e^{-t/T_{2,fr}} + n(t) \qquad \text{[Qian 2015]} \qquad (6.6)$$

where $n(t)$ is the noise with a Gaussian normal distribution N(0,σ), subscripts b and fr standing for "bounded" and "free" respectively, a is an intensity weighting factor between the two compartments, C is the compartment concentration, V the volumetric ratio between compartments and η represents the steady-state saturation correction factor for mono-exponential longitudinal relaxation given by equation 6.2.

6.2 Possible methods

In addition to the MQF methods introduced in Chapter 1, we briefly present few other possible methods to explore the compartmentalization of Sodium.

6.2.1 Shift reagents

Shift reagents are a convenient method, as they do not penetrate into the intracellular space and create a strong frequency shift [Seshan 1997]. They are typically lanthanide chelates such as Tm(DOTP)$^{5-}$ or Dy(TTHA)$^{3-}$. As they are toxic at high concentration, they are not authorized for clinical investigation but they can be used for preclinical studies. Unfortunately, their application to brain sodium imaging was hampered by their inability to cross the blood brain barrier (BBB) without help.

6.2.2 Multiple Quantum Filtering

Multiple Quantum Filtering (MQF) methods, presented in Chapter 1 can be used to acquire selectively the signals coming from the intracellular compartment (or rather from bound sodium nuclei). Unfortunately, MQF methods faces significant challenges as they are sensitive to B_0 heterogeneity, require several RF pulses leading to a higher SAR and finally, suffer from a very low SNR despite their long acquisition time due to the necessary phase cycling. These challenges have significantly limited the application of MQF methods for clinical research.

6.2.3 Other Single Quantum Imaging Methods

Few other methods were proposed to investigate the compartmentalization of Sodium. An interesting approach is the Inversion Recovery approach aiming at suppressing the fluid content [Kline 2000, Stobbe 2005, Nagel 2011, Madelin 2014] thanks to its longer T_1. Another is the Projection Acquisition in the steady state with Coherent MAgNetization sequence [Stobbe 2014] (PACMAN) , or the Double Readout DIM (DR-DIM) [Benkhedah 2014] or the Short T_2 imaging for bounded Sodium [Qian 2015].

6.3 Description of the MGE approach

Only few studies exploiting multiple gradient echoes (MGE) acquisitions were performed for non-proton MRI [Pilkinton 2010, Qian 2015, Bydder 2017]. An *in vivo* estimation of the long relaxation rate was performed at 7 T using a similar method based on two optimized echoes to fit a mono-exponential decay model of Sodium decay [Fleysher 2009].

6.3.1 MGE sequence

The multiple gradient echoes approach consists in a single RF impulsion to excite all sodium nuclei of the volume, followed by several signal readouts using the repetition of the same spatial encoding gradients. This way, the NMR signal can be sampled at different echo-times along its T_2* decay and different echo-images can be reconstructed and computed to estimate T_2* relaxation rates. The advantage of this method is its simplicity and the use of a single RF pulse to avoid any SAR issues. However, one must be cautious to preserve a sufficient SNR for each acquired echo-images.

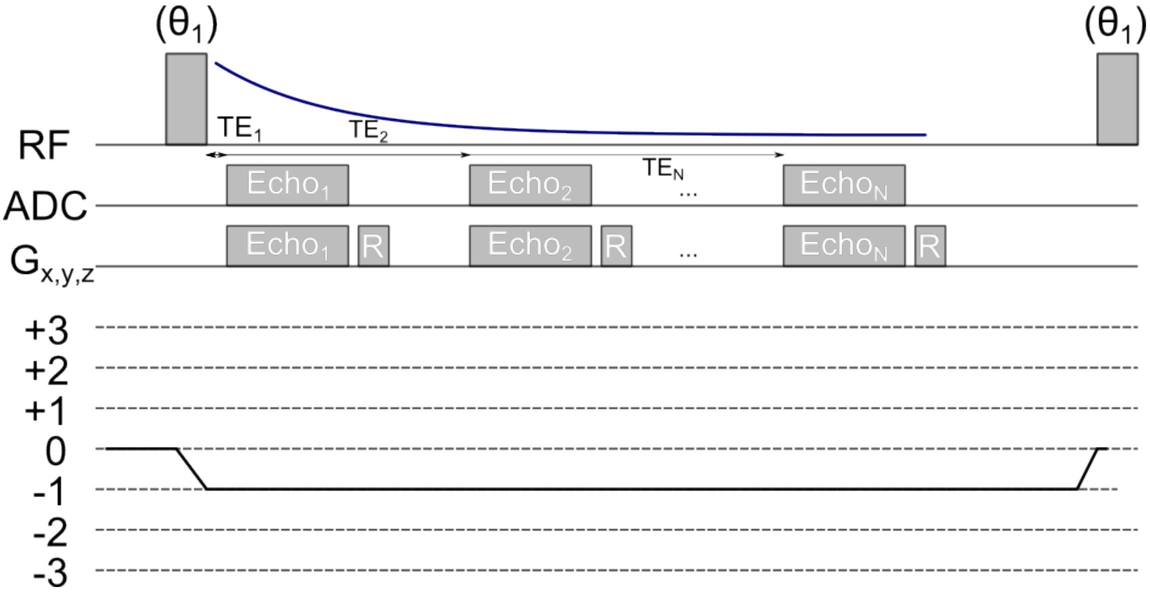

Figure 6.2: Chronogram of a Multi-gradient-echo sequence. A rectangular pulse of flip angle (θ) is applied and signal is then sampled at multiple echo times. R indicates that rewinders are applied after each signal readout.

Recently Qian et al. [Qian 2015] proposed to compute a "bounded" sodium map by the difference of two adequately chosen echoes. In some way, this approach could be seen as the simplest form of our multiple echo approach. The first echo, acquired with the shortest possible TE accounts for the total sodium content. On the opposite, the fast decaying component of the signal will have disappeared from the second echo leaving only the slow relaxing Sodium. As a consequence, by calculating their difference, areas where Sodium presents its fatest signal decay can be highlighted:

$$s_{T2_f} = S(TE_1) - S(TE_2) \qquad \text{[Qian 2015]} \tag{6.7}$$

Using the previously described signal model and some approximations, Qian et al. derive equation 6.7:

$$s_{T2_f} \approx V_b C_b \eta_b a_{b,s} e^{-TE_1/T_{2b,f}}[1 - e^{-\Delta TE/T_{2b,f}}] + (n(TE_1) - n(TE_2)) \qquad \text{[Qian 2015]} \tag{6.8}$$

The duration between echoes ΔTE has to be optimized to reduce the influence of longitudinal relaxation and acquire images when fast relaxing sodium signal is minimal. The method also takes into account static field inhomogeneity by computing a field map using the phase of acquired echoes:

$$\Delta_f = \frac{\Delta\phi}{2\pi\Delta TE} \tag{6.9}$$

and accounts for T_2^* signal decay by estimating using the link between T_2^*, T_2 and the B_0 map:

$$\frac{1}{T_2^*} = \frac{1}{T_2} + \kappa\Delta_f \tag{6.10}$$

Finally, when all corrections are performed a quantitative concentration measurement can be reached.

6.3.2 *In vivo* exploration at 3 T

An *in vivo* evaluation of the method proposed by Qian et al. was performed on a single healthy volunteer by acquiring two FLORET images, one with an ultra short Echo Time (UTE) of 0.1 ms and a second one with a TE of 5 ms as illustrated on Figure 6.3.

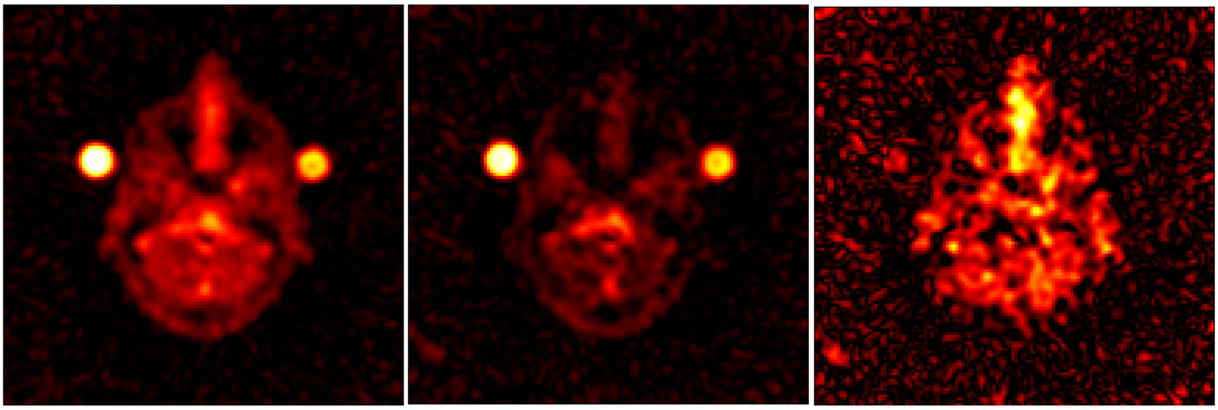

Figure 6.3: ^{23}Na MRIs acquired at TE=0.1 ms and TE=5 ms with the FLORET sequence (TR/FA=120 ms/90°) and computation of the bounded sodium image. Data were acquired with S. Romanzetti at Aachen University Hospital on a 3 T PRISMA MR scanner.

Figure 6.3 shows the two acquired echoes with the same intensity scale showing the fast signal decay. Their difference illustrates bounded Sodium of shortest T_2 clearly visible in nose cartilage or in brain tissues. One can also notice that side tubes filled with saline solution have completely disappeared from the bound ^{23}Na image.

6.3.3 implementation of a dedicated MGE sequence

Using Siemens sequence development environment (*IDEA*), the multiple echo acquisition was programmed and combined with the TPI sequence. For this first implementation, depending on chosen TR and readout duration up to 10 echoes can be acquired. Their temporal spacing is uniform to cover the full TR range or less if specified as illustrated by Figure 6.4.

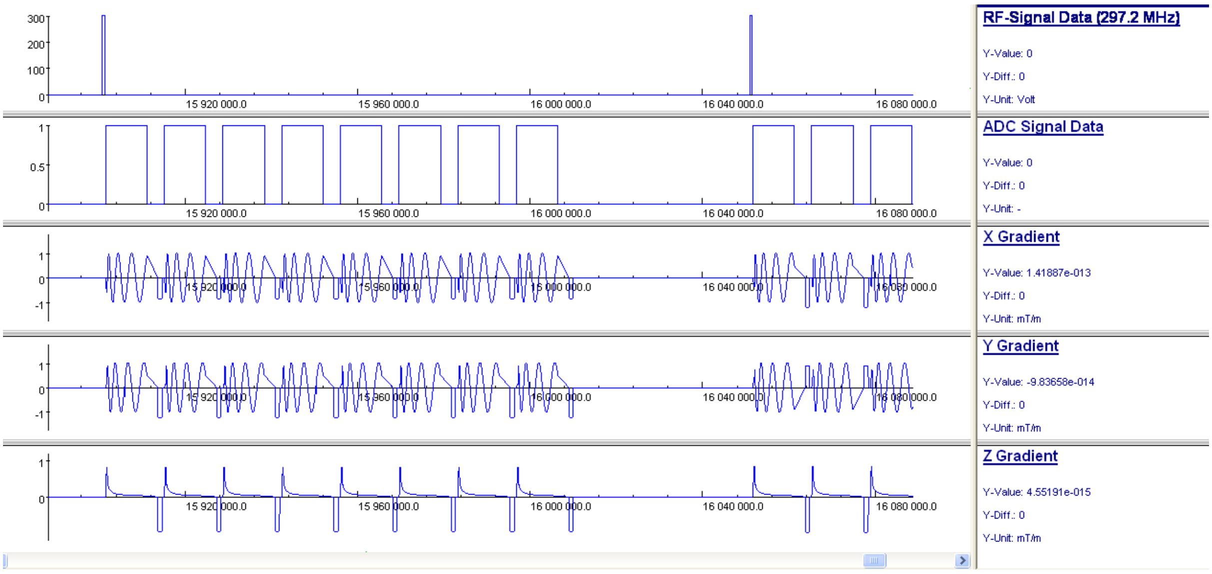

RF-Signal Data (297.2 MHz)
Y-Value: 0
Y-Diff.: 0
Y-Unit: Volt

ADC Signal Data
Y-Value: 0
Y-Diff.: 0
Y-Unit: -

X Gradient
Y-Value: 1.41887e-013
Y-Diff.: 0
Y-Unit: mT/m

Y Gradient
Y-Value: -9.83658e-014
Y-Diff.: 0
Y-Unit: mT/m

Z Gradient
Y-Value: 4.55191e-015
Y-Diff.: 0
Y-Unit: mT/m

Figure 6.4: Multi-gradient echo TPI sequence as visualized with Siemens simulation tool *POET* in the Siemens sequence development environment *IDEA*. 8 equispaced echoes are acquired after a rectangular pulse of 500 μs.

6.4 MC simulations and *in vitro* exploration

For various reasons, no more *in vivo* explorations of the MGE approach were conducted during this PhD thesis. Therefore, we focused our attention to Monte Carlo (MC) simulations so as to determine the best parametrization of our MGE acquisitions. This parametrization was tested *in vitro* at 7 T.

6.4.1 Monte Carlo Simulations

The T_2 mapping pipeline consists in a voxel-wise signal model exploiting all acquired echo-images. A Least Square regression enables the estimation of the slow and fast relaxation times and their respective fraction. Monte Carlo simulations were performed considering the bi-exponential signal decay model scaled by a calibration factor K:

$$S(t) = K(fe^{-TE/T_{2s}} + (1-f)e^{-TE/T_{2f}}) \tag{6.11}$$

Previous equation was implemented using MATLAB (The Mathworks, Natick, MA, USA) and hundred of thousands independent parameters estimations were performed. Initial input parameters were given to the algorithm and consisted of the theoretical component ratio of 0.4 and 0.6 for the extra and intra-cellular contributions respectively. Objectives of this simulation study were to determine the required SNR, the number and temporal coverage of acquired echoes to minimize the error in relaxation parameters estimation. The reference SNR considered for simulations was taken as a worst case scenario as the average SNR in our test object for the last echo we acquired at 33.3 ms (the image is presented on Figure 6.8). Then scaling coefficients are applied for our simulations. Multiple studies were made and some examples are presented in this section. Results are composed of histograms of estimated parameters distributions. They usually follow a Gaussian-like distribution.

A first simulation was performed with the following parameters: T_{2f} = 8 ms and T_{2s} = 60 ms and f = 40%. The simulated experiment was constituted by 13 echo-images at the following TE: 0.4/0.8/1/4/10/15/20/30/35/40/50/70/90 ms with a SNR 5 times the typical SNR observed for one average of our ^{23}Na UTE TPI at 7 T (see details in Chapter 1 or Figure 6.8 which illustrates reference Sodium images).

As shown on Figure 6.5, a good convergence is obtained (standard deviations of the simulated distributions are below 9%). A slight over-estimation of the relaxation times of about 5% is observed. This minor error is compensated by an estimated fraction f smaller than expected (38.8% instead of 40%). In a second simulation, Figure 6.6 demonstrates that doubling the SNR leads to a drastic improvement of our estimation, in particular of our deviation standards which decrease to around 3%. Yet, the over-estimation of our relaxation times remains the same at about 5%.

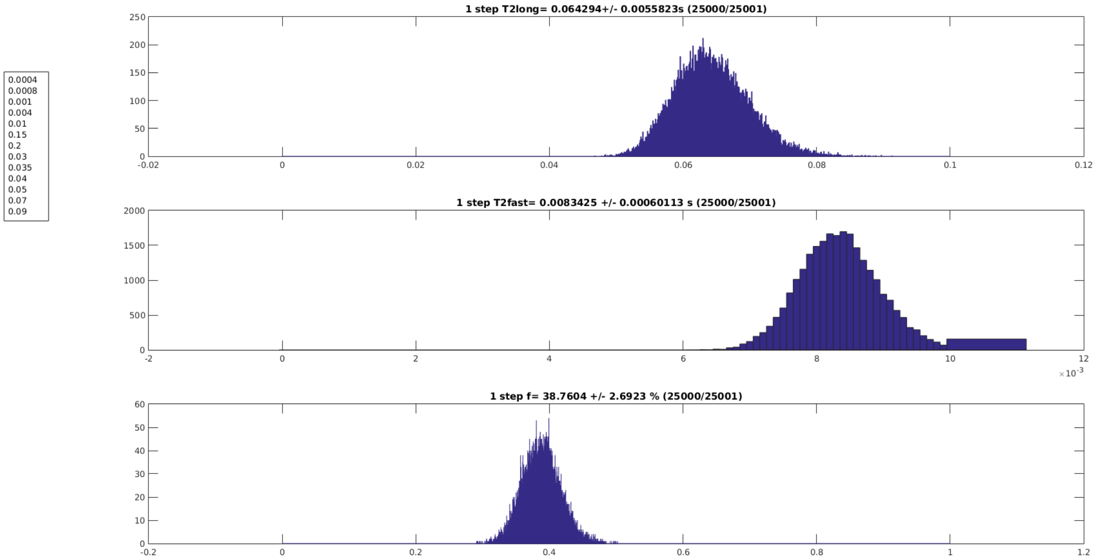

Figure 6.5: Monte Carlo Simulation results (T_{2f} = 8 ms, T_{2s} = 60 ms and f = 40%) with 25k iterations, a 5 times higher SNR in acquired images and 13 echoes acquired at: 0.4/0.8/1/4/10/15/20/30/35/40/50/70/90 ms

Unfortunately, this simulation is quite unrealistic, with a dense sampling of the T_2 decay at low TE to capture the fast component and a very high SNR which can not be achieved *in vivo* except with ^{23}Na MRS or very-low resolution MRI.

A last simulation was performed with more realistic parameters : T_{2f} = 3 ms and T_{2s} = 20 ms and f = 40% [Van Der Maarel 1989]. The simulated experiment was constituted by 8 echo-images with a inter-echo of about 5 ms at the following TE: 0.4/5/9.8/14.4/19.3/24.4/28.7/33.3 ms. The SNR was considered at only 3.4 times the reference SNR, corresponding to a degradation of the spatial resolution of our ^{23}Na TPI acquisitions at 7 T from 4 mm isotropic to 6 mm isotropic

As shown on Figure 6.7, a reasonably good convergence is obtained (standard deviations of the simulated distributions are below 10%). Yet, a much larger over-estimation of our relaxation times is observed : 25 ms instead of 20 ms and 4.3 ms instead of 3 ms. This error leads to an estimated fraction f much smaller than expected (33% instead of 40%).

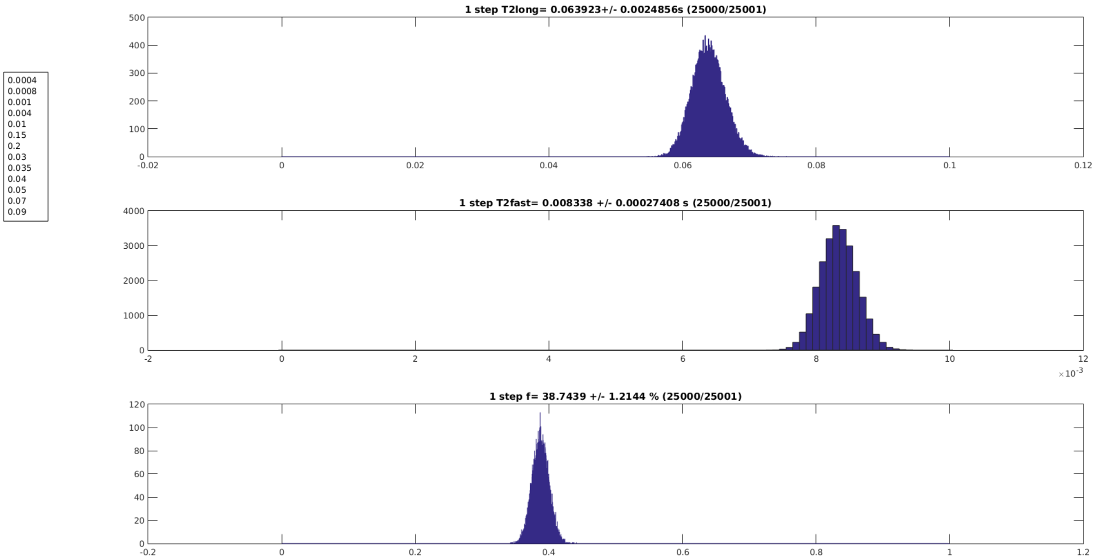

Figure 6.6: Monte Carlo Simulation results (T_{2f} = 8 ms, T_{2s} = 60 ms and f = 40%) with 25k iterations, a 10 times higher SNR in acquired images compared to SNR measured in our reference data set and 13 echoes acquired at: 0.4/0.8/1/4/10/15/20/30/35/40/50/70/90 ms

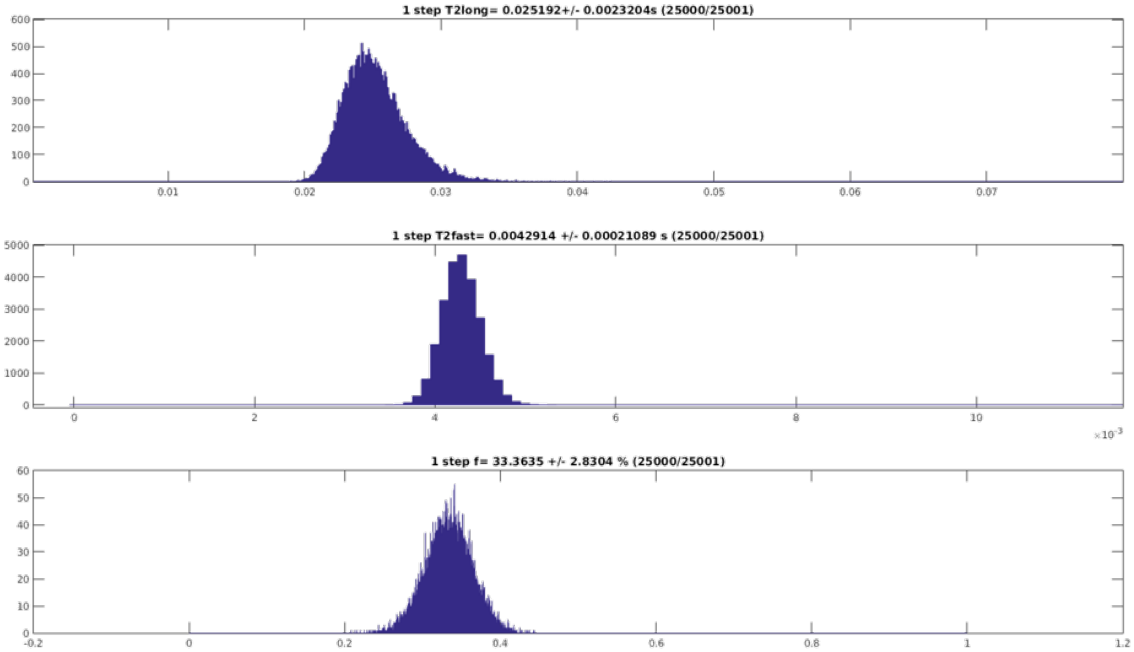

Figure 6.7: Monte Carlo Simulation results (T_{2f} = 3 ms, T_{2s} = 20 ms and f = 40%) with 25k iterations, a 3.4 times higher SNR in acquired images and 8 echoes acquired at: 0.4/5/9.8/14.4/19.3/24.4/28.7/33.3 ms

6.4.2 Phantom Exploration

Using one of our Sodium phantom (ref=23Na-7T-1), we acquired a set of ^{23}Na TPI echo-images with our MGE sequence, TE ranging from 0.4 to 33.3 ms milliseconds.

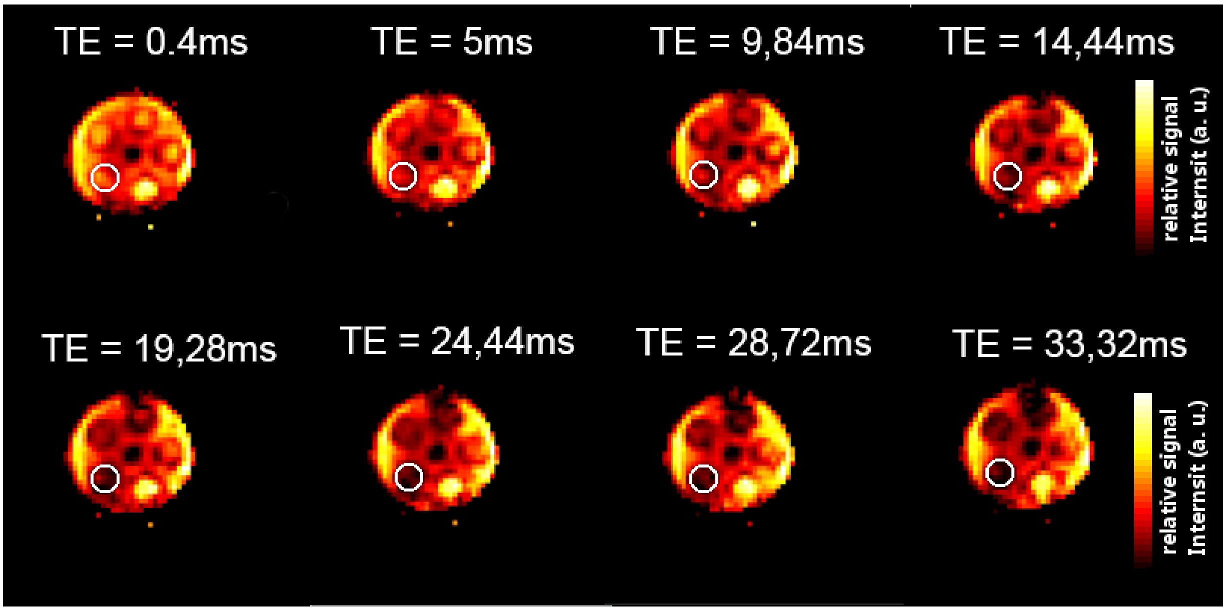

Figure 6.8: ^{23}Na MGE TPI echo-images with TE: 0.4/5/9.84/14.44/19.28/24.44/28.72/33.32 ms at a 6 mm isotropic resolution acquired at 7 T in XX minutes. The white circle surrounds the tube with the highest agar content of 8%. One can clearly notice that the signal in this tube is decaying faster than the signal coming from others compartments in particular the one immediately to its right.

Figure 6.8 shows our 8 echo-images. As expected a faster decay is observed in the tubes with higher agar content as illustrated by Figure 6.9.

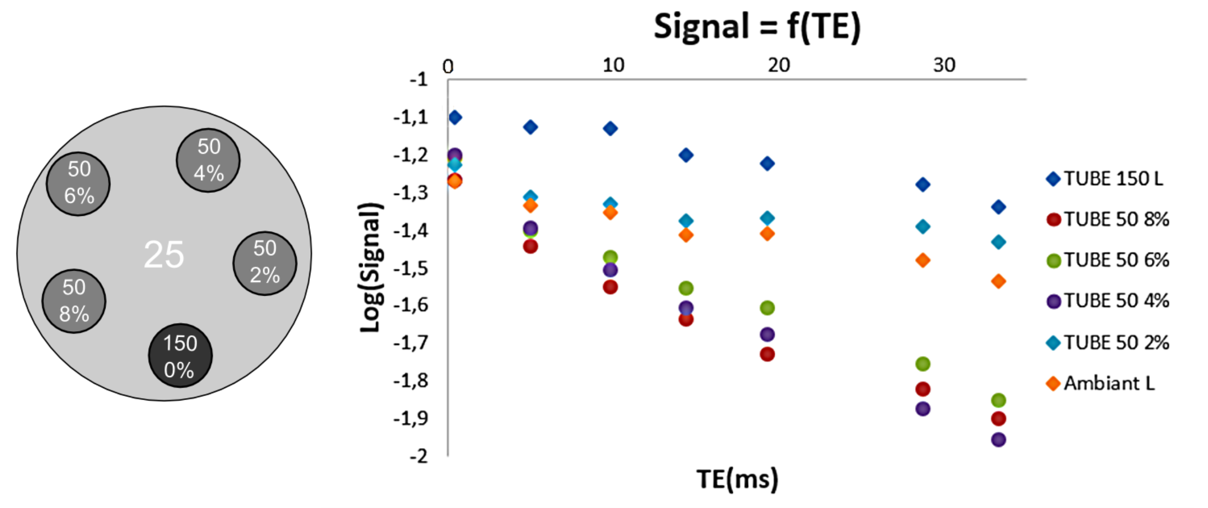

Figure 6.9: Phantom design (left) and semi-logarithm plot of average signal in the different chemical tubes and the central compartment for all TE. With increasing agar content, a bi-exponential decay becomes more manifest.

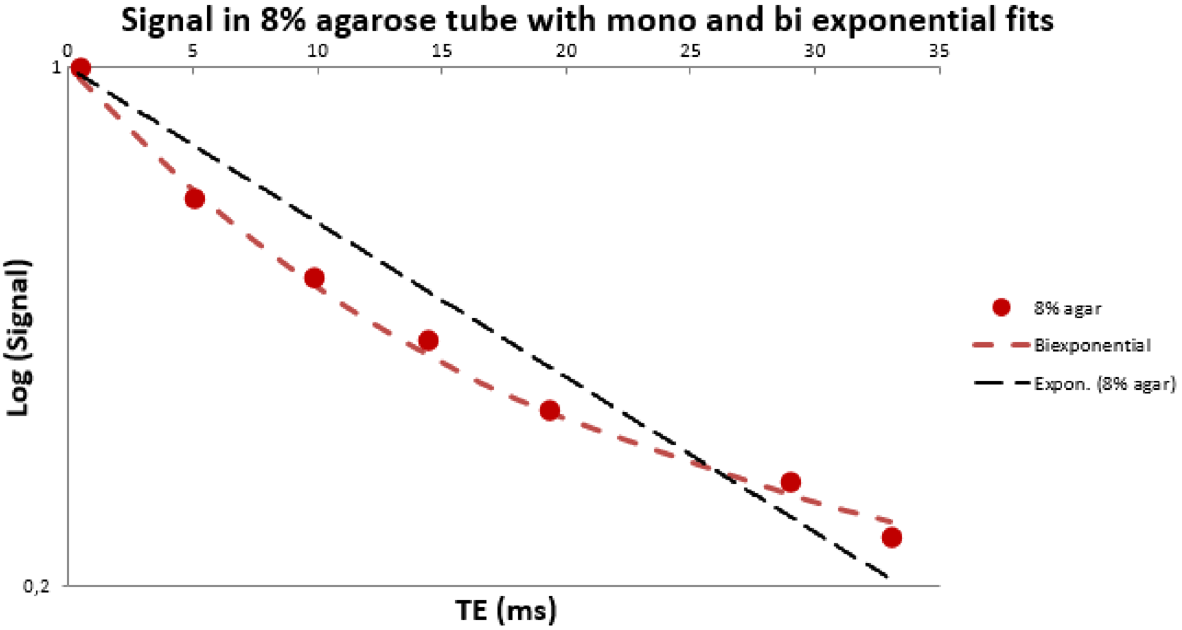

Figure 6.10: Semi-logarithmic plot of signal decay in the tube with 8% agar and associated mono- (dark dashed line) and bi-exponential (orange dashed curve) fits. The bi-exponential regression yielded a T_{2f} of 7.6 ms, a T_{2s} of 62.5 ms and a T_{2mono} of 20.7 ms with respective correlation factors R^2=0.99 for the bi-exponential fit and R^2=0.95 for the mono-exponential fit.

Figure 6.10 shows mono- and bi-exponential modeling of the signal decay in the 8% agar gel tube. As expected, the bi-exponential curve matches (R^2=0.99 vs R^2=0.95 for the mono-exponential fit) the nature of the T_2 decay in this tube with fast and slow relaxation times: T_{2f} = 7.6 ms and T_{2s} = 62.5 ms (assuming respective fractions of 0.6 and 0.4). The mono-exponential fit yields a T_{2mono} of 20.7 ms.

A voxel-wise estimation of the volumic fraction f, relaxation rates T_{2f} and T_{2s} was performed to map those parameters (without any assumption for f). Figure 6.11 presents the volumic fraction $(1-f)$ and T_{2f} maps corresponding to the fast decaying component. First, one can notice that our bi-exponential modelling converges quite consistently for all pixel. Yet, some pixels display unreliable T_{2f} values particularly at the bottom of the phantom. This should be linked to the heterogeneous B_1 profile of our hemi-volumic coil and subsequently low SNR in this area. Expectedly, the fast fraction decreases with the agar content and is above 0.8 in the liquid compartments. The relaxation times themselves do not change very clearly across the tubes and most of the contrast is visible in the volumic fraction map. Estimated values are consistent with the range of values previously reported for *in vitro* experiments. While our protocol seems appropriate for *in vivo* experiments or for the estimation of T_{2f}, our estimation of T_{2s} would have benefitted from the acquisition of echo-images at longer TE (if possible greater than 60 ms) to limit the significant spread of T_{2s} values observed in the corresponding map (not shown).

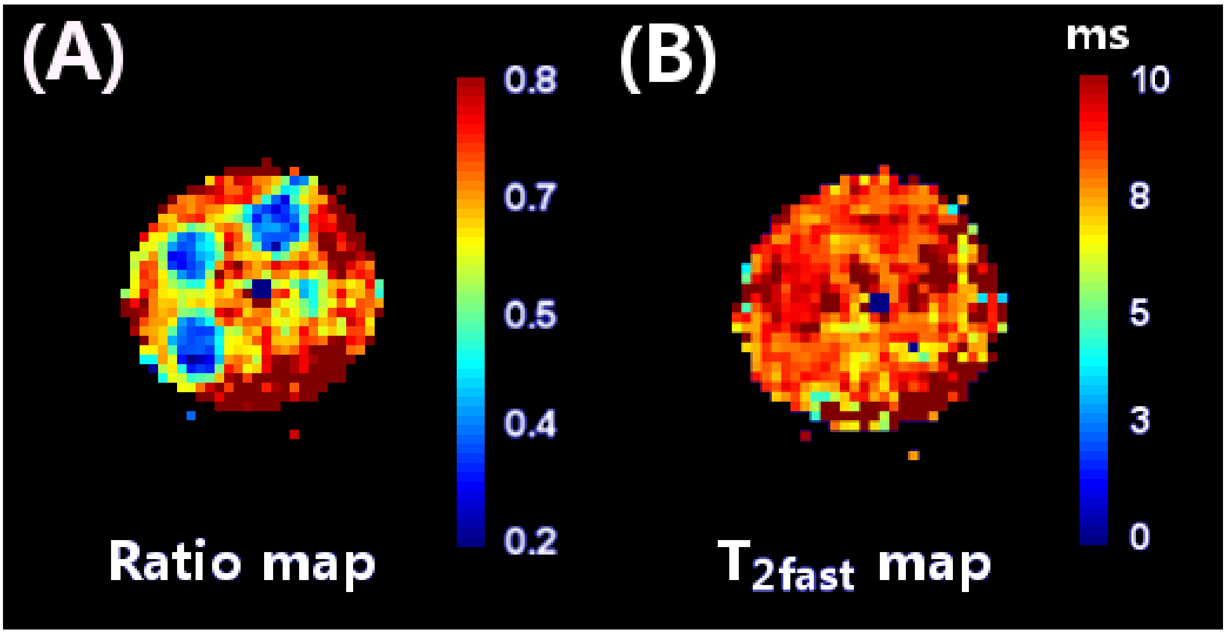

Figure 6.11: Maps obtained for the volumic fraction $(1 - f)$ (A) and T_{2f} relaxation time of the fast decaying component (B).

6.5 Conclusion and Perspectives

Multiple gradient echoes acquisitions are an interesting alternative to state-of-the-art Triple Quantum Filtering techniques.

The proposed MGE approach is relatively straightforward to implement and allows to obtain parametric maps for the slow and fast decaying components of the ^{23}Na signal *in vitro* in a reasonable time.

As pointed out by our MonteCarlo simulations and *in vitro* test, the precise estimation of those model parameters depends on the range of TE that must sample properly the range of possible T_{2s} with a good SNR. Those MC simulations could be useful to further optimize our MGE acquisitions (distribution of echo-time and number of averages) according to the complexity of the compartmental modeling and the available SNR.

Due to the lack of time, we could not confront our MGE data to TQF acquisitions or any other alternative sequence. However, a recent study from the CRMBM in Marseille has applied a similar approach *in vivo* and chose to acquire for more than an hour [BYDDER 2017] which is similar to what was done at the same field using MQF approaches [FLEYSHER 2012, PETRACCA 2015]. As a consequence, it is reasonable to consider that MGE as other approaches aiming at disentangle intra- and extra-cellular contributions should remain an advanced pre-clinical and clinical research tool for UHF ^{23}Na MRI.

Finally, it could be interesting in the future to think of a combined VFA+MGE approach to estimate simultaneously T_{1s}, T_{2s} and volumic fractions. Such acquisition would require slightly more complex compartmental models and an even more complex simulation tool to handle the optimization of TEs, TRs and flip angles.

CHAPTER 7

In vivo Application of Quantification Pipeline to Sodium MRI

Contents

7.1 *in vivo* ^{23}Na MRI protocol

Following its *in vitro* validation in Chapter 4, the VFA approach and its dedicated concentration and T_1 quantification pipeline was applied *in vivo* on human subjects to further evaluate its performances. Experiments were performed at 3T at Aachen University Clinic under the direct supervision of Dr. Sandro ROMANZETTI and with the support of Pr. Kathrin REETZ, chief of Aachen University Clinic neurology department.

Parts of this Chapter were submitted as abstracts to the International Society for Magnetic Resonance in Medicine conference in 2017. Parts of this chapter are under review for publication in Magnetic Resonance in Medicine:
A. COSTE, F. BOUMEZBEUR, A. VIGNAUD, G. MADELIN, K. REETZ, D. LE BIHAN, C. RABRAIT-LERMAN and S. ROMANZETTI, Sodium Concentration and T_1 assessment in the human brain using a Variable Flip Angle approach at 3T.

After local Internal Review Board (IRB) approval, four healthy volunteers were recruited and examined after providing written and informed consent. Information about volunteers are presented in Table 7.1.

Subject	Sex	Date of Birth	Weight	Height	Date of Scan
B0636	F	13/09/1994	75 kg	1.68 m	26/07/2016
B0643	M	06/12/1989	78 kg	1.68 m	29/07/2016
B0645	M	08/01/1995	72 kg	1.67 m	04/08/2016
B0664	M	17/08/1985	70 kg	1.74 m	18/08/2016

Table 7.1: Volunteer information.

MR data were acquired on a 3T PRISMA MR scanner using first the manufacturer 64 Rx channels Hydrogen coil and the 2 Tx channel body coil for the ^{1}H imaging session, then a dual resonance 1Tx/1Rx ^{1}H/^{23}Na RF birdcage coil (Rapid Biomedical, Rimpar, Germany) for the ^{23}Na imaging session.

Regarding the ^{1}H MRI session, high resolution T_1 and T_2 weighted images were acquired as anatomical references, along with more exploratory data: multi-band Diffusion Weighted Imaging (DWI) and quantitative T_1 and Spin Density acquisitions. This first part lasted about half an hour, then the volunteer took a short break out of the magnet to allow for the switch between RF coils. The ^{23}Na MRI session started with standard reference voltage calibration and B_0 shimming procedures. As detailed in Table 4.1, SD, VFA and DAM acquisitions were performed in the exact same conditions than for our *in vitro* experiment. For the SD acquisition, we considered a TR value of 120 ms which is widely used in literature [INGLESE 2010, ZAARAOUI 2012, PALING 2013, RIEMER 2014, MAAROUF 2017]. One additional acquisition with maximum reachable flip angle under SAR constraints was added for future explorations. Each acquisition was fragmented in 3 minutes blocks for retrospective correction of motion (see Figure 4.4) of the volunteer as staying steady for long non-proton acquisition can be challenging in clinical practice.

7.2 Results

7.2.1 Retrospective Motion Correction

Each block was reconstructed and processed as defined in Chapter 4. As illustrated by Figure 7.1, NUFFT reconstructions of each block for the SD or the two VFA acquisitions yielded images with relatively moderate SNR. However, it was sufficient for the co-registration step of our motion correction pipeline.

This block acquisition approach aimed at exploring a possible improvement of the pipeline for clinical application on unsteady patients that could not undertake long acquisition without moving. The duration of the block was taken to be small enough with regard to this possible motion, but long enough to get sufficient SNR for the full image reconstruction. In the case of healthy volunteers at the resolution of 4 mm isotropic this approach may not be ideal as it introduces additional post-processing steps that can incorporate some noise or bias in resulting images. Further explorations, especially on patients are needed to validate this approach and define the most accurate block duration.

While this approach can be an interesting optional feature of the pipeline, other approaches can be considered as interleaving into the sodium sampling sequence a ^{1}H highly under-sampled acquisition (to be very short) to probe motion at a higher temporal frequency as a navigator. Finally, another alternative is the use of independent field monitoring or motion correction device [ZAITSEV 2006, MACLAREN 2013, GODENSCHWEGER 2016].

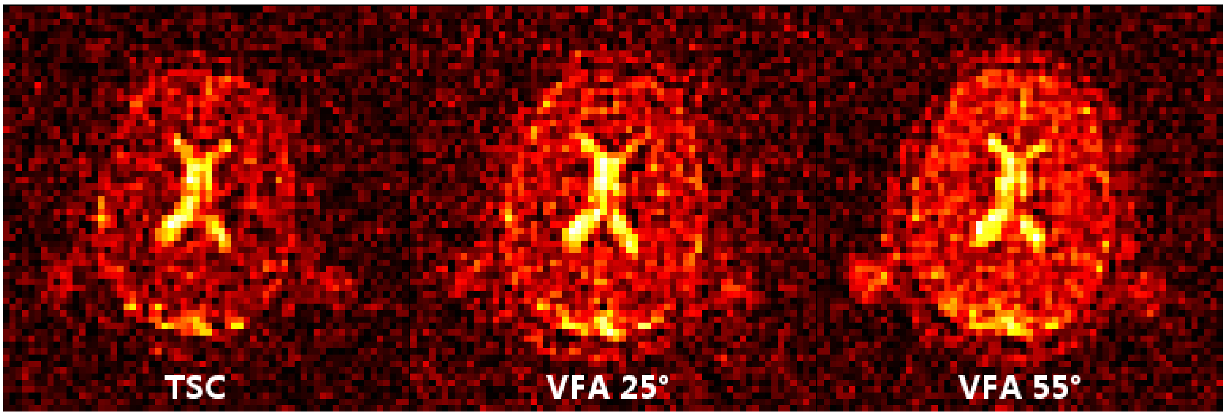

Figure 7.1: Reconstruction of a single block acquisition of SD and VFA at 25° and 55°.

7.2.2 NLM Filtering

As for our *in vitro* acquisitions (see Figure 4.6), a Non Local Mean filter was applied to denoise our images. Figure 7.2 demonstrates the positive effect of this NLM filter on an *in vivo* SD acquisition.

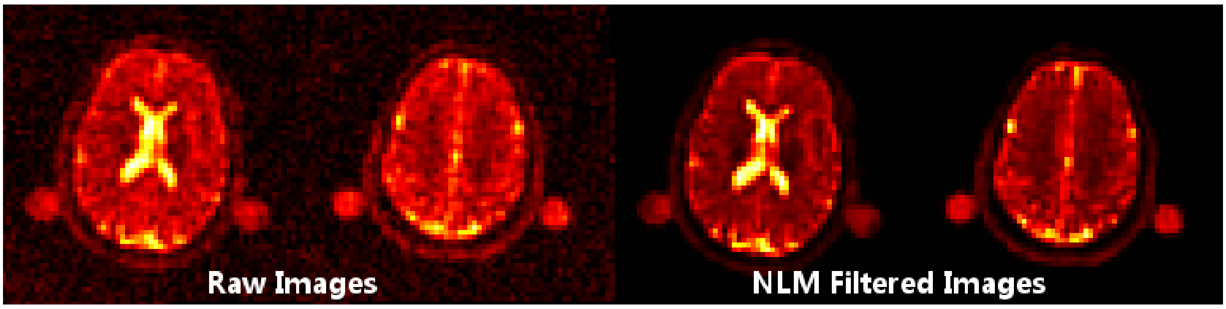

Figure 7.2: Denoising using the Non Local Mean Filter applied to one of our *in vivo* SD image.

7.2.3 TSC and T_1 maps

Figure 7.3 shows the four set of TSC and T_1 parametric maps extracted using our quantification pipeline. Images were reconstructed with the NUFFT algorithm dedicated to the FLORET sampling sequence implemented in MATLAB (The MathWorks, Natick, MA, USA). Signal intensity calibration was made using two external tubes visible on the sides of volunteers head.
Inter-subject variability and overall stability was evaluated using a ROI-based approach as illustrated in Figure 7.4. Box-plots of the TSC and T_1 distribution in those ROIs are shown in Figure 7.5. Our *in vivo* TSC values are close to 35 mmol.L^{-1} which is consistent with TSC values in the normal brain recently reported in the literature [ATKINSON 2011, PALING 2013, MAAROUF 2014, QIAN 2012a,

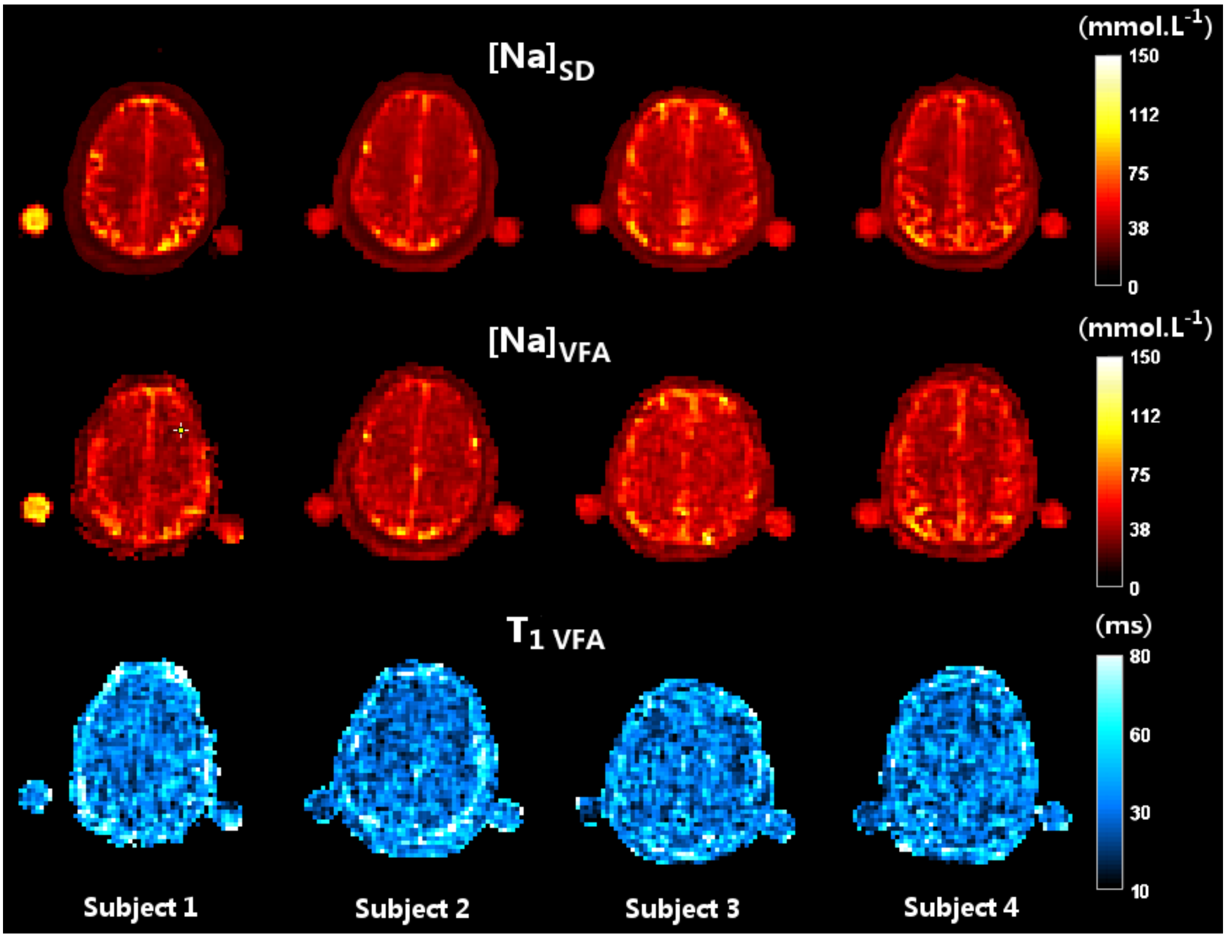

Figure 7.3: Similar axial slices of our *in vivo* validation experiment on four volunteers. Sodium concentration maps computed extracted from the SD data (first row) the VFA pipeline (middle row) and the associated T_1 map. Images were reconstructed using the NUFFT algorithm. For volunteer 1 external concentration calibration references were placed differently.

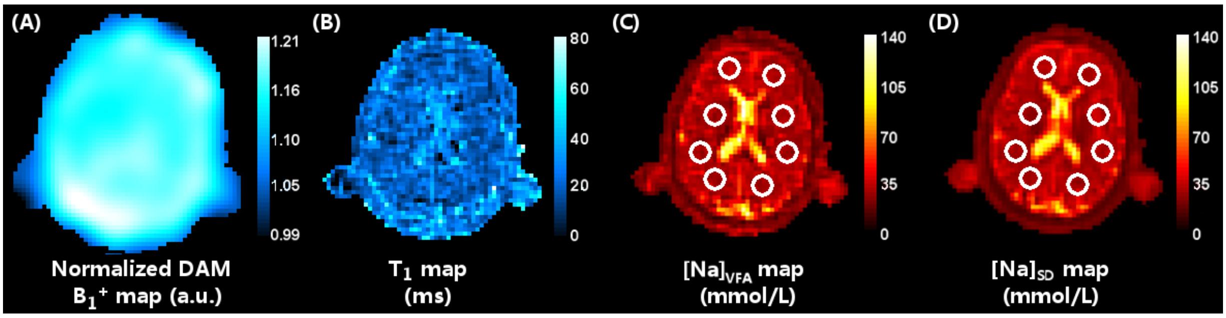

Figure 7.4: Volunteer 2 sodium data: the B_1^+ map (A), the VFA T_1 map (B), the $[\text{Na}]_{VFA}$ map (C) and the $[\text{Na}]_{SD}$ map (D). Concentrations maps (C) and (D) illustrate that measurements were conducted in a large number of small circular ROIs located on multiple slices throughout white matter of the whole brain.

THULBORN 2015, THULBORN 2017]. A simple model of Sodium distribution in brain tissues can be expressed as:

$$TSC = CVF \times [\text{Na}^+]_{ICC} + (1 - CFV) \times [\text{Na}^+]_{ECC} \tag{7.1}$$

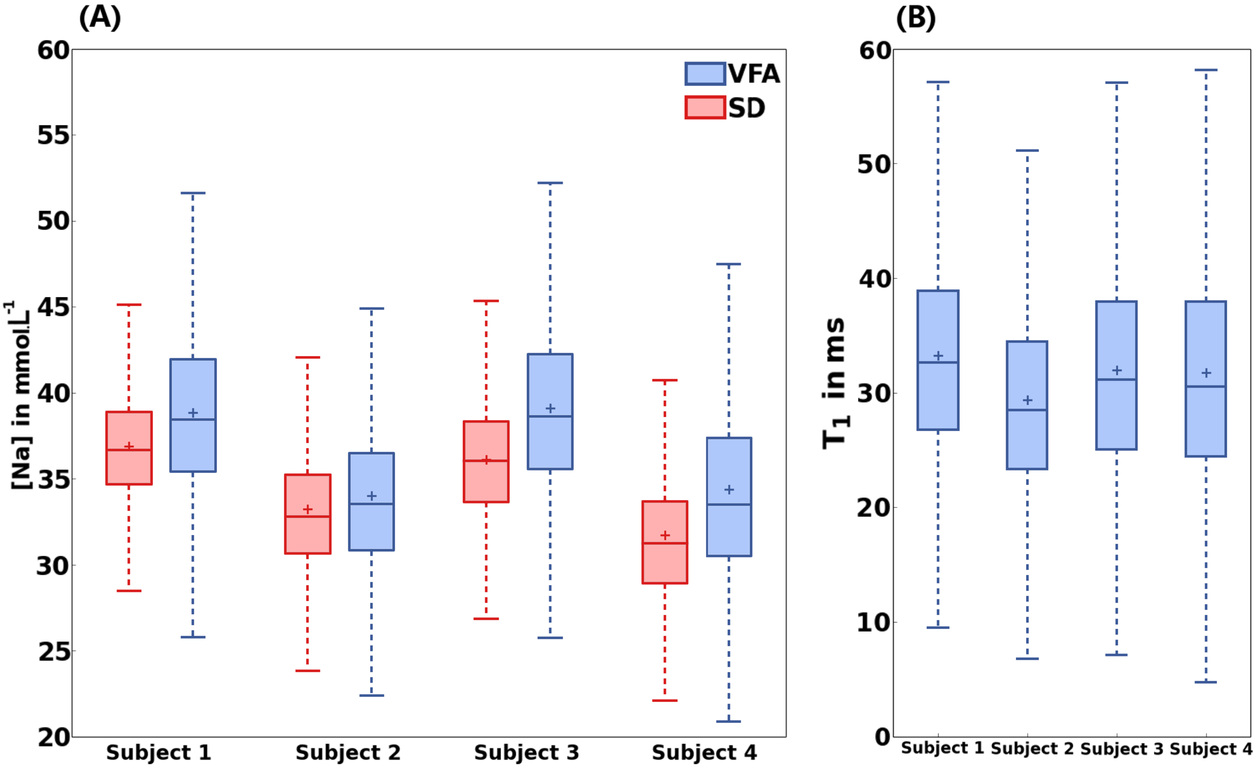

Figure 7.5: SD and VFA measured concentration and T_1 distributions in a large multi-slice ROI of homogeneous white matter.

with CVF being the cellular volume fraction recently estimated to be 0.81 [THULBORN 2015] and $[\mathrm{Na}^+]_{ICC} \in [10, 12]$, and $[\mathrm{Na}^+]_{ECC} \in [140, 150]$. Such method leads to expect tissular concentrations in the range of [30,40] mmol.L^{-1} which corresponds to the range of our measured values. As observed for our phantom measurements, TSC values are slightly higher in VFA than in SD (TR=120 ms) maps. If we were extending the conclusions already made for *in vitro* TSC maps to these *in vivo* data, we would state that our TSC measurements better reflect the actual total sodium concentration as T_1-weigthing is accounted for with our VFA approach. Regrettably, the intra-subject standard deviation was again greater with the VFA than with the SD approach (12% vs 8%) while the inter-subject variability was similar (15.8 vs 15.5%).

VFA estimated longitudinal relaxation times in white matter was relatively stable across volunteers at 31.6 ms with a inter-subject standard deviation of about 4% while the intra-subject standard deviation was close to 28%. While those T_1 values in WM are in agreement with values reported in the literature [MADELIN 2013, SHAH 2015], the wide spread of those T_1 distributions is the most crucial limit of our quantification pipeline. As such, our VFA pipeline would greatly benefit from using either more T_1-weighted acquisitions or anatomical masks (extracted from ^{1}H MPRAGE images) to constraint the T_1 fit.

7.3 Axis of Improvement

7.3.1 Increasing SNR

Another solution to improve the precision of our T_1 estimation would be to increase SNR. In order to appreciate the impact of SNR on the quality of our T_1 maps, two extra acquisition block (one at 25° and one at 55°) were acquired and added to the other blocks leading to a total acquisition time of 24 minutes instead of 18 minutes. Figure 7.6 illustrates the results obtained with a longer acquisition time. As can be appreciated based on the T_1 values given in Table 4.1, a 15% increase in SNR can lead to a reduction of the variance by about 10%.

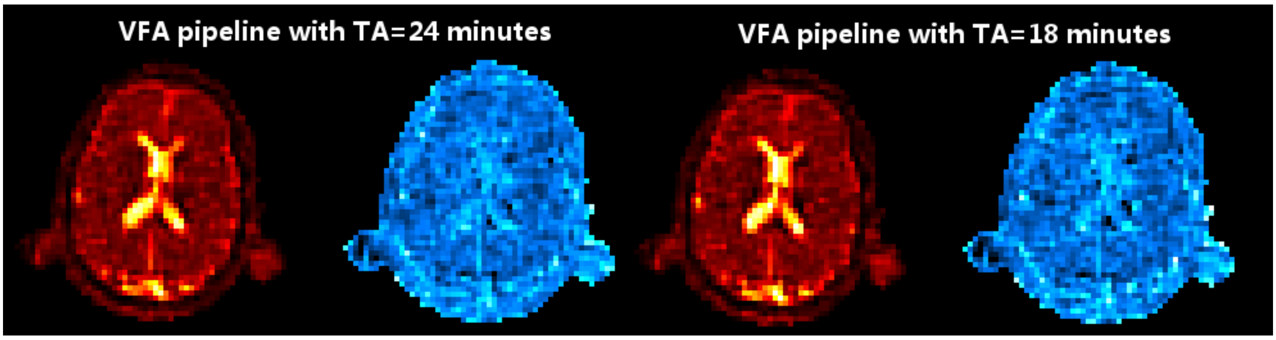

Figure 7.6: Comparison between M_0 and T_1 maps for the use of 3 acquired blocks and 4 acquired blocks.

ROI	4 blocks	3 blocks
Ventricular CSF	48.0 ± 9.5	49.6 ± 10.3
Homogeneous WM 1	28.5 ± 7.9	28.6 ± 9.7
Homogeneous WM 2	29.8 ± 7.1	28.7 ± 8.2
Homogeneous WM 3	29.4 ± 8.0	29.0 ± 7.7
Right eye	53.8 ± 9.1	55.6 ± 10.5
Left eye	53.3 ± 10.5	55.3 ± 11.3

Table 7.2: Comparison of measured T_1 for a 24 and 18 minutes acquisition time of the VFA method.

7.3.2 NUFFT and FISTA reconstruction

Beyond the challenge related to our T_1 estimation pipeline, other axis of improvement were explored *in vivo*. One such axis is to evaluate the impact of the chosen reconstruction algorithm. As all images were first reconstructed using the NUFFT [Fessler 2003] reconstruction algorithm, we then used the 3D wavelet regularized non-linear iterative FISTA algorithm [Beck 2009] based on the NFFT [Keiner 2008] for comparison. Figure 24 shows our quantitative TSC and T_1 maps obtained for the SD and VFA approaches.

Differences between the two reconstructions are small, the smoothing and denoising behavior of FISTA is clearly visible on results. Numerical value extracted from both methods were very similar and are summarized in Table 7.3. Therefore, while caution is still required to correctly set tuning parameters, the use of non-linear reconstruction algorithm is possible for *in vivo* data without jeopardizing quantitative measurements. In recent years, such algorithms have started to be used for non-proton MRI [Madelin 2012, Behl 2016].

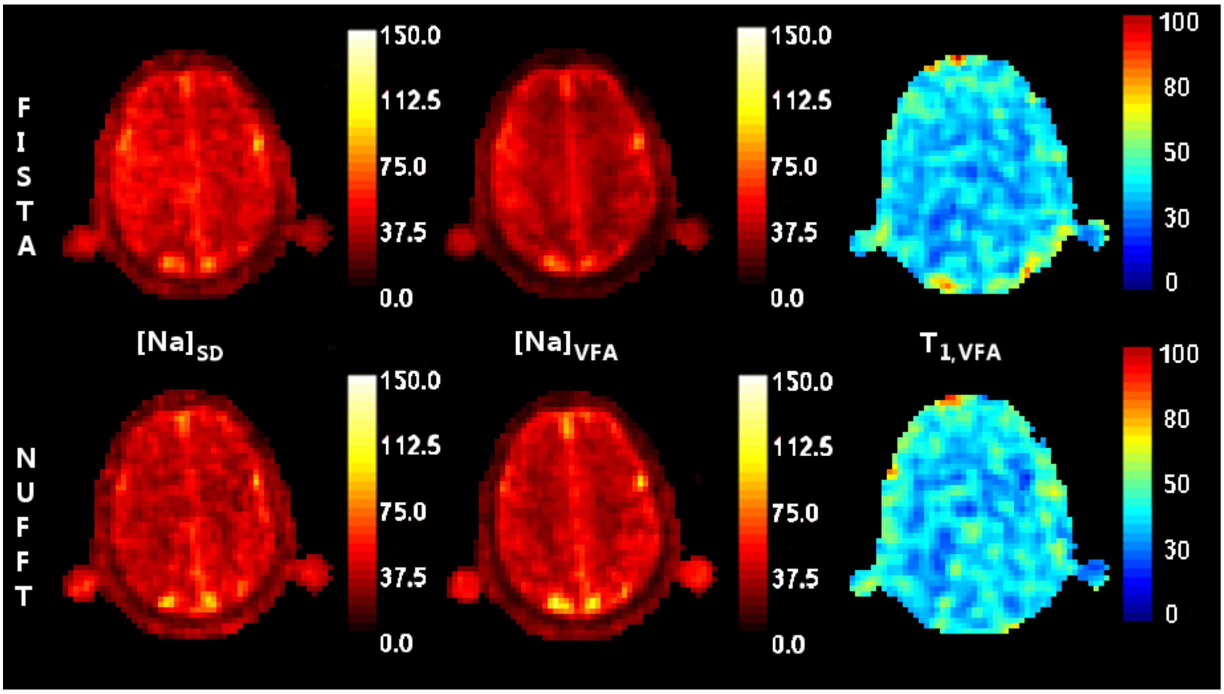

Figure 7.7: Concentration and T_1 maps reconstructed with either FISTA (top) or NUFFT (bottom).

	FISTA	NUFFT	unit
[Na] Homogeneous WM SD	31.9 ± 4.2	36.2 ± 5.4	$mmol.L^{-1}$
[Na] Homogeneous WM VFA	40.2 ± 4.3	36.4 ± 5.9	$mmol.L^{-1}$
T_1 Homogeneous WM VFA	30.4 ± 8.2	32.0 ± 9.7	ms

Table 7.3: Comparison of measured Sodium concentration and T_1 for FISTA and NUFFT reconstructions.

7.3.3 Acquisition time

Another axis of improvement could paradoxically to reduce the acquisition time (TA) of our VFA method so as to foster its application for clinical research. To do so, we explored two different options: (i) make use of fragmented acquisition to evaluate the possibility to use less acquisition blocks or (ii) use retrospective random under-sampling of Fourier data to reduce the number of acquired spokes with minimal impact on SNR and image structure.

7.3.3.1 Block reduction

Fragmented acquisitions to account and correct for possible patient motion is an opportunity to explore reconstruction and measurements with less blocks with the aim of reducing TA. Our comparison criterion is indeed quantitative concentration measurements. Figure 7.8 illustrates the reconstruction with all acquired blocks using NUFFT (panels B-D), a 33% time reduction removing one block on each VFA acquisition and 2 on SD to maintain identical TA and reconstructed with NUFFT (panels F-H).

For this test, data were not corrected by the NLM filter, therefore their visual quality is not as nice as previous images. Quantitative measurements performed on those data sets provided similar mean concentration values but at the price of an increased spread as illustrated in Table 7.4. Results were

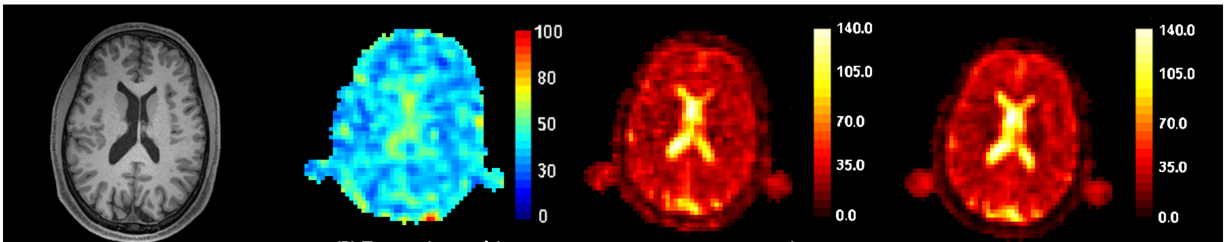

(A) Anatomy ^{1}H T_{1w} (B) T_1 map (seconds) (C) $[Na]_{VFA}$ map (mmol/L) (D) $[Na]_{SD}$ map (mmol/L)

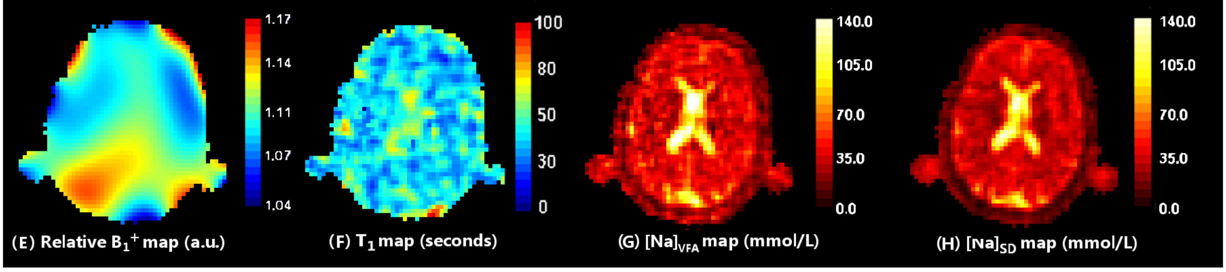

(E) Relative B_1^+ map (a.u.) (F) T_1 map (seconds) (G) $[Na]_{VFA}$ map (mmol/L) (H) $[Na]_{SD}$ map (mmol/L)

Figure 7.8: Comparison between the use of the 3 acquired blocks (TA=18 minutes) and 33% reduction by removing one block (TA=12 minutes).

obtained using ROI based measurements with several measures in different white matter areas.

	18 minutes	12 minutes	unit
[Na] Homogeneous WM SD NUFFT	35.4 ± 5.3	33.8 ± 5.7	$mmol.L^{-1}$
[Na] Homogeneous WM VFA NUFFT	37.3 ± 6.5	38.4 ± 8.8	$mmol.L^{-1}$
T_1 Homogeneous WM VFA NUFFT	34.1 ± 12.2	32.9 ± 14.6	ms

Table 7.4: Comparison of measured Sodium concentration and T_1 for 18 and 12 minutes acquisition time.

7.3.3.2 Retrospective under-sampling

To further reduce acquisition time, it is possible to under-sample K-space and compensate for the loss of samples by using a non-linear reconstruction algorithm. In our *in vivo* study, we did not aim at implementing this approach prospectively, so data were acquired with original full sampling scheme and were retrospectively under-sampled by randomly removing a certain number of spokes.

As illustrated on Figure 7.9, the resulting SNR after a 3 minutes Sodium acquisition is very low, which makes image reconstruction very challenging. Data under-sampling was performed up to 50% spoke removal and, as noticeable, image shape and quality remain pretty stable until 30% removal and then a strong degradation of the shape occurs. Application of the SSIM criterion was not conclusive on such data set. Other explorations were conducted on data sets with higher SNR allowing a most important under-sampling as illustrated by Figure 7.10. A FLORET SD acquisition was performed with a single long block and reconstructed using FISTA with 125 iterations and a regularization weight λ of 10^{-5}. Random spoke removal was performed with increasing under-sampling ratios going up to 75% spoke removal. First, one can notice that when removing too much data, the algorithm is no longer capable of reconstructing an image. Second, when SNR is high enough in acquired data set, larger under sampling ratios are reachable. Degradation of the image

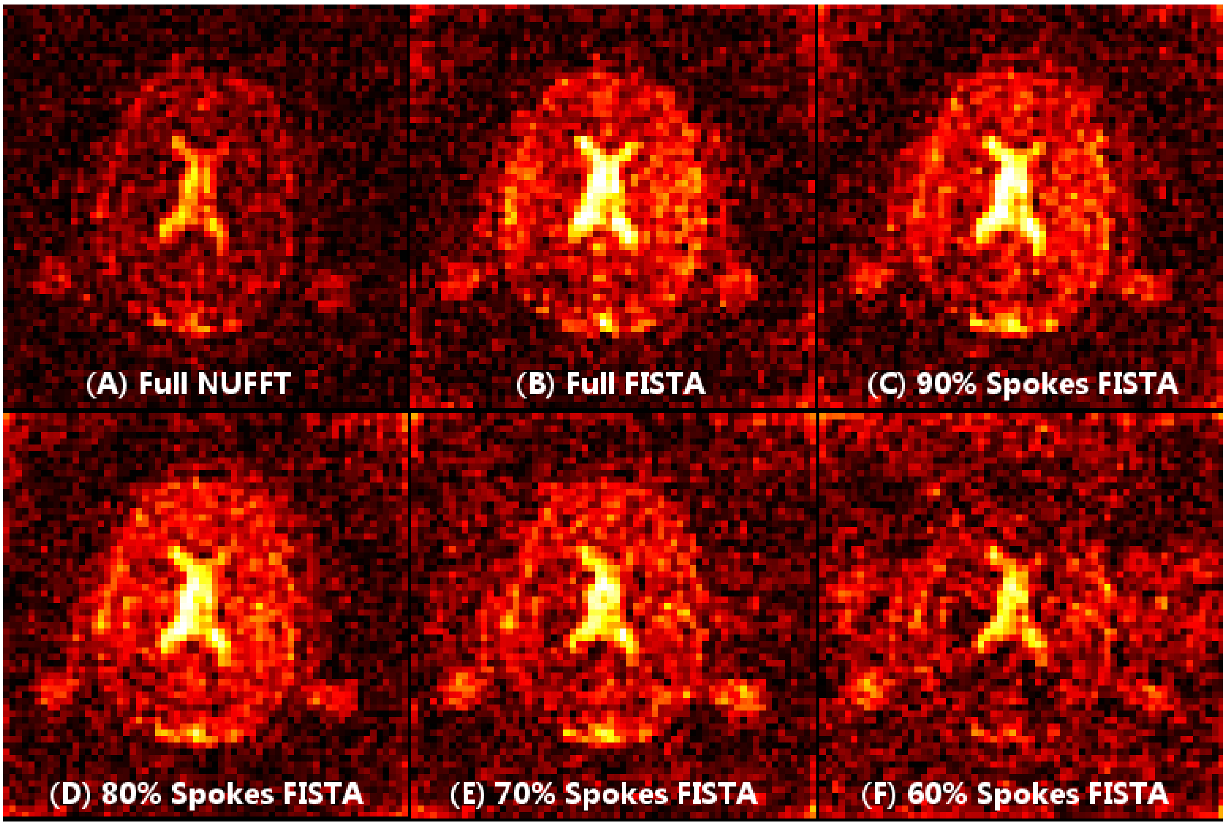

Figure 7.9: Under-sampling experiment on a single block acquisition using FISTA and compared with NUFFT reconstruction.

quality are also visible and the impact of under sampling on image contrast and structure would need to be quantified as well as the influence of algorithm tuning parameters.

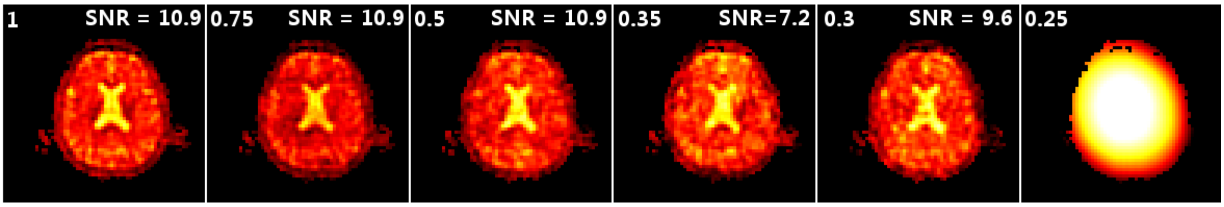

Figure 7.10: Under-sampling experiment of a longer Sodium SD acquisition using FISTA with sampling ratios: 1, 0.75, 0.5, 0.35, 0.3 and 0.25.

Influence of regularization weight in FISTA

Non linear iterative inverse problem based regularized algorithms need to specify the relative weights to assign to the different terms of the optimization problem. Those weights are real values favoring some aspects and properties of the reconstruction. In our case, we have a λ parameter weighting the wavelet decomposition of the image. As no automated process exists to accurately set this weight as it depends on the geometric complexity of studied object and the available level of signal, a prior exploration had to be performed. Figure 7.11 illustrate the smoothing and denoising effect of the algorithm with increasing λ value and illustrates pretty well the challenge of setting it properly. When no weight is used, reconstruction becomes an NFFT based linear least square image reconstruction with no wavelet decomposition. For our *in vivo* explorations, we noticed that a weighing factor of $\lambda \approx 10^{-5}$ was providing satisfying results.

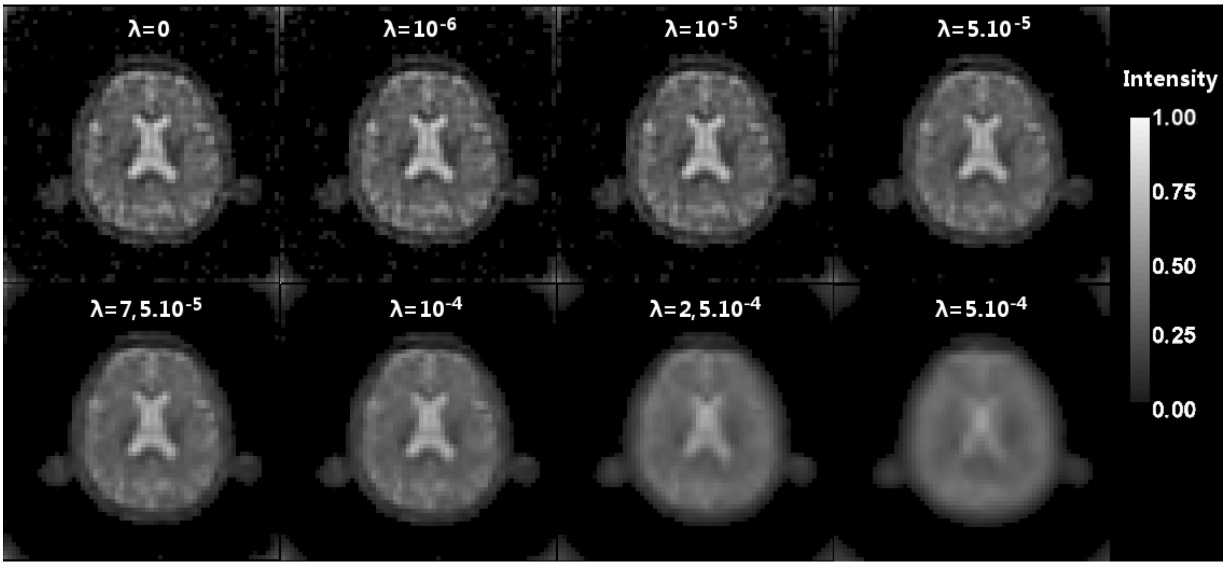

Figure 7.11: Influence of the wavelet regularization weighting parameter lambda in FISTA algorithm.

Influence of iteration number in FISTA

Another parameter that can have some influence is the number of iterations of the algorithm. An empirical criterion to set the number of iterations prior to stopping the algorithm was initially set and led us to explore the influence of the number of iterations on reconstructed images.

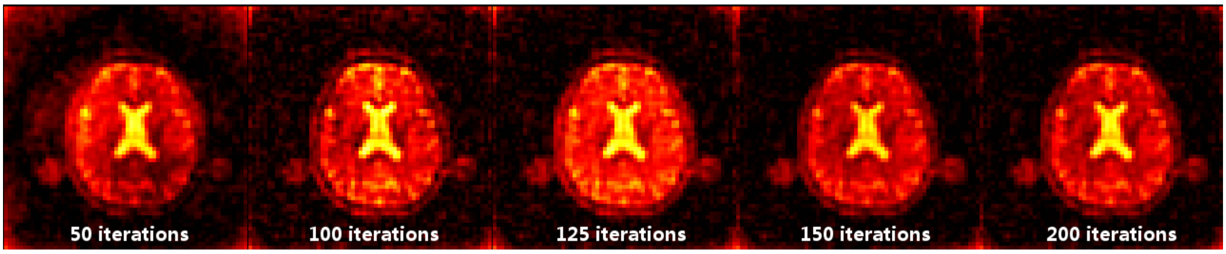

Figure 7.12: Influence of the number of iteration on reconstructed images for a fixed λ value of 10^{-5}.

As illustrated by Figure 7.12 SNR is increasing with iterations until about 125 and then is seems to decrease. This study was extended with several values of the regularization weight, SNR analysis in multiple ROI in different brain areas and tissues and structural analysis using the SSIM index. As this study requires an important number of reconstructions and is therefore time consuming, following results have been only obtained for a limited number of different data sets. As no ground truth exists, in this particular case of studying the influence of FISTA's reconstruction parameters, the NUFFT image reconstruction was used as reference.

Based on previous results, we observed that there seems to exist an optimal value for both the number of iterations and the weighting value (λ) which would concomitantly maximize SNR and SSIM.

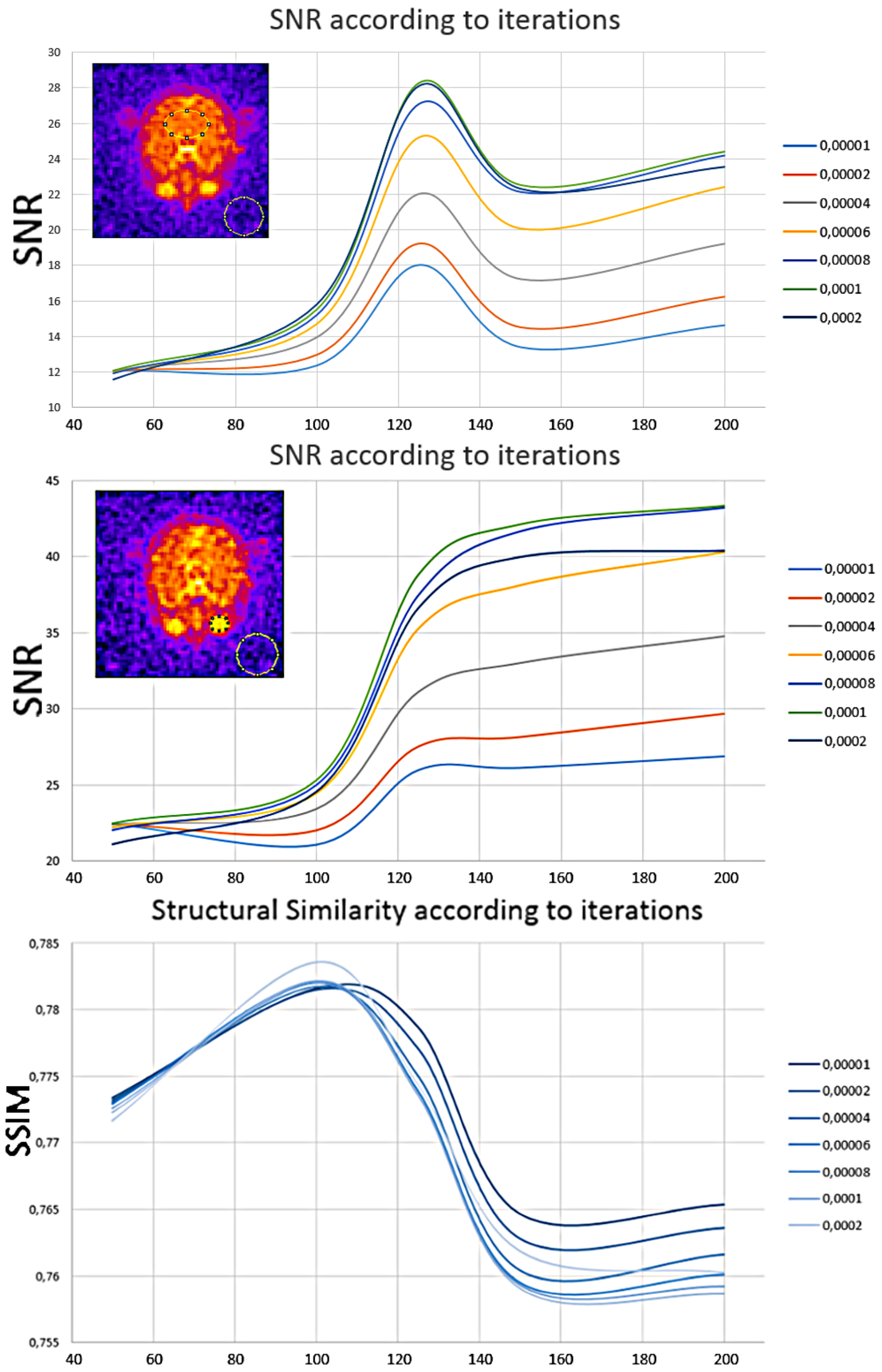

Figure 7.13: Influence of the number of iterations on SNR and SSIM index for various λ values. In White matter SNR in NUFFT image was 13.5 and 19.2 in the eye ROI.

Finally, we also tried to find a criterion to reach a satisfying number of iterations automatically based on the energy improvement between two consecutive iterations. This method provided number of iterations close to 125 which appeared to be in good agreement with the behavior previously observed. Further and extended explorations are needed to confirm these observations. For the time being, we think it is important to adjust these parameters for each new *in vivo* study.

7.4 Conclusion and Perspectives

With this small *in vivo* proof-of-concept study, we have demonstrated the feasibility of our VFA approach and have acquired precious data to improve our acquisition protocol and the quantification pipeline. The advantages of this VFA pipeline is that it leads to TSC values intrinsically corrected for T_1-weigthing and to T_1 values that could be of interest to further assess changes in local tissues environment. This could be particularly interesting for diseases such as Multiple Sclerosis where lesions exhibit increased extra-cellular content compared to healthy tissue [BONNIER 2014]. As demonstrated with our phantom data, the use of relatively short TR in many clinical studies results in an imperfect longitudinal magnetization regrowth in those lesions. Therefore, our T_1-corrected TSC maps could be alternative approach for the study of MS lesions or stroke.

However, our VFA approach remains a work-in-progress and deserves to be improved upon. The most promising step would be to use tissue probability maps (Figure 7.14) to take into account partial volume effects and correct accordingly T_1 and TSC estimations [NIESPOREK 2015]. More generally, any ^{1}H imaging modality could be used as prior knowledges to constrain a revised iterative reconstruction and quantification pipeline [GNAHM 2014].

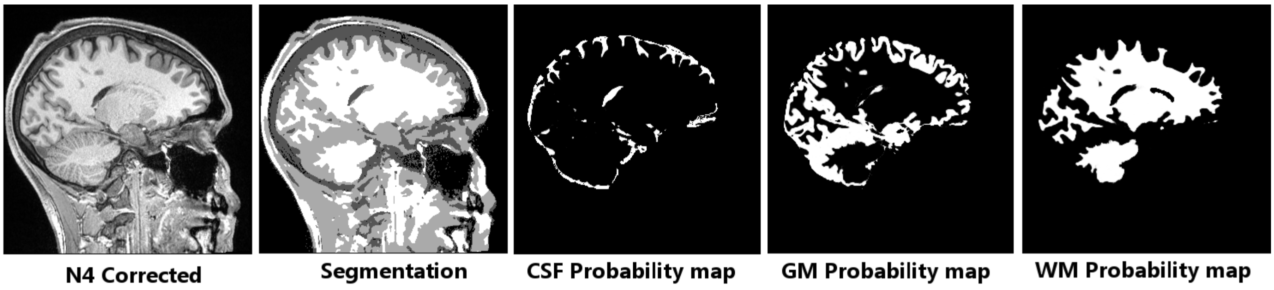

Figure 7.14: Anatomical Images processed using ANTs to correct intensity, segment images, perform brain extraction and compute tissues probability maps [AVANTS 2011].

The use of different reconstruction algorithms, linear and non linear, was studied to evaluate possible benefices and requirements. When conducted with data with sufficient SNR, our retrospective under-sampling tests confirmed the ability of non-linear algorithm such as FISTA to handle under-sampled datasets (up to 30%) with limited impact on the quality of the ^{23}Na images, opening the way for potential time reduction for clinical applications or increased spatial resolution especially for ultra-high field MRI. These results confirm a known fact in the Compressed Sensing domain that larger under-sampling factors can be obtained with larger data sets. However, one should be cautious to adjust certain tuning parameters before relying blindly on non-linear iterative algorithms. Indeed, a too heavy regularization weight would lead to a strong smoothing and denoising effect while a too light value would yield no benefit. Moreover, the number of iterations should be optimized to maximize the quality of the reconstructed images while remaining low enough to limit the computing time.

The VFA pipeline presented in Chapter 4 and validated *in vivo* in this chapter is currently used at Aachen University Hospital for explorations on patients suffering from Alzheimer's disease. Hopefully, the VFA approach will be applied at NeuroSpin for non-proton MRI in particular ^{23}Na MRI of both non-human primates and patients (if possible Alzheimer's patients in collaboration with Sainte Anne Hospital Center) at 7 T in 2018 and later at 11.75 T.

CHAPTER 8

Proof-Of-Concept Study in Phosphorus MRI

Contents

In this section, we present our developments of a spectrally-selective non-Cartesian SSFP sequence for Phosphorus (^{31}P) MRI. *In vivo* preliminary results are compared with state-of-the-art ^{31}P-MRSI acquisitions. Our quantification pipeline is detailed even though only localized concentration measurements are calculated.

8.1 Principle and Implementation

8.1.1 Principle of spectral selection

In order to image selectively a metabolite-of-interest, a selective excitation can be realized using a RF pulse whose operating frequency is set at its Larmor frequency (or at the resonance frequency of one of its moiety) and whose spectral bandwidth will be smaller than half the frequency gap with its closest neighbor as depicted by Figure 8.1.
For any given RF pulse, the pulse bandwidth is inversely proportional to its duration and depends on the time-bandwidth product R according to:

$$R = \Delta_\nu \tau_{RF}. \tag{8.1}$$

Consequently having a more selective pulse requires a longer RF pulse which also presents drawbacks. A trade-off thus needs to be found. As a general guideline, one should set the pulse duration

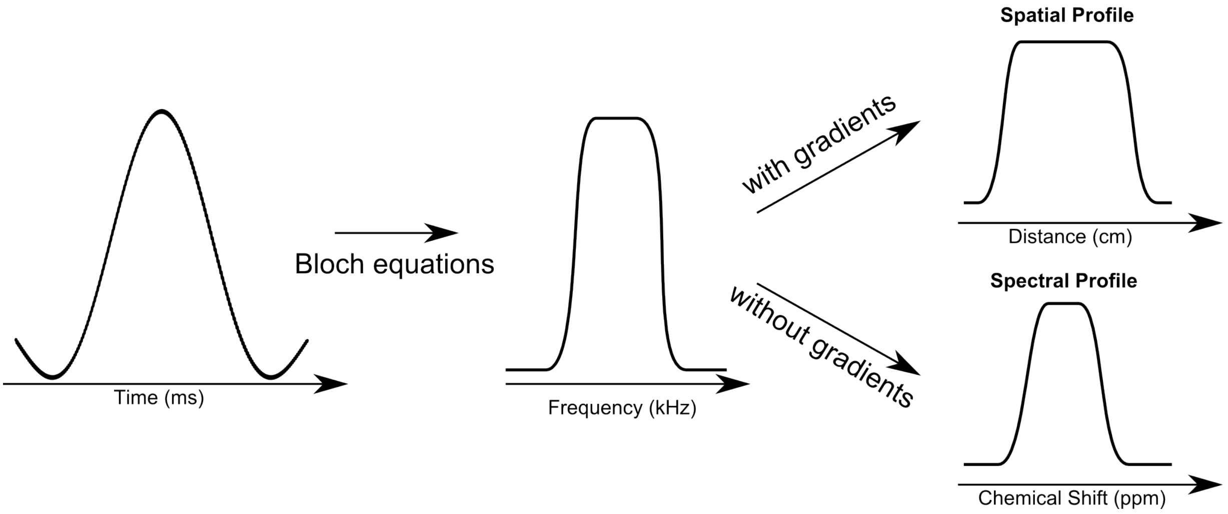

Figure 8.1: Principle of spectral and spatial selection [Bernstein 2004].

to achieve a satisfying spectral selectivity while preserving a short echo-time under SAR or B_1^+ constraints.

8.1.2 Implementation

Due to the relatively low concentration of phosphorylated metabolites, we chose to use the Twisted Projection Imaging sequence [Boada 1997c], detailed in Chapter 3 and already used for *in vitro* Sodium MRI at 7 T.

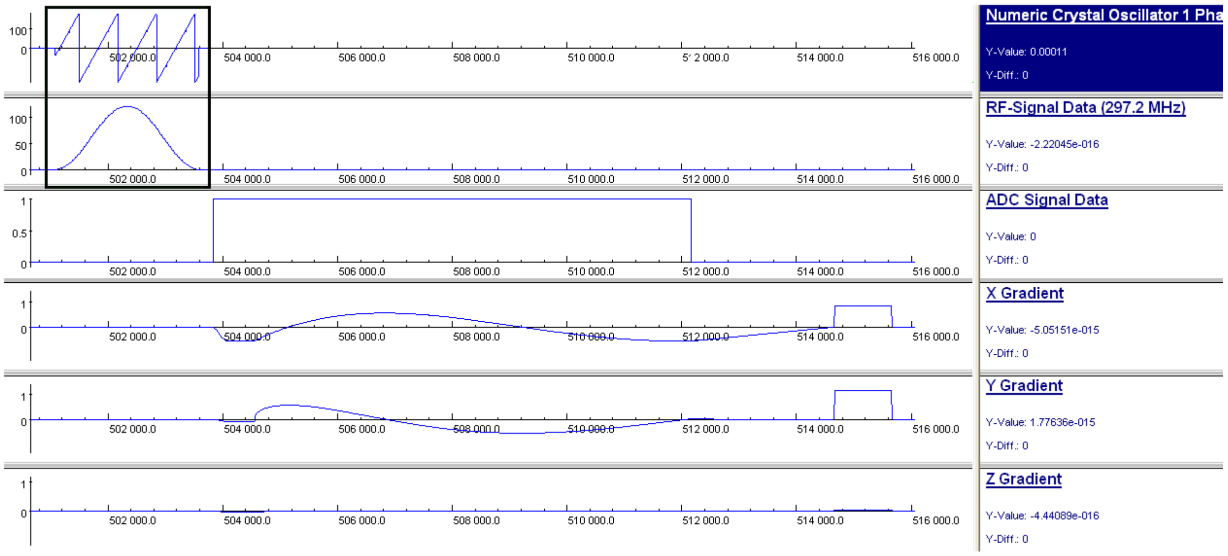

Numeric Crystal Oscillator 1 Pha
Y-Value: 0.00011
Y-Diff.: 0

RF-Signal Data (297.2 MHz)
Y-Value: -2.22045e-016
Y-Diff.: 0

ADC Signal Data
Y-Value: 0
Y-Diff.: 0

X Gradient
Y-Value: -5.05151e-015
Y-Diff.: 0

Y Gradient
Y-Value: 1.77636e-015
Y-Diff.: 0

Z Gradient
Y-Value: -4.44089e-016
Y-Diff.: 0

Figure 8.2: Spectrally selective TPI pulse sequence diagram simulated with POET, a tool of Siemens IDEA developing environment.

For the spectral selective excitation, a simple Gaussian pulse (R=2.73) was implemented with adjustable duration and frequency offset as depicted by Figure 8.2. A constant pulse duration of 4 ms was set for all our acquisitions yielding a pulse bandwidth 680 Hz and an effective echo-time of 2.3 ms.

8.2 *In vitro* explorations

8.2.1 Validation of the spectral selectivity

To validate our spectral selectivity, a dedicated phantom (ref=31P-7T-4) presented in Chapter 2 and illustrated in Figure 8.4 was filled with PhosphoCreatine (PCr at 20 and 40 mmol.L^{-1}), Adenosine Triphosphate (ATP at 20 and 40 mmol.L^{-1}) and Phosphate Buffered Saline (PBS at 50 mmol.L^{-1}) solutions.

The acquisition protocol consisted in: first, a non localized ^{31}P spectrum to check the resonance frequencies of each metabolite; then our dedicated SSFP sequence was used to acquire PCr, ATP and Pi images at a resolution of 10 mm isotropic in 10 minutes. The frequency offset used are given in Table 8.1. The TPI parameters were: TR of 100 ms, TE of 2.3 ms with a flip angle of 20°. No specific optimization of the FA (Ernst angle) was performed according to the T_1 of each metabolite.

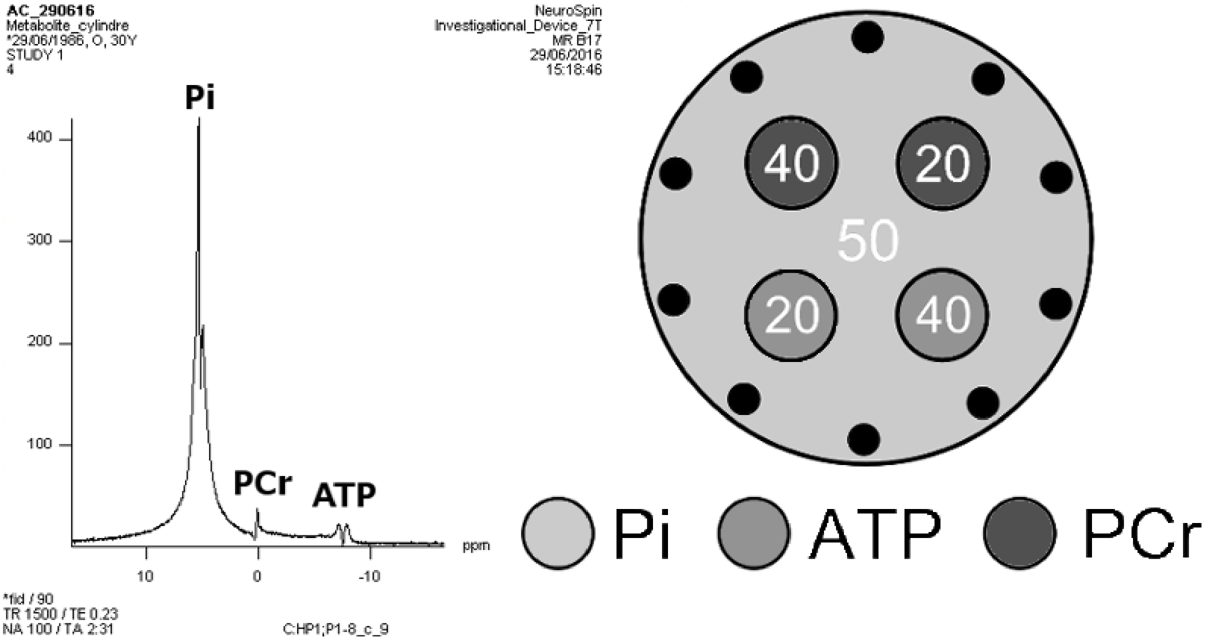

Figure 8.3: Non-localized ^{31}P magnitude spectrum (left) acquired from our multiple compartment ^{31}P phantom (right). Pi is the largest peak as its concentration and volume are dominant.

Metabolite	Frequency Shift (ppm)	Frequency shift (Hz)
PhosphoCreatine	0	0
Pi	5	600
ATP	-8.5	-1020

Table 8.1: Frequency and ppm offsets for the different phosphorylated metabolites of our phantom.

^{31}P MR images were reconstructed using our Kaiser-Bessel based gridding reconstruction algorithm presented in Chapter 1 and Chapter 3. As illustrated by Figure 8.4, Pi, PCr and ATP images were obtained with a sufficient SNR validating our spectrally selective SSFP sequence.

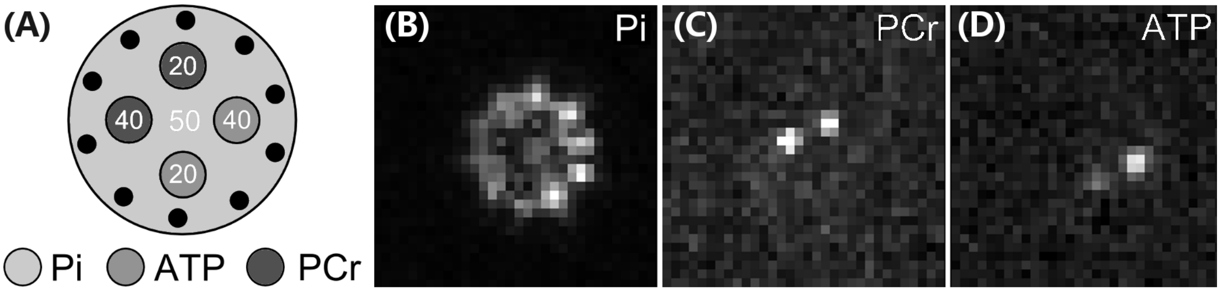

Figure 8.4: ^{31}P MR images of Pi (B), PCr (C) and ATP (D) at 10 mm isotropic spatial resolution. Acquisition parameters: TR/TE/FA/TA=100 ms/0.5 ms/20°/10 min with TPI parameters: 2 averages of 3000 spokes composed of 608 samples and linear fraction of 35%.

8.2.2 Gridding versus FISTA

Explorations regarding the use of our 3D wavelet regularized non-linear reconstruction algorithm were performed using a different phantom (ref=31P-7T-3), presented in Chapter 2. PhosphoCreatine images were acquired in similar conditions as before. Reconstructed images with our Kaiser-Bessel gridding method and FISTA algorithm were compared in terms of SNR. Figure 8.5 shows our four PCr tubes reconstructed with both methods and Table 8.2 provides the average SNR values over each tube.

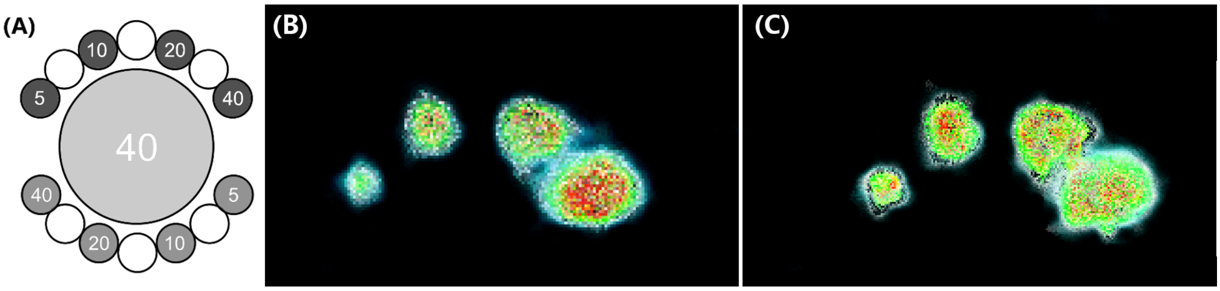

Figure 8.5: Phantom design (A) and 3D interpolated PCr images at 10 mm isotropic resolution and reconstructed using KB Gridding (B) and FISTA (C). FISTA number of iterations and regularization weight were set empirically based on visual inspection. Acquisition parameters: TR/TE/FA/TA=100 ms/2.5 ms/15°/7 min 45 sec with TPI parameters: 3 averages of 1500 spokes composed of 608 samples and linear fraction of 30%.

Reconstruction	40 mmol.L^{-1}	20 mmol.L^{-1}	10 mmol.L^{-1}	5 mmol.L^{-1}
KB Gridding	30.4 dB	28.16 dB	26.28 dB	20.17 dB
FISTA	32.3 dB	30.15 dB	27.71 dB	20.94 dB

Table 8.2: SNR comparison between Gridding and FISTA in the different PCr tubes.

As expected the proper use of FISTA led to improved SNR values for each PCr tubes (up to 1.9 dB for the most concentrated tube). Although not perfect, both reconstruction algorithm preserved the proportionality of SNR with increasing PCr concentration (R^2=0.96 for FISTA and 0.94 for KB gridding). Despite this advantage of FISTA, subsequent *in vivo* images were reconstructed using KB gridding for practical reasons (shorter time needed for computation and visual inspection).

8.3 *In vivo* study

8.3.1 Volunteers information

In order to further evaluate our spectrally selective ^{31}P MRI approach, we performed a proof-of-concept study after approval by NeuroSpin's internal scientific committee and a national ethics committee on two healthy human volunteers (see Table 8.3 for details) who provided written informed consent.

Volunteer	Sex	Date of Birth	Scan Date	Vref (V)
1	F	09/04/1992	28/06/2017	350
2	M	12/02/1982	28/06/2017	320

Table 8.3: Volunteers information and reference voltage used for *in vivo* Phosphorus MRI explorations.

8.3.2 Imaging Protocol

The study was performed at 7 T on our Siemens MAGNETOM MR scanner using our dual resonance ^{1}H/^{31}P 8Tx/8Rx transceiver phased array head coil (Resonant Research, Billerica, USA) operating at 297.2 MHz and 120.3 MHz for ^{1}H and ^{31}P respectively [AVDIEVICH 2011] (for details see Chapter 2). Table 8.4 summarizes the imaging protocol and Table 8.5 provides sequence detailed parameters.

Sequence	TA	Optional
^{1}H Localizer	30 secs	No
^{31}P FID 4 kHz	2 mins	No
^{31}P FID 10 kHz	2 mins	Yes
Voltage Calibration	3 min	No
B_0 Shim	5 mins	No
^{31}P TPI-PCr	18 mins	No
^{31}P TPI-ATP	18 mins	No
^{31}P 2D-CSI-V_1	18 mins	No
^{31}P 2D-CSI-V_2	18 mins	No
^{1}H MPRAGE	5 mins	No

Table 8.4: ^{31}P MRI protocol for our proof-of-concept study at 7 T.

The reference voltage for the ^{31}P channel was estimated based on *in vitro* measurements made using the ellipsoidal phantom (ref=31P-7T-1). Both reference voltages are given in Table 8.3. Chemical shift offsets for PCr (0 ppm) and αATP (-7.5 ppm) were verified from the non-localized ^{31}P spectrum presented in Figure 8.6.

	TPI	TPI	2D-CSI	2D-CSI	Unit
	PCr	α ATP	V_1	V_2	
$T_1^\dagger$	3.43	1.26			s
$T_2^\dagger$	132	26			ms
T_2^*	26	17			ms
TE	2.3	2.3	2.3	2.3	ms
TR	100	100	1800	200	ms
FA	15	23	60	20	degree (°)
Projections	1400	1400			
linear proportion	0.35	0.35			
Averages	8	8	12	122	
Shift	0	-7.7			ppm
TA	19	19	19	19	min
Spectral BW			6000	6000	Hz
Number of Points			2048	1024	points
voxel size	1728	1728	3125	3125	mm^3
Matrix	32 iso	32 iso	16 iso	16 iso	voxel
FOV	320 iso	320 iso	200 iso	200 iso	mm

Table 8.5: Acquisition parameters for our ^{31}P imaging with SSFP-TPI and CSI-FID. (†) T_1 and T_2 values are from [LEI 2003, LU 2014]. T_2* values were estimated from the FWHM of PCr and αATP resonances from CSI data. Flip angles were set approximately at the Ernst angle values depending on the TR and T_1 considered.

Due to the significant B_1^+ heterogeneity of our proton channel, an anatomical proton image (Turbo Flash TR/TE/FA/TA/Res/=2300 ms/2.98 ms/9°/7′46"/1 mm isotropic) was recovered for each volunteer from a prior examination at 3 T.

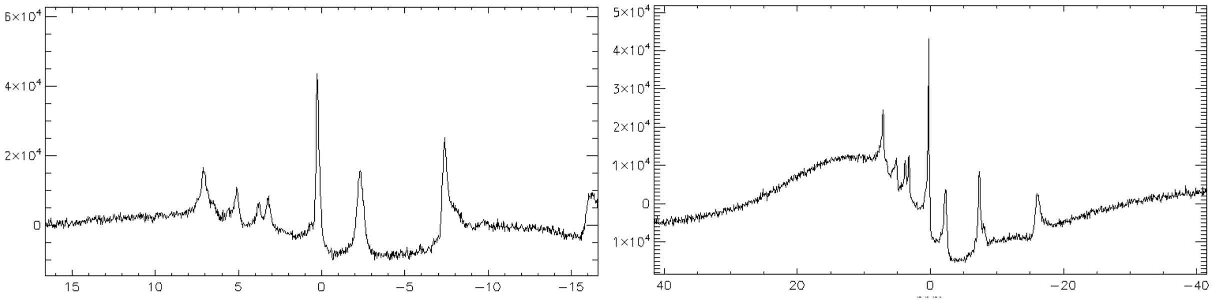

Figure 8.6: Non-localized *in vivo* Phosphorus spectra with a 4 kHz (left) and a 10 kHz (right) spectral bandwidth acquired from volunteer 2. One can notice on the 10 kHz spectra the presence of a large background signal from hydroxyapatite which is highly concentrated in bones (≈ 30 $mol.L^{-1}$) [LEBON 2017].

8.3.3 TPI post-processing

Raw ^{31}P TPI data were reconstructed using our homemade KB-gridding reconstruction algorithm and smoothed using the Non Local Mean filter with automated parameter estimation based on data (here σ=4.02×10^{-8} and global smoothing parameter h=2.958×10^{-8}) to reduce noise. The great advantage of such filter is that no modification of the PSF was observed as illustrated by Figure 8.7.

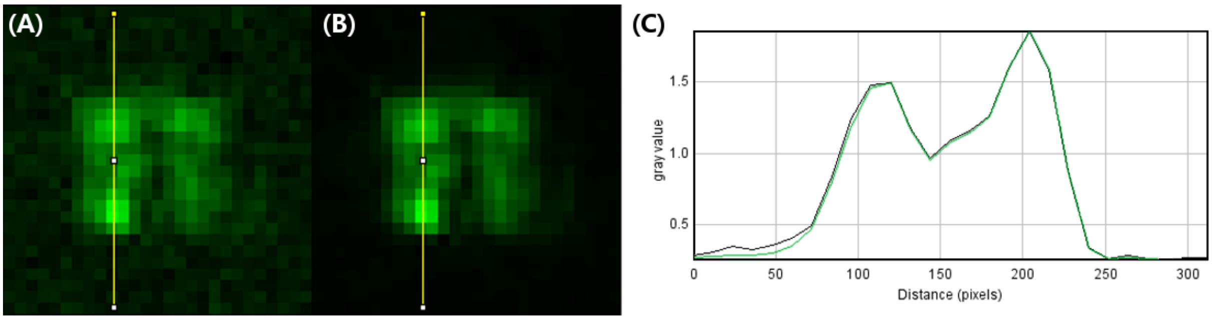

Figure 8.7: Comparison between the reconstructed TPI image (A) and the image denoised with the Non-Local Mean filter (B) on the PSF using profile plots (C).

Each TPI images were registered on the corresponding anatomical T_1w image of the volunteer acquired at 3 T using a rigid transformation matrix simplified to a simple translation adjusted manually:

$$T = \left(\begin{array}{ccc|c} a_{11} & a_{12} & a_{13} & T_x \\ a_{21} & a_{22} & a_{23} & T_y \\ a_{31} & a_{32} & a_{33} & T_z \\ \hline 0 & 0 & 0 & 1 \end{array}\right) \quad \rightarrow \quad T_0 = \left(\begin{array}{ccc|c} 1 & 0 & 0 & T_x \\ 0 & 1 & 0 & T_y \\ 0 & 0 & 1 & T_z \\ \hline 0 & 0 & 0 & 1 \end{array}\right) \tag{8.2}$$

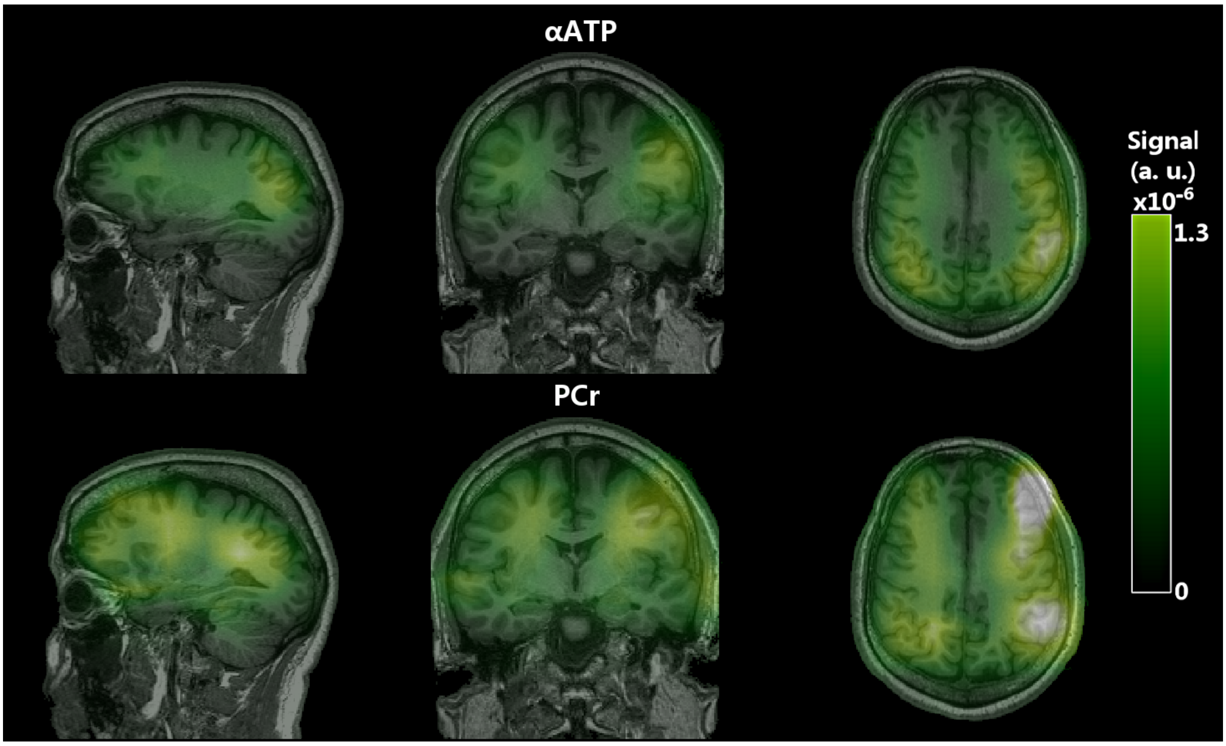

Figure 8.8: αATP and PCr images from our second volunteer using our spectrally selective SSFP sequence with TPI sampling overlaid on the T_{1w} MPRAGE image acquired at 3 T. Images are presented with the same intensity scaling. Acquisition parameters are given in Table 8.5.

As illustrated by Figure 8.9, similar PCr distribution patterns were obtained for both volunteer. One can notice hypersignals on the brain periphery due to contamination from extracranial muscles where PCr is much more concentrated than in the brain parenchyma. Indeed, it has been reported that PCr concentration in brain was circa 4 to 5 mmol.L^{-1}, with higher concentration localized grey matter than white matter [De Graaf 2013]. In muscles it PCr levels are about 30 to 35 mmol.L^{-1} [Kemp 2007]. The lowest amount of signal was observed at the center of the brain probably as the consequence of partial volume effect from the ventricles as well as the lower sensibility of our phased array coil there.

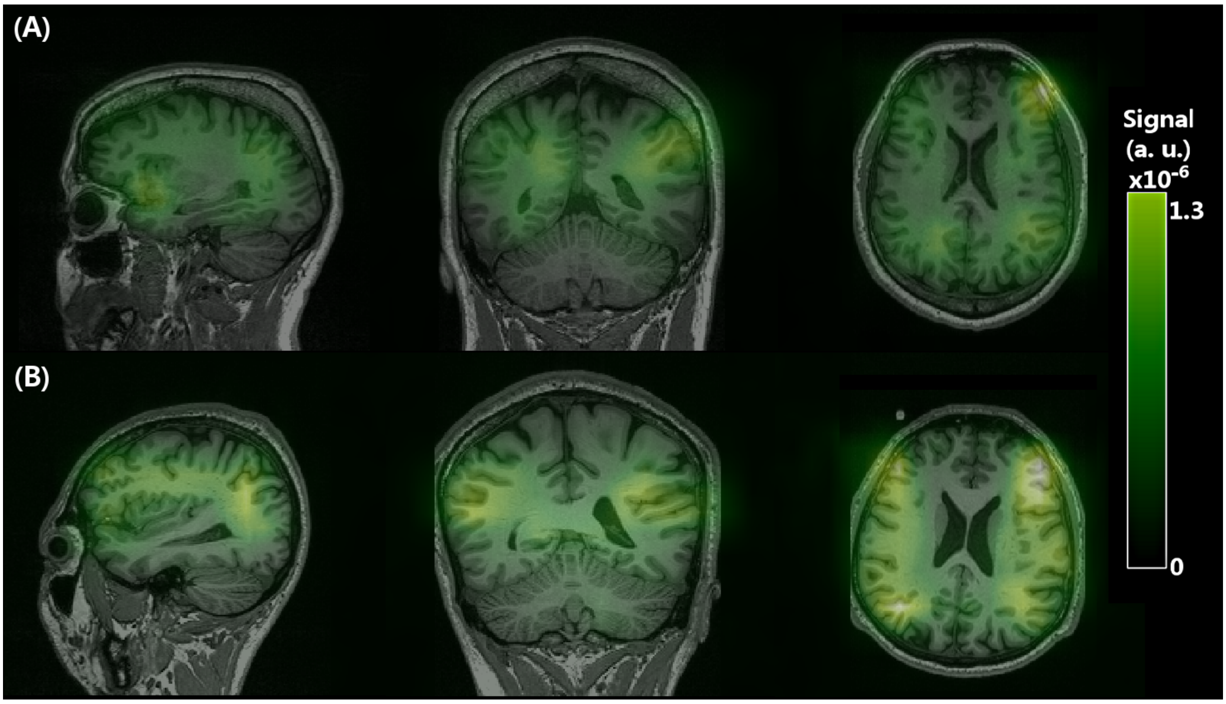

Figure 8.9: Orthogonal views of TPI-PCr images obtained from both volunteers 1 (A) and 2 (B).

8.3.4 CSI post-processing

DICOM CSI data were preprocessed using CSI-APO [Le Fur 2010]. Spectra were corrected for zero and first order phase and filtered with a 20 Hz Lorentzian temporal filter prior to the generation of a 16×16 matrix of ^{31}P MR spectra. Spectral decomposition was performed using LCModel [Provencher 1993, Lopez Kolkovsky 2015, Deelchand 2015]. Post-processing intermediate steps and results are presented in Figure 8.10 and metabolic maps are presented in Figure 8.12.

8.3.5 SNR comparison

In this section, SNR measurements are presented as normalized SNR per unit of volume (in cm^3) with V being the voxel volume and calculated over similar ROIs according to:

$$SNR_{VN} = \frac{1}{V} \times \frac{< S_{ROI} >}{\text{stdev}(ROI_{\text{background}})} \qquad (8.3)$$

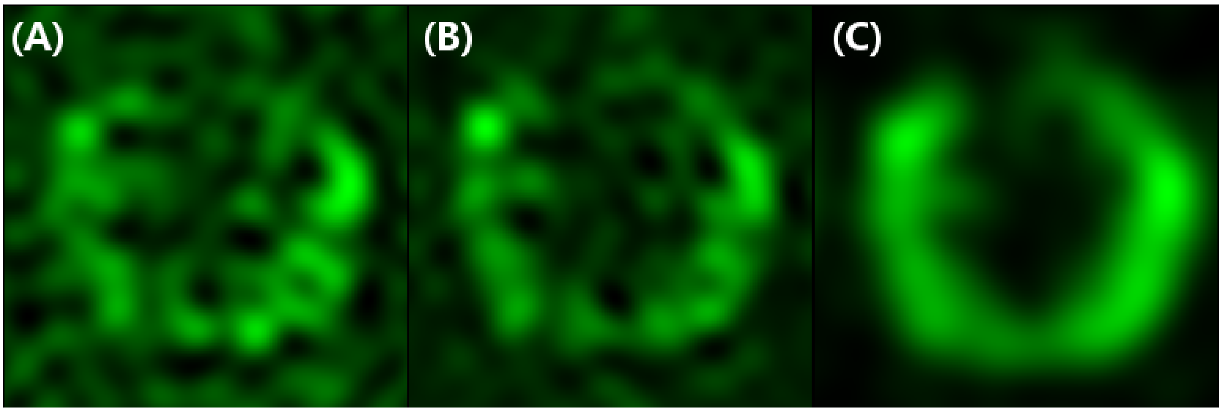

Figure 8.10: Post-processing steps of 2D-CSI v1 data for the PCr peak at 0 ppm. Data acquired with TR/TE/FA=1800 ms/2.3 ms/60° Raw magnitude image (A), magnitude image after a 20 Hz Lorentzian temporal filtering (B) and resulting PCr map obtained with LCmodel (C).

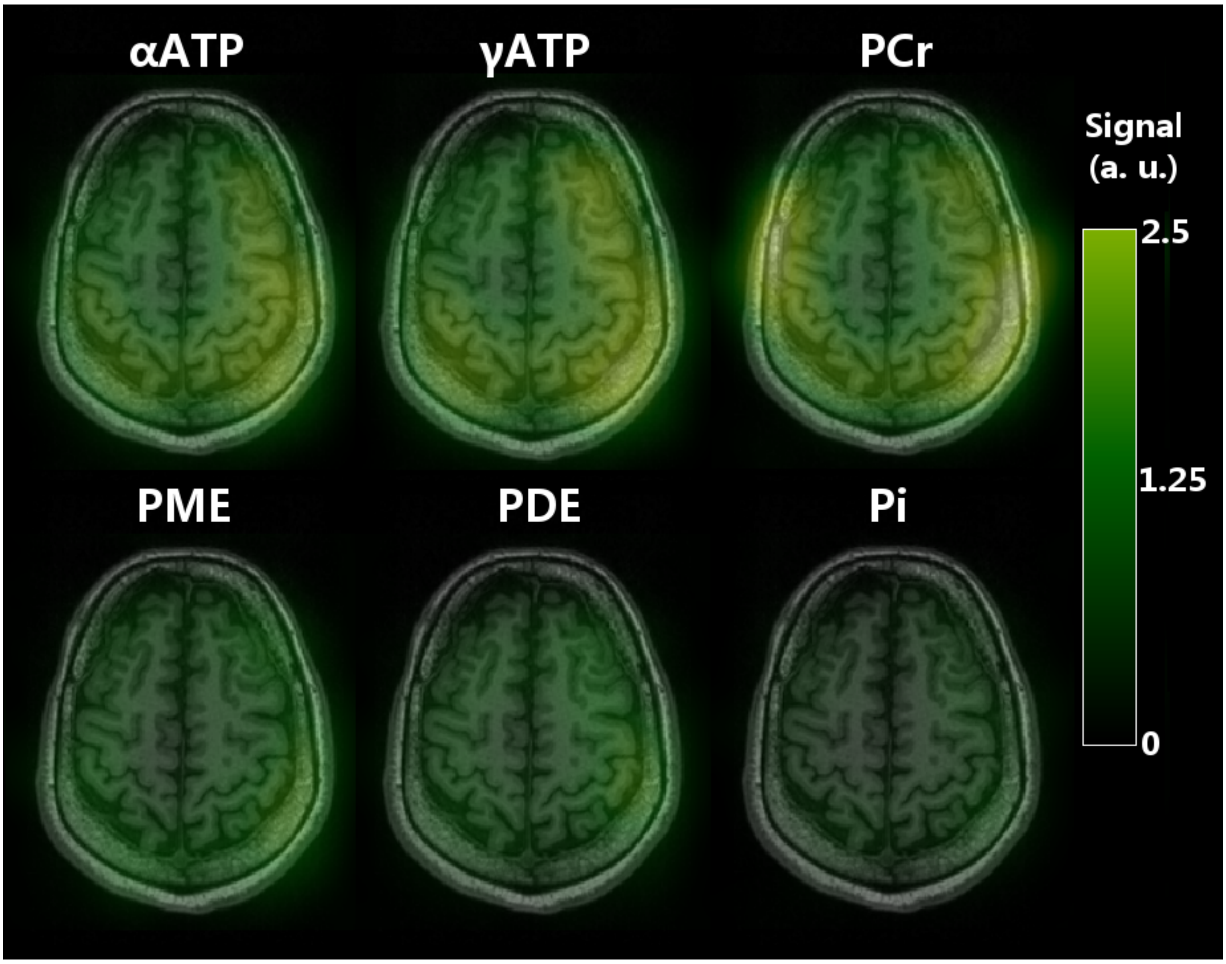

Figure 8.11: Maps of the six most prevalent group of resonances from 2D-CSI v2 data at 7 T (TR/TE/FA=200 ms/2.3 ms/20°): α and γ resonance of Adenosine TriPhosphate (αATP, γATP), PhosphoCreatine(PCr), Phospho-monoester(PME), Phospho-diester(PDE) and Inorganic Phosphate (Pi). All images are presented with the same intensity scaling.

8.3.5.1 CSI-V_1 vs CSI-V_2 comparison

^{31}P MRSI data can be acquired either in 2D with a relatively long repetition times to alleviate differential T_1 weighting between metabolites or in 3D with a much shorter TR to accommodate its very long sampling of K-space [HETHERINGTON 2001]. Typical voxel sizes for those acquisitions are about 12 cm^3 at 3 T [PANDA 2012] or 6 cm^3 at 7 T [RODGERS 2014] with acquisition times ranging from 10 to 50 minutes. For this proof-of-concept study, we acquired 2D-CSI data according to two sets of parameters to compare metabolic maps acquired with the spin-density and T_1-weighted approaches. For both acquisitions, the flip angle was set to a value close to the Ernst angle for PCr (T_1=3.4 s) and the number of averages was adjusted to maintain a constant acquisition time of 18 minutes.

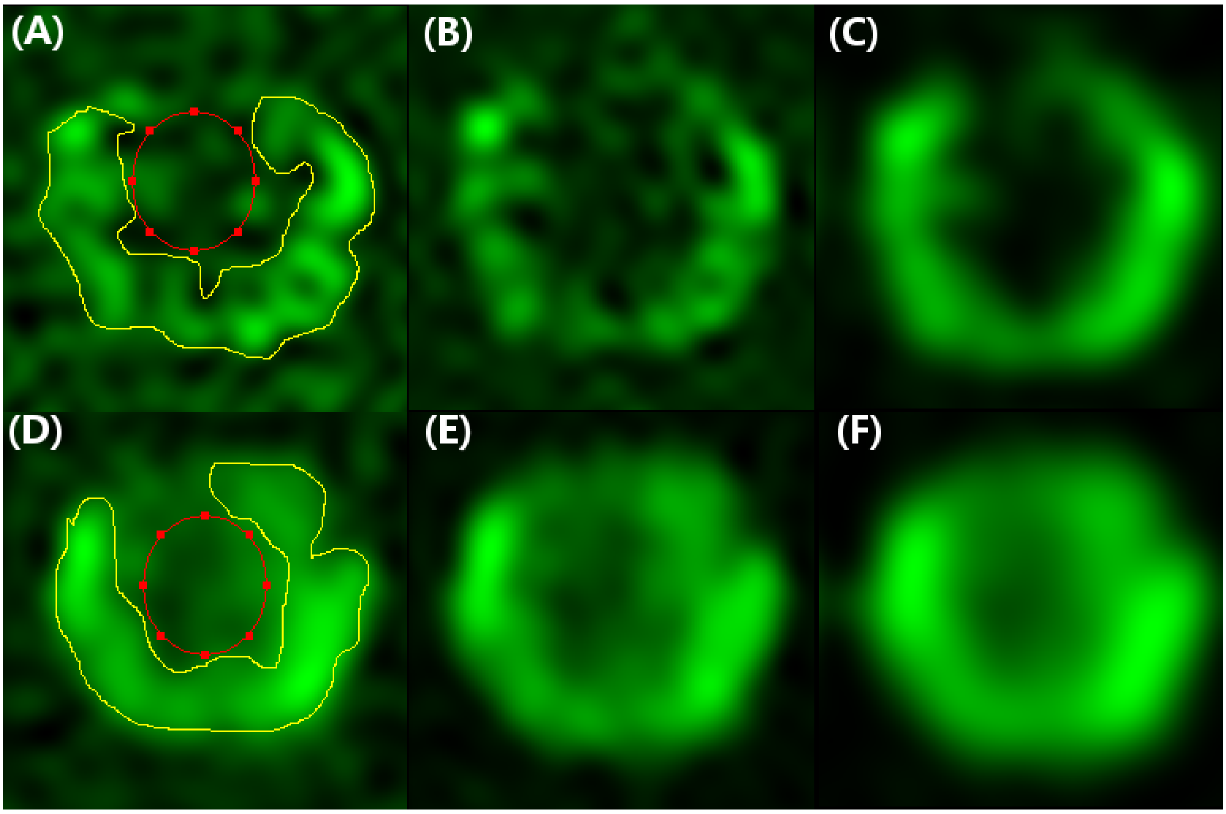

Figure 8.12: Post-processing steps of 2D-CSI v1 (top raw) and v2 (bottom raw) data for the PCr peak at 0 ppm. Raw magnitude image (A and D), magnitude image after a 20 Hz Lorentzian temporal filtering (B and E) and resulting PCr map obtained with LCmodel (C and F). The ROIs for the brain periphery and center are respectively represented in yellow and red on each set of raw CSI data.

As illustrated by Figure 8.12 both CSI acquisitions exhibited a satisfying SNR while being significantly impacted by the heterogeneous ^{31}P channel profiles. As summarized in Table 8.6, the CSI-V_1 tends to offer a slightly better SNR on raw images but CSI-V_2 PCr maps presents up to 2 dB higher SNR in the central area of interest.

SNR_{VN} cm^{-3}	Periphery	Center	Periphery dB	Center dB
CSI-V_1 Raw	2.4	1.9	3.5	3.22
CSI-V_1 filtered	1.9	0.7	3.2	2.0
CSI-V_1 Map	1.8	0.4	3.1	1.4
CSI-V_2	2.2	1.5	3.1	2.7
CSI-V_2 filtered	3.4	1.8	3.5	2.8
CSI-V_2 Map	5.0	2.9	3.9	3.3

Table 8.6: Voxel Volume Normalized SNR comparison between CSI-V_1 and CSI-V_2.

8.3.5.2 TPI vs CSI comparison

3D-TPI and 2D-CSI-V_2 data (see Table 8.5 for acquisition parameters) were compared in terms of sensitivity and spatial coverage. SNR values were estimated on the respective raw and unfiltered magnitude PCr images, images are presented on Figure 8.13 and results are summarized in Table 8.7.

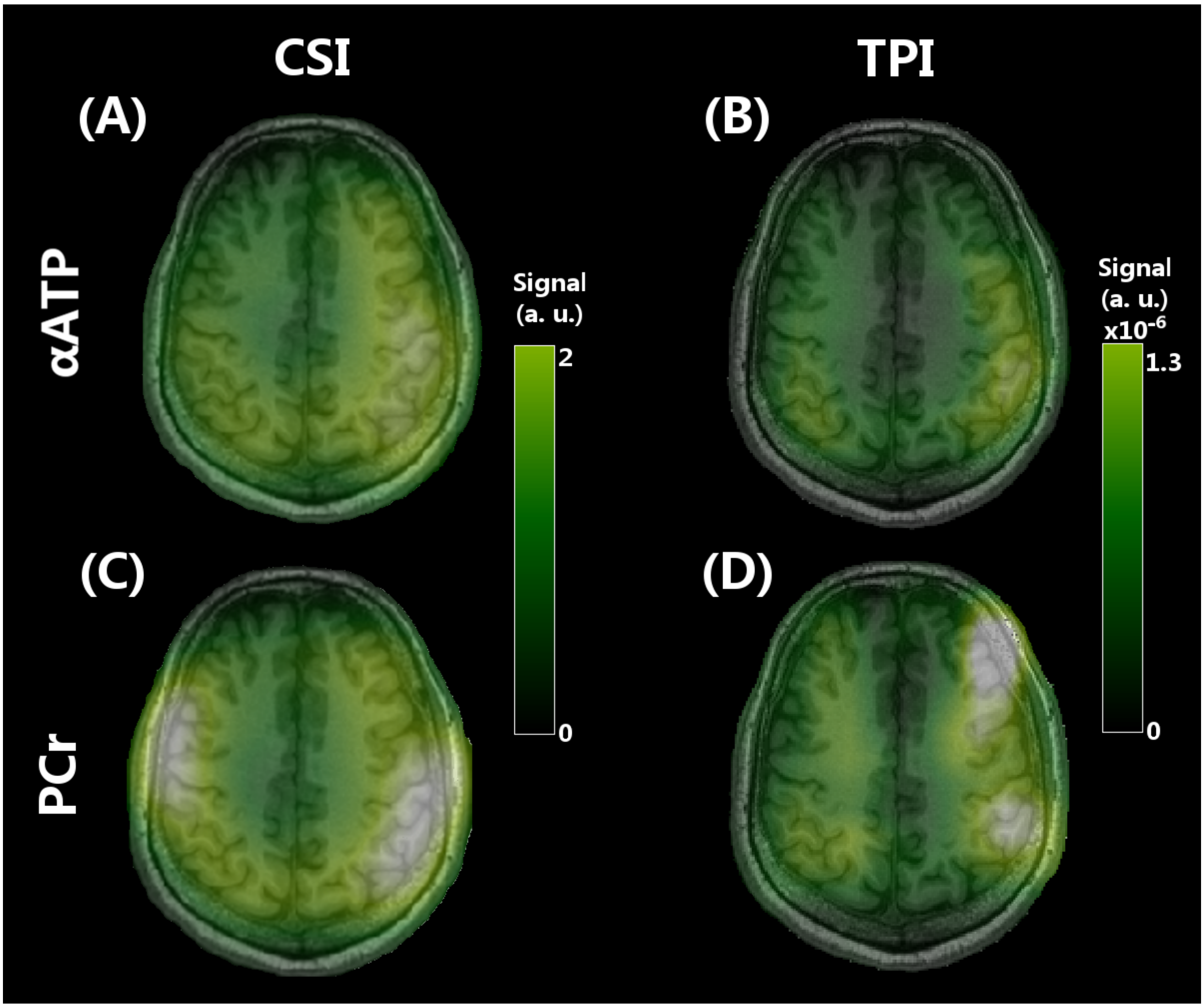

Figure 8.13: αATP (A,B) and PCr (C,D) images obtained with both CSI (A,C) and TPI (B,D). Images are presented with similar intensity scaling within acquisition but signal intensity dynamics are different between CSI and TPI. Acquisition parameters are given in Table 8.5.

SNR_{VN} cm^{-3}	Periphery	Center	Periphery dB	Center dB
CSI-V_2	2.2	1.5	3.1	2.7
CSI-V_2 Map	5.0	2.9	3.9	3.3
TPI Raw	9.6	5.7	13.1	10.8
TPI Filtered	49.6	30.3	20.3	18.1

Table 8.7: Voxel Volume Normalized SNR comparison between PCr maps acquired using CSI-V_2 or TPI.

As shown by SNR measurements, our 3D-TPI approach yields a significant sensitivity improvement (from 8-10 dB for raw data and up to +16 dB for processed/filtered maps) while covering the whole brain in less than 20 minutes.

8.4 *In vivo* quantification

8.4.1 Phantom replacement and calibration experiments

In the context of this proof-of-concept spectrally selective ^{31}P MRI sequence, we did not apply our variable flip angle approach despite the use of short TR. Therefore, our quantification pipeline needs to assume the values of the relaxation times for each metabolite-of-interest. As summarized in Table 8.5, we considered homogeneous T_1 and T_2 values measured at 7 T by CHEN *et al.* [LEI 2003, LU 2014]. While the acquisition of B_1 profiles were feasible for each volunteer of our Sodium MRI study, such acquisition would have been challenging for Phosphorus. As a consequence, we chose to adopt the phantom replacement and calibration approach [SOHER 1996, STOUT 2017]. Such approach rely on the acquisition of reference B_1 profiles on a phantom presenting similar dielectric properties than the human head. Moreover, identical TPI (and 2D-CSI) acquisitions are used as an external reference of concentration. Due to time constraints and struggle in properly managing the coil profile correction in the proposed pipeline, we decided to evaluate this calibration on two ROI corresponding to those used for SNR comparisons (see Figure 8.12). This way, we could estimate from the B_1^+ profile shown in Figure 2.16 average flip angle over each ROI. Figure 8.14 illustrates our general phantom replacement pipeline and the modifications we made for its application to *in vivo* ^{31}P MRI.

8.4.1.1 TPI calibration

Figure 8.15 shows the 3D-TPI acquisition of our calibration phantom (ref=31P-7T-1 presented in Figure 2.16) with the associated periphery and center ROI considered for analysis.
T_1 (6000 ms) and T_2 (170 ms) of Phosphate ions were estimated at 7 T from SVS PRESS acquisitions using respectively progressive saturation method (TR $\in$ [200, 20000] ms) or by increasing echo-time (TE $\in$ [50, 500] ms).

To determine the calibration factor k linking measured signal to the spin density ρ (mmol.L^{-1}), we used the SSFP signal model of our TPI acquisition :

$$S = k\rho B_1^- \frac{1 - E_1}{1 - (E_1 - E_2)\cos(\alpha) - E_1E_2}\sin(\alpha) \tag{8.4}$$

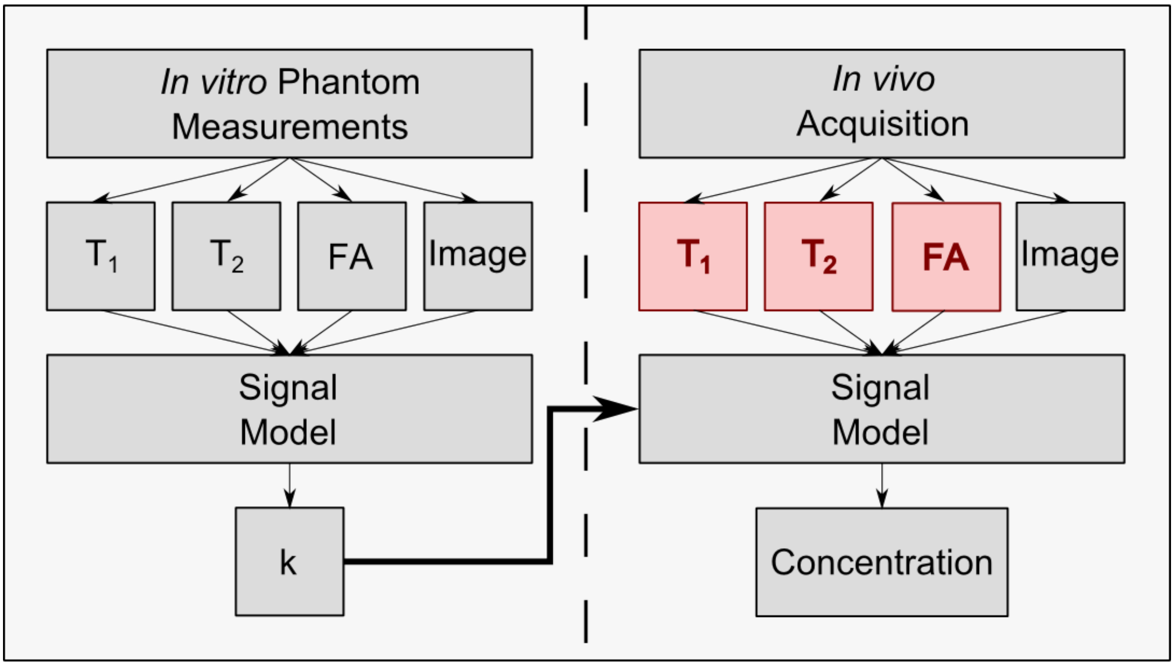

Figure 8.14: Schematic of phantom replacement pipeline for our ^{31}P MRI application. The red boxes indicate that parameters could not be acquired with this set up due to time constrains. T_1 and T_2 values were taken from literature ([LEI 2003, LU 2014]) and B_1 profile was extrapolated from phantom data shown in Chapter 2.

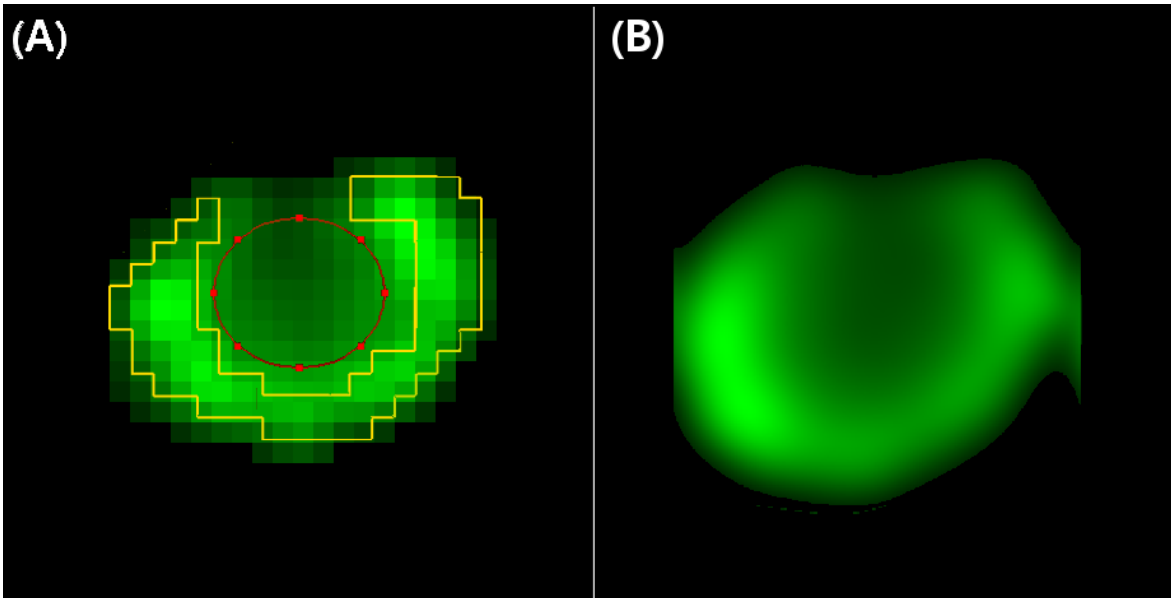

Figure 8.15: ^{31}P 3D-TPI Image (A) and CSI map (B) of our calibration phantom. Periphery and center ROIs are shown in yellow and red respectively. Both Pi images are fully processed.

As explained before, mean flip angles were estimated from *in vitro* B_1^+ profile over large ROIs corresponding to the periphery or the center of our calibration phantom. By assuming the reciprocity between flip angle values and the B_1^- field intensity, k was estimated. It is then possible to use the reference values of T_1 and T_2 as well as the estimated flip angles for both ROIs (about 15° at the periphery and 5° at the center for PCr TPI acquisitions) to convert signal intensities into concentration values as summarized in Table 8.8.

8.4.1.2 CSI calibration

A similar method was applied for 2D-CSI data by considering the following signal equation:

$$S = k\rho B_1^- \frac{1 - E_1}{1 - E_1 \cos(\alpha)} \sin(\alpha) e^{-TE/T_2^*} \tag{8.5}$$

CSI calibration data were acquired on the same PBS phantom (ref=31P-7T-1). Using the average flip angle in both ROIs, we computed a different calibration factor k for our CSI acquisitions. In a similar fashion, average signal intensities were converted to concentration values by considering reference values for T_1, experimental T_2^* values (estimated from the raw CSI data themselves) as well as estimated flip angles for both ROIs (about 60° at the periphery and 20° at the center for CSI-V_1; one third of these values for CSI-V_2 acquisitions). Resulting concentration values for CSI are presented in Table 8.8 as well.

	CSI Periphery	CSI Center	TPI Periphery	TPI Center	Unit
PCr					
• Volunteer 1	3.6	1.7	4.0	3.4	mmol.L^{-1}
• Volunteer 2	3.1	2.6	2.6	3.0	mmol.L^{-1}
ATP					
• Volunteer 1	2.2	1.8	0.9	0.8	mmol.L^{-1}
• Volunteer 2	2.7	2.0	*	*	mmol.L^{-1}

Table 8.8: Measured PCr and ATP concentration values with 2D-CSI-V_2 and 3D-TPI. * For volunteer 2, ATP TPI acquisition was interrupted and could not be fully processed.

Overall, those concentrations values are consistent between each other and are also in agreement with literature values for ATP and PCr concentrations in the brain [Hetherington 2001]. As expected the PCr content is higher in the periphery than in the center probably due to the contribution of extracranial muscles. ATP concentrations estimated from the sole ATP TPI image are remarkably low and could be the result of an experimental blunder (sometimes the B_0 shim currents are reset to their default values and the operating frequency is modified).

8.5 Conclusion and Perspectives

As introduced in Chapter 1, ^{31}P NMR has been used to investigate energy metabolism in the context of various pathologies: muscular [Prompers 2006], cardiac [Horn 2006], oncology [Maintz 2002, Ha 2013], neurology or psychiatric disorders [Martin 2007, Pan 2008]. Unfortunately, most studies have been limited to single voxel or non localized approaches by the low concentration of phosphorylated metabolites, especially in the brain. With the recent advent of ultra high field scanners and improved non-Cartesian sampling schemes, one can hope to overcome some of these limitations and map the distribution of several metabolites such as ATP and PCr in a clinical research setting.

By applying a spectrally selective non-Cartesian SSFP sequence, we were able to acquire high-resolution PCr and αATP images from the whole brain in less than twenty minutes at 7 T with a 12 mm isotropic nominal resolution (about 2 cm^3 voxel size). Regrettably, this proof-of-concept study require more experiments to draw definitive conclusions. Yet, we think that our approach could be compared to recent developments by ^{31}P MRI by Korzowski et al. [Korzowski 2017] or Ma et al. [Ma 2017] who managed to acquire ^{31}P MRI at compatible resolutions using respectively a frequency selective EPSI sequence at 7 T or a sparse FID-spiral-EPSI sequence at 9.4 T.

As demonstrated by comparing the SNR values, our TPI approach presents the advantage of a very efficient signal sampling compared to CSI but at the expense of a loss of additional metabolic information. However, some of this metabolic information could be recovered by performing an interleaved signal acquisition of several resonances as illustrated in Figure 8.16 [Lu 2013].

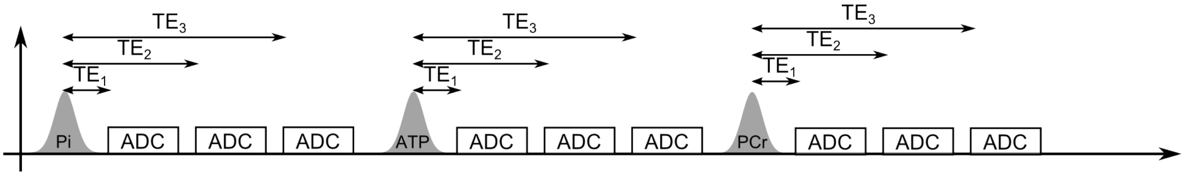

Figure 8.16: Multiple echoes with interleaved multiple metabolic acquisition inside a single TR.

Further work will be conducted to finalize this study notably our quantification pipeline. For now, the estimated PCr and ATP concentrations were quite consistent with previously reported values arguing in favor of the validity of our approach.

Finally, this proof-of-concept study should hopefully constitute a step towards the implementation of ^{31}P saturation transfer imaging approach [Matthews 1982, Parasoglou 2014] to investigate the rate of ATP synthesis in humans at UHF [Layec 2011].

CHAPTER 9

Lithium-7 MRI Pilot Study in Bipolar Patients

Contents

Lithium salts (typically monocarboxylate) are the first-line treatment for preventing maniac relapse in bipolar patients (BP). After administration, lithium (Li) is present in the body as a small cation (Li^+) with a chemical similarity to Na^+. Li exhibits a rather narrow therapeutic window with a maximum therapeutic dose of 1800 mg per day and an LD50 of about 500 mg per kg of body weight. The daily dosage of Li aims at maintaining a serum Li concentration of 0.4 to 0.8 $mmol.L^{-1}$. Despite its wide use and efficacy, little is understood about the mechanism of action of Lithium [MALHI 2013]. As detailed in Chapter 1, *in vivo* MRS explorations and measurements of Lithium were performed as early as 1985 by RENSHAW and colleagues [RENSHAW 1985, RENSHAW 1988]. More recently, 3D MRSI was performed at 4T by Lee [LEE 2012] to map brain Lithium distribution in few bipolar patients. Notably, Fernando BOADA has presented at the ISMRM in 2010 the first ^{7}Li MRI of the brain acquired using a non-Cartesian UTE sequence [BOADA 2010].

This last chapter presents the application to ^{7}Li MRI of some of our developments for ^{23}Na MRI. This work was done in collaboration with Jacques STOUT, another PhD student of our research team and a team of psychiatrists at NeuroSpin and University Paris-V: Pr. Frank BELLIVIER, Dr. Josselin HOUENOU and Dr. Franz HOZER. The goal of our collaboration project is to map quantitatively the brain distribution of Lithium and to use this unique information to help elucidating the variability in the response to the Lithium treatment. Following some preliminary work on rodents at 17 T [STOUT 2017], a pilot study was performed at NeuroSpin during the first semester of 2017 on 8 BP treated with Lithium salts.

9.1 *In vitro* exploration

9.1.1 SPGR versus SSFP

As discussed in Chapter 3, SSFP sequence offers an increased SNR compared to SPGR. First we aimed at validating our choice of the SSFP over SPGR sequence for ^{7}Li TPI imaging. Two images of a multicompartment lithium chloride (LiCl) phantom (ref=7Li-7T-2, Figure 9.2) were acquired at 7 T on our Siemens Magnetom MR scanner with a dual resonance ^{1}H/^{7}Li RF birdcage coil (Rapid Biomedical, Rimpar, Germany) and the following parameters: (TR/TE/FA/TA=200 ms/0.4 ms/10°/30′). Figure 9.1 compares both acquisitions with and without spoiling and demonstrate the benefice of using SSFP (up to 4.6 dB in the less concentrated tube). This result is consistent with the long T_2 of free Li and the signal equations given in Chapter 3.

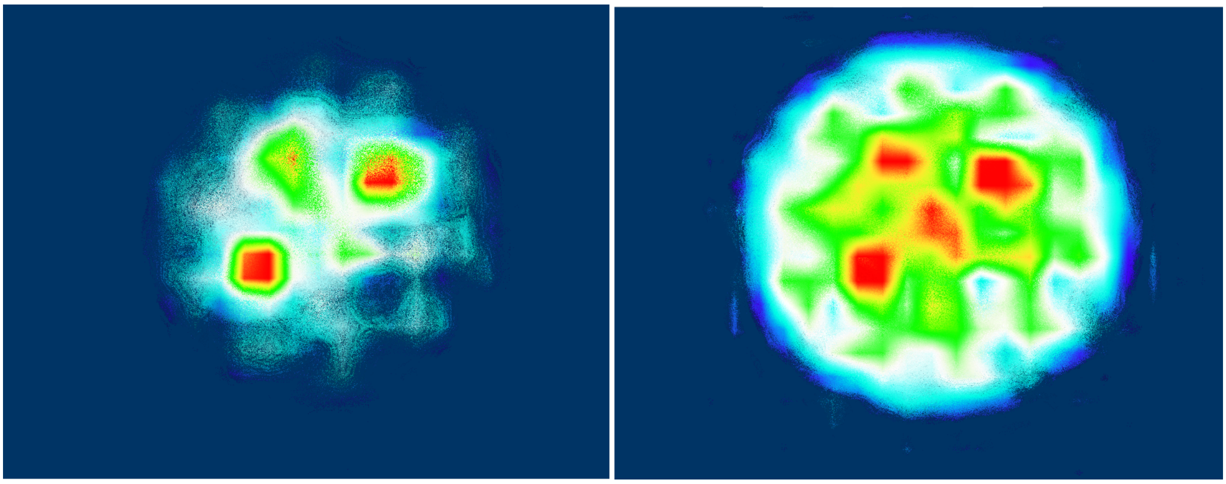

Figure 9.1: 3D volume rendering of SPGR (left) and SSFP (right) ^{7}Li TPI acquisitions. Images are shown with the same intensity scaling and were acquired with the same parameters (TR/TE/FA/TA=200 ms/0.4 ms/10°/30′).

Acquisition	20 mmol.L^{-1}	15 mmol.L^{-1}	10 mmol.L^{-1}	5 mmol.L^{-1}
SPGR	42.5 (32.5 dB)	36.6 (31.3 dB)	28.3 (29.0 dB)	15.6 (23.8 dB)
SSFP	57.0 (35.1 dB)	51.3 (34.2 dB)	38.5 (31.7 dB)	26.3 (28.4 dB)

Table 9.1: SNR comparison between SPGR and SSFP ^{7}Li TPI acquisitions in the different LiCl tubes.

9.1.2 Sensitivity estimation

To estimate the achievable sensitivity of our ^{7}Li SSFP TPI sequence, we acquired data using the following set of parameters: TR/TE/FA/TA = 200 ms/1 ms/10°/50 min, Nb of spokes = 15000, linear fraction = 0.4, FOV 320 mm isotropic, 1 cm isotropic resolution. Image were reconstructed with FISTA (50 iterations, λ=5×10^{-5}) presented in Chapter 3. From the SNR values obtained for each tube and summarized in Table 9.2, one can extrapolate that a SNR of about 5 should be achievable with our TPI sequence in less than 20 minutes at an isotropic spatial resolution of 15 mm as long the Li brain distribution exceed 0.1 mmol.L^{-1}.

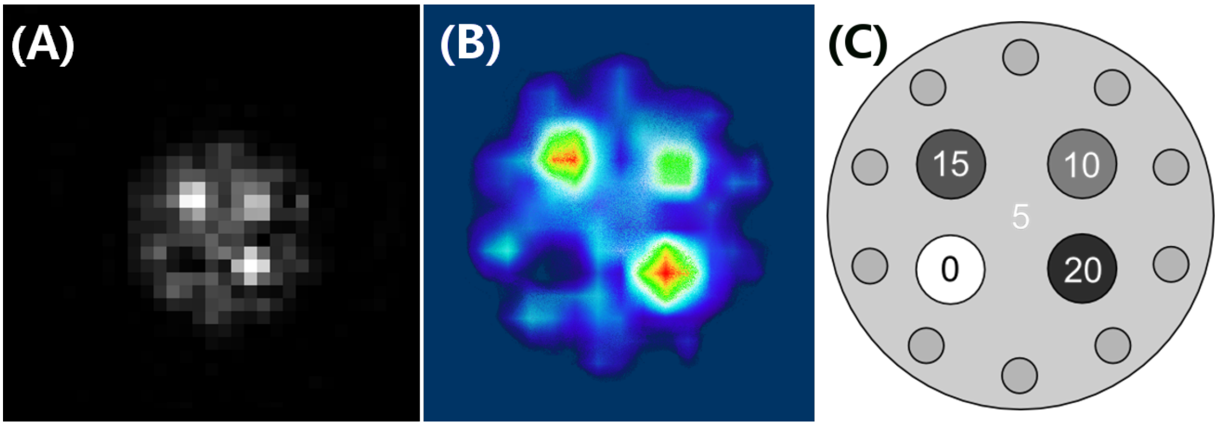

Figure 9.2: ^{7}Li phantom MR Image obtained at 7 T at spatial resolution of 10 mm isotropic in 50 minutes (A). Image (B) is presenting a 3D volume rendering of acquired data to better appreciate the result and panel (C) illustrates effective Lithium concentrations in the phantom.

Acquisition	20 mmol.L^{-1}	15 mmol.L^{-1}	10 mmol.L^{-1}	5 mmol.L^{-1}
SSFP	209.6 (46.4 dB)	139.2 (42.9 dB)	100.7 (40.1 dB)	60.3 (35.6 dB)

Table 9.2: Voxel normalized SNR (cm^{-3}) comparison between Gridding and FISTA in the different PCr tubes.

9.2 Pilot study

9.2.1 Patients recruitment

Normothymic bipolar patients (BD) were recruited by Pr. BELLIVIER and its team of psychiatrists from the Expert Center on Bipolar Disorders (ECBD, FondaMental Foundation) of Hospital Fernand Widal (AP-HP, Paris). The study was approved by a national ethic committee and NeuroSpin's scientific committee. All patients were treated with Lithium salts but not exclusively with some patients taking other drugs (valproate, olanzapine and venlafaxine). The study aims at scanning fifteen good versus fifteen poor responders to Li treatment as evaluated using the ALDA score [GROF 2002]. Table 9.3 summarizes information about the patients who have been recruited and scanned for this pilot study.

Patient	Sex	Age years	Scan Date	Lithium Dosage mg/day	Vref V	FA °	MRS T$_1$ ms	MRS T$_2f$/T$_2s$ ms | ms
1	M	32	24/01/2017	800	300	12	3009	15 | 66
2	M	55	07/02/2017	1400	300	20	No	No
3	M	32	14/02/2017	1200	340	20	No	No
4	F	42	21/02/2017	1000	320	20	No	No
5	F	43	21/03/2017	800	340	20	No	No
6	F	52	11/04/2017	800	350	20	No	No

Table 9.3: Patient information and special sequence parameters for *in vivo* Lithium MRI of the version 1 protocol.

At the eve of the MR examination, patients were asked to take their medication (*TÉRALITHE LP*) (see Tables 9.3 and 9.6) at 22:00 pm sharp. Patients were transported to NeuroSpin by taxi and each examination started between 9:00 and 9:30 am. Drs HOUENOU and HOZER (NeuroSpin's UNIACT team) were in charge of the inclusion of those selected BD patients for our 3/7 T examination and the coordination with the Expert Center.

9.2.2 Imaging protocol

9.2.2.1 3 T examination

A 45 minutes exam was performed on our 3 T Prisma MR scanner using a 20 channel head neck coil (Siemens Healthcare, Erlangen, Germany). Table 9.4 summarizes the imaging protocol conducted at 3 T. Anatomical T_{1w} and T_{2w} images were acquired and 10 acquisitions were made using the Variable Flip Angle method to compute T_1 maps. A Diffusion Weighted Imaging (DWI) acquisition was also performed to reconstruct Diffusion Tensor Images (DTI) and study water diffusion in brain tissues [LE BIHAN 1985]. Finally, an hydrogen spectroscopic imaging acquisition (2D CSI) using a semiLASER (Localization by Adiabatic SElective Refocusing) MR pulse sequence was performed [SCHEENEN 2008]. Among all these data, only the anatomical T_1w MPRAGE image (TR/TE/FA/TA/Res/=2300 ms/2.98 ms/9°/7'46"/1 mm isotropic) was used for co-registration with our ^{7}Li TPI image acquired at 7 T.

Sequence	TA	Optional
Localizer	40 secs	No
Calibrations and shim	2 min	No
B_0 Map	3 mins	No
B_1 Map	1 mins	No
T_1w MPRAGE	8 mins	No
qT1 mapping	7 mins	No
Multi-Band-DWI	9 mins	No
^{1}H 2D-CSI-sLASER	16 mins	No

Table 9.4: ^{7}Li MRI protocol at 3 T.

9.2.2.2 7 T examination

Table 9.7, summarizes the 75 minutes imaging protocol conducted on our 7 T Magnetom MR scanner (Siemens Healthcare, Erlangen, Germany) using a dual tune ^{1}H/^{7}Li birdcage coil (Rapid Biomedical, Rimpar, Germany). For calibration of the ^{7}Li reference voltage, non-localized ^{7}Li MR spectra were acquired at two probable voltage values based on a prior *in vitro* experiments. ^{7}Li reference voltage was set at the value yielding the most intense Lithium peak. Moreover, for our first patient, additional non-localized MRS (TR/TE/FA/TA=[400,20000] ms/0.35 ms/90°/0'42" for T_1 estimation and TR/TE/FA/TA=3000 ms/[30,200] ms/90°/0'48" for T_2 estimation) measurements were performed to estimate *in vivo* longitudinal and transverse relaxation constants.

9.2.3 ^{7}Li MRI post-processing

^{7}Li TPI data were reconstructed using the same gridding algorithm based on a Kaiser-Bessel kernel as depicted in Chapter 3 and smoothed using the Non Local Mean filter (with automated parameter estimation based on data) to reduce noise. A rigid transformation matrix T was used to manually register Lithium images with the T_1 weighted anatomical image acquired at 3 T.

Table 9.5: MR Imaging Protocol and associated parameters for TPI sequence.

Sequence	TA	Optional
^{1}H Localizer	30 secs	No
B_0 Shim	5 mins	No
B_0 mapping	2 mins	No
^{7}Li FID 1	2 mins	No
^{7}Li FID 2	2 mins	No
^{1}H Voltage Calibration	1 min	No
^{7}Li 3D-TPI	24 mins	No
^{7}Li 2D-MS-TSE	24 mins	No
^{1}H T_1w MPRAGE	4 mins	No
T_1w PRESS	10 mins	Yes
T_2w PRESS	10 mins	Yes

(a) BipLi protocol V_1.

^{7}Li TPI		Unit
T_1	3000	ms
TE	0.3	ms
TR	200	ms
Projections	1769	
Linear ratio	0.5	
Readout Duration	10.6	ms
FA	20	degree (°)
TA	24	min
Resolution	15 iso	mm
Matrix	32 iso	voxel
FOV	480 iso	mm

(b) SSFP TPI acquisition parameters.

9.2.3.1 Quantitative measurements

In the context of this project, both the spatial distribution of Lithium and its absolute concentration could be relevant. Therefore, we applied the phantom replacement approach already presented in Chapter 8. Considering the satisfying homogeneity of our Lithium coil profiles (see Figure 2.27 in Chapter 2), we assumed a spatially invariant transmission and reception profiles.

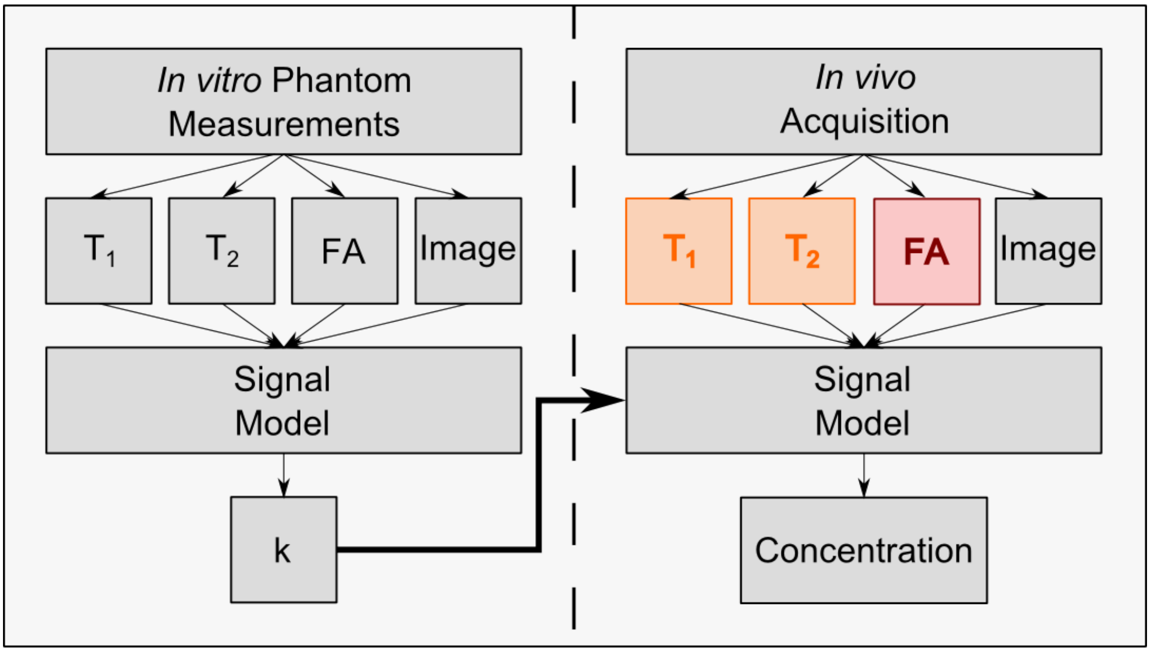

Figure 9.3: Schematic of the phantom replacement pipeline used for ^{7}Li quantification. The red box indicates that the acquisition could not be performed *in vivo*. In this case, coil transmission and reception profiles were considered spatially invariant as illustrated by Figure 2.23. Orange boxes indicate that measurements were not conducted for each volunteer.

9.2.3.2 T_1 and T_2 measurements

Lithium relaxation times are known to be relatively long, especially for a quadrupolar nucleus. Values as long as 20 seconds have been reported for T_1 in CSF and in the range [2400-5000] ms in brain tissues [GULLAPALLI 1991, MOORE 2003, KOMOROSKI 2004, SMITH 2011]. Fast and slow transverse relaxation times have also been reported *in vivo* with T_{2s} being in the [60,160] ms range while T_{2f} is found between 5 and 15 ms [KOMOROSKI 2008, PORT 2013].

As detailed in Chapter 1, this is attributed to its specific spatial nuclear charges distribution. In order to quantify our brain Lithium concentration at 7 T, we fitted T_1 and T_2 weighted non-localized MRS data acquired on the first patient. Figure 9.4 illustrates the mono and bi-exponential fits of T_1 and T_2 relaxation curves respectively. A T_1 of 3009 ms and a slow transverse relaxation time T_{2s} of 66 ms and a fast time T_{2f} of 15 ms. A mono-exponential fit of T_2 weighted data yields a T_{2mono} value of 41 ms. These obtained data for one patient are close to previously reported values of 3300 ms found in rat brain at 4.7 T [KOMOROSKI 2004] and 2100 ms obtained in human brain at 3 T [SMITH 2011] for T_1 and of T_{2s} and T_{2f} measured at about 5 ms and 68 ms respectively with a T_{2mono} of 47 ms [PORT 2013].

For calibration purpose, additional *in vitro* T_1 and T_2 estimations were performed using the ellipsoidal phantom (ref=7Li-7T-1) illustrated in Chapter 2 by Figure 2.16. In aqueous environment, we found a T_1 of about 14 seconds and a T_{2mono} of 310 ms using mono-exponential models as illustrated previously in Chapter 2 by Figure 2.23. Such value of T_{2mono} is consistent with previously reported of about 300 ms measured in extracellular compartment [KOMOROSKI 2013].

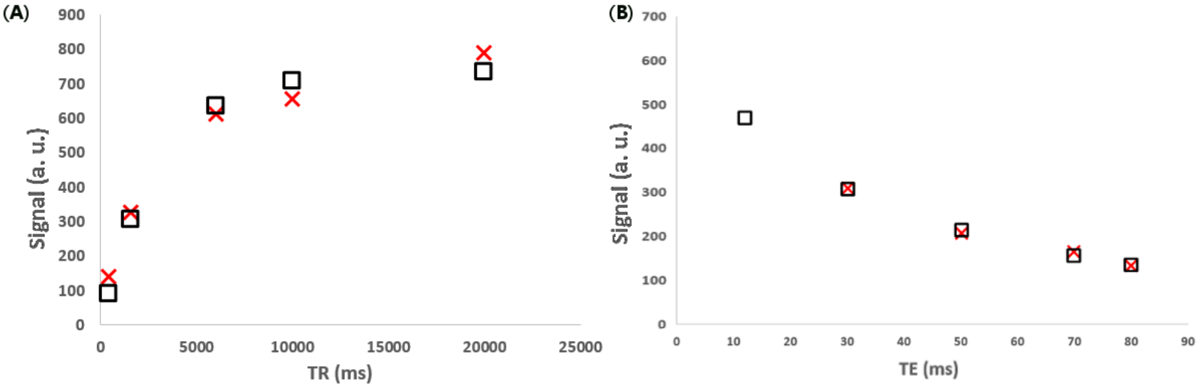

Figure 9.4: *In vivo* T_1 (A) and T_2 (B) relaxation curves from the first patient of the study. Amplitude of ^{7}Li peaks are plotted as red crosses and the fits with black squares. T_1 was estimated using a mono-exponential model and provides values of 3009 ms. Estimation of transverse magnetization decay was performed with a bi-exponential model leading to a T_{2s} of 66 ms and T_{2f} of 15 ms. Acquisitions were performed with two sets of non-localized MR spectroscopy sequences with parameters TR/TE/FA/TA=[400,20000] ms/0.35 ms/90°/0′42" for T_1 estimation and TR/TE/FA/TA=3000 ms/[30,200] ms/90°/0′48" for T_2 estimation.

9.2.3.3 Calibration using external reference

For our phantom replacement approach, we acquired ^{7}Li TPI reference image acquired with identical parameters as presented in Table 9.5b. Our ellipsoidal phantom was filled with a 15 mmol.L^{-1} aqueous Lithium chloride solution.

Based on phantom measurements, the SSFP equation was solved to determine the correcting factor k linking nuclei concentration with signal intensity:

$$S = k\rho B_1^- \frac{1 - E_1}{1 - (E_1 - E_2)\cos(\alpha) - E_1 E_2} \sin(\alpha) \tag{9.1}$$

Considering all known parameters (B$_1^-$ in Hertz, the Flip Angle α in rads, and relaxation times in seconds) a k factor was calculated for our specific TPI acquisition protocol based on the *in vitro* reference image. All acquired *in vivo* images were then corrected with this factor accounting for their specific T$_1$ and T$_2$ weighting (for robustness, the considered T$_1$ was the average of measurements from patients 1,7 and 8 at 4043 ms).

9.2.4 Results

Figure 9.5 illustrates the acquired raw image prior to quantification and the final resulting calibrated ^{7}Li concentration map overlaid on the associated anatomical image for spatial distribution analysis.

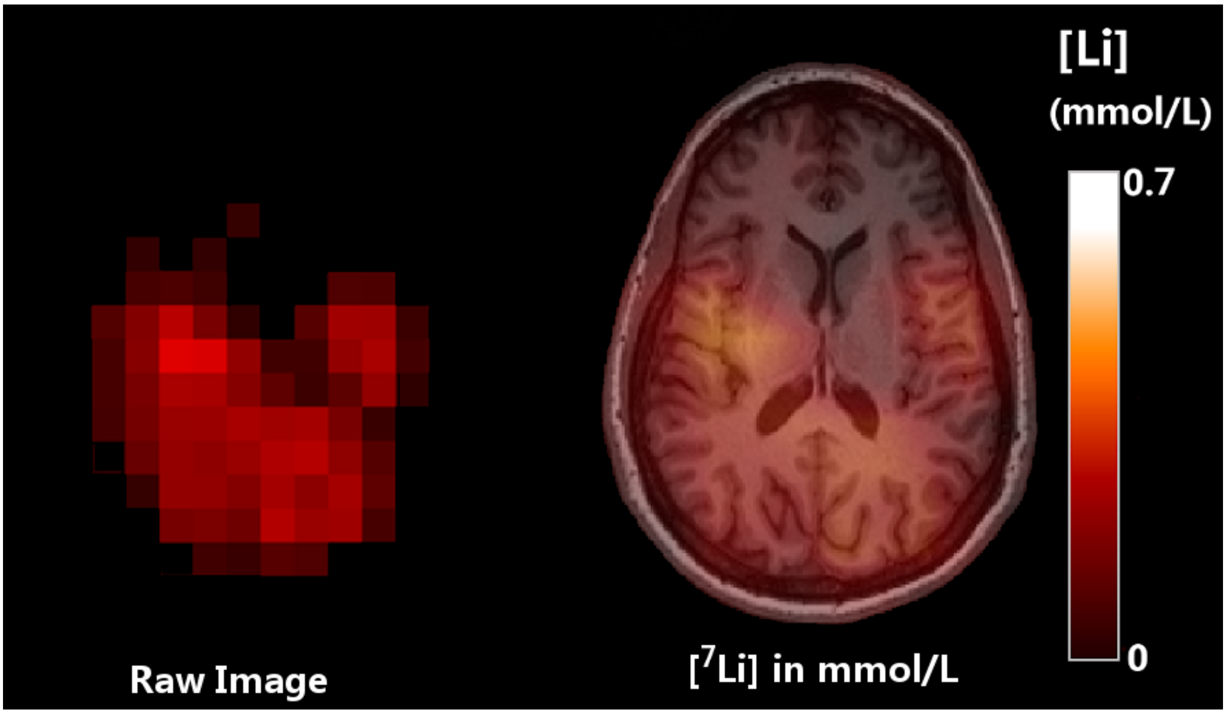

Figure 9.5: ^{7}Li TPI raw magnitude image (A) for patient 4 and corresponding [Li] map (B) after post-processing and calibration. The concentration map is overlaid on the anatomical reference image acquired at 3 T.

Figure 9.6 presents a gallery of ^{7}Li concentration maps obtained for all 6 patients of the pilot study (protocol v1). As expected the brain lithium distribution are not uniform which confirms previous observations [Lee 2012, Boada 2010, Smith 2011]. The range of concentration is also consistent with previously reported values. Even though plasma Lithium levels are not available for comparison at this stage of the study, it is interesting to notice a correlation between average brain concentrations with the daily lithium intake (Table 9.3).

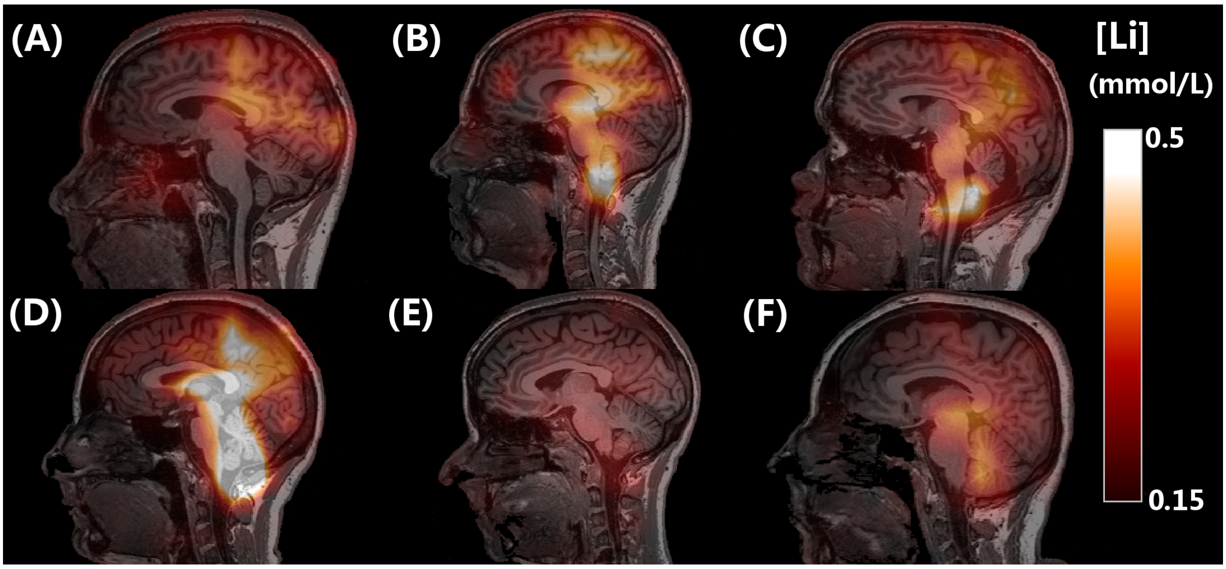

Figure 9.6: Sagittal views of our lithium concentration maps for every patient of the V_1 protocol (A-F). As all maps are displayed with the same dynamic ([0.15,0.5] $\mathrm{mmol.L^{-1}}$), one can appreciate the variability of Li concentration across patients.

9.3 Application of VFA to ^{7}Li MRI

Once the pilot study was concluded, we opted for a more ambitious ^{7}Li TPI protocol adapting the previously described VFA approach.

9.3.1 Patient recruitment

At this stage, only two patients have been investigated with this new protocol:

Patient	Sex	Age years	Scan Date	Lithium Dosage mg/day	Vref V	FA °	MRS T_1 ms
7	F	54	16/05/2017	800	350	21/10	5901
8	M	57	13/06/2017	1400	320	21/10	3220

Table 9.6: Patient information and experimental parameters for our *in vivo* ^{7}Li MRI protocol V_2.

9.3.2 Imaging protocol

This new imaging protocol includes the acquisition of two ^{7}Li TPI images with different flip angles. The choice of targeted angle was based on both LiCl phantom and brain tissues T_1 measurements (14000 and 3000 ms (for Patient 1) respectively). The associated Ernst angle for a TR of 200 ms yielded angles of 10° and 20° that were considered for imaging studies with TPI. This way, we are trying to perform a compartmental signal weighting for both liquid and tissues compartments by favoring one or the other with the adequate flip angle. Figure 9.8 shows the obtained TPI images obtained with this new protocol where one can notice bright lithium spots on the TPI image acquired with a flip angle of 21° which are not visible on the image acquired with the 10° flip angle.

Sequence	TA	Optional
Localizer	30 secs	No
Li FID	2 mins	No
Li Auto Voltage	3 mins	Yes
Voltage Calibration	1 min	No
B_0 Shim	5 mins	No
B_0 mapping	2 mins	No
Li TPI VFA I	24 mins	No
Li TPI VFA II	24 mins	No
MPRAGE	4 mins	No
T1 PRESS	10 mins	Yes
T2 MRS	10 mins	Yes

Table 9.7: Version 2 of the BipLi protocol with sequences and their duration.

9.3.3 ^{7}Li MRI post-processing

The SSFP signal model:

$$S = k\rho B_1^- \frac{1 - E_1}{1 - (E_1 - E_2)\cos(\alpha) - E_1 E_2} \sin(\alpha) \tag{9.2}$$

was simplified considering a fixed T_2 equal to T_{2mono} of 41 ms as measured on patient 1. Considering homogeneous coil transmission and reception profiles allows to only estimate two unknown parameters. As presented for Sodium explorations, based on the two TPI acquisitions and this simplified model, it is then possible to extract simultaneously a T_1 and M_0 maps. To improve robustness of the estimated T_1 map, some constrains were set to restrain the range of possible values between 2 and 20 seconds.

The phantom replacement approach depicted in Figure 9.7 was used to determine the calibrating constant k by applying the same imaging protocol to our ellipsoidal phantom. This calibration was then used directly on computed M_0 maps to obtain ^{7}Li concentration maps as they are already corrected for relaxation and flip angle.

9.3.4 Results

Figure 9.8 shows a comparison between the two ^{7}Li 3D-TPI acquisitions at flip angles of 10° and 21° from the same patient. One can notice that the lower flip angle image exhibit a much more homogenous signal than the larger flip angle acquisition. Those bright spots could correspond to area where intra-cellular (or bound) lithium dominates.

9.3.4.1 Concentration map

Figure 9.9 presents the obtained concentration maps using the VFA approach for the two volunteers of protocol V_2. Distribution patterns and concentrations values are quite similar to what was observed for our pilot study (protocol V_1).

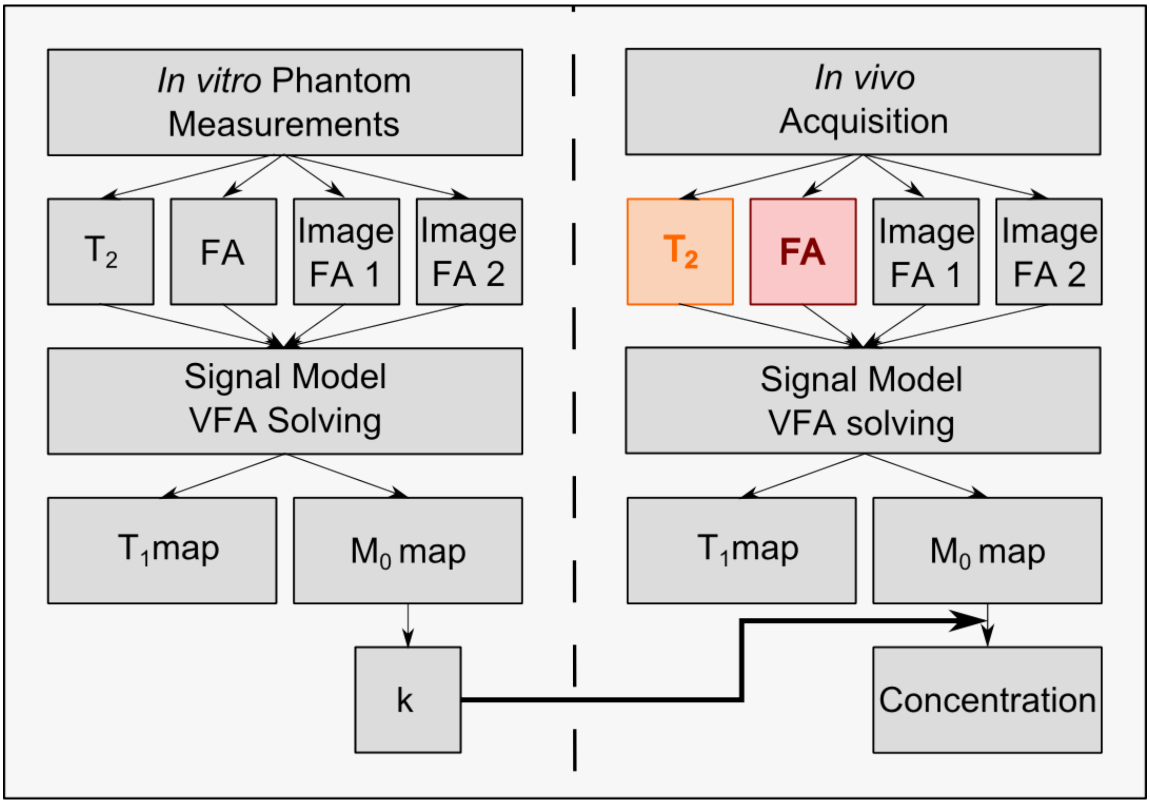

Figure 9.7: Schematic of the phantom replacement pipeline used for ^{7}Li calibration of the VFA pipeline. The red box indicates that the acquisition could not be performed *in vivo*. In this case, coil transmission and reception profiles were considered spatially invariant as illustrated by Figure 2.23. Orange boxes indicate that T_2 value was considered fixed at T_{2mono} 47 ms.

9.3.4.2 T_1 estimation

As illustrated by Figure 9.11, our T_1 maps suffer from a significant spread with unexpected values found in area where the lithium signal is smallest. In some case, partial volume effect due to the large voxel size could also be incriminated. Another limitation of our quantification pipeline is our assumption of a constant mono-exponential T_2.

Nevertheless, comparing T_1 values obtained with both MR Spectroscopy, presented in Figure 9.10 and Imaging is of interest to evaluate a mean *in vivo* longitudinal relaxation rate and appreciate the potential quantification errors when spatial variation of T_1 are not accounted for. Our results show that average values estimated using the VFA approach or the non-localized MRS and reasonably close considering the to the aforementioned issues.

9.4 Conclusion and Perspectives

In this Chapter, we adapted successfully our previous developments to the problematic of *in vivo* ^{7}Li MRI at 7 T and validated our imaging protocol and quantification pipeline for clinical investigation of bipolar patients treated with Lithium salts. As for ^{31}P MRI, we applied the phantom replacement method and obtained meaningful brain Lithium concentration maps. As for ^{23}Na MRI, we applied the VFA approach and estimated simultaneously concentration and T_1 maps.

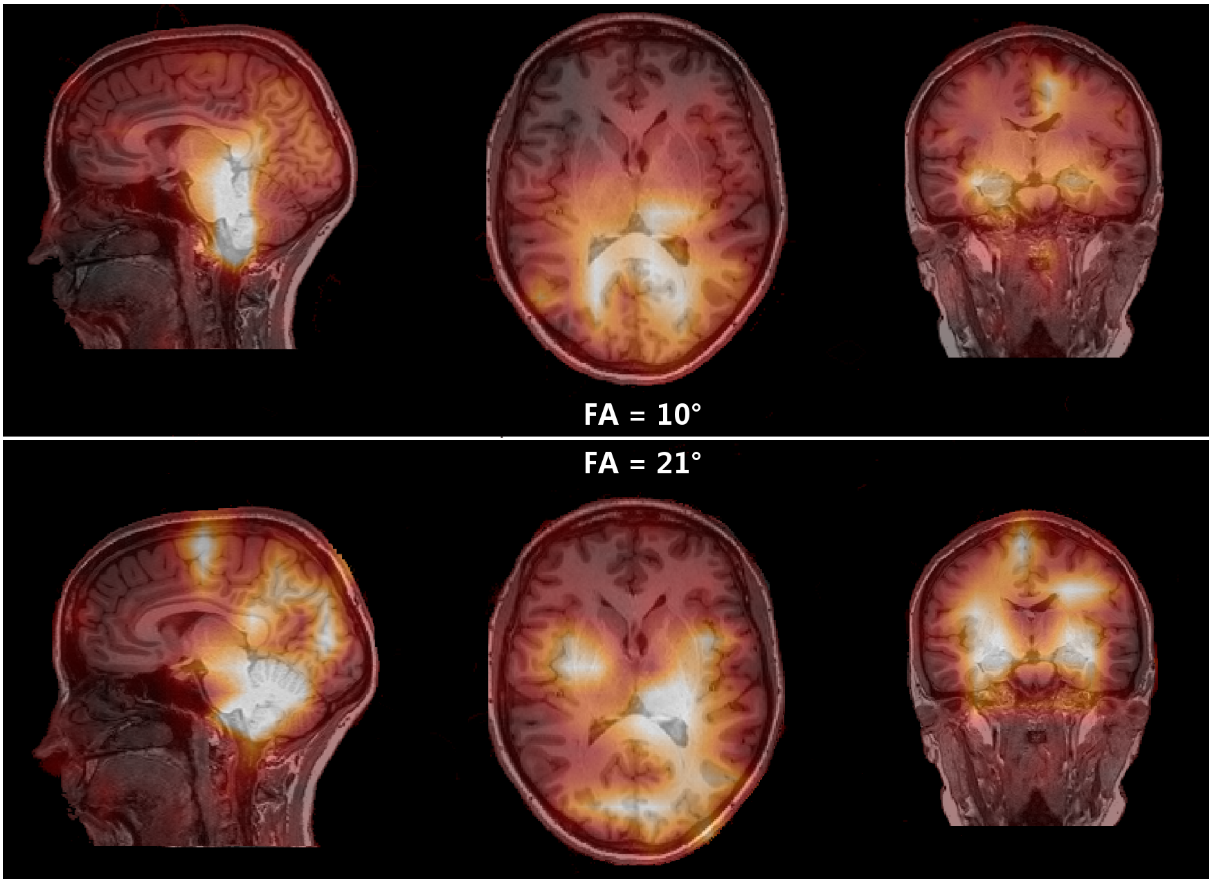

Figure 9.8: Orthogonal views of the two ^{7}Li TPI acquisitions from the same patient. While an almost homogeneous Li distribution can be seen for the shorter FA acquisition, bright spots are visible all over the brain with the larger FA acquisition. Images are presented with identical intensity scaling.

Lithium NMR is the only non-invasive method to get access to the clinically relevant lithium content in the brain of bipolar patients and get insights about its mechanism of action. Our study confirms the heterogeneous distribution of ^{7}Li in human brain as previously reported [BOADA 2010, SMITH 2011, LEE 2012]. Our measurements of lithium brain concentrations, longitudinal and transverse relaxations times *in vivo* are all in agreement with previously reported values.

This pilot study also demonstrates that NeuroSpin's non-proton imaging platform and research team can achieve the sufficient sensitivity and spatial specificity to be relevant for advanced clinical investigation overcoming the lower sensitivity and *in vivo* concentration of nuclei such as Lithium-7. As already stated for our ^{23}Na MRi explorations, the VFA pipeline need to be improved to better control the fit of T_1. Hopefully, this task will be undertaken soon so as to unleach the true potential of this method for ^{7}Li MRI among others. The BIP-Li7 project continues and more data will be acquired, opening the way for original hypothesis and correlations between Li concentrations and the anatomical, structural and metabolic data acquired at 3 T.

Finally, our ^{7}Li MR images played a role in mobilizing a European consortium with the objective to better understand Lithium mechanisms of action for Bipolar Disorder. The R-Link project was successful in convincing the European Research Council (H2020 call) to fund a large scale multi-

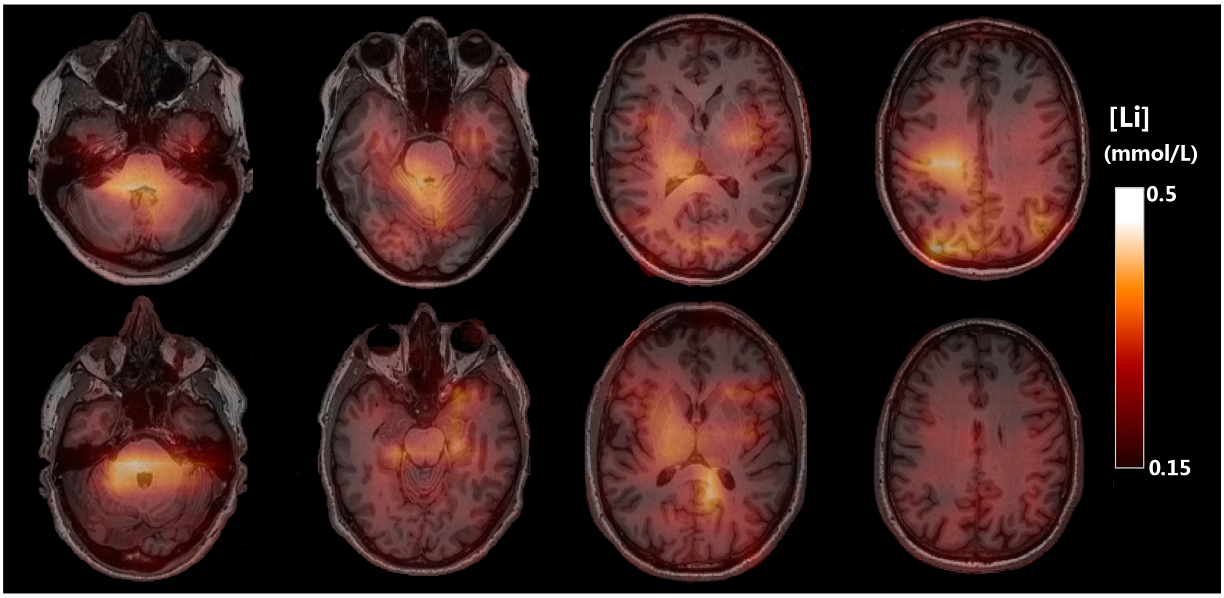

Figure 9.9: Axial views of the Lithium concentration maps obtained for patients 7 (top row) and 8 (bottom row). Images are presented with identical intensity scaling.

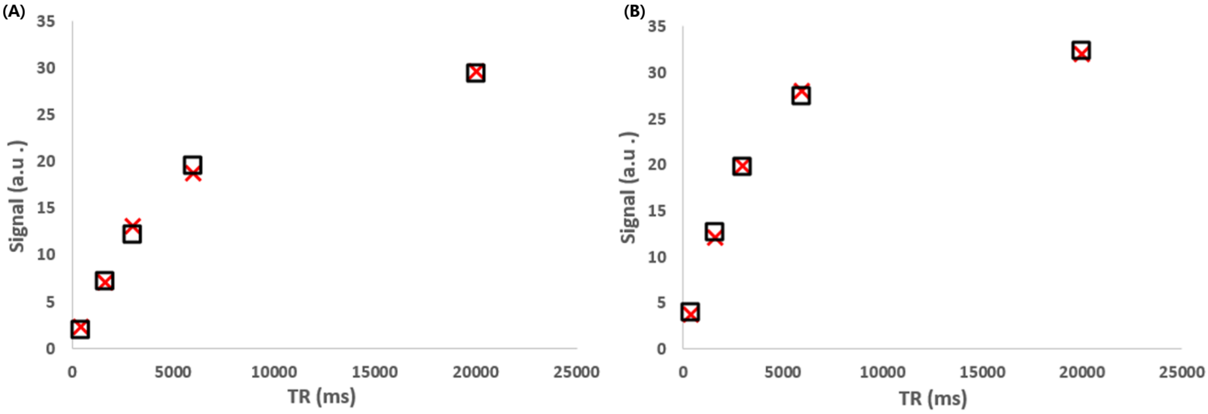

Figure 9.10: MR Spectroscopy estimation of the longitudinal relaxation time for a patients 7 (A) and 8 (B) of the V_2 protocol. T_1 was estimated at 5901 ms for patient 7 and 3220 ms for patient 8.

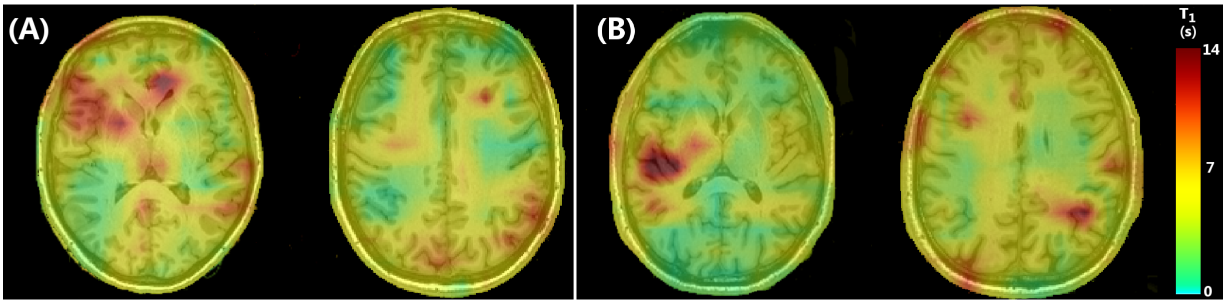

Figure 9.11: T_1 maps computed with the VFA pipeline for patients 7 (A) and 8 (B). Average T_1 was estimated at 4500 ms for patient 7 and 4000 ms for patient 8.

centric $^{1}H/^{7}Li$ MRI study. Hundreds of BP patients will soon be scanned at 3 T or 7 T and our developments are likely to constitute a basis for the quantitative ^{7}Li protocol.

Deeper analysis will be performed and results are expected to be submitted at the joint International Society of Magnetic Resonance in Medicine and European Society for Magnetic Resonance in Medicine and Biology meeting held in Paris in 2018. A multimodal analysis is also expected to be submitted for publication later this year or in 2018.

General Conclusion and Perspectives

Conclusions

The main objective of this PhD thesis was to develop a whole platform for non-proton MRI: acquisition reconstruction and quantification methods dedicated to Sodium, Phosphorus and Lithium MRI at ultra high magnetic field. We succeeded in implementing and validating, both *in vitro* and *in vivo*, our non-Cartesian ultra-short echo time acquisition protocol at 3 T and 7 T.

Our Sodium MRI developments aimed at improving the temporal efficiency of the current state-of-the-art spin-density weighted acquisition protocol. Indeed with our VFA approach we could improve the NMR signal sampling efficiency by a factor of 6 (TR reduced from 120 ms to 20 ms) while increasing signal accumulation to maintain SNR. The strong T_1 weighting brought by this approach was accounted for and corrected by the VFA pipeline leading to a simultaneous T_1 and spin-density estimation. Our validation studies, both *in vitro* and *in vivo* showed that VFA enables a T_1 independent concentration mapping which is of interest. Moreover, the simultaneous mapping T_1 could be of interest for lesion characterization in a clinical context.

Our explorations towards the use of similar fast imaging techniques combined to a spectrally selective module were successfully validated. Our *in vitro* experiments demonstrated the good spectral selection capacity and our *in vivo* explorations allowed to compare its efficiency and performances with state-of-the-art MRSI acquisitions. Despite some difficulties in accurate phosphorylated metabolite concentration mapping, we obtained images with better SNR and resolution than MRSI. The theoretical 12 mm isotropic resolution that we achieved is slightly higher than state-of-the-art acquisitions [Lu 2013] within comparable acquisition times. Indeed they acquired simultaneously PCr and ATP signals in 33 minutes, we achieved the same in 38 minutes (2×19).

The ongoing Lithium MRI protocol strongly benefited from this fast imaging approach as Lithium's longitudinal relaxation rate is tremendously long. Our approach allowed to obtain a theoretical 15 mm isotropic resolution with a whole brain coverage which is also slightly better than state-of-the-art MRSI ([Lee 2012]) and MRI ([Boada 2010]) approaches. It is likely that we could also gain SNR by increasing scan time as acquisitions, in previously cited studies, were respectively 92% and 33% longer than our acquisition. Our results being in agreement with previously reported findings it validates our choices.

For both Lithium and Phosphorus acquisition, the use of phantom replacement is well suited as *in vivo* acquisitions of coil properties and relaxation rates is long and challenging. Nevertheless, it requires additional post-processing steps and accounting for the different relaxation properties.

Perspectives

Our collaboration with Drs Sandro Romanzetti and Kathrin Reetz allowed the application of the VFA pipeline in pathological conditions. Further explorations around the clinical application of our developments are ongoing. In particular, acquisitions are currently performed on AD and HD patients. Unfortunately, due to time constraints they could not be analyzed and presented in this manuscript but we are confident they will yield valuable information Therefore, further explorations around application of our developments are ongoing. Moreover, this collaboration will be strengthen by a new *in vivo* Sodium MRI research project starting 2018 at NeuroSpin. With the reception of a new 7 T human Sodium head coil new explorations are possible. In particular, a deeper exploration of Sodium concentration between white and grey matter at a finer resolution as well a more accurate mapping of relaxation properties. In addition, the *in vivo* application of the multiple echoes approach could yield finer relaxation constant estimations as well as compartmental information.

Our Phosphorus explorations validated the spectrally selective approach as an interesting method with a better efficiency than MRSI techniques for single metabolite studies. Further studies aiming at exploring ATP synthesis through magnetization transfer techniques are foreseen using this Imaging technique and may be explored in the coming months at NeuroSpin. Moreover, a metabolic interleaved approach was implemented and needs to be adapted and validated to further improve the efficiency of this method.

Our preliminary Lithium MRI results obtained at 7 T on bipolar patients are of interest for clinicians. A large European consortium project, *R-Link*, headed by Pr Franck BELLIVIER was created and recently got funded by the H2020 program to further extend our developments and apply them on larger cohorts. Therefore our development will be carried on and probably improved and adapted for a larger use on multiple MR scanners across Europe.

An other non-proton project in collaboration with the Molecular Imaging Research Center (CEA-Mircen) with Drs Julien VALETTE and Julien FLAMENT about Oxygen 17 is currently developed. It is likely that our non-Cartesian UTE sequences, reconstruction techniques and concentration measurements methods can be extended to this application.

The adaptability of our non-proton MR Imaging platform, illustrated in this thesis to Sodium, Phosphorus and Lithium can of course be extended to any other nuclei. Adaptation of acquisition parameters and sequence sensitivity needs to be performed but other studies of Potassium [UMATHUM 2013] or Chlorine [NAGEL 2014] are possible. As Potassium concentration in cellular compartment is higher in the intra-cellular compartment, a joint Sodium/Potassium study could yield valuable insights into cellular compartmentalization and homeostasis. Moreover, Aluminum nuclei is also NMR sensitive and could be explored in the framework of certain disease that could be caused to its accumulation in certain body parts.

Finally, this PhD work has gathered many experimental and technical developments covering a large spectrum of NMR (MRS and MRI). We explored coils and phantoms designs, sequence developments and validations, image reconstruction and post-processing pipelines and *in vivo* clinical applications to healthy controls and patients with bipolar disorder or neurological diseases.

In the recent years, non-proton MRI gained interest due to the wider availability of high and ultra high magnetic field scanners in both research laboratories and hospitals as well as improved MR pulse sequences and reconstruction algorithms. The lower resonant frequency of these nuclei being a prominent factor for their application at fields higher than 7 T compared to proton which suffers already from significant dielectric artifacts. At those fields the higher available SNR will compensate for their low *in vivo* concentration and will offer high resolution images to better understand brain's biochemistry and metabolism. Non-proton MRI has therefore a promising future for clinical research about metabolism, physiology and pharmacology.

The recent arrival of the 11.7 T magnet at NeuroSpin opens the way to improve already existing protocols, extend their applications and tackle new challenges with higher resolution images.

Publications

Peer Reviewed Journal Publications

- **A. COSTE**, F. BOUMEZBEUR, A. VIGNAUD, G. MADELIN, K. REETZ, D. LE BIHAN, C. LERMAN, S. ROMANZETTI, Simultaneous Sodium Concentration and T1 assessment using Variable Flip Angle approach in vivo at 3T, Magnetic Resonance in Medicine, Submitted in June 2017.
- **A. COSTE** & L. LEROI , F. BOUMEZBEUR, L. DE ROCHEFORT, M. SANTIN, R. VALABREGUE, C. POUPON, D. LE BIHAN, C. LERMAN, A. VIGNAUD, Simultaneous multi-parametric and quantitative estimation of ^{23}Na physical properties at 7 Tesla using QuICS, Magnetic Resonance in Medicine, Submitted in June 2017.

International Conferences with Reading Committee and Proceedings

- **A. COSTE**, F. BOUMEZBEUR, A. VIGNAUD, G. MADELIN, K. REETZ, D. LE BIHAN, C. LERMAN, S. ROMANZETTI, Variable Flip Angle Pipeline for in vivo Sodium Concentration Measurements (VaSCo), Proceedings of the International Society for Magnetic Resonance in Medicine, Poster, Honolulu 2017.
- **A. COSTE**, N. CHAUFFERT, F. BOUMEZBEUR, A. VIGNAUD, P. CIUCIU, G. MADELIN, K. REETZ, D. LE BIHAN, C. LERMAN, S. ROMANZETTI, Improving Sodium Concentration Measurements using sub-sampled Non-Cartesian Trajectories and Non-Linear Iterative Reconstruction algorithm, Proceedings of the International Society for Magnetic Resonance in Medicine, ePoster, Honolulu 2017.
- L. LEROI & **A. COSTE**, F. BOUMEZBEUR, L. DE ROCHEFORT, M. SANTIN, R. VALABREGUE, C. POUPON, D. LE BIHAN, C. LERMAN, A. VIGNAUD, Simultaneous multi-parametric and quantitative estimation of ^{23}Na physical properties at 7 Tesla using QuICS, Proceedings of the International Society for Magnetic Resonance in Medicine, ePoster, Honolulu 2017.
- **A. COSTE**, A. VIGNAUD, P. CIUCIU, F. BOUMEZBEUR, F. MAUCONDUIT, A. AMADON, S. ROMANZETTI, D. LE BIHAN, C. LERMAN, ^{31}P MR Imaging and Concentration Measurements, Proceedings of the International Society for Magnetic Resonance in Medicine, ePoster, Singapore 2016.
- **A. COSTE**, N. CHAUFFERT, A. VIGNAUD, P. CIUCIU, F. BOUMEZBEUR, P. WEISS, S. ROMANZETTI, D. LE BIHAN, C. LERMAN, Assessment of benefit to use a non-Cartesian trajectory and non-linear reconstruction method compared to a Cartesian strategy for Fast ^{31}P MRI, Proceedings of the International Society for Magnetic Resonance in Medicine, ePoster, Singapore 2016.
- **A. COSTE**, F. MAUCONDUIT, A. VIGNAUD, A. AMADON, S. ROMANZETTI, D. LE BIHAN, C. LERMAN, ^{31}P MRI Transmission (B_1^+), sensitivity (B_1^-) and T_1 mapping at Ultra High Field, Proceedings of the European Society for Magnetic Resonance in Medicine and Biology, Oral and ePoster, Edinburgh 2015.
- **A. COSTE**, N. CHAUFFERT, A. VIGNAUD, P. CIUCIU, F. BOUMEZBEUR, P. WEISS, S. ROMANZETTI, D. LE BIHAN, C. LERMAN, ^{31}P Comparison of Image Reconstruction Approaches for sub-Nyquist Acquisitions at Ultra High Field, Proceedings of the European Society for Magnetic Resonance in Medicine and Biology, Oral and ePoster, Edinburgh 2015.

Oral Presentation at National Conferences

- **A. COSTE**, In vivo Sodium MR Imaging, Institut d'Imagerie Biomédicale, CEA 2016.
- **A. COSTE**, D. LE BIHAN, C. LERMAN, X Nuclei MR Imaging at High Field, Réseau de jeunes chercheurs en imagerie / France Life Imaging, Octobre 2015.
- **A. COSTE**, Phosphorus MRI Acquisitions and Reconstruction, Life Science Division Meeting, Octobre 2015

National Press Communication

- F. BOUMEZBEUR, J. HOUENOU, *Imagerie IRM du Lithium in vivo*, France Culture, Février 2017

Abbreviations and Acronyms

ADC	**A**pparent **D**ifusion **C**oefficient
ATP	**A**denosine **T**ri**P**hosphate
BP	**B**ipolar **P**atients
BW	**B**and **W**idth
CEA	**C**ommissariat à l'**É**nergie **Atomique** et aux **É**nergies **Al**ternatives
CEST	**C**ontrast **E**nhanced **S**aturation **T**ransfer
CSF	**C**erebro-**S**pinal **F**luid
CS	**C**ompressed **S**ensing
CSI	**C**hemical **S**hift **I**maging
dB	**d**eci**B**el
DAM	**D**ouble **A**ngle **M**ethod
DIM	**D**ifference **I**mage **M**ethod
EEG	**E**lectro**E**ncephalo**G**raphy
FID	**F**ree **I**nduction **D**ecay
FA	**F**lip **A**ngle
FFT	**F**ast **F**ourier **T**ransform
FISTA	**F**ast **I**terative **S**oft **T**hresholding **A**lgorithm
FLORET	**F**ermat **L**oop **OR**thogonaly **E**ncoded **T**rajectory
FOV	**F**ield **O**f **V**iew
FWHM	**F**ull **W**idth at **H**alf **M**axium
GM	**G**rey **M**atter
GPU	**G**raphical **P**rocessing **U**nit
GRE	**G**radient **R**ecalled **E**cho
IFT	**I**nverse **F**ourier **T**ransform
LASER	**L**ocalization by **A**diabatic **SE**lective **R**efocusing
MEG	**M**agneto**E**ncephalo**G**raphy
MQF	**M**ultiple **Q**uantum **F**iltering
MRI	**M**agnetic **R**esonance **I**maging
MRS	**M**agnetic **R**esonance **S**pectroscopy
MRSI	**M**agnetic **R**esonance **S**pectroscopic **I**maging
NMR	**N**uclear **M**agnetic **R**esonance
NUFFT	**N**on **U**niform **F**ast **F**ourier **T**ransform
NFFT	**N**on-equispaced **F**ast **F**ourier **T**ransform
PCr	**P**hospho**C**reatine
PIXEL	**Pi**cture **EL**ement
ppm	**p**arts **p**er **m**illion
PSF	**P**oint **S**pread **F**unction
QuICS	**Qu**antitative **I**maging using **C**onfiguration **S**tates
RF	**R**adio **F**requency
ROI	**R**egion **O**f **I**nterest
SAR	**S**pecific **A**bsorption **R**ate
SD	**S**pin **D**ensity
SE	**S**pin **E**cho
SNR	**S**ignal to **N**oise **R**atio
SPGR	**SP**oiled **GR**adient echo

SSIM	**S**tructural **SIM**ilarity
SVS	**S**ingle **V**oxel **S**pectroscopy
TA	**A**cquisition **T**ime
TE	**E**cho **T**ime
TPI	**T**wisting **P**rojection **I**maging
TQF	**T**riple **Q**uantum **F**iltering
TR	**R**epetition **T**ime
TSC	**T**otal **S**odium **C**oncentration
TSE	**T**urbo **S**pin **E**cho
TWIRL	**TWI**sting **R**adial **L**ine
UHF	**U**ltra **H**igh magnetic **F**ield
UTE	**U**ltra-short **E**cho **T**ime
VDS	**V**ariable **D**ensity **S**ampling
VFA	**V**ariable **F**lip **A**ngle
VTK	**V**isualization **T**ool**K**it
VOXEL	**V**olume **E**lement
WM	**W**hite **M**atter

Physical constants and Symbols

Speed of Light	c	2.997 924 58 $\times 10^{8}$ m.s^{-1} (exact)
Elementary electrostatic charge	q	1.602 $\times 10^{-19}$ A.s (C)
Planck Constant	h	1.05 $\times 10^{-34}$ J.s
Boltzmann Constant	k$_B$	1.38 $\times 10^{-23}$ J.K^{-1}
Mass of an electron	m$_e$	9.109 $\times 10^{-31}$ kg
Mass of a nucleon	m$_n$	1.67 $\times 10^{-27}$ kg
Avogadro Constant	N$_A$	1.06 $\times 10^{23}$ mol^{-1}

Apparent Diffusion Coefficient	ADC	m$^2 s^{-1}$
Molar Concentration	[]	mol.L^{-1}
Temporal frequency	ν	s^{-1} (Hz)
Larmor Frequency	γ	s^{-1} (Hz)
Spatial frequency	k	m^{-1}
Static Magnetic Field	B$_0$	kg.s^{-2}.A^{-1} (T)
Coil Transmission Field	B$_1^+$	kg.s^{-2}.A^{-1} (T)
Coil Reception Profile	B$_1^-$	kg.s^{-2}.A^{-1} (T)
Spin Lattice Relaxation Time	T$_1$	s
Spin Spin Relaxation Time	T$_2$	s
Effective Spin Spin Relaxation Time	T$_2^*$	s
Spin Lattice Relaxation Rate	R$_1$	s^{-1}
Spin Spin Relaxation Rate	R$_2$	s^{-1}
Effective Spin Spin Relaxation Rate	R$_2^*$	s^{-1}
Energy	E	kg.m^2.s^{-2} (J)
Power	P	J.s^{-1} (W)
Flip Angle	α	degree (°) radian (rad)
Dirac Function	δ	$\delta_a(x) = \lim\limits_{a \to 0} \frac{1}{a\sqrt{\pi}} e^{-x^2/a^2}$
Chemical Shift	δ	ppm
Larmor Angular Precession Frequency	ω_0	rad.s^{-1}
Magnetic Moment	μ	A.m^2 (J.T^{-1})
Macroscopic Equilibrium Magnetization	M$_0$	A.m
Macroscopic Magnetization	M	A.m
Temperature	T	K
Spin Density	ρ	
Spatial Field Gradients	G	kg.s^{-2}.A^{-1}.m^{-1} (T.m^{-1})
Field Gradient slew rate	S	kg.s^{-3}.A^{-1}.m^{-1} (T.m^{-1}.s^{-1})

Graphical Data plots

Box and whisker diagram

Box plots or box and whisker plots is a way of graphically representing groups of numerical data based on statistic splitting known as quartiles. Box plots are non-parametric plots as they display variation in samples with no assumptions about the underlying statistical distribution. Spacing between the different elements of the representation illustrates the spread and skewness properties of data. Figure 12 illustrates a graphical representation of a box plot and the associated statistical meaning of each element. On our representations the mean of data distribution was plotted as cross mark for comparison. Outliers that represent less than 0.5% were not plotted on the boxplot to avoid large spread and keep meaningful information.

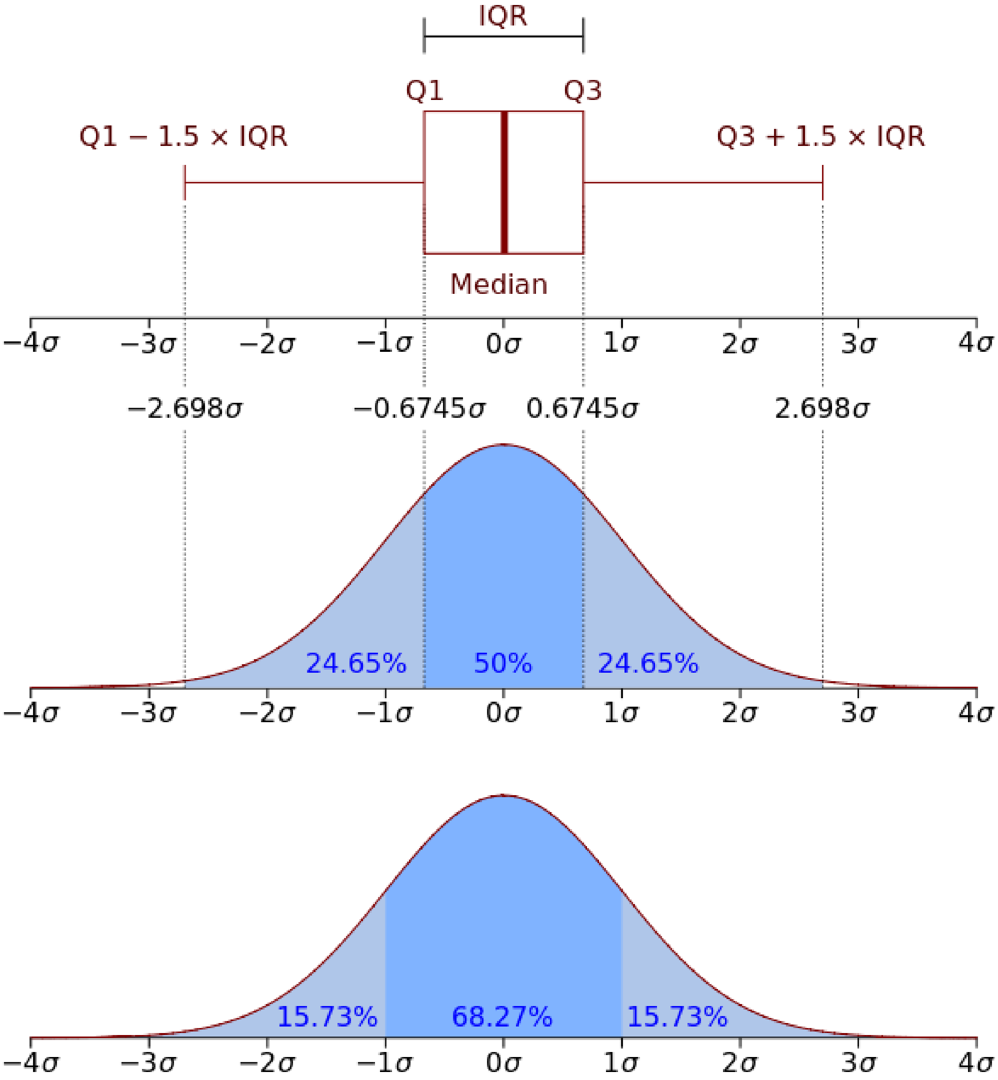

Figure 12: Illustration of the graphical representation of a boxplot with statistical comparison to a Gaussian probabity distribution

List of Figures

List of Tables

Résumé court en Français

Sujet : Développements Méthodologique pour l'IRM à haut champ magnétique du Sodium, du Phosphore et du Lithium : Application en recherche clinique à 3 Teslas et 7 Teslas.

Résumé :

L'Imagerie par Résonance Magnétique Nucléaire des noyaux non-proton (X) permet d'explorer in vivo le métabolisme et la physiologie en conditions normales ou pathologiques mais aussi d'étudier la pharmacologie de manière non-invasive. Toutefois, ces explorations souffrent de la moindre sensibilité de ces noyaux X et de leur plus faible concentration dans les tissus. Le Sodium (^{23}Na) est le second noyau le plus visible en RMN dans les tissus cérébraux et sa distribution, dans les compartiments intra et extra-cellulaires, est strictement régulée notamment par la pompe Na^+/K^+-ATPase. Les stocks d'adénosine triphosphate (ATP) et de phosphocréatine (PCr), réservoirs d'énergie pour l'activité enzymatique, doivent être perpétuellement reconstitués pour assurer le bon fonctionnement cellulaire. C'est pourquoi étudier les distributions cérébrales de ces deux métabolites phosphorylés en plus de celle du sodium permettrait d'avoir un aperçu de la viabilité et du métabolisme cellulaire. Enfin, le lithium est le traitement de référence pour la prévention de la crise maniaque chez le patient bipolaire. Pour autant, de nombreuses questions se posent quant à sa distribution cérébrale et son mécanisme d'action thérapeutique.

Durant ces trois années de thèse, nous nous sommes intéressés, en particulier, aux problématiques d'imagerie rapide par échantillonnage non-Cartésien, de reconstruction de ces images et de quantification de la concentration et des propriétés physiques de ces noyaux. Nous avons développé une méthode permettant la correction des différents biais à travers la cartographie du champ statique B_0 et des profils de transmission (B_1^+) et de réception (B_1^-) de l'antenne. De plus, la quantification des temps de relaxation longitudinale et transverse permet de compenser les effets de ces mécanismes de relaxation sur le signal RMN pour obtenir des mesures de concentrations robustes et fiables. En raison d'un moment quadripolaire important, l'emploi de séquences à temps d'écho ultra-court (UTE) est indispensable en IRM du ^{23}Na en combinaison de schémas non-Cartésiens d'encodage spatial. Des méthodes dédiées de reconstruction ont été évaluées ainsi que diverses stratégies de sous-échantillonnage. Enfin, une approche multi-gradient-écho, alternative aux approches de Filtrage Quantique Multiple (MQF), a été implémentée afin d'explorer la compartimentation cellulaire.

Ces développements ont donné lieu à des applications cliniques en Sodium à 3 T chez des volontaires sains en collaboration avec le service de Neurologie de l'Hôpital Universitaire d'Aix la Chapelle en Allemagne. Des études en recherche clinique, à 7 T à NeuroSpin, ont été réalisées en Phosphore (^{31}P) chez des sujets sains et en Lithium-7 (^{7}Li) chez des patients bipolaires sous traitement lithium en collaboration avec un service de Psychiatrie de l'Assistance Publique, Hôpitaux de Paris (AP-HP). Une application clinique en IRM ^{23}Na à 3 T est actuellement en cours chez des patients atteints par la maladie d'Alzheimer à Aix la Chapelle.

Mots clés : Imagerie Par Résonance Magnétique Nucléaire, Sodium, Phosphore, Lithium, Quantification

Abstract in English

Subject: Methodological Developments for Sodium, Phosphorus and Lithium MRI at high magnetic field: Application to clinical research at 3 and 7 Tesla.

Abstract:

Nuclear Magnetic Resonance Imaging of other nuclei than Hydrogen (X) allows to, non-invasively, probe in vivo metabolism and cellular physiology in both normal and pathological conditions and also to explore the pharmacological effect of certain drugs. However, such explorations suffer from the lower sensitivity of such X nuclei combined with a lower concentration in tissues. Sodium nuclei (23Na) is the second most NMR visible nuclei in brain tissues and its distribution in both intra and extra cellular compartments is tightly regulated by, in particular, the Na^+/K^+-ATPase pump. Stocks of Adenosine Triphosphate (ATP) and Phosphocreatine (PCr), main sources of cellular energy are perpetually maintained to ensure proper cellular function. This is why, study of spatial distributions of these two phosphorylated metabolites along with Sodium could yield insights about cellular viability and metabolism. Finally, Lithium is the reference treatment to prevent the onset of maniac events of patients suffering from bipolar disorder. Nevertheless, many questions are still unanswered about its spatial distribution in brain tissues and the underlying therapeutic mechanisms.

During these three years of research, we got particular interest to fast Imaging techniques through the use of non-Cartesian Fourier space sampling combined with dedicated and optimized reconstruction methods to perform accurate and robust quantification measurements of those nuclei. We developed a method that allows to account for acquisition bias through a mapping of the static magnetic field B_0 and of the coil transmission (B_1^+) and reception (B_1^-) profiles. Moreover, quantifying longitudinal and transverse relaxation time allows to adapt acquisition parameters and compensate the acquired NMR signal for the effect of these mechanisms. All these corrections allow to reach robust and reliable quantitative concentration measurements. Due to a strong quadrupolar moment, the use of an ultra-short echo time (UTE) sequence combined with non-Cartesian sampling schemes is mandatory for Sodium MRI. Various Fourier space sampling schemes along with undersampling strategies and reconstruction methods were evaluated and compared. Finally, a multiple echoes acquisition has been implemented to explore cellular compartmentalization and avoid the use of Multiple Quantum Filtration (MQF).

These developments were applied in a clinical research Sodium MRI setting on healthy volunteer in collaboration with the Neurology department of Aachen University Hospital. Research explorations were conducted, at 7 T at NeuroSpin, using Phosphorus (^{31}P) MRI on healthy volunteers. In collaboration with a Psychiatry service of Paris Public Hospital (AP-HP), Lithium (^{7}Li) MRI was used on patients with bipolar disorder and treated with Lithium based cure. A pathological study using Sodium (^{23}Na) MRI at 3 T is currently ongoing on patients suffering from Alzheimer's disease at Aachen University Clinic.

Key Words: Nuclear Magnetic Resonance Imaging, Sodium, Phosphore, Lithium, Quantification

Résumé en Français

Introduction

Ce document présente de manière synthétique les thématiques abordées durant ces trois années de thèse, les différentes méthodes utilisées ou développées et les résultats obtenus. Le plan de ce résumé diffère légèrement de celui du manuscrit de thèse et omet volontairement de nombreuses parties, en particulier les parties introductives sur la physique de l'IRM et sur le cerveau et ses pathologies, sujet d'application de nos études.

Contexte et Objectifs

Contexte de la thèse

Cette thèse s'inscrit dans le cadre du développement d'une nouvelle thématique de recherche au sein du laboratoire NeuroSpin du Département de la Recherche Fondamentale (DRF) du Commissariat à l'Énergie Atomique et aux Énergies Alternatives (CEA). L'Imagerie par Résonance Magnétique Nucléaire (IRM) basée sur le phénomène physique de la Résonance Magnétique Nucléaire (RMN) est une modalité d'imagerie médicale de fort intérêt en raison de son caractère non invasif et non ionisant. En effet, exceptés les explorations échographiques utilisant les ondes ultrasonores, la radiographie, le scanner X et la Tomographie par Emission de Positons (TEP) sont des modalités ionisantes en raison de l'utilisation de rayonnements de haute énergie (Rayons X) ou de radioactivité. Les images IRM réalisées en pratique clinique, mais aussi en recherche, sont basées sur les propriétés RMN de l'atome d'Hydrogène (aussi appelé proton en raison de sa structure), le plus présent dans l'organisme notamment au travers de la molécule d'eau (H_2O) qui compose environ 60% de la masse du corps humain. Une bonne sensibilité RMN et une forte concentration de noyaux permettent aujourd'hui d'obtenir des images anatomiques à haute résolution spatiale en un temps compatible avec la pratique clinique. De plus, différentes explorations peuvent également être réalisées telles que des études de la diffusion de l'eau ou des études d'IRM fonctionnelle illustrant l'activité cérébrale consécutive à une stimulation.

Imagerie des noyaux exotiques (Noyaux X)

L'étude par IRM d'autres noyaux que l'Hydrogène très impliqués dans les processus biochimiques tels que le Carbone (^{12}C) et l'Oxygène (^{16}O) est impossible en raison de leur insensibilité à la RMN. Mais, certains noyaux, sont eux sensible à la RMN et peuvent être étudié, principalement par Spectroscopie. Les études par spectroscopie RMN de ces noyaux étant très largement exploitées depuis plusieurs décennies, les chercheurs en IRM ont, très tôt, essayé d'appliquer les techniques d'imagerie pour produire des images de la distribution de ces noyaux: Lithium (^{7}Li) [Renshaw 1985, Renshaw 1988, Boada 2010, Lee 2012], Bore (^{11}B) [Glover 1992, Bendel 1998], Fluor (^{19}F)[Holland 1977, McFarland 1985, Ruiz-Cabello 2011], Sodium (^{23}Na) [Hilal 1985, Perman 1986], Phosphore (^{31}P) [Bendel 1969]. Malhreusement en raison de leur plus faible sensibilité et concentration dans les tissus, les images obtenues à l'époque étaient de très basse résolution spatiale et très longues à acquérir donc assez peu attractives pour les cliniciens. Néanmoins, l'utilisation de l'imagerie Spectroscopique offre la possibilité d'interpoler des cartes de concentration basée sur l'acquisition spectrale dans un ensemble de voxel basse résolution. Il faudra attendre plusieurs années et l'amélioration du matériel disponible et des techniques d'acquisition et méthodes de traitement du signal et de reconstruction des images pour voir ce type d'imagerie se développer en particulier l'IRM du Sodium [Qian 2012b, Madelin 2013], du Phosphore (^{31}P) [Lu 2013], du Potassium (^{39}K) [Parrish 1997] ou du Chlore (^{35}Cl) [Nagel 2014]. Le tableau 8 résume les propriétés physiques de quelques noyaux présentés précedemments et les compare avec l'Hydrogène. L'augmentation du champ magnétique des imageurs combinée à une amélioration des performances, intensité maximale et vitesses de commutation, des gradients de champs ainsi que de nouveaux designs d'antennes plus efficaces ont permis d'augmenter significativement le niveau du signal RMN crée par ces noyaux et donc de réduire le temps d'acquisition ou d'améliorer la résolution spatiale des images. L'augmentation des champs magnétiques disponibles pour l'imagerie chez l'Homme. En effet, plus d'une cinquantaine de scanners à, une dizaine de scanner à 9.4T et 1 scanner à 10.5T sont actuelements opérationnels et bientôt un scanner 11.75T Ã NeuroSpin. Ces machines IRM ouvrent de nouvelles perspectives pour la recherche en particulier pour l'imagerie des noyaux X. L'implantation croissante de scanner IRM à 3 T dans les hôpitaux permet également d'envisager des applications clinique de diagnostic avec, néanmoins, des optimisations nécéssaires pour palier un niveau de signal qui demeure relativement faible. D'autres techniques permettent également d'étudier d'autres noyaux comme l'utilisation d'isotopes sensibles à la RMN tels que l'Oxygène 17 (^{17}O) [Hoffmann 2011], l'Hélium 3 (^{3}He) [Kober 1999], le Xénon (^{129}Xe) [Alberts 1994] ou le Carbone 13 (^{13}C) [Day 2007, Valette 2017] dont il est possible d'amplifier le signal par hyperpolarisation.

Isotope	Spin	Abondance Naturelle (%)	Sensibilité Relative†	Rapport Gyromagnetique $\gamma/2\pi$ (MHz.T^{-1})	Fréquence RMN à 7 T (MHz)
^{1}**H**	1/2	99.985	1.00	42.58	298.03
^{2}H	1	0.015	1.45×10^{-6}	6.54	45.75
^{3}He	1/2	1.4×10^{-4}	5.75×10^{-7}	32.43	227.04
^{7}**Li**	3/2	92.4	0.272	16.55	115.82
^{11}B	3/2	80.42	0.133	13.66	95.61
^{13}C	1/2	1.108	1.76×10^{-4}	10.70	74.93
^{14}N	1	99.63	1.0×10^{-3}	3.08	21.54
^{15}N	1/2	0.370	3.86×10^{-6}	-4.32	-30.21
^{17}O	5/2	0.037	1.08×10^{-5}	5.77	40.40
^{19}F	1/2	100	0.834	40.05	280.36
^{23}**Na**	3/2	100	9.27×10^{-2}	11.26	78.83
^{27}Al	5/2	100	0.21	11.09	77.66
^{31}**P**	1/2	100	6.65×10^{-2}	17.24	120.65
^{35}Cl	3/2	75.53	3.55×10^{-3}	4.17	29.2
^{39}K	3/2	93.10	4.75×10^{-4}	1.99	13.92
^{129}Xe	1/2	26.44	5.71×10^{-3}	11.78	82.44

Table 8: Propriétés RMN de différents noyaux d'intérêt en recherche biomedicale. † La sensibilité relative est calculée comme le produit de la sensibilité RNM et de l'abondance naturelle et comparée au ^{1}H.

Cette thèse se décompose en deux volets, le premier présente les développements de différentes méthodes à NeuroSpin sur le scanner à 7 Tesla et le second présente leur application chez l'Homme à 3 T dans le service de neuroradiologie de l'Hôpital Universitaire d'Aix la Chapelle en Allemagne.

Applications Clinique

Durant cette thèse j'ai travaillé avec le Sodium, le Phosphore et le Lithium. Le Sodium étant le plus concentré dans les tissus, différentes études cliniques ont déjà été réalisées. De nombreux tissus tels que le tissu musculaire, le tissu cérébral ou le cartilage ont déjà été étudiés avec des applications pour les maladies neurodégénératives, cardiaques ou musculosqueletiques. La spécialisation de NeuroSpin à l'étude du cerveau et notre collaboration avec le service de Neuroradiologie de l'hôpital universitaire d'Aix la Chapelle en Allemagne nous a fait nous intéresser spécifiquement aux applications neurologiques de l'imagerie du Sodium:

- L'Accident Vasculaire Cérébral (AVC) Ischémique dont la cause est l'occlusion d'une artère cérébrale entraînant un arrêt de l'irrigation d'un territoire cérébral et une progressive mort cellulaire par manque d'oxygène et de nutriment.
  L'Accident Vasculaire Cérébral (AVC) Hémoragique dont l'origine est l'éclatement d'un vaisseau consécutive à une occlusion et qui entraîne une hémoragie. Différentes études ont permis de montrer que l'IRM du Sodium le diagnostic de l'AVC conjointement aux explorations par IRM de perfusion de diffusion (DWI/PWI) mais offre un potentiel pour évaluer le moment d'occurence de l'occlusion [THULBORN 2005, TSANG 2011, WETTERLING 2015].

- La Sclérose en Plaques (SeP) est une maladie démyelinisante qui crée des lésions interompant la communications entre différentes zones cérébrales entrainant des symptomes moteurs ou cognitifs. La maladie peut se présenter sous deux formes: une forme progressive qui évolue lentement au cours du temps et une forme rémittente qui est caractérisée par des périodes de poussées symptomatiques et des périodes de rémittence. Les études basée sur l'IRM du Sodium ont permis un diagnostic des lésions mais également une possible détermination du types de symptomes pouvant apparaitre [INGLESE 2010, ZAARAOUI 2012, PALING 2013, MAAROUF 2014, MAAROUF 2017].

- La Chorée de Huntington est une maladie génétique et héréditaire se manifestant par la destruction des neurones de certaines régions cérébrales et entraînant des symptomes moteurs ou comportementaux. Une étude de nos collaborateurs du service de Neurologie du Pr REETZ de l'Hôpital Universitaire d'Aix la Chapelle a montrée une augmentation de la concentration en sodium dans le tissu cérébral des patients comparés aux sujets sains [REETZ 2012].

- La Maladie d'Alzheimer qui est une maladie neurodégénérative entraînant une perte définitive des neurones en particulier ceux impliqués la mémoire et entraînant des amnésies rétrogrades à court terme au début, puis évoluant vers les neurones impliqués dans les l'humeur et le language et conduisant à une amnésie totale. Une étude a également montré une élévation de la concentration en Sodium chez les patients consécutive à la mort cellulaire et donc une augmentation de la fraction extracellulaire de plus forte concentration [MELLON 2009]. La complexité et la dépendance multi-factorielle de la maladie nécessite souvent des études plus spécifiques comme la détection des agrégats des protéines tau et βamyloide en particulier ce qui n'est possible qu'en imagerie pré-clinique.

- Les Tumeurs Cérébrales qui sont le résultat d'une prolifération incontrolée des cellules gliales support des neurones, les cellules nerveuses ne pouvant pas dégénérer. La tumeur cérébrale la plus fréquente est le Glioblastome multiforme et plus précisement un astrocytome provenant des cellules astrocytaires. Il s'agit d'une catégorie de tumeur très grave, nécéssitant des traitements lourds de chimiothérapie et de résection chirurgicale avec une très faible espérance de survie à moyen terme. Un suivi des traitements chimiothérapiques a été menée en sodium en 2005 [Babsky 2005] et plus récemment une équipe a utilisé l'IRM du Sodium pour caractériser différents types de tumeurs cérébrales [Biller 2015].

Le Phosphore est un atome très impliqué dans le métabolisme en particulier au travers des molécules d'Adénosine TriPhosphate (ATP), Adénosine DiPhosphate (ADP) et PhosphoCréatine (PCr) qui sont des support au stockage et au transfert d'énergie. Son étude par Spectroscopie RMN est ancienne et très utilisé pour de nombreuses explorations: cérébrales [Chaumeil 2009, Martin 2007, Kauv 2017, Du 2017], musculaires [Chance 2006, Bendahan 2006, Kemp 2007, Hooijmans 2017], cardiaque [Ingwall 1982, Bottomley 2009, Stoll 2016], hépathique [Norén 2004], prostatique [Komoroski 2011], sénographiques [Klomp 2011, van der Kemp 2014] ou pour mesurer les vitesses de synthèse ou de consommation musculaire ou cérébrale d'ATP ou de PCr. En raison de nombreuses molécules phosphorylées présentes dans l'organisme et de leur faible concentration il est complexe de faire de l'imagerie. L'augmentation des champs magnétiques des scanner IRM et le développement de nouvelles séquences d'acquisition et de reconstruction des données a permis aux premières applications en IRM d'avoir lieu [Lu 2013].
Le Lithium est le thymorégulateur le plus utilisé dans le trouble bipolaire pour réduire la fréquence, l'intensité et la durée des épisodes dépressifs ou maniaques des patients [Shorter 2009]. Grâce à de nombreuses études conduites en MRS [Renshaw 1985, Renshaw 1988, Gonzalez 1993] [Soares 2001, Smith 2011, Lee 2012, Cousins 2013], il a été observé que la réponse des patients au traitement varie entre les individus. L'objectif de cette étude est donc de réaliser une cartographie de la distribution de Lithium chez différents patients issus de deux groupes, rÃ©pondant plus ou moins bien au traitement, pour les comparer et tenter de mettre en évidence des différences. Il s'agit d'un projet financé par l'ANR (BipLi7) en collaboration avec les services de psychiatrie du Pr Frank Bellivier, du Dr Josselin Houenou et du Dr Franz Hozer de l'Assistance Publique des Hopitaux de Paris (APHP). Un premier volet pré clinique sur des rats a déjà eu lieu et a permis de comparer des études en IRM avec des études en spectroscopie de masse [Stout 2017].

Méthodes utilisées et outils développés

Acquisition du signal RMN

Comme illustré dans le tableau 1.1, chaque noyau a des propriétés RMN différentes liées à sa structure. En effet, la taille nucléaire et la forme de la distribution des charges va influencer grandement le comportement du noyau et en particulier ses temps de relaxation (T_1 et T_2) qui peuvent diminuer significativement rendant l'acquisition du signal RMN difficile. C'est en particulier le cas du Sodium, qui, en raison d'une asymétrie de la distribution des charges nucléaires va présenter un moment quadripolaire associé à un gradient de champ électrique (EFG) par interaction avec les électrons du nuage électronique entourant le noyau. Cette propriété a une conséquence importante car elle modifie les constantes de relaxation du noyau lors d'une expérience RMN. Un autre effet vient également interagir avec ce dernier phénomène : la diffusion du noyau dans le milieu. En effet, à cause son mouvement microscopique, le noyau va subir de légères variations du champ magnétique B_0. Selon l'environnement chimique, la combinaison de ces deux effets va être différente. Ainsi, dans un environnement liquide, où la diffusion des particules est rapide et isotrope, c'est à dire ne présentant aucune direction privilégiée de déplacement, les interactions de l'EFG ainsi que le moment quadripolaire peuvent, sur un petit intervalle de temps, être considérés de moyenne temporelle nulle. Il en résulte une relaxation mono-exponentielle avec des constantes de relaxation longitudinale T_1 et transversale T_2 de l'ordre de 50 ms. En revanche, dans le cas d'un tissu par exemple, la diffusion est anisotrope et ralentie et donc les temps de corrélations augmentent. L'EFG ne peut plus être considéré de moyenne temporelle nulle et l'interaction quadripolaire est importante. Ainsi, il est possible d'observer une modification de la relaxation qui devient bi-exponentielle avec un dédoublement des constantes de relaxation en une très rapide $T_{1,2R}$ et une plus lente $T_{1,2L}$. Les rapports de ces constantes de relaxation sont de 20%/80% pour la relaxation longitudinale et de 60%/40% pour la composante transversale. La domination de la composante rapide de décroissance de l'aimantation transversale est un problème important car elle conditionne la durée du signal RMN à acquérir la rendant de plus en plus faible. La valeur de ces constantes est fonction du champ utilisé pour l'exploration ainsi que de la densité du milieu.

Différents développements méthodologiques ont été réalisés pour palier ce problème. Le premier consiste en une acquisition à Temps d'Echo Ultra-court (UTE) qui permet de minimiser la durée entre l'excitation des noyaux et le moment ou le signal est recueilli. Ainsi, la quantité de signal perdue est minimisée car une très faible relaxation peu se réaliser avant de commencer à acquérir le signal. La durée minimale du TE est limitée par les capacités matérielles des gradients d'encodage par les différents temps de commutation du système. La combinaison de cette technique avec une stratégie optimisée de l'échantillonnage du signal permet de maximiser le signal et l'information spatiale acquis. En effet, le signal utile étant essentiellement localisé au centre de l'espace de Fourier il n'est pas optimal d'acquérir pendant un temps égal les zones périphériques pour une information peu pertinente. De plus, la basse résolution des acquisitions en noyaux X entraîne une absence intrinsèque de finesse et de détails spatiaux essentiellement localisés dans la périphérie de l'espace K, qu'il n'est pas pertinent d'acquérir. Ainsi, des schémas dits non-Cartésiens par comparaison aux acquisitions par lignes à échantillonnage uniforme ont été développés. Par exemple, les schémas radiaux où le centre de l'espace K est plus échantillonné que la périphérie ont permis d'augmenter considérablement les performances des acquisitions. Ainsi, en fonction des possibilités des gradients, il est possible de définir complètement une trajectoire selon une densité d'échantillonnage choisie au préalable ou un parcours particulier. Chaque trajectoire appartenant à un ensemble défini par

$$\mathcal{S}_T = \left\{ s : [0,T] \rightarrow \mathbb{R}^3, ||\dot{s}(t)|| \leq \gamma_X G_{max}, ||\ddot{s}(t)|| \leq \gamma_X S_{max}, \forall t \in [0,T] \right\} \tag{3}$$

Qui prend en compte les contraintes matérielles imposées par la valeur maximale d'intensité des gradients G_{max} et leur temps de commutation (Slew Rate): S_{max} défini par :

$$||G(t)|| \leq G_{max} \qquad ||\dot{G}(t)|| = \left|\left| \frac{dG(t)}{dt} \right|\right| \leq S_{max} \qquad \forall t \in [0,T] \tag{4}$$

Lors de mes explorations j'ai travaillé avec des séquences radiales, spirales et la combinaison des deux, à la fois pour des schémas 2D et 3D. Il s'agit en particulier des séquences TWIRL (TWIsting Radial Lines) [Jackson 1992] en 2D et de TPI (Twisted Projection Imaging) [Boada 1997c] en 3D qui comportent un segment radial de longueur variable et un segment spiralé ou de la séquence 3D FLORET (Fermat Loop ORthogonaly Encoded Trajectory) [Pipe 2011] composée de hubs de spirales entrecroisés. Le schéma d'acquisition de ces séquence est illustré par la Figure 13. De tels schémas d'encodage spatial de l'espace s'obtiennent à l'aide d'une forme prédéfinie du courant circulant dans les gradients et permettant de modifier localement le champ magnétique vu par les noyaux. En appliquant simultanément deux gradients dans différentes directions, il est possible, de générer des spirales avec une forme sinusoïdale du courant.

Reconstruction des images

L'utilisation de trajectoires non-Cartésiennes pose un problème de reconstruction de données qu'il faut résoudre. En effet, comme les données ne sont plus acquises selon une grille uniforme il

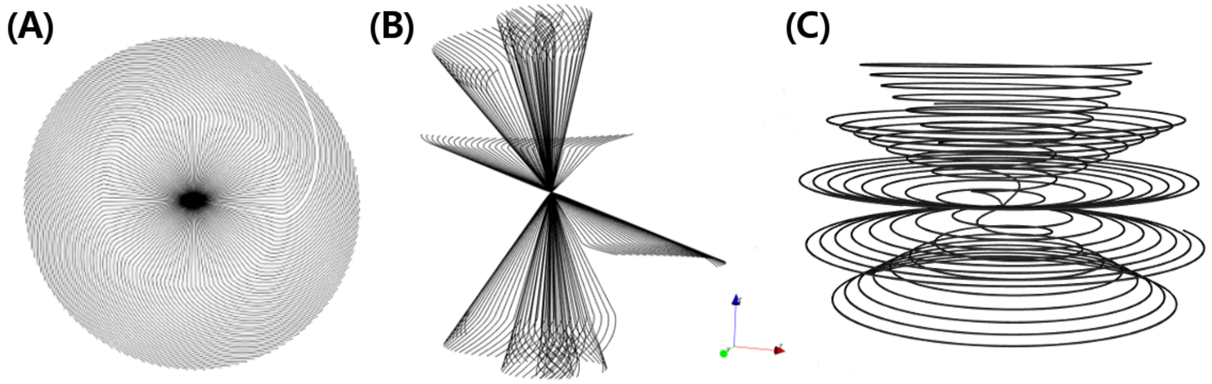

Figure 13: Exemples de trajectoires : 2D TWIRL [Jackson 1992], 3D TPI[Boada 1997c], 3D FLORET[Pipe 2011]

n'est pas possible d'utiliser la transformée de Fourier inverse permettant de passer de l'espace des fréquences spatiales (espace K) à l'espace image.
Pour résoudre ce problème différentes méthodes ont été développées:

- Le "*gridding*", qui consiste à projeter sur une grille cartésienne, grâce à une pondération spatiale des points acquis hors de celle-ci. Un noyau de pondération spécial est alors utilisé et dans notre implémentation il s'agit d'un noyau de Kaiser Bessel [Jackson 1991]. Ensuite, il est possible d'appliquer la transformée de Fourier inverse pour reconstruire l'image acquise selon:

  $$m(x,y,z) = \mathcal{F}^{-1}\left(\left(\frac{M(u,v,w).S(u,v,w)}{\rho(u,v,w)} * K(u,v,w)\right).\text{Ш}(u,v,w)\right) \qquad \text{[Jackson 1991]} \quad (5)$$

  Où M correspond aux valeurs échantillonnées du signal, S leur distribution spatiale, ρ est la fonction de compensation de densité liée à la trajectoire d'acquisition et à la distribution spatiale des échantillons, K est le noyau de pondération spatiale utilisé et Ш est un peigne de Dirac tridimensionnel modélisant une grille uniforme.

- Les transformées de Fournier Non Uniformes (NUFFT) [Dutt 1993][Fessler 2003] ou non équidistribuées (NFFT) [Keiner 2008] qui consistent en une redéfinition de la transformée de Fourier pour prendre en compte un espacement variable entre les différents échantillons.

- La modélisation par problème inverse qui permet de reconstruire une image par minimisation d'une fonction d'énergie convexe mais non nécessairement continue. Un tel problème permet de faire intervenir différents types de régularisation spatiale comme par exemple une décomposition en ondelettes [Guerquin-Kern 2011] ou différents types de contraintes sur les intensités de l'image reconstruite et ce avec différentes normes. Durant cette thèse, j'ai travaillé avec le problème suivant :

  $$\hat{x} = \frac{1}{2}\left(||\boldsymbol{A}x - y||_2^2 + \lambda||x||_1\right) \qquad (6)$$

  Où y est l'ensemble des mesures réalisées, $\hat{x}$ est l'estimation des coefficients de la décomposition en ondelette, $\boldsymbol{A} = F_\Omega^*\Psi$ est la matrice modélisant l'acquisition avec F_Ω^* la transformée de Fourier non uniforme, Ψ^* est la transformée en ondelettes telle que l'image reconstruite soit $\rho = \Psi x$.

J'ai implémenté une version d'un algorithme de gridding en python et un environnement complet de traitement des données brutes acquises par la machine a été développé. En effet, pour les acquisitions Cartésiennes, le système de traitement des images du scanner IRM est capable de reconstruire les images. Les résultats sont très souvent exportés sous format DICOM. En revanche, dans le cas d'acquisitions non-Cartésiennes, aucune fonction n'est implémentée et il est nécessaire de travailler directement sur les données brutes. La NUFFT et la NFFT ont été utilisées dans l'environnement Matlab (The Mathworks, Natick, USA) ainsi qu'une implémentation d'un algorithme d'optimisation nommé FISTA (Fast Iterative Shrinkage Thresholding Algorithm) [BECK 2009]. Cet algorithme, initialement développé pour de l'imagerie 2D par Nicolas CHAUFFERT durant sa thèse, a été modifié et appliqué à des données 3D issues de nos acquisitions.

Sous échantillonnage et acquisitions comprimées

Les schémas d'encodage non-Cartésiens sont très intéressants pour optimiser la quantité de signal acquis, offrant ainsi une possibilité de reduction du temps d'acquisition via un possible sous échantillonage. Il y a une dizaine d'années une équipe de recherche américaine [LUSTIG 2007] a développé une méthode de sous échantillonnage permettant de s'affranchir de la limite théorique formulée par le critère d'échantillonnage optimal de Shannon-Nyquist. En effet, en introduisant une connaissance a priori sur la structure et les caractéristiques du signal échantillonné, il est possible de réduire le nombre d'échantillons nécessaires à sa description: c'est l'acquisition comprimée ("*Compressed Sensing*"). L'application de cette technique a été faite pour les signaux RMN dont la structure peut être très bien décrite par un nombre restreint de coefficients en exploitant leur décomposition sur des bases de fonctions autres que les fonctions trigonométriques de l'analyse de Fourier. De nombreuses bases de fonctions telles que les ondelettes ou leurs dérivées (shearlet, curvelet,...) [TSAI 2012, **?**] peuvent être utilisées. Une contrainte importante est que le signal à analyser doit présenter une décomposition parcimonieuse ("*sparse*") selon la base de fonctions choisie, c'est à dire présenter un nombre minimal de coefficients non nuls. La méthode de sous échantillonnage doit également répondre à des contraintes précises en ayant un schéma stochastique pour ne pas introduire de bruit de structure causé par un schéma déterministe.

Nous avons appliqué et exploré ces nouvelles méthodes d'acquisition pour l'imagerie des noyaux X car elles présentent un fort potentiel de réduction du temps d'acquisition. Deux types d'explorations peuvent être réalisées: une exploration prospective où l'acquisition est directement réalisée avec un schéma aléatoire comme par exemple un "*golden angle radial*" [WINKELMANN 2007], ou alors de manière rétrospective en partant d'un échantillonnage complet qui est, lors de la reconstruction, sous-échantillonné selon différents schémas. Certaines précautions sont cependant à prendre car cette méthode présente un comportement intrinsèque de lissage des images. En effet, la suppression de coefficients de détails dans la décomposition en ondelette peut dégrader la fonction d'étalement du point (PSF) de l'acquisition et dégrader la résolution spatiale théorique de l'image. Une optimisation des paramètres de pondération (dans notre cas λ) permet de contrôler cet effet.

Post traitement, corrections et mesures

Une fois reconstruites, les données doivent être corrigées pour différents effets physiques et biais qui peuvent venir modifier le signal. En effet, les acquisitions à Echo de Gradient Spoilées (SPGR) produisent un signal qui dépend des constantes de relaxation du noyau étudié et des propriétés de l'antenne utilisée pour exciter et recueillir les signaux:

$$S = \rho B_1^- \frac{1 - e^{-TR/T_1}}{1 - cos(\alpha) e^{-TR/T_1}} sin(\alpha) e^{-TE/T_2^*} \text{[HAACKE 1999]} \tag{7}$$

Ce qui dans le cas de noyaux quadripolaires, dans un environnement entrainant un dédoublement des constantes de relaxations, tel que le Sodium dans les tissus se reformule suivant :

$$S = \rho B_1^- \frac{(1-(0.8e^{-TR/T_{1l}} + 0.2e^{-TR/T_{1r}}))sin(\alpha)}{1-cos(\alpha)(0.8e^{-TR/T_{1l}} + 0.2e^{-TR/T_{1r}})} \left(0.6e^{-TE/T_{2r}^*} + 0.4e^{-TE/T_{2l}^*}\right) \qquad (8)$$

Avec T_{Xl} et T_{Xr} les composantes lentes et rapides des relaxations biexponentielles et

$$\gamma_{Na} \approx \frac{1}{4}\gamma_H \qquad (9)$$

Un premier élément important est l'inhomogénéité du champ statique B_0 qui peut engendrer des variations locales des constantes de relaxation et qui résulte par exemple d'une hétérogénéité de l'objet comme par exemple les cavité sinusales ou auditives chez l'Homme. Pour corriger ces inhomogénéités, il existe une procédure spéciale: le "*shim*" qui consiste à homogénéiser le champ magnétique grâce à des bobines annexes. Grâce à l'aide de Franck MAUCONDUIT, l'ingénieur Siemens avec lequel nous travaillons, j'ai pu mettre en œuvre une procédure pour réaliser cette opération en noyaux X. Il est également possible, grâce à une imagerie de phase basée sur deux échos de calculer une carte du champ pour en visualiser les variations spatiales.
Un second élément important est lié à l'antenne, utilisée à la fois pour exciter l'échantillon, et manipuler son aimantation puis pour recueillir le signal RMN émis lors de la relaxation. Ainsi, selon sa géométrie et son design chaque antenne possède des propriétés spécifiques à savoir un champ d'excitation B_1^+ et un profil de réception B_1^-, qui ne sont pas nécessairement les mêmes et qui varient spatialement en fonction de la nature, la géométrie de l'objet étudié et l'intensité du champ magnétique auquel l'exploration a lieu. En effet, la fréquence de résonance des différents noyaux sensibles à la RMN est définie par la relation de Larmor:

$$\omega_0 = 2\pi f_0 = \gamma_X B_0 \qquad (10)$$

Ou γ_X est le rapport gyromagnétique propre à chaque noyau en raison de sa structure physique (voir le tableau 1.1). Ainsi, lorsqu'on augmente le champ, la fréquence d'excitation augmente, la longueur d'onde diminue de manière proportionnelle à l'intensité du champ. Si la longueur d'onde devient trop faible, c'est à dire inférieure à l'ordre de grandeur de l'objet étudié, des variations spatiales de l'excitation vont se produire et donner lieu à une inhomogénéité importante du champ d'excitation B_1^+. Il est donc nécéssaire selon le champ utilisé et le noyau étudié d'acquérir des cartes de champs pour corriger ses possibles variations spatiales. Pour ce faire différentes méthodes sont possibles, nous en avons essentielement utilisé deux: la méthode de l'angle double qui permet par acquisition de deux images avec un angle de bascule et l'angle double d'extraire une estimation de la carte de B_1^+ selon:

$$\alpha(r) = arccos\left(\left|\frac{I_{2\alpha}(r)}{2I_{\alpha}(r)}\right|\right) \qquad \text{[Stollberger 1988]} \qquad (11)$$

J'ai également utilisé la séquence XFL [AMADON 2010], développée à NeuroSpin par Alexis AMADON et Nicolas BOULANT, qui permet également d'obtenir une carte de l'angle de bascule réellement appliqué dans l'objet étudié. La carte obtenue peut, selon les cas, souffrir de la présence de bruit ce qui ne reflète pas ses variations spatiales lentes. Pour réduire l'impact du bruit, nous avons souvent procédé à son interpolation par des polynômes spatiaux multidimensionnels de bas ordre. Il est également nécessaire de caractériser le profil de réception de l'antenne grâce à différentes méthodes. Une méthode simple consiste à acquérir une image avec un faible angle de bascule puis à lisser l'image obtenue pour obtenir une relativement bonne estimation du profil de réception de l'antenne. Enfin, le dernier type de correction possible concerne les paramètres physique du noyau et ses constantes de relaxation. Il est souvent utile, selon le type d'acquisition de corriger pour T_2^* ou pour une repousse incomplète de l'aimantation longitudinale. Différentes méthodes sont possibles, en imagerie ou en spectroscopie pour estimer ces constantes. J'ai par exemple utilisé une méthode d'échos de gradients multiples avec différents temps d'échos pour estimer le T_2^* et la méthode de l'angle de bascule variable (VFA) pour obtenir des cartes de T_1. J'ai également utilisé des séquences de spectroscopie monovoxel ou non localisée pour caractériser les constantes de relaxation de différents noyaux dans différents environnements chimiques. Par exemple, dans le cas d'une acquisition pondérée en densité de spin du Sodium (TSC) il est nécéssaire de corriger pour une saturation incomplète selon [Mirkes 2015]:

$$f_{corr} = \left(\frac{1 - e^{-TR/T_1}}{1 - cos(\theta) e^{-TR/T_1}} \left(0.6 e^{-TE/T_{2f}^*} + 0.4 e^{-TE/T_{2s}^*} \right) \right)^{-1} \quad (12)$$

Après correction de ces paramètres, il est possible d'obtenir des cartes de concentration du noyau étudié. Pour cela, une dernière opération est nécessaire: convertir l'intensité du signal mesurée et corrigée en un niveau de concentration. Il faut donc une référence de concentration qui permettra d'obtenir une relation linéaire entre une intensité et une concentration. Après toutes ces opérations il est possible d'obtenir des cartes de concentration fiables ou les différents biais possibles lors de l'acquisition ont été pris en compte [Coste 2017].

Compartimentation

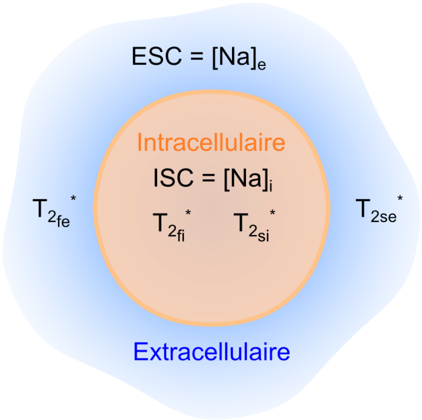

Figure 14: Compartiments cellulaires et de leurs concentrations en Sodium

Un aspect relativement important au regard des applications cliniques de l'IRM du Sodium est la capacité à distinguer la concentration en Sodium intracellulaire et extracellulaire. En effet, il existe un fort gradient de concentration entre les compartiments intra et extracellulaires qui est régulé au moyen de canaux ioniques et de pompes chimiques. C'est le cas en particulier de la pompe Sodium Potassium ATPase (Na^+/K^+ ATPase) dont l'energie de fonctionnement est apportée par l'Adénosine TriPhosphate (ATP). Une anomalie lors de la synthèse en ATP par les mitochondries a pour conséquence un ralentissement puis un arrêt de ces pompes et par conséquent une diminution puis une disparition du gradient de concentration en Sodium. L'étude de l'augmentation de la concentration intracellulaire qui occupe environ 80% du volume tissulaire [Thulborn 2015], typiquement de l'ordre de $[Na]_i \in$ [10-15] mmol.L^{-1} est un très bon indicateur. Malheureusement la mesure de ces concentrations est très compliquée, en raison de la domination de la concentration extra-cellulaire de l'ordre de $[Na]_e \in$ [145-150] mmol.L^{-1} et de la faible résolution des images.

Réaliser cette compartimentation est extrêmement long et demande la mise en œuvre de séquences complexes composées de nombreuses impulsions radio fréquence. Ces méthodes exploitent les cohérences quantiques d'ordres élevés qui correspondent à des transitions entre le niveau d'énergie le plus élevé du Sodium et le niveau fondamental. En effet, contrairement à l'Hydrogène qui par effet Zeeman présente deux niveaux d'énergie distincts correspondants aux orientations parallèles et antiparallèles des spins par rapport à B_0, le Sodium présente lui 4 niveaux d'énergie. Ainsi, plusieurs transitions entre les niveaux sont possibles et leur existence est fonction de l'environnement chimique du noyau. En effet, dans un environnement liquide avec diffusion isotrope rapide devant le temps de corrélation microscopique, le Sodium présente seulement des transitions uni quanta entre ses quatre niveaux. En revanche, dans un environnement organisé où la diffusion est anisotrope et ralentie fortement, le Sodium présente en particulier la transition de triple quanta entre le niveau de plus haute énergie et le niveau fondamental.

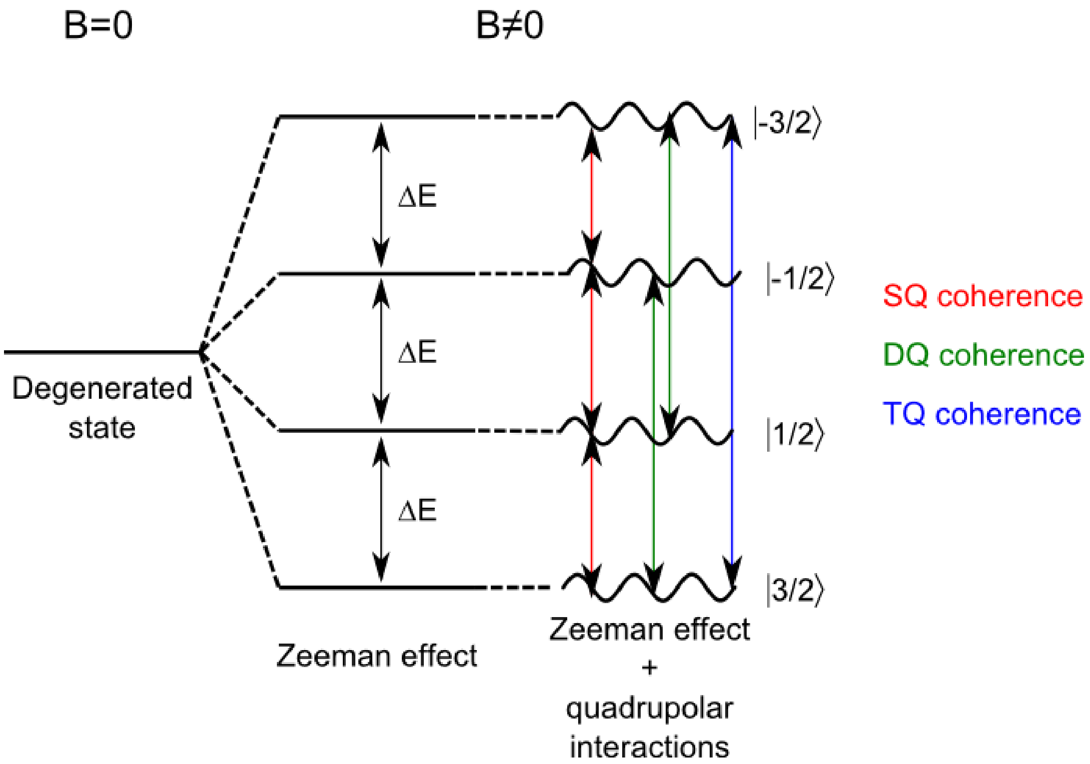

Figure 15: Transitions possibles pour un noyau quadripolaire dans un environnement tissulaire oú l'EFG n'est pas de moyenne temporelle nulle.

Ainsi, la méthode la plus avancée repose sur le principe du filtrage quantique (TQF) [Wimperis 1992] basé sur une excitation particulière de l'atome de Sodium, via trois impulsions radiofréquence de haute énergie combiné dans un cyclage de phase, pour ne selectionner que le seul signal provenant de cette transition a triple quanta.

Cette méthode de filtrage quantique est très coûteuse en énergie rayonnée (DAS ou SAR) et donne lieu à un signal très faible et très fugace à acquérir ce qui complexifie d'autant plus l'application à l'imagerie. Des applications ont néanmoins été réalisées chez l'Homme, à Ultra Haut Champ, par une équipe New Yorkaise très récemment [Petracca 2015]. D'autres méthodes basées sur des différences d'images ont été développées. La première soustrait une image du Sodium présetnatn les transition mono-quanta à une acquisition totale [Benkhedah 2013], la seconde se base sur les différents temps de relaxations pour soustraire une acquisition à long temps d'écho d'une acquisition totale faisant apparaitre les zones à courts temps d'écho [Qian 2015]. Enfin une autre solution, que nous avons commencé à explorer consiste en une estimation de la contribution du signal intracellulaire au signal total mesuré lors d'une exploration où le Sodium est excité sans sélection quantique. Une acquisition avec de multiple échos couvrant une large partie de la relaxation permet ensuite par comparaison à un modèle multiparamétrique d'estimer les différentes propriétés des tissus exprimées dans le signal mesuré.

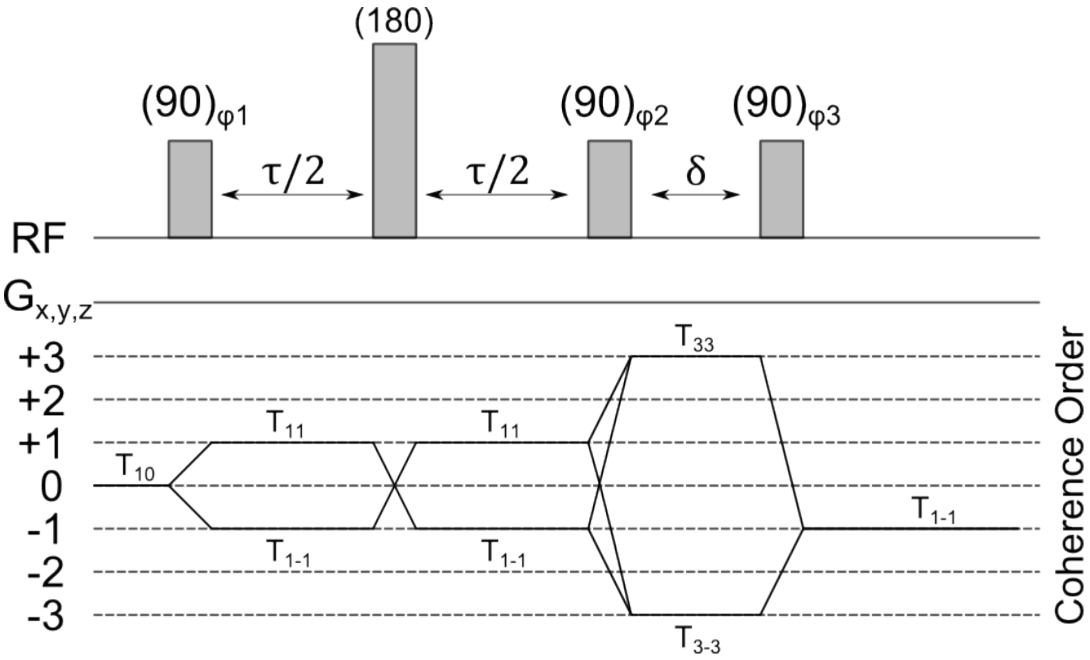

Figure 16: Chronogramme d'une séquence TQF insensible aux inhomogénéités de B_0 [Hancu 1999] ainsi que du diagramme de cohérences.

Expérimentations et applications cliniques des méthodes de caractérisation pour le Phosphore, le Sodium et le Lithium

Imagerie des métabolites phosphorés

L'étude des métabolites phosphorés par spectroscopie RMN est un domaine de recherche relativement ancien permettant l'étude de nombreux phénomènes biologiques ou métaboliques. En revanche, l'étude de ces métabolites par IRM est beaucoup plus récente [Lu 2013] et très peu d'équipes travaillent sur cet aspect. En effet, en raison d'une très basse concentration *in vivo*, de l'ordre de quelques millimoles par litre, le signal disponible est très faible rendant compliquée les applications d'imagerie. L'application de l'imagerie permet de s'intéresser à la distribution spatiale d'un seul métabolite en procedant à une excitation spectrale sélective de celui ci. Pour cela, il est nécessaire dans un premier temps d'acquérir le spectre du Phosphore présent dans l'objet étudié pour déterminer les fréquences de résonance des différents métabolites comme illustré Figure 17. Ensuite, il est nécessaire d'implémenter une impulsion de sélection spectrale, de bande passante adéquate, centrée autour de la fréquence du métabolite choisi. Le spectre illustre la présence importante de PhosphoCréatine (PCr), de deux des trois résonances de l'Adénosine TriPhosphate (γATP et αATP), de Phospho Mono et Di Ester (PME/PDE), de Phosphore Inorganique (Phosphate, Pi) et de Nicotinamide Adénine Dinucléotide (NAD). Ainsi en créant une impulsion RF centrée sur l'un d'eux et avec une bande passante suffisamment restreinte il est possible de réaliser une sélection spectrale qui se traduit ici par une sélection chimique. La bande passante de l'impulsion étant inversement proportionnelle à sa durée, il est souvent nécessaire de recourir à des impulsions longues afin d'obtenir une largeur de bande satisfaisante. Comme illustré Figure 18, nous avons choisi une impulsion Gaussienne. Le schéma d'encodage utilisé est indépendant de l'excitation et peut donc être libre. Néanmoins, le signal étant très faible et pouvant être de courte durée, il est intéressant d'employer une trajectoire Non Cartésienne avec un temps d'écho court comme présenté précedemment. Dans notre cas nous avons utilisé la trajectoire TPI [Boada 1997c] illustrée Figure 13. Pour

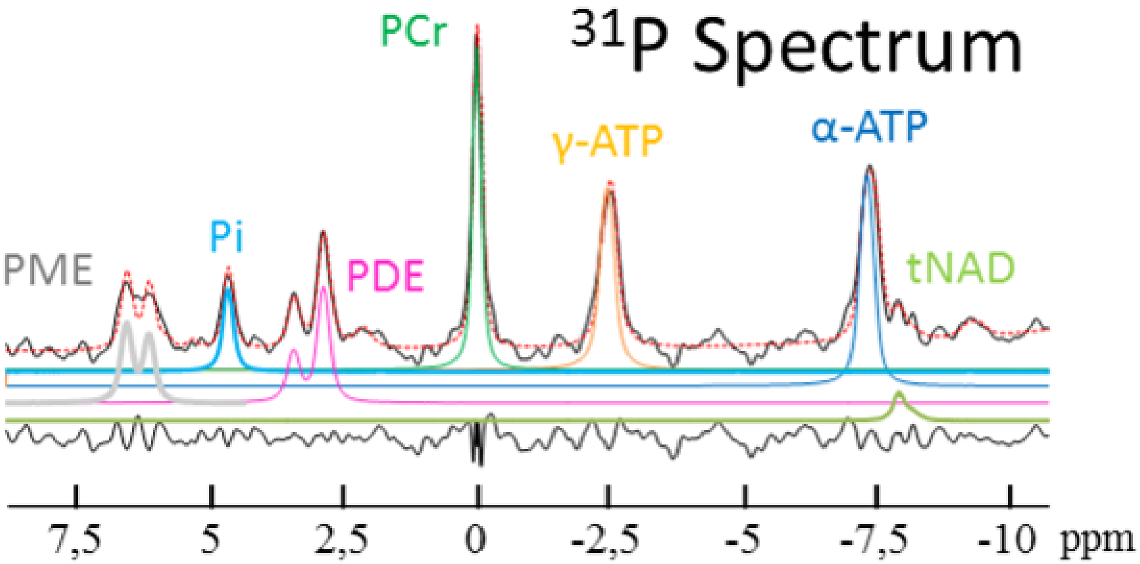

Figure 17: Spectre du Phosphore cérébral acquis à 7 T chez un volontaire sain (Figure d'Alfredo Lopez Kolkovsky)

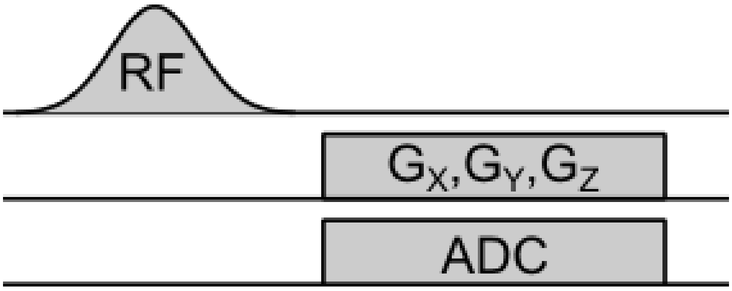

Figure 18: Illustration d'un chrono-gramme général d'une séquence avec sélection spectrale

tester l'implémentation de la séquence nous avons développé un fantôme dédié et composé de différents compartiments contenant différents métabolites phosphorés. L'expérimentation a consisté en 3 acquisitions de 10 minutes à une résolution de 10mm isotrope. Les angles de bascule ainsi que la largeur spectrale de l'impulsion ayant été au préalable optimisés. La Figure 19 illustre les résultats obtenus et montre que malgré une résolution spatiale assez basse il est possible de séparer proprement les différents métabolites de notre fantôme. Des applications *in vivo* à 7 T et à 3 T permettront d'optimiser plus finement les paramètres d'acquisition et en particulier la résolution spatiale visée vis à vis du temps d'acquisition disponible et des objectifs de l'étude. Malheureusement, par manque de temps des acquisitions *in vivo* n'ont pas encore pu être réalisées. Des améliorations pour des études spécifiques de transfert de saturation entre métabolites phosphorés pourraient être implémentées [Du 2007].

Une application *in vivo* a permis d'optimiser la résolution spatiale et la durée d'acquisition en fonction de la concentration réelle du métabolite étudié. De plus, il apparait nécessaire selon le métabolite considéré d'implémenter des bandes de saturation (*Outer Volume Suppression (OVS)*) pour s'affranchir du signal provenant des structures musculaires crâniennes. L'implémentation des méthodes de transfert de saturation nécessite également d'évaluer l'augmentation du DAS (Débit

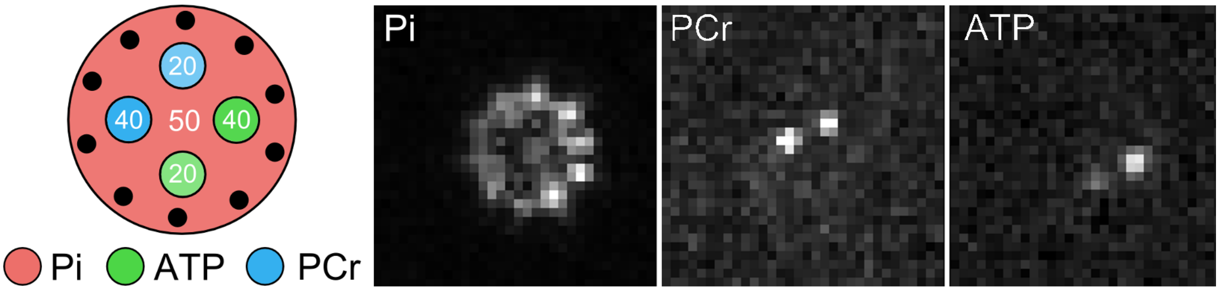

Figure 19: Design du phantom utilisé, des métabolites et de leur concentration ainsi que des acquisitions réalisées du Phosphate Inorganique, de la Phosphocréatine et de l'ATP

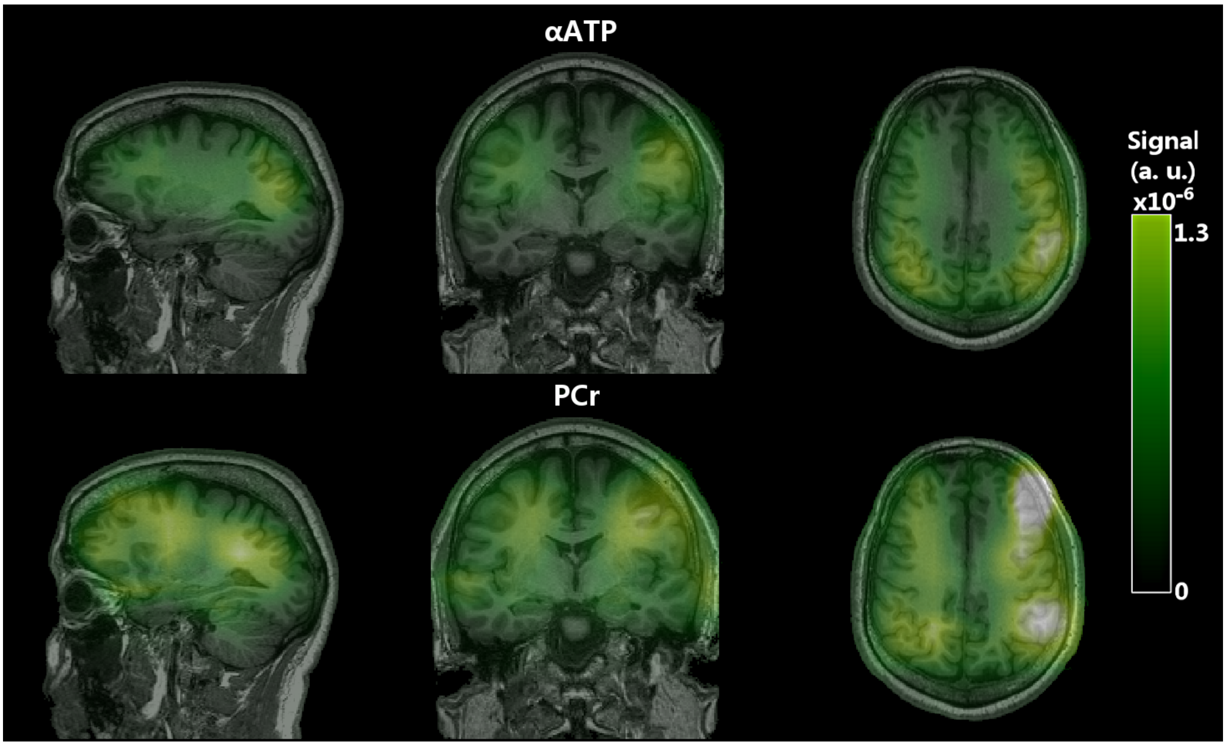

Figure 20: Images de Phosphocreatine et d'ATP obtenue à 7 T chez un volontaire sain.

d'Absorption Spécifique (*SAR*)) qui en résulterait en raison de l'utilisation de très nombreuses impulsions comme utilisé dans la séquence BISTRO [Luo 2001].

Mesures *in vivo* de la concentration et de la relaxation du Sodium

Mes recherches ont permis de développer un pipeline, *VaSCo* (**Va**riable Flip Angle pipeline for **S**odium **Co**ncentration Measurements) [Coste 2017], de quantification absolue de la concentration totale du Sodium en prenant en compte et en corrigeant les différents paramètres présentés précédemment. Notre pipeline nous permet également de produire une carte de la vitesse de relaxation longitudinale via le paramètre T_1. Les acquisitions étant réalisée avec une pondération T_1, elles permettent d'augmenter considérablement le signal acquis par unité de temps comparé à une acquisition pondérée en densité de spins. Des tests préliminaires ont été réalisés en IRM du Phosphore sur fantôme à 7 T pour valider la méthode. Ce pipeline a ensuite été implémenté sur un

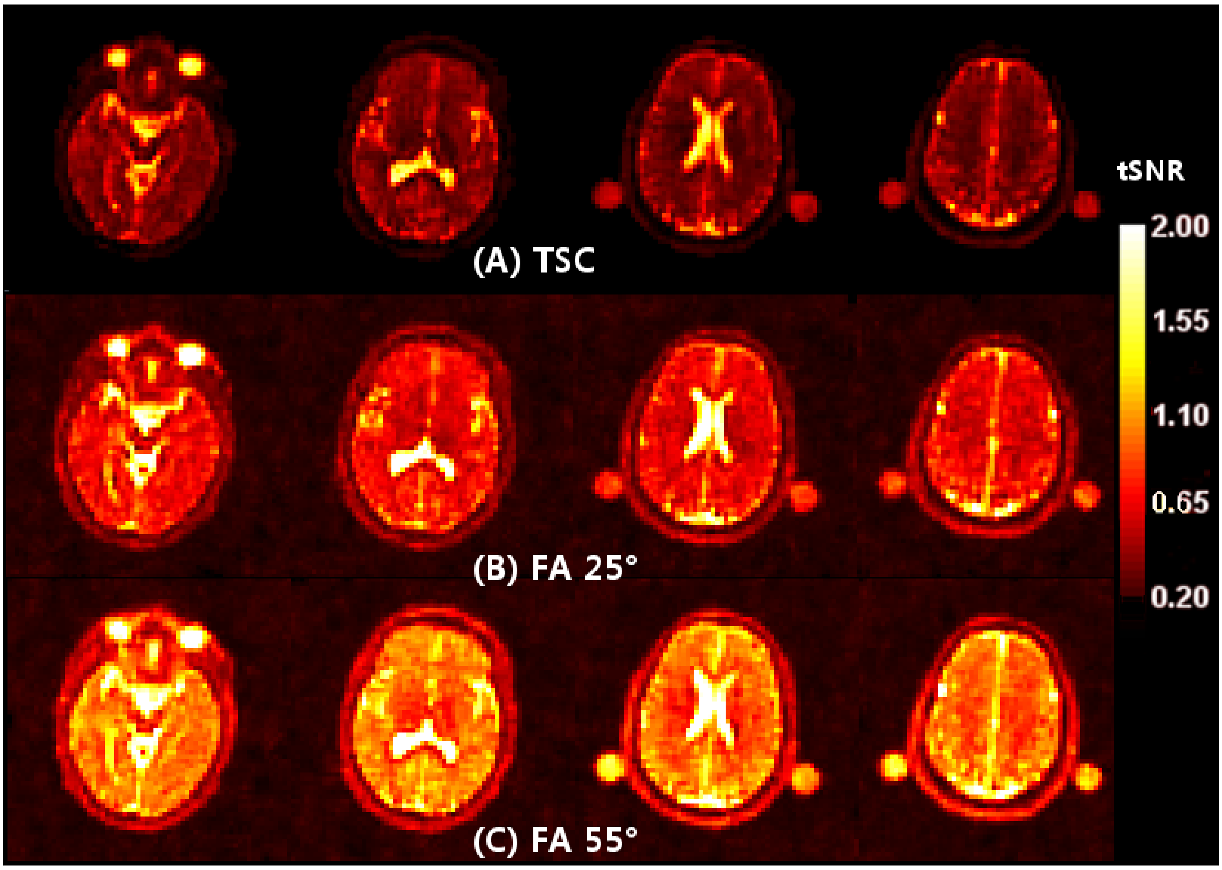

Figure 21: Comparaison du SNR par unité de temps de l'acquisition pondérée en densité de spin (TSC) et celles pondérées T_1

scanner clinique à 3 Tesla de l'Hôpital Universitaire d'Aix la Chapelle en Allemagne. Une validation a d'abord été réalisée sur un fantôme spécialement conçu puis appliqué chez des volontaires Humains sains. Notre pipeline a été comparé à l'acquisition de référence dans les études cliniques en Sodium: la TSC (Total Sodium Concentration) qui consiste en une acquisition pondérée en densité de spins avec une bascule complète dans le plan transverse de l'aimantation (angle de 90°) et un long temps de répétition (TR) pour permettre une repousse complète de l'aimantation longitudinale. Dans les deux acquisitions, la séquence FLORET [PIPE 2011] a été utilisé avec un temps d'écho ultra-court (UTE) de 100 μs pour minimiser les pertes de signal. Nous avons, dans les deux cas, corrigé les images acquises, soit avec notre pipeline en intégrant les champs B_1^+ et B_1^- et le T_1, soit avec une correction de saturation pour l'acquisition TSC. Nous avons ensuite calibré le signal à l'aide des références extérieures de concentration, pour enfin comparer les cartes de concentration obtenues avec les deux méthodes. En raison de la faible résolution de nos images : 4mm isotrope, nous avons choisi d'utiliser le modèle bicompartimental défini par :

$$[Na]_{tissus} = [Na]_{intra} \times V_{intra} + [Na]_{extra} \times V_{extra} \qquad \text{[CONSTANTINIDES 2001]} \tag{13}$$

$$[Na]_{tissus} = [10 - 12] \times 0.81 + [145 - 150] \times 0.19 = [36 - 39] mmol.L^{-1} \qquad \text{[THULBORN 2015]} \tag{14}$$

Nos résultats *in vivo* présentés Figure 23 fournissent des valeurs relativement proches de l'interval théorique défini par ce modèle ce qui est relativement satisfaisant. Une étude sur plusieurs sujets et différents tissus dans différentes aires cérébrales a confirmé ces résultats et montre qu'ils sont comparables à ce qui est reporté dans la littérature par différentes équipes de recherches. Concernant les

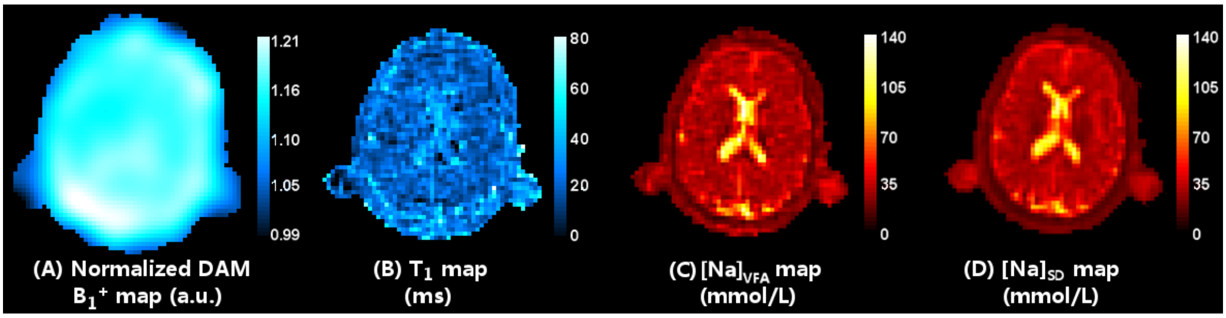

(A) Normalized DAM B_1^+ map (a.u.) (B) T_1 map (ms) (C) $[Na]_{VFA}$ map (mmol/L) (D) $[Na]_{SD}$ map (mmol/L)

Figure 22: Résultats obtenu avec notre pipeline (VaSCo) et l'état de l'art (TSC)

mesures de la constante de relaxation longitudinale T_1 nos mesures sont en accord avec les valeurs mesurées par d'autres équipes utilisant les méthodes de référence [Madelin 2013]. Il semblerait que les acquisitions TSC aient tendance à légèrement sous estimer la concentration tissulaire.

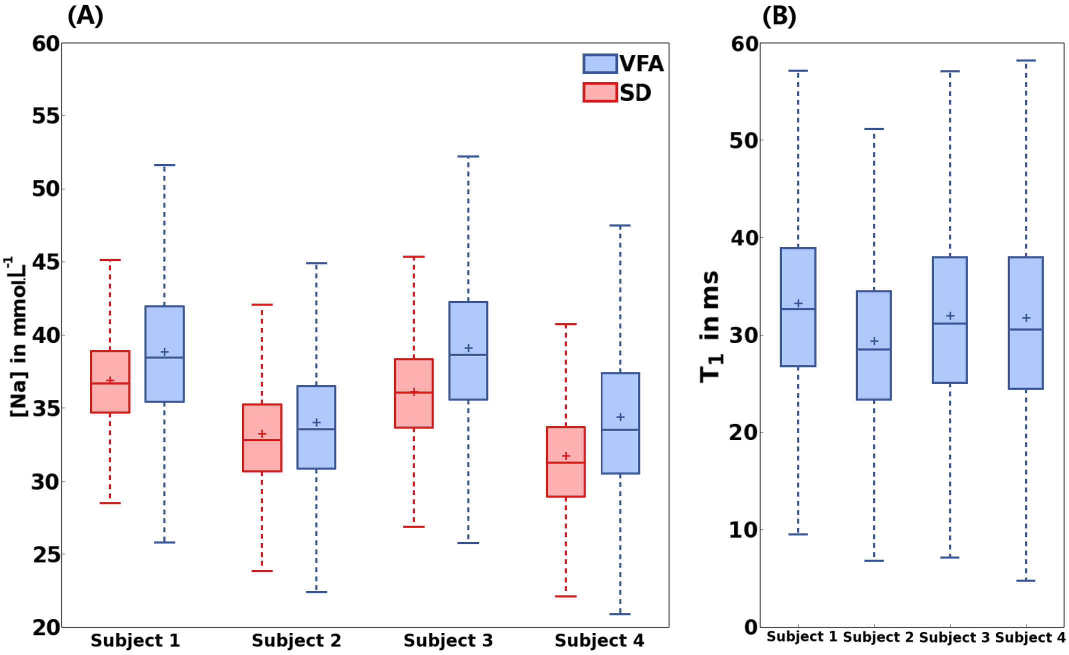

Figure 23: Résultats obtenu avec notre pipeline (VFA) et l'état de l'art (SD)

Des améliorations sont possibles et en particulier une correction de l'effet de volume partiel qui entâche les mesures d'une incertitude dans les régions frontalières de différents tissus, en particulier s'ils présentent des concentrations différentes. L'intérêt de ce pipeline est modéré pour les champs cliniques pour lesquels la fréquence de résonance du Sodium est relativement basse et donc engendrant peu d'inhomogénéités de B_1^+, en revanche il présente des avantages à très hauts champs en particulier pour les futures explorations à 7 T et 11.7T.

Nous nous sommes également intéressés à l'impact de l'algorithme de reconstruction et en particulier de savoir s'il était possible de reconstruire nos données à l'aide de FISTA. La Figure 24 présente nos résultats et les mesures que nous avons pu faire sont relativement similaires à celles réalisées avec une reconstruction NUFFT. Une comparaison des mesures des concentrations et de la constante de relaxation longitudinale a été réalisée et est illustrée Figure 28. Les résultats étant relativement proches l'utilisation d'un algorithme de reconstruction non-linéaire et itératif peut donc

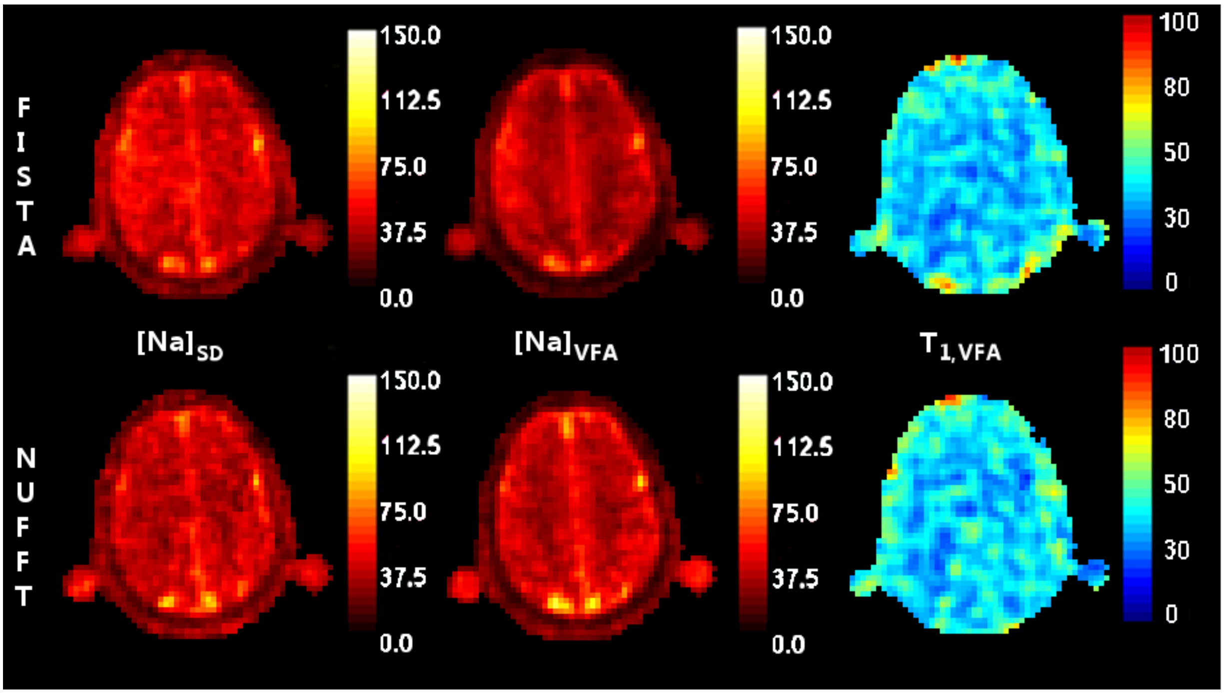

Figure 24: Illustration des résultats obtenu avec notre pipeline (VaSCo) et l'état de l'art (TSC) en comparant la reconstruction FISTA (haut) à la reconstruction NUFFT (bas)

être appliqué de manière satisfaisante à des données non-Cartésiennes d'IRM du sodium *in vivo*. Il faut cependant choisir une valeur adéquate du paramètre de régularisation pour obtenir une image exploitable et un contrôle qualité préalable est nécessaire.

De même, nous avons également tenté d'optimiser la durée d'acquisition du pipeline pour la réduire et le rendre le plus viable cliniquement pour son intégration dans des protocoles de recherche clinique. Nos mesures comparant les résultats entre les deux méthodes sont très encourageantes

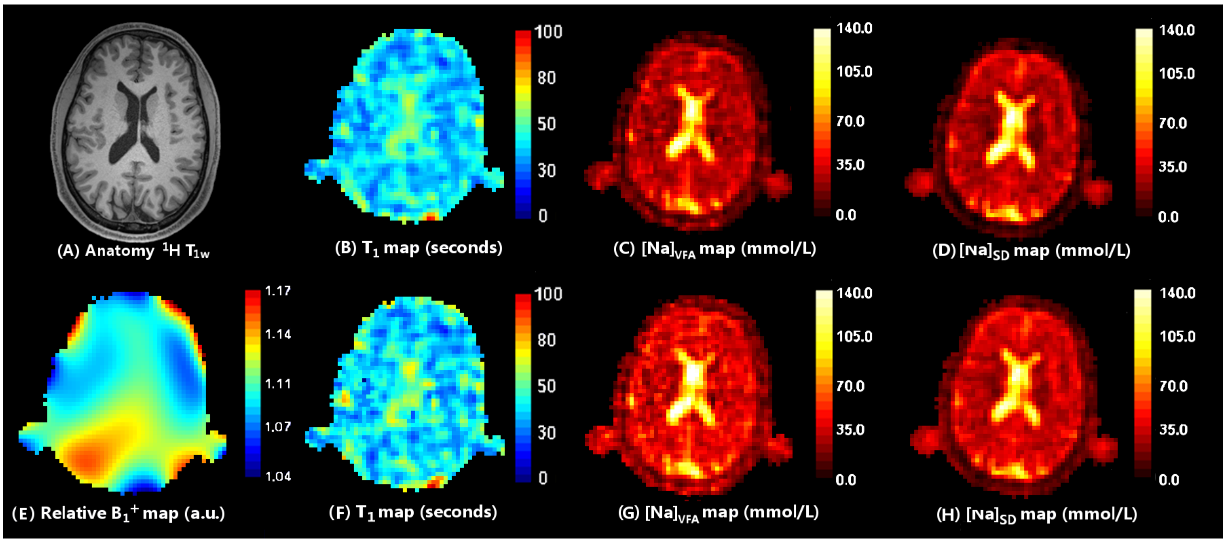

Figure 25: Illustration des résultats obtenu avec une durée de 18 minutes (B-D) et avec une durée de 12 minutes (F-H)

avec une différence d'estimation des paramètres relativement faible comme illustrée par la Figure 28. Les résultats obtenus indiquent qu'il est possible d'obtenir dans un temps clinique une mesure simultanée de la concentration et le T_1 du Sodium dans les tissus cérébraux et ce avec des valeurs en accord avec le modèle et similaires à celles reportées dans la littérature.

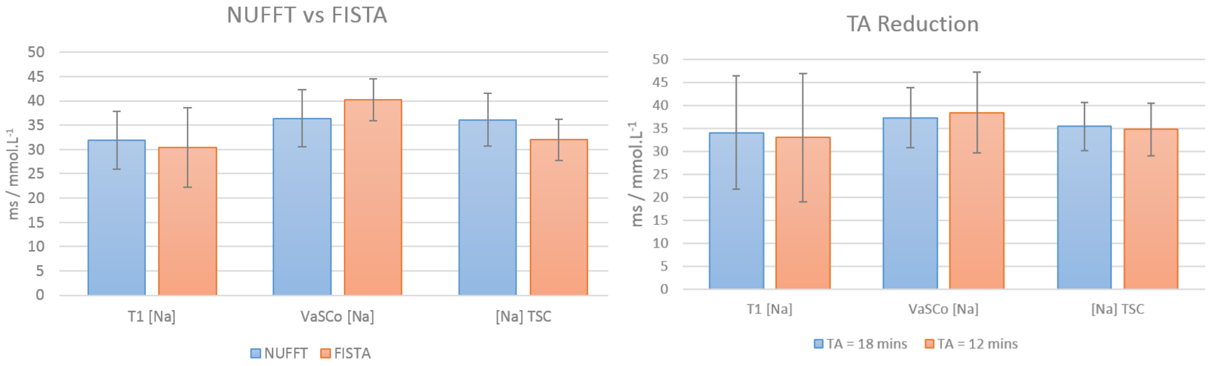

Figure 26: Comparaison des différentes mesures entre les deux méthodes de reconstruction et en réduisant le temps d'acquisition de 18 à 12 minutes.

L'obtention d'une antenne pour l'exploration du Sodium *in vivo* chez l'Homme à 7 T, fin 2017, permettra surement dans un futur proche l'implémentation de ce pipeline pour de nouvelles mesures avec une résolution plus élevée et donc des images de meilleure qualité permettant d'envisager une comparaison entre la matière grise et la matière blanche et l'étude de structures sous-corticales. De même il sera possible d'étudier l'existence d'une différence de concentration entre la matière blanche et la matière grise ainsi que des différences de constantes de relaxation. La séquence TPI que j'ai développée avec l'aide de Sandro ROMANZETTI étant bien indiquée pour ces études.

Caractérisation multiparamétrique de l'ion Sodium

En collaboration avec Lisa LEROI, doctorante au laboratoire, nous nous sommes intéressés à la question de la quantification simultanée des paramètres physiques du Sodium par IRM. L'intérêt de cette méthode est qu'elle évite d'avoir à utiliser plusieurs séquences différentes avec de nombreux paramètres à optimiser pour chacune d'elle. Nous avons pu estimer simultanément les constantes de relaxation longitudinale T_1 et transversale T_2, le Coefficient de Diffusion Apparent (ADC), l'aimantation M_0 ainsi qu'une cartographie de l'angle de bascule (FA) tout en étant robuste aux inhomogénéités du champ statique B_0. Cette méthode : QuICS [DE ROCHEFORT 2015, DE ROCHEFORT 2016b] utilise différents états d'équilibres, des états de configurations et l'effet du déphasage ("*spoiling*") d'aimantation généré par des gradients ou une impulsion RF comme illustré par la Figure 27.
L'extraction quantitative des paramètres est réalisée par une modélisation en problème inverse des données acquises avec différents incréments de spoiling RF. On estime tout d'abord la dérive en phase grâce aux acquisitions réalisées avec les incréments de 0° et 180°. Cette dérive est ensuite soustraite de chaque acquisition SSFP. Enfin l'estimation des cartes paramétriques est obtenue par une minimisation aux moindres carrés non linéaire (Gauss Newton) du fit des signaux complexes avec une simulation de l'équation de Bloch Torrey :

$$\frac{dM}{dt} = \gamma_X M \times B - \frac{M_x\vec{i} + M_y\vec{j}}{T_2} - \frac{(M_z - M_0)\vec{k}}{T_1} + \nabla \cdot D\nabla M \qquad [\text{TORREY 1956}] \tag{15}$$

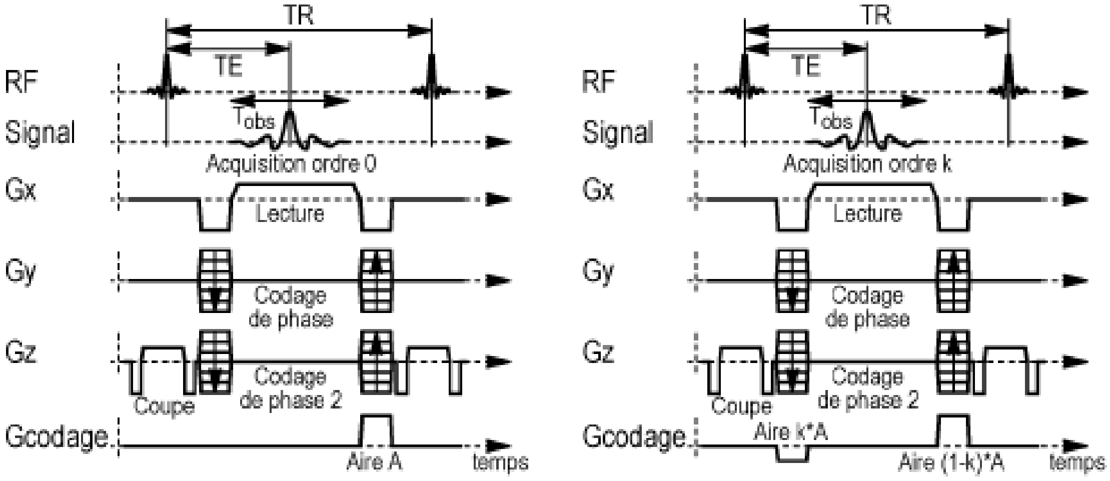

Figure 27: Chronogramme de la séquence QuICS [De Rochefort 2016b].

Ce type de mesures simultanées se développe rapidement en IRM de l'Hydrogène car les temps d'acquisition sont courts et la resolution satisfaisante. Une méthode concurente nommée Fingerprinting [Ma 2013] est actuelement implémentée par Siemens sur ses scanner IRM ce qui illustre l'intérêt croissant pour ces méthodes. L'application de telles méthodes aux Noyaux X n'a jamais été tentée en raison de leur faible concentration comme mentionné précedemment. L'objectif de nos recherches est, dans un premier temps d'appliquer QuICS à l'IRM du Sodium afin d'en évaluer les capacités sur fantôme en comparant rigoureusement nos résultats à la littérature, puis d'en optimiser et améliorer le fonctionnement pour essayer de la rendre viable pour des expériences chez l'Homme. Les différentes expériences que nous avons pu réaliser nous ont fourni des résultats comparables aux mesures obtenues par d'autres groupes de recherche [Leroi 2017]. Les expérimentations avec différents environnements chimiques ont permis de valider la sensibilité de la méthode aux variations possibles des différents paramètres.

Environnement Chimique	Paramètre	QuICS (ms)	Littérature (ms)	Erreur (%)
Solution salée	T_1	59.0 ± 6.85	55	4.4
	T_2	53.7 ± 6.63	55	2.4
2% agar	T_1	48.1 ± 8.92	45	5.3
	T_2	29.8 ± 3.73	24.3 ± 0.9	19.2

Table 9: Mesures de T_1 et T_2 obtenues avec QuICS et comparées avec la littérature [Nagel 2016] pour une concentration de 150 mmol.L^{-}1

La mesure du Coefficient de Diffusion Apparent (ADC) est la plus complexe car elle requiert un moment important des gradients de spoiling et est très sensible aux variations de signal. Ainsi, l'estimation de ce paramètre a entrainé des temps d'acquisition de plusieurs heures (autour de 5h) alors que la seule estimation des constantes de relaxation T_1 et T_2 est possible en moins d'une heure. Afin de réduire le temps d'acquisition, l'implémentation de trajectoires non Cartésiennes permettra une optimisation de la densité d'échantillonnage dans l'espace de Fourier et l'utilisation d'un temps d'écho ultra court augmentera le niveau de signal mesuré. Ainsi, la combinaison de ces deux éléments peut permettre de réduire encore plus le temps d'acquisition.

Imagerie du Lithium

Le protocole d'exploration par IRM clinique a débuté à NeuroSpin le 24 janvier 2017 et sera composé au total de 35 patients bipolaires traités aux sels de Lithium et représentant les deux groupes de patients. Le protocole se compose d'acquisitions réalisées à 3 T et à 7 T. A 3 T, nous avons défini un protocole comportant de l'imagerie anatomique pondérée T_1 une séquence d'imagerie quantitative pour quantifier le T_1, une séquence d'IRM fonctionnelle de repos ("*Resting State fMRI*") et une séquence de spectroscopie pour la quantification des neurotransmetteurs et métabolites. A 7 T différents tests de séquences ont été menés avec Jacques STOUT pour comparer les performances d'une séquence Turbo Spin Echo (TSE) 2D multi-coupes à schéma d'encodage Cartésien ou BLADE ("PROPELLER") [PIPE 1999] avec une séquence à Echo de Gradient non spoilée (FISP) 3D à trajectoire non Cartésienne (TPI). Dans le cas d'un objet fortement concentré avec un T_1 proche d'une dizaine de secondes, l'acquisition multi-coupes en Spin Echo est la plus efficace par la production d'un plus grand signal et une acquisition de toutes les coupes durant un long TR. En revanche, lors d'une expérience à concentration physiologique moyenne chez un patient de 0.5 mmol.L^{-1} la séquence non Cartésienne est redevenue compétitive grâce au schéma d'encodage qui permet d'acquérir l'information plus efficacement et avec une meilleure densité que le schéma Cartésien. J'ai participé à tous les tests et au développement et à l'optimisation du protocole pour son application clinique. Mon travail a permis de réaliser des images du Lithium *in vivo* chez des patients atteints de trouble bipolaire en faisant suite à la première image réalisée aux États Unis il y a quelques années [BOADA 2010]. En utilisant une technique de calibration dédiée, nous avons pu obtenir des cartes quantitatives de la distribution du Lithium dans les tissus cérébraux.

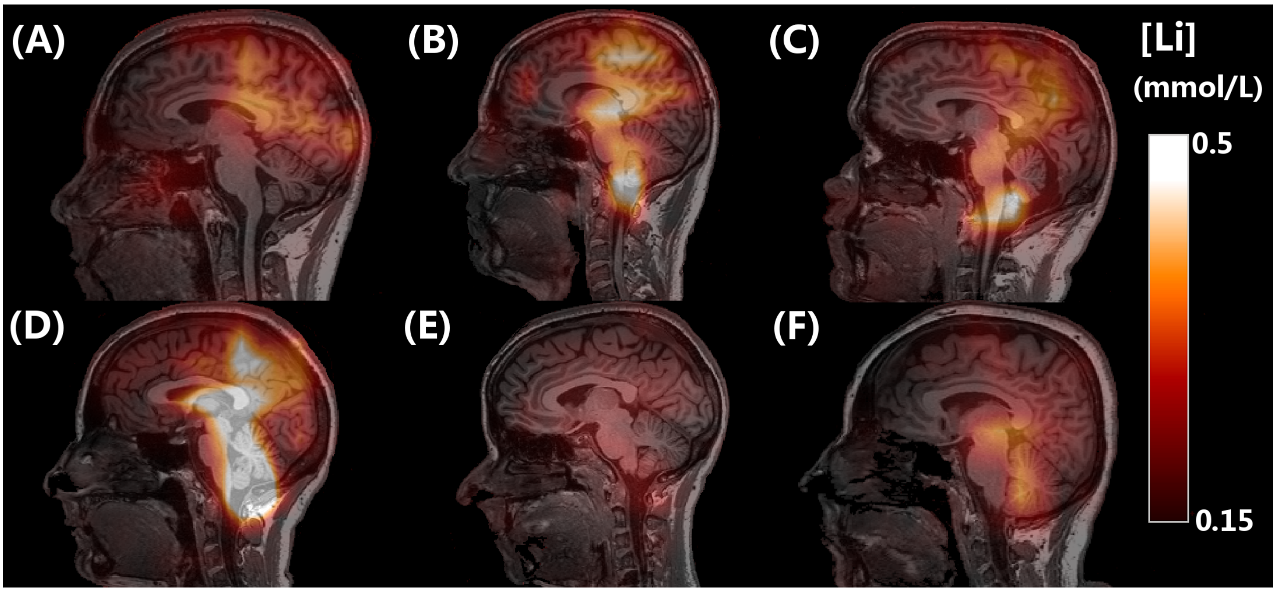

Figure 28: Cartographies quantitatives de la distribution de Lithium dans le cerveau de 6 patients bipolaires.

Conclusion

Le travail de recherche réalisé durant mes trois années de doctorat se situe au carrefour de la physique, des mathématiques, de l'imagerie médicale et de la médecine. Il a permis d'évaluer et de comparer différentes méthodes pour l'imagerie des noyaux X allant de l'acquisition du signal RMN à la reconstruction des images. Nous avons pu appliquer une partie des travaux de Nicolas CHAUFFERT, sur l'acquisition comprimée, aux noyaux X ouvrant la voie à de possibles améliorations. En effet, nous avons pu, dans le cas de l'imagerie des Noyaux X très faiblement concentrés, démontrer l'intérêt de la combinaison d'une séquence non-Cartésienne et d'une reconstruction itérative comparé à une acquisition Cartésienne reconstruite par transformée de Fourier inverse [COSTE 2016]. Les séquences développées et optimisées ainsi que le pipeline de correction et de quantification simultané de la concentration et de la constante de relaxation longitudinale (T_1) sont des outils intéressants qui ont pu être validé *in vivo* chez l'Homme en Sodium mais aussi en Phosphore et en Lithium [COSTE 2017]. L'étude en Lithium sera en particulier étendue à l'échelle européenne par un nouveau financement et la mise en place d'un consortium.

Nous avons également pu, en collaboration avec Lisa LEROI et Alexandre VIGNAUD, appliquer, pour la première fois, *in vitro*, une méthode de quantification multi-paramétrique des propriétés de l'ion Sodium dans différents environnements chimiques. Les résultats obtenus sont très satisfaisants et en accord avec les mesures faites par d'autres équipes de recherche avec d'autres méthodes [LEROI 2017]. Une optimisation de la méthode pour en améliorer l'efficacité en utilisant par exemple un schéma d'encodage non Cartésien combiné à un temps d'écho ultra court (UTE) pourrai permettre d'augmenter le signal acquis et donc de réduire le temps d'acquisition avec pour objectif la viabilité clinique de la méthode.

Les méthodes développées durant cette thèse sont pour certaines déjà utilisées dans le cadre de l'étude *in vivo* en Lithium. Les développements en Sodium et en Phosphore sont utilisés par nos collègues de l'hôpital Universitaire d'Aix la Chapelle, en Allemagne. En particulier pour une étude sur la maladie d'Alzheimer. De plus, certains outils informatiques spécialement développés seront surement utilisés pour d'autres études. En particulier, l'obtention d'une antenne Sodium pour le scanner IRM 7 T ainsi que l'arrivée de l'aimant 11.7 T [VEDRINE 2008] permettront possiblement d'approfondir mes travaux.

Bibliography

[ABRAGAM 1978] A. ABRAGAM and M. GOLDMAN. *Principles of dynamic nuclear polarisation*. Reports on Progress in Physics, vol. 41, no. 3, 1978. (Cited on page 8.)

[ADAM 1987] W.R. ADAM, A.P. KORETSKY and M.W. WEINER. *Measurement of tissue potassium in vivo using 39K nuclear magnetic resonance*. Biophysic Journal, vol. 51, no. 2, pages 265–271, 1987. (Cited on page 6.)

[AHN 1986] C.B. AHN, J.H. KIM and Z.H. CHO. *High-speed spiral-scan echo planar NMR imaging*. IEEE Transactions on Medical Imaging, vol. 5, no. 1, pages 2–7, 1986. (Cited on page 20.)

[ALBERTS 1994] M.S. ALBERTS, G.D. CATES, B. DRIEHUYS, W. HAPPER, B. SAAM, C.S. SPINGER JR and A. WISHNI. *Biological magnetic resonance imaging using laser-polarized 129Xe*. Nature, vol. 370, pages 199–201, 1994. (Cited on pages 6 and 194.)

[ALEXANDER 2008] D.C. ALEXANDER. *A general framework for experiment design in diffusion MRI and its application in measuring direct tissue-microstructure features*. Magnetic Resonance in Medicine, vol. 60, no. 2, pages 439–448, 2008. (Cited on page 108.)

[AMADON 2010] A. AMADON, M.A. CLOOS, N. BOULANT, M.F. HANG, C. J. WIGGINS and H.P. FAUTZ. *Validation of a very fast B1-mapping sequence for parallel transmission on a human brain at 7T*. Proceedings of the 18th International Society of Magnetic Resonance in Medicine, vol. 370, page 2828, 2010. (Cited on pages 44 and 200.)

[ANASTASIOU 2004] A. ANASTASIOU and L.D. HALL. *Optimisation of T2 and M0 measurements of bi-exponential systems*. Magnetic Resonance Imaging, vol. 22, no. 1, pages 67–80, 2004. (Cited on page 108.)

[ANDRASKO 1974] J. ANDRASKO. *Nonexponential relaxation of 23Na+ in agarose gels*. Journal of Magnetic Resonance, vol. 16, no. 3, pages 502–504, 1974. (Cited on page 112.)

[ATKINSON 2011] I.C. ATKINSON, A. LU and K.R. THULBORN. *Clinically Constrained Optimization of flexTPI Acquisition Parameters for the Tissue Sodium Concentration Bioscale*. Magnetic Resonance in Medicine, vol. 66, pages 1089–1099, 2011. (Cited on pages 29 and 126.)

[AVANTS 2011] B. AVANTS, N. TUSTISON and G. SONG G. *Advanced Normalization Tools (ANTS)*, 2011. (Cited on pages 134 and 182.)

[AVDIEVICH 2011] N.I. AVDIEVICH. *Transceiver-Phased Arrays for Human Brain Studies at 7 T*. Applied Magnetic Resonance, vol. 41, no. 2-4, pages 483–506, 2011. (Cited on pages 46 and 139.)

[BABSKY 2005] A.M. BABSKY, S.K. HEKMATYAR, H. ZANG, J.L. SOLOMON and N. BANSAL. *Application of ^{23}Na MRI to Monitor Chemotherapeutic Response in RIF-1 Tumors*. Neoplasia, vol. 7, no. 7, pages 658–666, 2005. (Cited on pages 32 and 196.)

[BABSKY 2008] A.M. BABSKY, S. TOPPER, H. ZANG, Y. GAO, J.R. JAMES, S.K. HEKMATYAR and N. BANSAL. *Evaluation of extra- and intracellular apparent diffusion coefficient of sodium in rat skeletal muscle: Effects of prolonged ischemia*. Neoplasia, vol. 59, no. 3, pages 485–491, 2008. (Cited on page 105.)

[BAE 2012] W.C. BAE, P.C. CHEN, C.B. CHUNG, K. MASUDA, D. D'LIMA and J. DU. *Quantitative Ultrashort Echo Time (UTE) MRI of Human Cortical Bone: Correlation with Porosity and Biomechanical Properties*. Journal of Bone and Mineral Research, vol. 27, no. 4, pages 848–857, 2012. (Cited on page 61.)

[BANGERTER 2016] N.K. BANGERTER, G.J. TARBOX, M.D. TAYLOR and J.D. KAGGIE. *Quantitative sodium magnetic resonance imaging of cartilage, muscle, and tendon*. Quantitative Imaging in Medicine and Surgery, vol. 6, no. 6, pages 699–714, 2016. (Cited on page 33.)

[BEATTY 2005] P.J. BEATTY, D.G. NISHIMURA and J.M. PAULY. *Rapid Gridding Reconstruction With a Minimal Oversampling Ratio*. IEEE Transactions on Medical Imaging, vol. 24, no. 6, pages 799–808, 2005. (Cited on page 23.)

[BECK 2009] A. BECK and M. TEBOULLE. *A fast iterative shrinkage-thresholding algorithm for linear inverse problems*. SIAM Journal of Imaging Science, vol. 2, pages 183–202, 2009. (Cited on pages 25, 77, 128 and 199.)

[BEHL 2016] N.G.R. BEHL, C. GNAHM, P. BACHERT, M.E. LADD and A.M. NAGEL. *Three-dimensional dictionary-learning reconstruction of 23Na MRI data*. Magnetic Resonance in Medicine, vol. 4, no. 75, pages 1605–1616, 2016. (Cited on pages 25 and 128.)

[BENDAHAN 2006] D. BENDAHAN, J.P. MATTEI, S. GUIS, G. KOZAK-RIBBENS and P.J. COZZONE. *Non-invasive investigation of muscle function using 31P magnetic resonance spectroscopy and 1H MR imaging*. Revue Neurologique, vol. 162, no. 4, pages 467–484, 2006. (Cited on pages 33 and 196.)

[BENDEL 1969] P. BENDEL, C.M. LAI and P.C. LAUTERBUR. *31P spectroscopic zeugmatography of phosphorus metabolites*. Journal of Magnetic Resonance, vol. 38, no. 2, pages 343–356, 1969. (Cited on pages 1, 6, 26 and 193.)

[BENDEL 1998] P. BENDEL, A. FRANTZ, J. ZILBERSTEIN, G.W. KABALKA and Y. SALOMON. *Boron-11 NMR of borocaptate: Relaxation and in vivo detection in melanoma-bearing mice*. Magnetic Resonance in Medicine, vol. 39, no. 3, pages 439–447, 1998. (Cited on pages 6 and 193.)

[BENKHEDAH 2013] N. BENKHEDAH, P. BACHERT, W. SEMMLER and A.M. NAGEL. *Three-Dimensional Biexponential Weighted 23Na Imaging of the Human Brain with Higher SNR and Shorted Acquisition Time*. Magnetic Resonance in Medicine, vol. 70, pages 754–765, 2013. (Cited on pages 30 and 202.)

[BENKHEDAH 2014] N. BENKHEDAH, P. BACHERT and A.M. NAGEL. *Two-pulse biexponential-weighted 23Na MRI*. Journal of Magnetic Resonance, vol. 240, pages 67–76, 2014. (Cited on pages 30 and 114.)

[BERNSTEIN 2004] M.A. BERNSTEIN, K.F. KING and X.J. ZHOU. Handbook of mri pulse sequences. Elsevier, 2004. (Cited on pages 6, 60, 61, 87, 103, 136 and 182.)

[BIERI 2011] O. BIERI, K. SCHEFFLER, G.H. WELSCH, S. TRATTNIG, T.C. MAMISCH and C. GANTER. *Quantitative mapping of T2 using partial spoiling. Magnetic Resonance in Medicine*. Magnetic Resonance in Medicine, vol. 66, no. 2, pages 410–418, 2011. (Cited on page 100.)

[BILLER 2015] A. BILLER, S. BADDE, A. NAGEL, J.-O. NEUMANN, X.W. WICK, A. HERTENSTEIN, X.M. BENDSZUS, F. SAHM, N. BENKHEDAH and J. KLEESIEK. *A, Improved Brain Tumor Classification by Sodium MR Imaging: Prediction of IDH Mutation Status and Tumor Progression*. American Journal of NeuroRadiology, 2015. (Cited on pages 32 and 196.)

[Biller 2016] A. Biller, I. Pflugmann, S. Badde, R. Diem, B. Wildemann, A.M. Nagel, J. Jordan, N. Benkhedah and J. Kleesiek. *Sodium MRI in Multiple Sclerosis is Compatible with Intracellular Sodium Accumulation and Inflammation-Induced Hyper-Cellularity of Acute Brain Lesions*. Scientific Reports, vol. 6, no. 31269, 2016. (Cited on pages 2 and 84.)

[Black 2010] J.A. Black, J. Newcombe and S.G. Waxman. *Astrocytes within multiple sclerosis lesions upregulate sodium channel Nav1.5*. Brain, vol. 133, pages 835–846, 2010. (Cited on page 31.)

[Blanc 2016] J. Blanc, F. Boumezbeur, Y. Le Fur, P. Aubourg, C. Chiron, C. Sevin and L. Hertz-Pannier. *Imagerie Spectroscopique à 3 T dans la Leucodystrophie Metachromatique*. 26ème congres de la Société Francaise de Neurologie Pédiatrique, 2016. (Cited on pages 16 and 175.)

[Bloch 1946] F. Bloch, W.W. Hansen and M. Packard. *The nuclear induction experiment*. Phys Rev, vol. 70, pages 474–485, 1946. (Cited on pages 6 and 9.)

[Block 1997] W. Block, J. Pauly and D. Nishimura. *RARE spiral T2-weighted imaging*. Magnetic resonance in medicine, vol. 37, no. 4, pages 582–590, 1997. (Cited on page 21.)

[Block 2007] K.T. Block, M. Uecker and J. Frahm. *Undersampled Radial MRI with Multiple Coils. IterativeImage Reconstruction Using a Total Variation Constraint*. Magnetic Resonance in Medicine, vol. 57, pages 1086–1098, 2007. (Cited on page 25.)

[Boada 1997a] F.E. Boada, G.X. Chen, S.Y. Chang and K.R. Thulborn. *Spectrally Weighted Twisted Projection Imaging: Reducing T_2 Signal Attenuation Effects in Fast Three-Dimensional Sodium Imaging*. Magnetic resonance in medicine, vol. 38, pages 1022–1028, 1997. (Cited on pages 29 and 63.)

[Boada 1997b] F.E. Boada, J.D. Christensen, J.S. Gillen and K.R. Thulborn. *Three Dimensional Projection Imaging with Half the Number of Projections*. Magnetic resonance in medicine, vol. 37, no. 3, pages 470–477, 1997. (Cited on page 64.)

[Boada 1997c] F.E. Boada, J.S. Gillen, G.X. Chen, S.Y. Chang and K.R. Thulborn. *Fast Three Dimensional Sodium Imaging*. Magnetic resonance in medicine, vol. 37, pages 706–715, 1997. (Cited on pages 1, 2, 21, 29, 136, 184, 197, 198 and 203.)

[Boada 2005] F.E. Boada, G. LaVerde, C. Jungreis, E. Nemoto and C. Tanase. *Triple/Single Quantum Filtered Sodium MRI Of Acute Brain Ischemia*. Proceedings of the 2005 IEEE Engineering in Medicine and Biology, 2005. (Cited on page 30.)

[Boada 2010] F. E. Boada, Y. Qian, A. Gildengers, M. Phillips and D. Kupfer. *In Vivo 3D Lithium MRI of the Human Brain*. In Proceedings of the International Society for Magnetic Resonance in Medicine 18, volume 70, pages 474–485, 2010. (Cited on pages 2, 6, 35, 36, 151, 157, 161, 165, 176, 193 and 211.)

[Bonnier 2014] G. Bonnier, A. Roche, D. Romascano, S. Simioni, D. Meskaldji, D. Rotzinger, Y-C. Lin, G. Menegaz, M. Schluep, R. Du Pasquier, T.J. Sumpf, J. Frahm, J-P. Thiran, G. Krueger and C. Granziera. *Advanced MRI unravels the nature of tissue alterations in early multiple sclerosis*. Annals of Clinical and Translational Neurology, vol. 6, no. 1, pages 423–432, 2014. (Cited on page 134.)

[Bottomley 1987] P.A. Bottomley. *Spatial localization in NMR Spectrocopy in vivo*. Annals of NY Academy of Science, vol. 508, pages 333–348, 1987. (Cited on page 14.)

[Bottomley 2009] P.A. Bottomley, K.C. Wu, G. Gerstenblith, S.P. Schulman, A. Steinberg and R.G. Weiss. *Reduced myocardial creatine kinase flux in human myocardial infarction*. Circulation, vol. 119, pages 1918–1924, 2009. (Cited on pages 33 and 196.)

[Bottomley 2015] P.A. Bottomley. *Sodium MRI in human heart: a review*. NMR in Biomedicine, 2015. (Cited on page 33.)

[Bracewell 1965] R.M. Bracewell. The fourier transform and its applications. McGraw-Hill, 1965. (Cited on page 11.)

[Brodsky 2009] E.K. Brodsky, A.A. Samsonov and W.F. Block. *Characterizing and correcting gradient errors in non-cartesian imaging: Are gradient errors linear time-invariant (LTI)?* Magnetic Resonance in Medicine, vol. 62, no. 6, pages 1466–1476, 2009. (Cited on page 42.)

[Brown 1982] T.R. Brown, B.M. Kincaid and K. Ugurbil. *NMR chemical shift imaging in three dimensions*. Proceedings of the Natinall Academy of Science, vol. 79, pages 3523–3526, 1982. (Cited on page 14.)

[Buades 2005] A. Buades, B. Coll and J.M. Morel. *A non-local algorithm for image denoising*. Computer Vision and Pattern Recognition, page 44, 2005. (Cited on page 87.)

[Bydder 2017] M. Bydder, A. Nagel, A. Maarouf, J. Verneuil, P. Viout, M. Guye, J.P. Ranjeva and W. Zaaraoui. *Sodium short and long T2* components in the normal human brain: a multi-TE 23Na MRI study at 7T*. Proceedings of the International Society of Magnetic Resonance in Medicine, vol. 5631, 2017. (Cited on pages 115 and 122.)

[Castillo 1996] M. Castillo, L. Kwock and S.K. Kwock. *Clinical Applications of Proton MR Spectroscopy*. American Journal of NeuroRadiology, vol. 17, pages 1–15, 1996. (Cited on page 14.)

[Chance 2006] B. Chance, J. Im, S. Nioka and M. Kushmerick. *Skeletal muscle energetics with PNMR: personal views and historic perspectives*. NMR in Biomedicine, vol. 19, pages 904–926, 2006. (Cited on pages 33 and 196.)

[Chauffert 2015] N. Chauffert. *Echantillonnage compressé le long de trajectoires physiquement plausibles en IRM*. PhD thesis, Université Paris XI, 2015. (Cited on pages 2, 21 and 59.)

[Chaumeil 2009] M.M. Chaumeil, J. Valette, M. Guillermier, E. Brouillet, F. Boumezbeur, A.S. Herard, G. Bloch, P. Hantraye and V. Lebon. *Multimodal neuroimaging provides a highly consistent picture of energy metabolism, validating 31P MRS for measuring brain ATP synthesis*. Proceedings of the National Academy of Science USA, vol. 106, no. 10, pages 3988–3993, 2009. (Cited on pages 2, 33 and 196.)

[Chen 1993] S.W.W. Chen and P.J. Rossky. *Influence of solvent and counterion on sodium-23(1+) spin relaxation in aqueous solution*. Journal of Physical Chemistry, vol. 97, no. 41, pages 10803–10812, 1993. (Cited on page 29.)

[Cheng 2006] H.L. Cheng and G.A. Wright. *Rapid high-resolution T(1) mapping by variable flip angles: accurate and precise measurements in the presence of radiofrequency field inhomogeneity*. Magnetic Resonance in Medicine, vol. 55, no. 3, pages 566–574, 2006. (Cited on page 83.)

[Choi 2014] N. Choi, J. Lee, M.O. Kim, J. Shin and D.H. Kim. *A modified multi-echo AFI for simultaneous B1(+) magnitude and phase mapping*. Magnetic Resonance Imaging, vol. 32, no. 4, pages 314–320, 2014. (Cited on page 45.)

[CHUNG 1990] C.W. CHUNG and S. WIMPERIS. *Optimum detection of spin-32 biexponential relaxation using multiple-quantum filtration techniques*. Journal of Magnetic Resonance, vol. 88, no. 2, pages 440–447, 1990. (Cited on page 30.)

[CLARE 1997] S. CLARE. *Functional MRI : Methods and Applications*. PhD thesis, University of Nottingham, 1997. (Cited on pages 40 and 176.)

[CLOOS 2016] M.A. CLOOS, F. KNOLL, T. ZHAO, K.T. BLOCK, M. BRUNO, G.C. WIGGINS and D.K. SODICKSON. *Multiparametric imaging with heterogeneous radiofrequency fields*. Nature Communications, vol. 7, page 12445, 2016. (Cited on page 110.)

[COLLINS 2011] C.M. COLLINS and Z. WANG. *Calculation of radiofrequency electromagnetic fields and their effects in MRI of human subjects.* Magnetic Resonance in Medicine, vol. 65, no. 5, pages 1470–1482, 2011. (Cited on page 10.)

[CONOLLY 1988] S. CONOLLY, D.G. NISHIMURA, A. MACOVSKI and G. GLOVER. *Variable-rate selective excitation*. Journal of Magnetic Resonance, vol. 78, pages 440–458, 1988. (Cited on page 62.)

[CONSTANTINIDES 2001] C.D. CONSTANTINIDES, D.L. KRAITCHMAN, K. O BRIEN, F.E. BOADA, J. GILLEN and P.A. BOTTOMLEY. *Noninvasive quantification of total sodium concentrations in acute reperfused myocardial infarction using 23Na MRI.* Magnetic Resonance in Medicine, vol. 46, pages 1144–1151, 2001. (Cited on page 206.)

[COSTE 2013] A. COSTE. Diffusion tensor imaging work. Scientific Computing and Imaging Institute, 2011-2013. (Cited on pages 17 and 175.)

[COSTE 2014] A. COSTE. Cortical thickness work. BioClinica, 2014. (Cited on pages 16 and 175.)

[COSTE 2015] A. COSTE, N. CHAUFFERT, A. VIGNAUD, F. BOUMEZBEUR, P. CIUCIU, P. WEISS, S. ROMANZETTI, D. LE BIHAN and C. LERMAN. *31P MRI: Comparison of Image Reconstruction Approaches for Sub-Nyquist Acquisitions at Ultra High Field*. Proceedings of the European Society of Magnetic Resonance in Medicine and Biology, 2015. (Cited on pages 74, 75 and 179.)

[COSTE 2016] A. COSTE, N. CHAUFFERT, A. VIGNAUD, P. CIUCIU, F. BOUMEZBEUR, P. WEISS, S. ROMANZETTI, D. LE BIHAN and C. LERMAN. *Assessment of benefit to use a non-Cartesian trajectory and nonlinear reconstruction method compared to a Cartesian strategy for Fast 31P MRI*. Proceedings of the 24th International Society of Magnetic Resonance in Medicine, 2016. (Cited on pages 66, 67, 110, 178 and 212.)

[COSTE 2017] A. COSTE, F. BOUMEZBEUR, A. VIGNAUD, G. MADELIN, K. REETZ, D. LE BIHAN, C. LERMAN and S. ROMANZETTI. *Variable Flip Angle Pipeline for in vivo Sodium Concentration Measurements (VaSCo)*. Proceedings of the 25th International Society of Magnetic Resonance in Medicine, 2017. (Cited on pages 82, 201, 205 and 212.)

[COUSINS 2013] D.A. COUSINS, B. ARIBISALA, I. NICOL FERRIER and A.M. BLAMIRE. *Lithium, gray matter, and magnetic resonance imaging signal*. Biological Psychiatry, vol. 73, no. 7, pages 652–657, 2013. (Cited on pages 35 and 196.)

[CUNNINGHAM 2006] C.H. CUNNINGHAM, J.M. PAULY and K.S. NAYAK. *Saturated Double-Angle Method for Rapid B1+ Mapping*. Magnetic Resonance in Medicine, vol. 55, pages 1326–1322, 2006. (Cited on page 44.)

[DAY 2007] S.E. DAY, M.I. KETTUNEN, F.A. GALLAGHER, D.E. HU, M. LERCHE, J. WOLBER, K. GOLMAN, J.H. ARDENKJAER-LARSEN and K.M. BRINDLE. *Detecting tumor response to treatment using hyperpolarized 13C magnetic resonance imaging and spectroscopy*. Nature Medicine, vol. 13, pages 1382–1387, 2007. (Cited on pages 6 and 194.)

[DE FIGUEIREDO 2006] R.J.P. DE FIGUEIREDO. *Generalized Nonlinear Impulse Response and Nonlinear Convolution in a Reproducing Kernel Hilbert Space*. page 2, 2006. (Cited on page 68.)

[DE GRAAF 2007] R.A. DE GRAAF. In vivo nmr spectrocopy: Principles and techniques. John Willey and Sons, Ltd, first edition édition, 2007. (Cited on pages 6, 8, 11, 43 and 176.)

[DE GRAAF 2013] R.A. DE GRAAF. In vivo nmr spectrocopy: Principles and techniques. John Willey and Sons, Ltd, second edition édition, 2013. (Cited on page 142.)

[DE ROCHEFORT 2009] L. DE ROCHEFORT, T. LIU, B. KRESSLER, J. LIU, P. SPINCEMAILLE, V. LEBON, J. WU and Y. WANG. *Quantitative susceptibility map reconstruction from MR phase data using bayesian regularization: Validation and application to brain imaging*. Magnetic Resonance in Medicine, vol. 63, no. 1, pages 194–206, 2009. (Cited on page 17.)

[DE ROCHEFORT 2015] L. DE ROCHEFORT. *Encoding with Radiofrequency Spoiling, Equilibrium States and Inverse Problem for Parametric Mapping*. In Proceedings of the International Society of Magnetic Resonance in Medicine, 2015. (Cited on pages 18, 97, 98 and 209.)

[DE ROCHEFORT 2016a] L. DE ROCHEFORT. Method and device for imaging by magnetic resonance. Patent, 2016. (Cited on pages 98, 100 and 180.)

[DE ROCHEFORT 2016b] L. DE ROCHEFORT. *Method and device for Imaging by Magnetic Resonance*, 2016. (Cited on pages 185, 209 and 210.)

[DE ROCHEFORT 2016c] L. DE ROCHEFORT, G. GUILLOT, R.M. DUBUISSON and R. VALABRËGUE. *In Vivo Feasibility of Multi-Parametric Mapping Based on Fast Steady-State Sequences*. In Proceedings of the International Society of Magnetic Resonance in Medicine, 2016. (Cited on pages 18, 97, 98 and 108.)

[DE SOUSA 2012] P.L. DE SOUSA, A. VIGNAUD, E. CALDAS DE ALMEIDA ARAÚJO and P.G. CARLIER. *Factors controlling T2 mapping from partially spoiled SSFP sequence: Optimization for skeletal muscle characterization*. Magnetic Resonance in Medicine, vol. 67, no. 5, pages 1379–1390, 2012. (Cited on page 100.)

[DEELCHAND 2015] D.K. DEELCHAND, T.M. NGUYEN, X.H. ZHU, F. MOCHEL and P.-G. HENRY. *Quantification of in vivo 31P NMR Brain Spectra using LCModel*. NMR in Biomedicine, vol. 28, no. 6, pages 633–641, 2015. (Cited on page 142.)

[DELAUNAY 1934] B.N. DELAUNAY. *Sur la sphere vide*. Bulletins Academie des Sciences USSR VII: Class. Sci. Math., pages 793–800, 1934. (Cited on page 70.)

[DRAGO 1992] R.S. DRAGO. Physical methods for chemists. SurfSide Scientific Publisher, second edition édition, 1992. (Cited on pages 27 and 176.)

[DU 2007] F. DU, X.-H. ZHU, H. QIAO, X. ZHANG and W. CHEN. *Efficient in vivo 31P magnetization transfer approach for noninvasively determining multiple kinetic parameters and metabolic fluxes of ATP metabolism in the human brain*. Magnetic Resonance in Medicine, vol. 57, no. 1, pages 103–114, 2007. (Cited on pages 14 and 204.)

[DU 2010] J. DU, M. CARL, M. BYDDER, A. TAKAHASHI, C.B. CHUNG and G.M. BYDDER. *Qualitative and quantitative ultrashort echo time (UTE) imaging of cortical bone*. Journal of Magnetic Resonance, vol. 207, pages 304–311, 2010. (Cited on page 61.)

[DU 2017] F. DU, C. YUKSEL, V.A. CHOUINARD, P. HUYNH, K. RYAN, B.M. COHEN and P.J. ÖNGÜR. *Abnormalities in High-Energy Phosphate Metabolism in First-Episode Bipolar Disorder Measured Using 31P-Magnetic Resonance Spectroscopy.* Biological Psychiatry, vol. 17, 2017. (Cited on pages 33 and 196.)

[DUMOULIN 1989] C.L. DUMOULIN, S.P. SOUZA, M.F. WALKER and W. WAGLE. *Three-Dimensional Phase Contrast Angiography*. Magnetic Resonance in Medicine, vol. 9, pages 139–149, 1989. (Cited on page 16.)

[DUTT 1993] A. DUTT and V. ROKHLIN. *Fast Fourier Transforms for Nonequispaced data*. SIAM Journal of Scientific Compututing, vol. 14, no. 4, page 1368, 1993. (Cited on pages 23 and 198.)

[EISELE 2015] P. EISELE, S. KONSTANDIN, M. GRIEBE, K. SZABO, M.E. WOLF, A. ALONSO, A. EBERT, J. SERWANE, C. ROSSMANITH, M.G. HENNERICI, L.R. SCHAD and A. GASS. *Heterogeneity of acute multiple sclerosis lesions on sodium (23Na) MRI*. Multiple Sclerosis, 2015. (Cited on pages 2, 29 and 31.)

[ELSTER 2016] A.D ELSTER. *mriquestions.com*. Available from `https://www.mriquestions.com`, Consulted 2016. (Cited on pages 60 and 178.)

[ENGEL 2015] M. ENGEL, N. BENKHEDAH and A.M. NAGEL. *Density-Adapted Spiral MRI sequence for 23Na imaging*. Proceedings of the International Society for Magnetic Resonance in Medicine meeting, vol. 23, no. 2443, 2015. (Cited on page 64.)

[EPSTEIN 1996] F.H. EPSTEIN, J.P. MUGLER and J.R. BROOKEMAN. *Spoiling of transverse magnetization in gradient-echo (GRE) imaging during the approach to steady state*. Magnetic Resonance in Medicine, vol. 35, no. 2, pages 237–245, 1996. (Cited on page 99.)

[FESSLER 2003] J.A. FESSLER. *Nonuniform Fast Fourier Transforms Using Min-Max Interpolation*. IEEE Transactions on Signal Processing, vol. 51, no. 2, pages 560–574, 2003. (Cited on pages 23, 128 and 198.)

[FIEGE 2013] D.P FIEGE, S. ROMANZETTI, D.H.Y. TSE, D. BRENNER, A. CELIK, J. FELDER and N.J. SHAH. *B0 insensitive multiple-quantum resolved sodium imaging using a phase-rotation scheme*. Journal of Magnetic Resonance, no. 228, pages 32–36, 2013. (Cited on pages 29 and 30.)

[FLEYSHER 2009] L. FLEYSHER, N. OESINGMANN, C. STOECKEL, I. GROSSMAN and M. INGLESE. *Sodium Long-Component T*2 Mapping in Human Brain at 7 Tesla*. Magnetic Resonance in Medicine, vol. 62, pages 1338–1341, 2009. (Cited on page 115.)

[FLEYSHER 2010] L. FLEYSHER, N. OESINGMANN and M. INGLESE. *B_0 inhomogeneity-insensitive triple-quantum-filtered sodium imaging using a 12-step phase-cycling scheme*. NMR in Biomedicine, vol. 23, no. 10, pages 1191–1198, 2010. (Cited on page 29.)

[FLEYSHER 2012] L. FLEYSHER, N. OESINGMANN, R. BROWN, D.K. SODICKSON, G.C. WIGGINS and M. INGLESE. *Noninvasive quantification of intracellular sodium in human brain using ultrahigh-field MRI*. NMR in Biomedicine, vol. 26, pages 9–19, 2012. (Cited on pages 30, 31, 122 and 176.)

[Flower 2012] M.A. Flower. Webb's physics of medical imaging. CRC Press, second edition édition, 2012. (Cited on pages 9 and 175.)

[Frahm 1969] J. Frahm, K.D. Merboldt and W. Hanicke. *Localised Proton Spectroscopy Using Stimulated Echoes*. Journal of Magnetic Resonance, vol. 72, pages 502–508, 1969. (Cited on page 14.)

[Friston 1994] K.J. Friston, A.P. Holmes, K.J. Worsley, J.-P. Poline, C.D. Frith and R.S. Frackowiak. *Statistical parametric maps in functional imaging: a general linear approach*. Human Brain Mapping, vol. 2, pages 189–210, 1994. (Cited on page 17.)

[Friston 1999] K.J. Friston, E. Zarahn, O. Josephs, R.-N. Henson and A.M. Dale. *tochastic designs in event-related fMRI*. NeuroImage, vol. 10, no. 3, pages 607–619, 1999. (Cited on page 17.)

[Gai 2015] N.D. Gai, C. Rochitte, M.S. Nacif and D.A. Bluemke. *Optimized Three-Dimensional Sodium Imaging of the Human Heart on a Clinical 3T Scanner*. Magnetic Resonance in Medicine, vol. 73, pages 623–632, 2015. (Cited on page 33.)

[Ganter 2006] C. Ganter. *Steady state of gradient echo sequences with radiofrequency phase cycling: Analytical solution, contrast enhancement with partial spoiling*. Magnetic Resonance in Medicine, vol. 55, no. 1, pages 98–107, 2006. (Cited on page 100.)

[Garwood 2001] M. Garwood and L. DelaBarre. *The return of the frequency sweep: Designing adiabatic pulses for contemporary NMR*. Journal of Magnetic Resonance, vol. 153, no. 2, pages 155–177, 2001. (Cited on page 14.)

[Geman 1995] D. Geman and C. Yang. *Nonlinear image recovery with half-quadratic regularization*. IEEE Transactions on Image Processing, vol. 4, pages 932–946, 1995. (Cited on page 25.)

[Glasser 2011] M. F. Glasser and D. C. Van Essen. *Mapping human cortical areas in vivo based on myelin content as revealed by T1- and T2-weighted MRI*. Journal of Neuroscience, vol. 31, no. 32, pages 11597–11616, 2011. (Cited on page 17.)

[Glover 1992] G.H. Glover, J.M. Pauly and K.M. Bradshaw. *Boron-11 imaging with a three-dimensional reconstruction method*. Journal of Magnetic Resonance Imaging, vol. 1, no. 2, pages 47–52, 1992. (Cited on pages 6 and 193.)

[Gnahm 2014] C. Gnahm, M. Bock, P. Bachert, W. Semmler, N.G.R. Behl and A.M Nagel. *Iterative 3D projection reconstruction of 23Na data with an 1H MRI constraint*. Magnetic Resonance in Medicine, vol. 71, no. 5, pages 1720–1732, 2014. (Cited on page 134.)

[Godenschweger 2016] F. Godenschweger, U. Kägebein, D. Stucht, U. Yarach, A. Sciarra, R. Yakupov, F. Lüsebrink, P. Schulze and O. Speck. *Motion correction in MRI of the brain*. Physics in medicine and biology, vol. 61, no. 5, pages R32–R56, 2016. (Cited on page 125.)

[Golman 2003] K. Golman, L.E. Olsson, O. Axelsson, S. Mansson, M. Karlsson and J.S. Petersson. *Molecular imaging using hyperpolarized 13C*. British Journal of Radiology, vol. 76, no. 2, pages 118–1227, 2003. (Cited on page 8.)

[Gonzalez 1993] R.G. Gonzalez, A.R. Guimaraes, G.S. Sachs, J.F. Rosenbaum, M. Garwood and P.F. Renshaw. *Measurement of Human Brain Lithium In Vivo by MR Spectroscopy*. American Journal of NeuroRadiology, vol. 14, pages 1027–1037, 1993. (Cited on pages 35 and 196.)

[GOODMAN 2005] J.A. GOODMAN, C.D. KROENKE, G.L. BRETTHORST, J.H.H. ACKERMAN and J.J. NEIL. *Sodium ion apparent diffusion coefficient in living rat brain*. Magnetic Resonance in Medicine, vol. 53, no. 5, pages 1040–1054, 2005. (Cited on pages 105 and 187.)

[GRAESSL 2015] A. GRAESSL, A. RUEHLE, H. WAICZIES, A. RESETAR, S.H. HOFFMANN, J. RIEGER, F. WETTERLING, L. WINTER, A.M. NAGEL and T. NIENDORF. *Sodium MRI of the human heart at 7.0T: preliminary results*. NMR in Biomedicine, 2015. (Cited on page 33.)

[GRANOT 1986] J. GRANOT. *Selected volume excitation using stimulated echoes (VEST): application to spatially localized spectroscopy and imaging*. Journal of Magnetic Resonance, vol. 70, pages 488–492, 1986. (Cited on page 14.)

[GRAS 2016] V. GRAS, E. FARRHER, F. GRINBERG and N.J. SHAH. *Diffusion-weighted DESS protocol optimization for simultaneous mapping of the mean diffusivity, proton density and relaxation times at 3 Tesla*. Magnetic Resonance in Medicine, 2016. (Cited on page 97.)

[GRODZKI 2012] D. M. GRODZKI, P. M. JAKOB and B. HEISMANN. *Ultrashort echo time imaging using pointwise encoding time reduction with radial acquisition (PETRA)*. Magnetic Resonance in Medicine, vol. 67, no. 2, pages 510–518, 2012. (Cited on page 29.)

[GROF 2002] P. GROF, A. DUFFY, P. CAVAZZONI, E. GROF, J. GARNHAM, M. MACDOUGALL, C. O'DONOVAN and M. ALDA. *Is response to prophylactic lithium a familial trait?* Journal of Clinical Psychiatry, vol. 63, pages 942–947, 2002. (Cited on page 153.)

[GUDBJARTSSON 1995] H. GUDBJARTSSON and S. PATZ. *The Rician Distribution of Noisy MRI Data*. Magnetic Resonance in Medicine, vol. 34, no. 6, pages 910–914, 1995. (Cited on page 77.)

[GUERQUIN-KERN 2011] M. GUERQUIN-KERN, M. HÄBERLIN, K. P. PRUESSMANN and M. UNSER. *A Fast Wavelet-Based Reconstruction Method for Magnetic Resonance Imaging*. IEEE Transactions on Medical Imaging, vol. 30, no. 9, 2011. (Cited on pages 24 and 198.)

[GULLAPALLI 1991] R.P. GULLAPALLI, R.M. HAWK and R.A. KOMOROSKI. *A 7Li NMR study of visibility, spin relaxation, and transport in normal human erythrocytes*. Magnetic Resonance in Medicine, vol. 20, pages 240–252, 1991. (Cited on page 156.)

[GURNEY 2006] P. T. GURNEY, B. A. HARGREAVES and D. G. NISHIMURA. *Design and analysis of a practical 3D cones trajectory*. Magnetic Resonance in Medicine, vol. 55, no. 3, pages 575–582, 2006. (Cited on page 29.)

[HA 2013] D.-H. HA, S. CHOI, J.Y. OH, S.K. YOON, M.J. KANG and K.-U KIM. *Application of 31P MR Spectroscopy to the Brain Tumors*. Korean Journal of Radiology, vol. 14, no. 3, pages 477–486, 2013. (Cited on page 148.)

[HAACKE 1999] E.M. HAACKE, R.W. BROWN, M.R. THOMPSON and R. VENKATESAN. Magnetic resonance imaging: Physical principles and sequence design. Wiley and sons, second edition édition, 1999. (Cited on pages 6, 19, 20 and 199.)

[HAACKE 2004] E.M. HAACKE, Y. XU and J.R REICHENBACH. *Susceptibility weighted imaging*. Magnetic Resonance in Medicine, vol. 52, pages 612–618, 2004. (Cited on page 17.)

[HALSE 2003] M. HALSE, D.J. GOODYEAR, B. MACMILLAN, P. SZOMOLANYI, D. MATHESON and B.J. BALCOM. *Centric scan SPRITE magnetic resonance imaging*. Journal of Magnetic Resonance, vol. 165, no. 2, pages 219–229, 2003. (Cited on page 29.)

[HANCU 1999] I. HANCU, F.E. BOADA and G.X. SHEN. *Three-Dimensional Triple-Quantum-Filtered 23Na Imaging of in vivo Human Brain*. Magnetic Resonance in Medicine, vol. 42, pages 1146–1154, 1999. (Cited on pages 30, 184 and 203.)

[HANEDER 2013] S. HANEDER, P. KETTNAKER, S. KONSTANDIN, J.N. MORELLI, L.R. SCHAD, S.O. SCHOENBERG and H.J. MICHAELY. *Quantitative in vivo 23Na MR imaging of the healthy human kidney: determination of physiological ranges at 3.0T with comparison to DWI and BOLD*. Magnetic Resonance Materials in Physics, Biology and Medicine, vol. 26, no. 6, pages 501–509, 2013. (Cited on page 33.)

[HANEDER 2014] S. HANEDER, M.M.L. ONG, R. SCHMIDT J.M. BUDJAN, S. KONSTANDIN, J.N. MORELLI, L.R. SCHAD, S.O. SCHOENBERG and U.H. KERL. *23Na-magnetic resonance imaging of the human lumbar vertebral discs: in vivo measurements at 3.0 T in healthy volunteers and patients with low back pain*. The Spine Journal, vol. 14, pages 1343–1350, 2014. (Cited on page 33.)

[HARA 2014] M. HARA, M. KURODA, Y. OHMURA, H. MATSUZAKI, T. KOBAYASHI, J. MURAKAMI, K. MATSUZAKI, M. ASHIDA, S. OHNO and J.-I ASAUMI. *A new phantom and empirical formula for apparent diffusion coefficient measurement by a 3 Tesla magnetic resonance imaging scanner*. Oncology Letters, vol. 8, no. 2, pages 819–824, 2014. (Cited on page 107.)

[HARRINGTON 2011] M.G. HARRINGTON, E.Y. CHEKMENEV, V.D. SCHEPKIN, A.N. FONTEH and X. ARAKAKI. *Sodium MRI in a rat migraine model and a NEURON simulation study support a role for sodium in migraine*. Cephalalgia, vol. 31, pages 1254–1265, 2011. (Cited on page 30.)

[HEILER 2011] P.M. HEILER, F.L. LANGHAUSER, F. WETTERLING, S. ANSAR, S. GRUDZENSKI, S. KONSTANDIN, M. FATAR, S. MEAIRS and L.R. SCHAD. *Chemical shift sodium imaging in a mouse model of thromboembolic stroke at 9.4 T*. Journal of Magnetic Resonance Imaging, vol. 34, no. 4, pages 935–940, 2011. (Cited on page 112.)

[HENNIG 1991a] J. HENNIG. *Echoes-how to generate, recognize, use or avoid them in MR-imaging sequences. Part I: Fundamental and not so fundamental properties of spin echoes*. Concepts in Magnetic Resonance, vol. 3, no. 3, pages 125–143, 1991. (Cited on page 99.)

[HENNIG 1991b] J. HENNIG. *Echoes-how to generate, recognize, use or avoid them in MR-imaging sequences. Part II: Echoes in imaging sequences*. Concepts in Magnetic Resonance, vol. 3, no. 4, pages 179–192, 1991. (Cited on page 99.)

[HETHERINGTON 2001] H.P. HETHERINGTON, D.D. SPENCER, J.T. VAUGHAN and J.W. PAN. *Quantitative 31P spectroscopic imaging of human brain at 4T: assessment of gray and white matter differences of phosphocreatine and ATP*. Magnetic Resonance in Medicine, vol. 45, no. 1, pages 45–52, 2001. (Cited on pages 144 and 148.)

[HEULE 2014] R. HEULE, C. GANTER and O. BIERI. *Triple echo steady-state (TESS) relaxometry*. Magnetic Resonance in Medicine, vol. 71, no. 1, pages 230–237, 2014. (Cited on pages 18 and 97.)

[HILAL 1985] S.K. HILAL, A.A. MAUDSLEY, J.B. RA, H.E. SIMON, P. ROSCHMANN, S. WITTEKOEK, Z.H. CHO and I.K. MUN. *In vivo NMR imaging of sodium-23 in the human head*. Journal of Computer Assisted Tomography, vol. 9, pages 1–7, 1985. (Cited on pages 1, 6, 26 and 193.)

[HOFFMANN 2011] S.H. HOFFMANN, P. BEGOVATZ, A.M. NAGEL, R. UMATHUM, K. SCHOMMER, P. BACHERT and M. BOCK. *A measurement setup for direct 17O MRI at 7 T*. Magnetic Resonance in Medicine, vol. 66, no. 4, pages 1109–1115, 2011. (Cited on pages 1, 6 and 194.)

[HOLLAND 1977] G.N. HOLLAND, P.A. BOTTOMLEY and W.S. HINSHAW. *19F magnetic resonance imaging*. Journal of Magnetic Resonance, vol. 28, pages 133–136, 1977. (Cited on page 193.)

[HOOIJMANS 2017] M.T. HOOIJMANS, N. DOORENWEERD, C. BALIGAND, J.J.G.M. VERSCHUUREN, I. RONEN, E.H. NIKS, A.G. WEBB and H.E. KAN. *Spatially localized phosphorous metabolism of skeletal muscle in Duchenne muscular dystrophy patients: 24 month follow-up*. PLoS ONE, vol. 12, no. 8, page e0182086, 2017. (Cited on pages 33 and 196.)

[HORCH 2010] A.H. HORCH, J.S. NYMAN, D.F. GOCHBERG, R.D. DORTCH and M.D. DOES. *Characterization of 1H NMR signal in human cortical bone for magnetic resonance imaging*. Magnetic Resonance in Medicine, vol. 64, no. 4, pages 680–687, 2010. (Cited on page 61.)

[HORN 2006] M. HORN. *Cardiac magnetic resonance spectroscopy: a window for studying physiology*. Methods in Molecular Medicine, vol. 124, no. 7, pages 225–248, 2006. (Cited on page 148.)

[HOULT 1976] D.I. HOULT and R.E. RICHARDS. *The signal-to-noise ratio of nuclear magnetic resonance experiment*. Journal of Magnetic Resonance, vol. 24, pages 71–85, 1976. (Cited on page 26.)

[HOULT 1979] D.I. HOULT and P.C. LAUTERBUR. *Sensitivity of the zeugmatography experiment involving human samples*. Journal of Magnetic Resonance, vol. 34, pages 425–433, 1979. (Cited on page 26.)

[HOULT 2000] D.I. HOULT. *The principle of reciprocity in signal strength calculations-A mathematical guide*. Concepts in Magnetic Resonance, vol. 12, no. 44, pages 173–187, 2000. (Cited on pages 83 and 104.)

[HUANG 2012] C. HUANG, C.G. GRAFF, E.W. CLARKSON, 1. BILGIN and M.I. ALTBACH. *T2 mapping from highly undersampled data by reconstruction of principal component coefficient maps using compressed sensing*. Magnetic Resonance in Medicine, vol. 5, no. 67, pages 1355–1266, 2012. (Cited on page 26.)

[HURLEY 2012] S.A. HURLEY, V.L. YARNYKH, K.M.JOHNSON, A.S. FIELD, A.L. ALEXANDER and A.A. SAMSONOV. *Simultaneous Variable Flip Angle-Actual Flip Angle Imaging (VAFI) Method for Improved Accuracy and Precision of Three-dimensional T1 and B1 Measurements*. Magnetic Resonance in Medicine, vol. 68, no. 1, pages 54–64, 2012. (Cited on page 45.)

[IDIYATULLIN 2006] D. IDIYATULLIN, C. CORUM, J.Y. PARK and M. GARWOOD. *Fast and quiet MRI using a swept radiofrequency*. Journal of Magnetic Resonance, vol. 181, no. 2, pages 342–349, 2006. (Cited on page 62.)

[IEC 2010] IEC. *International Electrotechnical Commission: Medical electrical equipment - Part 2-33: Particular requirements for the basic safety and essential performance of magnetic resonance equipment for medical diagnosis*. vol. 60601-2-33, 2010. (Cited on page 53.)

[IEC 2015] IEC. *International Electrotechnical Commission: Medical electrical equipment - Part 2-33: Particular requirements for the basic safety and essential performance of magnetic resonance equipment for medical diagnosis*. vol. 60601-2-33, 2015. (Cited on pages 53 and 84.)

[INGLESE 2010] M. INGLESE, G. MADELIN, N. OESINGMANN, J.S. BABB, W. WU, B. STOECKEL, J. HERBERT and G. JOHNSON. *Brain tissue sodium concentration in multiple sclerosis: a sodium imaging study at 3 tesla*. Brain, vol. 133, no. 1, pages 847–857, 2010. (Cited on pages 2, 31, 82, 95, 124 and 195.)

[INGWALL 1982] J.S. INGWALL. *Phosphorus nuclear magnetic resonance spectroscopy of cardiac and skeletal muscles*. American Journal of Physiology - Heart and Circulatory Physiology, vol. 242, no. 5, 1982. (Cited on pages 33 and 196.)

[ISO 1993] ISO. *Guide to the expression of uncertainty in measurement*. 1993. (Cited on pages 107 and 181.)

[JACCARD 1986] G. JACCARD, S. WIMPERIS and G. BODENHAUSEN. *Multiple Quantum NMR-Spectroscopy of S=3/2 Spins in Isotropic Phase: a New Probe for Multiexponential Relaxation*. Journal of Chemical Physics, vol. 85, no. 11, pages 6282–6293, 1986. (Cited on pages 29, 30, 112 and 176.)

[JACKSON 1991] J. I. JACKSON, C. H. MEYER and D. G. NISHIMURA. *Selection of a Convolution Function for Fourier Inversion Using Gridding*. IEEE Transactions on Medical Imaging, vol. 10, no. 3, pages 473–478, 1991. (Cited on pages 22, 69 and 198.)

[JACKSON 1992] J. I . JACKSON, D. G. NISHIMURA and A. MACOVSKI. *Twisting Radial Lines with Application to Robust Magnetic Resonance Imaging of Irregular Flow*. Magnetic Resonance in Medicine, vol. 25, pages 128–139, 1992. (Cited on pages 21, 29, 63, 184, 197 and 198.)

[JERECIC 2002] R. JERECIC, M. BOCK, C. WACKER, W. BAUER and L.R. SCHAD. *23Na-MRI of the human heart using a 3D radial projection technique*. Biomed Tech (Berl), vol. 47, pages 458–459, 2002. (Cited on page 19.)

[JUCHEM 2017] C. JUCHEM and R.A. DE GRAAF. *B0 magnetic field homogeneity and shimming for in vivo magnetic resonance spectroscopy*. Analytical Biochemistry, vol. 529, pages 17–29, 2017. (Cited on page 41.)

[KAUV 2017] P. KAUV, S.S. AYACHE, A. CRÉANGE, M.A. CHALAH, J.P. LEFAUCHEUR, J. HODEL and P. BRUGIÈRES. *Adenosine Triphosphate Metabolism Measured by Phosphorus Magnetic Resonance Spectroscopy: A Potential Biomarker for Multiple Sclerosis Severity*. European Neurology, vol. 77, no. 5-6, pages 316–321, 2017. (Cited on pages 33 and 196.)

[KEINER 2008] J. KEINER, S. KUNIS and D. POTTS. *Using NFFT 3 - a software library for various nonequispaced fast Fourier transforms*. ACM Transactions on Mathematical Software, vol. V, pages 1–23, 2008. (Cited on pages 23, 24, 128 and 198.)

[KEMP 2007] G.J. KEMP, M. MEYERSPEER and E. MOSER. *Absolute quantification of phosphorus metabolite concentrations in human muscle in vivo by 31P MRS: a quantitative review*. American Journal of Physiology - Heart and Circulatory Physiology, vol. 20, no. 6, pages 555–565, 2007. (Cited on pages 33, 142 and 196.)

[KLINE 2000] R.P. KLINE, E.X. WU, D.P. PETRYLAK, M. SZABOLCS, P.O. ALDERSON, M.L. WEISFELDT, P. CANNON and J. KATZ. *Rapid in vivo monitoring of chemotherapeutic response using weighted sodium magnetic resonance imaging*. Clinical Cancer Research, vol. 6, no. 6, pages 2146–2156, 2000. (Cited on page 114.)

[KLOMP 2011] D.W.J. KLOMP, B.L. VAN DE BANK, A. RAAIJMAKERS, M.A. KORTEWEG, C. POSSANZINI, V.O. BOER, C.A.T. VAN DE BERG, M.A.A.J. VAN DE BOSCH and P.R. LUIJTEN. *31P MRSI and 1H MRS at 7 T: initial results in human breast cancer*. NMR in Biomedicine, vol. 24, pages 1337–1342, 2011. (Cited on pages 34 and 196.)

[KOBER 1999] F. KOBER, P. WOLF, J. LEVIEL, VERMEULEN, G. DUHAMEL, A. DELON, J. DEROUARD, M. DESCORPS and A. ZIEGLER. *Low temperature polarized helium-3 for MRI applications*. Magnetic Resonance in Medicine, vol. 41, pages 1084–1047, 1999. (Cited on pages 6 and 194.)

[KOMOROSKI 2004] R.A. KOMOROSKI and J.M. PEARCE. *Localized 7Li MR spectroscopy and spin relaxation in rat brain in vivo*. Magnetic Resonance in Medicine, vol. 52, no. 1, pages 164–168, 2004. (Cited on pages 2 and 156.)

[KOMOROSKI 2008] R.A. KOMOROSKI and J.M. PEARCE. *Estimating Intracellular Lithium in Brain In Vivo by Localized 7Li Magnetic Resonance Spectroscopy*. Magnetic Resonance in Medicine, vol. 60, no. 1, pages 21–26, 2008. (Cited on page 156.)

[KOMOROSKI 2011] R.A. KOMOROSKI, J.C. HOLDER, A.A. PAPPAS, A.E. FINKBEINER and D.W. KLOMP. *31P NMR of phospholipid metabolites in prostate cancer and benign prostatic hyperplasia*. Magn Reson Med, vol. 65, pages 911–913, 2011. (Cited on pages 34 and 196.)

[KOMOROSKI 2013] R.A. KOMOROSKI, D.M. LINDQUIST and J.M. PEARCE. *Lithium Compartmentation in Brain by 7Li MRS: Effect of Total Lithium Concentration*. NMR in biomedicine, vol. 26, no. 9, pages 1152–1157, 2013. (Cited on page 156.)

[KONSTANDIN 2011] S. KONSTANDIN, A.M. NAGEL, P.M. HEILER and L.R. SCHAD. *Two-Dimensional Radial Acquisition Technique With Density Adaption in Sodium MRI*. Magnetic Resonance in Medicine, vol. 65, pages 1091–1097, 2011. (Cited on page 62.)

[KONSTANDIN 2014] S. KONSTANDIN and A.M. NAGEL. *Measurement techniques for magnetic resonance imaging of fast relaxing nuclei*. Magnetic Resonance Materials in Physics, Biology and Medicine, vol. 27, no. 1, pages 5–19, 2014. (Cited on page 64.)

[KORZOWSKI 2017] A. KORZOWSKI and P. BACHERT. *High-Resolution 31P Echo-Planar Spectroscopic Imaging In Vivo at 7T*. Magnetic Resonance in Medicine, 2017. (Cited on pages 34 and 149.)

[LAUBACH 1998] H.J. LAUBACH, P.M. JAKOB, K.O. LOEVBLAD, A.E. BAIRD, M.P. BOVO, R.R. EDELMAN and S. WARACH. *A Phantom for diffusion-weighted imaging of acute stroke*. Journal of Magnetic Resonance Imaging, vol. 8, no. 6, pages 1349–1354, 1998. (Cited on page 107.)

[LAUTERBUR 1973] P.C. LAUTERBUR. *Image formation by induced local interactions: examples employing nuclear magnetic resonance*. Nature, vol. 242, pages 190–1, 1973. (Cited on pages 6, 19 and 62.)

[LAYEC 2011] G. LAYEC, A. BRINGARD, Y. LE FUR, C. VILMEN, J.P. MICALLEF, S. PERREY, P.J. COZZONE and D. BENDAHAN. *Comparative determination of energy production rates and mitochondrial function using different 31P MRS quantitative methods in sedentary and trained subjects*. NMR in Biomedicine, vol. 24, no. 4, pages 425–438, 2011. (Cited on pages 34 and 149.)

[LE BIHAN 1985] D. LE BIHAN and E. BRETON. *Imagerie de diffusion in-vivo par resonance*. Academie des Sciences, Paris, vol. 301, no. 15, pages 1109–1112, 1985. (Cited on pages 1, 14 and 154.)

[LE FUR 2010] Y. LE FUR, F. NICOLI, S. CONFORT-GOUNY, P.J. COZZONE and F. KOBER. *Gridfree interactive and automated data processing for MR chemical shift imaging data*. Magnetic Resonance Materials in Physics, Biology and Medicine, vol. 23, pages 23–30, 2010. (Cited on page 142.)

[LE ROUX 1993] P. LE ROUX and R.S. HINKS. *Stabilization of echo amplitudes in FSE sequences*. Magnetic Resonance in Medicine, vol. 30, no. 2, pages 183–190, 1993. (Cited on page 99.)

[Lebon 2017] V. Lebon, S. Jan, Y. Fontyn, B. Tiret, G. Pottier, E. Jaumain and J. Valette. *Using 31P-MRI of hydroxyapatite for bone attenuation correction in PET-MRI: proof of concept in the rodent brain*. European Journal of Nuclear Medicine and Molecular Imaging Physics, vol. 4, no. 16, pages 18–27, 2017. (Cited on pages 140 and 182.)

[Lee 2009] J.S. Lee, R.R. Regatte and A. R.R. Jerschow. *Selective detection of ordered sodium signals by a jump-and-return pulse sequence*. Journal of Magnetic Resonance, vol. 200, pages 126–129, 2009. (Cited on page 30.)

[Lee 2012] J.H. Lee, C. Alder, M. Norris, W.J. Chu, E.M. Fugate, S. M. Strakowski and R.A. Komoroski. *4T 7Li 3D MRSI in the brains of bipolar disorder subjects*. Magnetic Resonance in Medicine, vol. 68, no. 2, pages 363–368, 2012. (Cited on pages 2, 6, 35, 36, 151, 157, 161, 165, 176, 193 and 196.)

[Lee 2016] J.S. Lee, D. Xia, G. Madelin and R.R. Regatte. *Sodium inversion recovery MRI on the knee joint at 7 T with an optimal control pulse*. Journal of Magnetic Resonance, vol. 262, pages 33–41, 2016. (Cited on page 33.)

[Lei 2003] H. Lei, X.-H. Zhu, X.-L. Zhang, K. Ugurbil and W. Chen. *In vivo 31P magnetic resonance spectroscopy of human brain at 7 T: An initial experience*. Magnetic Resonance in Medicine, vol. 49, no. 2, pages 199–205, 2003. (Cited on pages 34, 140, 146, 147, 183 and 187.)

[Leroi 2017] L. Leroi, A. Coste, L. de Rochefort, M. Santin, R. Valabrègue, F. Mauconduit, M.-F. Hang, E. Chazel, J. Bernard, M. Luong, E. Giacomini, D. Le Bihan, C. Poupon, F. Boumezbeur, C. Rabrait-Lerman and A. Vignaud. *Simultaneous multiparametric and quantitative estimation of 23Na physical properties at 7 Tesla using QuICS*. Proceedings of the 25th International Society of Magnetic Resonance in Medicine, 2017. (Cited on pages 210 and 212.)

[Linz 2014] P. Linz, D. Santoro, W. Renz, J. Rieger, A. Ruehle, J. Ruff, M. Deimling, N. Rakova, D.N. Muller, F.C. Luft, J. Titze and T. Niendorf. *Skin Sodium measured with ^{23}Na MRI at 7.0T*. NMR in Biomedicine, vol. 28, pages 54–62, 2014. (Cited on page 33.)

[Lopez Kolkovsky 2015] A.L. Lopez Kolkovsky. *1H and 31P NMR Spectroscopy for the study of brain metabolism at Ultra High Magnetic Field from Rodents to Men*. PhD thesis, Université Paris XI, 2015. (Cited on pages 2 and 142.)

[Lopez-Kolkovsky 2016] A.L. Lopez-Kolkovsky, S. Mériaux and F. Oatridge. *Metabolite and macromolecule T1 and T2 relaxation times in the rat brain in vivo at 17.2T*. Magnetic Resonance in Medicine, vol. 75, no. 2, pages 503–514, 2016. (Cited on page 14.)

[Lu 2010a] A. Lu, I.C. Atkinson, T.C. Claiborne, F.C. Damen and K.R. Thulborn. *Quantitative Sodium Imaging With a Flexible Twisted Projection Pulse Sequence*. Magnetic Resonance in Medicine, vol. 63, pages 1583–1593, 2010. (Cited on pages 29 and 82.)

[Lu 2010b] A. Lu, I.C. Atkinson and K.R. Thulborn. *Sodium Magnetic Resonance Imaging and its Bioscale of Tissue Sodium Concentration*. Encyclopedia of Magnetic Resonance, 2010. (Cited on page 113.)

[Lu 2013] A. Lu, I.C. Atkinson, X.J. Zhou and K.R. Thulborn. *PCr/ATP ratio mapping of the human head by simultaneously imaging of multiple spectral peaks with interleaved excitations and flexible twisted projection imaging readout trajectories at 9.4 T*. Magnetic Resonance in Medicine, vol. 69, no. 2, pages 538–544, 2013. (Cited on pages 2, 6, 34, 149, 165, 194, 196 and 203.)

[LU 2014] M. LU, W. CHEN and X-H. ZHU. *Field Dependence Study of In Vivo Brain 31P MRS up to 16.4 Tesla*. NMR in Biomedicine, vol. 27, no. 9, pages 1135–1141, 2014. (Cited on pages 140, 146, 147, 183 and 187.)

[LUO 2001] Y. LUO, R.A. DE GRAAF, L. DELABARRE, A. TANNÚS and M. GARWOOD. *BISTRO: an outer-volume suppression method that tolerates RF field inhomogeneity*. Magnetic Resonance in Medicine, vol. 45, no. 6, pages 1095–1102, 2001. (Cited on page 205.)

[LUSTIG 2007] M. LUSTIG, D. DONOHO and J. M. PAULY. *Sparse MRI: The Application of Compressed Sensing for Rapid MR Imaging*. Magnetic Resonance in Medicine, vol. 58, pages 1182–1195, 2007. (Cited on pages 19 and 199.)

[MA 2013] D. MA, V. GULANI, N. SEIBERLICH, K. LIU, J.L. SUNSHINE, J.L. DUERK and M.A. GRISWOLD. *Magnetic Resonance Fingerprinting*. Nature, vol. 495, pages 187–192, 2013. (Cited on pages 18, 97 and 210.)

[MA 2017] C. MA, B. CLIFFORD, Y. LIU, Y. GU, F. LAM, X. YU and Z.-P. LIANG. *High-Resolution Dynamic 31P-MRSI Using a Low-Rank Tensor Model*. Magnetic Resonance in Medicine, vol. 78, pages 419–428, 2017. (Cited on page 149.)

[MAAROUF 2014] A. MAAROUF, B. AUDOIN, S. KONSTANDIN, A. RICO, E. SOULIER, F. REUTER, A. LE TROTER, S. CONFORT-GOUNY, P. J. COZZONE, M. GUYE, L. R. SCHAD, J. PELLETIER, J. P. RANJEVA and W. ZAARAOUI. *Topography of brain sodium accumulation in progressive multiple sclerosis*. Magnetic Resonance Materials in Physics, Biology and Medicine, vol. 27, no. 1, pages 53–62, 2014. (Cited on pages 2, 31, 82, 95, 126 and 195.)

[MAAROUF 2017] A. MAAROUF, B. AUDOIN, F. PARIOLLAUD, S. GHERIB, A. RICO, E. SOULIER, S. CONFORT-GOUNY, M. GUYE, L. SCHAD, J. PELLETIER, J.-P. RANJEVA and W. ZAARAOUI. *Increased total sodium concentration in gray matter better explains cognition than atrophy in MS*. Neurology, vol. 88, no. 3, pages 289–295, 2017. (Cited on pages 2, 31, 82, 124 and 195.)

[MACLAREN 2013] J. MACLAREN, M. HERBST, O. SPECK and M. ZAITSEV. *MProspective Motion Correction in Brain Imaging: A Review*. Magnetic Resonance in Medicine, vol. 69, pages 621–636, 2013. (Cited on page 125.)

[MADELIN 2010] G. MADELIN, S.J. LEE, S. INATI, A. JERSCHOW and R.R. REGATTE. *Sodium inversion recovery MRI of the knee joint in vivo at 7T*. Journal of Magnetic Resonance, vol. 207, no. 1, pages 42–52, 2010. (Cited on page 83.)

[MADELIN 2012] G. MADELIN, G. CHANG, R. OTAZO, A. JERSCHOW and R.R. REGATTE. *Compressed Sensing Sodium MRI of Cartilage at 7T: Preliminary Study*. Journal of Magnetic Resonance, vol. 214, no. 1, pages 360–365, 2012. (Cited on pages 33 and 128.)

[MADELIN 2013] G. MADELIN and R.R. REGATTE. *Biomedical Applications of Sodium MRI In Vivo*. Journal of Magnetic Resonance Imaging, vol. 38, no. 3, pages 511–529, 2013. (Cited on pages 1, 6, 62, 105, 127, 187, 194 and 207.)

[MADELIN 2014] G. MADELIN, R. KLINE, R. WALVICK and R.R. REGATTE. *A method for estimating intracellular sodium concentration and extracellular volume fraction in brain in vivo using sodium magnetic resonance imaging*. Nature Scientific Reports, vol. 4, pages 47–63, 2014. (Cited on pages 61, 82, 88, 113 and 114.)

[Maintz 2002] D. Maintz, W. Heindel, H. Kugel, R. Jaeger and K.J. Lackner. *Phosphorus-31 MR spectroscopy of normal adult human brain and brain tumours*. NMR in Biomedicine, vol. 15, no. 1, pages 18–27, 2002. (Cited on page 148.)

[Malhi 2013] G.S. Malhi, M. Tanious, P. Das, C.M. Coulston and M. Berk. *Potential Mechanisms of Action of Lithium in Bipolar Disorder*. CNS Drugs, vol. 27, no. 1, pages 135–153, 2013. (Cited on page 151.)

[Malzacher 2015] M. Malzacher, R. Kalayciyan, S. Konstandin, S. Haneder and L.R. Schad. *Sodium-23 MRI of whole spine at 3 Tesla using a 5-channel receive-only phased-array and a whole-body transmit resonator*. Zeitschrift fÃ¼r Medizinische Physik, 2015. (Cited on page 33.)

[Mansfield 1977] P. Mansfield and A.A. Maudsley. *Medical imaging by NMR*. British Journal of Radiology, vol. 50, pages 188–194, 1977. (Cited on page 6.)

[Mansfield 1984] P. Mansfield. *Spatial mapping of the chemical shift in NMR*. Magnetic Resonance in Medicine, vol. 1, pages 370–386, 1984. (Cited on page 34.)

[Mariappan 2010] Y.K. Mariappan, K.J. Glaser and R.L. Ehman. *Magnetic Resonance Elastography: A review*. Clinical Anatomy, vol. 23, no. 5, pages 497–511, 2010. (Cited on page 17.)

[Maril 2006] N. Maril, Y. Rosen, G.H. Reynolds, A. Ivanishev, L. Ngo and R.E. Lenkinski. *Sodium MRI of the Human Kidney at 3 Tesla*. Magnetic Resonance in Medicine, vol. 56, pages 1229–1234, 2006. (Cited on page 33.)

[Martin 2007] W.R. Martin. *MR spectroscopy in neurodegenerative disease*. Biological Psychiatry, vol. 9, no. 4, pages 196–203, 2007. (Cited on pages 33, 148 and 196.)

[Mastikhin 1999] I.V. Mastikhin, B.J. Balcom, P.J. Prado and C.B. Kennedy. *SPRITE MRI with Prepared Magnetization and Centrick-Space Sampling*. Journal of Magnetic Resonance Imaging, vol. 136, no. 2, pages 159–168, 1999. (Cited on page 29.)

[Matsui 1985] S. Matsui, K. Sekihara and H. Kohno. *High-speed spatially resolved highresolution NMR spectroscopy*. Journal of the American Chemistry Society, vol. 107, pages 2817–2818, 1985. (Cited on page 34.)

[Matthews 1982] P.M. Matthews, J.L. Bland, D.G. Gadian and G.K. Radda. *A 31P-NMR saturation transfer study of the regulation of creatine kinase in the rat heart*. Epilepsia, vol. 721, no. 3, pages 312–320, 1982. (Cited on page 149.)

[Matthies 2010] C. Matthies, A.M. Nagel, L.R. Schad, P. Bachert and K. Scheffler. *Reduction of B0 inhomogeneity effects in triple-quantum-filtered sodium imaging*. Journal of Magnetic Resonance, no. 101, pages 239–244, 2010. (Cited on page 29.)

[Maudsley 1983] A.A. Maudsley, S.K. Hilal, W.H. Perman and H.E. Simon. *Spatially resolved high resolution spectroscopy by "four-dimensional" NMR*. Journal of Magnetic Resonance, vol. 51, pages 147–152, 1983. (Cited on page 14.)

[McFarland 1985] E. McFarland, J.A. Koutcher, B.R. Rosen, B. Teicher and T.J. Brady. *In vivo 19F NMR imaging*. Journal of Computer Assisted Tomographie, vol. 9, no. 1, pages 8–15, 1985. (Cited on pages 6 and 193.)

[MELLON 2009] E.A. MELLON, D.T. PILKINTON, C.M. CLARK, M.A. ELLIOTT, W.R. WITSCHEY, A. BORTHAKUR and R. REDDY. *Sodium MR Imaging Detection of Mild Alzheimer Disease: Preliminary Study*. AJNR American Journal of NeuroRadiology, vol. 30, no. 5, pages 978–984, 2009. (Cited on pages 32 and 195.)

[MIRKES 2015] C. MIRKES, J. HOFFMANN, G. SHAJAN, J. BAUSE, K. BUCKENMAIER and K. SCHEFFLER. *High-resolution quantitative sodium imaging at 9.4 tesla*. Magnetic Resonance in Medicine, vol. 73, no. 1, pages 342–351, 2015. (Cited on pages 1, 29, 83 and 201.)

[MIRKES 2016] C. MIRKES, G. SHAJAN, J. BAUSE, R. POHMANN and K. SCHEFFLER. *Triple-quantum-filtered sodium imaging at 9.4 Tesla*. Magnetic Resonance in Medicine, vol. 75, no. 3, pages 1278–1289, 2016. (Cited on page 29.)

[MOONEY 1969] E.F. MOONEY, P.H. WINSON and F. BOUMEZBEUR. *Nitrogen Magnetic Resonance Spectroscopy*. Annual Reports on NMR Spectroscopy, vol. 2, pages 125–152, 1969. (Cited on pages 6 and 26.)

[MOORE 2003] C.M. MOORE, B.D. FREDERICK, M.E. HENRY, C.C. STREETER, B.M. COHEN and P.F. RENSHAW. *Human in vivo lithium magnetic resonance spectroscopy at 4. 0 tesla: Initial findings*. Biological Psychiatry, vol. 53, pages –, 2003. (Cited on pages 2 and 156.)

[MORRELL 2008] G.R. MORRELL. *A phase-sensitive method of flip angle mapping*. Magnetic Resonance in Medicine, vol. 60, pages 889–894, 2008. (Cited on page 45.)

[MURPHY 2009] E. MURPHY and D.A. EISNER. *Regulation of intracellular and mitochondrial sodium in health and disease*. Circulation Research, vol. 104, no. 3, pages 292–303, 2009. (Cited on page 111.)

[NAGEL 2009a] A.M. NAGEL, M. BOCK, C. HARTMANN, L. GERIGK, J.O. NEUMANN, M.A. WEBER, M. BENDSZUS, A. RADBRUCH, W. WICK, H.P. SCHLEMMER, W. SEMMLER and A. BILLER. *The potential of relaxation-weighted sodium magnetic resonance imaging as demonstrated on brain tumors*. Investigative Radiology, vol. 46, no. 9, pages 539–547, 2009. (Cited on page 32.)

[NAGEL 2009b] A.M. NAGEL, F.B. LAUN, M.A. WEBER, C. MATTHIES, W. SEMMLER and L.R. SCHAD. *Sodium MRI Using a Density-Adapted 3D Radial Acquisition Technique*. Magnetic Resonance in Medicine, vol. 62, pages 1565–1573, 2009. (Cited on page 29.)

[NAGEL 2011] A.M. NAGEL, E. AMARTEIFIO, F. LEHMANN-HORN, K. JURKAT-ROTT, W. SEMMLER, L.R. SCHAD and M.A. WEBER. *3 Tesla sodium inversion recovery magnetic resonance imaging allows for improved visualization of intracellular sodium content changes in muscular channelopathies*. Investigative Radiology, vol. 46, no. 12, pages 759–766, 2011. (Cited on pages 33 and 114.)

[NAGEL 2014] A. M. NAGEL, F. LEHMANN-HORN, M.A. WEBER, K. JURKAT-ROTT, M.B. WOLF, A. RADBRUCH, R. UMATHUM and W. SEMMLER. *In vivo 35Cl MR imaging in humans: a feasibility study*. Radiology, vol. 271, no. 2, pages 585–595, 2014. (Cited on pages 6, 166 and 194.)

[NAGEL 2016] A.M. NAGEL, R. UMATHUM, M.B. RÖSLER, M.E. LADD, I. LITVAK, P.L. GOR'KOV, W.W. BREY and V.D. SCHEPKIN. *39K and 23Na relaxation times and MRI of rat head at 21.1T*. NMR in Biomedicine, vol. 46, 2016. (Cited on pages 110, 188 and 210.)

[NEHRKE 2009] K. NEHRKE. *On the steady-state properties of actual flip angle imaging (AFI)*. Magnetic Resonance in Medicine, vol. 61, no. 1, pages 84–92, 2009. (Cited on page 45.)

[NEHRKE 2012] K. NEHRKE and P. BÖRNERT. *DREAM - A Novel Approach for Robust, Ultra-Fast, Multi-Slice B1 Mapping*. Proceedings of the International Society for Magnetic Resonance in Medicine, vol. 605, 2012. (Cited on page 45.)

[NEUBERGER 2007] T. NEUBERGER, V. GULANI and A. WEBB. *Sodium Renal Imaging in Mice at High Magnetic Fields*. Magnetic Resonance in Medicine, vol. 58, pages 1067–1071, 2007. (Cited on page 30.)

[NIELLES-VALLESPIN 2007] S. NIELLES-VALLESPIN, M.A. WEBER, M. BOCK, A. BONGERS, P. SPEIER, S.E. COMBS, J. WÖHRLE, F. LEHMANN-HORN, M. ESSIG and L.R. SCHAD. *3D radial projection technique with ultrashort echo times for sodium MRI: Clinical applications in human brain and skeletal muscle*. Magnetic Resonance in Medicine, vol. 57, pages 74–81, 2007. (Cited on pages 29 and 64.)

[NIESPOREK 2015] S.C. NIESPOREK, S.H. HOFFMANN, M.C. BERGER, N. BENKHEDAH, A. KUJAWA, P. BACHERT and A.M. NAGEL. *Partial volume correction for in vivo (23)Na-MRI data of the human brain*. Neuroimage, vol. 57, no. 112, pages 353–363, 2015. (Cited on page 134.)

[NISHIMURA 1990] D.G. NISHIMURA. *Time-of-Flight MR Angiography*. Magnetic Resonance in Medicine, vol. 14, pages 194–201, 1990. (Cited on page 16.)

[NOLL 1997] D.C. NOLL. *Multishot Rosette Trajectories for Spectrally Selective MR Imaging*. IEEE Transactions on Medical Imaging, vol. 16, no. 4, pages 372–377, 1997. (Cited on page 21.)

[NORÉN 2004] B. NORÉN, P. LUNDBERG, M. RESSNER, S. WIRELL, S. ALMER, E.O. SMEDBY, S. NEUBAUER and C.T. RODGERS. *Absolute quantification of human liver metabolite concentrations by localized in vivo 31P NMR spectroscopy in diffuse liver disease*. European Radiology, vol. 15, pages 148–157, 2004. (Cited on pages 33 and 196.)

[OGAWA 1990] S. OGAWA, T.M. LEE, A.S. NAYAK and P. GLYNN. *Oxygenation-sensitive contrast in magnetic resonance image of rodent brain at high magnetic fields*. Magnetic Resonance in Medicine, vol. 14, no. 1, pages 68–78, 1990. (Cited on pages 1 and 17.)

[OUWERKERK 2005] R. OUWERKERK, R.G. WEISS and P.A. BOTTOMLEY. *Measuring Human Cardiac Tissue Sodium Concentrations Using Surface Coils, Adiabatic Excitation, and Twisted Projection Imaging With Minimal T2 Losses*. Journal of Magnetic Resonance Imaging, vol. 21, pages 546–555, 2005. (Cited on page 33.)

[OUWERKERK 2007] R. OUWERKERK, M.A. JACOBS, K.J. MACURA, A.C. WOLFF, V. STEARNS, S.D. MEZBAN, N.F. KHOURI, D.A. BLUEMKE and P.A. BOTTOMLEY. *Elevated tissue sodium concentration in malignant breast lesions detected with non-invasive 23Na MRI*. Breast Cancer Research and Treatment, vol. 106, no. 2, pages 151–160, 2007. (Cited on page 33.)

[OUWERKERK 2008] R. OUWERKERK, P.A. BOTTOMLEY, M. SOLAIYAPPAN, A.E. SPOONER, G.F. TOMASELLI, K.C. WU and R.G. WEISS. *Tissue sodium concentration in myocardial infarction in humans: a quantitative 23Na MR imaging study*. Radiology, vol. 248, no. 1, pages 88–96, 2008. (Cited on page 33.)

[PALING 2013] D. PALING, B. S. SOLANKY, F. RIEMER, D. J. TOZER, C. A. M. WHEELER-KINGSHOTT, R. KAPOOR, X. GOLAY and D. H. MILLER. *Sodium accumulation is associated with disability and a progressive course in multiple sclerosis*. Brain, vol. 136, pages 2305–2317, 2013. (Cited on pages 2, 31, 95, 124, 126 and 195.)

[PALOMBO 2016] M. PALOMBO, C. LIGNEUL, C. NAJAC, J. LE DOUCE, J. FLAMENT, C. ESCARTIN, P. HANTRAYE, E. BROUILLET, G. BONVENTO and J. VALETTE. *New paradigm to assess brain cell morphology by diffusion-weighted MR spectroscopy in vivo*. Proceedings of the Natinal Academy of Science USA, vol. 113, no. 24, pages 6671–6676, 2016. (Cited on page 14.)

[PAN 2008] J.W. PAN, A. WILLIAMSON, I. CAVUS, H.P. HETHERINGTON, H. ZAVERI, O.A. PETROFF and D.D. SPENCER. *Neurometabolism in human epilepsy*. Epilepsia, vol. 49, no. 3, pages 31–41, 2008. (Cited on page 148.)

[PANDA 2012] A. PANDA, S. JONES, H. JONES, R.S. RAGHAVAN, K. SANDRASEGARAN, N. BANSAL and U. DYDAK. *Phosphorus Liver MRSI at 3 T Using a Novel Dual-Tuned Eight-Channel 31P/1H Coil*. Magnetic Resonance in Medicine, vol. 68, no. 3, pages 1346–1356, 2012. (Cited on page 144.)

[PAPADAKIS 1997] N.G. PAPADAKIS, A.A. WILKINSON, T.A. CARPENTER and L.D. HALL. *A general method for measurement of the time integral of variant magnetic field gradients: application to 2D spiral imaging*. Journal of Magnetic Resonance Imaging, vol. 15, pages 567–578, 1997. (Cited on page 42.)

[PARASOGLOU 2014] P. PARASOGLOU, D. XIA, G. CHANG and R.R. REGATTE. *Three-dimensional Saturation Transfer 31P-MRI in Muscles of the Lower Leg at 3.0 T*. Scientific reports, 2014. (Cited on page 149.)

[PARASOGLOU 2016] P. PARASOGLOU, R. BROWN and G. MADELIN. *31P-MRI using A Spectrally Selective 3D non-Cartesian FLORET Sequence at 7 T*. Proceedings of the 25th International Society of Magnetic Resonance in Medicine, 2016. (Cited on pages 2, 34, 35 and 176.)

[PARKER 2014] D.L. PARKER, A. PAYNE, N. TODD and J.R. HADLEY. *Phase reconstruction from multiple coil data using a virtual reference coil*. Magnetic Resonance in Medicine, vol. 72, no. 2, pages 563–569, 2014. (Cited on page 110.)

[PARRISH 1997] T.B. PARRISH, D.S. FIENO, S. W. FITZGERALD and R.M. JUDD. *Theoretical Basis for Sodium and Potassium MRI of the Human Heart at 1.5T*. Magnetic Resonance in Medicine, vol. 38, pages 653–661, 1997. (Cited on pages 6, 29 and 194.)

[PAULY 1991] J. PAULY, P. LE ROUX, D. NISHIMURA and A. MACOVSKI. *Parameter relations for the Shinnar-Le Roux selective excitation pulse design algorithm [NMR imaging]*. EEE Transactions on Medical Imaging, vol. 10, no. 1, pages 53–65, 1991. (Cited on page 99.)

[PAYNE 1990] G.S. PAYNE, A.-M.L. SEYMOUR, P. STYLES and G. RADDA. *Multiple Quantum Filtered 23Na NMR Spectroscopy in the Perfused Heart*. NMR in Biomedicine, vol. 3, no. 3, pages 139–146, 1990. (Cited on page 112.)

[PERMAN 1986] W.H. PERMAN, P.A. TURSKI, L.W. HOUSTON, G H. GLOVER and C.E. HAYES. *Methodology of in Vivo Human Sodium MR Imaging at 1.5T*. Radiology, vol. 160, pages 811–820, 1986. (Cited on pages 112 and 193.)

[PETRACCA 2015] M. PETRACCA, L. FLEYSHER, N. OESINGMANN and M. INGLESE. *Sodium MRI of multiple sclerosis*. NMR in Biomedicine, 2015. (Cited on pages 31, 122 and 202.)

[PETRACCA 2016] M. PETRACCA, R.O. VANCEA, L. FLEYSHER, L.E. JONKMAN, N. OESINGMANN and M. INGLESE. *Brain intra- and extracellular sodium concentration in multiple sclerosis: a 7 T MRI study*. Brain, vol. 139, no. 3, pages 795–806, 2016. (Cited on pages 30, 31 and 176.)

[Phlypo 2014] R. Phlypo, B. Thirion and G. Varoquaux. *Deriving a multi-subject functional-connectivity atlas to inform connectome estimation*. Proceedings of Medical Image Computing and Computer-Assisted Intervention meeting, vol. 8675, pages 185–192, 2014. (Cited on pages 18 and 176.)

[Pilkinton 2010] D.T. Pilkinton, M.A. Elliott, J. Magland and R. Reddy. *Sodium MRI Multi-Echo Sequence for Simultaneous Ultra-Short Echo Imaging and T2L* Mapping at 7T with a 12 Channel Phased-Array Coil*. Proceedings of the International Society of Magnetic Resonance in Medicine, vol. 1002, 2010. (Cited on page 115.)

[Pipe 1999] J.G. Pipe. *Motion correction with PROPELLER MRI: application to head motion and free-breathing cardiac imaging*. Magnetic Resonance in Medicine, vol. 42, pages 963–969, 1999. (Cited on page 211.)

[Pipe 2011] J. G. Pipe, N. R. Zwart, E. A. Aboussouan, R. K. Robison, A. Devaraj and K. O. Johnson. *A New Design and Rationale for 3D Orthogonally Oversampled k-Space Trajectories*. Magnetic Resonance in Medicine, vol. 66, pages 1303–1311, 2011. (Cited on pages 1, 21, 29, 65, 184, 197, 198 and 206.)

[Pohmann 2016] R. Pohmann, O. Speck and K. Scheffler. *Signal-to-Noise Ratio and MR Tissue Parameters in Human Brain Imaging at 3, 7, and 9.4 Tesla Using Current Receive Coil Arrays*. Magnetic Resonance in Medicine, vol. 75, pages 801–809, 2016. (Cited on page 26.)

[Port 2013] J.D. Port, K.E. Rampton, Y. Shu, A. Manduca and M.A. Frye. *Short TE 7Li-MRS confirms Bi-exponential lithium T2 relaxation in humans and clearly delineates two patient subtypes*. Journal of Magnetic Resonance Imaging, vol. 37, no. 6, pages 1451–1459, 2013. (Cited on page 156.)

[Posse 1994] S. Posse, C. DeCarli and D. Le Bihan. *Three-dimensional echo-planar MR spectroscopic imaging at short echo times in the human brain*. Radiology, vol. 192, pages 733–738, 1994. (Cited on page 34.)

[Preibisch 2009] C. Preibisch and R. Deichmann. *Influence of RF spoiling on the stability and accuracy of T1 mapping based on spoiled FLASH with varying flip angles*. Magnetic Resonance in Medicine, vol. 61, no. 1, pages 125–135, 2009. (Cited on page 83.)

[Prompers 2006] J.J. Prompers, J.A. Jeneson, M.R. Drost, C.C. Oomens, G.J. Strijkers and K. Nicolay. *Dynamic MRS and MRI of skeletal muscle function and biomechanics*. NMR in Biomedicine, vol. 19, no. 7, pages 927–953, 2006. (Cited on page 148.)

[Provencher 1993] S.W. Provencher. *Estimation of metabolite concentrations from localized in vivo proton NMR spectra*. Magnetic Resonance in Medicine, vol. 30, no. 6, pages 672–679, 1993. (Cited on page 142.)

[Purcell 1946] E.M. Purcell, H.C. Torrey and R.V. Pound. *Resonance absorption by nuclear moments in a solid*. Phys Rev, vol. 69, pages 37–38, 1946. (Cited on page 6.)

[Qian 2008] Y. Qian and F.E. Boada. *Acquisition-weighted stack of spirals for fast high-resolution three-dimensional ultra-short echo time MR imaging*. Magnetic Resonance in Medicine, vol. 60, no. 1, pages 135–145, 2008. (Cited on page 29.)

[Qian 2009] Y. Qian, V.A. Stenger and F.E. Boada. *Parallel imaging with 3D TPI trajectory: SNR and acceleration benefits*. Journal of Magnetic Resonance Imaging, vol. 27, no. 5, pages 656–663, 2009. (Cited on page 29.)

[QIAN 2012a] QIAN, T. ZHAO, G.C. WIGGINS, L.L. WALD, H. ZHENG, J. WEIMER and F.E. BOADA. *Sodium imaging of human brain at 7 T with 15-channel array coil*. Magnetic Resonance in Medicine, vol. 68, no. 6, pages 1807–1814, 2012. (Cited on pages 1, 29 and 126.)

[QIAN 2012b] Y. QIAN, T. ZHAO, G.C. WIGGINS, L.L. WALD, H. ZHENG, J. WEIMER and F.E. BOADA. *Sodium imaging of human brain at 7 T with 15-channel array coil*. Magnetic Resonance in Medicine, vol. 68, no. 6, pages 1807–1814, 2012. (Cited on page 194.)

[QIAN 2015] Y. QIAN, A. PANIGRAHY, C. M. LAYMON, V. K. LEE, J. DRAPPATZ, F. S. LIEBERMAN, F. E. BOADA and J. M. MOUNTZ. *Short-T2 imaging for quantifying concentration of sodium (23Na) of bi-exponential T2 relaxation*. Magnetic Resonance in Medicine, vol. 74, pages 162–174, 2015. (Cited on pages 114, 115 and 202.)

[QUETTIER 2017] L. QUETTIER, G. AUBERT, J. BELORGEY, C. BERRIAUD, A. BOURQUARD, P. BREDY, O. DUBOIS, G. GILGRASS, F.-P. JUSTER, H. LANNOU, F. MOLINIE, M. NUSBAUM, F. NUNIO, A. PAYN, T. SCHILD, M. SCHWEITZER, L. SCOLA, A. SINANNA, V. STEPANOV and P. VEDRINE. *Iseult/INUMAC Whole Body 11.7 T MRI Magnet*. IEEE Transactions on Applied SuperConductivity, vol. 27, no. 4, pages 1346–1356, 2017. (Cited on page 1.)

[RABI 1938] I.I. RABI, J.R. ZACHARIAS, S. MILLMAN and P. KUSCH. *A New Method of Measuring Nuclear Magnetic Moment*. Physical Review, vol. 53, page 318, 1938. (Cited on page 6.)

[RASCHE 1999] V. RASCHE, R. PROKSA, R. SINKUS, P. BORNERT and H. EGGERS. *Resampling of Data Between Arbitrary Grids Using Convolution Interpolation*. IEEE Transactions on Medical Imaging, vol. 18, no. 5, pages 385–392, 1999. (Cited on pages 69 and 70.)

[REETZ 2012] K. REETZ, S. ROMANZETTI, I. DOGAN, C. SAβ, C.J. WERNER, J. SCHIEFER, J.B. SCHULZ and N.J. SHAH. *Increased brain tissue sodium concentration in Huntington's Disease - a Sodium imaging study at 4T*. NeuroImage, vol. 63, pages 525–524, 2012. (Cited on pages 32 and 195.)

[RENSHAW 1985] P.F. RENSHAW, J.C. HASELGROVE, J.S. LEIGH and B. CHANCE. *In Vivo Nuclear Magnetic Resonance Imaging of Lithium*. Magnetic Resonance in Medicine, vol. 2, no. 5, pages 5–16, 1985. (Cited on pages 6, 35, 151, 193 and 196.)

[RENSHAW 1988] P.F. RENSHAW and S. WICKLUND. *In Vivo measurements of Lithium in humans by nuclear magnetic resonance spectroscopy*. Biological Psychiatry, vol. 23, no. 5, pages 465–475, 1988. (Cited on pages 35, 151, 193 and 196.)

[RIBEIRO 2010] J.A. RIBEIRO. *Diffusion Coefficients of Sodium Fluoride in Aqueous Solutions at 298.15 K and 310.15 K*. ResearchGate, vol. 57, no. 2, pages 410–414, 2010. (Cited on page 105.)

[RIEMER 2014] F. RIEMER, B.S. SOLANKY, M. CLEMENCE C. STEHNING, C.A.M. WHEELER-KINGSHOTT and X. GOLAY. *Sodium (23Na) ultra-short echo time imaging in the human brain using a 3D-Cones trajectory*. Magnetic Resonance Materials in Physics, Biology and Medicine, vol. 27, pages 35–46, 2014. (Cited on pages 29, 82, 84, 95 and 124.)

[RINK 2016] K. RINK, M.C. BERGER, N. BENKHEDAH, C. GNAHM, P. BACHERT and A.M. NAGEL. *31P MR Imaging with Radial bSSFP Data Acquisition and 1H Constraint Iterative Reconstruction*. Proceedings of the International Society of Magnetic Resonance in Medicine, vol. 3938, 2016. (Cited on page 34.)

[ROBSON 2003] M.D. ROBSON, P.D. GATEHOUSE, M. BYDDER and G. BYDDER. *Magnetic resonance : An introduction to ultrashort te (UTE)*. Journal of Computer Assisted Tomographie, vol. 27, no. 6, pages 825–846, 2003. (Cited on page 61.)

[RODGERS 2014] C.T. RODGERS, W.T. CLARKE, C. SNYDER, J.T. VAUGHAN, S. NEUBAUER and M.D. ROBSON. *Human cardiac 31P magnetic resonance spectroscopy at 7 Tesla*. Magnetic Resonance in Medicine, vol. 72, pages 304–315, 2014. (Cited on pages 34 and 144.)

[ROMANZETTI 2006] S. ROMANZETTI, M. HALSE, J. KAFFANKE, K. ZILLES, B.J. BALCOM and N.J. SHAH. *A comparison of three SPRITE techniques for the quantitative 3D imaging of the 23Na spin density on a 4T whole-body machine*. Journal of Magnetic Resonance, vol. 179, no. 1, pages 64–72, 2006. (Cited on page 29.)

[ROMANZETTI 2014] S. ROMANZETTI, C.C. MIRKES, D.P. FIEGE, A. CELIK, J. FELDER and N.J. SHAH. *Mapping tissue sodium concentration in the human brain: A comparison of MR sequences at 9.4 Tesla*. NeuroImage, vol. 96, no. 1, pages 44–53, 2014. (Cited on pages 65, 66, 78 and 178.)

[ROONEY 1991] W. ROONEY and C.S. SPRINGER Jr. *A Comprehensive Approach to the Analysis and Interpretation of the Resonances of Spins 3/2 from-Living Systems*. NMR in Biomedicine, vol. 4, pages 209–226, 1991. (Cited on pages 28 and 176.)

[ROSE 1994] A.M. ROSE and R. VALDES. *Understanding the sodium pump and its relevance to disease*. Clinical Chemistry, vol. 40, pages 1674–1685, 1994. (Cited on page 111.)

[ROSS 2001] B. ROSS and S. BLUML. *Magnetic Resonance Spectroscopy of the Human Brain*. The anatomicl record, vol. 265, pages 54–84, 2001. (Cited on page 14.)

[RUIZ-CABELLO 2011] J. RUIZ-CABELLO, B.P. BARNETT, P.A. BOTTOMLEY and J.W.M. BULTE. *Fluorine (19F) MRS and MRI in biomedicine*. NMR in Biomedicine, vol. 24, no. 2, pages 144–129, 2011. (Cited on pages 6 and 193.)

[SABATI 2013] M. SABATI and A.A. MAUDSLEY. *Fast and high-resolution quantitative mapping of tissue water content with full brain coverage for clinically-driven studies*. Magnetic Resonance Imaging, vol. 31, no. 44, pages 1752–1759, 2013. (Cited on pages 83 and 85.)

[SACOLICK 2007] L.I. SACOLICK, F. WIESINGER, I. HANCU and M.W. VOGEL. *B1 Mapping by Bloch-Siegert Shift*. Magnetic Resonance in Medicine, vol. 63, pages 1315–1322, 2007. (Cited on page 45.)

[SAIB 2017] G. SAIB, V. GRAS, F. MAUCONDUIT, N. BOULANT, A. VIGNAUD, D. LE BIHAN, L. LE BRUSQUET and A. AMADON. *Double-Spoke Slab-Selective Ramp Pulse Design for UHF TOF MR Angiography*. Proceedings of the International Society of Magnetic Resonance in Medicine 25th meeting, vol. 1319, 2017. (Cited on pages 17 and 176.)

[SARTY 2001] G.E. SARTY, R. BENNETT and R.W. COX. *Direct reconstruction of non-Cartesian k-space data using a nonuniform fast Fourier transform*. Magnetic Resonance in Medicine, vol. 45, no. 5, pages 908–915, 2001. (Cited on page 24.)

[SCHEENEN 2008] T.W. SCHEENEN, A. HEERSCHAP and D.W. KLOMP. *Towards 1H-MRSI of the human brain at 7T with slice-selective adiabatic refocusing pulses*. Magnetic Resonance Materials in Physics, Biology and Medicine, vol. 21, no. 1-2, pages 95–101, 2008. (Cited on page 154.)

[SCHEFFLER 1999] K. SCHEFFLER. *A pictorial description of steady-states in rapid magnetic resonance imaging*. Concepts in Magnetic Resonance, vol. 11, no. 5, pages 291–304, 1999. (Cited on page 99.)

[SCHEPKIN 2006] V.D. SCHEPKIN, K.C. LEE, K. KUSZPIT, M. MUTHUSWAMI, T.D. JOHNSON, T.L. CHENEVERT, A. REHEMTULLA and B.DROSS. *Proton and sodium MRI assessment of emerging tumor chemotherapeutic resistance*. NMR in Biomedicine, vol. 19, no. 8, pages 1035–1042, 2006. (Cited on page 30.)

[SCHMITT 2004] P. SCHMITT, M.A. GRISWOLD, P.M. JAKOB, M. KOTAS, V. GULANI, M. FLENTJE and A. HAASE. *Inversion Recovery TrueFISP: Quantification of T1, T2 and Spin Density*. Magnetic Resonance in Medicine, vol. 51, pages 661–667, 2004. (Cited on pages 17 and 97.)

[SCHNEIDER 2011] J. T. SCHNEIDER, M. HAAS, W. RUHM, J. HENNIG and P. ULLMANN. *Robust spatially selective excitation using radiofrequency pulses adapted to the effective spatially encoding magnetic fields*. Magnetic Resonance in Medicine, vol. 65, no. 2, pages 409–421, 2011. (Cited on page 42.)

[SCHROEDER 2006] W. SCHROEDER, K. MARTIN and B. LORENSEN. The visualization toolkit. Kitware, fourth edition édition, 2006. (Cited on pages 21, 64, 176 and 178.)

[SESHAN 1997] V. SESHAN, A.D. SHERRY and N. BANSAL. *Evaluation of triple quantum-filtered 23Na NMR spectroscopy in the in situ rat liver*. Magnetic Resonance in Medicine, vol. 38, pages 821–827, 1997. (Cited on page 114.)

[SHAH 2015] N.J. SHAH, W.A. WORTHOFF and K.J. LANGEN. *Imaging of sodium in the brain: a brief review*. NMR in Biomedicine, 2015. (Cited on pages 30, 105, 127 and 187.)

[SHAJAN 2016] G. SHAJAN, C. MIRKES, K. BUCKENMAIER, J. HOFFMANN, R. POHMANN and K. SCHEFFLER. *Three-layered Radio Frequency Coil Arrangement for Sodium MRI of the Human Brain at 9.4 Tesla*. Magnetic Resonance in Medicine, vol. 75, pages 906–906, 2016. (Cited on pages 1 and 110.)

[SHIMIZU 1992] T. SHIMIZU, H. NARITOMI, Y. KURIYAMA and I. SAWADA. *Sequential changes of sodium magnetic resonance images after cerebral hemorrhage*. Neuroradiology, vol. 34, pages 301–304, 1992. (Cited on page 32.)

[SHORTER 2009] E. SHORTER. *The history of lithium therapy*. Bipolar Disorder, vol. 11, no. 2, pages 4–9, 2009. (Cited on pages 35 and 196.)

[SLOTBOOM 1991] J. SLOTBOOM, A.F. MEHLKOPF and W.M.M.J. BOVEE. *A single-shot localization pulse sequence suited for coils with inhomogeneous RF fields using adiabatic slice-selective RF pulses*. Journal of Magnetic Resonance, vol. 95, no. 3, pages 396–404, 1991. (Cited on page 14.)

[SMITH 2011] F.E. SMITH, D.A. COUSINS, P.E. THELWALL, I.N. FERRIER and A.M. BLAMIRE. *Quantitative Lithium Magnetic Resonance Spectroscopy in the Normal Human Brain on a 3 T Clinical Scanner*. Magnetic Resonance in Medicine, vol. 66, pages 945–949, 2011. (Cited on pages 2, 35, 156, 157, 161 and 196.)

[SOARES 2001] J.C. SOARES, F.E. BOADA, S. SPENCER, A.G. MALLINGER, C.S. DIPPOLD, K.F. WELLS, E. FRANK, M.S. KESHAVAN, S. GERSHON and D.J. KUPFER. *Brain lithium concentrations in bipolar disorder patients: preliminary (7)Li magnetic resonance studies at 3 T*. Biological Psychiatry, vol. 49, no. 5, pages 437–443, 2001. (Cited on pages 35 and 196.)

[SOHER 1996] B.J. SOHER, P.C. VAN ZIJL, J.H. DUYN and P.B. BARKER. *Quantitative proton MR spectroscopic imaging of the human brain*. Magnetic Resonance in Medicine, vol. 35, pages 356–363, 1996. (Cited on page 146.)

[Stejskal 1965] E.O. Stejskal and J.E. Tanner. *Spin Diffusion Measurements: Spin Echoes in the presence of a Time-Dependent Field Gradient*. The Journal of Chemical Physics, vol. 42, no. 1, page 288, 1965. (Cited on page 14.)

[Stobbe 2005] R.W. Stobbe and C. Beaulieu. *Rapid in vivo monitoring of chemotherapeutic response using weighted sodium magnetic resonance imaging*. Magnetic Resonance in Medicine, vol. 54, pages 1305–1310, 2005. (Cited on page 114.)

[Stobbe 2008] R.W. Stobbe and C. Beaulieu. *Sodium Imaging Optimization Under Specific Absorption Rate Constraint*. Magnetic Resonance in Medicine, vol. 59, pages 345–355, 2008. (Cited on page 84.)

[Stobbe 2014] R.W. Stobbe and C. Beaulieu. *Exploring and enhancing relaxation-based sodium MRI contrast*. Magnetic Resonance Materials in Physics, Biology and Medicine, vol. 27, no. 1, pages 21–33, 2014. (Cited on page 114.)

[Stöcker 2014] T. Stöcker, F. Keil, K. Vahedipour, D. Brenner, E. Pracht and N.J. Shah. *MR parameter quantification with magnetization-prepared double echo steady-state (MP-DESS)*. Magnetic Resonance in Medicine, vol. 72, no. 1, pages 103–111, 2014. (Cited on page 97.)

[Stockmann 2017] J.P. Stockmann and L.L. Wald. *In vivo B0 field shimming methods for MRI at 7T*. Neuroimage, 2017. (Cited on page 41.)

[Stoll 2016] V.M. Stoll, W.T. Clarke, E. Levelt, A. Liu, S.G. Myerson, M.D. Robson, S. Neubauer and C.T. Rodgers. *Dilated cardiomyopathy: phosphorus 31P MR spectroscopy at 7T*. Radiology, vol. 281, pages 409–417, 2016. (Cited on pages 33 and 196.)

[Stollberger 1988] R. Stollberger, P. Wach, G. McKinnon, E. Justich and F. Ebner. *Rf-field mapping in vivo*. Proceedings of the 7th Annual Meeting of SMRM, page 106, 1988. (Cited on pages 44, 45, 83 and 200.)

[Stout 2017] J. Stout, A.-S. Hanak, L. Chevillard, B. Djemaï, P. Risède, E. Giacomini, J. Poupon, D. A. Barrière, F. Bellivier, B. Mégarbane and F. Boumezbeur. *Investigation of lithium distribution in the rat brain ex vivo using lithium-7 magnetic resonance spectroscopy and imaging at 17.2 T*. NMR in Biomedicine, 2017. (Cited on pages 146, 151 and 196.)

[Stucht 2015] D. Stucht, K.A. Danishad, P. Schulze, F. Godenschweger, M. Zaitsev and O. Speck. *Highest Resolution In Vivo Human Brain MRI Using Prospective Motion Correction*. PLoS One, vol. z0133921, no. 7, pages 900–919, 2015. (Cited on page 1.)

[Stys 2005] P.K. Stys. *General mechanisms of axonal damage and its prevention*. Journal of the Neurological Sciences, vol. 233, pages 3–13, 2005. (Cited on page 31.)

[Sukstanskii 2016] A.L. Sukstanskii, J. Wen, A.H. Cross and D.A. Yablonskiy. *Simultaneous multi-angular relaxometry of tissue with MRI (SMART MRI): Theoretical background and proof of concept*. Magnetic Resonance in Medicine, 2016. (Cited on page 18.)

[Szomolanyi 2001] P. Szomolanyi, D. Goodyear, B. Balcom and D. Matheson. *SPIRAL-SPRITE: a rapid single point MRI technique for application to porous media*. Journal of Magnetic Resonance Imaging, vol. 19, no. 3-4, pages 423–428, 2001. (Cited on page 29.)

[Tanase 2005] C. Tanase and F.E. Boada. *Triple-quantum-filtered imaging of sodium in presence of B(0) inhomogeneities*. Journal of Magnetic Resonance, vol. 174, no. 2, pages 270–278, 2005. (Cited on pages 29 and 30.)

[THULBORN 2005] K. R. THULBORN, D. DAVIS, J. SNYDER, H. YONAS and A. KASSAM. *Sodium MR imaging of acute and subacute stroke for assessment of tissue viability*. Neuroimaging Clin North America, vol. 15, no. 3, pages 639–653, 2005. (Cited on pages 32 and 195.)

[THULBORN 2015] K. R. THULBORN, E. LUI, J. GUNTIN, S. JAMIL, Z. SUN, T. C. CLAIBORNE and I. C. ATKINSON. *Quantitative sodium MRI of the human brain at 9.4T provides assessment of tissue sodium concentration and cell volume fraction during normal aging*. NMR in Biomedicine, 2015. (Cited on pages 126, 127, 201 and 206.)

[THULBORN 2017] K.R. THULBORN. *Quantitative sodium MR imaging: A review of its evolving role in medicine*. NeuroImage, 2017. (Cited on page 126.)

[TORO 2016] R. TORO and *et al. Brainspell*. Available from `http://brainspell.org/`, Consulted 2016. (Cited on pages 18 and 176.)

[TORREY 1956] H.C. TORREY. *Bloch Equations with Diffusion Terms*. Physical Review, vol. 104, no. 3, pages 563–565, 1956. (Cited on pages 100 and 209.)

[TSAI 2012] K. TSAI, J. MA, D. YE and J. WU. *Curvelet processing of MRI for local image enhancement*. International Journal for Numerical Methods in Biomedical Engineering, vol. 28, pages 661–677, 2012. (Cited on pages 78 and 199.)

[TSANG 2011] A. TSANG, R.W. STOBBE, N. ASDAGHI, M.S. HUSSAIN, Y.A. BHAGAT, C. BEAULIEU, D. EMERY and K.S. BUTCHER. *Relationship Between Sodium Intensity and Perfusion Deficits in Acute Ischemic Stroke*. Journal of Magnetic Resonance Imaging, vol. 33, pages 41–47, 2011. (Cited on pages 32 and 195.)

[TSANG 2013] A. TSANG, R.W. STOBBE and C. BEAULIEU. *Evaluation of B0-inhomogeneity correction for triple-quantum-filtered sodium MRI of the human brain at 4.7 T*. Journal of Magnetic Resonance, vol. 230, pages 134–144, 2013. (Cited on page 29.)

[TSANG 2015] A. TSANG, R.W. STOBBE and C. BEAULIEU. *In Vivo Double Quantum Filtered Sodium Magnetic Resonance Imaging of Human Brain*. Magnetic Resonance in Medicine, vol. 73, no. 2, pages 497–504, 2015. (Cited on page 29.)

[TUCH 2002] D.S. TUCH, T.G. REESE, M.R. WIEGELL, N. MAKRIS, J.W. **Belliveau** and V.J. WEDEEN. *High Angular Resolution Diffusion Imaging reveals intravoxel white matter fiber heterogeneity*. Magnetic Resonance in Medicine, vol. 48, pages 577–582, 2002. (Cited on page 14.)

[TUCH 2004] D.S. TUCH. *Q-ball imaging*. Magnetic Resonance in Medicine, vol. 52, pages 1358–1372, 2004. (Cited on page 14.)

[UGURBIL 2014] K. UGURBIL. *Magnetic Resonance Imaging at Ultrahigh Fields*. IEEE Transactions on Biomedical Engineering, vol. 61, no. 5, pages 1364–1379, 2014. (Cited on page 36.)

[UMATHUM 2013] R. UMATHUM, M.B. RÖSLER and A.M. NAGEL. *In vivo 39K MR Imaging of the Human Muscle and Brain*. Radiology, vol. 269, pages 569–576, 2013. (Cited on pages 6 and 166.)

[VALABRÈGUE 2016] R. VALABRÈGUE and L. DE ROCHEFORT. *Fisher Information Matrix for Optimizing the Acquisition Parameters in Multi-Parametric Mapping Based on Fast Steady-State Sequences*. Proceedings of the International Society of Magnetic Resonance in Medicine, page 1569, 2016. (Cited on page 108.)

[VALETTE 2017] J. VALETTE, B. TIRET and F. BOUMEZBEUR. *Experimental strategies for in vivo 13C NMR spectroscopy*. Analytical Biochemistry, vol. 529, no. 15, pages 216–228, 2017. (Cited on pages 1, 6 and 194.)

[VAN DER KEMP 2013] W.J.M. VAN DER KEMP, V.O. BOER, P.R. LUIJTEN, B.L. STEHOUWER, W.B. VELDHUIS and D.W.J. KLOMP. *Adiabatic multi-echo 31P spectroscopic imaging (AMESING) at 7 T for the measurement of transverse relaxation times and regaining of sensitivity in tissues with short T2* values*. NMR in Biomedicine, vol. 26, pages 1299–1307, 2013. (Cited on page 34.)

[VAN DER KEMP 2014] W.J. VAN DER KEMP, B.L. STEHOUWER, P.R. LUIJTEN, M.A. VAN DEN BOSCH and D.W. KLOMP. *Detection of alterations in membrane metabolism during neoadjuvant chemotherapy in patients with breast cancer using phosphorus magnetic resonance spectroscopy at 7 Tesla*. Springerplus, vol. 3, page 634, 2014. (Cited on pages 34 and 196.)

[VAN DER MAAREL 1989] J.R.C. VAN DER MAAREL. *Relxation of Spin 3/2 in a Non Zero Average Electric Field Gradient*. Chemical Physics Letters, vol. 3, no. 155, 1989. (Cited on pages 28, 29, 118 and 176.)

[VAN DER MAAREL 2001] J.R.C. VAN DER MAAREL. *Dynamics of Spin I 3/2 under Spin-Locking Conditionsin an Ordered Environment*. Journal of Magnetic Resonance Imaging, vol. 151, pages 298–313, 2001. (Cited on page 29.)

[VAN DER MAAREL 2003] J.R.C. VAN DER MAAREL. *Thermal Relaxation and Coherence Dynamics of Spin 3/2. I. Static and Fluctuating Quadrupolar Interactions in the Multipole Basis*. Concepts in Magnetic Resonance Part A, vol. 2, no. 19A, pages 97–116, 2003. (Cited on page 29.)

[VAN ZIJL 2011] P.C.M. VAN ZIJL and N.N. YADAV. *Chemical Exchange Saturation Transfer (CEST): what is in a name and what isn't?* Magnetic Resonance in Medicine, vol. 65, no. 4, pages 927–948, 2011. (Cited on page 14.)

[VEDRINE 2008] P. VEDRINE, G. AUBERT, F. BEAUDET, J. BELORGEY, J. BELTRAMELLI, C. BERRIAUD, P. BREDY, P. CHESNY, A. DONATI, G. GILGRASS, G. GRUNBLATT, F.P. JUSTER, F. MOLINIE, C. MEURIS, F. NUNIO, A. PAYN, L. QUETTIER, J.M. REY, T. SCHILD and A. SINANNA. *The Whole Body 11.7 T MRI Magnet for Iseult/INUMAC Project*. IEEE Transactions on Applied Superconductivity, vol. 18, no. 2, pages 868–873, June 2008. (Cited on pages 1 and 212.)

[VOGEL 1979] H. VOGEL. *A better way to construct the sunflower head*. Mathematical Biosciences, vol. 44, no. 44, pages 179–189, 1979. (Cited on page 72.)

[VORONOI 1908] G. VORONOI. *Nouvelles applications des paramètres continus Ã la théorie des formes quadratiques*. Journal fÃ$\frac{1}{4}$r die Reine und Angewandte Mathematik, vol. 133, pages 97–178, 1908. (Cited on page 69.)

[WANG 2004] Z. WANG, A.C. BOVIK, H.R. SHEIKH and E.P. SIMONCELLI. *Image quality assessment: From error visibility to structural similarity*. IEEE Transactions on Image Processing, vol. 4, no. 13, pages 600–612, 2004. (Cited on pages 26 and 74.)

[WARNTJES 2007] J.B. WARNTJES, O. DAHLQVIST and P. LUNDBERG. *Novel method for rapid simultaneous T1, T2* and proton density quantification*. Magnetic Resonance in Medicine, vol. 57, no. 3, pages 528–537, 2007. (Cited on pages 17 and 97.)

[WARNTJES 2008] J.B. WARNTJES, O.D. LEINHARD, J. WEST and P. LUNDBERG. *Rapid magnetic resonance quantification on the brain: Optimization for clinical usage*. Magnetic Resonance in Medicine, vol. 60, no. 2, pages 320–329, 2008. (Cited on pages 18 and 97.)

[WATTS 2011] A. WATTS, R.W. STOBBE and C. BEAULIEU. *Signal-to-noise optimization for sodium MRI of the human knee at 4.7 Tesla using steady state*. Magnetic Resonance in Medicine, 2011. (Cited on page 33.)

[WAXMAN 2008] S.G. WAXMAN. *Mechanisms of Disease: sodium channels and neuroprotection in multiple sclerosis current status*. Nature Clinical Practice Neurology, vol. 4, no. 3, 2008. (Cited on page 31.)

[WEBER 2011] M.A. WEBER, A.M. NAGEL, K. JURKAT-ROTT and F. LEHMANN-HORN. *Sodium (23Na) MRI detects elevated muscular sodium concentration in Duchenne muscular dystrophy*. Neurology, vol. 77, no. 23, pages 2017–2024, 2011. (Cited on page 33.)

[WEDEEN 2005] V.J. WEDEEN, P. HAGMANN, W.I. TSENG, T.G. REESE and R.M. WEISSKOFF. *Mapping complex tissue architecture with diffusion spectrum magnetic resonance imaging*. Magnetic Resonance in Medicine, vol. 54, pages 1377–1386, 2005. (Cited on page 14.)

[WEIGEL 2015] M. WEIGEL. *Extended phase graphs: Dephasing, RF pulses, and echoes-pure and simple*. Journal of Magnetic Resonance Imaging, vol. 41, no. 2, pages 266–395, 2015. (Cited on page 99.)

[WEIGER 2011] M. WEIGER, K.P. PRUESSMANN and F. HENNEL. *MRI with zero echo time: hard versus sweep pulse excitation*. Magnetic Resonance in Medicine, vol. 66, no. 2, pages 379–389, 2011. (Cited on page 62.)

[WEISKOPF 2013] N. WEISKOPF, J. SUCKLIN, G. WILLIAMS, M.M. CORREIA, B. INKSTER, R. TAIT, C. OOI, E.T. BULLMORE and A. LUTTI. *Quantitative multi-parameter mapping of R1, PD*, MT and R2* at 3T: a mutli-center validation*. Frontiers in Neuroscience, vol. 7, 2013. (Cited on pages 17, 18 and 176.)

[WELSCH 2009] G.H. WELSCH, K. SCHEFFLER, T.C. MAMISCH, T. HUGHES, S. MILLINGTON, M. DEIMLING and S. TRATTNIG. *Rapid estimation of cartilage T2 based on double echo at steady state (DESS) with 3 Tesla*. Magnetic Resonance in Medicine, vol. 62, pages 544–549, 2009. (Cited on page 97.)

[WETTERLING 2012] F. WETTERLING, D.M. CORTEVILLE, R. KALAYCIYAN, A. RENNINGS, S. KONSTANDIN, A.M. NAGEL, H. STARK and L.R. SCHAD. *Whole body sodium MRI at 3T using an asymmetric birdcage resonator and short echo time sequence: first images of a male volunteer*. Physics in Medicine and Biology, vol. 57, pages 4555–4567, 2012. (Cited on pages 33 and 176.)

[WETTERLING 2015] F.F. WETTERLING, L. GALLAGHER, J. MULLIN, W.M. HOLMES, C. MCCABE, I.M. MACRAE and A.J. FAGAN. *Sodium-23 Magnetic Resonance Imaging Has Potential for Improving Penumbra Detection but Not for Estimating Stroke Onset Time*. Journal of Cerebral Blood Flow Metabolism, vol. 35, no. 1, pages 103–110, 2015. (Cited on pages 32 and 195.)

[WIMPERIS 1992] S. WIMPERIS, P. COLE and P. STYLES. *Triple-Quantum-Filtration NMR Imaging of 200 mM Sodium at 1.9 Tesla*. Journal of Magnetic Resonance, vol. 98, no. 1, pages 628–636, 1992. (Cited on pages 29 and 202.)

[WINFIELD 2016] J.M. WINFIELD, D.J. COLLINS, A.N. PRIEST, R.A. QUEST, A. GLOVER, S. HUNTER, V.A. **MORGAN**, S. FREEMAN, A. ROCKALL and N.M. DESOUZA. *A framework for optimization of diffusion-weighted MRI protocols for large field-of-view abdominal-pelvic imaging in multicenter studies*. Medical Physics, vol. 43, no. 1, pages 95–110, 2016. (Cited on page 107.)

[WINKELMANN 2007] S. WINKELMANN, T. SCHAEFFTER, T. KOEHLER, H. EGGERS and O. DOESSEL. *An optimal radial profile order based on the Golden Ratio for time-resolved MRI*. IEEE Transactions on Medical Imaging, vol. 26, no. 1, pages 68–76, 2007. (Cited on pages 19 and 199.)

[YARNYKH 2007] V.L. YARNYKH. *Actual Flip-Angle Imaging in the Pulsed Steady State: A Method for Rapid Three-Dimensional Mapping of the Transmitted Radiofrequency Field*. Magnetic Resonance in Medicine, vol. 57, pages 192–200, 2007. (Cited on page 45.)

[YOUNG 1994] I.R. YOUNG, J.W. HAND, A. OATRIDGE and M.V. PRIOR. *Modeling and observation of temperature changes in vivo using MRI*. Magnetic Resonance in Medicine, vol. 32, pages 358–369, 1994. (Cited on page 17.)

[ZAARAOUI 2012] W. ZAARAOUI, S. KONSTANDIN, B. AUDOIN, A.M. NAGEL, A. RICO, I. MALIKOVA, E. SOULIER, P. VIOUT, S. CONFORT-GOUNYand P.J. COZZONE, J. PELLETIER, L.R. SCHAD and J.P. RANJEVA. *Distribution of Brain Sodium Accumulation Correlates with Disability in Multiple Sclerosis: a Cross-sectional 23Na MR Imaging Study*. Radiology, 2012. (Cited on pages 2, 31, 32, 82, 84, 95, 124, 176 and 195.)

[ZAITSEV 2006] M. ZAITSEV, C. DOLD, G. SAKAS, J. HENNIG and O. SPECK. *Magnetic resonance imaging of freely moving objects: prospective real-time motion correction using an external optical motion tracking system*. NeuroImage, vol. 31, no. 3, pages 1038–1050, 2006. (Cited on page 125.)

[ZBÝN 2015] S. ZBÝN, V. MLYNÁRIK, V. JURAS, P. SZOMOLANYI and S. TRATTNIG. *Evaluation of cartilage repair and osteoarthritis with sodium MRI*. NMR in Biomedicine, 2015. (Cited on page 33.)

[ZHANG 2012] H. ZHANG, T. SCHNEIDER, C.A. WHEELER-KINGSHOTT and D.C. ALEXANDER. *NODDI: practical in vivo neurite orientation dispersion and density imaging on the human brain*. NeuroImage, vol. 61, no. 4, pages 1000–1016, 2012. (Cited on page 14.)

[ZHANG 2015] Y. ZHANG, S. WANG, G. JI, Z. DONG and J. YAN. *Preliminary Research on Combination of Exponential Wavelet and FISTA for CS-MRI*. Bioinformatics and Biomedical Engineering, pages 175–182, 2015. (Cited on page 78.)

[ZHAO 2016] B. ZHAO, J.P. HALDAR, K. SETSOMPOP and L.L. WALD. *Optimal experiment design for magnetic resonance fingerprinting*. Proceedings of the 38th Annual International Conference of the IEEE Engineering in Medicine and Biology Society (EMBC), pages 453–456, 2016. (Cited on page 108.)

[ZHOU 1998] X. ZHOU, Z.P. LIANG, S.L. GEWALT, G.P. GOFER, P.C. LAUTERBUR and G.A. JOHNSON. *A fast spin echo technique with circular sampling*. Magnetic Resonance in Medicine, vol. 39, no. 1, pages 23–27, 1998. (Cited on page 21.)

[ZÖLLNER 2015] F. G. ZÖLLNER, S. KONSTANDIN, J. LOMMEN, J. BUDJAN, S.O. SCHOENBERG, L.R. SCHAD and S. HANEDER. *Quantitative sodium MRI of kidney*. NMR in Biomedicine, 2015. (Cited on page 33.)

[ZUR 1991] Y. ZUR, M.L. WOOD and L.J. NEURINGER. *Spoiling of transverse magnetization in steady-state sequences*. Magnetic Resonance in Medicine, vol. 21, no. 2, pages 251–263, 1991. (Cited on page 100.)

[The Blender Foundation] The Blender Foundation. *Blender - a 3D modelling and rendering package*. Blender Institute, Amsterdam. (Cited on page 51.)

ÉCOLE DOCTORALE
Physique et ingénierie :
électrons, photons,
sciences du vivant (EOBE)

Title : Methodological Developments for Sodium, Phosphorus and Lithium MRI at high magnetic field: Applications to clinical research at 3 and 7 Tesla.

Keywords : Magnetic Resonance Imaging, X Nuclei, Sodium, Lithium, Metabolism, Phosphorus

Abstract : Nuclear Magnetic Resonance Imaging of exotic (X) nuclei, other than Hydrogen, allows to probe in vivo metabolism and cellular physiology in normal or pathological conditions. Moreover, X-MRI can be used in pharmacology studies. However, X-MRI suffers from the relatively low sensitivities and in vivo concentrations of these nuclei. Sodium nuclei (^{23}Na) is the second most NMR visible nuclei in brain tissues and its distribution in both intra- and extra-cellular compartments is tightly regulated by, in particular, the Na^+/K^+-ATPase pump. Stocks of Adenosine Triphosphate (ATP) and Phosphocreatine (PCr), main sources of cellular energy are perpetually maintained to ensure proper cellular function. This is why, study of spatial distributions of these two phosphorylated metabolites along with Sodium could yield insights about cellular viability and metabolism. Finally, Lithium is the reference treatment to prevent the onset of maniac events for patients suffering from bipolar disorders. Nevertheless, many questions are still unanswered about its spatial distribution in brain tissues and its underlying therapeutic mechanism.

During these three years of PhD, we implemented efficient Acquisition and Reconstruction protocols for ^{23}Na, ^{31}P and ^{7}Li MRI using Ultra-Short Echo-Time (UTE) sequences and non-Cartesian sampling combined with dedicated quantification pipelines to obtain accurate and robust concentration measurements in the brain. In particular, our proposed method accounts for signal bias due to the heterogeneities in coil transmission (B_1^+) and reception (B_1^-). Additionally, longitudinal (T_1) and transverse (T_2) relaxation times were assessed and the NMR signal was corrected for their respective weighting. Our quantification pipeline was validated in vitro for ^{23}Na MRI. Various Fourier space sampling schemes along with undersampling strategies and reconstruction methods were evaluated and compared. Finally, a multiple-gradient-echo (MGE) acquisition was implemented to explore cellular compartmentalization as an alternative to Multiple Quantum Filtering (MQF) approaches.

These developments were applied at 3 T in a clinical research setting for ^{23}Na MRI on healthy volunteers in collaboration with the Neurology department of Aachen University Clinic, opening the way for an ongoing study of Alzheimer's disease patients. Proof-of-concept studies were conducted at 7 T at NeuroSpin for ^{31}P MRI on healthy volunteers and for ^{7}Li MRI in bipolar patients to study brain lithium distribution in collaboration with Hospital Fernand Widal in Paris.

Université Paris-Saclay
Espace Technologique / Immeuble Discovery
Route de l'Orme aux Merisiers RD 128 / 91190 Saint-Aubin, France

université
PARIS-SACLAY

ÉCOLE DOCTORALE
Physique et ingénierie :
électrons, photons,
sciences du vivant (EOBE)

Titre : Développements Méthodologiques pour l'IRM à haut champ magnétique du Sodium, du Phosphore et du Lithium : Applications en Recherche Clinique à 3 et 7 Tesla.

Mots clefs : IRM, Noyaux X, Sodium, Lithium, Métabolisme, Phosphore

Résumé : L'Imagerie par Résonance Magnétique Nucléaire des noyaux exotiques (X), autres que l'Hydrogène, permet d'explorer in vivo le métabolisme et la physiologie en conditions normales ou pathologiques mais aussi d'étudier la pharmacologie de manière non-invasive. Toutefois, ces explorations souffrent de la moindre sensibilité en IRM de ces noyaux et de leur plus faible concentration dans les tissus. Le Sodium-23 (^{23}Na) est le second noyau le plus visible en RMN dans les tissus cérébraux et sa distribution, dans les compartiments intra- et extra-cellulaires, est strictement régulée notamment par la pompe Na^+/K^+-ATPase. Les stocks d'adénosine triphosphate (ATP) et de phosphocréatine (PCr), réservoirs d'énergie pour l'activité enzymatique, doivent être perpétuellement reconstitués pour assurer le bon fonctionnement cellulaire. C'est pourquoi étudier les distributions cérébrales de ces deux métabolites phosphorylées en plus de celle du sodium permettrait de définir des indicateurs quantitatifs de la viabilité et du métabolisme cellulaire. Enfin, le lithium est le traitement de référence pour la prévention de la crise maniaque chez le patient bipolaire. Pour autant, de nombreuses questions se posent, encore aujourd'hui, quant à sa distribution cérébrale et à son mécanisme d'action thérapeutique.

Durant ces trois années de thèse, nous nous sommes intéressés, en particulier, aux problématiques d'imagerie rapide par échantillonnage non-Cartésien, de reconstruction de ces images et de quantification du ^{23}Na, du Phosphore-31 (^{31}P) et du Lithium-7 (^{7}Li). Nous avons développé une méthode permettant la correction des différents biais d'acquisition à travers la cartographie du champ statique B_0 et des profils de transmission (B1+) et de réception (B1-) des antennes utilisées. De plus, la quantification des temps de relaxation longitudinale (T_1) et transverse (T_2) permet de compenser les effets de ces mécanismes de relaxation sur le signal RMN pour obtenir des mesures de concentrations robustes et fiables. En raison d'un moment quadripolaire important, l'emploi de séquence à temps d'écho ultra-court (UTE) est indispensable en IRM du 23Na en combinaison avec des schémas non-Cartésiens d'encodage spatial. Des méthodes de reconstruction dédiées aux acquisitions non-Cartésiennes ont été évaluées et comparées en termes de qualité d'image mais aussi de robustesse des stratégies de sous-échantillonnage. Enfin, une approche multi-gradient-écho (MGE), alternative aux approches de Multiple Filtrage Quantique (MQF), a été implémentée afin d'approcher la quantification dans les différents compartiments cellulaires.

Ces développements ont donné lieu à des applications cliniques en Sodium à 3 T chez des volontaires sains en collaboration avec le service de Neurologie de l'Hôpital Universitaire d'Aix la Chapelle en Allemagne. Une application clinique en IRM ^{23}Na à 3T est actuellement en cours chez des patients atteints par la maladie d'Alzheimer à Aix la Chapelle. Des preuves de concept en recherche clinique, à 7 T à NeuroSpin, ont été réalisées en IRM du ^{31}P chez des sujets sains et en ^{7}Li chez des patients bipolaires sous traitement lithium en collaboration avec l'hôpital Fernand Widal à Paris et son centre expert Bipolaire.

La complexité de ces acquisitions peut être réduite en augmentant la quantité de signal disponible par augmentation du champ magnétique statique. Le Centre NeuroSpin qui dispose d'une plateforme unique d'imageurs par résonance magnétique à très hauts champs permet donc ce genre d'études. Il comporte en particulier le premier IRM 7 T clinique en France et sera équipé dans le courant de l'année 2017 d'un IRM 11.7 T clinique unique au monde.

Université Paris-Saclay
Espace Technologique / Immeuble Discovery
Route de l'Orme aux Merisiers RD 128 / 91190 Saint-Aubin, France